ANTENNA SYSTEMS RESEARCH

Keith Malcolm Keen

A Thesis submitted to the University of Greenwich
for the degree of Doctor of Philosophy,
based on published work.

February 1999

Abstract

This thesis is an overview of a number of investigations on antenna systems and related subjects over a period of 28 years, which has resulted in 44 publications in the technical literature, one current patent, and an M.Sc. thesis.

The investigations have been grouped into 7 categories:

- **Log periodic antennas,**
- **Antenna performance measurement techniques,**
- **Spacecraft Antenna Systems,**
- **Satcom Terminal Antennas,**
- **Transmission lines and baluns,**
- **High Radar Cross Section Reflectors for Spaceborne Radar Calibration,**
- **Miscellaneous Antenna Investigations.**

These investigations have resulted in various outcomes: in new antenna types and in improved antenna configurations; in improved techniques for antenna rf performance evaluation; in new knowledge relating to materials used with spacecraft antenna systems; in the development of computer software and computer-numerical methods for specific purposes; and in the advancement of accurate radar cross section prediction methods for spaceborne radar calibration targets.

In the discipline of log-periodic antennas, a planar 'printed circuit' antenna structure has been devised which has a toroidal shaped radiation pattern distribution with horizontal linear polarization. A non-planar form of this radiating structure with a unidirectional beam has also been demonstrated.

Some new techniques for measuring the rf characteristics of antenna systems have been devised. These include special techniques for frequency scaled ship model hf radar antenna measurements, and techniques for measuring scattering from the feed support struts of large Earth station parabolic reflector antennas. A novel method of acquiring near field phase and amplitude data using an interference technique for determining antenna far field performance characteristics by near field to far field data processing transformation has been demonstrated. Correction factors which allow gain comparison measurements to be made in short range length facilities, such as certain types of anechoic chamber, have also been presented. Antenna measurement techniques which are applicable to spacecraft antenna systems have been reviewed.

With regard to spacecraft antenna systems, a number of diverse studies have been carried out, one of which has resulted in the composition of a mathematical procedure for predicting the complex beamshapes of contoured beam satellite reflector antenna systems. Also, experimental work has been described which showed that spacecraft reflector antennas constructed with carbon fibre reinforced plastics do not require metallic surface coatings, and that thermal control paint applied to spacecraft does not cause antenna performance degradation. Other programmes of research involved VHF turnstile antenna systems on large satellites, and future technology, geostationary orbit multi-role satellites with 'plug-in' payloads.

New satcom terminal antenna configurations has been a very important area of research, resulting in high performance circularly polarized antenna configurations for small terminals for maritime, aeronautical and land-mobile applications. A patent has also been granted on a very compact antenna system for a satellite paging receiver.

Many types of antenna require a balun system of some type, often with impedance transformation, for excitation of the radiating elements. A mathematical analysis which allows the design of one type of impedance transforming balun has been presented, and a new microstrip and coaxial cable balun system with progressive quadrature phase output (for the excitation of quadrifilar antennas) has been demonstrated.

Very large radar cross section (RCS) passive radar reflectors are used for the monostatic calibration of spaceborne synthetic aperture radars on Earth resource monitoring satellites. A computer-numerical technique for accurately determining the RCS of these large reflectors was devised and has been extensively used. Other aspects of large radar reflector operation were also investigated, such as RCS reduction due to construction errors and radome covers.

Publications relating to a number of other miscellaneous antenna investigations are also included in this thesis. Among these are descriptions

and performance details of choked waveguide and printed dipole feeds for parabolic reflector antennas, a special purpose antenna for a remotely piloted vehicle, and some results from an investigation on a double offset reflector antenna system.

The publications which are the subject of this thesis, are introduced here in their historical context, and are presented in the Appendix at the back of this volume.

Table of Contents

Abstract i

1. Introduction 1

1.1 Log-Periodic Antennas 2

1.2 Antenna Performance Measurement Techniques 3

1.3 Spacecraft Antenna Systems 9

1.4 Satcom Terminal Antennas 10

1.5 Transmission Lines and Baluns 12

1.6 High Radar Cross Section Reflectors for Spaceborne Radar Calibration 13

1.7 Miscellaneous Antenna Investigations 14

2. List of Publications and Patent by K.M. Keen 16

3. Conclusions 22

4. References 25

Appendix. Copies of Publications and Patent P2 - P46

1. Introduction

Over a period of 28 years, the author of this thesis has carried out a number of diverse investigations on antenna systems and related subjects, mostly pertaining to the VHF, UHF and microwave frequency bands (approximately 100 MHz to 40 GHz). These investigations, which are the subject of the publications listed in **section 2** of this thesis, have resulted in various outcomes: in new types or configurations of antennas; in new or improved techniques for antenna system rf performance evaluation; in new knowledge relating to materials used with spacecraft antenna systems; in the development of computer software and computer numerical techniques for special purposes; in the development of radar cross section (RCS) prediction techniques; and in methods of implementing large radar targets for calibrating synthetic aperture radars on Earth sensing satellites. For the purposes of this thesis, these diverse investigations have been grouped into 7 categories, as listed below.

- **Log periodic antennas.**
- **Antenna performance measurement techniques.**
- **Spacecraft Antenna Systems.**
- **Satcom Terminal Antennas.**
- **Transmission lines and baluns.**
- **High Radar Cross Section Reflectors for Spaceborne Radar Calibration.**
- **Miscellaneous Antenna Investigations.**

In this introduction, **sub-sections 1.1 to 1.7** below correspond to the above

listed categories. In each of these sub-sections, there is first a brief overview of the historical development of knowledge in that particular field of research. The overview is then followed by an introduction to the author's published work in this field.

In this thesis, references to the author's publications as listed in **section 2**, are denoted using 'P' prefixes and are in boldface type, e.g. **[P37]**, to distinguish them from general references which are listed in **section 4**, and which are denoted using numbers only in the usual way, e.g. [56].

Copies of the publications P2 to P46 (the M.Sc. thesis is not included) are presented in the Appendix at the back of this volume.

1.1 Log-Periodic Antennas

Until about 1955, experience showed that all antennas were highly frequency selective. Most antenna systems were, in fact, based on the use of resonant length devices such as the half wavelength dipole and the quarter wavelength monopole. The discovery of frequency independent and log-periodic radiating structures produced a radical improvement in antenna technology.

With frequency independent antennas, the structure is defined entirely by angles, without any characteristic length dimension [1][2][3]. This concept led to the well known planar spiral and conical spiral antennas [4][5]. A development which closely paralleled the frequency independent concept was that of log-periodic antennas. As described by DuHamel and Isbell in 1957 [6], the geometry of log-periodic antenna structures is chosen so that the electrical properties repeat periodically with the logarithm of the frequency. The period width is relatively narrow in order that the variation in antenna characteristics is small within each period. With an infinite structure

composed of radiating elements having successive lengths defined by a scaling factor τ, the antenna performance at a frequency f will be repeated at all other frequencies given by $\tau^n f$ where n is any integer. When plotted on a logarithmic scale, these frequencies are equally spaced with a separation or period of $\ln\tau$; hence the choice of the name logarithmically periodic antennas by DuHamel and Isbell. The log-periodic structure principle led to very broad frequency band (quasi frequency independent) planar antennas [7] and to the extensively used log-periodic dipole array (LPDA) antenna [8][9].

The log-periodic antenna described by the author **[P2]** is a symmetrical planar structure defined by the geometry

$$Y_{n+1} = X_{n+1} = \tau Y_n = \tau X_n \qquad (1)$$

where τ is a scaling factor. This 'printed circuit' form of antenna is unique in that it exhibits toroidal shaped radiation patterns similar to those of a half wavelength dipole, but with a bandwidth which can essentially be made as broad as required. Polarization is horizontal linear.

It was also demonstrated that the log-periodic antenna could be configured in a non-planar form, with the structure inclined about one axis of symmetry **[P11]**. In this form, the antenna has a unidirectional beam with E and H plane half power beamwidths of the order of 85° and 120° respectively.

1.2 Antenna Performance Measurement Techniques

Evaluation of the rf performance characteristics of antennas is an essential part of antenna system engineering, and encompasses many aspects of antenna behaviour. Modern antenna measurement techniques stem from wartime pioneering work carried out in the USA (especially at the M.I.T.

Radiation Laboratory [10]) and in the UK in the early 1940s, following the invention of the magnetron by Randell and Boot in 1940 [11] and the advent of airborne centimetric radar using 'pencil beam' antennas for accurate target location [12]. Since that time there has been an enormous expansion in the types of, and requirements for, antennas for military and civil radar and communications [13], and for radio astronomy [14], and particularly for satellite communications [15][16][17]. There has also been a corresponding increase in the number of, and improvements in, antenna measurement techniques [18][19][20][21] [22].

Most antennas exhibit **reciprocity**, which means that the performance characteristics are the same whether the antenna operates as a transmitting or as a receiving device. The main characteristics which usually have to be determined for any given antenna system are: **radiation patterns** in various planes, to show the beamshape, **wave polarization** and **cross-polarization** i.e. orthogonal polarization to main polarization ratio, **gain** or **directivity**, impedance match usually measured as **return loss** or voltage standing wave ratio (**VSWR**), and **antenna noise temperature**.

Usually, the most important antenna parameter which has to be established is the **gain** in some direction (θ,ϕ) of a Cartesian/spherical co-ordinate system defined by the antenna geometry, and which can be expressed as

$$G(\theta,\phi) = \frac{4\pi U(\theta,\phi)}{P_{IN}} \tag{2}$$

where $U(\theta,\phi)$ is the far zone radiation intensity (in watts rad^{-2}) and P_{IN} is the power ***supplied to*** the antenna. The related parameter **directivity** in direction (θ,ϕ) is defined as

$$D(\theta,\phi) = \frac{4\pi U(\theta,\phi)}{P_T} \tag{3}$$

where P_T is the total power ***transmitted by*** the antenna. Directivity and gain are related by **antenna efficiency**, η,

$$G(\theta,\phi) = \eta D(\theta,\phi) \tag{4}$$

where η is a measure of the losses associated with the antenna (i.e. internal dissipation loss, impedance mismatch loss, and cross-polarization loss). N.B. Antenna efficiency as defined here should not be confused with 'aperture efficiency'.

Directivity can be expressed in integral form as

$$D(\theta,\phi) = \frac{4\pi U(\theta,\phi)}{\int_0^{2\pi}\int_0^{\pi} U(\theta,\phi)\sin\theta \, d\theta \, d\phi} \tag{5}$$

and directivity evaluation is often carried out with the aid of this relationship, as the expression can be interpreted in terms of measured far zone relative radiation pattern levels, represented by $P(\theta,\phi)$. Suppose we have an antenna with its main beam peak in direction (0,0) and with directivity D in direction (0,0). Also, during measurements, relative power levels would be normalised to the value corresponding to the beam peak direction, i.e.

$$P(0,0) = 1 = 0\,\text{dB}$$

and therefore from expression 5,

$$D = \frac{4\pi}{\int_0^{2\pi}\int_0^{\pi} P(\theta,\phi)\sin\theta \, d\theta \, d\phi} \tag{6}$$

and if a number of far field radiation pattern 'cuts' are recorded in N equispaced 'constant ϕ' planes, the directivity value can be closely approximated by

$$D = \frac{2N}{\sum_{N} \int_{0}^{\pi} P(\theta) \sin\theta \, d\theta} \qquad (7)$$

For an antenna where the losses can be estimated with good accuracy, it is often preferable to measure the antenna directivity based on a technique using expression 7 and to then find the antenna gain from expression 4, rather than to measure the gain directly. Antenna gain measurements are normally made by the gain substitution method, using a gain 'standard' (an antenna with a known gain/frequency curve, usually a pyramidal horn antenna). However, such measurements are difficult and are of limited accuracy, for a variety of reasons including inaccurate gain standard calibration [23] and finite measurement range length [24].

The definitions of gain and directivity given above are appropriate for an antenna system which essentially operates in one polarization only, e.g. horizontal or vertical linear, or right hand circular (RHCP) or left hand circular (LHCP), which is usually the case. Sometimes, however, an antenna system will be designed to operate in a 'mix' of polarizations. This is the case with VHF turnstile antennas on satellites, used for the transmission of telemetry and telecommand data (TTC). These antennas provide omnidirectional radiation pattern coverage with orthogonal circular polarizations at the 'poles' above and below the satellite, which degenerates through elliptical polarization away from the poles, down to linear polarization in the azimuth plane of the satellite [25] [26]. At the ground station, polarization diversity reception is employed; that is, reception is in two orthogonal polarizations, and the received powers in the separate polarizations are added together, to give 'total power' reception. To evaluate the satellite antenna system coverage performance therefore, partial directivities (in two orthogonal polarizations) are measured separately, and then the 'total power' directivity is determined by data processing. The author's publication **[P16]** describes a method which was devised for carrying this out.

The author's publication **[P26]** is an extensive review of satellite antenna measurement techniques, which was commissioned by the Institution of Electrical Engineers. In this publication, it is shown that there are two distinct classes of spacecraft antenna system, i.e. low gain (omnidirectional and quasi-omnidirectional) and medium and high gain antennas, for which quite different performance evaluation methods are appropriate. The various measurement range configurations and test methods that have been devised to evaluate spacecraft antenna systems are reviewed.

Antennas are measured on ranges of various types; these include outdoor ranges and indoor anechoic chamber facilities. The conventional range is the 'far field' type in which far zone conditions are simulated with quasi plane wave excitation over the aperture of the antenna under test. In some circumstances this can be achieved with a 'compact range' which utilises the plane wave behaviour found just in front of the aperture of a very large reflector or lens system [27][28][29], but facilities of this type are usually only applicable for measurements at relatively high microwave frequencies. On conventional 'far field' ranges, however, the test and source antennas are situated a significant distance, R, apart so that the spherical wavefront at the test antenna aperture approximates a plane wave. The usual criterion for far field distance approximation is

$$R \geq \frac{2D^2}{\lambda} \qquad (8)$$

where λ is the wavelength and D is the largest test antenna aperture dimension. Expression 8 is equivalent to an aperture edge phase error of $\pi/8$ radians (22.5°).

One consequence of equation 8 is that large electrical diameter, narrow beam antennas such as large parabolic reflector antennas or many element array antennas, require test ranges with values of R that are considerable, sometimes as much as a kilometre or more. To overcome the practical

difficulties associated with very long range distances, near field and intermediate distance measurement techniques have evolved, based on computer data processing methods to perform near field to far field transformations using measured near field amplitude and phase data [30][31]. However, such techniques can only be applied at test range facilities which have quite sophisticated phase and amplitude measurement receivers. In the 1970s, such receivers were very expensive and consequently rare. For this reason, the author devised an interference pattern technique which only required the use of a conventional amplitude only measurement receiver, and phase data was digitally extracted from the interference patterns prior to the far field transformation process **[P12][P13][P14][P18]**.

A review of intermediate distance antenna measurement techniques was presented by Keen, Bennett and Wood in the conference publication **[P19]**.

A special purpose surface wave range for measuring ship antenna systems using scale models, at the Admiralty Research Establishment, Funtington, was described by Keen, Grime and Stemp in publication **[P28]**.

In publication **[P24]** the author presented a novel measurement technique for modelling the effects of feed support struts on the radiation patterns of large parabolic reflector antennas.

Publication **[P27]** by Keen and Brown and **[P32]** addressed the measurement of cross-polarization radiation patterns of satellite ground station antennas.

Publication **[P44]** by Keen, Smith and Lee shows how correction factors can be calculated for gain comparison measurements on short length measurement ranges.

1.3 Spacecraft Antenna Systems

In the 1960s, carbon fibre reinforced plastic (CFRP) was developed as a very strong but light material for aerospace structures [32][33]. Because it can be shaped by 'laying-up' over a mould, this material is particularly suitable for ultra lightweight parabolic reflector antennas on satellites. In the last stage of the construction process of a CFRP 'dish', a high reflectivity surface such as a stretch formed aluminium skin would normally be added [34], but rf investigations by the author **[P5][P8][P9]** showed that the addition of a metallic reflecting surface was often not necessary (depending on the CFRP composition and the antenna operating frequencies) and could be omitted, giving a significant mass reduction benefit.

The surface reflectivity measurement technique that was developed for the investigation of non-metallised CFRP parabolic antenna reflectors was also used to validate the electrically conductive thermal control paint that had to be applied to the surfaces of satellites, including the antennas **[P6]**.

During the launch of a spacecraft in a multi-stage rocket such as a Thor-Delta, the spacecraft is housed within an ejectable, two part, nose fairing. The fairing will typically be made of aluminium alloy with a gridded internal structure, and to allow the reception of telemetry from the spacecraft during the launch phase, a small number of glass reinforced plastic (GRP) rf windows may be fitted in the fairing, between the gridded framework. The author's publication **[P4]** describes an investigation to determine rf window configurations that allow downlink coverage to be achieved until fairing ejection takes place.

The results of some computer software modelling of the rf performance of VHF, four monopole, turnstile antenna systems on large satellites (such as

ESA GEOS and ESA COS-B), with conclusions on antenna configuration optimisation, are shown in the author's publication **[P15]**.

In publication **[P30]**, the author addresses an aspect of future technology, whereby a single multi-payload spacecraft with a large, shared, antenna main reflector would be maintained in geostationary orbit (GSO) to take the place of a number of separate GSO satellites. This concept depends on the advent of space shuttle type maintenance vehicles with high orbit distance capabilities. The idea is that 'plug-in' modules would facilitate the addition or replacement of services. It is shown that a double offset parabolic cylinder reflector system would be appropriate for this concept.

The advent of direct broadcast satellite TV created the need for broadcast satellite antennas with highly non-symmetrical beamshapes to give coverage 'footprints' over extended and inconveniently shaped geographical regions. Coverage is usually achieved by combining a number of overlapping circular beams using a reflector antenna system with a cluster of feed horns [35]. The author's publication **[P38]** presents a mathematical procedure for predicting the beamshape of contoured beam satellite reflector antenna systems.

1.4 Satcom Terminal Antennas

The first generation of geostationary orbit communications satellites were only capable of providing relatively low EIRP (equivalent isotropic radiated power) levels at the surface of the Earth, and therefore the ground stations that were used at that time utilised very large, high gain, reflector antenna systems [36][37][38]. In order to avoid interfering with satellites other than the one in the ground station main beam, low radiation pattern sidelobe level performance was essential. The factors which cause high sidelobe levels,

and methods of reducing sidelobe levels, were considered by Claydon, Harris, and the author in publications **[P20]** and **[P22]**.

With the advent of larger and more complex communications satellites having 'spot beam' antennas and high power output amplifiers, satcom terminals with small, low gain antennas are now commonplace. The author's publication **[P39]** shows a simple analysis which can be used for the calculation of the gain values of very broad beam satcom terminal antennas. One such very broad beam antenna is the quadrifilar helix antenna described in **[P41]**. This satcom antenna was developed by the author, using a conformal mapping technique for the volute elements, for Inmarsat, for their 'Standard-C' maritime satcom service. Many of the Inmarsat-C terminals sold around the world have antennas which are based on this design.

The very compact cavity antenna devised by the author and described in publications **[P42]** and **[P43]** was also developed primarily for satcom terminal use, in this case for a vehicle terminal incorporating a medium gain azimuthally tracking antenna. For vehicle satcom terminals where this level of antenna gain is necessary, it is sometimes possible to achieve satisfactory terminal operation without recourse to a tracking antenna system, using a conical beam antenna which has a narrow elevation angle beamwidth [39]. The non-resonant length backfire bifilar helix antenna is one type of antenna which achieves this type of beam with the required circular polarization, but it also exhibits some rf performance defects. An improved form of conical beam bifilar helix satcom antenna which overcomes at least some of the performance shortcomings, has been described recently by the author, with Smith and Lee **[P45]**.

Finally here, US Patent 5539414 was granted for a satellite paging receiver antenna invented by the author **[P46]**.

1.5 Transmission Lines and Baluns

A significant percentage of antennas which are designed to operate at VHF, UHF and the lower microwave frequencies, incorporate one or two baluns. A balun is a balanced to unbalanced mode transformer' and is necessary to convert between, for example, a coaxial transmission line (unbalanced mode) and a twin wire transmission line (balanced). The classic example of the need for a balun is the excitation of a half wavelength dipole antenna from a coaxial cable, and the well known Pawsey stub (or quarter wavelength stub) balun was invented in the 1940s for this purpose [40]. Since that time many different balun arrangements have been devised. In the development of any specific antenna arrangement, the design of the balun system is quite often the greatest challenge.

In publication **[P40]**, the author described an impedance transforming balun feeder system that was devised for low gain bifilar and quadrifilar antennas such as helices and spirals. And in publication **[P10]**, the author presented a mathematical analysis and procedure for the determination of the characteristic impedance of dielectric filled slotted coaxial transmission line as a function of angular slot extent. This analysis facilitates the design of the stepped form of the Duncan and Minerva tapered balun [41][42].

In the semi-tutorial publication **[P7]**, the author presented interpretation nomographs for transmission lines with complex impedance terminations. The nomographs enable the easy conversion of measured reflection coefficient amplitude and phase data into the resistance and reactance values of the load impedance.

1.6 High Radar Cross Section Reflectors for Spaceborne Radar Calibration

The ESA ERS-1 and ERS-2 Earth resources satellites, launched in 1991 and 1995 respectively, each carry a synthetic aperture radar (SAR) which provides high resolution images of the Earth's surface, even at night and through cloud, unlike optical sensors. The spaceborne SAR systems have to be calibrated at regular intervals using high radar cross section (RCS) targets at known locations on the ground, and which have accurately known values of RCS as a function of monostatic radar incidence angle. The author has been involved with the SAR calibration programme from 1981, and the publications introduced here are the result of some of the work that has been carried out.

One early idea for the provision of an ultra high RCS target for SAR calibration, was to modify a large parabolic reflector radio telescope or satellite terminal antenna for this purpose. Publication **[P34]** describes how this could be done and an expression for RCS as a function of parabolic reflector diameter is given.

The plan to use a modified radio telescope for SAR calibration was superseded by the use of a number of 'SAR-580' trihedral corner reflectors. These reflectors consist of three orthogonal flat plates, two triangular plates above a square base plate. A 'farm' of SAR-580 reflectors has been set up in the South of England for calibrating the ERS-1 and ERS-2 satellites. In publication **[P31]**, the author described a computer-numerical technique that was devised to accurately determine the RCS values of SAR-580 and other trihedral radar reflectors. The technique is based on the projected aperture method described by Robertson in 1947 [43]. The computer-numerical technique determines the corner reflector effective aperture A_{eff} , for any

given monostatic direction defined by direction cosines (l, m, n) relative to the corner reflector axes, and then the RCS value, σ , is simply found from the relationship :

$$\sigma(l,m,n) = \frac{4\pi}{\lambda^2}\left[A_{eff}(l,m,n)\right]^2 \qquad (9)$$

The author's later publication **[P35]** describes an improved mathematical technique which produced a faster computer algorithm for determining $A_{eff}(l,m,n)$.

Also for trihedral radar reflectors, including SAR-580 reflectors, the author's publication **[P33]** presents an analysis for predicting the reduction in the RCS values of real reflectors due to plate orthogonality errors. And the author's publication **[P37]** described how planar 'A-sandwich' radomes could be added to trihedral reflectors for weather protection, without performance degradation.

1.7 Miscellaneous Antenna Investigations

In the author's publication **[P3]** the very interesting apparent paradox in antenna theory whereby an endfire array of small physical transverse area can give significant gain [44], is addressed. It is shown that an effective aperture is formed by the fields near to the array.

In publication **[P17]** the author presents design information for the choked waveguide feed. This is a compact but relatively high performance feed with equal E and H plane beamwidths for parabolic reflector antennas.

In the conference publication with Williams, Foster and Wright **[P21]**, the author describes a novel broad beam antenna he devised for installation on the underside of a remotely piloted vehicle (RPV) aircraft. This antenna incorporated a parasitically excited element adjacent to a driven 'bent' monopole, to provide a circularly polarized beam component, so that data acquisition by a remote tracking antenna could be maintained for all aircraft attitudes.

In publication **[P23]**, Adatia and the author describe the results of an investigation into a double offset reflector antenna system that was carried out for the European Space agency.

In publication **[P25]** the author described a low blockage feed for parabolic reflector antennas consisting of a broadside array of two half wavelength dipoles, with a configuration that provides equal E and H plane beamwidths.

In publication **[P29]** the author described a simple method of mathematically modelling antenna radiation patterns, using a Fourier series. A short computer program which determines coefficients using Gaussian elimination, was presented.

Finally, in publication **[P36]**, expressions for predicting deterioration in the boresight polarization axial ratio of circularly polarized antennas, due to feeder errors or radome performance asymmetries, are presented.

2. List of Publications and Patent by K.M. Keen

Where publications have joint authorship, the approximate percentage contribution made by KMK in the reported work, is noted.

P1. M.Sc. Thesis, *To construct a facility for measuring the patterns of primary feeds of large reflecting aerials.* The Victoria University of Manchester, 1970.

P2. K.M. KEEN, *A planar log-periodic antenna.* IEEE Trans AP-22, May 1974, pp 489-490.

P3. K.M. KEEN, *On the equivalent aperture formation of an endfire array.* IEEE Trans AP-22, Nov. 1974, pp 831-832.

P4. K.M. KEEN and H. MAREIS, *The radiation characteristics of a metallic launch vehicle fairing with r.f. windows.* International Conference on Antennas for Aircraft and Spacecraft. IEE London, Conference publication, June 1975, pp 70-75. (75%)

P5. K.M. KEEN, *Gain loss measurements on a carbon fibre composite reflector antenna.* Electronics Letters, Vol. 11, No. 11, May 29 1975, pp 234-235.

P6. K.M. KEEN, *The effect of conductive thermal control paint on spacecraft antenna performance.* Electronics Letters, Vol. 11, No. 17, Aug. 1975, pp 412-413.

P7. K.M. KEEN, *Load impedance from complex reflection coefficient curves.* MICROWAVES, Nov. 1975, pp 53-54.

P8. K.M. KEEN, *Surface efficiency measurements on a high modulus carbon fibre composite reflector antenna at L- and S-band frequencies.* Electronics Letters, Vol. 12, No. 7, April 1976, pp 160-161.

P9. K.M. KEEN, P. MOLETTE *et al, Development and testing of a new CFRP reflector design.* RAUMFAHRTFORSCHUNG, Band 20, Heft 4, Juli/August 1976, pp 173-181. (25%)

P10. K.M. KEEN, *Characteristic impedance of dielectric filled slotted coaxial transmission line.* Proceedings IEE, Vol. 123, No. 10, October 1976, pp 981-983.

P11. K.M. KEEN, *A log-periodic antenna with unidirectional radiation characteristics.* Electronics Letters, Vol. 12, No. 19, Sept. 16 1976, pp 498-500.

P12. K.M. KEEN, *Simulation of a proposed near field to far field measurement system.* Electronics Letters, Vol. 13, No. 8, April 14 1977, pp 223-224.

P13. K.M. KEEN, *An interference pattern intermediate distance antenna measurement method.* ESA Workshop, 'Antenna Testing Techniques' ESA SP-127, May 1977, pp 137-141.

P14. K.M. KEEN, *Antenna measurements on an intermediate distance range by using an interference pattern technique.* Electronics Letters, Vol. 13, No. 13, June 23 1977, pp 375-376.

P15. K.M. KEEN, *VHF turnstile antenna performance as a function of satellite geometry.* Electronics Letters, Vol. 13, No. 21, Oct. 1977, pp 654-656.

P16. K.M. KEEN, *A computer program system for evaluating partial and total antenna directivities from measured data.* Proceedings IEE, Vol. 124, No. 10, Oct. 1977, pp 1117-1120.

P17. K.M. KEEN, *Beamwidth variation with aperture diameter of the choked waveguide feed antenna.* Electronics Letters, Vol. 14, No. 13, June 22 1978, pp 406-407.

P18. K.M. KEEN, *Interference pattern intermediate distance antenna measurement technique.* Microwaves, Optics and Acoustics, Vol. 2, No. 4, July 1978, pp 113-116.

P19. K.M. KEEN, J.C. BENNETT and P.J. WOOD, *Intermediate distance antenna measurement techniques.* IEE Conference 'Antennas and Propagation', Nov. 1978, Conference Publication 169, pp 106-110. (35%)

P20. B. CLAYDON, K.M. KEEN and A.B. HARRIS, *Wide angle radiation from Earth station antennas.* IBID., pp 218-222. (50%)

P21. N. WILLIAMS, P.R. FOSTER, P. WRIGHT, and K.M. KEEN, *Antennas for RPVs.* International Conference on Remotely Piloted Vehicles, Bristol, England, Sept. 1979. (40%)

P22. A.B. HARRIS, B. CLAYDON and K.M. KEEN, *Reducing the sidelobes of Earth station antennas.* International Conference on Communications, Boston, USA, June 1979, Conference Proceedings, pp 6.6.1-6.6.5. (40%)

P23. N.A. ADATIA and K.M. KEEN, *Radiation characteristics of a double offset antenna; theory and experiment.* IEEE/URSI APS Symposium Publication, Quebec, June 1980, pp 545-548. (45%)

P24. K.M. KEEN, *A measurement technique for modelling the effects of feed support struts on large reflector antennas.* IEEE Trans-AP, Vol. 28, July 1980, pp 562-564.

P25. K.M. KEEN, *A low blockage, dipole array reflector antenna feed for the lower microwave frequencies.* IEEE Trans-AP, Vol. 28, Nov. 1980, pp 914-916.

P26. K.M. KEEN, *Satellite antenna measurement techniques* Commissioned IEE Review. IEE Proc. Vol. 127, Part A, No. 7, Sept. 1980, pp 417-434.

P27. K.M. KEEN and A.K. BROWN, *Techniques for the measurement of the cross-polarization radiation patterns of linearly polarized, polarization diversity, satellite ground station antennas.* Proceedings IEE, Vol. 129, Part H, No. 3, June 1982, pp 103-108. (85%)

P28. K.M. KEEN, R.R. GRIME, and B.E. STEMP, *Improvements to a surface wave antenna measurement range with troublesome site effects.* Electronics Letters, Vol. 18, No. 11, May 27 1982, pp 439-440. (80%)

P29. K.M. KEEN, *Simple expressions model antenna radiation patterns.* MICROWAVES & RF, Dec. 1982, pp 65-87.

P30. K.M. KEEN, *Antenna system for a new geostationary applications satellite concept.* Microwave Systems News, Vol. 13, No. 2, February 1983, pp 64A-64F.

P31. K.M. KEEN, *New technique for the evaluation of the scattering cross-sections of radar corner reflectors.* IEE Proceedings, Vol. 130, Part H, No. 5, August 1983, pp 322-326.

P32. K.M. KEEN, *Ground station antenna cross-polarization measurements with an imperfectly polarized ancillary antenna.* Electronics Letters, Vol. 18, No. 21, Oct. 14 1982, pp 924-926.

P33. K.M. KEEN, *Prediction of scattering cross-section reductions due to plate orthogonality errors in trihedral radar reflectors.* Electronics Letters, Vol. 19, No. 3, February 3 1983, pp 115-117.

P34. K.M. KEEN, *Use of radio telescopes or satellite Earth station antennas as ultra-high scattering cross-section calibration targets for spaceborne remote sensing radars.* Electronics Letters, Vol. 19, No. 6, March 17 1983, pp 225-226.

P35. K.M. KEEN, *Fast algorithm for the exact determination of the mapped effective areas of trihedral corner reflectors.* Electronics Letters, Vol. 19, No. 24, November 1983, pp 1014-1015.

P36. K.M. KEEN, *Antenna circular polarization deterioration due to feeder errors.* Microwave Systems News, May 1984, pp 102-108.

P37. K.M. KEEN, *Design criterion for inclined planar radomes on radar corner reflectors used for spaceborne SAR calibration.* Electronics Letters, Vol. 21, No. 12, June 6 1985, pp 548-549.

P38. K.M. KEEN, *Simple pattern prediction procedure for satellite antenna contoured beams.* Microwave Journal, October 1985, pp 149-153.

P39. K.M. KEEN, *Method permits gain estimation for very wide beam satellite terminal antennas.* Microwave Systems News, October 1985, pp 83-87.

P40. K.M. KEEN, *Simple impedance transforming feed system for low-gain quadrifilar and bifilar satellite terminal antennas.* Electronics Letters, Vol. 24, No. 5, March 1988, pp 278-279.

P41. K.M. KEEN, *Developing a Standard-C antenna.* Microwave Systems News, June 1988, pp 52-54.

P42. K.M. KEEN, *Low profile cavity antenna with small pitch angle helix feed.* Electronics Letters, Vol. 29, No. 5, 4th March 1993, pp 501-502.

P43. K.M. KEEN, *Antenna design offers compact size and low cost.* Microwaves and RF, August 1996, pp 77-78.

P44. K.M. KEEN, D. SMITH, and B.S. LEE, *Reduced range antenna measurements for small satellite terminal applications*, Eighth International Seminar on Electrodynamics and Techniques of Microwaves and EHF, Moscow, September 1996, pp 36-40. (80%)

P45. K.M. KEEN, D. SMITH, and B.S. LEE, *Improved form of backfire bifilar helix conical beam antenna.* Microwave and Optical Technology Letters, Vol. 14, No 5, April 5 1997, pp 278-280. (95%)

P46. United States Patent No. 5,539,414, *Folded Dipole Microstrip Antenna.* July 23 1996. Inventor: K.M. Keen. Assignee: Inmarsat, London.

3. Conclusions

A large number of diverse investigations on antenna systems and related subjects have been carried out over a period of 28 years, and have resulted in 44 publications in the technical literature, plus one current patent, and an M.Sc. thesis.

These investigations have resulted in the development of new antenna types and configurations, new and improved methods for antenna rf performance evaluation, new techniques for radar cross section prediction, and in the implementation of large radar cross section targets for calibrating spaceborne radars.

Many of the new developments which are described in this thesis were a consequence of the enormous expansion in the utilisation of antenna systems for satellite communications and other spacecraft applications. This expansion continues with the advent of the new LEO (low Earth orbit) and MEO (medium Earth orbit) satellite communications systems which will perhaps eventually replace GSO (geostationary Earth orbit) satellites, and which will provide complete global communications coverage with a wide variety of services; and also with the advent of the low cost 'microsatellites' which are now being made in significant numbers for a variety of purposes.

With regard to spacecraft antenna research and the space environment, the author's past work on the suitability and choice of engineering materials, which is described in the publications referred to in **sub-section 1.3**, is still proceeding. For example the new family of STRV satellites which will be launched during and after 1999, will travel into orbits where very high ionizing radiation levels are predicted. Situated on the outside of the satellite body, the antennas will not be shielded from the ionizing radiation by the

peripheral surfaces of the spacecraft. For this reason, the antennas can not be constructed with conventional dielectric materials such as PTFE, polyethylene, Rexolite, RT/Duroid, etc., which would seriously erode, eventually degenerating into dust, in the high radiation environment. After an investigation into this problem, the author has designed Lindenblad antennas for this application which incorporate PEEK 450G polyetheretherketone, polyimide film and 10G40 reinforced epoxy composite components where dielectrics are needed for rf and mechanical functions. To date, prototype versions of the antennas have passed all the rf performance and the space and launch environment tests which have been carried out at DERA Farnborough and elsewhere.

The author's work on radar cross section prediction, which is described in the publications referred to in **sub-section 1.6**, is also continuing, albeit along a new path, in the form of investigations relating to 'stealth' aircraft and methods of achieving very low RCS levels for 'radar invisibility'.

Continuing satcom terminal antenna system research and development is, however, the largest part of the author's current involvement. This is partly due to the evolution of the latest generation of highly capable, steerable spot beam, civil and military GSO communications satellites, but also a consequence of the advent of intermediate circular orbit communications satellites, as already mentioned. New technology challenges continue to emerge. As an example, the author is currently carrying out a research programme aimed at the evolution of a compact multi band maritime satcom terminal antenna system which would operate with Inmarsat satellites (1530-1646.5 MHz), with ICO satellites (1980-2200 MHz), with terrestrial GSM mobile telephone networks (880-960 MHz) and also acquire satellite global positioning (GPS) data at 1575 MHz. This type of investigation can only be carried out in the light of previous research into the type of antenna and feeder system configurations which are described in the publications referred to in **sub-section 1.4**, **sub-section 1.5**, and **sub-section 1.7**. The publications referred to in **sub-section 1.2** are also relevant to this type of

investigation, with regard to the measurement techniques for rf performance evaluation.

4. References

1. V.H. Rumsey, *Frequency Independent Antennas,* Academic Press 1966.

2. H. Jasik (Ed.), *Antenna Engineering Handbook,* Chapter 18 *Frequency independent antennas,* by G.A. Deschamps and R.H. DuHamel, McGraw-Hill Book Co., 1961.

3. E.C. Jordan and K.G. Balmain, *Electromagnetic Waves and Radiating Systems*, (2nd Ed.), Prentice-Hall Inc., 1968.

4. J.D. Dyson, *The equiangular spiral antenna*, IRE Trans. Antennas and Propagation, April 1959, pp 181-187.

5. J.D. Dyson, *The characteristics and design of the conical log-spiral antenna*, IEEE Trans. Antennas and Propagation, July 1965, pp 488-499.

6. R.H. DuHamel and D.E. Isbell, *Broadband logarithmically periodic antenna structures,* IRE Nat. Conv. Record Part 1, 1957, pp 119-128.

7. R.H. DuHamel and F.R. Ore, *Logarithmically periodic antenna designs,* IRE Nat. Conv. Record Part 1, 1958, pp 139-151.

8. D.E. Isbell, *Log periodic dipole arrays*, IRE Trans. Antennas and Propagation, May 1960, pp 260-267.

9. R. Carrel, *The design of log-periodic dipole antennas*, IRE Wescon. Conv. Record Part 1, 1961, pp 61-75.

10. S. Silver (Ed.) *Microwave Antenna Theory and Design*, M.I.T. Radiation Laboratory Series Vol. 12, McGraw-Hill Book Co., 1949.

11. S.J. Nightingale, *Filings, filaments, and FETs: technologies for harnessing the waves*, IEE Electronics and Communication Engineering Journal, Oct. 1997, pp 209-220.

12. M.I. Skolnik, *Introduction to Radar Systems*, McGraw-Hill Book Co., 1976.

13. P.E. Law, *Shipboard Antennas,* Artech House, 1983.

14. J.D. Kraus, *Radio Astronomy,* McGraw-Hill Book Co., 1966.

15. L.J. Ricardi, *Communication satellite antennas*, Proc. IEEE Vol. 65, No. 3, March 1977, pp 356-369.

16. G. Maral and M. Bousquet, *Satellite Communications Systems*, John Wiley and Sons, 1986.

17. A. Kumar, *Fixed and Mobile Terminal Antennas*, Artech House, 1991.

18. J.S. Hollis, T.J. Lyon, L. Clayton, *Microwave Antenna Measurements*, Scientific Atlanta Inc., 1970.

19. G.H. Bryant, *Principles of Microwave Measurements*, Peter Peregrinus Ltd., 1993.

20. W.L. Weeks, *Antenna Engineering*, McGraw-Hill Book Co., 1968.

21. H. Jasik (Ed.), *Antenna Engineering Handbook*, Chapter 34 *Antenna Measurements* by R. Rubin, McGraw-Hill Book Co., 1961.

22. A.W. Rudge, K. Milne, A.D. Olver and P. Knight, *The Handbook of Antenna Design Volume 1*, Chapter 8 *Antenna Measurements* by J. Appel-Hansen, J.D. Dyson, E.S. Gillespie and T.G. Hickman, Peter Peregrinus Ltd., 1982.

23. E.V. Jull, *Errors in the predicted gain of pyramidal horns*, IEEE Trans. Antennas and Propagation AP-21, Jan. 1973, pp 25-31.

24. E.V. Jull, *Finite range gain of sectoral and pyramidal horns,* Electronics Letters Vol. 6, Oct. 15 1970, pp 680-681.

25. R.B. Jackson, *The canted turnstile as an omnidirectional spacecraft antenna system*, NASA Report X-712-67-441, 1967.

26. S. Nichols, *Satellite turnstile antennas*, Naval Research Laboratory report 6907, 1969.

27. W. Burnside, *Dual chamber design reduces quiet zone ripple/taper errors*, Microwaves and RF, May 1987, pp 168-174.

28. W. Mendel and B. Huder, *Compact range for millimetre-wave frequencies using a dielectric lens*, Electronics Letters, Vol. 20, No. 19, 13 September 1984, pp 768-769.

29. A.D. Olver and G. Tong, *Compact antenna range at 35 GHz*, Electronics Letters, Vol. 13, No. 8, 14 April 1977, pp 223-224.

30. C.F. Stuberrauch and A.C. Newell, *Some recent near-field antenna measurements at NBS*, Microwave Journal, Nov. 1980, pp 37-41.

31. E.B. Joy, *Near field testing of radar antennas*, Microwave Journal, Jan. 1990, pp 119-130.

32. W.T. Gunston, *Carbon Fibres*, Science Journal, Feb. 1969, pp 39-49.

33. R.M. Gill, *Carbon Fibres in Composite Materials*, Iliffe Books, 1972.

34. H.L. Hillesland, *Development of an advanced composite antenna reflector*, Fourth Nat. SAMPE Tech. Conf.,Vol. 2, Oct. 1972, pp 235-248.

35. D.J. Brain, A. Brunt, W.T. Costello, Y. Koi, M.S. Sidat and R. Waugh, *A circularly polarized antenna for contoured beam coverage of Europe*, Int. Conf. on Antennas and Propagation 1985, pp 536-540.

36. A.W. Love (Ed.), *Reflector Antennas*, IEEE Press, 1978.

37. W.V.T. Rusch and P.D. Potter, *Analysis of Reflector Antennas*, Academic Press, 1970.

38. P.J. Wood, *Reflector Anatenna Analysis and Design*, Peter Peregrinus Ltd., 1980.

39. C.D. McCarrick, *A vertically mounted, elevation steerable, vehicular antenna for mobile satellite communications*, Via Satellite, Oct. 1991, pp 64-65.

40. R.A. Burberry, *VHF and UHF Antennas*, Peter Peregrinus Ltd., 1992.

41. B.G. Evans, *Chebyshev quarter-wave stepped balun transformer*, Electronics Letters, Vol. 9, No. 22, 1st Nov.1973, pp 514-516.

42. J.W. Duncan and V.P. Minerva, *100:1 bandwidth balun transformer*, Proc. IRE, Vol. 48, 1960, pp 156-164.

43. S.D. Robertson, *Targets for microwave radar navigation*, Bell System Technical Journal, Vol. 26, 1947, pp 852-869.

44. E.A. Wolff, *Antenna Analysis*, Artech House, 1988.

Appendix

Copies of Publications and Patent P2 - P46

Publication P2. **K.M. KEEN, *A planar log-periodic antenna.***
IEEE Trans AP-22, May 1974, pp 489-490.

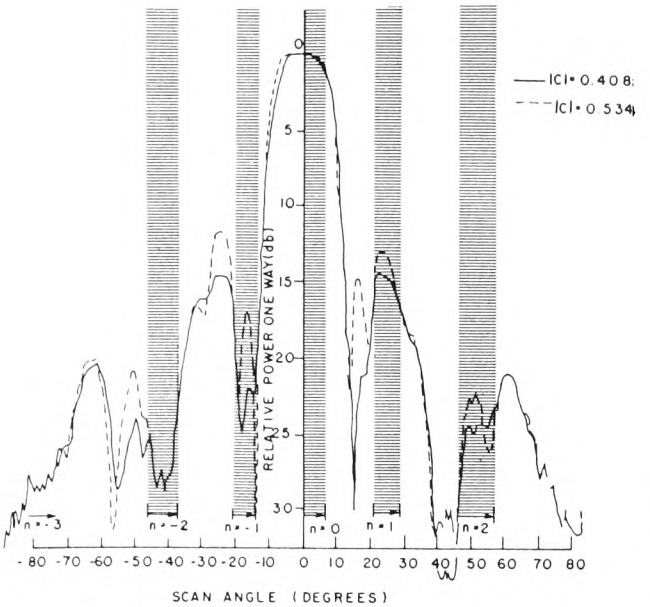

Fig. 4. Experimental element patterns.

respect to the main beam, as compared with the −15-dB prediction. They are also more strongly suppressed for wider angles (near 70°) than at 60°, thus indicating that diffraction effects are limiting the wide angle radiation.

The loci of beam and grating lobe positions for positive scan angle are indicated on this figure. Several features which distinguish the scanning characteristics of the experimental subarray pattern are that the $n = -1$ grating lobes are at the −14-dB level for the array at broadside, and so these sidelobe levels (not the sidelobe at ±17°) determine the highest grating lobe level for the scanned array, and that the $n = +2$ and $n = -3$ grating lobes see substantially lower sidelobes for the experimental than for the theoretical cases. These data imply that it may be possible to suppress all grating lobes to nearly −20 dB if dielectric lenses were used to correct the element phase distributions so that the nulls at ±21° could be maintained. This modification would leave the subarray sidelobes at ±60° virtually unchanged below the −20-dB level and should provide excellent E-plane scanning characteristics over the ±7° scan region.

III. CONCLUSION

A new and practical technique was described for synthesis of a flat-topped subarray pattern for limited scan applications. The technique requires overlapping of nearest neighbor elements only, relies on the excitation of a higher order mode to approximate the required subarray aperture illumination, and is simply implemented in waveguide or other microwave transmission circuitry.

ACKNOWLEDGMENT

The author gratefully acknowledges the contributions of Dr. A. Schell for introducing him to the concept of overlapped subarrays, of P. Franchi who first suggested the possibility of extending our continuing odd mode work in this direction, and of G. Forbes for his able assistance in the measurement program.

REFERENCES

[1] P. Shelton, "Multiple-feed systems for objectives," *IEEE Trans. Antennas Propagat.*, vol. AP-13, pp. 992–994, Nov. 1965.
[2] R. J. Mailloux, "Surface waves and anomalous wave radiation nulls on phased arrays of TEM waveguides with fences," *IEEE Trans. Antennas Propagat.*, vol. AP-20, pp. 160–166, March 1972.
[3] H. R. Phelen and J. L. Harrison, "Phased array costs cut by new radiating elements," *Microwaves*, vol. 12, no. 1, pp. 40–43, Jan. 1973.
[4] R. Tang, "Survey of time-delay beam steering techniques," in *Proc. 1970 Phased Array Antenna Symp.*, A. A. Oliner and G. H. Knittel, Eds. Dedham, Mass.: Aertech House, Inc., 1972, pp. 254–260.
[5] R. J. Mailloux and G. R. Forbes, "An array technique with grating-lobe suppression for limited-scan applications," *IEEE Trans. Antennas Propagat.*, vol. AP-21, pp. 597–602, Sept. 1973.

A Planar Log-Periodic Antenna

KEITH M. KEEN

***Abstract*—A planar log-periodic antenna structure that has radiation characteristics similar to those of a half-wave dipole has been found. The bandwidth can be as large as desired, and antennas can be easily fabricated by using printed circuit techniques. When fed with a suitable balun, VSWR's lower than 1.8:1 can be obtained over a wide-frequency band.**

The antenna configuration is defined by joining the points given by

$$Y_{n+1} = X_{n+1} = \tau Y_n = \tau X_n$$

on a set of orthogonal XY axes, where τ is a scaling factor. The resulting geometrical pattern is then considered as two complementary shapes, one of which forms the antenna. Two feeder lines have to be added to the pattern giving the antenna shape shown in Fig. 1. The dotted portions represent metal and the rest is dielectric.

Antennas have been constructed with τ values between 0.75 and 0.92. In general, antennas of $\tau = 0.85$ give the cleanest radiation patterns, and antennas with τ lower than 0.8 show poor impedance match characteristics. The antennas were made from ordinary glass fiber fabric printed circuit board with copper on one side. Although photo etching techniques could have been used, it was found that the antennas were easily cut out with a sharp knife and the unwanted copper peeled away in strips. Fig. 2 shows an antenna with a scaling ratio of $\tau = 0.8$ and a frequency range of 1000–2000 MHz. A semirigid coaxial cable has its outer conductor soldered to one feed line of the antenna, and the inner conductor is soldered to the other line to form a frequency independent balun of the type used on log-periodic dipole arrays. The coaxial cable is terminated in an N-type connector. All the antennas were constructed with a feed line width of $C = 3$ mm, which was convenient for taking the semirigid cable.

It was found experimentally that the antennas could be designed for a particular operating band by assuming that the radiating elements, the "teeth" between the X and Y axes, become resonant when their lengths are equal to a quarter of a wavelength.

The structure was found to have linearly polarized radiation properties with the electric field direction orthogonal to the feeder axis as shown in Fig. 1. Cross-polarization levels were measured as a function of frequency on the radiation pattern peaks and found to be lower than −20 dB below the in-line polarization. Fig. 3 shows a typical set of radiation pattern curves for a $\tau = 0.85$ antenna at 1200 MHz. When placed a quarter of a wavelength in front of a metal screen, the antennas were seen to give unidirectional radiation patterns similar to that of a dipole and ground plane.

If direct feeding with a 50 Ω cable was used as shown in Fig. 2, input VSWR's of the order of 3:1 were encountered, indicating input impedances of the order of 150 Ω. Theoretically the impedance should be higher, with a value of 189 Ω, as the structure is self-complementary [1]. However, the impedance plot of Fig. 4 taken with a 600–2000 MHz bandwidth $\tau = 0.85$ antenna, shows that the mean impedance is approximately 150 Ω. Fig. 4 indicates that with a suitable transforming balun an input VSWR less than 1.8:1 should be possible. To test this, a Bawer and Wolfe microstrip balun [2] was made for a center frequency of 1200 MHz and used to feed the wide band $\tau = 0.85$ antenna. This balun incorporates an impedance transformer. Fig. 5 shows the VSWR curve; it is less than 1.8:1 over the 860–1510 MHz frequency range.

When the experimental antennas were constructed in the way mentioned earlier, the first knife cut was always along the X axis. The effect of this was to make a gap of approximately 0.005 in between the ends of the radiating elements. It has been found that it is important to ensure that the ends of the elements do not make contact; if they do, then the smaller elements short circuit the larger

Manuscript received October 9, 1973; revised November 23, 1973.
U.K. Patent applied for.
The author was with the GEC-Marconi Research Laboratories, Great Baddow, England. He is now with the Antenna Section, Telecommunications Division, European Space Research and Technology Center, Noordwijk, The Netherlands.

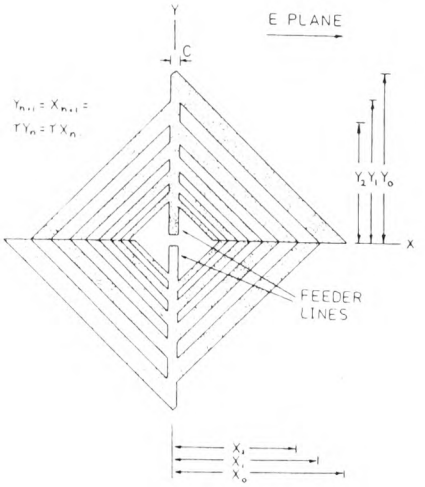

Fig. 1. Antenna structure.

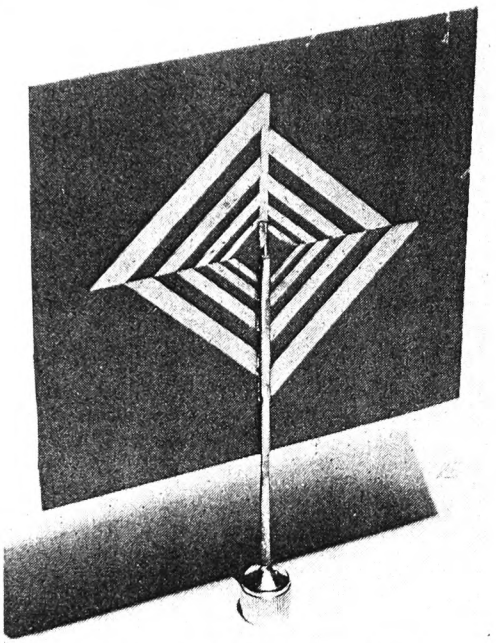

Fig. 2. Photograph of $\tau = 0.8$ antenna.

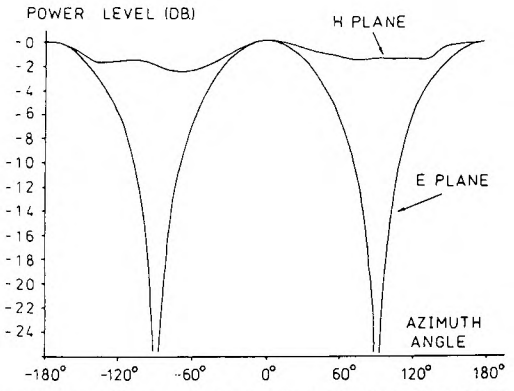

Fig. 3. Far field patterns for $\tau = 0.85$ antenna at 1200 MHz.

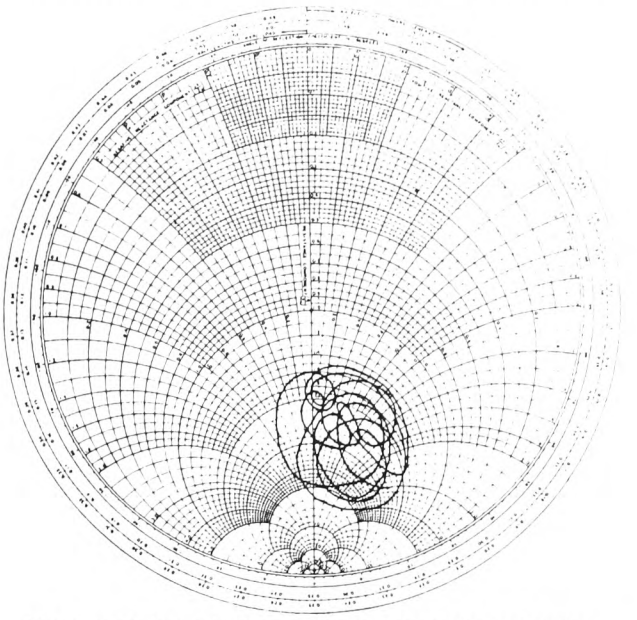

Fig. 4. Impedance plot of $\tau = 0.85$ antenna at 600–2000 MHz.

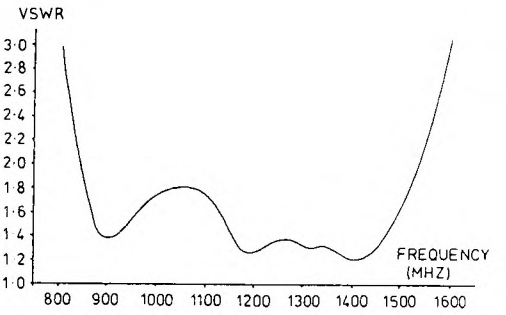

Fig. 5. VSWR of $\tau = 0.85$ antenna with microstrip balun.

ones. Measurements with an antenna that had small pieces of wire soldered across the element ends have shown that the effect of this is to give the antenna an extremely high input VSWR.

REFERENCES

[1] H. Jasik, *Antenna Engineering Handbook*. New York: McGraw-Hill, 1961, p. 14–18.
[2] R. Bawer and J. J. Wolfe, "A printed circuit balun for use with spiral antennas," *IRE Trans. Microwave Theory Tech.*, vol. MTT-8, pp. 319–325, May 1960.

A Linear Aperture Radiating Maximum Power Within Prescribed Angular Constraints

J. T. MAYHAN, MEMBER, IEEE

Abstract—For fixed aperture size, the aperture taper which maximizes the power radiated into a specified interval $(-\theta_0, \theta_0)$ is determined, and the properties of the corresponding pattern are compared to the ideal space pattern introduced by Taylor [1]. We consider the case of the linear aperture with no supergaining, although the results are directly applicable to the principal plane

Manuscript received October 10, 1973; revised November 27, 1973. This work was sponsored by the U. S. Department of the Navy.
The author is with the M.I.T. Lincoln Laboratory, Lexington, Mass. 02173.

Publication P3. **K.M. KEEN, *On the equivalent aperture formation of an endfire array*. IEEE Trans AP-22, Nov. 1974, pp 831-832.**

On the Equivalent Aperture Formation of an Endfire Array

KEITH M. KEEN

Abstract—**Wavefront diagrams are presented for the near-field region of a 10-element ordinary endfire array and its Hansen–Woodyard counterpart. The diagrams, which show phase and amplitude distributions, give a visual insight into the radiation mechanism of endfire arrays.**

At first sight, endfire array theory seems to present a paradox in that a directive antenna can be formed with a small physical area of cross section. This is sometimes baffling to engineering students who learn at an early stage that antenna gain is proportional to the antenna aperture area. Clearly, an endfire array simply has an electrical aperture that is much larger than, and unrelated to, its physical cross section; the amplitude and phase distribution about an endfire array is such that an equivalent aperture is formed. Because of this, it is interesting to look at the near-field wavefronts around an endfire array. Some experimental data can be found in the literature for parasitic arrays [1]–[3], but it is of interest to see the shape of the phase contours around a simple array. This gives a visual insight into the radiation mechanism.

In this communication, wavefront diagrams are presented for ordinary and Hansen–Woodyard arrays of 10 dipole elements with an interelement spacing of a quarter of a wavelength. An ordinary (or "classical") endfire array is one in which the elements are fed with equal amplitudes and with an interelement phase retardation equal to the element spacing in radians. If the phase retardation is changed so that the total phase delay along the array is increased by 2.94 rad, the directivity is maximized; this is the Hansen–Woodyard condition [4]. For each array the phase of the electric field was computed in a plane through the center of the array and orthogonal to the dipoles, and the amplitude variations along constant phase contours were studied. Phase contours were plotted from rectangular grids of more than 4000 phase values computed from the simple relationship

$$E_{XY} \propto \sum_{n=1}^{10} \frac{1}{r_n} \exp j(\chi_n - kr_n)$$

where E_{XY} is the electric field value at some point (X,Y) on the grid, r_n is the distance of the nth dipole to (X,Y), and χ_n is the phase on the nth dipole. The equation, which easily gives phase and amplitude values, is only true for regions beyond the static and induction fields of the dipoles. For distances greater than $\lambda/2\pi$ the radiation fields predominate [5]. For the wavefront diagram computations, the minimum distance taken was equal to half a wavelength.

Figs. 1 and 2 show near-field constant phase contours spaced at 90° intervals around the two arrays. Each array is phased to give the main lobe of its radiation pattern towards the right hand side of the diagram. Some interesting points can be found from these diagrams. Consider first Fig. 1. Using a set of compasses, it was found that the front sections of the phase curves are arcs of circles whose centers coincide with the center of the array (i.e. midway between elements 5 and 6). This suggests that over this region, which by comparing angles can be seen to correspond to the main beam of the array, the phase center coincides with the geometrical center of the array. Furthermore, the shapes of the wavefronts are clearly linked to the main and sidelobe structures of the radiation pattern shown in Fig. 3. Going round a wavefront from the boresight point, a series of ripples followed by relatively flat regions are seen. By examining angles it can be seen that the flat regions correspond to the radiation pattern sidelobes.

Fig. 2 is the Hansen–Woodyard array counterpart of Fig. 1. Analysis of the wavefront shapes with respect to the radiation pattern shown in Fig. 3 is again interesting. The front portions of the wavefronts, which correspond to the radiation pattern main beam, deviate very slightly from circular arcs. These curves are slightly flattened in three places, but when approximated to circles, still subtend a phase center between the fifth and sixth dipole elements. Once again, the

Manuscript received March 24, 1974; revised May 23, 1974.
The author is with European Space Research and Technology Centre, Domeinweg-Noordwijk, The Netherlands.

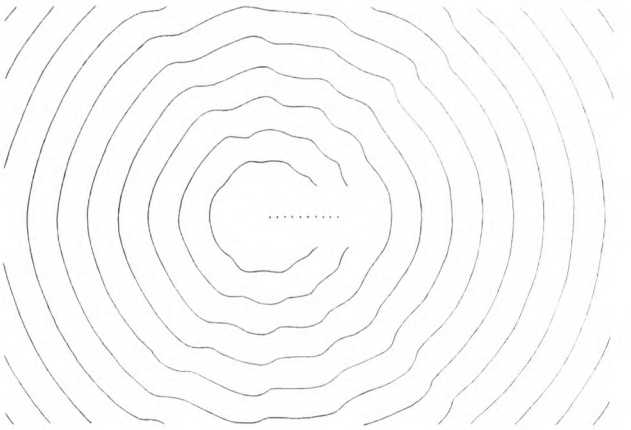

Fig. 1. Phase contours around 10-element array.

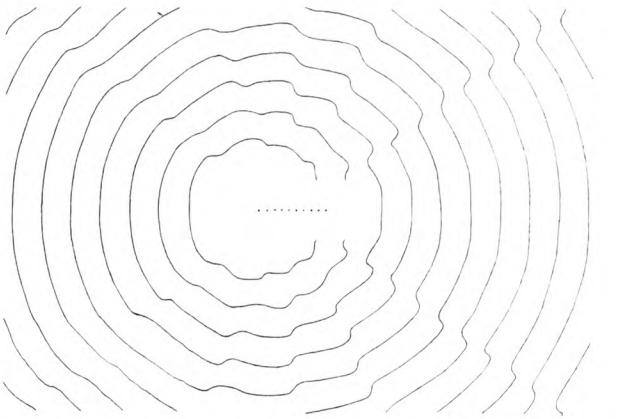

Fig. 2. Corresponding phase contours around Hansen–Woodyard array.

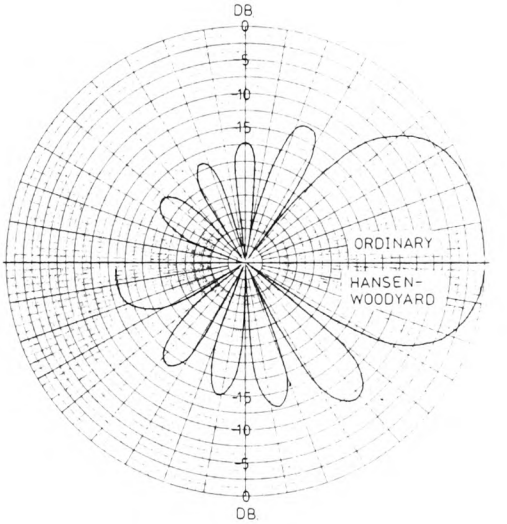

Fig. 3. Far-field radiation patterns from 10-element ordinary and Hansen–Woodyard arrays.

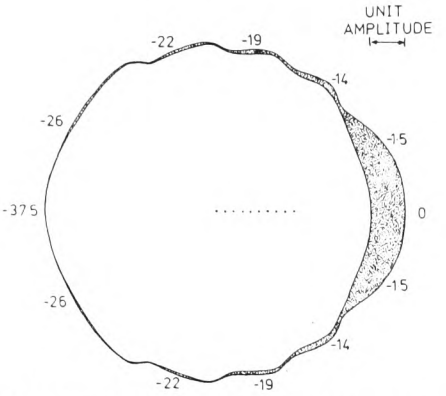

Fig. 4. Near-field amplitude distribution around ordinary endfire array.

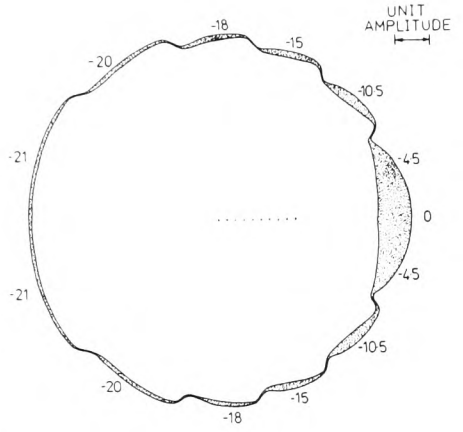

Fig. 5. Near-field amplitude distribution from Hansen–Woodyard array.

relatively flat regions beyond the ripplies on the wavefronts can be seen to correspond with sidelobes.

Figs. 4 and 5 illustrate the near-field amplitude distributions along the wavefronts for the two types of array, and these diagrams were made in the following way. The amplitudes were computed for points on the fourth wavefronts on Figs. 1 and 2. The amplitudes are represented by proportional length lines drawn orthogonal to, and with their centers at, the wavefronts. Joining the inner and outer line extremities gave the forms shown. These then are wavefront diagrams where the thickness of the figure represents the relative electric field amplitude. The relative amplitudes at certain points are also given in numbers although these, unlike the figure thicknesses, are expressed in decibels. As would be expected, the near-field amplitudes are highest at the angular positions corresponding to the main and sidelobe maxima. This is particularly evident in the Hansen–Woodyard case.

REFERENCES

[1] E. K. Damon, "The near fields of long end-fire dipole arrays," *IRE Trans. Antennas Propagat.*, vol. AP-10, pp. 511–523, Sept. 1962.
[2] E. G. Neumann, "Radiation mechanism of dielectric rod and Yagi aerials," *Electron. Lett.*, vol. 6, p. 528, 1970.
[3] H. W. Ehrenspeck and H. Poehler, "A new method for obtaining maximum gain from Yagi antennas," *IRE Trans. Antennas Propagat.*, vol. AP-7, pp. 379–386, Oct. 1959.
[4] W. W. Hansen and J. R. Woodyard, "A new principle in directional antenna design," *Proc. IRE*, vol. 26, pp. 333–345, Mar. 1938.
[5] S. Silver, *Microwave Antenna Theory and Design*. New York: McGraw-Hill, 1949.

Coupling Between Minimum Scattering Antennas

J. BACH ANDERSEN, H. A. LESSOW, AND H. SCHJÆR-JACOBSEN

***Abstract*—Coupling between minimum scattering antennas (MSA's) is investigated by the coupling theory developed by Wasylkiwskyj and Kahn. Only rotationally symmetric power patterns are considered, and graphs of relative mutual impedance are presented as a function of distance and pattern parameters. Crossed-dipoles and helices are considered in order to establish a correspondence with simple antenna structures.**

INTRODUCTION

In many applications, e.g., phased arrays and multibeam antennas, the interaction between antenna elements is often important in the evaluation of the total antenna system performance. This communication is concerned with an idealized class of elements consisting of minimum scattering antennas (MSA's) [1]. Works have been published, notably by Wasylkiwskyj and Kahn [2], [3], on coupling theory for MSA's. The power of the technique is that the complex relative mutual impedance is completely given by the power pattern of a single element, where the mutual impedance is taken relative to the real part of the self-impedance of one element. The MSA concept is used here to compute the relative mutual impedance between two elements for various spacings between the elements and for various power patterns. Once the relative mutual impedance is known it is a simple matter to find coupling loss, scattered patterns, etc.

The practical usefulness of the MSA concept depends on the extent to which coupling among realistic antennas is adequately covered by the theory. Therefore another purpose of this communication is to investigate two commonly used element types, namely crossed-dipoles and helices, and compare coupling data obtained by the MSA approach with other calculations and experimental data.

MUTUAL IMPEDANCE THEORY

Consider two identical reciprocal MSA's I and II situated along the z' axis in Fig. 1. From Wasylkiwskyj and Kahn [2, eqs. (71b) and (72)] we find for the normalized mutual impedance

$$Z_{12} = 2\int_0^{2\pi} d\phi' \int_\Gamma \sin\alpha\, d\alpha \exp(-j\boldsymbol{k}\cdot\boldsymbol{d}) P(\alpha,\phi') \qquad (1)$$

where $P(\alpha,\phi')$ is the power pattern for one antenna. $P(\alpha,\phi')$ is normalized such that the total radiated power is unity. This means that the real part of the self-impedance of one element is equal to unity. α and ϕ' are spherical coordinates and the α integration is to be taken in the complex α plane, with $0 \leq \alpha \leq \pi/2$ along the real α axis and $0 \leq \mathrm{Im}(\alpha) < j\infty$ along the line $\mathrm{Re}(\alpha) = \pi/2$. $\boldsymbol{d} = d\hat{z}'$ is a vector with direction from antenna I to antenna II and its length equals the distance between the two antennas. $\boldsymbol{k}$ is the propagation vector.

To simplify things we consider only power patterns with rotational symmetry, the axis of symmetry being the y' axis. Thus we assume that $P(\alpha,\phi')$ is a function of θ only, θ being measured from the y' axis. The pattern function is expanded in a power series in $\cos\theta$, each term in the series contributing both to the real and imaginary part of the mutual impedance. Restricting ourselves to two terms, we find

$$P(\theta) = 1 + A\cos^N(\theta), \qquad 0 \leq \theta \leq \frac{\pi}{2} \qquad (2)$$

Manuscript received March 27, 1974; revised May 30, 1974. This work was supported by ESRO under ESTEC Contract 1698/72AA.
J. Bach Andersen is with the Danish Engineering Academy, Aalborg, Denmark.
H. A. Lessow and H. Schjær-Jacobsen are with the Electromagnetics Institute, Technical University of Denmark, Lyngby, Denmark.

Publication P4. **K.M. KEEN and H. MAREIS, *The radiation characteristics of a metallic launch vehicle fairing with r.f. windows.* International Conference on Antennas for Aircraft and Spacecraft. IEE London, Conference publication, June 1975, pp 70-75.**

THE RADIATION CHARACTERISTICS OF A METALLIC LAUNCH VEHICLE FAIRING WITH R.F. WINDOWS.

K.M. Keen and H. Mareis

Introduction

The THOR-DELTA is probably the most widely used of all launch vehicles and will be employed for most of the ESRO satellites now under development. In 1972 the vehicle was uprated and given a new mechanical configuration which includes a larger fairing; this is of aluminium in contrast to the fibreglass unit used previously. The fibreglass unit was transparent at r.f. and allowed a direct telemetry link with the enshrouded satellite during the launch phase, but the new unit normally does not until the fairing ejects. This presents a problem for the ESRO GEOS and ESRO METEOSAT satellites, with which it is desired to monitor VHF telemetry throughout launch. Fortunately, the fairing manufacturers can provide options whereby the prelaunch access doors can be in fibreglass, as can part of the tapered nose section. These options can be used as r.f. windows, but no information regarding transparency is available.

The metal fairing problem was first encountered in connection with GEOS. This satellite will be mounted in the main cylindrical body of the fairing with its antenna whips underneath. The GEOS configuration needs three access doors for prelaunch checkout so it was hoped that if these were of fibreglass with possibly a fourth door in the position facing the ground station, the system would radiate sufficiently. The problem was, though, that the order of magnitude of transparency of the $10\frac{1}{2}$ inch diameter circular windows was unknown, and the system is a very complicated one to treat theoretically.

There are two parts to the problem really. First the fraction of energy that couples through the hole, and second the gain of the radiating system consisting of the fairing and its surface currents. If the field distribution set up by the satellite antennas within the fairing could be determined, the coupling through the hole could be found[1]; the radiation patterns could also be predicted.[2] But when the problem arose some quick answers were needed, in particular to know if a link was feasible with this system. To answer this some experiments were made with a simplified model.

Initial Investigation

Figure 1 shows the model geometry, where a cylinder was used to crudely approximate the fairing. The model, of 5.3:1 scale, contained a fibreglass window of the correct size and thickness. The chamber was excited by a monopole antenna constructed from semi-rigid cable, and measurements were made with the monopole in the positions shown.

K.M. Keen is at the European Space Research and Technology Centre, Noordwijk, The Netherlands.
H. Mareis is with Messerschmitt-Bölkow-Blohm, Ottobrunn, near Munich, W. Germany.

The measurements were made under ESRO contract, by Messerschmitt-Bölkow-Blohm at their antenna facility in Ottobrunn near Munich. The facility consists of a large anechoic chamber in the top of a specially constructed building which forms part of an elevated antenna range. The facility has a fully automated system for measuring the directivity and isotropic level of an antenna under test. This is done by making successive pattern 'cuts' along cones about one of the test antenna axes. The cones are 5° apart and power level data is registered digitally at 2° intervals within each cone. So the radiation distribution is sampled over a complete sphere and 6,660 power levels are registered. Computer processing of the data yields the isotropic level and gives a printout of directive gains as a function of position. The system can work in one polarisation or with two orthogonal polarisations; with the latter case the computer also gives the total power isotropic level and directive gains printout.

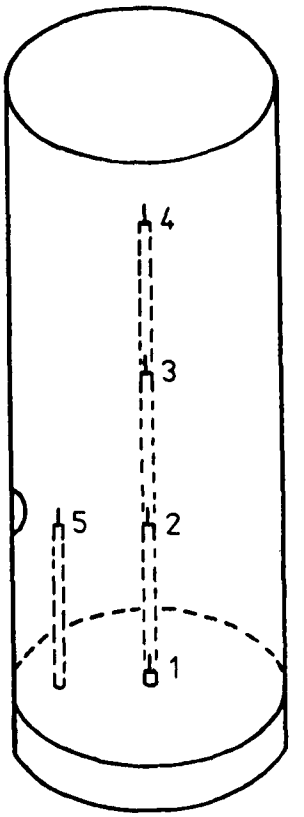

FIG. 1 CYLINDER GEOMETRY USED FOR INITIAL EXPERIMENTS

The cylinder measurements were carried out in the following way. For each position in the cylinder (1 to 5 in fig. 1) the monopole was first measured alone in parallel linear polarisation to establish its isotropic level (this was called the 'first isotropic level'). With the monopole installed, the cylinder was then measured using the same linear polarisations (cross-polar levels were small) and the data was processed using a modified computer program. This computed the new isotropic level and gave the directive gains, but these were referenced to the first isotropic level. So the directive gain printout showed the radiation distribution with both insertion loss and directive gain taken into account. Furthermore, by comparison of the isotropic level from the cylinder with the first isotropic level, the insertion loss alone could be seen.

Insertion losses of between 35 and 49 decibels were recorded, and the directive gains on the boresight of the hole were as follows. Position 1) -38 db, 2) -49.1 db, 3) -43.8 db, 4) - 31.8 db, 5) -31.6 db. As it was known that a directive gain referred to first isotropic level of about -45 db was sufficient to establish a link, the results were encouraging, particularly that of position 5 which is approximately where one of the GEOS whips would be. For this reason it was decided to do some further measurement work with more realistic models.

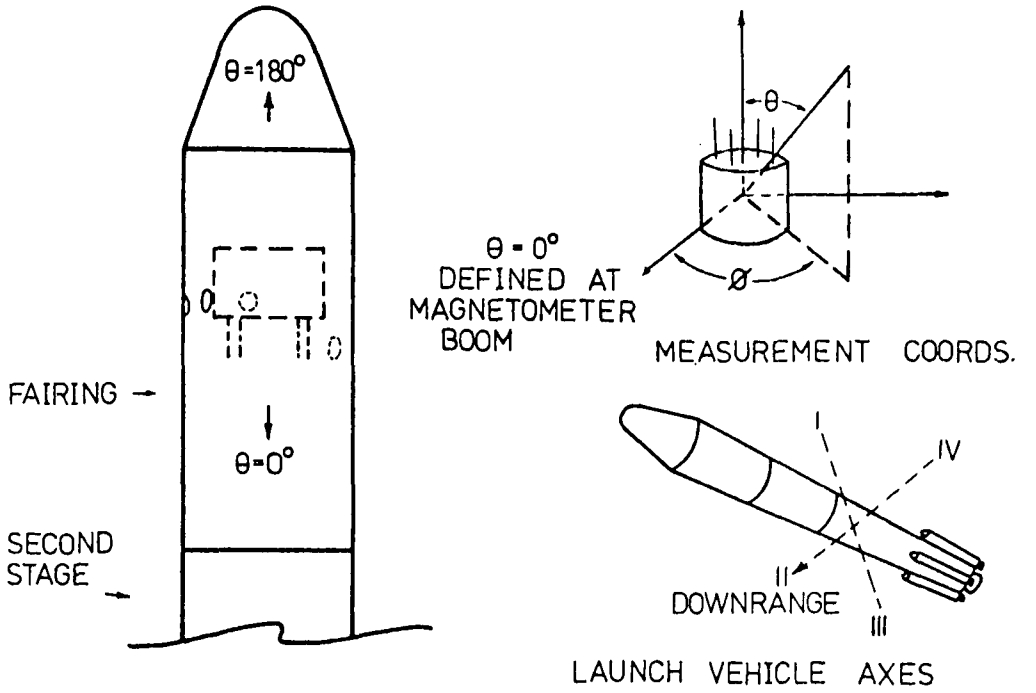

FIG.2 GEOS SATELLITE POSITION IN FAIRING & MEASUREMENT AND LAUNCH VEHICLE COORDINATE SYSTEMS

GEOS Configuration Measurements

Before making the measurements it was necessary to know something of the fairing construction and some details of the launch mission.

The aluminium fairing is made in two halves which fit together in a gas tight metal to metal joint. It consists of a 96 inch diameter cylindrical section with ISOGRID internal structure, topped by a ring stiffened monocoque structure in the form of a conical section with rounded nose cap. Fig. 2 shows the position that GEOS will have in the shroud.

A launch mission runs as follows. Lift off occurs with main engine and solid boost motors burning; the solids separate after 95 seconds. Main engine cutoff occurs at 219 seconds from lift and 8 seconds later the first and second stages separate. The second stage motor fires at 231 seconds from liftoff, and 48 seconds later the fairing halves are ejected. This is at a height

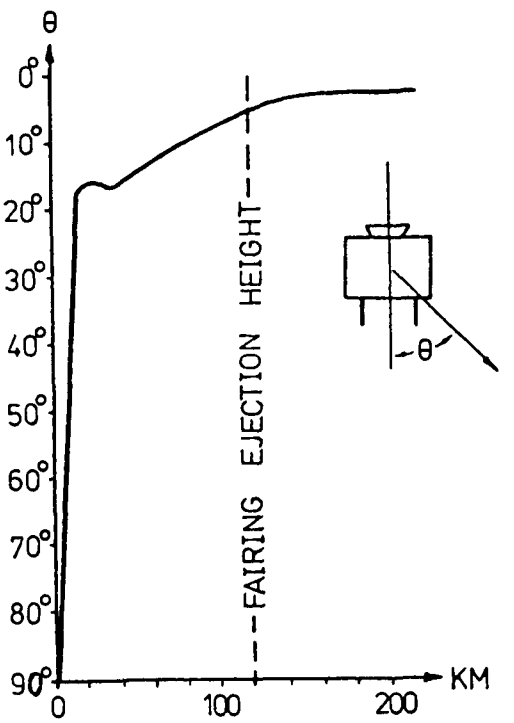

FIG.3 SPACECRAFT ATTITUDE v. DISTANCE FROM CAPE GROUND STATION

of 120 Km, fig.3 shows the attitude angle of the launch vehicle from the ground station during ascent. The second stage engine is stopped after fairing ejection, but is used again for a short time after approximately 20 minutes. The third stage is spin stabilised and this is achieved via a spin table with 8 spin rockets. After the final stage two motor cutoff, spin up is started and after 25 minutes from liftoff, the second stage separates.

Two important features are, firstly that the launch vehicle does not roll until third stage spin up (axis two is always in the downrange plane), and secondly that, because the plume of a rocket exhaust is opaque[3], the first stage main engine and solid boosters cutoff before small spacecraft attitudes are seen. The lowest value of θ (fig. 1) is about 6°, but this is not small enough to give problems with the second stage motor plume. In fact, the nozzle of this motor is small in relation to the vehicle body, and the plume is mainly contained within this diameter.

A 5.3:1 scale model of the satellite was loaned by the L.M. Ericsson Company of Molndahl, Sweden, who are the antenna subcontractors for GEOS. The model has a working 4 whip turnstile antenna system. A fairing model was made from aluminium and fibreglass and some of the parts can be seen in fig. 4. The fibreglass top section was coated with conducting paint. A further aluminium cylindrical section was used to simulate at least part of the rest of the launch vehicle. The spin table and attach fitting in the fairing were not modelled, and the satellite was simply held in place with plastic foam.

The Cape ground station can work in either of two orthogonal polarisations or power diversity which is essentially total power, and it is this that would be used. The measurements were made in orthogonal linear polarisations and these were combined to give results in total power. As with the cylinder measurements, the satellite was measured first to get the actual isotropic level.

Fig. 5 shows the results; the directive gains are presented as a contour plot. Axis two of the launch vehicle corresponds to $\phi = 28^{\circ}$ and this is marked as a dashed line. The θ variation during launch will be $\theta = 90^{\circ}$ to $\theta = 6^{\circ}$, and the corresponding directive gains are between - 36.5 db and - 32.2 db.

The allowable directive gain can be assessed from the free space path length attenuation difference between geostationary orbit distance and fairing ejection height. The difference is 49.5 db. A reduction of transmitter power of 3 db that would be caused by working into high mismatch conditions must also be taken into account, leaving over 46 db. The above is a simplified calculation and does not include all factors, but it can be shown that at least 46 db would be available. So it can be seen that with this system, a link would exist with a safety margin of about 10 db.

METEOSAT Configuration Measurements

METEOSAT will be situated at the top of the fairing with its antenna whips uppermost and inside the tapered nosecone. The obvious solution for this case is the partially dielectric nose section, two forms of which are available, i.e. large or small slots. Models were made as before and the two forms of

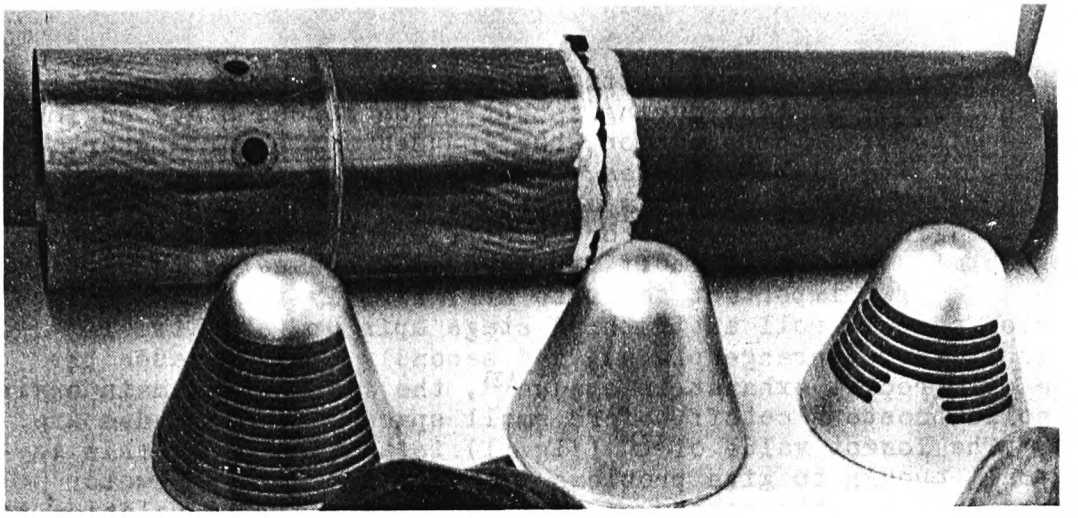

Fig. 4 Photograph of model fairing parts.

slotted nosecone can be seen in fig. 4. As no other was available, the GEOS model was used again, although this has a smaller diameter than METEOSAT.

Measurements were carried out and it was found that the nose section with the larger slots gave the best results; these are shown in fig. 6. In fact, the system worked as an excellent antenna and in the directions toward the ground station, the directional gain can be seen to be greater than 0 db at all times. And because the GEOS link requirements delineated earlier also apply to METEOSAT, it is clear that a link would exist with a very large safety margin.

References

(1) C.C. CHEN 'Transmission of Microwaves through perforated flat plates of finite thickness' IEEE Trans MTT-21 pp 1-6 Jan 1973

(2) S. SILVER and W.K. SAUNDERS 'The external field produced by a slot in an infinite circular cylinder' Journal of Applied Physics Vol. 21 no. 2 Feb. 1950 pages 153 - 158.

(3) K.E. GOLDEN, E.C. TAYLOR, F.A. VICENTE 'Diffraction by rocket exhausts' IEEE Trans AP-16 pp 614 - 616.

A – DIRECTIVITY GREATER THAN -30 DB.
B – DIRECTIVITY BETWEEN -30DB. & -35 DB.
C – DIRECTIVITY BETWEEN -35DB. & -40 DB.
D – DIRECTIVITY BETWEEN -40DB. & -45 DB.
E – DIRECTIVITY LOWER THAN - 45 DB.

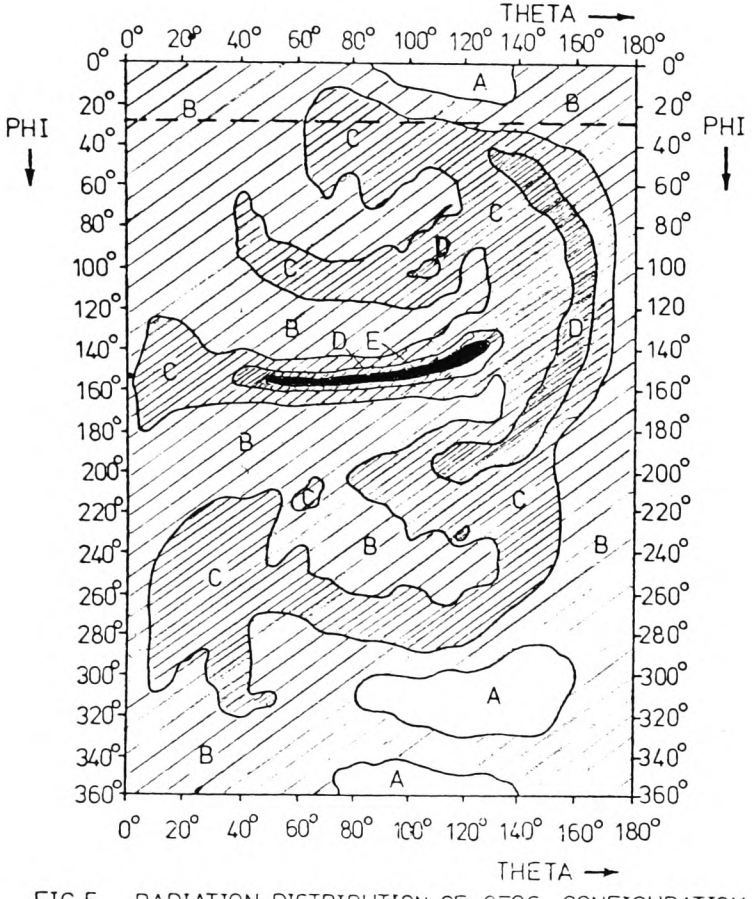

FIG. 5 RADIATION DISTRIBUTION OF GEOS CONFIGURATION

M – DIRECTIVITY GREATER THAN + 4DB.
N – DIRECTIVITY BETWEEN +4DB. & - 3DB.
O – DIRECTIVITY BETWEEN -3DB. & -10 DB.
P – DIRECTIVITY BETWEEN -10DB. & -17 DB.
Q – DIRECTIVITY LOWER THAN -17DB.

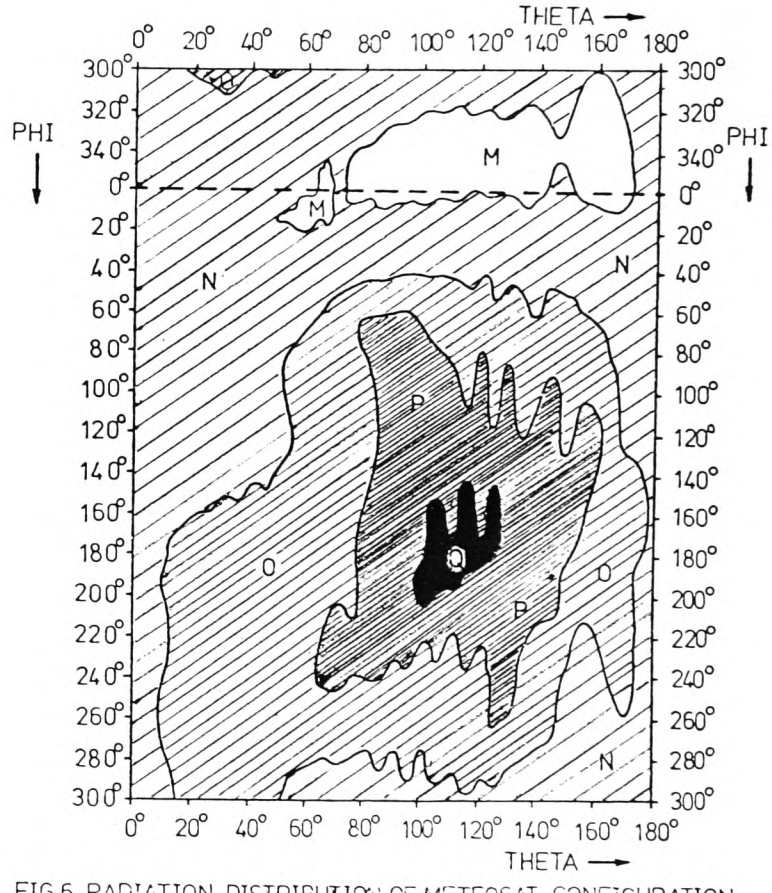

FIG. 6 RADIATION DISTRIBUTION OF METEOSAT CONFIGURATION

Publication P5. **K.M. KEEN,** ***Gain loss measurements on a carbon fibre composite reflector antenna.*** **Electronics Letters, Vol. 11, No. 11, May 29 1975, pp 234-235.**

method is suitable for determining impurity profiles in silicon. A direct C/V output enables one to obtain $N(W)$ plots with an analogue convertor.

J. OLEŃSKI

Institute of Electron Technology CEMI
Al. Lotników 32/46, 02-668 Warsaw, Poland

10th April 1975

P. MACHALICA

Institute of Industrial Electronics CEMI
Długa 44/50, 00-241 Warsaw, Poland

References

1 VAN GELDER, W., and NICOLLIAN, E. H.: 'Silicon impurity distribution as revealed by pulsed MOS C–V measurements', *J. Electrochem. Soc.*, 1971, **118**, pp. 138–141
2 OLEŃSKI, J., and MARCINIAK, W.: 'Pomiar rozkładu koncentracji domieszek w obszarze przypowierzchniowyn półprzewodnika', *Elektronika*, 1973, **14**, pp. 282–286
3 GOETZBERGER, A., and NICOLLIAN, E. H.: 'MOS avalanche and tunneling effects in silicon surfaces', *J. Appl. Phys.*, 1967, **38**, pp. 4582–4588
4 BULUCEA, C. D.: 'Investigation of deep-depletion régime of m.o.s. structures using ramp-response method', *Electron. Lett.*, 1970, **6**, pp. 479–481
5 SVENSSON, C., LUNDSTRÖM, I., and CHRISTENSSON, S.: 'Pulsed C–V measurements on MIS devices', *Phys. Status Solidi a*, 1970, **1**, pp. 389–394
6 NICOLLIAN, E. H., and GOETZBERGER, A.: 'The Si–SiO_2 interface—electrical properties as determined by the metal–insulator–silicone conductance technique', *Bell Syst. Tech. J.*, 1967, **56**, pp. 1055–1131

GAIN-LOSS MEASUREMENTS ON A CARBON-FIBRE COMPOSITE REFLECTOR ANTENNA

Indexing terms: Antenna reflectors, Carbon fibres, Composite materials, Microwave antennas

The loss of gain due to surface-current attenuation on an uncoated carbon-fibre-reinforced-plastics reflector antenna has been investigated by comparing an uncoated antenna with the same unit with the addition of a metallised surface. The measurements show that the gain loss of the test antenna is of the order of 0·5 dB at X band frequencies.

Two European satellites under development, OTS and MAROTS, will use reflector antennas constructed from carbon-fibre-reinforced plastics (c.f.r.p.). This is a light-weight, high-strength, yet rigid, composite material of fine graphite fibres in an epoxy-resin matrix, which, since the advent of a process for the large-scale production of the fibre,[1] is being used increasingly for aerospace applications.[2]

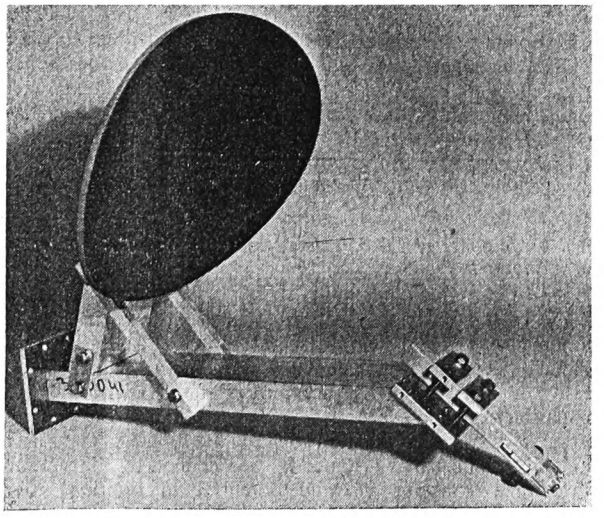

Fig. 1 *Photograph of antenna with carbon-fibre-composite reflector*

Broadly speaking, there are two categories of carbon fibre: type I, which has a high modulus of elasticity, and type II, which exhibits high tensile strength.

Several c.f.r.p. reflector antennas have been developed in the past in connection with US space projects.[3–5] Of particular interest is the 1.47 m antenna developed for the Viking Orbiter 1975 spacecraft.[3] This antenna, which operates at S and X band frequencies, was originally to have had an aluminium-foil surface to give a good r.f. reflectivity. However, it was found that the uncoated type I material was itself satisfactory. It is hoped that the European c.f.r.p. antennas will also give satisfactory r.f. performance without recourse to metallic surface coatings, as such coatings would not only raise the mass of the antenna, but could also introduce thermal problems. Further, elimination of a coating would save development time and costs.

Little data is available on the reflectivity of c.f.r.p., although it is known that type I material gives the smallest losses[5]. Some simple tests with plane sheets of c.f.r.p. forming a short circuit in a waveguide have shown that material with crossed layers exhibits a high reflectivity, but a sheet of unidirectional fibres is polarisation sensitive and can reflect less than half of the incident power.[6] To gain more information, a programme of measurements is now being carried out at ESTEC, and the results of the first part of the programme are reported here.

Poor reflectivity from the surface of a reflector antenna would result in gain loss; therefore, to evaluate a c.f.r.p. at r.f., a gain comparison between an antenna using a bare c.f.r.p. reflector and the same antenna with a metallic coating on the reflector is the most meaningful type of measurement. An offset parabolic c.f.r.p. reflector with elliptical aperture became available for r.f. measurements; this had been built for mechanical-feasibility evaluation using the tooling that was constructed for the glass-reinforced-plastics antenna of the 'Symphonie' satellite. The reflector was fabricated in type II c.f.r.p. with a sandwich construction. Six layers of c.f.r.p. with successive layers at 30° relative orientations form the outer skins, and these were bonded to an aluminium honeycomb.[7]

An X band antenna was built using the 655 mm × 405 mm reflector and a ridged-waveguide feed. The feed had dual polarisation so that the reflector could be illuminated in vertical (electrical field parallel to minor axis) or horizontal (electric field parallel to major axis) polarisation. The feed and reflector were joined by a very rigid support structure to ensure that no changes occurred in the antenna geometry throughout the measurement period. The antenna with the black c.f.r.p. reflector can be seen in Fig. 1.

The metal surface with which the performance of the c.f.r.p. was compared was formed from a single sheet of 0·02 mm aluminium foil. This was hand applied to the front face of the reflector, which had been covered with double-sided adhesive tape. It was found that surfaces with deviations smaller than 0·2 mm could be formed; this corresponds to a surface error gain loss of less than 0·05 dB,[8] which is negligible. The experimental procedure was to make a gain measurement with the metal coating present, then to remove the coating and adhesive tape without disturbing anything

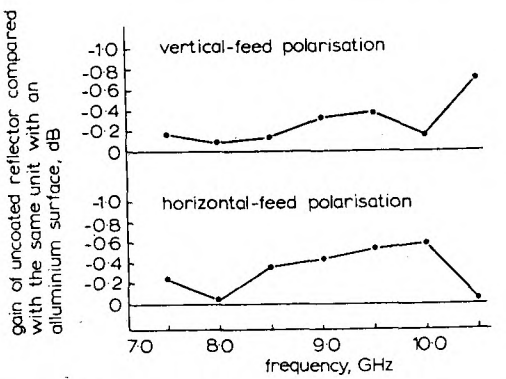

Fig. 2 *Measured values of gain loss due to c.f.r.p. material*

else and to make a new gain measurement. Gain measurements were carried out between 7·5 and 10·5 GHz and using both feed polarisations. The measurements were made by boresight comparison with a standard-gain horn using a coaxial switch to switch between antennas; the fast switching was found to be necessary to minimise the effect of receiver drift. Each measurement was repeated five times and a mean was taken. The results of the measurements are shown in Fig. 2. These show that the uncoated reflector does have a small gain loss and that the loss is a function of frequency and is polarisation sensitive.

It can be concluded that at X band frequencies, uncoated type II material is suitable for spacecraft antenna applications where the additional loss of even a fraction of a decibel is undesirable. However, the small loss is probably acceptable for other applications.

Further tests will shortly be made with a 0·88 m-diameter parabolic reflector, which is being constructed of type I c.f.r.p.

Acknowledgment: The interest and technical advice of N.W.T. Neale is gratefully acknowledged.

K. M. KEEN

15th April 1975

European Space Technology Centre
Noordwijk, The Netherlands

References

1 JOHNSON, W., PHILLIPS, L. N., and WATT, W.: British Patent 1110791, April 1964
2 HAM, A. C.: 'Carbon fibre composites for aerospace structures', *Phys. Bull.*, 1969, 20, pp. 474–478
3 STONIER, R. A., and HILLESLAND, H. L.: 'Fabrication of a graphite/epoxy antenna for the Viking Orbiter spacecraft'. Proceedings of SAMPE, 1974, pp. 596–608
4 HILLESLAND, H. L.: 'Development of an advanced composite antenna reflector'. Proceedings of fourth national SAMPE technical conference, 1972, 2, pp. 235–248
5 ROBINSON, E. Y., STONIER, R. A., and LOFGREN, C. L.: 'Development of a unique graphite/epoxy antenna subreflector'. Report of ASTM third conference, 1974, pp. 632–650
6 MESSERSCHMITT, BÖLKOW and BLOHM: 'Study of deployable antennas for satellites'. Second Progress Report, ESRO contract 2070/73HP, 1974
7 'Étude sur l'utilisation de plastiques renforcés par filaments de carbone dans les structures de satellites'. Rapport de synthèse 3586 CA/80 Société Nationale Industrielle Aerospatiale, 1975
8 RUE, J.: 'Antenna tolerance theory—a review', *Proc. Inst. Elec. Electron. Eng.*, 54, pp. 633–640

ALGORITHM FOR THE EVALUATION OF $(sI-A)^{-1}B$ FROM SIGNAL-FLOW GRAPHS NOT INVOLVING THE COMPLEX VARIABLE s

Indexing terms: Graph theory, Laplace transforms, Matrix algebra

A method of evaluating the Laplace transform of the state vector by a simple signal-flow graph of the state equations is presented. The coefficients of the numerator and denominator polynomials in Mason's gain formula are obtained from subgraphs whose transmittances are real numbers.

Given the state equations

$$\dot{X}(t) = AX(t) + BU(t) \quad . \quad . \quad . \quad . \quad . \quad . \quad . \quad . \quad . \quad (1)$$

where $X(t)$ is the n-state vector, $\dot{X}(t)$ is its derivative with respect to t, $U(t)$ is the $r \times 1$ input vector, $A = [a_{ij}]$ and $B = [b_{ij}]$ are constant $n \times n$ and $n \times r$ real matrices, respectively, the evaluation of $(sI-A)^{-1}B$ is of importance in control, systems and network theories. In this letter, considering a simple signal-flow graph of eqn. 1, an algorithm that gives the coefficients of the numerator and denominator polynomials of Mason's gain formula, i.e. of $(sI-A)^{-1}B$, from subgraphs whose transmittances are real numbers is developed. The following definition and theorem on determinants are needed for this development:

Definition: The matrix $A(k_1, k_2, \ldots, k_j)$ is obtained by deleting the rows and columns numbered $k_1, k_2, \ldots, k_j$ from the matrix $-A$ for $j = 1, 2, \ldots, n$), where A is $n \times n$; for $j = 0$, $A(k_1, k_2, \ldots, k_j) \triangleq -A$. Moreover, $\det A(1, 2, \ldots, n) \triangleq 1$.

Theorem 1:[1] The coefficients of the characteristic polynomial

$$\det(sI-A) = s^n + \alpha_{n-1}s^{n-1} + \ldots + \alpha_1 s + \alpha_0 \quad . \quad . \quad (2)$$

are given by

$$\alpha_j = \sum_{k_p} \det A(k_1, k_2, \ldots, k_j) \qquad j = 0, 1, \ldots, \ldots n \quad (3)$$

In eqn. 3, the summation is over all combinations of $\{k_1, k_2, \ldots, k_j\}$ from $\{1, 2, \ldots, n\}$.

By taking the zero-state Laplace transform, eqn. 1 can be written as

$$X(s) = (A-sI+I)X(s) + BU(s) \quad . \quad . \quad . \quad . \quad . \quad . \quad (4)$$

where $X(s)$ and $U(s)$ denote the Laplace transform of $X(t)$ and $U(t)$, respectively. This form of eqn. 4 is suitable because

(*a*) If nodes corresponding to $x_1(s), \ldots, x_n(s)$ are numbered as $1, 2, \ldots, n$ and nodes corresponding to $u_1(s), \ldots, u_r(s)$ are numbered as $n+1, \ldots, n+r$, the signal-flow graph G of eqn. 4 can be directly obtained by taking the transmittances t_{ij} to be

$$\left.\begin{aligned} t_{ij} &= a_{ji} && \text{for } i \neq j \quad \text{and} \quad i \leqslant n, j \leqslant n \\ t_{ii} &= a_{ii} - s + 1 && \text{for } i \leqslant n \\ t_{ij} &= b_{i-n,j} && \text{for } n+r \geqslant i > n \quad \text{and} \quad j \leqslant n \end{aligned}\right\} \quad (5)$$

(*b*) Excluding the self loops, all the transmittances are scalars and, as a result, the numerator and the denominator of Mason's gain formula are polynomials.

Since the denominator of Mason's gain formula for the graph G defined by eqns. 5 is the characteristic polynomial of A^2, the following theorem shows how this denominator can be obtained from subgraphs not involving s:

Theorem 2: Let $G(k_1, k_2, \ldots, k_j)$ be obtained from G by deleting the nodes $k_1, k_2, \ldots, k_j$ for $s = 0$. The coefficients of the characteristic polynomial in eqn. 2 are given by

$$\alpha_j = \sum_{k_p} \det G(k_1, k_2, \ldots, k_j) \qquad j = 0, 1, \ldots, n \qquad \text{and}$$

$$k_l \in \{1, 2, \ldots, n\} \quad (6)$$

$\sum_{k_p}$ is as defined as in theorem 1.

Proof: The proof follows by considering that to delete rows and columns $k_1, k_2, \ldots, k_j$ from A is equivalent to deleting nodes with the same number from G.

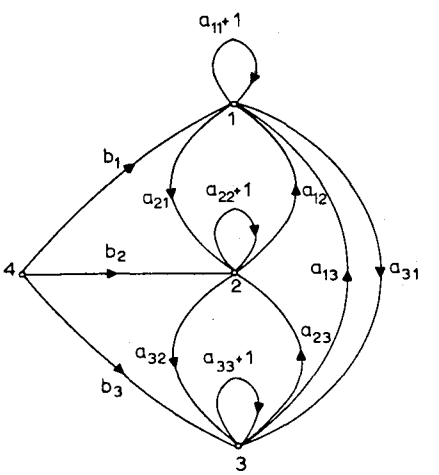

Fig. 1 *Signal-flow graph of state equations*
$n = 3, \quad r = 1, \quad s = 0$

Publication P6. **K.M. KEEN,** ***The effect of conductive thermal control paint on spacecraft antenna performance.*** **Electronics Letters, Vol. 11, No. 17, Aug. 1975, pp 412-413.**

Validation: The complete derivation will appear in Reference 4 and can be deduced by duality from Reference 3. Here, we only give some indications of validation.

First, we know, from Reference 5, that eqn. 10 has a unique solution if the characteristic polynomials of $A+\alpha I$ and $-(A+\alpha I)^T$ are relatively prime. This is so if $A+\alpha I > 0$, which asserts condition 8. On the other hand, the closed-loop system $\dot{x} = (A - BR^{-1}B^T\bar{P}^{-1})x$ can be shown to be asymptotically stable by investigating $V(x) = x^T\bar{P}^{-1}x$ as a Lyapunov function. Finally, the eigenvalues of the closed loop system are obtained as follows: by right multiplying eqn. 10 by $\bar{P}^{-1}$, the resulting equation

$$\bar{P}(A+\alpha I)^T\bar{P}^{-1} = -(A+\alpha I)+BR^{-1}B^T\bar{P}^{-1}$$

indicates that $A+\alpha I$ and $-(A-BR^{-1}B^T\bar{P}^{-1})-\alpha I$ are similar and thus have the same eigenvalues. This implies that, if λ_i is an eigenvalue of A, $-\lambda_i-2\alpha$ is an eigenvalue of $A-BR^{-1}B^T\bar{P}^{-1}$.

Conclusion: Among various versions of the linear quadratic optimal control theory, which allow an easier implementation of regulators, we have suggested a control algorithm which requires the computation of algebraic Lyapunov equations instead of the classical Riccati equations. On the other hand, a scalar coefficient can be chosen by the designer to adjust the settling time of the closed-loop system.

D. SARLAT
Y. A. THOMAS

École Nationale Supérieure de Mécanique
Université de Nantes
3 Rue du Maréchal-Joffre
44041 Nantes, France

21st July 1975

References

1 ANDERSON, B. D. O., and MOORE, J. B.: 'Linear optimal control' (Prentice Hall, 1971)
2 THOMAS, Y. A.: 'Linear quadratic optimal estimation and control with receding horizon', *Electron. Lett.*, 1975, **11**, pp. 19-21
3 DE LARMINAT, P., SARLAT, D., and THOMAS, Y.: 'Invariant imbedding and filtering: a moving horizon criterion', *JACC*, Jun. 1974, Austin, Texas
4 SARLAT, D.: Thèse de doctorat d'état. ENSM, Nantes (to appear)
5 GANTMACHER, F. R.: 'The theory of matrices—Vol. 1' (Chelsea, 1960)

EFFECT OF CONDUCTIVE THERMAL-CONTROL PAINT ON SPACECRAFT-ANTENNA PERFORMANCE

Indexing terms: Microwave antennas, Mobile antennas, Reflector antennas, Thermal-variables control

The effect of applying a conductive thermal-control paint to the surface of a reflector antenna has been investigated at X band frequencies using a swept-frequency technique. With a particular space-qualified paint, a maximum boresight gain loss of 0·1 dB was recorded.

Over the last few years it has become apparent that spacecraft in Earth orbits are subject to a previously unsuspected form of environmental hazard. System malfunctions and even, occasionally, the complete failure of satellites have led to the conclusion that differential electrical charging from hot plasmas can cause highly destructive vacuum arcs. The plasmas are a manifestation of a phenomena known as sub-storms, which occur in the Earth's magnetosphere, owing to interactions between the solar wind, the Earth's magnetic field and the interplanetary magnetic fields. If a satellite encounters a substorm region, the high-energy electrons in the plasma can cause charging of its component parts to the order of 20 kV. Subsequent electrical breakdown in dielectric materials can cause electromagnetic interference, transient pulses in electronic circuitry and burnout of electronic components.[1,2]

A way to prevent charge build-up would be to ensure that satellites are entirely electrically conductive on their external surfaces. This conflicts with the use of thermal-control paints, normally dielectric materials, which are often applied to spacecraft bodies or appendages for temperature control. If, however, the paint has some additive to make it slightly conductive, it fulfils the dual role of thermal control and charge-build-up inhibition.

Making thermal-control paint conductive leads to the possibility of problems with antenna systems, particularly for reflector antennas. It is known that the r.f. performance of a reflector antenna is virtually unaffected by a thin dielectric layer on its surface, as with normal paint, but, if the paint is conductive, there is a possibility of surface-current losses and hence antenna gain reduction. This problem of needing a thermal-control surface with electrostatic cleanliness was encountered with the reflector antenna of an ESA satellite now under development. It was hoped that a particular paint,* which was recently space qualified,[3] could be used, but no information was available regarding its r.f. performance. Because of this an investigation was carried out and the results are reported here.

An estimation of the effects of the paint can be made by calculating its skin depth. For a homogeneous partially conducting medium the depth of penetration δ is given by[4]

$$\delta = \frac{1}{\omega\left\{\frac{\mu_0\varepsilon_0\varepsilon_r}{2}\left(\sqrt{\left(1+\frac{\sigma^2}{\omega^2\varepsilon_0^2\varepsilon_r^2}\right)}-1\right)\right\}^{\frac{1}{2}}}$$

with the usual symbols. The value of conductivity σ for the paint was unknown, so samples were prepared on p.v.c. substrates and resistance measurements made. An average surface resistivity of $22{\cdot}4\times10^3\ \Omega$/square was found; the average thickness of correctly applied paint is 20 μm; therefore the conductivity of the paint was found to be 2·23 S/m. The relative permittivity ε_r of the paint was unknown, but estimated at 2. Using these values and a frequency of 10 GHz in the above equation reveals a depth of penetration of 4 mm. This is large compared with the paint thickness of 20 μm, so it can be assumed that with a painted reflector nearly all of the surface currents would flow in the metal beneath the paint, and the surface-current losses would be small. To verify this some direct measurements were carried out.

Measurements were carried out at X band using a front-fed parabolic reflector antenna of 334 mm diameter and $f/D = 0{\cdot}38$. The losses caused by the conductive thermal paint were measured by monitoring the boresight gain of the antenna under the same conditions, first with the reflector painted and then after the paint had been removed. The measurement of very small gain differences is difficult and time consuming; a method used recently which involves switching between the test and a reference antenna[5] was rejected in favour of a swept-frequency method. Fig. 1 shows the measurement arrangement. The parabolic antenna was illuminated by a horn at a separation distance of 9 m. The frequency was swept from 8 to 12 GHz.

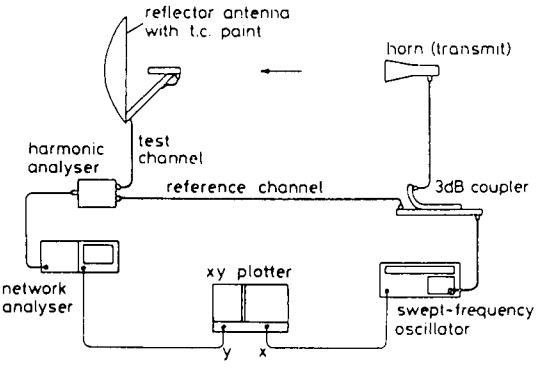

Fig. 1 *Swept-frequency measurement system*

* Hughson T (1960/71

The experimental technique was to take a recording on the xy plotter of the test-channel-to-reference-channel-level difference with the reflector antenna painted; the paint was then carefully removed with chemical paint stripper, and a new level-difference recording was made with everything, apart from the paint, as before. Fig. 2 shows the experimental result. It can be seen that there is a small gain loss which increases with frequency and reaches a maximum of 0·1 dB at 12 GHz.

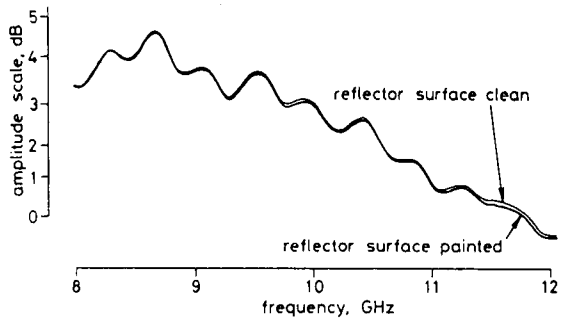

Fig. 2 *Test-channel-to-reference-channel-level difference*

The conclusion is that the type of conductive thermal-control paint tested can be applied to the surface of a reflector antenna without serious degradation of the r.f. performance, at least up to X band frequencies.

Acknowledgments: I would like to thank N.W.T. Neale for suggesting this investigation, and F. G. M. Levadou for supplying and preparing the Hughson paint.

K. M. KEEN

10th July 1975

European Space Technology Centre
Noordwijk, The Netherlands

References

1 ROSEN, A.: 'Large discharges and arcs on spacecraft', *Astronautics & Aeronatics*, Jun. 1975, pp. 36–44
2 DEFOREST, S. E.: 'Spacecraft charging at synchronous orbit', *J. Geophys. Res.*, 1972, 77, pp. 651–659
3 HUSMANN, O. K.: 'Conductive black paint qualification tests', Messerschmitt–Bolkow–Blohm GmbH Report UR-281-75, 1975 (ESTEC contract 2329/74 SK)
4 JORDAN, E. C., and BALMAIN, K.: 'Electromagnetic waves and radiating systems' (Prentice Hall, 1968)
5 KEEN, K. M.: 'Gain-loss measurements on a carbon-fibre composite reflector antenna', *Electron. Lett.*, 1975, **11**, pp. 234–235

SELF-REGULATING PICARD-TYPE ITERATION FOR COMPUTING THE PERIODIC RESPONSE OF A NEARLY LINEAR CIRCUIT TO A PERIODIC INPUT

Indexing terms: Iterative methods, Network analysis

Previous publications described the computation of the steady-state periodic response of a nearly linear circuit by solving the Volterra integral equation using a Picard-type iteration with a diagonal damping matrix. A new self-adaptive process not only has a much larger region of convergence, but also economises in computational effort.

The problem of finding the steady-state response of a nearly linear circuit to a periodic driving force has been dealt with by the first author in a number of publications.[1,2,4] The response was represented as the asymptotic solution of the Volterra integral equation

$$v(t) = v^{(0)}(t) + \int_0^t H(t-\tau) f[v(\tau)]d\tau \quad . \quad . \quad . \quad . \quad (1)$$

where $v^{(0)}(t)$ is the response of the linearised circuit, $H(t)$ is the impulse response matrix of the circuit and f is a vector of nonlinear functions representing the nonlinearities of the circuit, all of which can be represented by nonlinear voltage-dependent current generators. The same result may be more tidily expressed as the solution of

$$v_p(t) = v_p^{(0)}(t) + \int_{-\infty}^{t} H(t-\tau) f[v_p(\tau)]d\tau \quad . \quad . \quad . \quad (2)$$

where $v_p(t)$ and $v_p^{(0)}(t)$ are the steady-state responses of the complete and linearised circuits, respectively. Initially,[1,2] the solution was sought via the iteration

$$v_p^{(j+1)}(t) = v_p^{(0)}(t) + \int_{-\infty}^{t} H(t-\tau) f[v_p^{(j)}(\tau)]d\tau \qquad j = 0, 1, \ldots \quad (3)$$

the evaluation of the convolution integral being carried out by the fast Fourier transform (f.f.t.). If the nodal-analysis representation of eqns. 1–3 refers to an n-node circuit and an N-point f.f.t. is used, the nN sample values of $v_p(t)$ and $v_p^{(j)}(t)$ may be combined as single vectors $V(t)$ and $V^{(j)}(t)$. Proceeding similarly by writing U for $v_p^{(0)}(t)$ and $W(V)$ for the convolution integral as evaluated by the f.f.t., eqns. 2 and 3 reduce to

$$V = U + W(V) \quad . \quad . \quad . \quad . \quad . \quad . \quad . \quad . \quad . \quad . \quad (4)$$

to be solved by the iteration

$$V^{(0)} = U,\ V^{(j)} = U + W(V^{(j)}) \triangleq U + W^{(j)},\quad j = 0, 1, \ldots \quad (5)$$

It was quickly realised[3] that this simple process had not a wide enough region of convergence even for all nearly linear

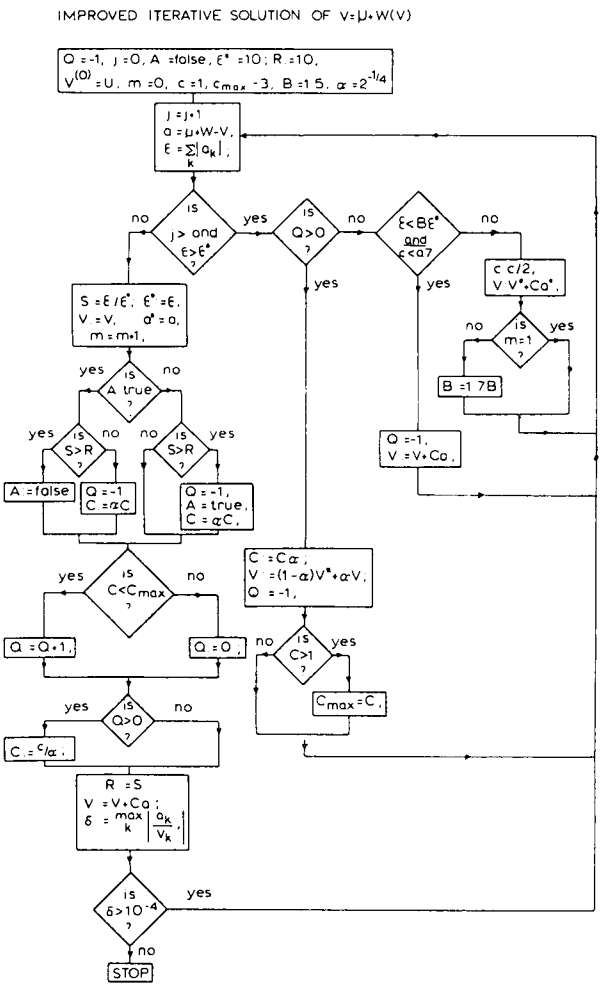

Fig. 1 *Flow diagram for improved iterative solution of* $V = U + W(V)$

Publication P7. **K.M. KEEN,** ***Load impedance from complex reflection coefficient curves.*** **MICROWAVES, Nov. 1975, pp 53-54.**

(re-titled *Graphs Simplify Load Impedance Measurements*)

Graphs Simplify Load Impedance Measurements

Here are some handy curves for converting measured phase and amplitude data to complex impedance values.

CLASSICALLY, transmission line loads of unknown impedance have been measured using a slotted line and plotting VSWR and position of first null on a Smith Chart. This method is time consuming since it can only be done at spot frequencies. Usually a network analyzer is employed instead, which compares the amplitude and phase at a test port with a reference channel and displays the values on a meter.

This article provides graphs (Fig. 1) for converting reflection coefficient and phases to impedance values; namely, R/Z_o and X/Z_o. The charts are derived from computer data, applicable to any kind of load and frequency.

Converting amplitude and phase data

To make a complex impedance measurement on a load with only a basic network analyzer, one must convert the measured phases and amplitudes to complex impedance values. A typical measurement setup used for spot frequency or swept frequency measurement is shown in Fig. 2. Here the load is a log-periodic antenna which terminates a 50-ohm coaxial cable. After a short is used correctly for calibration, (a short gives a voltage-reflected wave phase of 180 degrees) the network analyzer displays the voltage reflection coefficient amplitude, $|\rho|$, and phase angle, ϕ, directly in dB and degrees.

There are two ways to convert to normalized load impedance values. The first is to use the relationships

$$\frac{R}{Z_o} = \frac{1 - |\rho|^2}{1 + |\rho|^2 - 2|\rho|\cos\phi} \quad (1)$$

$$\frac{X}{Z_o} = \frac{2|\rho|\sin\phi}{1 + |\rho|^2 - 2|\rho|\cos\phi} \quad (2)$$

Keith M Keen, European Space Research Organization, European Space Research and Technology Center, Domeinweg-Noordwijk-Netherlands.

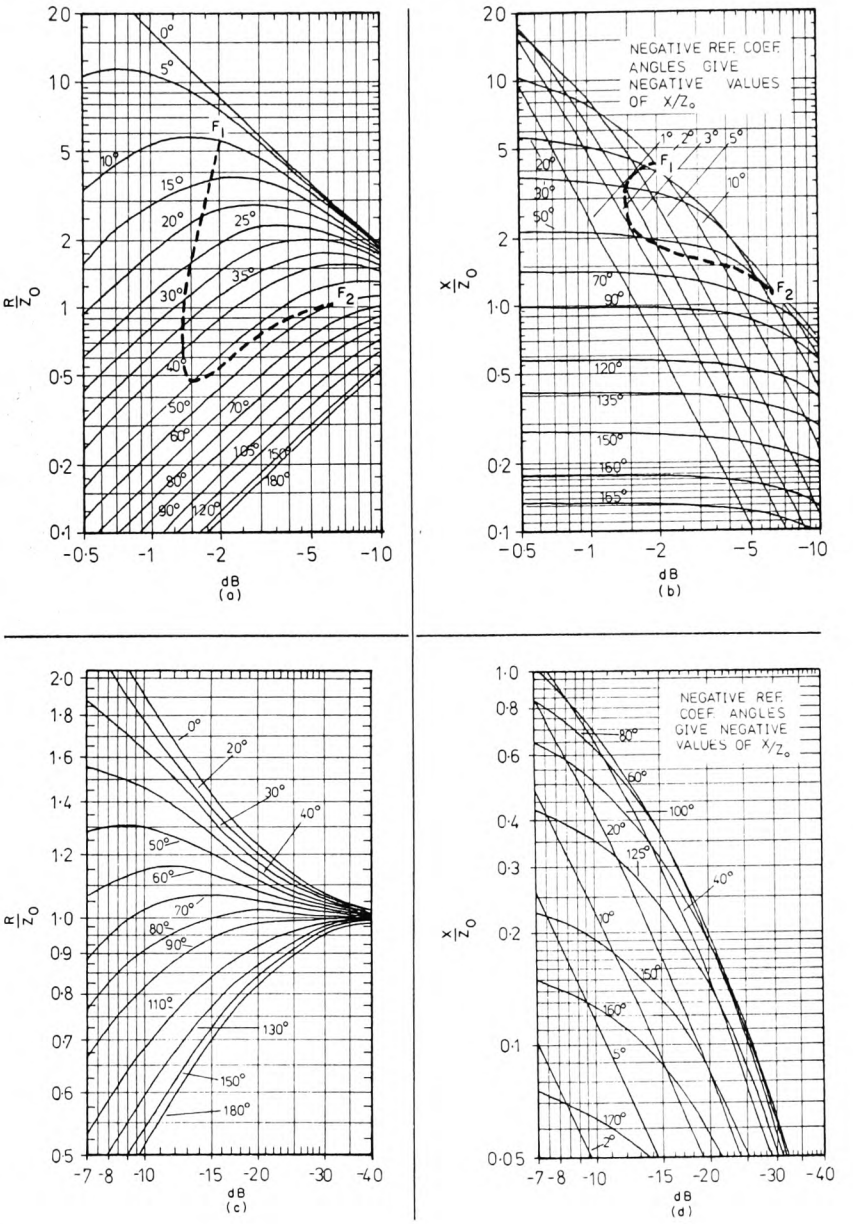

1. Curves of normalized resistance and reactance versus reflection coefficient for relatively large reflected wave amplitudes, (a) and (b), and for relatively small reflected wave amplitudes, (c) and (d), are plotted for constant phase angles. Reflection coefficient amplitudes are expressed in dB.

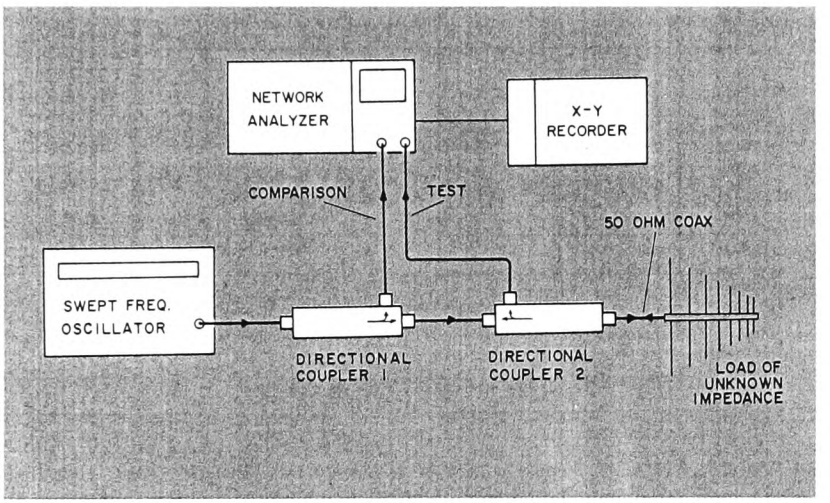

2. **In this typical test setup,** coupler 1 provides a constant reference signal, while coupler 2 monitors the reflected wave.

where $\rho = |\rho|e^{j\phi}$ is the complex reflection coefficient, R and X refer to the load impedance and Z_o is the characteristic impedance of the transmission line.

Alternatively, a Smith Chart can be employed in the way used for slotted-line measurements where the VSWR and position of the first standing wave minima are plotted to give the load impedance. The VSWR is found from:

$$\text{VSWR} = \frac{1 + |\rho|}{1 - |\rho|}$$

except that $|\rho|$ must be converted from decibel units. Most Smith Charts are already calibrated in degrees of reflection coefficient phase, but if not the phase must be converted to the corresponding first minima position, χ_{min}, using

$$\chi_{min} = \frac{\lambda}{4}\left(1 - \frac{\phi}{\pi}\right)$$

An alternative method and a very convenient one is to use the set of graphs in Fig. 1 which make the conversion given by Eqns. (1) and (2). The graphs are also useful in that they show the general relationship between load impedance and reflection coefficient in a simple way. They are, of course, applicable to any sort of transmission line termination.

Spot or swept measurements

Consider the test setup in Fig. 2 in which the log-periodic antenna used as a load is found to have a reflection coefficient of −12.5 dB amplitude and −65 degrees phase at some frequency F_{cw}.

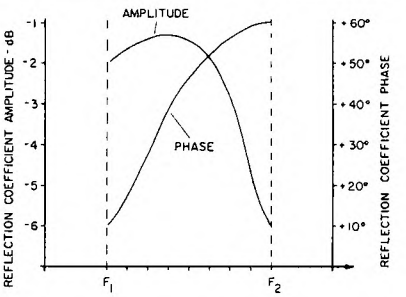

3. **Swept frequency measurement** records amplitude and phase of the reflection coefficient.

From 1(c) and 1(d), the normalized impedances are:

$$R/Z_o = 1.11, \quad X/Z_o = -0.48$$

As the transmission line has a characteristic impedance, Z_o, of 50-ohm the impedance values of the log-periodic antenna at F_{cw} are

$R = 55.5$ ohms $\quad X = -24$ ohms

The curves are also suited for swept measurements. Suppose, for example, that the input impedance of a stripline device with one coaxial input port is required over the band between frequencies F_1 and F_2. The amplitude and phase of the reflection coefficient is plotted by the X-Y recorder as shown in Fig. 3. To find the corresponding impedance values, the data from the X-Y recorder is plotted in Figs. 1(a) and 1(b) as shown by the boldfaced dotted lines. From these, the normalized impedance values can be read off for any frequency within the band. For $Z_o = 50$ ohms, the input impedance of the device varies between $Z = 275$ ohms, $X = -210$ ohms at F_1 to $Z = 50$ ohms, $X = 58$ ohms at F_2. ••

Publication P8. **K.M. KEEN,** ***Surface efficiency measurements on a high modulus carbon fibre composite reflector antenna at L- and S-band frequencies.*** **Electronics Letters, Vol. 12, No. 7, April 1976, pp 160-161.**

Discussion and conclusions: In practice, limitations are imposed on the signal amplitude and frequency ranges that can be accommodated by the scheme. The lower amplitude limit is set by the analogue-multiplier noise levels, which are noticeably higher than the op. amp. noise levels. The upper limit is set by the output voltage swing of the multipliers—typically ± 10 V for ± 15 V supply lines. No lower frequency limit appears to exist, except for the necessity of providing a low-frequency sinusoid at the input with a low distortion. The upper frequency limit of the individual frequency-multiplier stages and the number of frequency multiples that can successfully be generated are limited by distortion in the input signal, distortion produced in intermediate and final stages, phase shifts in multipliers and op. amps., failure to cancel exactly unwanted terms at the outputs of individual stages and spurious direct voltages that are generated at the outputs of the various op. amp. stages, owing to offset voltages.

It should be pointed out that certain minor variations are possible in the implementation of the principles, and, that for certain special cases of input voltage and K_x, simplifications are possible.

The system can provide the basis for a waveform generator in which required fractions of each output frequency are taken and added. This enables triangular and square waveforms, for example, to be generated.

R. W. J. BARKER
E. P. J. REILLY

Department of Electronic & Electrical Engineering
University of Sheffield
Sheffield S1 3JD, England

18th February 1976

SURFACE EFFICIENCY MEASUREMENTS ON A HIGH-MODULUS CARBON FIBRE COMPOSITE REFLECTOR ANTENNA AT L- AND S-BAND FREQUENCIES

Indexing terms: Antenna reflectors, Carbon fibres, Composite materials, Reflector antennas

The r.f. surface reflectivity of a parabolic antenna reflector fabricated from carbon fibre reinforced plastic with high modulus fibres, has been investigated at L- and S-band frequencies by a swept frequency gain comparison method. The gain of the antenna with the reflector uncoated was compared with that of the same unit but with a metal coating on the reflector.

Carbon fibre reinforced plastic is a strong, rigid, and lightweight material which is being used increasingly for aerospace applications including the fabrication of parabolic antenna reflectors. As c.f.r.p. is electrically conductive, it is in some circumstances unnecessary to add a metallic surface to ensure good reflectivity,[1] thus saving manufacturing time and expense and, for space applications, additional unwanted mass and the fear of delamination. However, for spacecraft communications, antenna gain losses of even a few tenths of a decibel are undesirable and a lossy reflector surface which gave, for example, an antenna gain reduction of 0·25 dB compared with an identical antenna with a metal reflector, would probably need to be metallised. To acquire some information on the relationship between reflector antenna gain loss as a function of c.f.r.p. surfaces, some direct antenna measurements have been made and the results of gain loss measurements with a high tensile strength (type II) fibre composite reflector have been published.[2] Since then, further measurements have been made on a high modulus (type I) material reflector and the results are reported here.

Fig. 1 shows the 880 mm diameter rotationally symmetric parabolic reflector with the feed system that was added for the tests. The f/D ratio of the reflector was 0·44 and a radome-covered log-periodic dipole array, longitudinally moveable along the parabola axis for optimisation, was used as the primary feed. Poor reflectivity from the surface of a reflector antenna would result in gain loss; therefore, to evaluate a c.f.r.p. reflector at r.f., a gain comparison between an antenna using a bare reflector and the same antenna but with a metallic coating on the reflector is the most meaningful type of measurement. This was done using the swept frequency gain comparison technique developed in connection with conductive paints.[3] With a swept frequency oscillator as a microwave power source, the gain of the antenna with its reflector coated in metal foil was monitored as a function of a reference channel level, the reference channel deriving from a directional coupler at the swept frequency oscillator output. An elevated outdoor range of length 16 m and height 7 m was employed; the remote antennas were a log-periodic dipole array at L-band frequencies and a ridged horn at S-band frequencies. The reference surfaces were made from aluminium foil in sections reminiscent of the panels of a parachute. These were laid over a convex parabolic former and welded together along the seams by a new welding process developed for metal and plastic films.* For each measurement, the reference surface was adhered to the reflector by a thin layer of heavy automotive grease.

Figs. 2 and 3 show measured gain comparisons, Fig. 2 for the frequency range 1·3 to 1·7 GHz, and Fig. 3 for 2·8 to 3·2 GHz. Each result consists of two recordings, the first taken with the metal reference surface in place and the second taken after its removal. The most striking feature of these results is that, in both cases, the two recordings are identical and appear as one over most of the frequency range. Some small departures can be seen, however, both positive and negative. The positive signs indicate where the gain with the bare reflector was actually better than with the aluminium reference, and the negative signs show the opposite. Departures are very small, less than 0·1 dB except for the extended region between approximately 3·05 and 3·15 GHz. In this region the bare reflector surface is more lossy than the equivalent metal coated case by about 0·12 dB.

To conclude, the measurements show that the high modulus material has an extremely good r.f. surface at L- and S-band

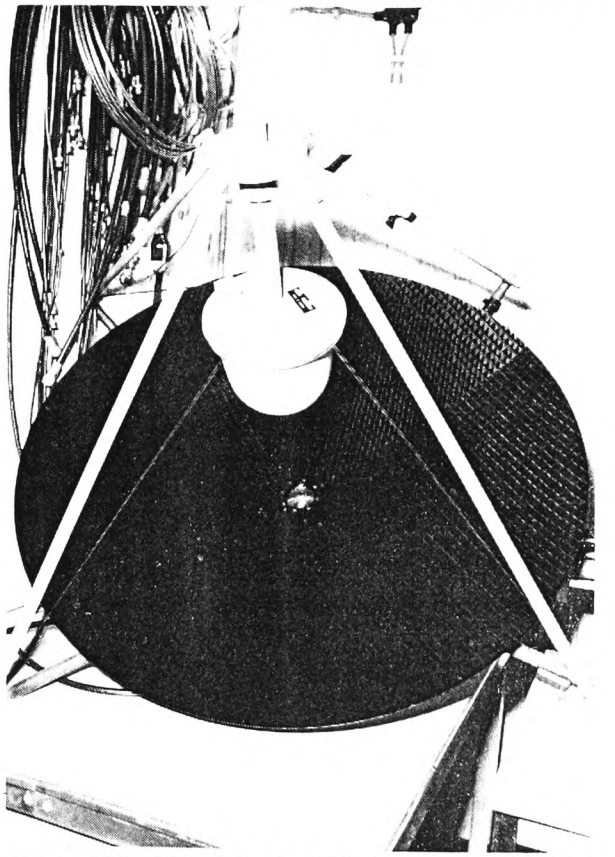

Fig. 1 *Photograph of the c.f.r.p. reflector and the antenna feed system*

* Luc welding

frequencies, in some cases better than the welded metal surface used for comparison. It is interesting to compare these results with those seen earlier with the high tensile material reflector.[2]

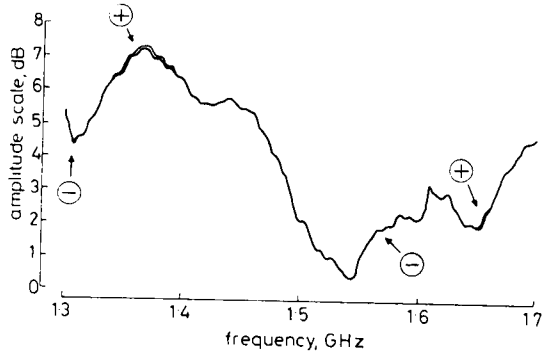

Fig. 2 *Test channel to reference channel level recordings with and without the reference surface, 1·3 to 1·7 GHz*

This was measured at a higher frequency band, but even so it is clear that the r.f. reflectivity of its surface is poor whereas that of the high-modulus reflector is very good. Part of the reason for this may be due to the fact that the electrical conductivity of high-modulus carbon fibres is approximately twice that of high-tensile fibres,[4] but it is believed that surface roughness is the most significant parameter. The effect of surface roughness has been demonstrated by Robinson *et al.*[1] who measured the reflectivity of some flat c.f.r.p. samples at 8·448 GHz with the surface roughness as a variable, and found that smooth surface samples gave normal incidence reflectivities of better than 0·15 dB, but rough surface samples gave reflectivities worse than 0·4 dB. The most noticeable difference between the surfaces of the two reflectors measured was that the high-modulus material reflector had a very smooth surface, but in contrast, the high-tensile-material reflector surface was rough to the touch.

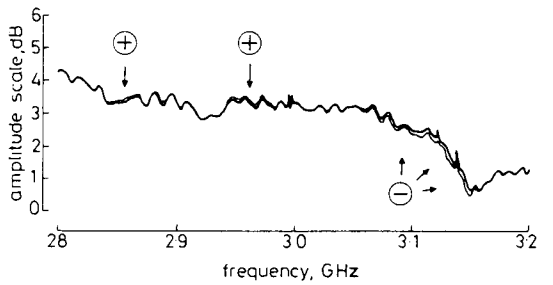

Fig. 3 *Test channel to reference channel level recordings with and without the reference surface, 2·8 to 3·2 GHz*

Acknowledgments: I would like to thank P. Molette for requesting the measurements, Messerschmitt-Bolkow-Blohm GMBH, Munich, for loaning the antenna, and I. Smit, Head of ESTEC Engineering Section, for procuring the Luc welding equipment and supplying the reference surfaces.

K. M. KEEN

European Space Research and Technology Centre
Noordwijk, The Netherlands

4th March 1976

References

1 ROBINSON, E. Y., STONIER, R. A., and LOFGREN, C. L.: 'Development of a unique graphite/epoxy antenna subreflector'. Report of the 3rd ASTM Conference, 1974, pp. 632–650
2 KEEN, K. M.: 'Gain-loss measurements on a carbon fibre composite reflector antenna', *Electron. Lett.*, 1975, **11**, pp. 234–235
3 KEEN, K. M.: 'Effect of conductive thermal control paint on spacecraft antenna performance', *Electron. Lett.*, 1975, **11**, pp. 412–413
4 GILL, R. M.: 'Carbon fibres in composite materials' (Iliffe Books, London, 1972) p. 73

TOTALLY SELECTIVE CONVOLUTIONAL DECODING

Indexing terms: Codes, Decoding

A modification of the Viterbi decoding algorithm is suggested for faster convergence.

Viterbi decoding[1–4] is best explained in terms of the trellis diagram[4] of a convolutional coder. Fig. 1 shows a particular rate 1/2 convolutional coder over $GF(2)$ and its trellis diagram. At time $t = 4T$ in the present example, there are two paths converging on every node representing a state of the coder. One computes the Hamming distance of all these paths from the received vector and, for every node, retains that path which has a smaller Hamming distance. All these retained paths are then extended through the trellis to the next time instant at which, once again, on every node two paths converge. The path having a smaller Hamming distance from the received vector is retained at every node and this procedure is recursively continued. Very frequently, there comes a time at which all the retained paths have the same common prefix, which corresponds to the corrected version of the received vector over that section. At every instant, the retained paths are called survivors. A more expressive terminology uses phrases like 'killing a path' and 'keeping a path alive'.[5] Thus the basic concept in the Viterbi algorithm is that of achieving consensus about the common prefix among all the survivors selected on the criterion of small Hamming distance from the received vector, selection being made on the nodal basis.

Let the two paths converging on a particular node have Hamming distances d_i and d_j, $d_i \leqslant d_j$, from the received vector, and let the two paths converging on some other node have Hamming distances d_p and d_q, $d_p \leqslant d_q$, from the received vector. In the nodally selective Viterbi algorithm, at these two nodes, the paths having Hamming distances d_i and d_p from the received vector are retained and the paths having Hamming distances d_j and d_q are rejected, even if $\min(d_j, d_q) < \max(d_i, d_p)$. This is a direct consequence of conducting selection on the nodal basis.

Heuristically, it seems more reasonable to have a stricter selection on the criterion of Hamming distance from the received vector without enforcing quota for every node. In this totally selective scheme, at every instant the paths are ordered according to increasing Hamming distance from the received vector, and the fixed number of paths from the top are retained. The retained paths are then extended to the next instant, and selection is performed again. Some nodes may therefore have more than one survivor converging on them. Such a situation is not necessarily objectionable. In fact, the list-of-L version of the Viterbi algorithm[6] retains $L > 1$ paths converging on every node. In the totally selective scheme, very frequently there comes a time when all the survivors pass through a common node. Between the starting common node and this subsequent common node, different survivors could have different routes, unlike the common prefix for a nodally selective Viterbi algorithm. The decision is taken on this section on the basis of smaller Hamming distance from the received vector. If there is a tie on this criterion, it is resolved on the basis of majority vote. If there is a tie then, the decision could be arbitrary.

As an example, let the all-zero vector be transmitted and let the received vector be 01 01 01 00 00 ... with triple error. The survivors would be denoted by their nodal codes, i.e. by the sequence of nodes through which a path passes. Using the trellis of Fig. 1, for the totally selective decoding algorithm, the nodal codes of eight survivors at $t = 4T$ are

0 1 2 5 3 (1)
0 0 0 0 0 (3)
0 1 2 5 2 (3)
0 0 1 2 4 (3)
0 0 1 2 5 (3)
0 1 2 4 0 (4)
0 1 2 4 1 (4)
0 0 0 1 2 (4)

Publication P9. **K.M. KEEN, P. MOLETTE *et al*, *Development and testing of a new CFRP reflector design.* RAUMFAHRTFORSCHUNG, Band 20, Heft 4, Juli/August 1976, pp 173-181.**

Für das seitlich überlappte Schlitzrohr ergeben sich ähnliche Ergebnisse, wobei mit wachsender Überlappung α die Resonanzen bei höheren Werten liegen (BILD 7a, 7b, 7c). Regt man den in der Drehachse liegenden Satellitenboom im Inertialsystem mit $x_o \sin \omega t$ an, so ergeben sich für die Vergrößerungsfunktionen jeweils zwei Teile in jeder Richtung ξ und η.

Der mit sin $(\omega + \Omega)$ t kommende Vergrößerungsfunktionsanteil ist mit $\xi_n^{(+)}$ und der mit sin $(\omega - \Omega)$ t vorkommende Anteil mit $\xi_n^{(-)}$ bezeichnet (BILD 8 und 9). Ähnliches gilt für die η-Richtung, wo der mit cos $(\omega + \Omega)$ t vorkommende Vergrößerungsfunktionsanteil mit $\eta_n^{(+)}$ und der mit cos $(\omega - \Omega)$ t vorkommende Teil mit $\eta_n^{(-)}$ bezeichnet wurde (BILD 10 und 11).

Man erkennt im Falle des Schlitzrohres, daß für $x = 1$ eine hebbare Resonanz (scheinbare Resonanz) vorhanden ist (BILD 8), so daß nur der größere Wert für die Schwingungsform $n = 1$ zur Resonanz führt. Bei dem seitlich überlappten Rohr tritt diese Resonanz de facto auf (BILD 9). Außerdem tritt bei der Drehgeschwindigkeit $x = 2$ noch eine zusätzlich kleinere Resonanz auf, in deren Umgebung allerdings die Vergrößerungsfunktion sehr schnell ganz kleine Werte annimmt.

Für wachsende Überlappung α verschieben sich die Resonanzen zu größeren Anregungsfrequenzwerten, wobei die für $x = 2$ auftretende niedrigste Resonanz mit wachsendem α sich gegen Null verschiebt. Die Vergrößerungsfunktionen $\eta_1^{(+)}$, $\eta_1^{(-)}$ sind in den Bildern 10 und 11 dargestellt. Die Kurven zeigen ähnliches Verhalten wie im vorhergehenden Falle.

LITERATUR:

[1] PILKINGTON, W. C.: Vehicle Motions as Inferred from Radio Signal Strength Records Jet Propulsion Laboratory External Publication 551, Sept. 5, 1958.

[2] ETKIN, B., and P. C. HUGHES: Explanation of the Anomolous Spin Behavior of Satellites with Long Flexible Antennae, Journal of Spacecraft and Rockets, Vol. 4, 1967, S. 1139-1145.

[3] BAUER, H. F.: Nichtlineares Verhalten von Sonnenpaddel-Elementen, WGLR-Jahrbuch 1974.

[4] BAUER, H. F.: Lineare Dynamik des rotierenden Schlitz- und Lapprohres. ERNO Raumfahrttechnik, TB TS 28/74 (1974).

Development and Testing of a new CFRP Antenna Reflector for Communication Satellites

K. KEEN, P. MOLETTE, and B. PIEPER, European Space Technology Centre, Noordwijk,

C. M. HERKERT, W. SCHAEFER, Messerschmitt-Bölkow-Blohm GmbH, Ottobrunn

A CFRP (**C**arbon **F**ibre **R**einforced **P**lastics) antenna reflector with 88 cm diameter has been designed and manufactured at MBB, consisting of a parabolic dish and a tangential conical support structure. The design is based on detailed structural calculations, which are described and discussed. The manufacturing steps for the reflector are given, the design concept and its main features are shown. Mechanical and thermal environmental tests with the reflector have been conducted at ESTEC, the results are presented and discussed. RF-surface reflectivity measurements resulted in extremely high reflectivity values of the CFRP surface at L and S band frequencies, in some cases better than the welded metal surface used for comparison. Finally the measured mechanical eigenfrequencies of the reflector have been compared to the calculated values resulting in a good correspondence.

Ein KfK-Antennen-Reflektor mit 88 cm Durchmesser wurde bei MBB entworfen und hergestellt, der aus einer Parabolschale und einem tangentialen Stützkegel besteht. Der Entwurf basiert auf detaillierten strukturmechanischen Berechnungen, die beschrieben und diskutiert werden. Die Fertigungsschritte für den Reflektor werden angegeben, der Entwurf und seine Hauptmerkmale aufgezeigt. Mechanische und thermische Umwelttests wurden bei der ESTEC durchgeführt; ihre Ergebnisse werden angegeben und diskutiert. Messungen der HF-Reflexion der Reflektoroberfläche resultierten in extrem hohen Reflexionswerten der KfK-Oberfläche bei L- und S-Band Frequenzen, die in einigen Fällen besser als die der geschweißten metallischen Referenzoberfläche waren. Schließlich wurden die gemessenen mechanischen Eigenfrequenzen des Reflektors mit den berechneten Werten verglichen, wobei sich eine gute Übereinstimmung ergab.

1. INTRODUCTION

For communication satellites microwave antennae with high pointing accuracy high directivity and/or small beam width are required. Parabolic antennae with a suitable aperture diameter (depending on frequency and coverage area) in general fulfill these RF-requirements satisfactorily. Beside the weight constraints combined with the high stiffness requirements, typical for spacecraft structures, severe requirements concerning manufacturing tolerances and especially thermal distortions of the antennae have to be considered. An antenna design made in CFRP (**C**arbon **F**ibre **R**einforced **P**lastics) seems to be the most favourable approach because of the low density, high modulus of elas-

ticity and low thermal expansion coefficient of the CFRP material. In addition also the RF-reflectivity of CFRP in the microwave range is close to that of a metallic surface. Aim of the development activity described in this paper was the verification of a simple low cost/low weight CFRP-technology reflector design with a reasonable, large enough aperture diameter.

2. REFLECTOR DESIGN

2.1 Design Requirements

The design requirements for the high gain technology reflector described in this chapter are resulting from the RF-requirements on one hand and from the spacecraft side on the other hand. The RF-requirements had to be met with a lightweight structural design.
The CFRP structure fulfills the requirement for high stiffness and minimum thermal deformation at low weight in addition to a very high RF-reflectivity using a high modulus carbon fiber.
The design requirements for the mission are derived from the launching vehicle (TD 3914) and the space environment of a synchronous orbit. That means that acceleration, vibration and acoustic excitation resulting from the launch vehicle and the high vacuum and solar radiation of the orbit environment have to be considered. Eclipse and/or shadow cases (antennae in satellite shadow) may result in temperature changes (temperature cycles) between about -160° C and $+100^\circ$ C. Under certain mission conditions (critical sun incidence cases) the antenna should be able to endure high temperature gradients without disturbing distortions.
The third point that had to be met by the design was that of a cheap and economic manufacturing of the reflector.

2.2 Design Description

The reflector shown in FIG. 1 consists of a parabolic dish (f = 383 mm, Dmax = 880 mm) which was tangentially met by a truncated cone. Each of these two parts is built from four equally spaced sectors. The sectors overlap one another by a certain amount. Fiberorientation of each sector (dish and cone) is $\pm$ 45° at the centerline. The cross of the dish produced by the overlaps of the sectors is turned against the cross of the cone through an angle of 45°. Between cone and dish there is a central tube which is attached to the dish with a bonded flange. The short part of the tube fits in the long central tube where it is bonded on one end and the other end is bonded in the inner flange of the cone. In this way there is a connection between the dish and cone in the center of the part, additional to the tangential bonding area between cone and dish at the edge. To reinforce the weak point where the support cone is truncated three layers of CFRP skins are introduced both inside and outside. The fastening of the antenna will be made at six points on a PCD of 90 mm. The "heli coils" for the M6 screws are incorporated in the CFRP inner and outer cone flange.
Measurements on pure 75 S/epoxy specimen conducted at MBB gave reflectivity factors at 12 GHz of about 98% [1] which eliminated the need for a metallic coating.

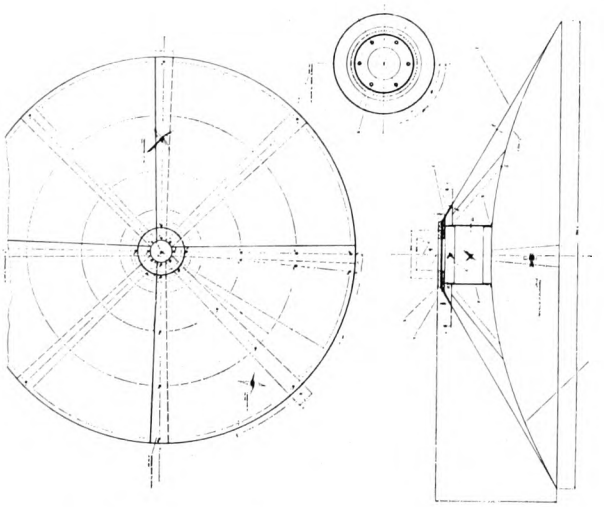

FIG. 1: **Antenna Reflector Geometry**

2.3 Materials

The materials used for the antenna are carbon fiber type HM (THORNEL 75 S) and epoxy resin (CIBA ARALDIT CY 209/HT 972). With these components filament wound flat skins with closed surface were fabricated. Fiberorientation of the skin is $\pm 45^\circ$. Using templates with the exact shape of the sectors for the cone and dish the cut of the skin parts was done with fiberorientation angles of $\pm 45^\circ$ to the centerline of the sector. The requirement of thermal stability of the antenna during thermal cycles in orbit can be fulfilled with this high modulus fiber and the fiber direction of $\pm$ 45° in the laminate at a fiber volume content of 60%. When all these specifications for the graphite skin are met one can find a coefficient of thermal expansion for the laminate of $0 \cdot 10^{-6}\ 1/^\circ\text{C} \leq |\bar{\alpha}| < 2 \cdot 10^{-6}\ 1/^\circ\text{C}$ in the temperature range of 100 K to 400 K. Such a carbon fiber reinforced epoxy skin has a wall-thickness of $\sim$ 0.45 mm.
The adhesive used for this antenna is the CIBA GEIGY ARALDIT AV 100/HV 100 which is as well space qualified as the carbon fiber THORNEL 75 S and Ciba resin CIBA GEIGY ARALDIT CY 209/HT 972. These materials are also used for the OTS (Orbital Test Satellite) and MAROTS (Maritime Orbital Test Satellite) solar panels built at MBB for ESA.

3. STRUCTURAL ANALYSIS

3.1 Assumptions and Input Data

The employed laminate-material has isotropic properties of thermal expansion and orthotropic properties of elasticity. The laminate application in four sections results in anisotropic elastic behaviour of the dish and cone. The input data used for all structural computations are given as follows:

Material selected: THORNEL 75 S with CY 209/HT 972
Fiberorientation = $\pm$ 45°
Thickness of dish and cone t = 0.45 mm
Thickness of tube t = 0.90 mm

Elastic properties of components:

a) **THORNEL 75 S**
$E_{\parallel F} = 523\,800$ N/mm²
$E_{\perp F} = 5\,600$ N/mm²
$G_F = 17\,460$ N/mm²
$\nu_{F\parallel\perp} = 0.39$
b) **CY 209/H 972**
$E_{\parallel B} = 4\,700$ N/mm²
$E_{\perp B} = 4\,700$ N/mm²
$\nu_B = 0.35$

From these properties, the material property matrix was derived:

$G_{11} = 73\,100$ N/mm²
$G_{12} = 67\,100$ N/mm²
$G_{22} = 73\,100$ N/mm²
$G_{33} = 68\,375$ N/mm²

For all numerical calculations the *Finite Element Method* and the computer program NASTRAN were used. The electronic computations were performed on the IBM system/370 Model 165 computing system at the MBB-plant Ottobrunn.

3.2 **Static Calculations**

Because of the anisotropic elastic behaviour of the dish and cone plane anisotropic plate elements were used instead of shell-ring-elements.
In FIG. 2 the undeformed and deformed shapes of the idealised model are shown for two load cases of thermal distortion. The model is a 90°-section of the antenna idealised in a polar-coordinate system. The boundary conditions consist of constraints on circumferential deflection and the corresponding rotation along the 0°- and 90°-cross-section and of constraints on axial deflection and on all rotational degrees of freedom of the lower flange area.

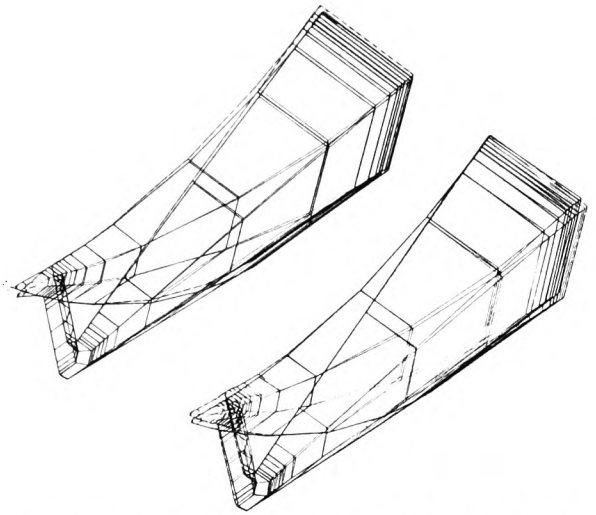

FIG. 2: **Thermal Deformations (a) Caused by an Overall Temperature Change of 300° C (upper drawing) (max. deformation ≈ 0.30 mm) and (b) by a Temperature Difference of 100° C between the Inner Cylindrical Tube and the Outer Parabolic Dish and Cone (max. deformation ≈ 0.01 mm)**

Four load cases were calculated:

- 1 g-acceleration in axial direction
- 1 g-acceleration in lateral direction
- thermal load caused by an overall temperature change of 300° C
- thermal load caused by a temperature difference of 100° C between the inner cylindrical tube and the outer parabolic dish and cone (FIG. 2).

For the two first load cases (acceleration in axial and lateral direction) the maximum deformations and the inforced stresses in the flange area are of special interest. By 1 g-acceleration the greatest deformation in lateral direction (worst case) was found to be 0.37 mm. The highest stresses in bending were 13.5 N/mm² in the case of 1 g-acceleration in axial direction (worst case). This leads to a maximum acceleration for break of 35–40 g.

3.3 **Dynamic Calculations**

3.31 Topology

3.311 Idealization of Structure

FIG. 3 shows the entire idealized structure of the dish with

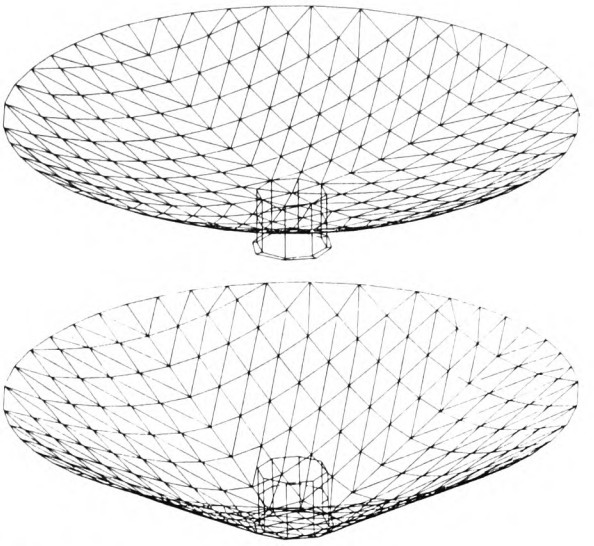

FIG. 3: **Idealized Structure of Dish and Support Cone**

tube and support cone in separated undeformed geometric projections. In establishing the Finite Element Model, the advantages of quarter-symmetry for dish, cone and tube were used in order to keep the idealized system at a reasonable size and still holding the numeric solution at the required level of accuracy.
The curvature of the structural components was idealized by a network of flat triangular plates for dish and cone. For the central tube and its flange, quadrilateral plates were used. The mathematical model consisted of

132 grid points,
216 triangular elements,
8 quadrilateral elements and
16 bars, representing a ring at the tangential point of cone to dish.

The dynamic system was comprised of 631 degrees of freedom, partially determined by the boundary conditions at the planes of symmetry. The entire system of the quarter-structure was then condensed to 42 degrees of freedom and eigenvalues extracted.

3.312 Choice of Finite Elements

All components of the entire reflector antenna consist of pure CFRP-fibre structure. The elastic behaviour of this type of structural elements was considered when selecting the proper input data for the computer program: All triangular and quadrilateral plates have both inplane and bending stiffness with solid homogeneous cross section and consist of linear, temperature-independent anisotropic material. For these combined membrane and bending elements with two different stress systems, the plate stiffness was generated by the computer program from additional input data such as fibre orientation and elastic constants. All bar elements include extension, torsion, bending in two perpendicular planes, and the associated shears.

3.313 Mass Distribution

For the CFRP-fibre structure, a mass density of ϱ = 0,000015696 N sec²/cm² was used. Mass terms are generated from element geometric and material properties and distributed to the system-points by the NASTRAN computer program.

3.32 Results of Dynamic Analysis (Normal Mode Analysis)

TABLE I shows the natural frequencies for symmetric boundary conditions (Z), TABLE II for anti-symmetric boundary conditions (X) each together with the measured natural frequencies.
As can be seen, the minimum natural frequency is close to 140 Hz. A discussion of calculated versus measured natural frequencies is given in Chapter 7.1.

TABLE I: **CALCULATED AND MEASURED NATURAL FREQUENCIES FOR SYMMETRIC BOUNDARY CONDITIONS (Z)**

Mode No.	Frequency [Hz] calculated	Frequency [Hz] measured
1	142	165
2	241	245
3	255	260

TABLE II: **CALCULATED AND MEASURED NATURAL FREQUENCIES FOR ANTI-SYMMETRIC BOUNDARY CONDITIONS (X)**

Mode No.	Frequency [Hz] calculated	Frequency [Hz] measured
1	139	136
2	247	210
3	277	250

4. REFLECTOR MANUFACTURING

Before manufacturing there was a material acceptance control for all reinforced plastic components and bought-out parts.
Two carbon fiber/epoxy skins were produced by a filament winding procedure. The pattern of each skin was fully closed. After this winding procedure the skin was cut from the drum and placed on a cutting table. On this table each of the four sectors for the dish and the truncated cone were cut out with the aid of templates. In the same way circular rings were cut out and put in a press mould to preproduce the inner and outer flange for the truncated cone and the dish flange which is bonded to the rear side of the dish. The four overlapping sectors were laid up on the moulds for the dish and cone respectively and cured.
The cured dish was left on the mould in which a central locating pin was positioned. With the aid of this pin and additional discs the rear-side dishflange was bonded. In a third step the previously manufactured long central tube was fixed and bonded to the fastened dishflange (FIG. 4).
To complete the support cone, first of all, the previously fabricated inner flange of the cone was fixed on the smaller diameter area of the cone mould. Then the three doubling rings were laid up on the mould. Following this the cured cone was positioned and the three outer doubling plies were laid up. After lay up this sub-assembly was co-curred in an autoclave under a vacuum at 120° C for 4 hours. Following curing the outer flange was bonded to the cone and heli-coils were positioned and inserted. Lastly the short central tube was bonded to the inner flange.
The final manufacturing process involved the bonding of the dish assembly to the cone assembly on the dish mould, and with the aid of locating centralizing pins and discs.
After manufacturing the reflector mass has been determined. The total reflector mass measured was 1030 g.

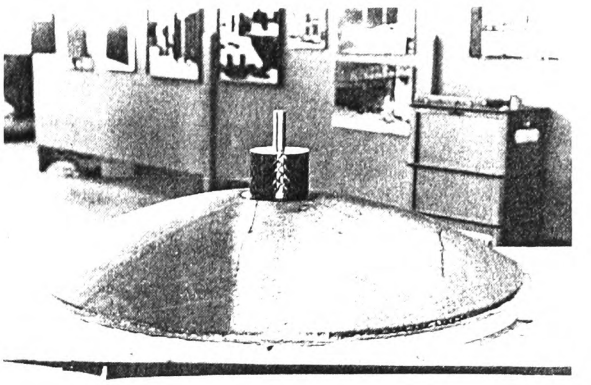

FIG. 4: **Bonding of the Central Tube to the Parabolic Dish on the Mould**

5. ENVIRONMENTAL TESTS

A complete series of environmental tests was performed at ESTEC. The most important tests concerning the operational life of the reflector are the thermal tests because they can show what distortions of the profile can be expected in orbit. These distortions can be divided in two types:

- permanent deformations due to hysteresis after a certain number of thermal cycles, and
- instantaneous deformations, which will add to the previous type, and which are distortions due to temperature level and distribution on the reflector.

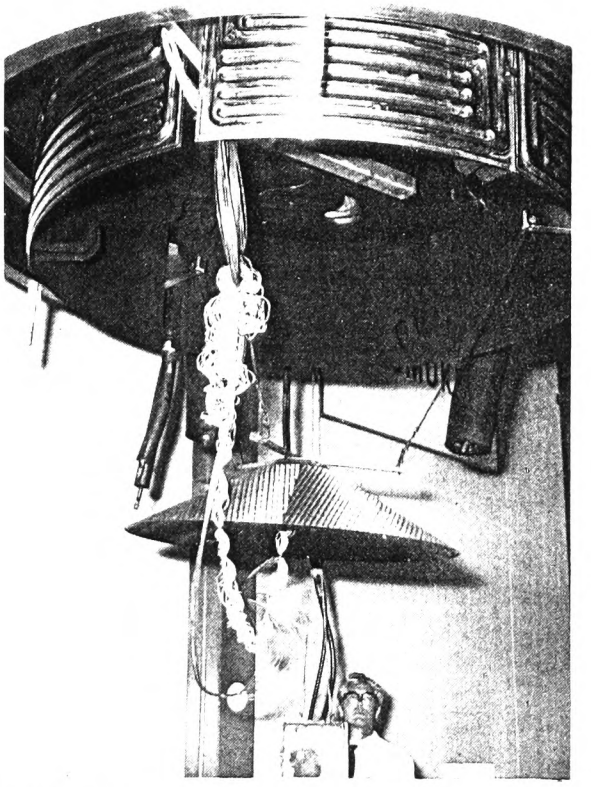

FIG. 5: **Test Arrangement for Thermal Cycling Test**

The distortions due to hysteresis have been measured after the reflector has been subjected to a certain number of thermal cycles, while the instantaneous deformations can be predicted by mathematical analysis when the field of temperatures is known: a solar simulation test has therefore been performed. The instantaneous deformations could also be measured directly under solar simulation by using the photogrammetry technique: this is being implemented in the HBF 3 chamber at ESTEC, but was not operational at the time of the test.
The other environment to which the reflector would be subjected is due to the vibrations during the launch of the spacecraft. Sine vibration tests are usually carried out and, in addition, for items such as antenna reflectors where the area/mass ratio is large, an acoustic vibration test is necessary. These two types of tests were therefore performed on this reflector.

5.1 **Thermal Cycling Tests**

An ageing tests of the reflector has been carried out in the ESTEC V.T.C. facility. FIG. 5 shows the test arrangement prior to test.
The test objective was to verify the amount of lasting distortion after exposure to extreme temperature excursions. A typical temperature cycle is shown in FIG. 6 simulating approximately (with regard to facility constraints) the temperature excursion of spacecraft antennae of this specific design in geostationary orbit.

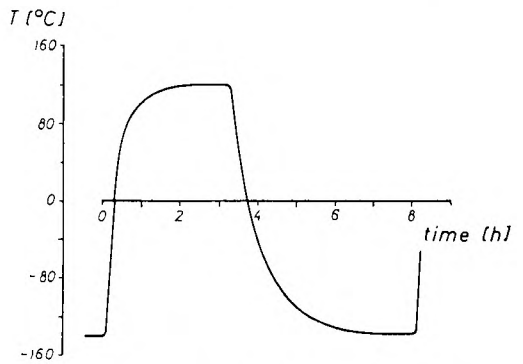

FIG. 6: **Typical Cycle during Thermal Cycling Tests**

Approximately 8 hrs. were required to reach quasi equilibrium temperatures during one cycle. The profile of the reflector was measured with a 3dB machine at ESTEC. A horizontal grid measurement points (10 cm by 10 cm) was applied to record the vertical coordinates of the reflector surface. A metal ring was employed fitting in the center hole of the reflector to provide a reference for exact centering and zero-distortion thus enabling unbiased comparison of different measurements to be done (see FIG. 7).

The following profile measurements were carried out:

- prior to thermal cycling
- after 25 cycles
- after 49 cycles
- after 70 cycles.

Some results are presented in FIG. 8 comparing the contour of the reflector surface after 70 cycles with that prior to test.
The contour maps indicate non-uniform lasting distortions of the reflector with maximum values of about .3 mm at the circumferential. The measurement accuracy is ± .05 mm.

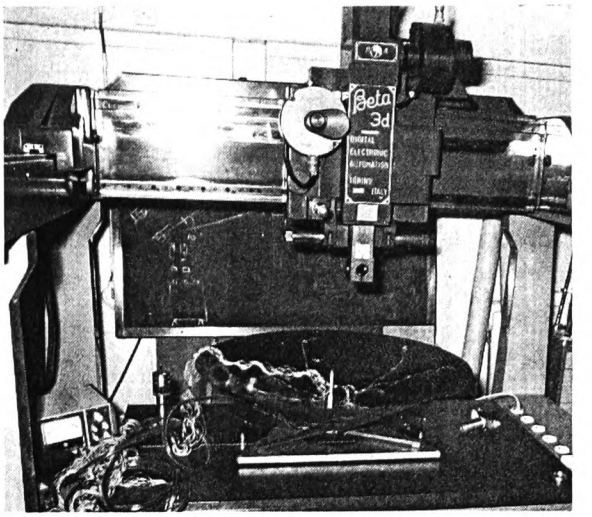

FIG. 7: **Profile Measurement of the Reflector**

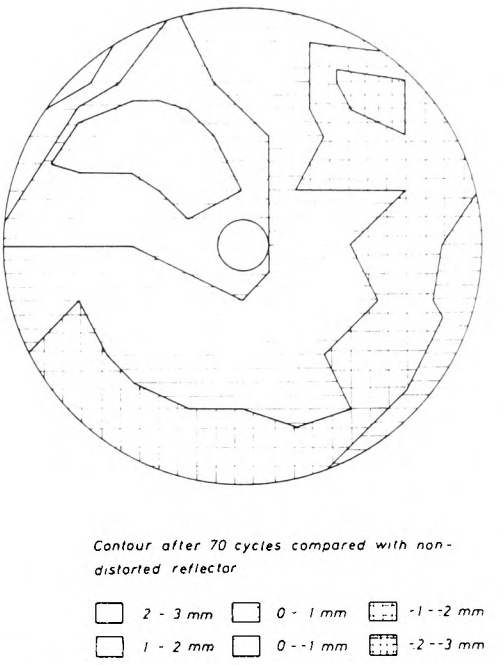

FIG. 8: **Contour after 70 Cycles Compared with Nondistorted Reflector**

5.2 **Solar Simulation Test**

After thermal cycling the reflector was subjected to a solar simulation test in the ESTEC HBF-3 facility. The purpose of this test was to simulate thermally extreme conditions to be encountered in a geosynchronous orbit with respect to temperature levels and local and temporal temperature gradients. In this context the following test phases have been determined covering the above extreme conditions for this particular antenna design:

Phase 1: Cold equilibrium, without simulated sun.
- symmetrical temperature distribution at min. temperature level

Phase 2: Hot equilibrium, with sun radiation perpendicular* to reflector aperture area (see FIG. 9)
- symmetrical temperature distribution at max. temperature level

Phase 3: 72 min. eclipse simulation, starting with temperatures of phase 2, and subsequent warm-up phase with sun as in phase 2,
- max. temporal temperature gradients

Phase 4: Intermediate equilibrium, sun incidence angle to reflector normal: 20°
- asymmetric temperature distribution at intermediate temperature level

Phase 5: max. local gradient equilibrium, solar radiation parallel to reflector aperture,
- max. local temperature gradients in reflector.

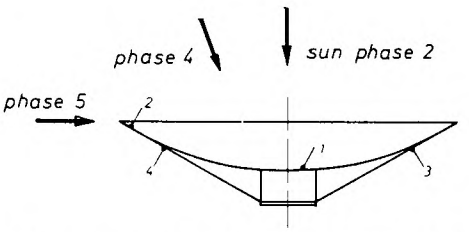

FIG. 9: **Thermocouple Location and Definition of Solar Incidence Angles for Different Test Phases**

Test temperatures of the reflector are measured by means of 36 thermocouples. The temperature excursion of some selected measurement points (see FIG. 9) are shown in FIG. 10.

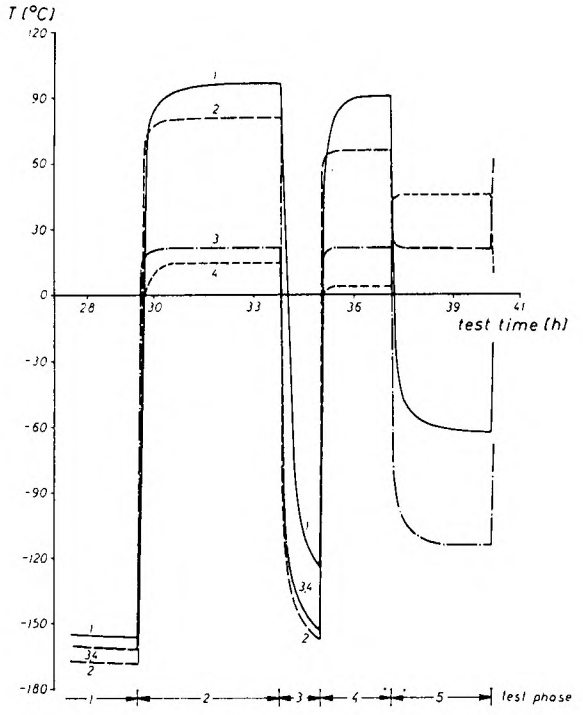

FIG. 10: **Temperature Excursion of some Selected Measuring Points during Solar Simulation Test**

* Simplified to get symmetrical temperature distribution – in orbit solar incidence angle in these cases is 9° from normal.

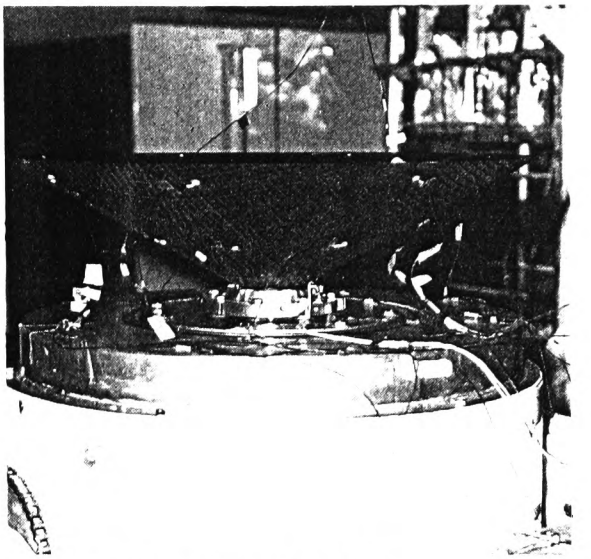

FIG. 11: Sine Vibration Test Set-up (Z-Axis)

5.3 Sine Vibration Test

This test was performed on the 7T installation at ESTEC. It consists of one vibrator Ratier VRF 60 for the vertical excitation and one vibrator LING 335 coupled to the slip table for the horizontal excitation.

The test was performed along two axes of the reflector:

- the longitudinal axis (Z), which is the axis of the parabola;
- one lateral axis (X).

The test configuration is shown on FIG. 11 for one axis excitation. Twelve accelerometers have been used to monitor the behaviour of the reflector. In order to limit the possible damages to the front face of the reflector, only two accelerometers were placed on the parabola, and the 10 other ones on the cone (see FIG. 12).

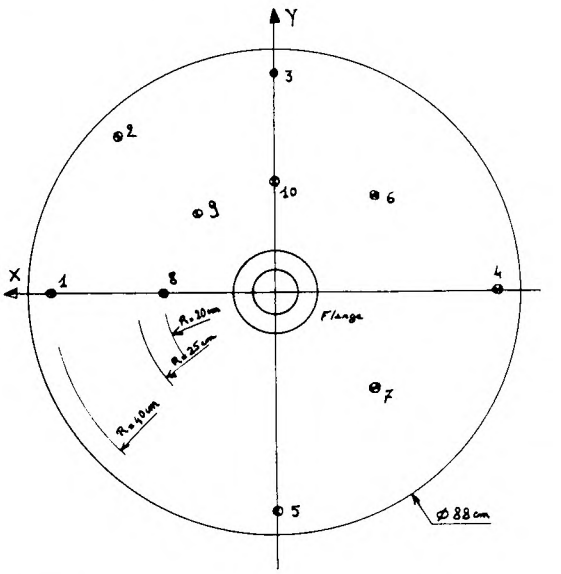

FIG. 12: **Positions of the Accelerometers on the Cone**

The test levels were based on the expected performances of an OTS (Orbital Test Satellite) type satellite as they were known at the time of the test. The qualification test levels were defined as follows:

	Frequency (Hz)	Levels (g)
Z-axis	5–15	2.5
	15–21	8.5
	21–100	3.5
X-axis	5–20	3.5
	20–30	5.0
	30–100	3.5

at a sweep rate of 2 oct/min.

The achieved levels were limited in the low frequency range (below 8 Hz in Z-axis and 10 Hz in X-axis), due to amplitude limitations of the vibrators.

The test sequence was a classical one:

- a resonance search at low level (0.5 g) between 5 and 2000 Hz;
- test at qualification levels between 5 and 100 Hz (a test at intermediate level is normally performed at $^2/_3$ of the qualification levels before the qualification test. However, due to the fact that the first resonance frequency of the reflector was well above 100 Hz, this intermediate level run was deleted).
- a second resonance search at low level (0.5 g) between 5 and 2000 Hz, which allows for detection of potential failures by comparison of the response curves with the ones of the first resonance search.

This same sequence was applied along the 2 axes. At the end of each run, the responses of the accelerometers were plotted and compared with the results of the previous runs. The results show that the first resonance frequency of the reflector is well above 100 Hz. Typical response curves are shown on FIG. 13 (Z-axis test) and FIG. 14 (X-axis test) for accelerometers 1 and 8 (they are non-filtered curves).

5.4 Acoustic Vibration Test

This test was performed in the reverberant chamber at ESTEC. The 12 accelerometers which were on the reflector for the sine vibration test have been kept and another one has been added on the support of the reflector, in order to monitor the random excitation transmitted by the reflector. Four microphones were also used to monitor the sound pressure level in the chamber. Prior to installation of the specimen, the 4 microphones were placed at the center of

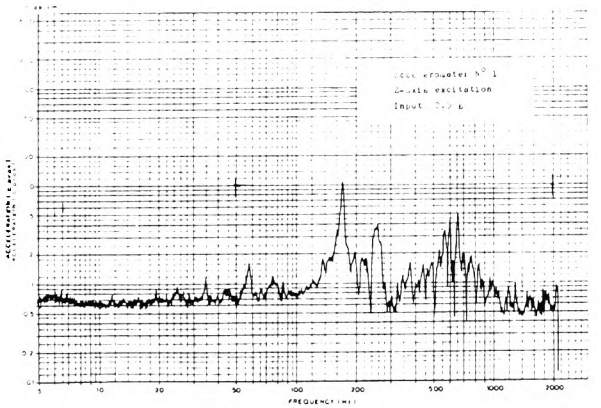

FIG. 13: **Accelerometer No. 1, Z-Axis Excitation Input 0.5 g**

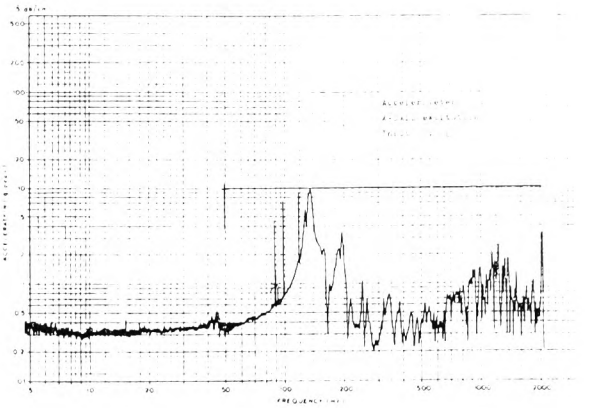

FIG. 14: **Accelerometer No. 8, X-Axis Excitation Input 0.5 g**

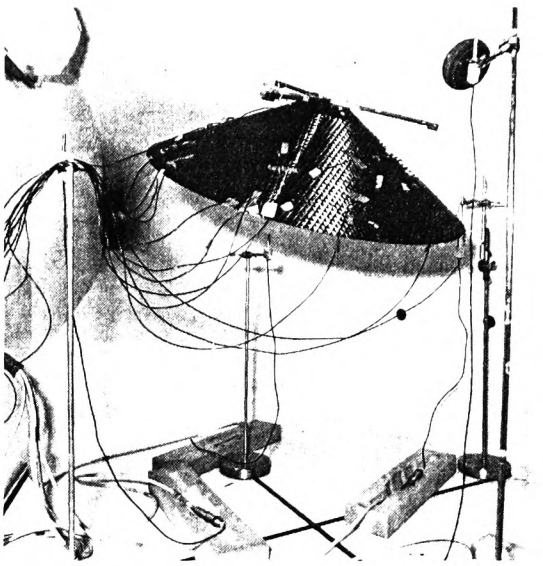

FIG. 15: **Test Set-up for the Acoustic Test**

the chamber, and the spectrum was adjusted to the specified levels.
The antenna was then suspended in the chamber and was orientated so that creation of standing waves between the reflector and the walls of the chamber was avoided. The four microphones were then placed, one in front of the reflector, one behind, and one on each side. This configuration is shown on FIG. 15.

The test sequence is a succession of three runs at increasing levels, up to qualification:

- qualification levels – 12 dB
- qualification levels – 4 dB (acceptance levels)
- qualification levels

These qualification levels were chosen assuming a Thor Delta 3914 launch as shown in TABLE III.
The duration of the qualification run is 120 sec., but for the 2 runs at reduced levels, a smaller duration of 60 sec. is sufficient. At the end of each run the results of the accelerometers and microphones were plotted, and the chamber opened for inspection of the reflector. The levels measured on the reflector during the qualification run were above 70 grms, and reached more than 100 grms on the parabola and at one point on the cone (accelerometer 2). A level of

TABLE III: **ACOUSTIC VIBRATION TEST LEVELS**

Octave Band Centre frequency (Hz)	Sound pressure level (dB, ref. 0.0002 dynes/cm²)
31.5	128
63	131
125	135
250	140
500	144
1000	137
2000	134
4000	130
8000	127
Overall	147 dB

38 grms was transmitted to the support of the antenna.

5.5 Test Results Summary and Discussion

The test results of the environmental tests performed on the reflector showed its good behaviour:
The thermal cycling test, performed between – 140° C and + 120° C, resulted in permanent deformations which are rather small (0.1 to 0.2 mm with a maximum at 0.3 mm in one place) and which tend to stabilize. This indicates a good thermal stability under the severe orbital conditions that such a reflector is susceptible to see.
The Solar simulation test has been finished successfully. The extreme temperatures and extreme temperature gradients represent approximately the worst conditions that a large spacecraft antenna reflector can experience in geostationary orbit. The optically black surfaces largely contribute to the high maximum temperatures (about 100° C) and to the large temperature gradients (maximum about 160° C) in the reflector.
The sine vibration test shows that this type of construction is quite stiff and no problem would be expected when it would be integrated on a spacecraft.
The response of the reflector to the high acoustic environment shows that this test is a severe one for such a lightweight structure, but the reflector passed successfully the test.
It must be noticed that through all the environment tests, the reflector did not suffer any apparent damage at any stage.

6. R. F. SURFACE REFLECTIVITY MEASUREMENTS

Carbon fibre reinforced plastics have appreciable electrical conductivities ([2]), although not as high as commonly used metals such as aluminium. Even so, this fact suggests that an antenna reflector fabricated from CFRP might not need a surface coating of metal to ensure good conductivity. However, for spacecraft communications antenna gain losses of even a few tenths of a decibel are undesirable and a reflector surface which gave, for example, an antenna gain reduction of 0.25 dB compared with an identical antenna with a metal reflector would probably need to be metallised. Past investigations ([3], [4]) have shown that the reflectivity of CFRP depends on several factors such as the type of materials, the filling fraction and the surface finish. To determine whether the type of CFRP used for the 880 mm diameter reflector was sufficiently good for spacecraft use without metallisation, some direct RF-measurements were made on it.
As shown in FIG. 16, the reflector was converted into a front fed antenna system using a radome covered log periodic dipole array – longitudinally moveable along the parabola axis for optimisation – as a primary feed, this being supported by a 4 arm structure. Poor reflecticity from the surface of a reflector antenna would result in gain loss; therefore, to evaluate a CFRP reflector at RF a gain comparison between an antenna using a bare reflector and the same antenna but with a metallic coating on the reflector is the most meaningful type of measurement. This was done using the swept frequency gain comparison technique developed in connection with conductive paints ([5]) and illustrated in FIG. 17. With a swept frequency oscillator as a microwave power source, the gain of the antenna with its reflector coated in metal foil was monitored as a function of a reference channel level, the reference channel deriving from a directional coupler at the swept frequency oscillator output. An elevated outdoor range of length 16 metres and height 7 metres was employed; the remote antennas were a log periodic dipole array at L band frequencies and a ridged horn at S band frequencies. The reference surfaces were made from aluminium foil in sections reminiscent of the panels of a parachute. These were laid over a convex parabolic former and welded together along the seams by a new welding process developed in the U. K. for metal and plastic films (Luc welding). For each measurement a reference surface was adhered to the reflector.

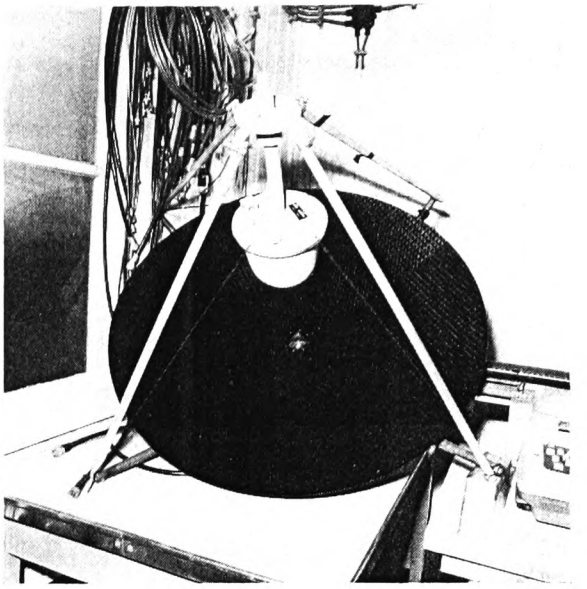

FIG. 16: **Photograph of the CFRP Reflector and the Antenna Feed System**

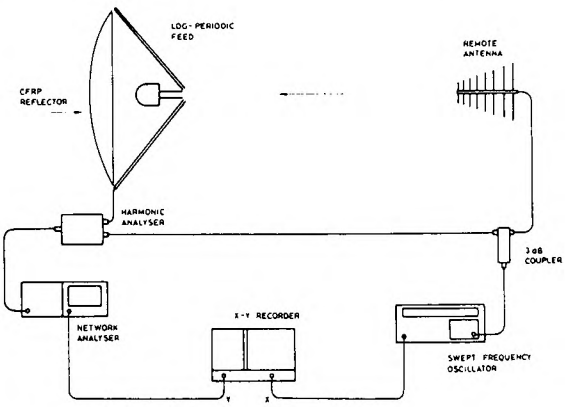

FIG. 17: **RF-Surface Reflectivity Measurement System**

FIG. 18 and 19 show two measured gain comparisons, FIG. 18 for the frequency range 1.3 to 1.7 GHz, and FIG. 19 for 2.8 to 3.2 GHz. Each result consists of two recordings, the first taken with the metal reference surface in place and the second taken after its removal. The most striking fea-

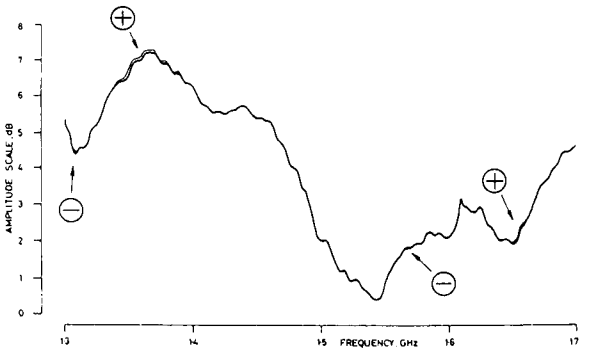

FIG. 18: **Test Channel to Reference Channel Level Recordings with and without Reference Surface 1.3 to 1.7 GHz**

ture of these results is that in both cases the two recordings are identical and appear as one over most of the frequency range. Some small departures can be seen, however, both positive and negative. The positive signs indicate where the gain with the bare reflector was actually better than with the aluminum reference, and the negative show the opposite. Departures are very small – less than 0.1 dB except for the extended region between approximately 3.05 and 3.15 GHz. In this region the bare reflector surface has a greater deficit than the equivalent metal coated case by about 0.12 dB.

To conclude, the measurements show that the high modulus material has an extremely good RF-surface at L and S band frequencies, in some cases better than the welded metal surface used for comparison. Clearly this type of CFRP can be used without recourse to a metallic surface to ensure good reflectivity, thus saving manufacturing time and expense as well as additional mass and the fear of de-laminition.

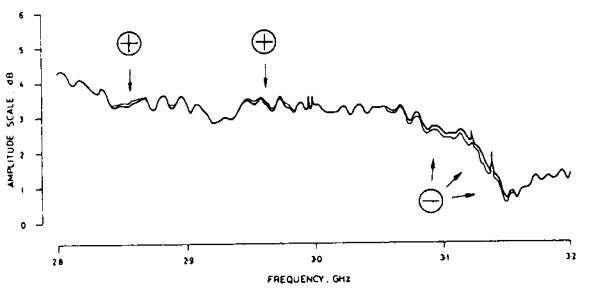

FIG. 19: **Test Channel to Reference Channel Level Recordings with and without Reference Surface 2.8 to 3.2 GHz**

7. SUMMARY AND CONCLUSIONS

7.1 Comparison of Calculated and Measured Natural Frequencies

A comparison of the calculated and the measured results shows that the first natural frequencies are almost identical (see TAB. I and II). The slightly larger deviation in the symmetric case (Z-direction) was caused by the support condition at the base, which could be only approximated to the computer model.
Comparing plotted frequency responses with calculated natural frequencies, it will be noticed that certain eigenfrequencies are present at the plots which did not show up at the computer solution. It can be assumed that these effects are local modes which were most likely induced by the attached accelerometers.

7.2 Conclusions

From the development program described in this paper the following conclusions can be drawn:

(1) The CFRP-reflector design of a parabolic dish with a tangential support cone has a high stiffness combined with a low weight and a very good thermal stability and allows a relatively cheap and economic manufacturing of the reflector.

(2) The reflector showed an outstanding good behaviour under all environmental tests performed and did not suffer any damage at any stage even under the critical thermal cycling and acoustic noise tests.

(3) The calculated first natural frequencies are almost identical to the measured eigenfrequencies; that means that the calculation method is suitable and accurate enough to allow a reasonable prediction of reflector frequency response without additional tests.

(4) The reflector can be used without additional metallic surface, ensuring maximum reflectivity.

Acknowledgement:

The authors wish to thank Mssrs. S. HOGL, H. J. HÜTTMANN and P. WACKERLE from MBB Ottobrunn, for valuable contributions to this paper.

LITERATURE:

[1] MBB/DS-Study: Schlußbericht – Phase 1 des Vorhabens „Bau und Test einer Satelliten-Sendeantenne", GfW-Vertrag Nr. RV 21-V 36/74-QH, 1975.

[2] GILL, R. M.: "Carbon fibres in composite materials", ILIFFE Book, London 1972, p. 73.

[3] ROBINSON, E. Y., STONIER, R. A., LOFGREN, C. L.: "Development of a unique graphite/epoxy antenna subreflector" Report of ASTM Third Conference 1974, p. p. 632–650.

[4] KEEN, K. M.: "Gain – loss measurements on a carbon fibre composite reflector antenna", Elec. Letts., Vol. 11, No. 11, May 29, 1975 p. p. 234–235.

[5] KEEN, K. M.: "Effect of conductive thermal control paint on spacecraft antenna performance", Elec. Letts. Vol. 11, No. 17, August 21, 1975, p. p. 412–413.

Publication P10. **K.M. KEEN,** ***Characteristic impedance of dielectric filled slotted coaxial transmission line.*** **Proceedings IEE, Vol. 123, No. 10, October 1976, pp 981-983.**

Characteristic impedance of dielectric-filled slotted coaxial transmission line

K.M. Keen, M.Sc., C.Eng., M.I.E.E.

Indexing terms: *Coaxial cables, Electrical impedance, Electrical impedance measurement, Microwave measurement, Transmission-line theory*

Abstract

A solution is presented for the determination of the impedance of slotted dielectric-filled transmission lines of the type that could be formed from semi-rigid coaxial cable, and theoretical results are compared with measured values. The solution is a composite one: over the region of greatest impedance variation, a method involving the conformal transformation of the slotted line to microstrip geometry is used, and a matched exponential function is used for the remaining part. The experimental method for finding the line impedance values, which is generally useful as it can be applied to any type of transmission line of unknown phase velocity, is also presented.

List of symbols

α = angular extent of slot, degrees
α' = angular extent of slot, radians
r_1 = radius of inner conductor of slotted coaxial line
r_2 = outer radius of dielectric filling of slotted coaxial line
r_3 = outer radius of outer conductor of slotted coaxial line
w = width of equivalent microstrip conductor
t = thickness of microstrip conductor
h = distance between microstrip conductor and its ground plane
a = width of microstrip ground plane
Z_0 = characteristic impedance of slotted coaxial line
Z_c = characteristic impedance of reference coaxial line used during measurements
Z_{IN} = input impedance at position AA'
ϵ_r = relative permittivity of slotted-line dielectric
ϵ_{EFF} = effective relative permittivity
ϵ_0 = permittivity of free space
μ_0 = permeability of free space
$|\rho|$ = voltage reflection coefficient magnitude
ϕ = voltage reflection coefficient phase
l = length of slotted coaxial line
m, s, k = constants

1 Introduction

The only really wideband microwave frequency balun suitable for feeding many of the log-periodic and frequency independent antennas now known, is the one from Duncan and Minerva.[1] Their balun is based on the use of slotted coaxial transmission line, the characteristic impedance of which depends on the angular extent of the slot. The original balun used a continuous taper in the outer conductor of the coaxial line which is difficult to fabricate, but Evans[2] has shown that the tapered impedance transforming section can be replaced by a stepped transformer of quarter-wavelength sections. Only air-spaced slotted lines have been described in this context, the impedance values deriving from Duncan and Minerva's expressions for homogeneous media. There are, however, practical situations where dielectric-filled slotted coaxial lines would be preferable. For example, semi-rigid (solid copper outer conductor) cable is now commonly used to feed antenna systems, and baluns could be formed directly on this by machining or chemical etching, thus making a balun and feeder cable in one unit. But to do this a knowledge of the impedance as a function of line geometry is necessary. A method of finding such impedance values is described here.

2 Impedance determination by conformal mapping

Fig. 1 shows the cross section of a line formed by removing a section of its outer jacket. Hatsuda and Matsumoto[3] have described a relaxation method for finding the impedance of partially dielectric-filled line, but for their case the dielectric contained within the angular region 2α, in Fig. 1, is also removed. This is quite a different line from the one considered here, as for high α values the Hatsuda and Matsumoto line approaches an air-filled line.

Paper 7739E, first received 16th March and in revised form 2nd June 1976

Mr. Keen is with the European Space Research & Technology Centre, Domeinweg, Noordwijk, The Netherlands

A convenient way to analyse the line is by conformal transformation into microstrip geometry and then to apply known microstrip impedance equations.

Assadourian and Rimai[4] have shown that the impedance of a transmission line is invariant under conformal transformation. Fig. 2 shows the line cross section in the complex Z plane where

$$Z = x + jy$$

and the equivalent microstrip geometry in the W-plane where

$$W = u + jv$$

under the conformal transformation

$$Z = \exp W$$

The microstrip parameters are then related to those of the slotted line as follows

$$h \equiv \ln\left(\frac{r_2}{r_1}\right)$$
$$w \equiv 2(\pi - \alpha') \quad (1)$$
$$t \equiv \ln\left(\frac{r_3}{r_2}\right)$$

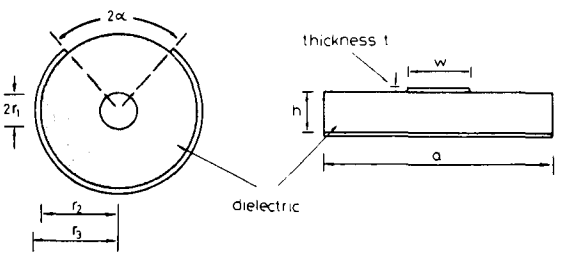

Fig. 1
Cross section of coaxial line and equivalent microstrip

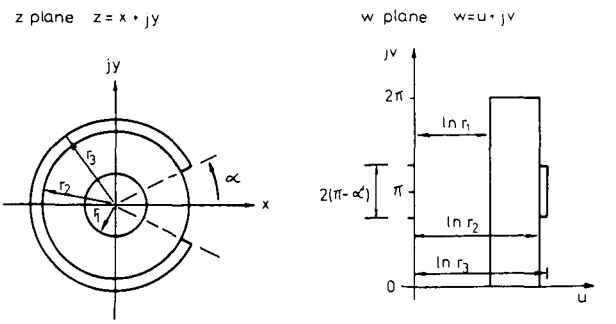

Fig. 2
Conformal mapping of slotted coaxial line to microstrip line geometry

where α' refers to radian measure and, in general, the absence of the dash refers to the angle in degrees.

Dukes[5] has shown that the ground plane of microstrip is effectively infinite for $a \geq 3w$, which corresponds to $2\alpha \geq 240°$, and, therefore, known microstrip impedance solutions cannot be used for values below this. Nevertheless, the region $360° \geq 2\alpha \geq 240°$ is the one in which over 80% of the impedance variation with 2α takes place. The graphically presented data of Reference 6 are probably the most widely used source of microstrip-impedance information, and these graphs are based on the work of Wheeler.[7] Substituting the transformed parameters of identities into Wheeler's expressions, and using his 'shape ratio of 0·5, for the criterion for the changeover from wide to narrow strip approximations, gives the following expressions for slotted dielectric-filled line impedance:

For $\pi - \alpha' > 0{\cdot}5 \ln\left(\frac{r_2}{r_1}\right)$

$$Z_0 = \frac{120\pi\epsilon_r^{-1/2}}{2\left[\frac{\pi-\alpha'}{\ln\left(\frac{r_2}{r_1}\right)}\right] + 0{\cdot}882 + \frac{\epsilon_r + 1}{\pi\epsilon_r}} \left\{ \ln\left[\frac{\pi-\alpha'}{\ln\left(\frac{r_2}{r_1}\right)} + 0{\cdot}94\right] + 1{\cdot}451 \right\} + 0{\cdot}164\left(\frac{\epsilon_r - 1}{\epsilon_r^2}\right) \quad (2)$$

And for

$$\pi - \alpha' < 0{\cdot}5 \ln\left(\frac{r_2}{r_1}\right)$$

$$Z_0 = 60\sqrt{\left(\frac{2}{\epsilon_r + 1}\right)}\left\{ \ln\left[\frac{4\ln\frac{r_2}{r_1}}{\pi - \alpha'}\right] + \frac{1}{8}\left[\frac{\pi-\alpha'}{\ln\left(\frac{r_2}{r_1}\right)}\right]^2 - 0{\cdot}5\frac{\epsilon_r - 1}{\epsilon_r + 1}\left(\ln\frac{\pi}{2} + \frac{1}{\epsilon_r}\ln\frac{4}{\pi}\right)\right\} \quad (3)$$

For both equations, ϵ_r is the relative permittivity of the slotted-line dielectric.

3 Outer jacket thickness correction

Eqns. 2 and 3 are for negligible thickness strips (outer coaxial jackets), and although this is sufficient for many cases, a correction for thick strips can be made, for example using the line width correction graph of Reference 6. The source of this graph is not given, but is presumably based on experimental results. From the identities 1 and numerical data from the graph, a correction for the angular extent of the outer jacket $2(\pi - \alpha')$ can be made. Denoting the effective value of the extent by the subscript *EFF* it can be shown that

$$2(\pi - \alpha')_{EFF} = 2(\pi - \alpha') + \ln\left(\frac{r_3}{r_2}\right)\left\{0{\cdot}54 + 0{\cdot}74\log_{10}\left[\frac{\ln\left(\frac{r_2}{r_1}\right)}{\ln\left(\frac{r_3}{r_2}\right)}\right]\right\} \quad (4)$$

4 Impedance expression for lower α values

For the region $240° \geq 2\alpha \geq 0°$, an impedance expression can be prepared from the following knowledge. At $2\alpha = 0°$ the line becomes a fully enclosed coaxial one; at $2\alpha = 240°$ the equation must give the same impedance and slope as eqn. 2; and from a knowledge of TEM mode transmission lines in general, the impedance variation can be expected to be exponential. These considerations lead to the following identity.

$$Z_0 = \frac{1}{2\pi}\sqrt{\left(\frac{\mu_0}{\epsilon_0\epsilon_{EFF}}\right)} \ln\left(\frac{r_2}{r_1}\right) \exp\left[(m\alpha')^s\right] \quad (5)$$

where

$$\epsilon_{EFF} = \epsilon_r(1 - k\alpha') \quad (6)$$

and m, s and k are constants. For the effective relative permittivity ϵ_{EFF} it is considered that a nonvarying function as proposed by Kaupp[8] is not sufficiently representative, as the proportion of fields within dielectric and within air is bound to change with α. Eqn. 6 is therefore proposed and the value of k found in the following way.

In basic terms, the impedance of a TEM mode transmission line is inversely proportional to the square root of the relative permittivity. If the dielectric medium of the line is not homogeneous, then the relative permittivity has some effective value. The effective value of the slotted coaxial line permittivity can be found by comparing the equivalent microstrip impedance with the impedance of the same microstrip geometry, but with an air dielectric (using the curves of Reference 6), and then applying the inverse square root relationship.

5 Impedance graphs for practical cases and a comparison with measured values

Figs. 3 and 4 are graphs of impedance as a function of slot angle, for cases with polythene and p.t.f.e. dielectrics. Fig. 4 is for slotted 0·141 inch semi-rigid cable, and Fig. 3 is for modified RG213U cable, which was convenient for measurements. In each case, region 3 was found from eqn. 3, region 2 from eqn. 2, and region 1 from eqn. 5. There are noticeable discontinuities between regions 2 and 3 owing to slight disagreement between wide and narrow strip impedance approximations,[7] but the error is only of the order of 2 or 3 Ω. The values from eqns. 5 and 6 for computing the impedance in regions 1 were as follows:

Fig.3: $s = 2{\cdot}5, m = 0{\cdot}2804, k = 0{\cdot}075$

Fig. 4: $s = 2{\cdot}8, m = 0{\cdot}3064, k = 0{\cdot}0644$

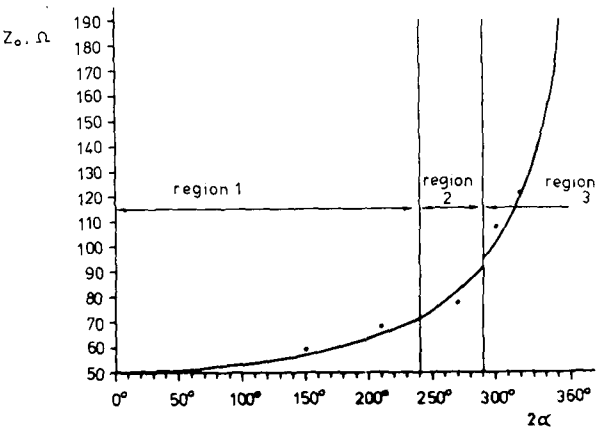

Fig. 3
Impedance of slotted polythene dielectric cable

Line with $\epsilon_r = 2{\cdot}3$ and $\ln(r_2/r_1) = 1{\cdot}265$
Dots are experimental values

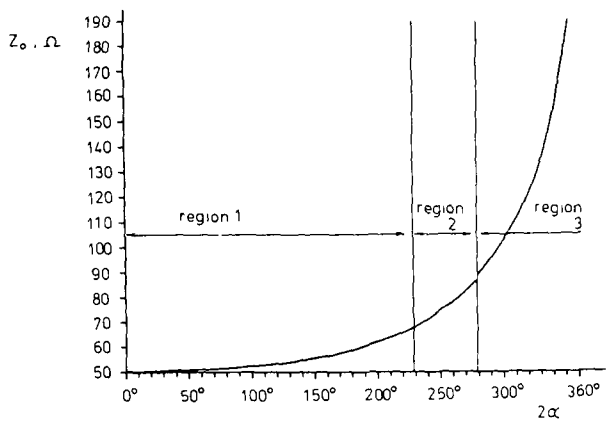

Fig. 4
Impedance of slotted 0·141 inch semi-rigid cable (p.t.f.e. dielectric)

Line with $\epsilon_r = 2{\cdot}1$ and $\ln(r_2/r_1) = 1{\cdot}187$

As a check on the foregoing, some experimental impedance values were obtained using a measurement method described in Section 6. Measurements were made on a modified RG21 3U cable, the braided outer conductor having been replaced with aluminium adhesive tape which was easily modified to a slotted configuration. The results are shown in Fig. 3 and good agreement can be seen.

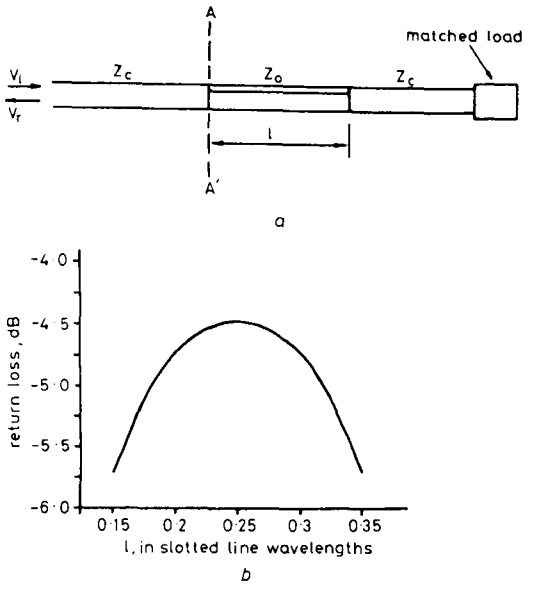

Fig. 5
Measurement of impedance

a Section of slotted line in terminated cable
b Typical return-loss/slotted-line-length graph

6 The impedance measurement method

The main problem for the direct microwave measurement of the slotted line impedance was that the wavelength was not accurately known, so the method shown in Fig. 5 was developed. Fig. 5*a* shows a terminated coaxial line of impedance Z_c, with a section of length l, approximately a quarter of a wavelength long, of slotted line of impedance Z_0. At AA' the input impedance is

$$Z_{IN} = Z_0 \frac{Z_c + jZ_0 \tan\beta l}{Z_0 + jZ_c \tan\beta l} \tag{7}$$

and the measureable reflection coefficient before AA' is

$$\frac{V_r}{V_i} = |\rho| \exp j\phi = \frac{j\,[Z_0^2 - Z_c^2]}{\dfrac{2Z_0 Z_c}{\tan\beta l} + j\,[Z_0^2 + Z_c^2]} \tag{8}$$

with the usual symbols. The quantities $|\rho|$ and ϕ are measureable with a network analyser, although the phase term ϕ is not useful as it is a linear function of l. However, the amplitude term $|\rho|$ has the form shown in Fig. 5*b*, and the peak of the curve is reached when l is a quarter of a line wavelength. When this occurs, the amplitude term, expressed here in decibels return loss, becomes

$$\text{return loss} = 20 \log_{10} \left[\frac{Z_0^2 - Z_c^2}{Z_0^2 + Z_c^2} \right] \tag{9}$$

and this outlines the measurement method: a return loss peak is first found by varying the applied frequency, then the return loss yields Z_0 from eqn. 9.

The method is most useful when Z_0 and Z_c differ by a factor of more than 1·5. When Z_0 approaches the value of Z_c, the reflections from the connectors at the return loss monitoring device/cable interface are significant, and the return loss/frequency curve has fast ripples superimposed on it, making the determination of the correct measurement frequency difficult.

Although this measurement technique was developed for slotted dielectric-filled coaxial transmission lines, it is applicable to any type of transmission line where the phase velocity is unknown.

7 References

1 DUNCAN, J.W., and MINERVA, V.P.: '100:1 bandwidth balun transformer', *Proc. IRE*, 1960, **48**, pp. 156–164
2 EVANS, B.G.: 'Chebyshev quarter-wave stepped balun transformer', *Electron. Lett.* 1973, 9, (22), pp. 514–516
3 HATSUDA, T., and MATSUMOTO, T.: 'Computation of impedance of partially filled and slotted coaxial line', *IEEE Trans.* 1973, MTT-15, pp. 643–644
4 ASSADOURIAN, F., and RIMAI, E.: 'Simplified theory of microwave transmission systems', *Proc. IRE*, 1952, 40, pp. 1651–1657
5 DUKES, J.M.C.: 'An investigation into some fundamental properties of strip transmission lines with the aid of an electrolytic tank', *Proc. IEE*, 1956, 103B, pp. 319–333
6 'Microwave engineers handbook – Vol. 1' (Horizon House – Microwave Inc., 1971)
7 WHEELER, H.A.: 'Transmission line properties of parallel strips separated by a dielectric sheet', *IEEE Trans.*, 1965, MTT-13, pp. 172–184
8 KAUPP, H.R.: 'Characteristics of microstrip transmission lines', *ibid.*, 1967, EC-16, pp. 185–193

Publication P11. **K.M. KEEN,** ***A log-periodic antenna with unidirectional radiation characteristics.*** **Electronics Letters, Vol. 12, No. 19, Sept. 16 1976, pp 498-500.**

where X is a random normal variable having the probability-density function

$$p(x; m, \sigma) = \frac{1}{\sigma\sqrt{(2\pi)}} \exp\left[-\frac{(x-m)^2}{2\sigma^2}\right] \quad \sigma > 0. \quad (5)$$

m is the mean value and σ^2 is the variance of X. The parameters m and σ^2 are related to a and p of the log-normal distribution by

$$m = \ln a \quad (6)$$

$$\sigma^2 = 2 \ln p \quad (7)$$

Problem formulation: Let $\boldsymbol{Z} = (Z_1, Z_2, \ldots, Z_N)$ be a random vector formed of N correlated clutter samples identically distributed according to eqn. 1. A random vector is fully characterised by its N-dimensional density function, which often cannot be easily determined. Therefore it is preferable to adopt a less complete, but sufficient for practical purposes, characterisation. For instance, the random vector $\boldsymbol{Z}$ can be characterised by the 1-dimensional density function of eqn. 1 and the correlation matrix $[s]$, formed of elements s_{ij} defined by

$$s_{ij} = \frac{E\{Z_i Z_j\} - E\{Z_i\}E\{Z_j\}}{\sqrt{(D^2\{Z_i\}\, D^2\{Z_j\})}} \quad i, j = 1, 2, \ldots, N \quad (8)$$

where E denotes statistical expectation and D^2 denotes the variance.

We shall focus our attention on generating a random log-normal vector $\boldsymbol{Z}$ with the prescribed correlation matrix $[s]$ and the specified parameters a and p.

Analysis: The quantity $E\{Z_i Z_j\}$ may be expressed as

$$E\{Z_i Z_j\} = \int_{-\infty}^{\infty}\int_{-\infty}^{\infty} \exp(x_i + x_j) p(x_i, x_j)\, dx_i\, dx_j \quad (9)$$

where $p(x_i, x_j)$ denotes the 2-dimensional normal density function given by

$$p(x_i, x_j) = \frac{1}{2\pi\sigma^2\sqrt{(1-r_{ij}^2)}}$$

$$\times \exp\left[-\frac{(x_i-m)^2 - 2r_{ij}(x_i-m)(x_j-m) + (x_j-m)^2}{2\sigma^2(1-r_{ij}^2)}\right] \quad (10)$$

and r_{ij} is the correlation coefficient between the variables X_i and X_j. Substituting eqn. 10 into eqn. 9,

$$E\{Z_i Z_j\} = \exp\left[2m + \sigma^2(1 + r_{ij})\right] \quad (11)$$

hence

$$s_{ij} = \frac{\exp(\sigma^2 r_{ij}) - 1}{\exp(\sigma^2) - 1} \quad (12)$$

The quantity r_{ij} may now be expressed in terms of s_{ij} and p:

$$r_{ij} = \frac{\ln\left[s_{ij}(p^2-1)+1\right]}{2 \ln p} \quad (13)$$

Procedure for generating log-normal vectors: We may now summarise the steps required to generate the random log-normal vector $\boldsymbol{Z}$ with the desired correlation matrix $[s]$ and the specified parameters a and p:

(1) The variance σ^2 and the mean value m of normal variables X_i, $i = 1, 2, \ldots, N$, are evaluated according to eqns. 6 and 7.

(2) The correlation matrix $[\boldsymbol{r}]$ of the normal vector $\boldsymbol{X}$ is formed of elements r_{ij} from eqn. 13.

(3) The random normal vector $\boldsymbol{X}$, with specified parameters m and σ^2, and the prescribed correlation matrix $[\boldsymbol{r}]$ are generated by one of several known methods.[3, 4]

(4) The components of the vector $\boldsymbol{X}$ are then transformed according to eqn. 4, and the correlated components Z_i of the random log-normal vector $\boldsymbol{Z}$ are thus obtained.

W. J. SZAJNOWSKI

Institute of Telecommunication
Warsaw Technical University
Nowowiejska 15/19
00-665 Warsaw, Poland

9th August 1976

References

1 EDGAR, A. K., DODSWORTH, E. J., and WARDEN, M. P.: 'The design of a modern surveillance radar' *in* 'Radar—present and future'. *IEE* Conf. Publ. 105, 1973, pp. 8–13
2 MEYER, D. P., and MAYER, H. A.: 'Radar target detection' (Academic Press, 1973), pp. 67–68
3 HURST, R. L., and KNOP, R. E.: 'Generation of random correlated normal variables', *Commun. ACM*, 1972, **15**, pp. 355–357
4 SCHEUER, E. M., and STOLLER, D. S.: 'On the generation of normal random vectors', *Technometrics*, 1962, **4**, pp. 278–281

LOG-PERIODIC ANTENNA WITH UNIDIRECTIONAL RADIATION CHARACTERISTICS

Indexing terms: Antenna radiation patterns, Antennas

The properties of an inclined form of a planar log-periodic antenna are described. The planar antenna has radiation characteristics similar to those of a halfwavelength dipole, but with a bandwidth as large as desired. It is shown that, when the planar antenna is inclined about one axis of symmetry, the resulting structure has unidirectional radiation patterns.

An antenna is described which is an inclined form of a previously reported planar log-periodic antenna.[1] The planar antenna is based on the structure formed by joining, in all four quadrants, the points given by

$$y_{n+1} = \tau y_n = \tau x_n = x_{n+1} \quad (1)$$

on a set of orthogonal xy-axes; τ is a scaling factor. If the geometry is considered as two complementary patterns, and one of these is realised in metal, and if feeder lines are added along the positive and negative y-axes, the resulting structure forms an antenna which exhibits radiation patterns similar to those of a halfwavelength dipole, but which has a bandwidth that can be extended as far as desired by choice of the maximum and minimum x and y values in eqn. 1. DuHamel and Ore[2] have shown that two types of planar log-periodic antenna, the 'circular-tooth' antenna of DuHamel and Isbell[3] and their own 'trapezoidal-tooth' antenna,[2] can be inclined about their axes of symmetry perpendicular to the feed lines to form antennas which give undirectional radiation patterns. This approach has been applied to the above mentioned planar antenna also, and results are described below.

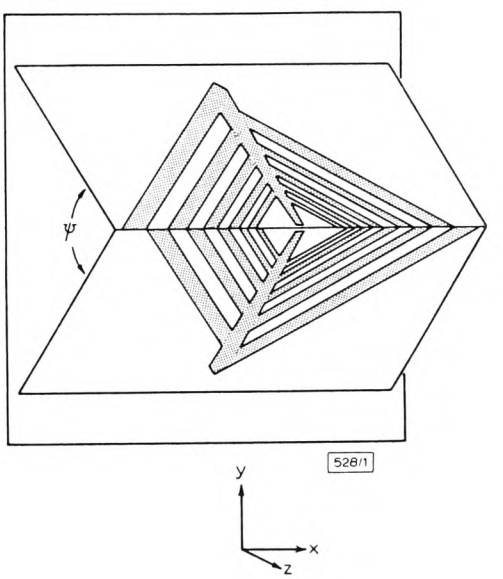

Fig. 1 *Log-periodic antenna*
Only five of the eight elements per quadrant are shown

A 4:1 bandwidth antenna with a scaling factor of $\tau = 0.85$ was constructed as illustrated in Fig. 1. The antenna was fabricated from two rectangular pieces of copper-clad glass-fibre/epoxy printed-circuit board,* the unwanted copper being removed by cutting and peeling. Dimensions of the printed-circuit boards were 304 × 152 mm and these were mounted above a square Perspex plate of 305 mm side, in such a way that the included angle ψ was variable. The antenna was designed for a frequency range of 500 to 2000 MHz by a semiempirical method. When operating at any one frequency, it is believed that a band of elements, or teeth, are excited on each side of the antenna about the x axis, and that the centre of the bands occurs where teeth are a quarter of a wavelength long. Therefore, for an antenna to cover a free-space wavelength range of λ_1 to λ_2, where $\lambda_2 > \lambda_1$, it is not sufficient to choose the x and y values from eqn. 1 to give extreme teeth lengths of $\lambda_1/4$ and $\lambda_2/4$; rather, it is necessary to have extreme lengths $k_1(\lambda_1/4)$ and $k_2(\lambda_2/4)$, where k_1 and k_2 are empirically determined constants. Further, if the radiating metal structure is on a dielectric base, as in this case, the dielectric loading must be taken into account. Bawer and Wolfe[4] have shown that an approximate effective permittivity for strip transmission lines on one side of a dielectric board is 0·75 times the permittivity of the base material. This approximation is applied here and leads to the maximum and minimum x and y values:

$$\left.\begin{aligned} x_{min} = y_{min} &= \frac{k_1 \lambda_1}{2\sqrt{\{6\varepsilon_r\}}} \\ x_{max} = y_{max} &= \frac{k_2 \lambda_2}{2\sqrt{\{6\varepsilon_r\}}} \end{aligned}\right\} \quad \ldots\ldots\ldots \quad (2)$$

The relative permittivity ε_r of the printed-circuit-board dielectric was taken as 2 and the constants were determined from a 1·9:1 bandwidth antenna and found to be $k_1 = 0.6$ and $k_2 = 1.75$. Using these factors and taking into account practical constraints, maximum and minimum x and y values of 151 and 13 mm were chosen. The antenna was constructed with 5°-included-angle feeder line sections on the y-axis to make a truly log-periodic structure, in contrast to previous antennas where parallel-sided lines have been used. The structure was fed with a 2·159 mm semirigid cable with its outer jacket soldered to one feeder line and its inner conductor soldered to the start of the other feeder arm to form a frequency-independent balun.

Radiation-pattern measurements were made on an elevated outdoor range of 14 m length and 9 m height.

Table 1 VARIATION OF AVERAGE BEAMWIDTH WITH ψ

ψ	Average 3 dB beamwidth (E plane)	Average 3 dB beamwidth (H-plane)
90°	84°	100°
60°	85°	123°
30°	83°	138°

The antenna was found to exhibit linear polarisation with the E-field direction parallel to the x-axis on the co-ordinate system of Fig. 1. Patterns were found to be undirectional with main lobe peaks in the $+z$-direction. Boresight cross-polarisation levels were measured at 1000 MHz and found to be −28·3 dB at $\psi = 90°$, −27·4 dB at $\psi = 60°$ and −29·3 dB at $\psi = 30°$. Radiation patterns were recorded at 100 MHz intervals over the band for three values of ψ, and it was seen that halfpower beamwidths varied by approximately plus and minus 20° about an average value. Table 1 shows these, and, comparing these data with those for the planar antenna ($\psi = 180°$), it can be seen that the average E-plane beamwidth does not vary with ψ, but the average H-plane beamwidth decreases from 360° at $\psi = 180°$ to, it is supposed, some maximum value between $\psi = 180°$ and $\psi = 90°$. Thereafter, as ψ decreases, the beamwidth increases to 138° at $\psi = 30°$. Fig. 2 shows some measured patterns. Experiments showed that if the Perspex mounting plate was replaced by a metal one, the pattern backlobes were greatly decreased without significant effect on the main lobe.

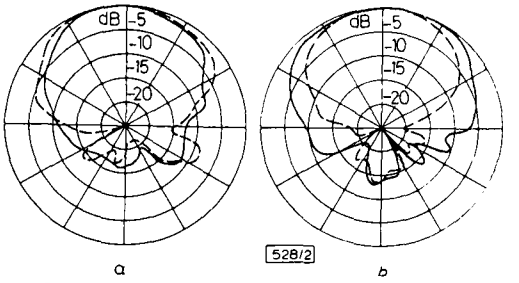

Fig. 2 *Radiation polar diagrams of antenna at 1400 MHz*
Solid lines are H-plane patterns, broken lines are E-plane patterns
(*a*) $\psi = 90°$
(*b*) $\psi = 30°$

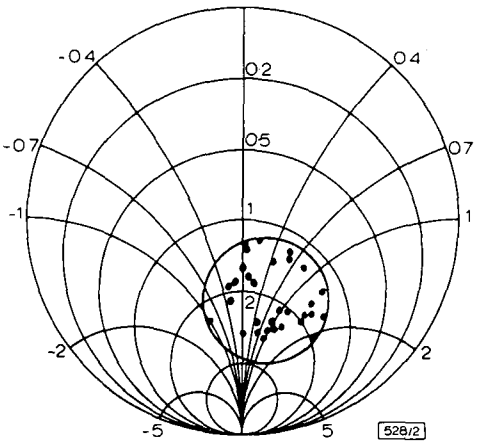

Fig. 3 *Input impedance of antenna*
$\psi = 90°$. From 500 to 2000 MHz in 50 MHz intervals

Fig. 3 shows a Smith-chart plot of the input impedance of the antenna with $\psi = 90°$. All measured points are under a circle which, if transferred to the centre of the chart, would represent a v.s.w.r. of 1·8:1. This shows the impedance-match potential of the antenna if fed with a wideband transforming balun, as has been demonstrated for the planar antenna.[1] One interesting feature of this antenna was that the average impedance was found to be 120 Ω rather than 150 Ω as seen with previously constructed antennas of this type. It is thought that the impedance change was due to the tapered feeder line.

It can be seen from Fig. 3 that the impedance is slightly inductive. This is a well known effect with log-periodic antennas and is caused by element truncation; it can be compensated for by shunt capacitance at the feed point.[5]

Variation of impedance with ψ is small. Measurements at $\psi = 180°$, 90°, 60° and 30° showed that the average impedance (the centre of the impedance circle) was constant, but that the radius of the circle increased slightly as ψ was decreased, from a v.s.w.r. of 1·7:1 relative to the mean at $\psi = 180°$ to 2:1 at $\psi = 30°$.

It is interesting to compare these measured characteristics with the reported characteristics of the circular- and trapezoidal-tooth antennas. Both of these exhibit a large decrease in average impedance with decreases in ψ; for the trapezoidal antennas a variation of 170 to 105 Ω was noted for a decrease in ψ from 180° to 60°. The normalised v.s.w.r. of the trapezoidal antenna increases only slightly to 1·6:1 at $\psi = 60°$, but the circular-tooth antenna attains a normalised v.s.w.r. of 3·5:1. No information is apparently available concerning the variation of beamwidth of the two antennas with ψ, but it seems that, in general, the beamwidths were smaller; typical E- and H-plane beamwidths of 60° and 90° are quoted for the circular-tooth antenna; for the trapezoidal antenna the corresponding figures are 65° and 85°.

In conclusion, it is worth noting that the inclined antenna may prove useful as a low-cost wideband feed for

* Formica CGP75

parabolic-reflector antennas at the lower microwave frequencies in the way that log-periodic dipole arrays are now used,[6] except that, because of its more compact structure and therefore smaller phase-centre variation, the inclined-antenna-and-reflector combination has a potentially larger available bandwidth.

K. M. KEEN

16th August 1976

European Space Research & Technology Centre
Noordwijk, The Netherlands

References

1 KEEN, K. M.: 'A planar log-periodic antenna', *IEEE Trans.*, AP-22, pp. 489–490
2 DUHAMEL, R. H., and ORE, F. R.: 'Logarithmically periodic antenna designs'. IRE National Convention Record, 1958, Pt. 1, pp. 139–151
3 DUHAMEL, R. H., and ISBELL, D. E.: 'Broadband logarithmically periodic antenna structures'. *ibid.*, 1957, Pt. 1, pp. 119–128
4 BAWER, R., and WOLFE, J. J.: 'A printed circuit balun for use with spiral antennas', *IRE Trans.*, 1960, MTT, pp. 319–325
5 RADFORD, M. F.: 'Logarithmic aerial for bands 4 and 5', *Wireless World*, Oct. 1964, pp. 526–528
6 MCINNES, P. A., MUNRO, E. W., and WHITTAKER, A. J. T.: 'Radiation patterns of paraboloid with log-periodic dipole feed', *Electron. Lett.*, 1971, 7, pp. 669–671

CLASS OF WAVE DIGITAL FILTERS CONSISTING ONLY OF ADDERS AND MULTIPLIERS

Indexing terms: Adders, Digital filters, Multiplying circuits

In the letter, a class of wave digital filters is indicated which can be realised without using any subtraction operation. This simplifies the hardware circuit to be constructed.

In a recent article,[1] Fettweis and Meerkötter have given some new adaptor realisations and equivalences. We may conclude that we now have available a 2-port adaptor and 3-port adaptors (with or without a matched port) having the following property: the sign invertors necessary in these realisations are situated directly at an adaptor input or output. This is shown symbolically in Fig. 1, showing an n-port adaptor having a sign invertor directly at input a_1 and output b_n. This property can be used to obtain a class of wave-digital-filter structures having no internal subtraction operation. We shall only indicate this class by giving two examples.

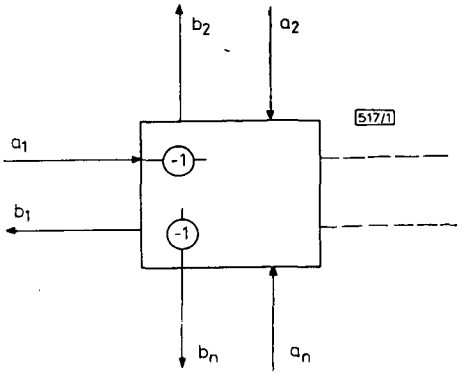

Fig. 1 *n-port adaptor having invertor at input a_1 and output b_n*

Example 1: In Fig. 2, a possible translation of a cascade of two unit elements[2] is shown. The internal structure of the 2-port adaptor is shown in Fig. 3, as given by Fettweis and Meerkötter.[1] Using the equivalence given in Fig. 4, the two invertors internal in Fig. 2 can be shifted to the filter input or output. If we then neglect the invertors resulting at inputs or outputs, having no essential influence on the filter characteristic, we have obtained a structure without any subtraction operation. It follows easily that this remains true for a cascade of an arbitrary number of unit elements. Replacing some or all delay elements of delay T by delay elements of delay $2T$ does not affect this property. This way a bandpass or bandstop filter with centre frequency $\frac{1}{4}\omega_s$ may be obtained.

Example 2: A translation of Fig. 5 is given in Fig. 6, where matched ports are indicated as in Reference 3. The internal structure of the adaptors is given in Reference 1. It is readily seen in Fig. 6 that the invertors cancel out (possibly except for an invertor at inputs or outputs, which can mostly be neglected). Again, a structure results without subtraction operations. Additionally, it can be shown that Fig. 6 is not the only translation of Fig. 5 having this property.

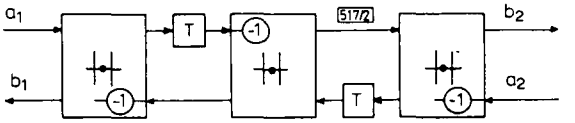

Fig. 2 *Wave-digital translation of a cascade of two unit elements*

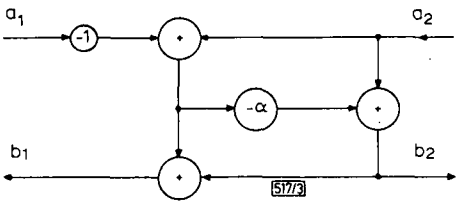

Fig. 3 *Internal structure of adaptors used in Fig. 2*
$\alpha = 2R_2/(R_1+R_2)$. R_1 and R_2 are the corresponding port resistances

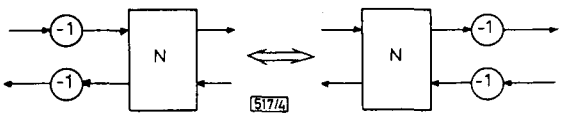

Fig. 4 *Equivalence showing possibility of shifting two invertors*

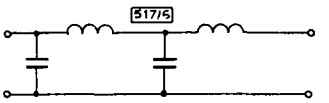

Fig. 5 *Fourth-order lowpass ladder filter*

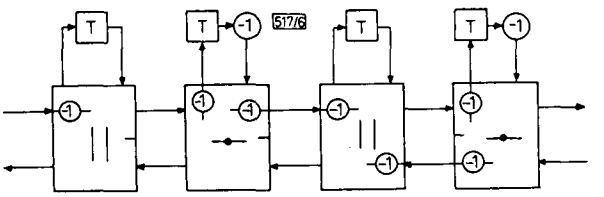

Fig. 6 *Wave-digital translation of Fig. 5*
Using 3-port adaptors given in Reference 1

It follows that the property remains if a lowpass ladder of arbitrary order is translated. Again, replacing some or all of the delay elements of delay T by delay elements of delay $2T$ does not affect the property. It can be shown that all other cases of introducing resonant circuits in shunt or series arms of the ladder results in the appearance of one invertor per resonant circuit whic cannot be removed. More details of the above indicated class of filter structures will be published elsewhere. In any case, the hardware realisation will be simplified, owing to the fact that no adder/subtractor building blocks are needed, but only adders and 2s complement multipliers.

Publication P12. **K.M. KEEN,** ***Simulation of a proposed near field to far field measurement system.*** **Electronics Letters, Vol. 13, No. 8, April 14 1977, pp 225-226.**

Gaussian process obtained from evaluation of the a_is by using

$$m_k = \frac{1}{n}\sum_{1}^{n} a_i^k \quad \ldots \quad (12)$$

While skewness and curtosis do not exhibit remarkable differences from those of the pure Gaussian process (or from theoretical values), the variance μ_2 for g.f.s.w. is surprisingly low. To obtain more information about g.f.s.w., the cumulative distribution was also evaluated by using 10^5 single events. From the properly scaled diagram (Fig. 1), it can be seen that it hardly deviates from true Gaussian; instead of a straight line, the actual curve is very slightly S-shaped.

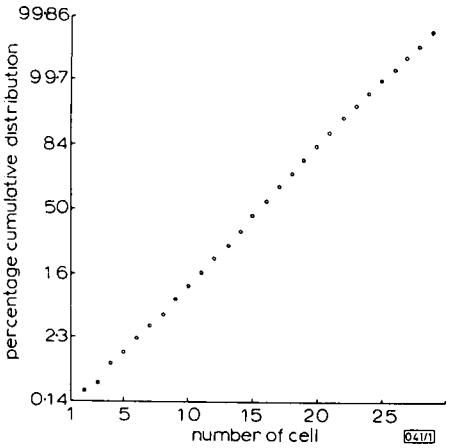

Fig. 1 *Cumulative distribution of 10^5 g.f.s.w. data*

The variance of variance is even greater than for a Gauss–Poisson square wave. While $\sigma_{GP}^2/\mu_{2GP} = 0{\cdot}055$, we have $\sigma^2{}_{GF}/\mu_{2GF} = 0{\cdot}123$, and, for comparison, $\sigma_G^2/\mu_{2G} = 0{\cdot}02$ for a true Gaussian process, supposing the conditions above hold.

Conclusion: In an earlier letter[1] it was shown that the high variance of variance of some kinds of excess noise can be explained by supposing a square-wave-like stochastic process, which corresponds well to certain physical models. The former simulations for Poissonian changeover distribution gave a threefold increased variance compared with that of a true Gaussian process. Now, a reciprocal changeover distribution which may lead to the $1/f$ power spectrum has been investigated, and it exhibited even higher variance of variance. The physical background and topology of the model suggested earlier (Fig. 2 of Reference 1) remains unchanged with the new stochastic process.

A. AMBRÓZY

14th March 1977

Department of Electronics Technology
Technical University, Budapest
H-1521 Budapest, Hungary

References

1 AMBRÓZY, A.: 'Variance noise', *Electron. Lett.*, 1977, **13**, pp. 137–138
2 VAN DER ZIEL, A.: 'Fluctuation phenomena in semiconductors' (Butterworths, London, 1959)
3 SHREIDER, YU. A.: 'Method of statistical tests (Monte Carlo methods)' (Fizmatgiz, Moscow, 1962) (In Russian)

SIMULATION OF A PROPOSED NEAR-FIELD-TO-FAR-FIELD ANTENNA MEASUREMENT SYSTEM

Indexing terms: Antenna radiation patterns, Digital simulation

A new antenna-pattern measurement method for antennas with large far-field distances is proposed. The method is applicable to conventional antenna ranges with two axis mounts and with pattern recording in amplitude only. It requires only a few minor items of additional equipment. A computer simulation has been carried out and the results are presented.

The far-field characteristics of the majority of microwave antennas can be determined on conventional measurement ranges in the normal way, i.e. by rotating the antenna and monitoring its radiation pattern with a remote antenna situated a sufficient distance away. However, there are cases —either because the Rayleigh criterion does not apply, or because the antenna aperture is large in terms of the operating wavelength—where the need for very large range distances precludes conventional methods and some form of near-field measurement method may be necessary. A current example is a shaped-beam satellite antenna for Earth coverage,[1] for which an 'intermediate-range-distance' facility has been set up.[2] On this range, both phase and amplitude are monitored, and the quasi-near-field information is transformed by computer processing to give the far-field radiation patterns. This type of range has the additional usefulness that it can be operated in the conventional mode for measuring the majority of antennas.

From the reverse point of view, existing conventional ranges could be adapted to this system for the measurement of antennas with large far-field distances. The only drawback being that the above mentioned range uses a sophisticated (and expensive) phase and amplitude receiver, which most ranges do not have. In an attempt to extend the capabilities of the ESTEC measurement facility without recourse to a phase-and-amplitude receiver, a new intermediate-range method has been devised, whereby the phase information is extracted from interference patterns, but in a different way from that accomplished with the holographic technique.[3] The new technique, described below, has been simulated by a series of computer programs prior to implementing it. Results of the simulation are presented.

In Fig. 1, antenna *A* is the antenna to be measured and is situated on a 2-axis mount, *B* is a reference antenna, which is static, and *C* is the remote antenna. The Figure shows the measurement hardware in an anechoic chamber, but the system is the same for indoor or outdoor ranges. Fig. 2 shows the feeding circuit, which includes a phase shifter able to switch from some arbitrary zero to +90° and +180° relative to that zero.

The method can be illustrated by first considering the treatment of data from azimuth (equatorial cut) rotations. Eqn. 1 represents the near-field distribution at *C* of the antenna *A*

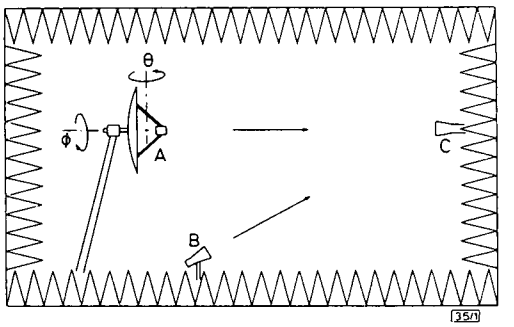

Fig. 1 *Measurement-method geometry*
A is the antenna undergoing measurement, *B* is a fixed reference antenna and *C* is the fixed remote antenna

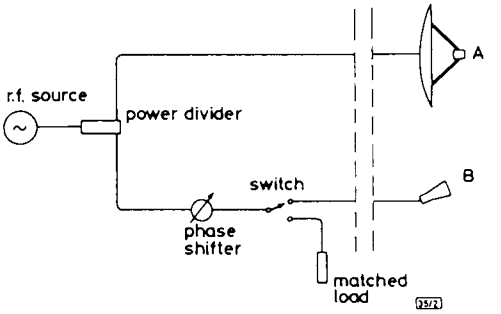

Fig. 2 *Feeding circuit of antennas A and B*

radiating alone, and eqn. 2 represents its far-field distribution:

$$D_1(\theta) = A_1(\theta)\exp(j\psi_1(\theta)) \quad . \quad . \quad . \quad . \quad . \quad . \quad . \quad (1)$$

$$D_2(\theta) = A_2(\theta)\exp(j\psi_2(\theta)) \quad . \quad . \quad . \quad . \quad . \quad . \quad . \quad (2)$$

What is required is the far-field radiation pattern, i.e.

$$P_{dB}(\theta) = 20\log_{10}\left[\frac{A_2(\theta)}{A_2(0)}\right] \quad . \quad . \quad . \quad . \quad . \quad . \quad . \quad (3)$$

The amplitude distribution $A_2(\theta)$ is linked to the parameters $A_1(\theta)$ and $\psi_1(\theta)$, and these are found as follows:

With antenna B switched out, a near-field power-level pattern is recorded. Ignoring the decibel scaling and constant of proportionality, this can be described by

$$P_1(\theta) = A_1^2(\theta) \quad . \quad . \quad . \quad . \quad . \quad . \quad . \quad . \quad . \quad . \quad (4)$$

Then, with the reference antenna switched in and the phase shifter set to 0°, 180° and then 90°, three more power-level patterns are recorded. These are $P_2(\theta)$, $P_3(\theta)$ and $P_4(\theta)$, respectively. The near-field amplitude can be obtained from eqn. 4 directly, and it can be shown that the phase is given by

$$\cos[\psi_1(\theta)-\phi_0] = \frac{P_2(\theta)-P_3(\theta)}{4\sqrt{\left\{\frac{P_1(\theta)}{2}[P_2(\theta)+P_3(\theta)-2P_1(\theta)]\right\}}} \quad . \quad . \quad . \quad (5)$$

and

$$\sin[\psi_1(\theta)-\phi_0] = \frac{2P_4(\theta)-[P_3(\theta)+P_2(\theta)]}{4\sqrt{\left\{\frac{P_1(\theta)}{2}[P_2(\theta)+P_3(\theta)-2P_1(\theta)]\right\}}} \quad . \quad . \quad . \quad (6)$$

The constant ϕ_0 has no effect on the subsequent transformation and can be ignored; it is actually the real value of the arbitrary zero of the phase shifter. To extract $\psi_1(\theta)$ from eqns. 5 and 6, it is only necessary to evaluate one equation and find the arithmetic sign of the other.

The above outlines the basis of the measurement technique; sets of four patterns are recorded, three of these being interference patterns, and, from each set, a phase distribution and an amplitude distribution are extracted by data processing. If this is done over the entire spherical envelope about the antenna undergoing measurement, and in two orthogonal polarisations, the resulting phase and amplitude information can be processed by a near-field-to-far-field-transformation computer program. The data sampling about antenna A requires a 2-axis positioner, but many conventional ranges have these, as sampling in this fashion is carried out for the measurement of directivity.[4] Although eqns. 5 and 6 were derived from azimuth rotations only, they can be extended to either conical (constant θ) or great-circle (constant ϕ) sampling over the spherical envelope.

Before trying the technique in practice, a computer simulation was made with a mathematical model of an array of 17 halfwave dipoles with interelement spacings of 1·2 wavelengths at a frequency of 2·4 GHz. In the array, the dipoles were equally fed in amplitude and phase, giving a far-field radiation pattern with a main beam of 2·5° halfpower beamwidth in the array plane, two prominent sidelobes and many minor lobes. The Rayleigh distance for the array is 92 m. The near-field sampling was made in E_θ and E_ϕ components, and, to simplify the simulation, the array was placed along the $\theta = 0°$ axis of the measurement co-ordinate system, so that the E_ϕ field was always zero. The near-field range length was set at 5 m and antenna B was placed this same distance below A and inclined at 45° to the horizontal. The parameters of the feeding circuit were chosen such that, with the main-beam peak of the array directed towards C, the field amplitudes from antennas A and B were equal at C.

Fig. 3 shows the power-level pattern $P_1(\theta)$ of the array, and the unbroken curve of Fig. 4 shows the directly calculated far-field pattern of the array. In the measurement simulation, after the amplitude and phase data was extracted from the sets of four near-field distributions, it was transformed to the far-field pattern by using the computer program SNIFT.[5] Outputs from this are shown as dots on Fig. 4, and agreement with the directly calculated pattern is apparent.

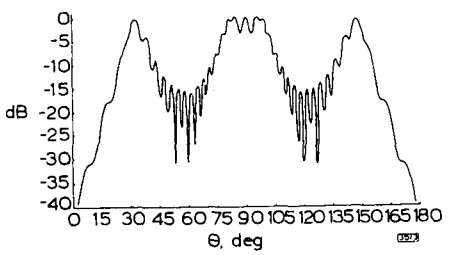

Fig. 3 *Power-level pattern $P_1(\theta)$ of 17-dipole array at 5 m distance*

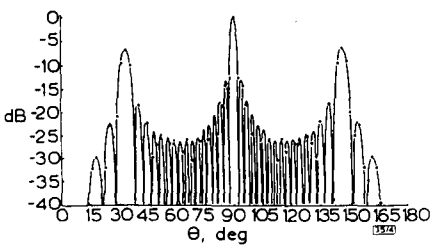

Fig. 4 *Far-field pattern of 17-dipole array*

Unbroken line is the calculated pattern at infinity, dots are from the simulated near-field measurements, phase extraction and near-field-to-far-field transformation

K. M. KEEN

9th March 1977

European Space Research & Technology Centre
Noordwijk, The Netherlands

References

1 COWAN, J. H.: 'A shaped beam antenna for a maritime communications satellite' *in* 'Antennas for aircraft and spacecraft'. IEE Conf. Publ.,128, 1965, pp. 101–106
2 WOOD, P. J., and LOCKETT, N. J.: 'A new type of test range for satellite-antenna polar-diagram measurements'. *ibid.*, pp. 186–191
3 BENNETT, J. C., ANDERSON, A. P.,, MCINNES, P. A., and WHITAKER, A. J. T.: 'Microwave holographic metrology of large reflector antennas', *IEEE Trans.*, 1976, AP-24, pp. 295–303
4 HOLLIS, J. S., *et al.*: 'Microwave antenna measurements' (Scientific-Atlanta Inc., 1970)
5 JENSEN, F.: 'SNIFT—computer program for spherical near-field far-field technique'. Appendix E to TICRA Final Report S-45-01 under ESTEC contract 2478/75AK

MILLIMETRE-WAVE S.S.B. MIXER WITH INTEGRATED LOCAL-OSCILLATOR INJECTION

Indexing term: Mixers

A description of a mixer mount with integrated image filter and l.o. injection filter is presented. The image filter is a high-pass filter using the cut-off properties of a circular waveguide section. The l.o. power is coupled selectively via a TE_{111}-mode filter into the mixer waveguide. The i.f. matching transformer has been designed by a microstrip technique.

Introduction: Usual mm-wave mixers[1,2] need additional filter and coupling components for the suppression of the image frequency and the injection of the l.o. power. These components are lossy and reduce the performance of low-noise mixers. To minimise noise temperature, the filters have been integrated into the mixer mount, giving a substantial improvement in the total noise figure, compared with the former design presented in Reference 1. The local oscillator used is a Gunn diode with centre frequency at 75 GHz and a tuning range of ± 100 MHz. The intermediate frequency of the mixer is 3·7–4·2 GHz.

Publication P13. K.M. KEEN, *An interference pattern intermediate distance antenna measurement method.* ESA Workshop, 'Antenna Testing Techniques' ESA SP-127, May 1977, pp 137-141.

AN INTERFERENCE PATTERN INTERMEDIATE DISTANCE ANTENNA MEASUREMENT METHOD

K.M. Keen

European Space Research and
Technology Centre (ESTEC)
Noordwijk, The Netherlands

ABSTRACT

A new antenna pattern measurement technique for antennas with large far field distances is described. The method, the essence of which is phase extraction from interference patterns, is applicable to conventional ranges with 2 axis positioners and amplitude only receivers. It requires only a few minor items of additional equipment.

The philosophy behind the method is that antennas not amenable to conventional far field measurement techniques are comparatively rare, and therefore the construction of special facilities for these cases is, in normal circumstances, counter cost effective. A better solution is to have some method whereby both phase and amplitude can be monitored at an intermediate distance on a conventional range, then to use data processing to get the far field patterns.

Keywords: Antenna measurements, interference, far field, intermediate distance.

1. INTRODUCTION

The far field characteristics of the majority of microwave antennas can be determined on conventional measurement ranges in the normal way, i.e. by rotating the antenna and monitoring its radiation pattern with a remote antenna situated a sufficient distance away. However, there are cases,-either because the Rayleigh criterion does not apply, or because the antenna aperture is large in terms of operating wavelength,- where the need for very large range distances precludes conventional methods and some form of near field measurement method may be necessary. A current example is the MAROTS satellite antenna for Earth coverage (Ref.1) for which an 'intermediate range distance' facility has been set up (Ref.2). On this range, both phase and amplitude are monitored, and the quasi near field information is transformed by computer processing to give the far field radiation patterns. This type of range has the additional usefulness in that it can be operated in the conventional mode for measuring the majority of antennas.

From the reverse point of view, existing conventional ranges could be adapted to this system for the measurement of antennas with large far field distances. The only drawback being that the above mentioned range uses a sophisticated (and expensive) phase and amplitude receiver,

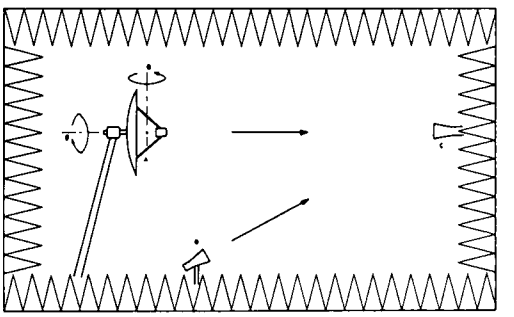

Figure 1. Measurement system configuration. A is the antenna undergoing measurement, B is a fixed reference antenna, and C is the fixed remote antenna

which most ranges do not have. In an attempt to extend the capabilities of the ESTEC measurement facility without recourse to a phase and amplitude receiver, a new intermediate range method has been devised whereby the phase information is extracted from interference patterns, but in a different way from that accomplished with the well known holographic technique (Ref.3) This new technique, described below, has been simulated by a series of computer programs and at the time of writing is being tried in practice.

In figure 1. antenna A is the antenna to be measured and is situated on a 2 axis

positioner, B is a fixed reference antenna and C is the remote antenna. The diagram shows the measurement hardware in an anechoic chamber, but the system is the same for indoor or outdoor ranges. Fig.2 shows the feeding circuit which includes a phase shifter able to switch from some arbitrary zero to +90 degrees and +180 degrees relative to that zero.

The method can be explained as follows. Let the field distribution at the chosen intermediate' distance (i.e. somewhere between, say, the Rayleigh distance and the close proximities of conventional near field probing methods of measurement) and in one known polarisation be represented by

$$D_1(\theta,\phi) = A_1(\theta,\phi)\, e^{j\gamma_1(\theta,\phi)} \qquad (1)$$

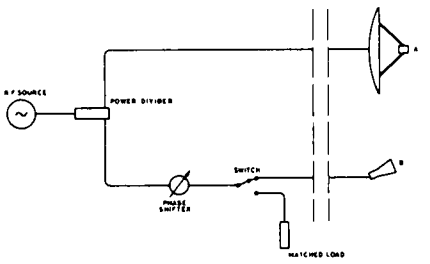

Figure 2. Feeding circuit of antennas A and B

and let the corresponding far field distribution be

$$D_2(\theta,\phi) = A_2(\theta,\phi)\, e^{j\gamma_2(\theta,\phi)} \qquad (2)$$

where A_1 and A_2 are amplitudes and γ_1 and γ_2 are phases. The desired description of the radiating characteristics of the antenna is $A_2(\theta,\phi)$, usually expressed in decibels, together with its orthogonal polarisation counterpart (OPC). These are the far field radiation distributions, and often only certain 'cuts' i.e. radiation patterns, are required. From electromagnetic theory it is known that $A_2(\theta,\phi)$ and its OPC can be found from $A_1(\theta,\phi)$ and $\gamma_1(\theta,\phi)$ plus their OPCs, and there are a number of near field to far field transformation computer programs in existence which do this. The interference method provides a way of determining the quasi near field phase and the procedure is as follows.

With antenna B switched out, the quasi near field power level distribution $P_1(\theta,\phi)$ is recorded. This determines $A_1(\theta,\phi)$ since, ignoring decibel scaling and a constant of proportionality

$$P_1(\theta,\phi) = A_1^2(\theta,\phi) \qquad (3)$$

Then, with the reference antenna switched in and the phase shifter set to zero degrees, +180 degrees, then +90 degrees, three more power level distributions are recorded. These are $P_2(\theta,\phi)$, $P_3(\theta,\phi)$ and $P_4(\theta,\phi)$ respectively. The phase distribution can then be extracted from the four power level distributions using the following relationships.

$$\cos\left[\gamma_1(\theta,\phi)-\delta\right] = \frac{P_2(\theta,\phi) - P_3(\theta,\phi)}{\sqrt{8P_1(\theta,\phi)\left[P_2(\theta,\phi)+P_3(\theta,\phi)-2P_1(\theta,\phi)\right]}} \qquad \ldots\ (4)$$

and

$$\sin\left[\gamma_1(\theta,\phi)-\delta\right] = \frac{2P_4(\theta,\phi)-\left[P_3(\theta,\phi)+P_2(\theta,\phi)\right]}{\sqrt{8P_1(\theta,\phi)\left[P_2(\theta,\phi)+P_3(\theta,\phi)-2P_1(\theta,\phi)\right]}} \qquad \ldots\ (5)$$

The constant δ has no effect on the subsequent transformation and can be ignored; it is actually the real value of the arbitrary zero of the phase shifter. To extract $\gamma_1(\theta,\phi)$ from 4 and 5 it is only necessary to evaluate one equation and find the arithmetic sign of the other.

The above outlines the basis of the measurement technique; four power level distributions are recorded, and from these a phase distribution and an amplitude distribution are extracted by data processing. If this is done in two orthogonal polarisations, the resulting phase and amplitude information can be processed by a near field to far field transformation computer program. The data sampling about antenna A requires a 2 axis positioner, but many conventional ranges have these, as sampling in this fashion is carried out for the measurement of directivity (Ref.4). The spherical envelope about the antenna can be monitored by either great circle (constant ϕ) or conical (constant θ) rotations.

2. COMPUTER SIMULATION

Before trying the technique in practice, a computer simulation was carried out to see if the method was viable and to get some feel for the magnitude of the data processing. The simulation was made with a mathematical model of an array of 17 half wave dipoles (fig. 3) with inter-element spacings of 1.2 wavelengths at a frequency of 2.4GHz. The dipoles were modelled as equally fed in amplitude and phase, and for mathematical convenience the array was oriented along the Z axis of the measurement co-ordinate system. This way, all radiation is in the E_θ polarisation (plus, in the near field, a radial component which we ignore) with zero cross (E_ϕ) polarisation. If R is the range distance (i.e. distance from array co-ordinate system origin to remote antenna) then the near field is given by

$$\bar{E}(\theta) = K\sum_{n=1}^{17}\left[\hat{\theta}\cdot\bar{E}_0(\theta_n)\frac{e^{-jkr_n}}{r_n}\right] \qquad (6)$$

where K is a constant and r_n is related to R, θ and Z_n by

$$r_n^2 = R^2 + Z_n^2 - 2RZ_n\cos\theta \qquad (7)$$

and θ_n is related to θ, R and Z_n by

$$\tan\theta_n = \frac{R\sin\theta}{R\cos\theta - Z_n} \qquad (8)$$

In the above Z_n refers to dipole position relative to the Z axis origin. The expression for the far field is much simpler and is

$$E(\theta) = K\sum_{n=1}^{17}E_0(\theta)e^{jkZ_n\cos\theta} \qquad (9)$$

where the dipole pattern in (9) and (1) is, of course, given by

$$E_0(\theta) = \frac{\cos\left(\frac{\pi}{2}\cos\theta\right)}{\sin\theta} \qquad (10)$$

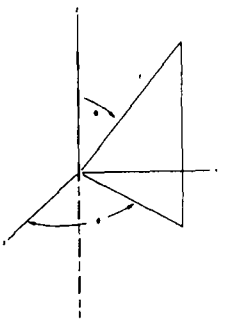

Figure 3. Dipole array geometry (only 7 of 17 dipoles shown)

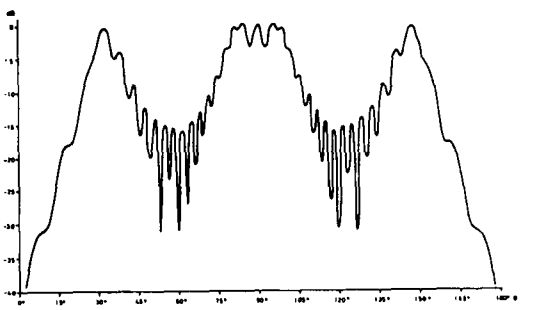

Figure 4. Power level pattern $P_1(\theta)$ of the 17 dipole array at 5 metres distance.

The 17 dipole array has a Rayleigh distance of 97 metres and a far field radiation pattern which exhibits a main beam of 2.5 degrees half power beamwidth in the array plane, two prominent side-lobes and many minor lobes. The near field range length of the simulated system was set at 5 metres, and antenna B was placed the same distance below A and inclined at 45 degrees to the horizontal. The parameters of the feeding circuit were chosen such that with the main beam peak of the array directed toward C, the field amplitudes from antennas A and B were equal at C. Radiation distribution samplings were made at intervals of 2.25 degrees in θ and 90 degrees in ϕ. These spacings were

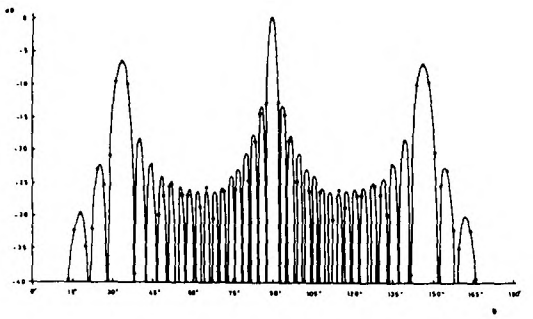

Figure 5. Far field pattern of the 17 dipole array. Continuous line is the calculated pattern at infinity, dots are from the simulated near field measurement and subsequent data evaluation.

dictated by the computer program subsequently used for transformation, and represents the minimum number of samples necessary for the matching of spherical modes for this size of antenna.

Figure 4 shows the quasi near field power level pattern $P_1(\theta)$ of the array, and the continuous line curve of fig. 5 shows the directly computed far field pattern. In the measurement simulation, after the amplitude and phase data was extracted from the sets of four near field distributions, it was transformed to the far field using the computer program SNIFT (Ref.5). Output from this is shown as dots on figure 5, and it can be seen that there is good agreement with the directly computed far field pattern.

3. PRACTICAL IMPLEMENTATION

At the time of writing, trial measurements are proceeding and fig.6 shows the first experimental arrangement. A 1.3m diameter reflector antenna with a log-periodic feed operating at 1.2GHz was chosen as a test case; this has a convenient Rayleigh distance of 13.5 metres, so by making direct measurements well into the far field at 20 metres and then comparing patterns from quasi near field measurements at 3 metres, it is hoped that agreement will be demonstrated. As can be seen from the photograph, crossed log-periodic antennas were initially used for the remote and reference antennas, but it was quickly learned that a wide beam reference antenna was not acceptable as scattering from the rotating model

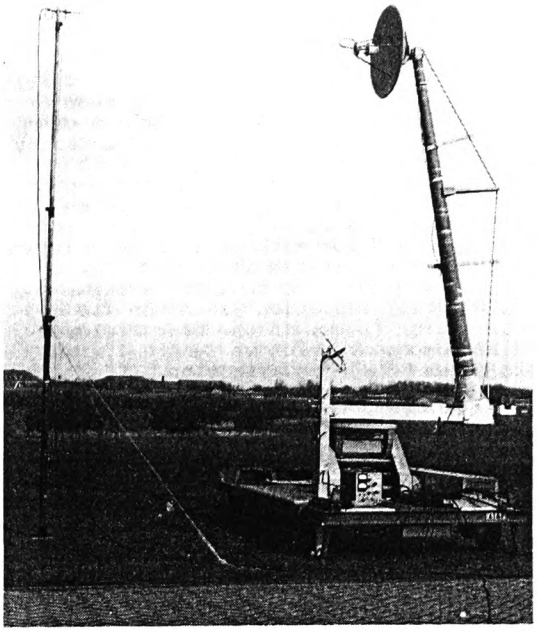

Figure 6. Initial measurement arrangement on the ESTEC site.

tower base caused the reference wave to be far from constant. At this time it was suggested (see acknowlegment) that an alternative to combining the main and reference waves at the remote antenna would be to combine them further on in the microwave circuit, i.e. instead of air propagation for the reference wave, a cable path could be used and the two waves combined in a directional coupler at a point before the receiver. This idea was adopted and fig.7 shows how a coupler can be used in this way.

The upper diagram of fig.7 shows a directional coupler in normal use; if a wave of voltage V is applied at the input port, then K_1V and K_2V are seen at the output ports where K_1 and K_2 are complex constants each composed of an insertion phase and an amplitude reduction term. If the coupler is used to combine two waves of voltage V_B and V_C (lower diagram) applied at ports B and C, then a certain amount of the input energy goes to the load, and an output $K_1V_B + K_2V_C$ is seen at port A. The phase constant introduced by K_1 and K_2 is unimportant as all measurements are in relative phase anyway. The amplitude constants are also unimportant as they have the same effect as changing the amplitude of the reference signal, and this can be set to anything convenient - the only requirement being that it stays constant throughout data recording.

A practical point that has arisen from the use of a coupler in this way is that extra cable must be put into the

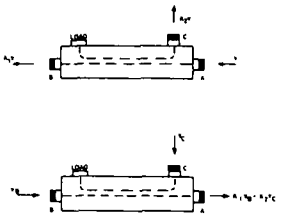

Figure 7. Use of a directional coupler for a two channel combiner. Top - coupler in normal use. Below - coupler combining the reference and direct channel signals.

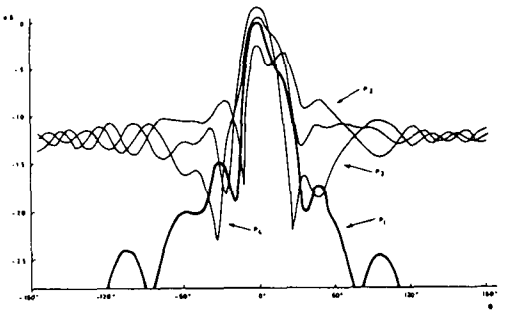

Figure 8. A set of azimuth patterns for the parabolic antenna using a coupler as a combiner.

direct circuit to approximately equalise the direct and reference path lengths in order to minimise dispersion.

Figure 8 shows a typical set of four patterns taken at 3 metres distance while choosing the amplitude relationship of the direct and reference channels. The interference effect can be clearly seen.

4. CONCLUDING REMARKS

A new intermediate distance antenna measurement method has been proposed and has been substantiated by a computer simulation. At the time of writing trial measurements are being carried out and it is hoped that the results from the subsequent data processing will be available in the near future.

5. ACKNOWLEGMENT

The author would like to thank Mr B.E. Westerman and Mr W.B.S.M. Kneefel of the Christiaan Huygenslaboratorium B.V. Noordwijk aan Zee, Holland who are carrying out all measurements and who suggested the use of the directional coupler combiner and the coaxial cable reference wave medium.

6. REFERENCES

1. Cowan J.H. 'A shaped beam antenna for a maritime communications satellite' IEE conference Antennas for Aircraft and Spacecraft June 1975 Conf. publication 128 pp 101-106

2. Wood P.J. and Lockett N.J. 'A new type of test range for satellite antenna polar diagram measurements' IEE conference Antennas for Aircraft and Spacecraft June 1975 Conf. Publn. 128 pp 186-191

3. Bennett J.C., Anderson A.P., McInnes P.A. and Whitaker A.J.T. 'Microwave holographic metrology of large reflector antennas' IEEE Trans Ant. and Prop. AP-24 No 3 May 1976 pp 295-303

4. Hollis J.S. et al 'Microwave antenna measurements' Scientific-Atlanta Inc. July 1970

5. Jensen F. 'SNIFT - computer program for spherical near-field far-field technique' Appendix E to TICRA final report S-45-01 under ESTEC contract 2478/75AK.

Publication P14. K.M. KEEN, *Antenna measurements on an intermediate distance range by using an interference pattern technique.* Electronics Letters, Vol. 13, No. 13, June 23 1977, pp 375-376.

ANTENNA MEASUREMENTS ON AN INTERMEDIATE DISTANCE RANGE BY USING AN INTERFERENCE-PATTERN TECHNIQUE

Indexing term: Antenna radiation patterns

Far-field antenna-pattern measurements have been made by using a recently proposed intermediate-distance technique, whereby phase information is extracted from interference patterns. A comparison between these and radiation patterns obtained on a conventional far-field range demonstrates the viability of the measurement method.

A new intermediate-distance antenna-pattern measurement method was recently proposed and results of a computer simulation were presented.[1] The purpose of the technique is to extend the capabilities of conventional ranges for cases where the Rayleigh distance of antennas to be measured greatly exceeds the available range distance. Only a few simple items of additional equipment are necessary, and, as phase information is extracted from interference patterns, nothing more sophisticated than a conventional amplitude receiver is required. The technique has been tried in practice, and results are presented below.

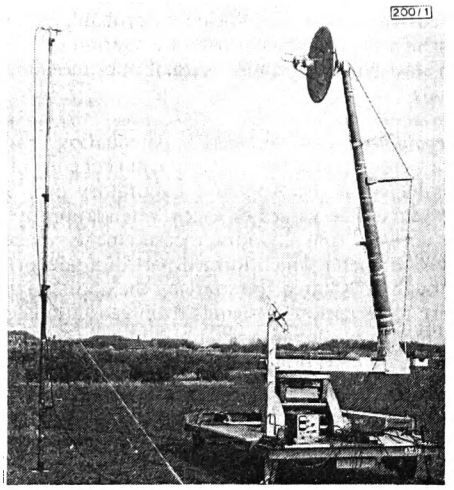

Fig. 1 *Initial measurement arrangement*

Fig. 1 shows the first intermediate-distance measurement arrangement, although, as will be described, this was subsequently modified. In the photograph, the antenna undergoing measurement is a 1·3 m paraboloid and feed. This size of antenna was convenient as a test case, as its Rayleigh distance was small enough for conventional far-field measurements to be made and used as a comparison. The feed was a linearly polarised log-periodic antenna; no attempt was made to optimise its position for the best secondary patterns, as this was not important to the present study. The remote antenna was a crossed log-periodic dipole array as was the interference-wave antenna. Measurements were made at 1200 MHz, ultimately at 3 m range length (the photograph shows a 5 m separation) and also at 20 m range length on a conventional elevated range for comparison. The Rayleigh distance of the paraboloid antenna is 13·5 m.

The purpose of the interference-wave antenna is to provide a constant reference wave for interference-pattern formation at the remote antenna, and, on the original measurement set-up, the ability to do this was tested for by transmitting with the interference antenna alone, receiving with the remote antenna and rotating the test antenna. When this was done, the interference wave was seen to be far from constant because of scattering from the test antenna and its tower and metal base. The obvious solution to this problem would be the use of a more directive interference antenna, but another scheme was proposed at this time and ultimately adopted. With this modification, instead of forming the interference pattern in air from two waves propagated by antennas, the interference-wave antenna is removed, a cable link takes the reference wave to a point beyond the receive antenna and interference is caused by combination of the two waves in a directional coupler. Fig. 2 shows how a directional coupler can be used in this way.

The upper diagram of Fig. 2 shows a directional coupler in normal use; if a wave of voltage V is applied at the input

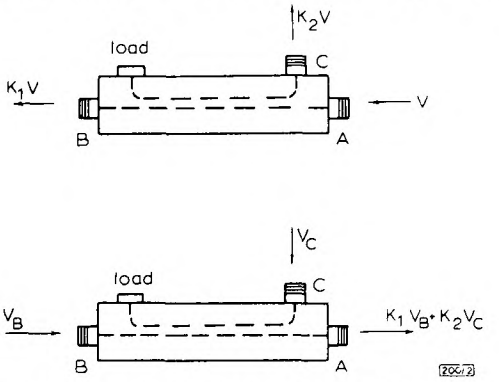

Fig. 2 *Use of directional coupler for 2-channel combiner*
Top: coupler in normal use. Below: coupler combining the reference- and direct-channel signals

port, K_1V and K_2V are seen at the output ports, where K_1 and K_2 are complex constants, each composed of an insertion-phase and an amplitude-reduction term. If the coupler is used to combine two waves of voltage V_B and V_C (lower diagram) applied at ports B and C, a certain amount of the input energy goes to the load, and an output $K_1V_B+K_2V_C$ is seen at port A. The phase constant introduced by K_1 and K_2 is unimportant, as all measurements are in relative phase anyway. The amplitude constants are also unimportant, as they have the same effect as changing the amplitude of the reference signal, and this can be set to anything convenient, the only requirement being that it stays constant throughout data recording.

A practical point that has arisen from the use of a coupler in this way is that extra cable must be put into the direct circuit to approximately equalise the direct and reference path lengths to minimise dispersion.

The direct and interference radiation distributions were sampled in orthogonal linear polarisations at intervals of 5° in θ and 6° in ϕ over the spherical region about the parabolic antenna. The sampled relative power levels were recorded on 8-level punched paper tape to give a resolution of 0·25 dB; this data was transferred to a digital computer for processing with two computer programs. The first of these extracted the amplitudes and phases from the recorded power levels, as described previously,[1] and these values were treated by the near-field-to-far-field transformation program, SNIFT,[2] to give far-field radiation patterns.

Figs. 3 and 4 indicate how the far-field patterns obtained by the interference technique compare with those measured conventionally. Fig. 3 shows H-plane patterns of the paraboloid antenna and Fig. 4 shows E-plane patterns (this plane

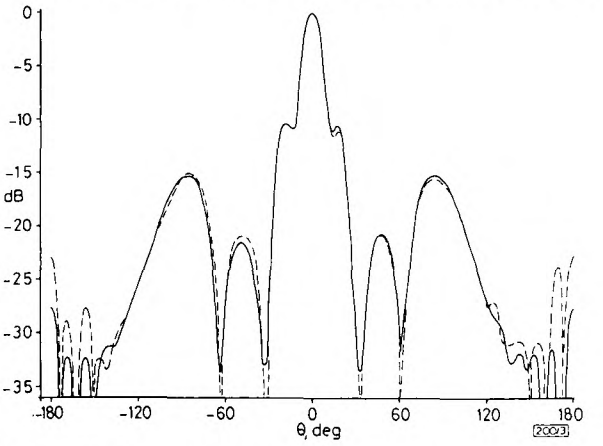

Fig. 3 *H-plane patterns of parabolic antenna*
Full line is from conventional pattern measurement at 20 m, broken line is pattern from interference method at 3 m

contained a feed strut, hence the asymmetry) and in each case the full line represents the conventionally measured pattern

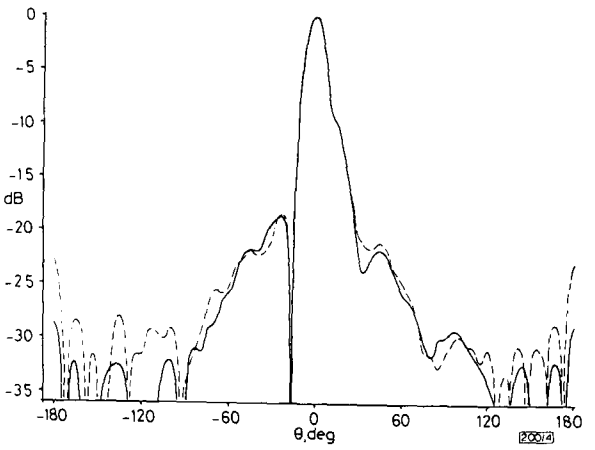

Fig. 4 *E-plane patterns of parabolic antenna*
Full line is from conventional pattern measurement at 20 m, broken line is pattern from interference method at 3 m

and the broken line shows where the interference-technique pattern deviates from it. It can be seen that there is good agreement between patterns measured by the two techniques down to low levels. In general, it is believed that the conventionally measured patterns which were made at a finite distance and in the presence of a ground-reflection level of the order of -30 to -35 dB are the less accurate of the two sets.

Acknowledgments: The author would like to thank B. E. Westerman and W. B. S. M. Kneefel of the Christiaan Huygenslaboratorium B.V., Noordwijk, The Netherlands, for carrying out measurements and for suggesting the use of the directional-coupler combiner. He would also like to thank J. Aasted, Head of the Antennas & Propagation Section, ESTEC, for encouragement, and D. J. Brain, also of ESTEC, for several helpful discussions.

K. M. KEEN* *16th May 1977*

European Space Research & Technology Centre
Noordwijk, The Netherlands

References

1 KEEN, K. M.: 'Simulation of a proposed near-field-to-far-field antenna measurement system', *Electron. Lett.*, 1977, **13**, pp. 225–226
2 JENSEN, F.: 'SNIFT—computer program for spherical near field far field technique'. Appendix E to TICRA Final Report S4501, under ESTEC contract 2478/75AK

* Now with Department of Electrical & Electronic Engineering, Queen Mary College, Mile End Road, London E1 4NS, England

PREDICTION OF MICROWAVE SLANT-PATH ATTENUATION FROM POINT RAINFALL-RATE MEASUREMENTS

Indexing terms: Microwave links, Radiowave propagation, Rain, Satellite links

An experiment is described in which a rapid-response (10 s) raingauge was operated for 3 years with an 11·6 GHz radiometer directed along an inclined radio path such as might be used with a communications satellite. Cumulative statistics of the path attenuation due to rain are computed from the radiometer results and compared with cumulative rainfall-rate statistics for each of the 3-year periods. The spread between successive years is considered to be small enough for reliable predictions of attenuation to be made from the raingauge results. The application to data obtained from slower-response raingauges is considered.

Introduction: The adverse effects of rain on Earth–space propagation, particularly for frequencies above 10 GHz, are well known. Future communications-satellite systems will use frequencies above 10 GHz, and, for planning to proceed, the statistics of the fading that will be obtained on any desired link must be predicted from data already obtained on other links. Such data will relate to climatic conditions different from those occurring on the desired links, and, for predictions to be made, the statistical rainfall characteristics for all the required areas must be known with sufficient accuracy, particularly the statistics relating to the short-term peak rainfall. Unfortunately, the response time of conventional raingauges in the worldwide network is not sufficiently fast for the peak rainfall rate to be recorded accurately. In recent years, however, rapid-response raingauges have been installed in various places, and it is therefore of interest to examine the possibility of using them to estimate long-term attenuation statistics. Much work has been carried out at the Appleton Laboratory by using fast-response raingauges in conjunction with ground–ground links, the results being in course of preparation for publication,* but, in the present letter, an experiment is described in which a rapid-response raingauge was placed near an experimental satellite communications link, so that rainfall rate and excess slant-path attenuation could be compared simultaneously. Resuts obtained are discussed and used to indicate the probable limits of accuracy to which the statistics of path attenuation can be predicted from fast-response point rainfall-rate measurements.

Experimental equipment and technique: Attenuation and rainfall-rate data were obtained from separate, but concurrent, experiments conducted at the Appleton Laboratory over a period of three years. The values of excess attenuation due to rainfall were derived from sky-noise measurements, made by an 11·6 GHz radiometer which formed part of a network set up in the Slough (UK) area for studying the application of space diversity to reception of signals from geostationary satellites.[1] The antenna of the radiometer was 1 m in diameter and was directed at an elevation angle of 29·5° on a bearing of 198·25°. The sky-noise temperature T (kelvins), was sampled every 2·5 s and converted into excess path attenuation A by using the formula

$$A = \log\left(\frac{275}{275-T}\right) \quad \text{decibels}$$

In this expression, a temperature of 275 K is assumed for the absorbing medium. The rapid-response raingauge[2] was approximately 400 m west of the radiometer site on level ground and formed part of an experimental programme designed to investigate rainfall-rate/attenuation profiles on a number of ground–ground links.[3, 4] The integration time was 10 s.

Observations: Fig. 1 shows the cumulative excess-attenuation results for 1973, 1974 and 1975. Other curves were produced for the 3 years which gave rainfall rates exceeded for given percentages of the time. The data for 1974 and 1975 are

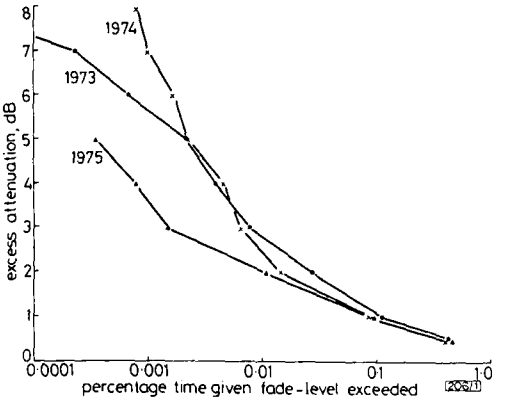

Fig. 1 *Cumulative statistics of excess attenuation at 11·6 GHz*
Elevation angle: 29·5°
Azimuth angle: 198·25°
The 1973 curve excludes data for May and August

* HARDEN, B. N.: Private communication

Publication P15. K.M. KEEN, *VHF turnstile antenna performance as a function of satellite geometry*. Electronics Letters, Vol. 13, No. 21, Oct. 1977, pp 654-656.

the signal when N and f_{ltm} are such that the humps merge together to form a nearly continuous spectrum.

The amplitude and frequency profiles of optimum 4- and 8-pulse signals are shown in Fig. 2 for $f_{ltm} = 10$. These profiles illustrate a general conclusion that, for $N \ll f_{ltm}$, the amplitude profile is nearly flat and the frequency profile is of staircase form. The signal is thus a discrete approximation of a linear chirp signal. When N is of the same order as f_{ltm}, there is no apparent general order in the profiles of the signals.

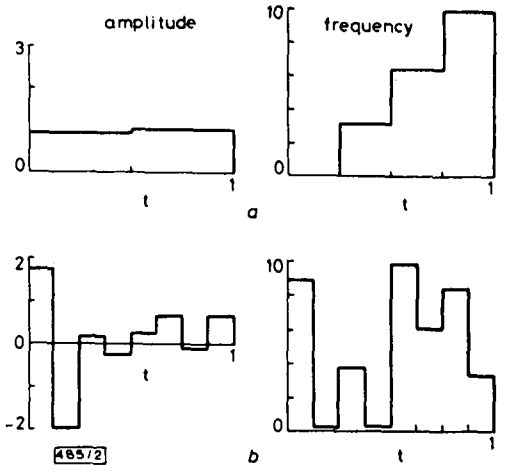

Fig. 2 *Amplitude and frequency profiles of optimum N-pulse amplitude f.s.k. burst*

$f_{ltm} = 10$

Forcing the individual pulse amplitudes to be equal results in a pure f.s.k. signal without any amplitude modulation. The broken line of Fig. 1 shows the variation of C_{min} with f_{ltm} for such a burst with $N = 8$. Again, it is seen that the pure f.s.k. burst is significantly inferior to an amplitude-modulated f.s.k. burst only when N is comparable to f_{ltm}. For $N \ll f_{ltm}$, flattening the signal amplitude results in little loss of clutter performance.

The ambiguity surfaces of several optimum signals have been plotted to obtain their combined range-Doppler resolution and clutter-rejection behaviour. Some of these signals exhibit excellent combined close-target range-Doppler resolution, as shown by a slender central ambiguity peak. For moderate f_{ltm}, the narrow central spike is accompanied by acceptable sidelobe levels elsewhere on the range-Doppler plane. This is not so with higher values of f_{ltm}, for which, although the central spike is finer than for moderate f_{ltm}, the sidelobes are numerous. Many of these sidelobes are unacceptably high and are located very close to the central spike.

P. R. MAHAPATRA

Department of Aeronautical Engineering
Indian Institute of Science
Bangalore 560012, India

30th August 1977

References

1 SPAFFORD, L. J.: 'Optimum radar signal processing in clutter', *IEEE Trans.*, 1968, IT-14, pp. 734–743
2 DELONG, D. F., and HOFSTETTER, E. M.: 'On the design of optimum radar waveform for clutter rejection', *ibid.*, 1967, IT-13, pp. 454–463
3 RUMMLER, W. D.: 'Clutter suppression by complex weighting of coherent pulse trains', *ibid.*, 1966, AES-2, pp. 689–699
4 RIHACZEK, A. W.: 'Principles of high resolution radar' (McGraw-Hill, New York, 1969), chap. 8, pp. 316–323
5 MAHAPATRA, P. R.: 'Optimum compact discrete coded signals for clutter rejection'. Ph.D. thesis, Indian Institute of Science, Bangalore, 1976, chap. 2
6 MAHAPATRA, P. R., and RAMAKRISHNA, S.: 'Compact AM signals for maximum clutter rejection', *IEEE Trans.*, 1977, AES-13, pp. 414–418

V.H.F.-TURNSTILE-ANTENNA PERFORMANCE AS A FUNCTION OF ANTENNA GEOMETRY ON LARGE CYLINDRICAL SATELLITES

Indexing terms: Antennas, Artificial satellites, Computer-aided design

Until recently, development of v.h.f.-turnstile-antenna systems for satellites was carried out mainly empirically by using r.f. models, but computer programs are now available to assist in this. One of these programs has been used to model turnstile systems on large cylindrical satellites (of the size of current European scientific satellites) and some general conclusions have been reached concerning the choice of monopole base radius and inclination.

Since first seen on Sputnik 1, the most common type of satellite antenna for telemetry and telecommand at v.h.f. frequencies has been the 4-whip turnstile antenna. This consists of four monopoles, usually mounted on one surface of the spacecraft, which are fed in progressive phase quadrature but equal amplitudes.[1,2] With such an antenna, a perfectly symmetrical spacecraft, as in Fig. 1*a*, will exhibit circular-polarisation characteristics at the $\theta = 0°$ and $\theta = 180°$ poles (the 'hand' of polarisation depending on the sense of the quadrature phase feeding) and linear polarisation in the equatorial ($\theta = 90°$) zone. The monopoles are approximately a quarter of a wavelength long—small variations are sometimes made in practice for impedance matching—and far-field radiation from such a system derives from the monopoles themselves and from surface currents which are induced on the spacecraft body. For small satellites of the order of one-quarter wavelength in diameter, such as those launched in the late 1950s and early 1960s, most radiation comes from the monopoles. But, for larger satellites, the situation is reversed and it can be difficult to obtain adequate coverage, free of deep dips in the radiation distribution, from satellites larger than about half a wavelength in diameter.

Until recently, v.h.f. antenna systems for satellites were developed almost entirely empirically by using r.f. models (sometimes called 'tinsats') with which measurements are

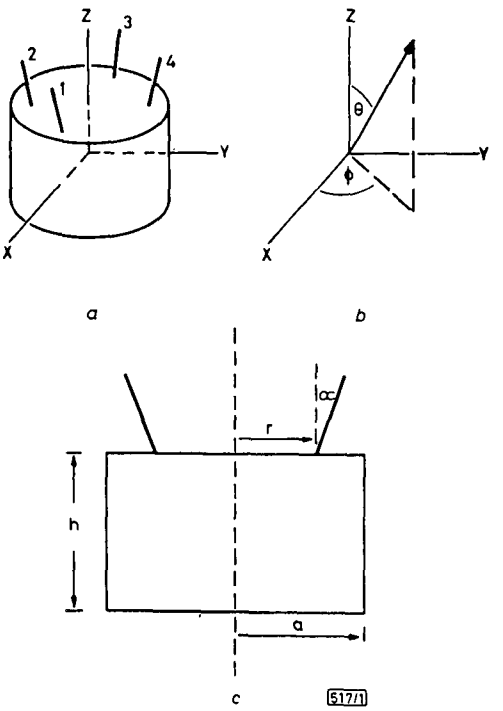

Fig. 1

a Four-whip turnstile antenna on cylindrical satellite
b Co-ordinate system
c Satellite and antenna geometry

carried out on suitable antenna measurement ranges.[3] This procedure can now be augmented by computer simulations using the radiation-pattern-prediction programs developed for the European Space Agency.[4] One of these programs—ROT 2—[5] has been used to model large cylindrical satellites with turnstile antennas. Some general conclusions have been reached concerning the choice of turnstile geometry, which could be of use in the development of future systems. These are the subject of this letter and are outlined below.

Four sizes of 'large' cylindrical satellite were modelled during this study, but most work was concentrated on a spacecraft of 0·71-wavelength diameter and 0·544-wavelength height, this being a mean of the ESA COS-B and the ESA GEOS satellites. These large scientific satellites represent very nearly the limit of satellite size with currently available launch-vehicle fairing space. The modelling frequency was chosen as 142 MHz, halfway between the usual telemetry and telecommand frequencies. Only simple turnstile antennas were modelled, i.e. those with monopoles either vertical or with radial inclination at some angle α, as these are used in the majority of cases.

The effect of monopole inclination on the polar (constant-ϕ plane) radiation patterns is illustrated in Fig. 2. These patterns are for the above-mentioned-size satellite with a monopole-base-radius/satellite-radius ratio fixed at $r/a = 0{\cdot}63$, and the cut is at $\phi = 0°$, although the patterns, which are total power, i.e. the sum of the power densities in the individual polarisations, are almost independent of ϕ. Total-power radiation patterns are of most interest with this type of satellite antenna, as the ground stations generally monitor in two orthogonal polarisations and, in reception at least, employ diversity combination, which, in effect, is very similar to total-power reception. Computations were made for 10° increments in α from $\alpha = 0°$ (vertical whips) to $\alpha = 70°$. It was seen that, as the monopoles are inclined, the radiation decreases in the $+Z$ direction and increases in the $-Z$ direction. This effect increases to a maximum at between $\alpha = 40°$ and $\alpha = 50°$, and then slowly reverses as α increases further. Similar computations that were made with a slightly different satellite geometry (0·78-wavelength diameter, 0·53-wavelength height), but with a much larger monopole base radius at $r/a = 0{\cdot}87$, indicate that inclination effects are much more dramatic with large r/a; in fact, a complete null was seen at 40° for this geometry. However, as will be shown below, large r/a cause excessive equatorial-plane-pattern ripple, and should normally be avoided if possible.

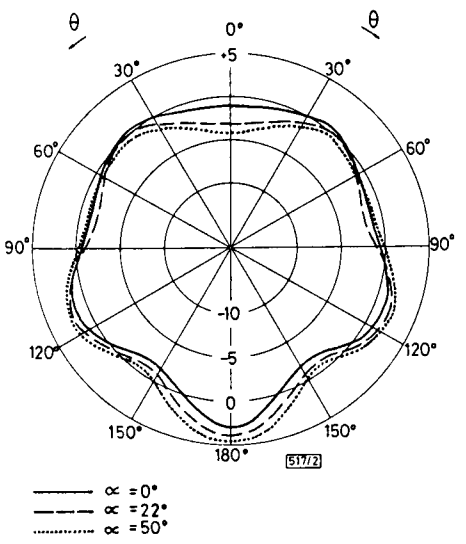

Fig. 2 *Total-power radiation patterns in $\phi = 0°$ plane for three monopole inclination angles*

Radial scale is in dBI

The practical usefulness of this information is as follows. Satellites are rarely simple structures, as they often have deployable booms and other appendages, which, along with the rest of the outer surface of the spacecraft, have currents flowing on them. These boom currents can be thought of as causing radiation which disturbs the distribution from the satellite and turnstile antenna alone. This disturbance is usually detrimental to the radiation distribution; thus the surface currents in the vicinity of the boom should be minimised. For example, if the majority of the booms of a satellite are concentrated on the top ($+Z$ end) surface, the monopoles should be inclined to $\alpha = 40°$ or thereabouts. This gives minimum radiation in the $+Z$ direction, and therefore minimum surface currents on the top surface of the spacecraft. As these currents are minimised, the currents induced on the top surface booms will also be minimised; hence the corresponding disturbance from boom radiation in all regions around the spacecraft can be expected to be as small as possible. Similarly, if there are more booms or objects on the bottom surface than elsewhere, vertical monopoles could be expected to give the most satisfactory radiation patterns.

One final thing to note concerning monopole inclination is that inclination slightly increases the pattern ripple in the equatorial region. For example, with $r/a = 0{\cdot}63$, as described above, the peak/trough ripple changed from 2 dB at $\alpha = 0°$ to 3 dB at $\alpha = 70°$.

Whether the monopoles are inclined or not, changes in the monopole base radius affect the equatorial-plane-pattern ripple such that large r/a give relatively large ripples. Fig. 3, which is from computations on the 0·71-wavelength-diameter space-

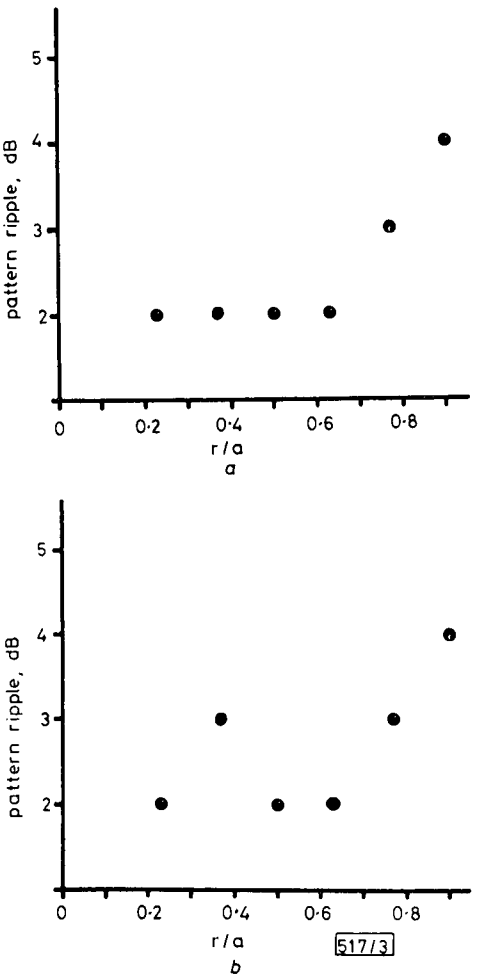

Fig. 3 *Equatorial plane ($\theta = 90°$) peak/trough pattern ripple as a function of r/a*

a $\alpha = 0°$
b $\alpha = 30°$

craft, shows this, and it can be seen that to obtain minimum ripple, r/a should be no greater than about 0·63. The ripples of Fig. 3 are for the total-power equatorial-plane patterns. Incidentally, the computer-derived data from Fig. 3 were only calculated to the nearest decibel. This explains the apparent abruptness of the ripple increase beyond $r/a = 0{\cdot}63$ and of the anomolous hump for the $\alpha = 30°$ case, which is almost certainly far less severe in reality.

Two further sizes of spacecraft were studied, one being about 10% larger than the 0·71-wavelength diameter spacecraft, at 0·78-wavelength diameter and 0·598-wavelength height, and the other about 10% smaller, at 0·64-wavelength diameter and 0·49-wavelength height. The same general behaviour as reported above was seen for these sizes of spacecraft; it seems that the conclusions concerning the choice of monopole base radius and inclination are true in general for large cylindrical satellites.

To sum up, the study shows that, for a v.h.f. turnstile antenna system on a large cylindrical satellite, the monopole base radius should be chosen to be no greater than about 0·6 of the satellite radius, and that the monopole inclination should be chosen according to the presence of booms or other appendages which are likely to be troublesome as regards unwanted 'parasitic' radiation. This study also highlights the usefulness of the pattern-prediction computer programs.

Acknowledgment: This investigation was carried out while the author was at the European Space Research & Technology Centre, Noordwijk, The Netherlands.

K. M. KEEN

Department of Electrical & Electronic Engineering
Queen Mary College
Mile End Road, London E1 4NS, England

12th September 1977

References

1 JACKSON, R. B.: 'The canted turnstile as an omnidirectional spacecraft antenna system'. NASA Report X-712-67-441, 1967
2 NICHOLS, S.: 'Satellite turnstile antennas'. NRL Report, Aug. 1969
3 HOGG, R. W.: 'Measurement techniques for satellite VHF telemetry antennas'. ESTEC Workshop 'Antenna testing techniques', June 1977, Publication SP 127, pp. 77-83
4 BRAIN, D. J., and JENSEN, N. E.: 'ESA computer programs for satellite antenna pattern prediction'. *ESA Sci. & Tech. Rev.*, 1976, 2, pp. 79-90
5 RYDAHL, O.: 'A numerical technique to predict scattering from bodies of revolution (users guide to the computer program ROT 2)'. Technical University of Denmark, Dec. 1975, ESA Contractor Report CR(P)-769

Publication P16. K.M. KEEN, *A computer program system for evaluating partial and total antenna directivities from measured data.* Proceedings IEE, Vol. 124, No. 10, Oct. 1977, pp 1117-1120.

Computer-program system for evaluating partial and total antenna directivities from measured data

K.M. Keen, M.Sc., C.Eng., M.I.E.E.

Indexing terms: *Antenna radiation patterns, Communications computing*

Abstract

A system of three computer programs is described which process data from far-field amplitude antenna pattern measurements to give partial and total directivity mappings (where 'partial directivity' refers to one polarisation only). The measurement data is acquired by sampling the radiation distribution over a spherical region enclosing the test antenna, first in one polarisation and then in the orthogonal polarisation, so that two 'spheres' of information are contained in a measurement data set. A small binary/decimal conversion program processes the two parts of the data set individually, and a data package with a heading containing measurement specifications is then set up. The data package is processed by the main program which integrates to find the isotropic level and then the partial and total directivities, and prints out the values in tabular form. As well as the conversion and main programs, there is an optional program that prints out the contents of the data package in an easily viewable form. This is useful if the input data contains errors.

1 Introduction

If, on a far-field antenna measurement range, the antenna or radiating system under investigation is mounted on a positioner with two independent rotational axes at right angles, then it is possible to make polar diagram measurements that cover the entire spherical region about the antenna. If two 'spheres' of information are recorded, the first in some convenient polarisation and the second in the orthogonal polarisation, then the information can be computer processed to find the isotropic level; and then radiation pattern maps, normalised to the isotropic level, can be printed out in digital form. As an example, Fig. 1 shows a full scale r.f. model of a current ESA satellite undergoing v.h.f. antenna-system measurements on the ESTEC antenna test range; the 4-whip turnstile antenna system can be seen on the foremost face of the spacecraft model. It was mounted on a measurement tower with the geometry and co-ordinate system shown in Fig. 2. This is probably the most common 2-axis measurement geometry and 'spheres' of radiation patterns are made by a continuous ϕ rotation over 360° with θ constant, followed by a θ increment which is then followed by another ϕ rotation and so on, until a 'sphere' consisting of a set of conical cut radiation patterns is collected.

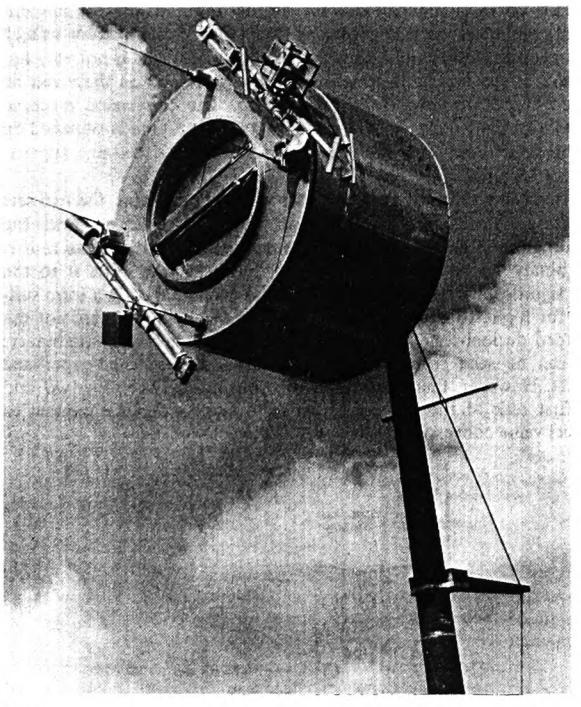

Fig. 1
Photograph of full-scale r.f. model of satellite undergoing v.h.f. antenna measurements

A computer program set is described below which processes 'spheres' of radiation pattern data recorded in digital form and gives partial and total directivity printouts in tabular form. The term 'directivity' used here is a general one and refers to the value in any direction θ, ϕ (see Appendix 8). Directivity information is useful for the following reasons: If the directivity and gain of an antenna are measured, then, within the limits of measurement error, the antenna efficiency can be deduced. Conversely, in some circumstances it is impracticable to measure the gain of an antenna or radiating system, so the directivity is measured instead, and the gain determined by estimating a value for the antenna efficiency. This is often done for omnidirectional v.h.f. satellite antenna systems where efficiencies of $-0{\cdot}5$ dB are typical. Although for some antenna types, e.g. unidirectional narrow-beam types, only the directivity in the boresight direction may be of interest, there are many others where full directivity mapping is of great use. Omnidirectional satellite antenna systems for telemetry and telecommand at either v.h.f. or *S*-band frequencies fall into this category; during launch phase, transfer orbit and final orbit manoeuvres, the spacecraft attains various attitudes with respect to the ground stations with which it must have a 2-way link. Obviously, before the spacecraft is 'flown', its radiation properties must be known fully so that link budgets can be established, and partial and total directivity mappings can be used for this. In such cases, the total-power directivities can be of special importance as many ground stations receive telemetry simultaneously in orthogonal polarisations and mix the powers received in the two channels together in a way which, in many cases, is equivalent to total power reception.

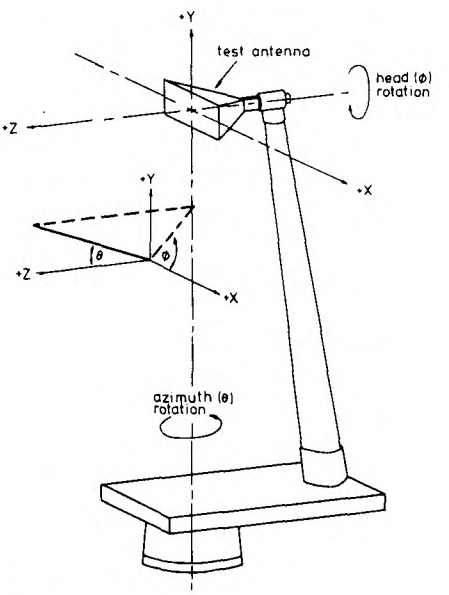

Fig. 2
Measurement geometry and co-ordinate system

Program CP156 E, received 23rd December 1976. The program and accompanying documentation are held in the IEE Program Library, IEE, Savoy Place, London WC2R OBL, England. Copies are available on application and on payment of a charge of £30.50

Mr. Keen is with the ERA RF Technology Centre, Cleeve Road, Leatherhead, Surrey, England

The measurement technique described here has been in existence for, perhaps, 15 years; however, there are comparatively few European establishments (perhaps 5 or 6) that use it. The purpose of this paper is to make the technique more widely known, and to describe a computer program system which can be used for data evaluation.

2 Theory

Let the total radiated power of an antenna system be P_T. If $U_a(\theta, \phi)$ represents the power radiated per unit solid angle in direction θ, ϕ in some polarisation a, and $U_b(\theta, \phi)$ represents the corresponding quantity in the orthogonal polarisation b, then, using the definitions described in Appendix 8, partial directivities for each polarisation can be written as follows:

$$D_a(\theta, \phi) = \frac{4\pi U_a(\theta, \phi)}{P_T} \tag{1}$$

$$D_b(\theta, \phi) = \frac{4\pi U_b(\theta, \phi)}{P_T} \tag{2}$$

In practical measurement cases, the orthogonal polarisations would be either left- and right-hand circular polarisations or orthogonal linear polarisations, such as vertical and horizontal, defined by the electric-field direction relative to the ground. The important property of orthogonal polarisations, so far as directivity measurements are concerned, is that, for a given direction, the powers in each polarisation can be added to give the total power in that direction.[2] That is, if $U_T(\theta, \phi)$ represents the total power radiated per unit solid angle in direction θ, ϕ, then

$$U_T(\theta, \phi) = U_a(\theta, \phi) + U_b(\theta, \phi) \tag{3}$$

and it can be seen that the total power directivity given by

$$D_T(\theta, \phi) = \frac{4\pi U_T(\theta, \phi)}{P_T} \tag{4}$$

is simply the sum of the partial directivities

$$D_T(\theta, \phi) = D_a(\theta, \phi) + D_b(\theta, \phi) \tag{5}$$

The required outputs from the computer processing are numerical maps of D_a, D_b, and D_T values as a function of θ and ϕ. The computer inputs are groups of U_a and U_b values (measured data) as functions of θ and ϕ. From these inputs the computer program must first determine P_T by integration, then find the directivities from eqns. 1, 2 and 5.

Now

$$P_T = \iint_{4\pi} U_T(\theta, \phi) \sin\theta \, d\theta \, d\phi$$

which, from eqn. 3, can be written

$$P_T = \iint_{4\pi} U_a(\theta, \phi) \sin\theta \, d\theta \, d\phi + \iint U_b(\theta, \phi) \sin d\theta \, d\phi \tag{6}$$

The recording of U_a and U_b is made in the following way: the θ parameter is fixed and a ϕ rotation is made from 0 to 360° during which a 'line' of data is recorded. A θ increment is then made and for this new θ value another 360 degree ϕ rotation and data recording is made, and so on until a complete sphere of space about the radiating device under test is covered. Hence, it is convenient to write eqn. 6 in the form

$$P_T = \int_0^{\pi} \left\{ \int_0^{2\pi} U_a(\theta, \phi) d\phi \right\} \sin\theta \, d\theta + \int_0^{\pi} \left\{ \int_0^{2\pi} U_b(\theta, \phi) d\phi \right\} \sin\theta d\theta \tag{7}$$

The quantities in curly brackets represent integrations for each 'line' of data from a ϕ rotation. The integrations are made in the computer by the application of Simpson's rule. If $A(\theta)$ represents the integration of $U_a(\theta, \phi)$ with θ constant and $B(\theta)$ likewise for the other polarisation, then eqn. 7 is reduced by the first set of integrations to

$$P_T = \int_0^{\pi} A(\theta) \sin\theta \, d\theta + \int_0^{\pi} B(\theta) \sin\theta \, d\theta \tag{8}$$

A second set of integrations, again using Simpson's rule, yields P_T. This value is then used via eqns. 1 and 2 with the original data sets of U_a and U_b values to give printouts of D_a and D_b. Finally, the partial directivities are added in the computer according to eqn. 5 to give a printout of total directivities.

An important practical point is evident from the above theory. During measurements it is necessary to ensure that no power-level changes or drifts occur in the measurement system; i.e. each conical cut radiation pattern must have the correct recorded levels in relation to the others in the 'sphere'. Furthermore, the two recorded 'spheres' of data must have the true power-level relationship to each other.

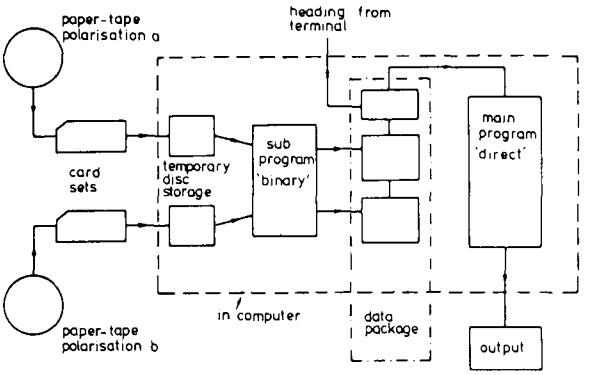

Fig. 3
Data-processing sequence of events

3 Data-processing organisation

Fig. 3 shows the data-processing sequence of events. On the ESTEC antenna test range for which this program set was written, measurement data from 'spheres' of conical cut radiation patterns is recorded on eight level punched paper tape using commercially available equipment. During each ϕ (head) rotation, the received power level is recorded in a pseudobinary code on the tape at intervals of 2°. Between the ϕ rotations, the intermediate θ increments are 5° in magnitude. So two paper tapes, one for each polarisation, are punched and each contains 37 'lines' of numbers, each 'line' having 180 pattern-level samples. This sampling system, i.e. 6660 radiation distribution samples per polarisation, is a convenient value which gives sufficient information for accuracy without excessive and impractical measurement time. The main program described in Section 4 is written for these increments but can be easily modified for others.

Cards or magnetic tape are the normal input media for modern digital computers; so it is necessary to change to one of these using a conversion machine, and although the choice of media is not very important, it was found that card sets were preferable as these can be looked at before entry to the computer. The conversion machine makes a straight copy; i.e. the coded data on the tape is punched on the cards without alteration. Each card set then contains approximately 85 cards.

After being fed into the computer via its card reader, the two sets of data are stored on disc files. Each file is then processed with the sub program BINARY. This subprogram reads the 'raw' data as if it was binary coded, into a word of 2 bytes length, shifts it to the least significant byte, then writes it out as decimal data in a form suitable for input to the main program. The decimal values are not the recorded decibel-scale values as the recording code is not pure binary; this can be seen from Fig. 4 which shows the punched-paper-tape format. However, there are simple relationships between the two, and the first task of the main program is to make a decimal number to decibel value conversion.

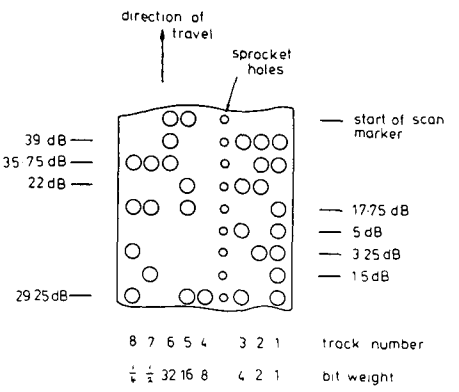

Fig. 4
8-level punched-paper-tape code format

The two 'spheres' of data are individually treated by BINARY and are appended to a 4-line heading to make a data package as shown in Fig. 3. A typical heading is given as follows:

TAPE A IS (8 spaces) LEFT-HAND CIRCULAR POLARISATION
TAPE B IS (8 spaces) RIGHT-HAND CIRCULAR POLARISATION
ANTENNA IS (7 spaces) 1·5 METRE PARABOLOID WITH LPDA FEED
FREQUENCY IS (5 spaces) 1550 MHZ

This heading is split up by the main program and used to provide titles for the final output sheets. The number of spaces is not critical but there should be at least five, and preferably a few more.

When the data package has been set up it is ready to be run with the main program; however, it may subsequently be found to contain errors. But with its format of one number per line, the data package is in an inconvenient form for inspection. For this reason, the program VIEW has been written. This takes the information in the data package and converts it into the more readily viewable format of the 4-line heading followed by the numbers arranged in groups of 20 per line.

The last stage of the data processing is to run the data package using DIRECT, the main program. If the data package is error free, partial and total directivity values are printed out in tubular form. If not, an error message giving the location of the error is produced.

4 Main program 'direct'

The main program can be divided into three sections: a data input stage, a conversion and integration stage and an output stage. A program run starts by reading the 4-line heading, storing it in sections, then printing out a copy in its original form as an overall output heading. After this, the first number is read and ignored. This number should be 48; the reason for this is that when the radiation distributions are sampled and recorded each line is terminated by a binary equivalent of 48 (see Fig. 4). In addition, each complete 'sphere' of information is ended with a 56 and started with a 48, and it is this 48 which is initially read. Following this, the first 'sphere' of data is read into a 2-dimensional array with data 'lines' as rows. At the end of each 'line', the 48 is read and identified. If the number proves to be other than 48, then there is an error on the data – perhaps one character was missed by the tape punch – and the computer run terminates with an error message identifying the polarisation and the line number. One or two missing characters at the end of a data 'line' happens occasionally, but can be corrected for by interpolation without significant loss of accuracy. The next operation by the computer is to see if the 56 which terminates the 'sphere' is present. If not, the 'sphere' contains an incorrect number of 'lines', and an appropriate error message is given and the run halted. But if, as is usually the case, the polarisation A data is read in without a hitch, then the entire operation described above is repeated for the polarisation B data, and a second 2-dimensional array is set up.

The first task in the next program stage is conversion from the decimal numbers in the two arrays to their equivalent decibel values. The first six tracks of the source-data paper tapes contain integer decibel values in pure binary, but tracks 7 and 8 hold fractional decibel values. If the 8-track tapes were read as if they were wholly binary, then the resulting decimal numbers are related to recorded decibel values in the following way. If Y_{DB} is the decibel equivalent of a decimal number X, then for X in the range 0–40,

$$Y_{DB} = X$$

for X in the range 64–104,

$$Y_{DB} = X - 63{\cdot}5$$

for X in the range 128–168,

$$Y_{DB} = X - 127{\cdot}75$$

and for X in the range 192–233,

$$Y_{DB} = X - 191{\cdot}25$$

When the conversion has been made, the decibel values are changed to power levels. Absolute values are, of course, not possible, or necessary, and the following type of relationship is used:

$$U_a(\theta, \phi) = 10^{(-Y_{DB}/10)} \quad (9)$$

This takes into account the fact that although no sign is encoded on the paper tapes, all decibel values are negative ones below an arbitrary 0dB. The integrations in the curly brackets of eqn. 7 are then carried to produce $A(\theta)$ and $B(\theta)$ of eqn. 8. These are then separately integrated with a $\sin\theta$ weighting and added to give P_T.

In the manner shown by eqns. 1 and 2, the power levels which were derived by equations such as eqn. 9 and stored in two arrays are then normalised to give the partial directivities $D_a(\theta, \phi)$ and $D_b(\theta, \phi)$ which are themselves stored in two arrays before printout. Finally, the partial directivities are added to give the total directivities $D_T(\theta, \phi)$ which are also stored in an array. Before storage, all directivity values are converted to decibel units and are therefore in decibels compared to the isotropic level (dBI) units.

The output stage prints the three directivity tables with job description headings plus θ and ϕ scales. A directivity table contains 6660 directivity values, each to one decimal place and with an arithmetic sign, and is too large to be contained in a single printout of standard 37·5 cm width. To overcome this, tables are printed in halves, each half using almost the full width of the printer. These have to be joined to form a table measuring 66 × 90 cm. Fig. 5 shows the top left-hand corner of a typical table; only this small portion is shown to give an idea of the table format. If a complete sheet was shown the characters would be too small to be seen.

The program normally assumes that measurements are started at $\theta = 0°$ and terminated at $\theta = 180°$, but it is sometimes more convenient to start at $\theta = 180°$. For this situation, the θ scale printout can be reversed by changing a parameter near the beginning of the program. There is a line as follows; START = 0. If this is changed to START = 180 the θ scale heading begins at 180 degrees and decreases to 0 degrees.

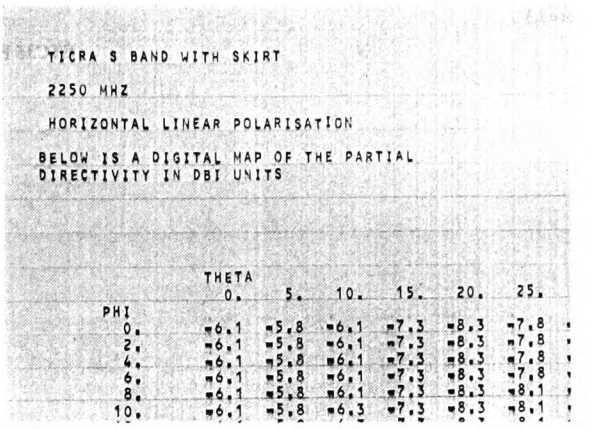
TICRA S BAND WITH SKIRT

2250 MHZ

HORIZONTAL LINEAR POLARISATION

BELOW IS A DIGITAL MAP OF THE PARTIAL DIRECTIVITY IN DBI UNITS

PHI	THETA 0.	5.	10.	15.	20.	25.
0.	-6.1	-5.8	-6.1	-7.3	-8.3	-7.8
2.	-6.1	-5.8	-6.1	-7.3	-8.3	-7.8
4.	-6.1	-5.8	-6.1	-7.3	-8.3	-7.8
6.	-6.1	-5.8	-6.1	-7.3	-8.3	-7.8
8.	-6.1	-5.8	-6.1	-7.3	-8.3	-8.1
10.	-6.1	-5.8	-6.3	-7.3	-8.3	-8.1

Fig. 5
Photograph of upper left-hand corner of one output sheet

5 Program details

Computer used: ICL system 4
Length of DIRECT: 368 cards
Length of BINARY: 13 cards
Length of VIEW: 35 cards
The program language is FORTRAN IV.
Single precision arithmetic is used throughout.
The main program DIRECT requires 490 storage units and 21 e.t.u.

6 Acknowledgment

The author is grateful to G.K. Smith of ESTEC who wrote BINARY, the binary-to-decimal conversion program, and who gave much valuable advice and help.

7 References

1 FORD, E.T.: 'Use of a computer to process the radiation patterns of omnidirectional antenna systems'. *IEE Conf. Publ.* 77, 1971, pp. 98–105
2 HOLLIS, J.S., LYON, T.J., and CLAYTON, L.: 'Microwave antenna measurements' (Scientific Atlanta Inc. 1970), chap. 7.
3 'IEEE standard definitions of terms for antennas', *IEEE Trans.*, 1969, AP-7 pp. 262–269

8 Appendix

Note on the definitions of directivity and gain

The definition of directivity used in this description is as follows:

$$D(\theta, \phi) = \frac{4\pi U(\theta, \phi)}{P_T}$$

where the directivity $D(\theta, \phi)$ and the radiation intensity $U(\theta, \phi)$ are in one specified polarisation or total power, and P_T is the power radiated by the antenna.

The above equation is distinct from gain which is defined by

$$G(\theta, \phi) = \frac{4\pi U(\theta, \phi)}{P_{IN}}$$

where, again, $G(\theta, \phi)$ and $U(\theta, \phi)$ are in one specified polarisation or total power. P_{IN} is the power supplied to the antenna input port. It can be seen that gain takes into account the efficiency of the antenna whereas directivity does not.

These definitions are not exactly as specified by the IEEE standards,[3] but it is the author's contention that the above are the ones in common usage. Generally speaking, 'gain' is an antenna parameter which is related to the power supplied to the antenna, and is measured by comparison with a gain standard such as a calibrated horn. In contrast, 'directivity' only depends on the shape of the radiation patterns and is determined by pattern measurements and integration. To introduce a third definition 'directive gain' is, in the author's opinion, confusing and unnecessary. This also applies to the term 'power gain'. Furthermore, 'directivity' as defined in Reference 3, i.e. as a maximum value only, has no useful meaning for an omnidirectional type of antenna system.

Errata

WOODS, D.: 'Reappraisal of computer-corrected network analyser design and calibration; *Proc. IEE*, 1977, **124**, (3), pp. 205–211:

The footnote on page 206 should be:

‡In this analysis we shall adopt a common normalising impedance ζ_1 for all ports so that $\zeta_3 = \zeta_2 = \zeta_1$. The port mismatches Z_1, Z_2 and Z_3 are, of course, all different.

On page 211, in the denominator of eqn. 34d, P' should be D'.

(The erratum entry concerning the footnote published in *Proc. IEE*, 1977, **124**, (8), p. 680, itself contained an error and should be ignored.)

ETC35 E

NANDA, J., and HURRY, S.: 'Self-excitation of dual-excited synchronous machines', *Proc. IEE*, 1977, **124**, (7), pp. 607–612

In the contents list of the July Proceedings IEE, the name of the second author of the above paper was omitted.

ETC36 E

Publication P17. K.M. KEEN, *Beamwidth variation with aperture diameter of the choked waveguide feed antenna.* Electronics Letters, Vol. I. 14, No. 13, June 22 1978, pp 406-407.

Fig. 2 shows typical learning curves for a stationary environment. With $c_1 = 0{\cdot}875$ and $c_2 = 0{\cdot}75$ the curves show Addie 2 (estimating c_2) counting up to its steady-state value of 0·75. The higher trace shows Addie 1 counting up and then being held at a steady-state value (~ 0·8) just above c_2. The reason for Addie 1 stopping counting up at ~ 0·8 is that when Addie 2 reaches a steady-state condition, and this estimate is lower than the value in Addie 1, then the automaton will always select the action resulting in c_2 being selected, thus inhibiting Addie 1. Similar results are obtained with the c_is reversed and also with an initial condition such that c_1 is chosen first. To investigate the operation of the two Addies in their count up and inhibit modes, Fig. 3 was taken with a fast time base. The learning curves illustrate the alternate counting modes until a steady state condition with $c_2 = 0{\cdot}875$ is reached. In order to compare Addies of varying bit size the results of Fig. 4 were obtained. This shows the learning behaviour of a 12, 16 and 20-bit Addie system. As expected a compromise has to be met between speed of operation and accuracy in the penalty-probability estimate. If a very small bit size of Addie is used and the two c_is are close together than there is the possibility that the wrong state will be chosen. This fact means that the automaton is no longer optimal, even with β equal to zero, thus contradicting the theoretical prediction of eqn. 4. In practice a 12-bit Addie was found to provide a satisfactory compromise solution.

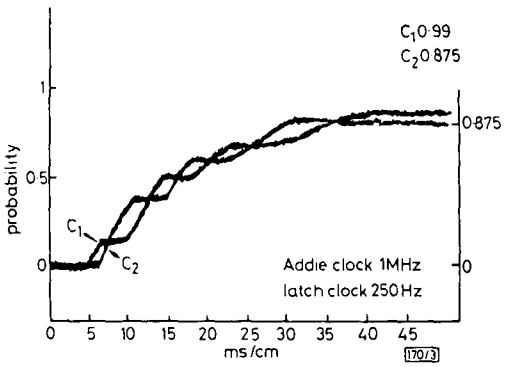

Fig. 3 *Alternative Addie count modes during learning*

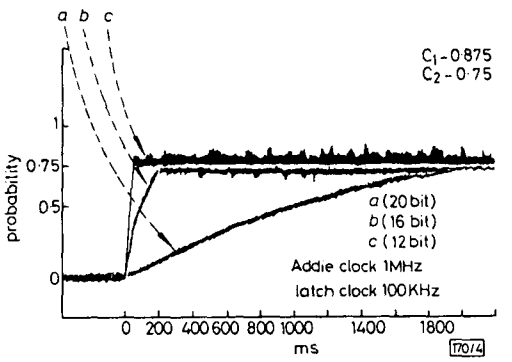

Fig. 4 *Influence of bit size on learning characteristics*

Conclusions: The hardware synthesis of a modified-estimating automaton based on digital stochastic computing techniques has been described. Experimental results for the operation of the automaton in stationary stochastic environments have shown that learning times are similar to those obtained for other automata structures.[7,8] A significant application area for the modified-estimating automaton is in nonstationary environments and this will be reported subsequently. It is intended to apply a hierarchical array of m.e. automata to the adaptive routing control of telephone traffic systems.[9]

Acknowledgment: The authors wish to gratefully acknowledge the support of a UK Science Research Council Grant.

M. J. COUTTS
P. MARS

School of Electronic & Electrical Engineering
Robert Gordon's Institute of Technology
Aberdeen AB9 1FR
Scotland

24th May 1978

References

1 NARENDRA, K. S., and THATHACHAR, M. A. L.: 'Learning automata–a survey', *IEEE Trans.*, 1974, SMC-4, pp. 323–334
2 LOUI, M. C., and NARENDRA, K. S.: 'Comparison of learning automata operating in nonstationary environments', Technical Report CT-65, Becton Centre, Yale University, 1975
3 GAINES, B. R.: 'Stochastic computing', *AFIPS SJCC*, 1976, 30, pp. 149–156
4 MILLER, A. J., BROWN, A. W., and MARS, P.: 'Adaptive logic circuits for digital stochastic computers', *Electron. Lett.*, 1973, 9, pp. 500–502
5 MILLER, A. J., BROWN, A. W., and MARS, P.: 'Study of an output interface for digital stochastic computers', *Int. J. Electron.*, 1974, 37, pp. 637–655
6 MILLER, A. J., and MARS, P.: 'Theory and design of a digital stochastic computer random number generator', *Trans. IMACS*, 1977, 19, pp. 198–216
7 NEVILLE, R. G., NICOL, C. R., and MARS, P.: 'Synthesis of stochastic learning automata', *Electron. Lett.*, 1978, 14, pp. 206–208
8 NEVILLE, R. G., NICOL, C. R., and MARS, P.: 'Design of stochastic learning automata using adaptive digital logic elements', *ibid.*, 1978, 14, pp. 324–326
9 NARENDRA, K. S., WRIGHT, E. A., and MASON, L. G.: 'Application of learning automata to telephone traffic routing and control', *IEEE Trans.*, 1977, SMC-7, pp. 785–792

0013-5194/78/1170-0404 $1.50/0

BEAMWIDTH VARIATION WITH APERTURE DIAMETER OF THE CHOKED WAVEGUIDE FEED ANTENNA

Indexing terms: Antenna feeders, Reflector antennas, Waveguide antennas

The choked waveguide feed antenna, which exhibits *E*- and *H*-plane radiation pattern equality, good pattern symmetry and low cross polarisation, is an excellent feed for symmetrical reflector antennas with *f/D* ratios in the range of about 0·3 to 0·4. An experimental programme has been carried out to determine the variation of beamwidth with feed aperture diameter, and the results are presented here.

It is now well known that for a certain aperture size, flanged smooth wall cylindrical waveguide or narrow flare angle conical horn feeds operating in the TE_{11} fundamental mode exhibit *E*- and *H*-plane radiation pattern equality and low cross-polarisation performance. The aperture diameter at which this occurs has been shown to be 1·15 wavelengths.[1] This effect is a narrow bandwidth one, but the range over which pattern equality is maintained can be extended for smaller aperture diameter waveguides or horns by the addition of a coaxial choke as in Fig. 1. The choked waveguide has been shown to be an excellent low blockage feed of relatively simple construction for front fed symmetrical parabolic reflector antennas with *f/D* ratios in the range of about 0·3 to 0·4, and it can even be extended to dual band operation by the addition of a second choke.[2] However, there appears to be little information in the literature which can be used for

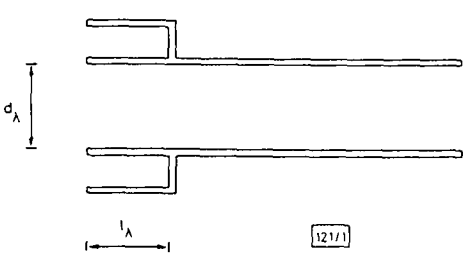

Fig. 1 *Choked horn configuration*

the direct design of such feeds, in particular there is no published data on the relationship between radiation pattern beamwidths and feed aperture diameters. An experimental programme has been carried out to determine this data, and results are presented here.

A feed element was constructed from a length of circular section waveguide and two short concentric tubes, the larger of which fitted over the other, which in turn fitted over the waveguide. By moving the smaller diameter tube relative to the outer tube and the waveguide, chokes of different depths could be formed. Also, by operating at different frequencies, the feed aperture diameter (in wavelengths) could be altered. The essential dimensions of the element components were as follows: waveguide–7·15 mm inner diameter, 8·0 mm outer diameter; inner concentric tube–8·0 mm i.d., 10·0 mm o.d.; outer concentric tube–10·0 mm i.d., 12·25 mm o.d. Although the tubes were a good 'push fit', a high conductivity silver loaded paste was applied to ensure good electrical contact. The circular waveguide was interfaced to a transition to WG22 rectangular waveguide for TE_{11} mode feeding, and measurements were made over the frequency range of 28 GHz to 39 GHz.

The two important dimensions of a choked waveguide feed are the aperture diameter in wavelengths (d_λ) and the choke depth in wavelengths (l_λ) as shown in Fig. 1. The measurement technique involved choosing the operating frequency to give the required d_λ value and then setting l_λ to a value of 0·255, this value deriving from Reference 2. Fig. 2 shows measured radiation pattern 12 dB half beamwidth values for the E- and H-planes as functions of d_λ, and it can be seen that the beamwidths in the two planes are always equal to within a few degrees.

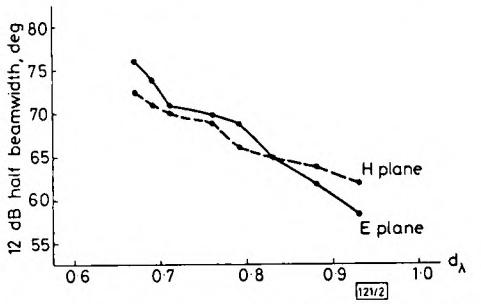

Fig. 2 *12 dB half beamwidth for choked waveguide feed as a function of aperture diameter*

To conclude, the relationship between the E- and H-plane radiation pattern beamwidths and the aperture diameter of the fundamental mode choked waveguide feed has been determined experimentally, and this information can be used directly in the design of front fed reflector antenna systems. It is interesting to compare the beamwidths of the choked waveguide feed with published data for similar size circular waveguides without chokes.[3] With these, as the aperture diameter decreases below 1·15 wavelengths, the E-plane pattern becomes progressively wider than the H-plane pattern and beamwidth equality is soon lost; typical values are 65° H-plane 12 dB half beamwidth and 75° E-plane 12 dB half beamwidth at a d_λ value of about 0·8. The choked waveguide feed, however, shows beamwidth equality within a few degrees, down to at least a d_λ value of 0·67.

K. M. KEEN

RF Technology Centre at ERA
Cleeve Road
Leatherhead
Surrey KT22 7SA
England

8th May 1978

References

1 ADATIA, N. A., RUDGE, A. W., and PARINI, C.: 'Mathematical modelling of the radiation from microwave primary feed antennas'. Proceedings of the 7th European microwave conference Copenhagen 1977
2 COWAN, J. H.: 'Dual-band reflector feed element for frequency reuse applications', *Electron. Lett.*, 1973, 9, pp. 596-597
3 JAMES, G. L., and GREENE, K. J.: 'Effect of wall thickness on radiation from circular waveguides', *ibid.*, 1978, 14, pp. 90-91

0013-5194/78/1121-0406 $1.50/0

DEGRADATION IN SHORT WAVELENGTH (AlGa)As LIGHT-EMITTING DIODES

Indexing terms: Light-emitting diodes, Semiconductor junction lasers

Degradation in short-wavelength (AlGa)As lasers is investigated through lifetests of such devices operated in the incoherent mode. It is shown that degradation increases with emission energy for diodes containing zinc in the p-type (AlGa)As bounding region, whereas diodes containing Ge in this region, although not satisfactory as c.w. lasers because of high resistivity, show no degradation. A way out of this difficulty is proposed through double doping with Ge and Zn, in which case degradation appears to be brought down to the Ge level.

Double-heterojunction $Al_xGa_{1-x}As/Al_yGa_{1-y}As$ laser diodes have been produced with room-temperature lasing wavelengths ranging from about 0·9 μm to 0·68 μm. Reliable devices have been reported in the spectral region of 0·82 to 0·87 μm,[1] but no data are available concerning devices emitting closer to the visible region. This paper reports reliability test results on diodes emitting between 0·73 and 0·82 μm.

Owing to the difficulty of achieving adequate conductivity for c.w. operation in Ge-doped $Al_xGa_{1-x}As$ as x approaches 0·5,[2] it is necessary to use Zn as the acceptor dopant in the liquid phase epitaxial growth of shorter wavelength lasers. However, the substitution of zinc for germanium as the dopant in the p-type bounding layer introduces fabrication problems and potential reliability issues. Nevertheless, it is only with zinc doping that room-temperature c.w. laser diodes operating near 0·73 μm have been achieved.[3] The substitution of Zn for Ge introduces a factor which we study with respect to the degradation of these devices. We show that Zn doping leads to accelerated degradation compared to Ge-doped diodes as the emission wavelength moves from the infra-red toward the visible, but double-doping with Ge and Zn yields reliable diodes.

The devices studied consisted of the structure shown in Fig. 1, the parameters of main interest being the dopants used (Ge, Zn, or Ge + Zn) in the p-type $Al_yGa_{1-y}As$ bounding region, and the x and y values employed. The recombination region was not deliberately doped. The devices were grown by a conventional liquid phase epitaxial process, and every attempt was made to keep the growth conditions similar to those employed in the fabrication of reliable (AlGa)As lasers emitting in the 0·80 and 0·87 μm range. A summary of the materials parameters used is given in Table 1.

All of the lasers discussed here were formed using the oxide-isolated stripe-contact process, with a stripe width of 10–15 μm. The diodes were mounted with In solder, p-side down, on Cu heat sinks. This process of fabrication is known to generally produce very reliable devices when used for

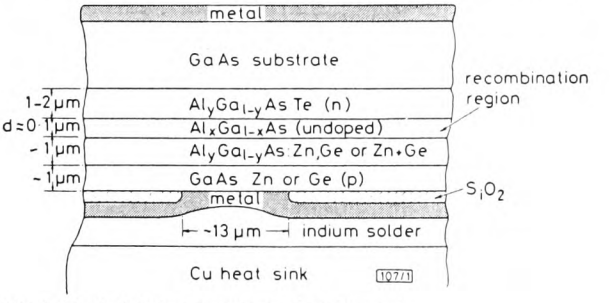

Fig. 1 *Typical device structure used in this work*

Publication P18. **K.M. KEEN,** ***Interference pattern intermediate distance antenna measure ment technique.*** **Microwaves, Optics and Acoustics, Vol. 2, No. 4, July 1978, pp 113-116.**

Interference-pattern intermediate-distance antenna measurement technique

K.M. Keen

Indexing terms: *Antenna radiation problems, Communications, Computing, Microwave antennas, Microwave measurement*

Abstract: A new antenna-pattern measurement technique for antennas with large-field distances is described. The method is applicable to conventional ranges with 2-axis positioners and receivers that work in amplitude only. Basically, the technique is to make pattern measurements on a conventional finite-length range in the normal way but with a third antenna or an auxiliary circuit that causes interference. Interference patterns and finite-distance amplitude patterns are recorded and the finite-distance phase distribution extracted by data processing. This finite-distance data is then the input to a near-field/far-field transformation computer program that gives the far-field patterns.

1 Introduction

The far-field characteristics of the majority of microwave antennas can be determined on conventional measurement ranges in the normal way, i.e. by rotating the antenna and monitoring its radiation pattern with a remote antenna situated a sufficient distance away. However, there are cases – either because the Rayleigh criterion does not apply, or because the antenna aperture is large in terms of the operating wavelength – in which the need for very large range distances precludes conventional methods and some form of near-field measurement method may be necessary. A recent example was a shaped-beam satellite antenna for earth coverage,[1] for which an 'intermediate-range distance' facility was set up near Chelmsford, England.[2] On this range both phase and amplitude are monitored, and the quasi near-field information is transformed by computer processing to give the far-field radiation patterns. This type of range has additional usefulness in that it can be operated in the conventional mode for measuring the majority of antennas.

From the reverse point of view, existing conventional ranges could be adapted to this system for the measurement of antennas with large far-field distances; the only drawback being that the above mentioned range uses a sophisticated (and expensive) phase and amplitude receiver, which most ranges do not have. In an attempt to extend the capabilities of the antenna measurement facility at the European Space Research and Technology Centre without recourse to a phase and amplitude receiver, a new intermediate-range technique has been devised whereby the phase information is extracted from interference patterns, but in a more direct way from that accomplished by the holographic method developed at the University of Sheffield.[3]

The new technique was first simulated by a series of computer programs to establish its viability and give some 'feel' for the extent of the data processing that would be involved. This was followed by a practical trial with encouraging results, and the technique is now considered as a generally available feature of the facility at which it was developed.[4] Aspects of the development have been reported previously,[5-7] but this paper gives a comprehensive review of the technique and the investigation and implementation of it.

Paper T198 M, first received 3rd April and in revised form 17th May 1978

Mr. Keen is with the RF Technology Centre, Electrical Research Association, Cleeve Road, Leatherhead, Surrey KT22 7SA, England

2 Description of the technique

In Fig. 1, antenna A is the antenna to be measured and is situated on a 2-axis mount, B is a static reference antenna and C is the remote antenna. The diagram shows the measurement hardware in an anechoic chamber, but the system is the same for indoor or outdoor ranges. Fig. 2 shows the feeding circuit, which includes a phase shifter able to switch from some arbitrary zero to +90° and

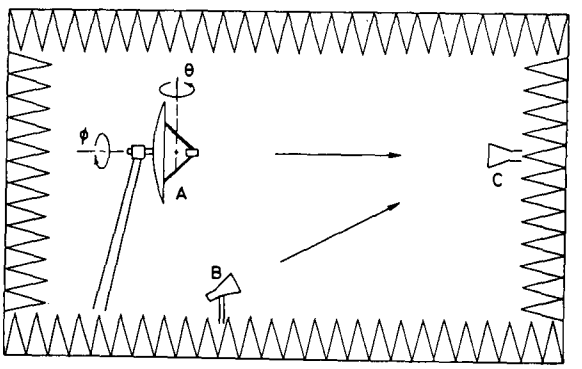

Fig. 1 *Measurement-method geometry*

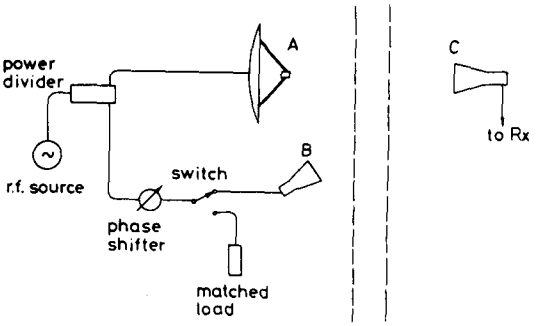

Fig. 2 *Feeding circuit – method 1*

0308–6976/78/198M–0113 $1·50/0

+ 180° relative to that zero. The purpose of antenna B is to act as a fixed reference for interference patterns set up at antenna C by interference between radiation from A and B. Fig. 3 shows an alternative circuit for causing the desired interference and this will be described later, but for the moment the technique is best explained by reference to Fig. 2.

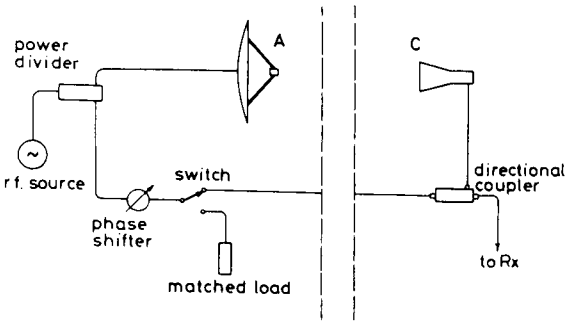

Fig. 3 *Feeding circuit – method 2*

Let the field distribution at the chosen intermediate distance (i.e. somewhere between, say, the Rayleigh distance and the close proximities of conventional near-field probing methods of measurement) and in one known polarisation be represented by

$$D_1(\theta, \phi) = A_1(\theta, \phi)\, e^{j\psi_1(\theta, \phi)} \tag{1}$$

and let the corresponding far-field distribution be

$$D_2(\theta, \phi) = A_2(\theta, \phi)\, e^{j\psi_2(\theta, \phi)} \tag{2}$$

where A_1 and A_2 are amplitudes and ψ_1 and ψ_2 are phases. The desired description of the radiating characteristics of the antenna is $A_2(\theta, \phi)$, usually expressed in decibels, together with its orthogonal polarisation counterpart (o.p.c.). These are the far-field radiation distributions, and often only certain 'cuts' i.e. radiation patterns, are required. From electromagnetic theory it is known that $A_2(\theta, \phi)$ and its o.p.c. can be found from $A_1(\theta, \phi)$ and $\psi_1(\theta, \phi)$ plus their o.p.c.s, and there are a number of near-field to far-field transformation computer programs in existence that do this. The interference method provides a way of determining the quasi near-field phase, and the procedure is as follows.

With antenna B switched out, the quasi near-field power-level distribution $P_1(\theta, \phi)$ is recorded. This determines $A_1(\theta, \phi)$, since, ignoring decibel scaling and a constant of proportionality,

$$P_1(\theta, \phi) = A_1^2(\theta, \phi) \tag{3}$$

Then, with the reference antenna switched in and the phase shifter set to 0°, + 180° and + 90°, three more power level distributions are recorded. These are $P_2(\theta, \phi), P_3(\theta, \phi)$ and $P_4(\theta, \phi)$, respectively. The phase distribution can then be extracted from the four power-level distributions using the following relationships:

$$\cos\,[\psi_1(\theta, \phi) - \delta] = \frac{P_2(\theta, \phi) - P_3(\theta, \phi)}{\sqrt{\{8P_1(\theta, \phi)[P_2(\theta, \phi) + P_3(\theta, \phi) - 2P_1(\theta, \phi)]\}}} \tag{4}$$

and

$$\sin\,[\psi_1(\theta, \phi) - \delta] = \frac{2P_4(\theta, \phi) - [P_3(\theta, \phi) + P_2(\theta, \phi)]}{\sqrt{\{8P_1(\theta, \phi)[P_2(\theta, \phi) + P_3(\theta, \phi) - 2P_1(\theta, \phi)]\}}} \tag{5}$$

The constant δ has no effect on the subsequent transformation and can be ignored; it is actually the real value of the arbitrary zero of the phase shifter. To extract $\psi_1(\theta, \phi)$ from eqns. 4 and 5 it is only necessary to evaluate one equation and find the arithmetic sign of the other.

The above outlines the basis of the measurement technique; four power-level distributions are recorded, and from these a phase distribution and an amplitude distribution are extracted by data processing. If this is done in two orthogonal polarisations, the resulting phase and amplitude information can be processed by a near-field to far-field transformation computer program. The data sampling about antenna A requires a 2-axis positioner, but many conventional ranges have these, as sampling in this fashion is carried out for the measurement of directivity.[8, 9] The spherical envelope about the antenna can be monitored by either great circle (constant ϕ) or conical (constant θ) rotations.

3 Computer simulation

Before trying the technique in practice, a computer simulation was made with a mathematical model of an array of 17 halfwave dipoles with interelement spacings of 1·2 wavelengths at a frequency of 2·4 GHz. In the array, the dipoles were axially aligned and equally fed in amplitude and phase, giving a far-field radiation pattern with a main beam of 2·5° half-power beamwidth in the array plane, two prominent sidelobes and many minor lobes. The Rayleigh distance for the array is 97 m. The near-field sampling was made in E_θ and E_ϕ components, and to simplify the simulation the array was placed along the $\theta = 0°$ axis of the measurement co-ordinate system, so that the E_ϕ field was always zero. The near-field range length was set at 5 m, and antenna B was placed this same distance below A and inclined 45° to the horizontal. The parameters of the feeding circuit were chosen so that, with the main-beam peak of the array directed toward C, the field amplitudes from antennas A and B were equal at C. Radiation-distribution samplings were made at intervals of 2·25° in θ and 90° in ϕ. These spacings were dictated by the computer program subsequently used for transformation, and represent the minimum number of samples necessary for the matching of spherical modes for this size of antenna.

Fig. 4 shows the quasi near-field power-level pattern $P_1(\theta)$ of the array, and the continuous line curve of Fig. 5 shows the directly computed far-field pattern. In the

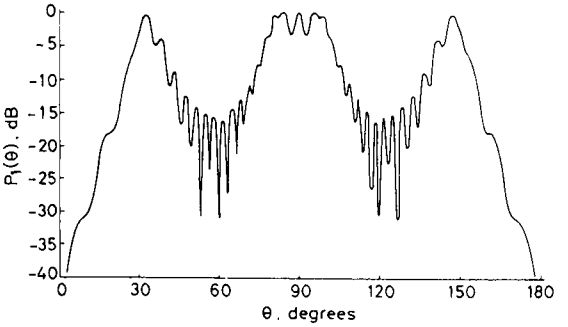

Fig. 4 *Power-level pattern $P_1(\theta)$ of the 17-dipole array at 5 m distance*

measurement simulation, after the amplitude and phase data were extracted from the sets of four near-field distributions, they were transformed to the far field using the computer program SNIFT.[10] This is a spherical-mode matching program that makes use of fast-Fourier-transform techniques. Output from this is shown as dots on Fig. 5, and it can be seen that there is good agreement with the directly computed far-field pattern.

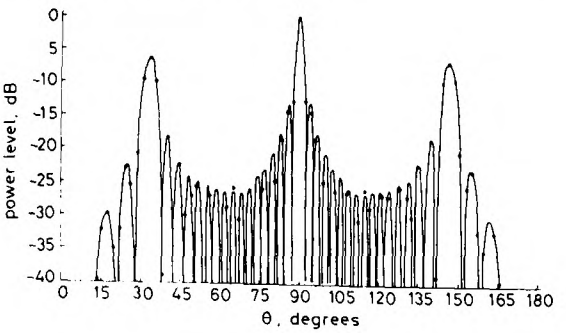

Fig. 5 *Far-field pattern of the 17-dipole array*

Continuous line is the calculated pattern at infinity, dots are from the simulated near-field measurement

4 Trial measurements using the technique

Fig. 6 shows the first intermediate-distance measurement arrangement although, as will be described, this was subsequently modified. In the photograph the antenna undergoing measurement is a 1·3 m paraboloid and feed. This size of antenna was convenient as a test case, as its Rayleigh distance was small enough for conventional far-field measurements to be easily made and used as a comparison.

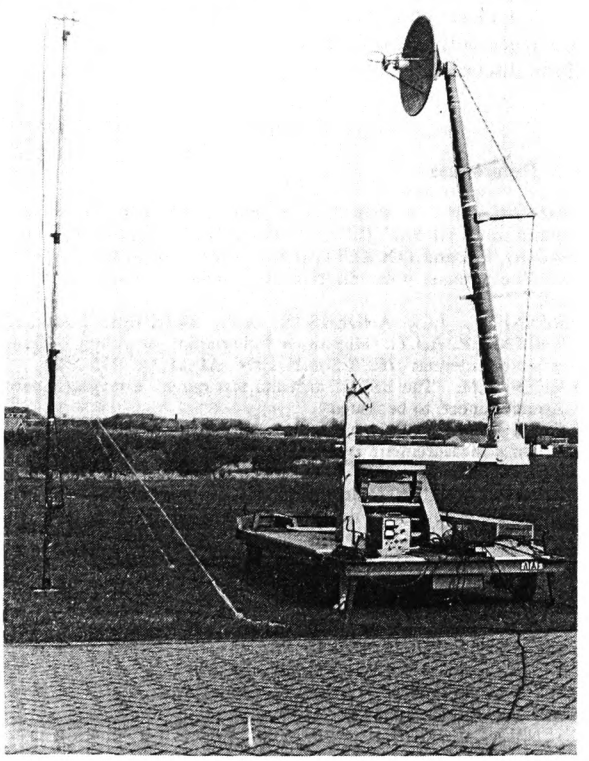

Fig. 6 *Initial measurement arrangement*

The feed was a linearly polarised log-periodic antenna. No attempt was made to optimise its position for the best secondary patterns, as poor patterns would not have been detrimental to the investigation. In fact, high sidelobes seen with the H-plane secondary pattern and a deep null just off the main beam in the E-plane secondary pattern (caused by a feed strut in this plane) were considered useful for monitoring the accuracy of the technique at different levels and angular positions. The remote antenna was a crossed log-periodic dipole array, as was the interference-wave antenna. Measurements were made at 1200 MHz, ultimately at 3 m range length (the photograph shows a 5 m separation) and also at 20 m range length on a conventional elevated range for comparison. The Rayleigh distance of the paraboloid antenna is 13·5 m.

The purpose of the interference-wave antenna is to provide a constant reference wave for interference-pattern formation at the remote antenna, and on the original measurement set-up the ability to do this was tested by transmitting with the interference antenna alone, receiving with the remote antenna and rotating the test antenna. When this was done, the interference wave was seen to be far from constant because of scattering from the test antenna and its tower and metal base. The obvious solution to this problem would be to use a more directive interference antenna, but an alternative scheme was proposed at this time and adopted for the trial measurements. With this scheme, shown in Fig. 3, instead of forming the interference pattern in air from two waves propagated by antennas, the intereference-wave antenna is removed, a cable link takes the reference wave to a point beyond the receive antenna, and interference is caused by combination of the two waves in a directional coupler. Fig. 7 shows how a directional coupler can be used in this way.

The upper diagram of Fig. 7 shows a directional coupler in normal use; if a wave of voltage V is applied at the input port, then K_1V and K_2V are seen at the output ports, where K_1 and K_2 are complex constants each composed of an insertion phase and an amplitude reduction term. If the coupler is used to combine two waves of voltage V_B and V_C (lower diagram) applied at ports B and C, then a certain amount of the input energy goes to the load, and an output $K_1V_B + K_2V_C$ is seen at port A. The phase constant

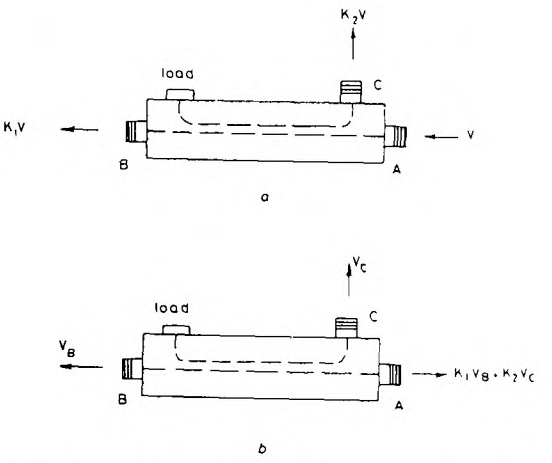

Fig. 7 *Use of a directional coupler for a 2-channel combiner*

a Coupler in normal use
b Coupler combining the reference- and direct-channel signals

introduced by K_1 and K_2 is unimportant, as all measurements are in relative phase anyway. The amplitude constants are also unimportant as they have the same effect as changing the amplitude of the reference signal, and this can be set to anything convenient – the only requirement being that it stays constant throughout data recording.

A practical point that has arisen from the use of a coupler in this way is that extra cable must be put into the direct circuit to approximately equalise the direct and reference path lengths to minimise dispersion.

The direct and interference radiation distributions were sampled in orthogonal linear polarisations at intervals of 5° in θ and 6° in ϕ over the spherical region about the parabolic antenna; the number of data points corresponding to this spacing were in accordance with the input requirements of the transformation program,[10] and are the minimum number of samples necessary for spherical-mode matching over this particular size of antenna. The sampled relative power levels were recorded on 8-level punched paper tape to give a resolution of 0·25 dB, and then this data was transferred to a digital computer for processing with two computer programs. The first of these extracted the amplitudes and phases from the recorded power levels according to eqns. 3, 4 and 5, and then these values were treated by the near-field to far-field transformation program SNIFT to give far-field radiation patterns. The program requires only relative phase values and is able to allow for an added phase variation due to the phase centre of the antenna under test being not precisely on the axes of rotation.

Figs. 8 and 9 show how the far-field patterns obtained by the interference technique compare with the conventionally measured ones. Fig. 8 shows *H*-plane patterns of the paraboloid antenna and Fig. 9 shows *E*-plane patterns, and in each case the hard line represents the conventionally measured pattern and the dashed line shows where the interference-technique pattern deviates from it. It can be seen that there is good agreement between patterns measured by the two techniques down to low levels. There are, of course, some discrepancies, but it must be remembered that the comparison is being made between patterns measured at 20 m (i.e. 1·5 times the Rayleigh distance of the antenna) and patterns in the true far field i.e. projected to infinity. Also, the conventional measurements were made in the presence of a ground reflection level of the order of −30 to −35 dB. In general, it is believed that the conventionally measured patterns are the less accurate of the two sets.

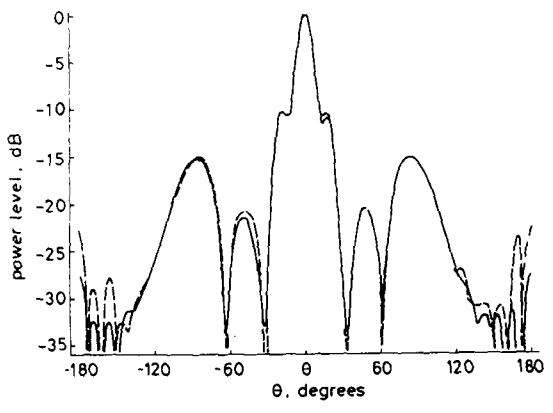

Fig. 8 *H-plane patterns of parabolic antenna*

Full line is from conventional pattern measurement at 20 m, broken line is pattern from interference method at 3 m

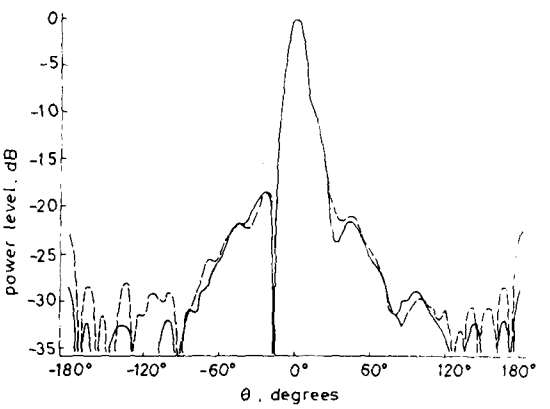

Fig. 9 *E-plane patterns of parabolic antenna*

Full line is from conventional pattern measurement at 20 m, broken line is pattern from interference method at 3 m

5 Acknowledgments

The author would like to thank B.E. Westerman and W.B.S.M. Kneefel of the Christiaan Huygenslaboratorium B.V., Noordwijk, Holland for carrying out measurements and for suggesting the use of the directional coupler combiner. He would also like to thank J. Aasted, Head of the Antennas and Propagation Section, ESTEC, for encouragement, and D.J. Brain, also of ESTEC, for several helpful discussions.

6 References

1 COWAN, J.H.: 'A shaped beam antenna for a maritime communications satellite'. IEE Conf. Publ.128, 1975, pp. 101–106
2 WOOD, P.J. and LOCKETT, N.J.: 'A new type of test range for satellite antenna polar diagram measurements', *ibid.*, pp. 186–191
3 BENNETT, J.C., ANDERSON, A.P., McINNES, P.A. and WHITAKER, A.J.T.: 'Microwave holographic metrology of large reflector antennas', *IEEE Trans.*, 1976, AP-24, pp. 295–303
4 KEEN, K.M.: 'The ESTEC antenna test range'. European Space Agency report, to be issued
5 KEEN, K.M.: 'Simulation of a proposed near-field to far-field antenna measurement system', *Electron. Lett.*, 1977, 13, (8), pp. 225–226
6 KEEN, K.M.: 'An interference pattern intermediate distance antenna measurement method'. ESTEC workshop on antenna test techniques: ESA preprint handbook SP127, June 1977
7 KEEN, K.M.: 'Antenna measurements on an intermediate distance range by using an interference method', *Electron. Lett.*, 1977, 13, (13), pp. 375–376
8 HOLLIS, J.S., *et al.*: 'Microwave antenna measurements' (Scientific-Atlanta Inc., 1970)
9 KEEN, K.M.: 'A computer program system for evaluating partial and total antenna directivities from measured data', *Proc. IEE*, 1977, 124, (12), pp. 1117–1120
10 JENSEN, F.: 'SNIFT – computer program for spherical near-field far-field technique'. Appendix E to TICRA final report S–45–01, under ESTEC contract 2478/75AK

Publication P19. K.M. KEEN, J.C. BENNETT and P.J. WOOD, *Intermediate distance antenna measurement techniques.* IEE Conference 'Antennas and Propagation', Nov. 1978, Conference Publication 169, pp 106-110.

INTERMEDIATE DISTANCE ANTENNA MEASUREMENT TECHNIQUES

K.M. Keen*, J.C. Bennett** and P.J. Wood***

*RF Technology Centre at ERA, UK. **University of Sheffield, UK. *** Marconi Research Labs. UK

INTRODUCTION

The far field radiation patterns of the majority of microwave antennas can be determined in the classical way, i.e. by rotating the antenna in an electromagnetically clean environment (usually either an outdoor range with low ground reflections or an anechoic chamber indoor range) and monitoring the radiation patterns with a remote antenna situated a sufficient distance away. This distance is usually chosen from the criterion $2D^2/\lambda$, where D is the major antenna dimension, which is a good approximation to the far field distance (1). However there are cases - either because the distance criterion is not valid, or because the antenna aperture is large in terms of the operating wavelength - where the need for very large range distances precludes classical methods and some form of near field measurement method may be necessary.

Due to the emergence of an increasing number of antennas which would be difficult or impossible to measure in the normal way, for example shaped beam and fine pencil beam satellite and radar antennas, the last two or three decades have seen a great deal of work in the development of what may be termed 'conventional' near field measurement techniques (2). Leaving aside the compact range technique, which is a special case and limited in application to relatively small antennas such as feeds, conventional near field techniques can be described as methods where a probe is moved across the aperture of the test antenna, and the near field phase and amplitude sampled. Sampling may be over spherical, planar or cylindrical surfaces, and, after data collection, a near field to far field transformation is carried out by computer processing to give the far field radiation patterns. These near field methods do have their drawbacks; for example there are measurement errors associated with the probe. These are of two types. Firstly, the physical presence of the probe alters the field being measured (e.g. energy is re-scattered on to the antenna under test). This effect cannot be corrected for in practice. Secondly, because the probe has a finite aperture, it measures an average of the field over this aperture rather than the field at a point. This can be corrected for at the cost of some complexity ('probe correction'). Also, large probe carriage structures are needed which must be capable of positioning with very high accuracy. These structures are housed in anechoic chambers, and obviously, to facilitate the measurement of physically large antennas, both probe carriage and chamber must themselves be large, making a near field system a very expensive facility to set up. Two other points worth noting, both involving planar near field probing, are as follows. Planar probing mechanisms are to some extent restricted in bandwidth. For example, for J and Q band frequencies, extremely good resolution/planarity is important; whilst for L band the overall size of the structure is considerable. It is difficult to get both with one carriage structure. The other point is that with planar probing, 'all round' radiation patterns cannot be determined. In practice, patterns can only be defined within a cone of semi angle of 60 degrees or so about the boresight axis.

With these limitations as a spur, a new class of antenna measurement method is emerging. In Europe, particularly in England, intermediate distance measurement methods have come forward, and although only a relatively small amount of development has taken place so far, it is clear that these methods have some operational and cost advantages over conventional near field systems.

As the name implies, intermediate distance methods employ range lengths somewhere between the $2D^2/\lambda$ distance and the close near field region. Both amplitude and phase are monitored at the intermediate distance, and an intermediate to far field (IDFF) transformation is made in some way to give the far field radiation patterns. One obvious advantage of the technique is that conventional far field test ranges can be adapted to intermediate distance working for the relatively few antenna measurements that can not be made in the normal manner. Temporarily adapting an existing range by keeping the test and remote towers, positioners etc., and merely reconfiguring the receiving and recording system is a far more attractive proposition than having a purpose built near field facility which, because the majority of antenna measurements are best carried out in the conventional way, would probably be under utilised.

In this paper, three particular intermediate distance measurement techniques are outlined. These are the holographic technique developed at the University of Sheffield, the Marconi Research Laboratories technique as used for satellite antenna measurements, and the interference pattern technique developed at the European Space Research and Technology Centre (ESTEC). All these techniques rely on some sort of transformation process; amplitude and phase distribution are recorded in some way and in two orthogonal polarisations, then an intermediate distance to far field transformation is carried out to give the far field distribution.

The University of Sheffield Holographic Technique

The holographic technique developed at the University of Sheffield (3) uses the arrangement shown in Fig. 1. A static microwave horn provides the reference wave which is combined with the antenna signal via a hybrid-T. The antenna elevation/azimuth positioning system is utilised to obtain the hologram in a raster format defined by the positioner axes.

The data array formed by regular sampling of the hologram signal is then computer processed using fast Fourier transform techniques to provide a variety of antenna diagnostics. One feature of the 'pure' holographic technique is that only an amplitude receiver is required (rather than a phase and amplitude receiver) because the storage of phase information is inherent in the holographic process.

Fig.2 shows a comparison of far-field radiation patterns obtained for a 3.66m paraboloid antenna both by direct, conventional measurement and by the holographic prediction process. Good agreement is seen between the predicted and experimantal results except in the -2^{o} to -4^{o} region of the elevation patterns. The measured results were obtained in conditions of deep snow and the high sidelobes obtained in the above region are due to ground reflections. Small differences in the azimuth patterns are due to positioning errors.

6B

A further feature of the holographic approach is that a transformation can be readily made from the measured data to the aperture region for the purpose of antenna metrology (4). Holographic phase and amplitude measurements have, for example, been made a 10GHz on the reflector antenna shown in Fig.3b. The surface profile error generated from the measured data is shown in Fig.3a and its interpretation leads to the identification of localised deformations, spinning errors and astigmatic distortion. Optimisation of the prime focus feed position has also been obtained from the data and the corresponding improvements in measured radiation patterns have been demonstrated.

The scanning geometry employed enables the investigation of very large antennas such as radio telescopes and satellite earth station antennas, with regard to both far-field radiation patterns and surface profile error. The 76m diameter Jodrell Bank Mark 1A radio telescope has been investigated by the holographic technique, using the Mark II radio telescope as a reference. In this case the antenna was illuminated by 31cm radiation from a stellar radio source. Recently, a comprehensive survey of the SRC 25m radio telescope was carried out and is reported elsewhere in these Proceedings.

The Marconi Research Laboratories Technique

The Marconi intermediate field range was originally developed for bread-board and flight model testing of the MAROTS (now MARECS) satellite antenna. This is basically an outdoor facility using two 13m towers at 107m spacing (Figs.4 and 5). For MAROTS L-band tests the range length is $\approx 4D^2/\lambda$. This length would ordinarily have been sufficient to permit conventional far field measurements, but for the special characteristics of a shaped reflector/shaped beam antenna. True near field probing would also be unsuitable for this type of antenna, because this would place unwanted emphasis on phase measurement accuracy - e.g. 1^{o} phase measurement error would result in o.2 dB error in the predicted antenna gain.

The range uses conventional azimuth and polar antenna positioners, effectively giving spherical surface probing. Previous computer orientated test range implementations (2) have required that a tape (paper or magnetic) be transferred from the range to the processing centre. For the Marconi range this drawback is overcome by an on-line interconnection. With reference to Fig.6, synchronising pulses are generated at regular increments of the antenna azimuth angle. They initiate both the digitisation of the received signal and also the serialisation of the signal to permit transmission by GPO telephone to the central computer. Thus antenna patterns and other data can be displayed on a V.D.U. screen at the range, and are immediately available to the antenna development engineer.

The time taken to characterise an antenna at one frequency is limited by the number of cuts required and the positioner turning speed. The latter in turn is limited by the digitisation time for a pattern point. Phase is measured as well as amplitude, since this reduces measurement time by a factor of 4 in compariso to amplitude only measurements. For MAROTS, a complete test is of about 1¾ hours duration.

The spherical probing data is processed by a spherical wave expansion technique (8). This is essentially a rigorous electromagnetic transformation. It is valid regardless of measurement range, and ideally permits all six electromagnetic field quantities (3 components E, 3 components H) to be individually specified at near or far-field range. The spherical wave spectrum for the antenna is a standard interface which can be used to transfer data to other computer programs. The 'cut-off' property of the spectrum gives a filtering action to eliminate spurious components of the measured pattern not compatible with the size of the aperture under test. The Marconi processing technique (7)(8) places no restrictions on data sampling interval, and the latter may be reduced to improve the smoothing action of the transform.

The Marconi range also incorporates many special features (9) to further suppress measurement errors, e.g. rigorous compensation for off-centre mounting of the test antenna, compensation of linear equipment drift and reference horn multipath, and polynomial fitting to the standard gain horn reference cuts. An overall absolute measurement accuracy of $\pm$ 0.07 dB at J-Band has been established experimentally (6),(9), some 4 times better than a conventional test range.

The Marconi range has been operated at frequencies from L-Band to J-Band, and can measure 'near-in' or 'all-round' patterns. With processing, the limit on test antenna size is 50λ - 100λ , to avoid computer time /storage difficulties. In common with other intermediate range techniques, the facility can also be used in a 'conventional' mode without IDFF and without this limitation.

The ESTEC Technique

The technique developed at ESTEC (10)(11)(12) is in some ways a hybrid of the two previously described methods, and was developed to extend the capabilities of the conventional far-field approximation antenna test range on the ESTEC site. Basically, the antenna under test is fed in parallel with a second antenna, in orde to make interference patterns which are monitored at an intermediate distance. As wit the holographic technique, the interference patterns contain the essential phase information, although with the ESTEC method the formation of the interference patterns, the phase data extraction, and the intermediate to far field distance transformation are carried out in different ways.

Fig.7 shows the antenna measurement geometry and Fig.8 illustrates the circuit which feeds the test and reference antennas. Actually,

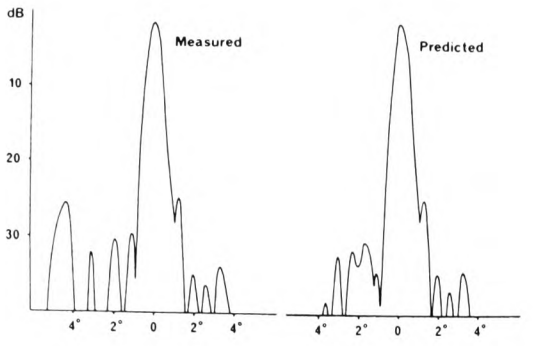

(a)

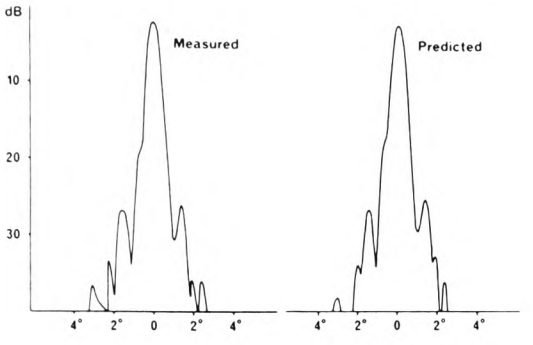

(b)

Figure 2 (a) Far-field radiation patterns (H-plane).
(b) Far-field radiation patterns (E-plane).

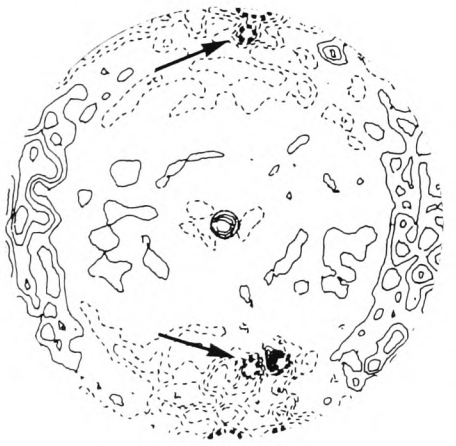

Figure 3a Contour map of profile error

——— + 0·15λ
——— + 0·12λ, + 0·09λ, + 0·06λ, + 0·03λ
– – – – – 0·03λ, – 0·06λ, – 0·09λ, – 0·12λ
– – – – – 0·15λ

zero height contour omitted for clarity

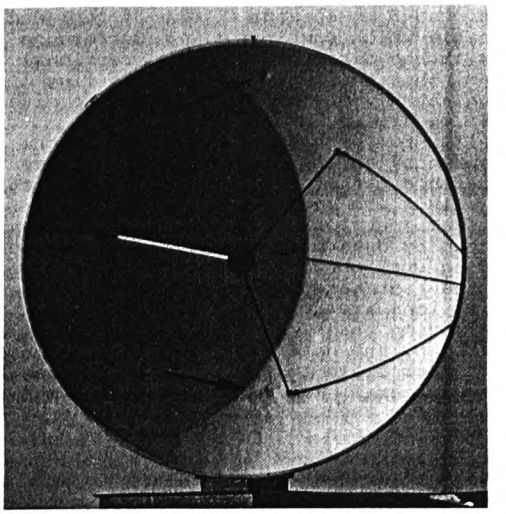

Figure 3b The 3.66 m paraboloid antenna

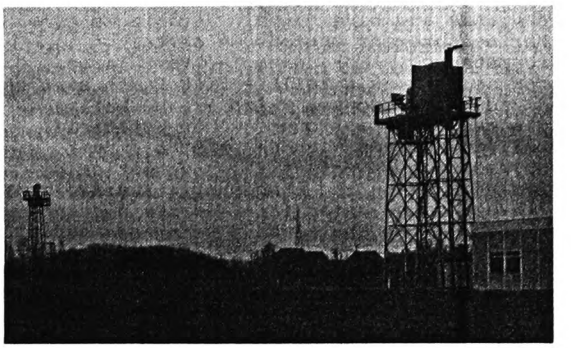

Figure 4 MAROTS antenna measurement facility

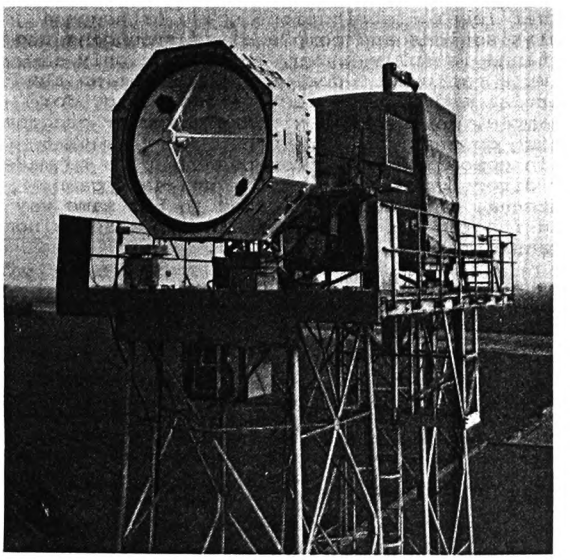

Figure 5 Receive tower with a development antenna in test container.

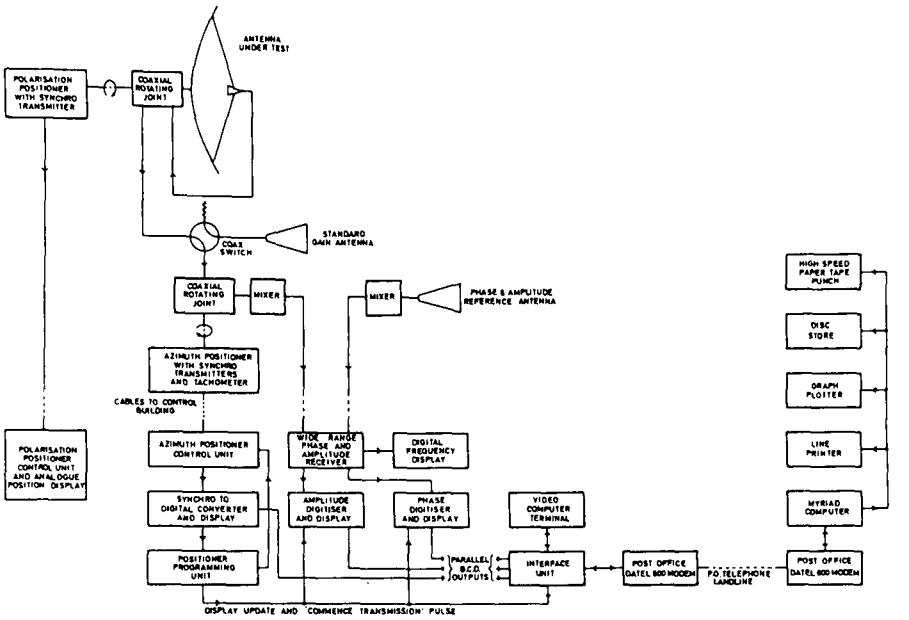

Figure 6 Marconi 'MAROTS' antenna test range instrumentation

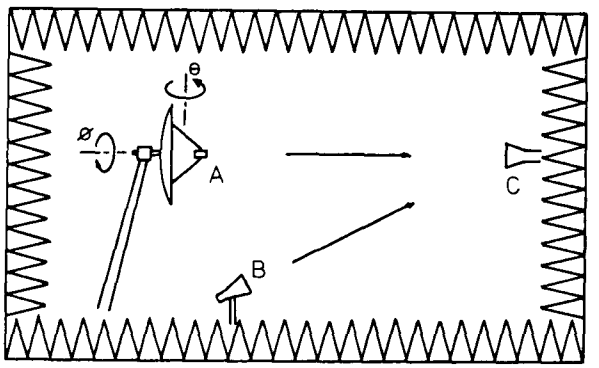

Figure 7 Measurement method geometry

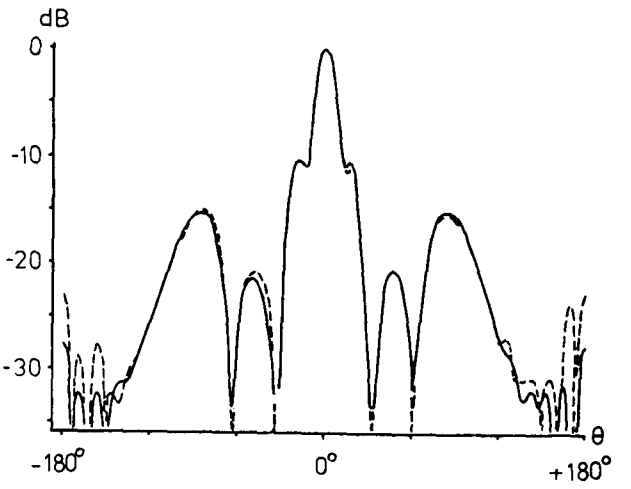

Figure 9 H-plane patterns of parabolic antenna

Full line is from conventional pattern measurement at 20 m, broken line is pattern from interference method at 3 m.

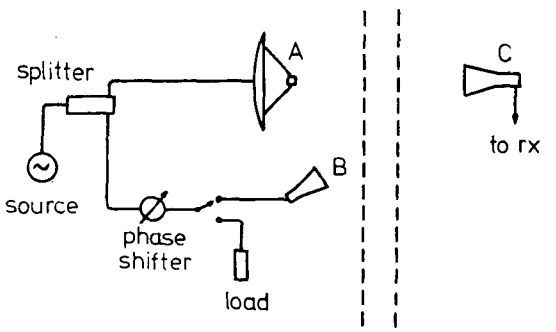

Figure 8 Feeding circuit of antennas A and B

Publication P20. B. CLAYDON, K.M. KEEN and A.B. HARRIS, *Wide angle radiation from Earth station antennas*. IBID, pp 218-222.

WIDE ANGLE RADIATION FROM EARTH-STATION ANTENNAS

B Claydon,* K M Keen,* A B Harris**

* RF Technology Centre, ERA, UK. ** Post Office Telecommunications Headquarters, UK

INTRODUCTION

With the increasing usage of the geostationary orbit for satellite radio-communication systems and the constant pressure upon the available frequency spectrum for space applications, the sidelobe radiation performance of earth-station antennas is rapidly becoming a parameter of critical importance. The present generation of earth-station antennas has been designed and constructed with considerable emphasis placed upon performance parameters such as gain, efficiency and figure of merit, and with much less attention given to the suppression of sidelobe radiation. Although the figure of merit parameter implies some interest in spurious radiation, this is more in relation to noise temperature considerations and is not primarily concerned with sidelobes which are directed toward the relatively cold sky.

It is generally accepted that the use of antennas with the best achievable radiation patterns will lead to the most efficient use of the available radio-frequency spectrum and the geostationary orbit. However, it is also clearly desirable that any specifications on sidelobe performance while providing an adequate electrical performance will also be realisable with good design and construction practice without imposing excessive cost requirements.

Most satellite earth-stations employ the axisymmetric Cassegrain design of antenna. The major factors influencing the wide-angle radiation of such an antenna can be identified as:

(a) primary-feed spillover
(b) diffraction from the edges of both the main and sub-reflectors
(c) scattering from the subreflector support structure
(d) main reflector profile errors.

Each of these factors is discussed and their relative importance clarified.

The so-called reference curve $32-25\log\theta$ dBi originated from the need for a generalised radiation pattern for earth-station antennas for use in estimating interference between earth-stations and terrestrial radio-relay stations. This curve can usefully be employed as a measure of the sidelobe performance of different antennas and the relative importance of the component factors giving rise to that performance.

PRIMARY-FEED SPILLOVER

A prime objective in the design of primary-feeds for high-gain earth-station antennas is efficient illumination of the Cassegrain subreflector. For an axisymmetric system, primary-feed radiation pattern symmetry is a first step towards achieving this. For good overall sidelobe suppression it is also essential that the wide-angle radiation pattern, including the first sidelobe, of the primary-feed itself be well controlled. An example of an antenna employing a primary-feed not compatible with low sidelobe radiation is illustrated in Fig 1. Here the E-plane radiation pattern from the feed has been superimposed on satellite measurements of the antenna radiation pattern. From an angle of 10° off-boresight (the edge of the subreflector) outwards the sidelobe structure of the feed can be identified on the antenna pattern. A necessary condition for overall antenna sidelobe suppression is, therefore, the adoption of high performance primary-feeds whose own wide-angle radiation pattern satisfies the overall specification. The corrugated conical horn has been shown to be capable of very low sidelobe radiation over a wide frequency band and when employed in a Cassegrain configuration results in a significant improvement in the wide-angle radiation.

DIFFRACTION FROM REFLECTOR EDGES

A further high contribution to the wide-angle radiation is due to the blockage and scattering effects caused by the Cassegrain subreflector. The Geometrical Theory of Diffraction may be used to determine the edge diffraction from the subreflector due to the incident radiation from the primary-feed. These diffraction effects depend on the geometry of the antenna and on the level of edge illumination. Fig 2 depicts the diffraction effects, in the vicinity of the incident shadow boundary, when the primary-feed edge illumination is varied. The absolute level of the diffraction pattern changes with the edge illumination, with the maximum coinciding with the semi-angle subtended by the subreflector at the primary-feed. This maximum level of the spillover-diffraction lobe can be approximated by the simple formula,

$$S_p = G_F + T - 6 \quad \text{dBi}$$

where G_F is the primary-feed gain and T is the edge illumination taper.

The edge illumination taper is a critical parameter; Fig 3 shows the maximum level of the spillover-diffraction lobe for various subreflector semi-angles and primary-feed edge tapers. In the case of the paraboloid-hyperboloid Cassegrain configuration, the choice of primary-feed illumination taper at the edge of the subreflector directly influences the attainable aperture efficiency and a taper of about -13dB is generally found to optimise the product of aperture and subreflector spillover efficiencies. However, this level of edge taper is not compatible with a low spillover-diffraction lobe and efficiency must be degraded to ensure a spillover-diffraction lobe whose level falls below the reference curve. For the high-efficiency shaped Cassegrain reflector, a low level of primary-feed edge illumination can be compensated by shaping the subreflector profile so that the main reflector aperture distribution is essentially uniform. It is therefore feasible to ensure both high efficiency and spillover-diffraction lobes below the reference curve using edge tapers of about -20dB. However, communications antennas need to operate over a fairly wide frequency band with the design frequency generally chosen nearer the lower end. The primary-feed illumination taper will therefore increase as the frequency increases and the efficiency will decrease. A compromise value of the edge taper at the design frequency would appear to be -15dB.

In contrast to the variation of the edge illumination taper, when the diameter of the subreflector is varie the absolute level of the diffraction pattern at the incident shadow boundary remains unaltered but the

periodicity of the ripple and the rate of fall-off change. This rate of fall-off, in any case, decreases faster than 25 logθ so that any violation of the reference curve will be restricted to angles in the vicinity of the incident shadow boundary.

Two other sources of diffracted fields are associated with Cassegrain antennas,

(a) subreflector blockage diffraction due to the fields reflected by the main reflector incident on the rim of the subreflector,
(b) main reflector edge diffraction due to the reflected fields from the subreflector.

The former is dominant close to the main beam of the antenna but for most practical cases is exceeded by the diffraction at the subreflector edge due to the incidence of the primary-feed radiation. The main reflector edge diffraction leads to a maximum in the direction of the reflection shadow boundary of the subreflector. In the case of the paraboloid-hyperboloid configuration this maximum level depends on the illumination taper at the edge of the subreflector. For high-efficiency shaped Cassegrains, the illumination distribution across the main reflector aperture is, generally, highly tapered towards the edge thus minimising the diffraction effects.

SCATTERING FROM THE SUBREFLECTOR SUPPORT STRUCTURE

The contribution of subreflector support blockage to the wide-angle radiation of an axisymmetric Cassegrain antenna arises from two factors:

(a) the spherical wave reflected from the subreflector being blocked before reaching the extremities of the main reflector,
(b) the plane wave emanating from the main reflector aperture being blocked by the support struts.

Spherical wave blocking leads to trapezium shape shadowed areas at the periphery of the main reflector. The scattered radiation associated with this may be determined by application of aperture-field techniques since the major contribution is contained close to boresight. For a typical earth-station Cassegrain geometry, the level of radiation reduces quickly away from boresight, reaching the isotropic level of the antenna at 5-10^{o} from axis.

The more dominant contribution to the wide-angle radiation is due to the scattering by the support struts of the plane wave reflected from the main reflector aperture. By approximating each strut as a plane strip whose surface current distribution is determined by application of the field boundary conditions, an approximate theoretical model can be constructed for determining the wide-angle radiation envelope (1). For a single strut, the predicted scattered field resembles that of a phased line source, maximising on a conical surface whose angular position depends solely on the inclination of the strut to the aperture plane.

An experimental programme has been carried out to investigate the validity of this theoretical model. Isolation of the scattered field associated with a strut from the far-field response of an antenna is generally difficult as the contribution is of a similar order of magnitude to the sidelobe levels of the reflector. However, by placing a strut in the near-field of an offset reflector antenna with very low sidelobes of its own, a "pattern difference" technique has been devised which allows this isolation with reasonable accuracy. The measurement system is illustrated in Fig 4. The strut model is supported by blocks of expanded polystyrene which is almost invisible at microwave frequencies. Strut responses are isolated by comparing in each case a "with strut" pattern with its "without strut" counterpart, as shown in Fig 5. Fig 6 compares the predicted and measured overall -10dBi contour levels for a 3.8λ diameter circular strut; good agreement is evident. The peak values of the co- and cross-polar responses were also in good agreement to within 5dB.

The overall radiation envelope due to plane wave blocking from a tripod or quadrupod, as used in earth-station antennas, can be derived from the sum of the patterns of constituent single struts. An approximate contour plot for a tripod with parameters typical of those associated with a 30m diameter Cassegrain antenna in the receive frequency band is shown in Fig 7.

MAIN REFLECTOR PROFILE ERRORS

Random profile errors in earth-station antennas arise from several causes. Changes in the gravitational loading with elevation angle, wind and thermal expansion will all tend to cause profile errors with large correlation intervals of the order of the reflector radius, resulting in an average gain function which is directive and largely contained in the boresight region. On the other hand, errors in the setting of individual reflector panels or in the original manufacture of the panels, will give rise to errors with correlation intervals of the order of a panel size or less. Panel dimensions will vary to some extent with aperture size, but in most antenna designs lie between 1m and 3m. The effects of typical profile errors for earth-station antennas of diameter 30m operating at 6GHz (2) are shown in Fig 8. Only the errors associated with small correlation intervals are seen to affect the wide-angle radiation and these effects rapidly become negligible with increasing angle. The curves are drawn such that 90% of the sidelobe peaks are contained below them; for all the peaks to be enclosed, a further 5dB should be added.

SUMMARY

The interference between satellite systems plays a major role in determining the allowable spacing between communications satellites sharing the same frequency band (3). If a curve of the form A-Blogθ is used to represent the antenna sidelobe envelope, the minimum allowable spacing is dependent on both coefficients A and B. For the reference curve 32-25logθ and with typical system parameters, the minimum acceptable spacing would be 2.9^{o}. By reducing A, the envelope level at 1^{o} off-axis, and increasing B, the fall-off rate of the envelope with angle, this allowable spacing can be decreased.

This poses the question - what are the limitations on sidelobe specifications and hence on satellite separation ? The limitations on the coefficients Aand B, given a primary-feed with low sidelobes, are principally due to subreflector edge illumination, subreflector blocking and profile errors. For example, most earth-station antennas employ an axisymmetric design with blocking diameter ratio of approximately 0.1. This sets a lower limit on A of between 26 and 28dB. The use of an offset antenna, where central blockage is avoided, could reduce this value by a further 2dB.

Table 1 summarises the major requirements on the earth-station antenna to achieve sidelobe envelopes of 32-25logθ, 29-25logθ and 26-33logθ resulting in allowable satellite spacings of 2.9^{o}, 2.2^{o} and 1.6^{o} respectively. Certain present-day earth-station antennas have been designed with these requirements in view and have attained the first envelope. The second envelope represents a design challenge which is feasible using an axisymmetric Cassegrain antenna. The third envelope offers a possible insight into the future when the restrictions due to aperture blockage will be removed by the use of offset configurations.

TABLE 1 - Antenna requirements for specified sidelobe envelopes

ANTENNA REQUIREMENT	SIDELOBE ENVELOPE		
	32-25logθ	29-25logθ	26-33logθ
Antenna type	High-efficiency shaped axisymmetric Cassegrain	High-efficiency shaped axisymmetric Cassegrain	Dual-offset - high-efficiency shaped Cassegrain
Primary-feed	Corrugated horn	Corrugated horn	Corrugated horn
Subreflector edge taper	-15dB	-20dB	-20 to -25dB
Main reflector profile errors correlated over less than 1m	0.5mm rms	0.25mm rms	less than 0.25mm rms
Subreflector support structure	Due attention necessary	Due attention necessary	Not applicable

The table assumes that each factor can be treated individually. To ensure that the overall radiation envelope formed by the combination of each of these effects lies below a certain level even tighter restrictions should be applied. The wide-angle spikes due to the plane-wave scattering from struts in an axisymmetric antenna have not been considered in relation to the achievable sidelobe envelope since they only occur over a limited angular range. However, they do represent a potential interference hazard and can only be eliminated by employing an offset design.

ACKNOWLEDGEMENTS

The authors acknowledge the permission of the Senior Director of Development of the British Post Office to publish this paper.

REFERENCES

1. Kreutel, R W., 1976, COMSAT Technical Review, 6, 71-88

2. Harris, A B., 1978 Elect.Letters, 114, 343-345

3. Withers, D J., 1977, Proc.IEEE, 65, 308-317

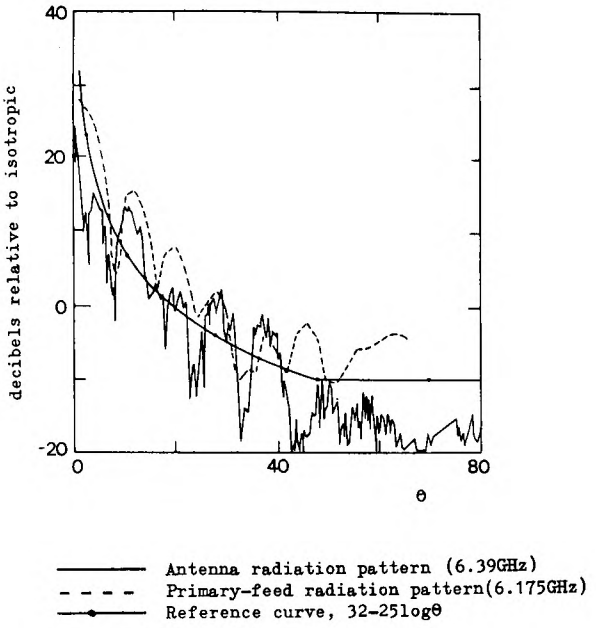

Fig 1 Effects of primary-feed spillover

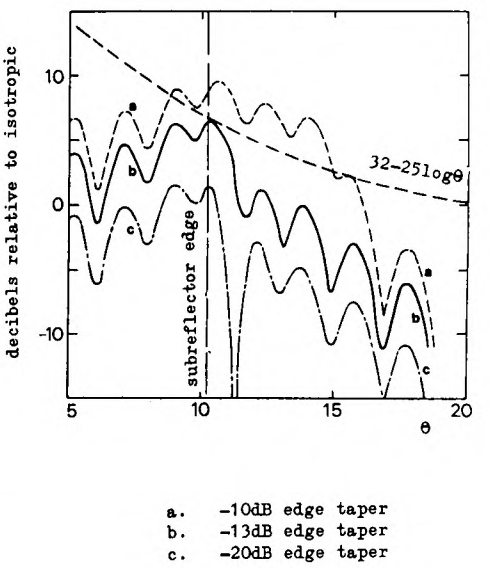

a. -10dB edge taper
b. -13dB edge taper
c. -20dB edge taper

Fig 2 Variation of subreflector diffraction wit edge illumination taper

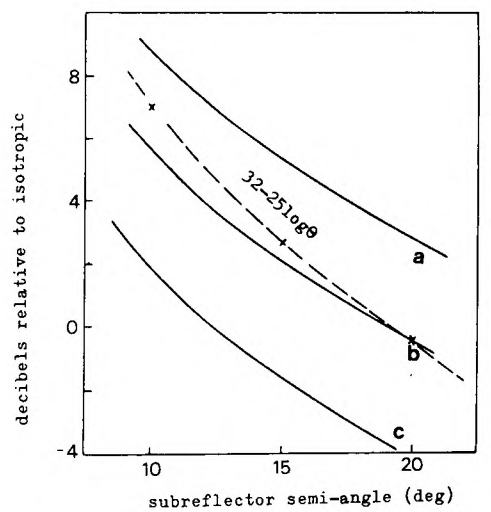

a. -10dB edge taper
b. -15dB edge taper
c. -20dB edge taper

Fig 3 Variation in level of spillover-diffraction lobe with subreflector semi-angle and edge illumination taper

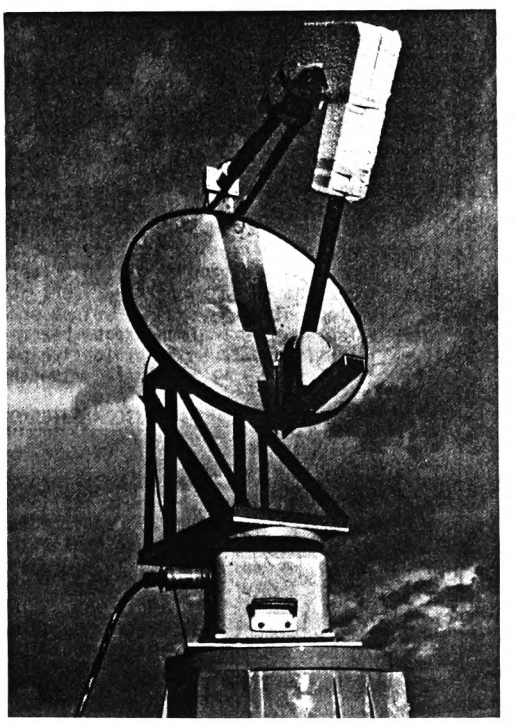

Fig 4 Measurement system for strut radiation

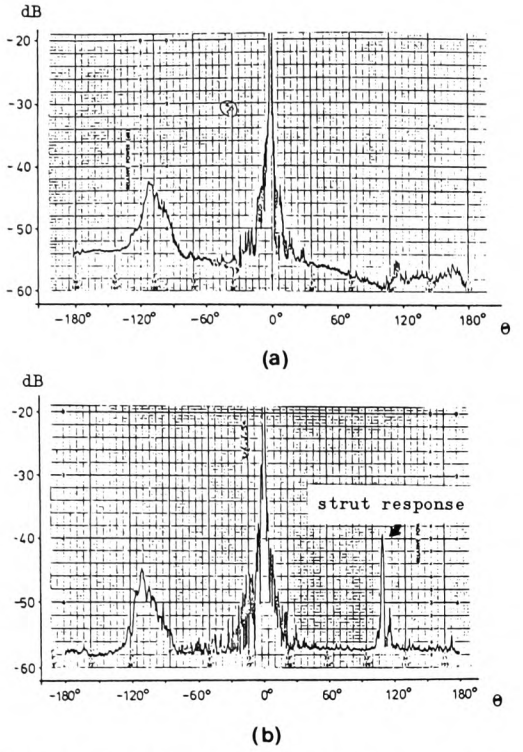

Fig 5 Wide angle radiation patterns from offset reflector relative to peak gain
(a) without strut; (b) with strut

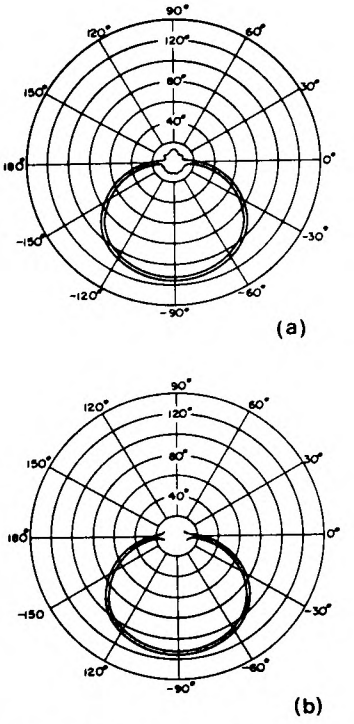

Fig 6 -10dBi contour plot of radiation from 3.8λ diameter strut (a) predicted; (b) measured.

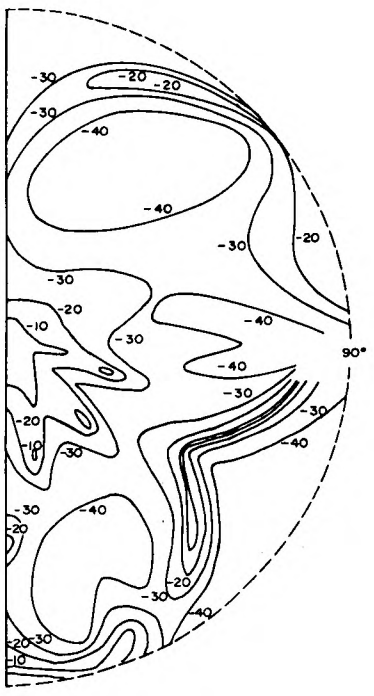

Main reflector diameter 400λ, strut width 4λ, strut length 156λ

Fig 7 Approximate contour plot of plane wave radiation envelope due to tripod blocking
(contours in decibels relative to isotropic)

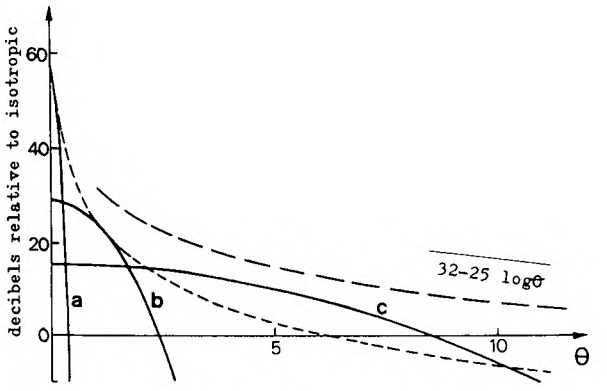

(a) 1mm rms errors correlated over 10m
(b) 0.5mm rms errors correlated over 1m
(c) 0.5mm rms errors correlated over 0.2m
- - - - diffraction envelope for uniformly illuminated aperture

Fig 8 Contribution of profile errors to radiation envelope of a 30m earth-station antenna at 6GHz

Publication P21. N. WILLIAMS, P.R. FOSTER, P. WRIGHT, and K.M. KEEN, *Antennas for RPVs*. International Conference on Remotely Piloted Vehicles, Bristol, England, Sept. 1979.

RPVs
Int Conf. Bristol 3-5 Sept 1979

ANTENNAS FOR RPV's

N Williams, P R Foster, P Wright and K Keen

RF Technology Centre, ERA, U.K

(Dr Foster is now with British Aerospace, Filton, U.K)

Introduction

Antennas on RPV's are employed for communication links and with microwave sensors. The former vary from narrowband Telemetry, Telecommand and Control (TT and C) channels to a wideband secure video data link. Microwave sensors generally operate at frequencies extending well into the millimetre wave band to achieve higher resolutions. Although many of the problems associated with mounting antennas on RPV's are similar to those encountered with manned aircraft, there are important differences which demand special attention. This is particularly true of the smaller RPV's considered in the work reported here.

Perhaps the most important area is protection against enemy interference with the communications/data link between the RPV and the control station. Federhen [1] of the Defense Advance Research Products Agency writes:

"Command, telemetry and data links are the weakest part of the RPV system and, unless a way can be found to provide reliable links in a hostile electromagnetic environment, the utility of the entire (RPV) system will be severely restricted".

Although many techniques are available, one of the most effective approaches is to control the radiation pattern of the antenna. Consideration must also be given to the scattering properties of the antenna, particularly in those RPV's which are specifically designed to minimise the radar cross section.

The choice of antennas is limited by the constraints of the RPV platform. Small RPV's are subject to severe limitations on weight and volume with the payload mass, perhaps, 20-30% of all up weight; the antenna mass budget is a fraction of this, typically 0.5 Kg. The radiation characteristics of the antenna must take account of the manoeuvring of the RPV; this generally implies a coverage of 360° in azimuth with an elevation plane pattern which is shaped in accordance with the pitch and roll characteristics of the aircraft and the operating range limits. Unless facilities for tracking and scanning the beam can be incorporated (at the expense of increased weight and complexity) small gain antennas must be employed. At high frequencies, however, the tail, wings and fuselage projections will cause deep nulls over wide angular regions of the antenna coverage pattern and several correctly sited antennas may be required to provide full azimuth coverage. Again, this is at the expense of additional mass and complexity. Lower frequency antennas do not suffer from obscuration effects to such an extent and may be similar in design to those employed with manned aircraft although more flexibility in mounting position should be available because of the lower flying speeds. An added advantage is that smaller vehicles can be mounted on conventional antenna positioning equipment and the antenna radiation patterns measured directly. Also the airframe geometry may be simpler and more amenable to theoretical analysis.

In the paper, the antennas used in current RPV experiments are reviewed and the development of a microwave antenna system for a secure data link is described which indicates the improvements which may be made with careful design.

Review of existing RPV antennas

Although at least 20 RPV's have been operational in the United States and perhaps half that number in Europe and elsewhere, the antenna design has received little attention. [2] The literature gives the impression that the final installation in an RPV is the communications/control link antenna which is placed as close to the electronics equipment as possible without regard to the effects of the airframe on the radiation characteristics. The whip configuration is generally used at low frequencies, whilst the higher frequency video links have employed skin mounted stub or discone elements.

Considerable attention has been given to the reduction of unwanted interfering signals using adaptive arrays, including null steering arrays (where with N elements, N-1 interfering signals may be nulled out). [1,3,4] However, few practical examples have been reported and the weight restrictions are likely to limit their application in the immediate future to large RPV's. Nulls of -30dB to -40dB on unwanted signals have been achieved in prototype systems with 3 to 5 element arrays. In order to maximise the desired signal it is, of course, necessary to either know its angular position or identify it by known parameters (exact frequency, bit rate or spread spectrum code).

To date, RPV mounted microwave sensors have mainly been radars although some development of radiometric sensors has been undertaken. [5] The trend is towards higher operating frequencies to obtain greater resolutions without a corresponding increase in aperture dimensions. Conventional

radars have generally used reflector antennas of lightweight construction. Synthetic aperture radar techniques are attractive in that 2D resolution can be achieved with a single line feed. A Slotted waveguide configuration has generally been preferred but printed circuit approaches may be required in lightweight, low cost applications. At millimetre wavelengths, however, feed and radome losses become increasingly important, particularly in radiometer systems.

Summarising, the antennas required in RPV's must satisfy very demanding specifications, particularly those used with secure data links. Existing designs, developed largely for experimental purposes, appear inadequate for eventual systems operating close to the horizon and in the presence of unwanted interference. The complexity of adaptive arrays make them unattractive in the short term, certainly for small RPV's. Against this background, antennas for a secure data link operating in I band and installed on the Stabileye fixed wing RPV are under development. A compromise solution has been chosen involving the use of multiple element switched beam antennas which provide some discrimination against interfering signals with the elements differently sited to maximise the overall coverage.

Antennas for I band secure data link

The coverage requirements for the vertically polarised antenna system are summarised in Figure 1. Maximum gain is required in the yaw plane for horizon operation. Increased gain and some discrimination against interfering signals is realised with a number of switched beams, each providing sector coverage. The radiation patterns in the pitch and roll planes have, ideally, constant gain over the range of angles corresponding to the pitch and roll of the aircraft during manoeuvres, and are shaped in the remaining sectors to provide constant signal at the ground station with range. In practise, a separate antenna is required for extremely close ranges which provides a circularly polarised component at angles near to the vertical. The development was carried out in two phases: a single omni-directional antenna was designed for use in initial short range data link trials; in parallel, the problems associated with the provisioning of the switched beam antennas were examined and a preferred design established.

The short range antenna is mounted underneath the fuselage and is integrated with the payload. The radiation characteristics are shown schematically in Figure 2. A simple monopole element produces a vertically polarised pattern with a null on its axis. To provide the additional circularly polarised component for close ranges, the configuration shown in Figure 3 was devised. The parasitic element provides the required orthogonal vector in phase quadrature with the principal vector. Typical radiation patterns (of the isolated antenna) are plotted in Figure 4 and the VSWR characteristics in the band of interest are presented in Figure 5. The antenna is protected with a wedge-faired radome, compatible with low sub-sonic air speeds as illustrated in Figure 6.

The outline specifications of the antennas for long range coverage are summarised below:

1. Beamwidth a) yaw plane: full 360° coverage provided by 4 switched beams,
   b) pitch and roll plane: maximum gain in sectors $\pm 25^{\circ}$ about the horizontal and $\mathrm{cosec}^2\theta$ coverage at low angles.
2. Polarisation: vertical
3. Frequency: I band
4. Bandwidth: approximately 5%
5. Target mass: $\leq$ 0.5 Kg.
6. Compatible with Stabileye airframe

It was realised that a major problem would be obscuration of the antenna radiation by the airframe which is large in terms of wavelengths. The principal effects are shown schematically in Figure 7. A number of radiation pattern measurements were performed with a monopole mounted at various sites in the fuselage skin and with a biconical antenna, elevated above the airframe, to examine the magnitude of these effects. Sample radiation patterns are presented in Figures 8 and 9. The results demonstrate that, first, a single antenna mounted on the fuselage will not provide adequate 360° coverage at angles close to the horizontal and second, multipath effects seriously degrade the performance of elevated antennas which provide adequate coverage in the pitch and roll planes. It was concluded that several antennas were needed to obtain acceptable performance and that the wing tips offered the best sites since they introduced least obscuration.

The wing tip antenna system is shown schematically in Figure 10. Three single pole-double throw switches are required to direct energy to the appropriate radiating element. The driving signals to control these are derived from the navigation equipment and the circuitry required is being developed by RAE and BAe. Obviously, the penalty to be paid in this scheme is the mass and insertion losses of the switches and semi-rigid feeder; this is estimated to be 350gms and 1.4dB respectively.

The Stabileye wing assembly consists of a metal skin and ribs, with the wing tips formed in rigid plastic foam covered with a GRP skin. It is therefore appropriate to mount the antennas on the end metal rib and use the present wing tip moulding as a protective radome. A prototype antenna system was constructed using dipole radiating elements as shown in Figure 11. Representative patterns of one wing tip assembly providing 180° coverage in the yaw plane are shown in Figure 12. No interaction with the edges of the wing were noted but the patterns are

strongly influenced by the surface of the end wing rib and the patterns shown were recorded with radio-absorbent material on the rib. An optimised antenna configuration is currently under development.

Conclusions

The problems associated with mounting antennas on RPV's have been discussed and the need for improved designs was highlighted. The design of a high frequency antenna system for the video data links of a fixed wing, mini-RPV was described which represents one possible approach to achieve improved performance.

References

1. FEDERHEN, H.M. RPV - remotely piloted vehicle, command and control. Signal (USA), Vol 29, No.10, pp 64-67, August 1975.

2. FOSTER, P.R. and WILLIAMS, N. Antennas for RPV's. Final report on MoD Contract, Report No: RFTC 280976, ERA, Leatherhead, June 1978.

3. RASSWEILER, G.G., MARTIN, G.P., PAYNE, L.M. and LEHMAN, D.F. Null steering arrays for RPV applications. IEEE International Communications Conference Paper 10E, 1974.

4. The search for smarter and scrappier drones, Microwaves, Vol 12, pp 42-54, October 1973

5. DAVIS, R. Millimetre waves: a solution that's finally found a problem. Microwave System News, Vol 7, pp 63-70, September 1977.

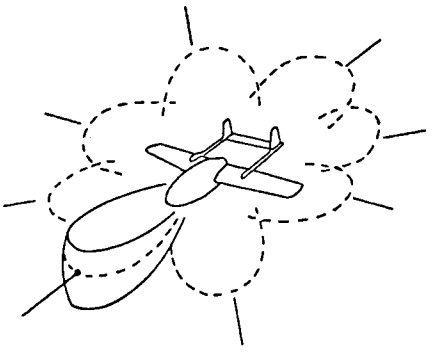

Figure 1: Multiple switched beam configuration providing full azimuth coverage

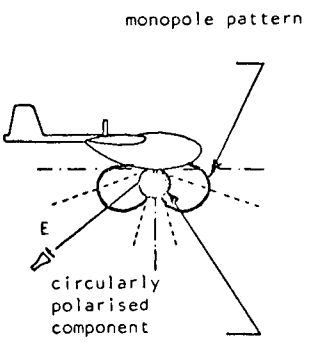

Figure 2: Close range coverage requirements

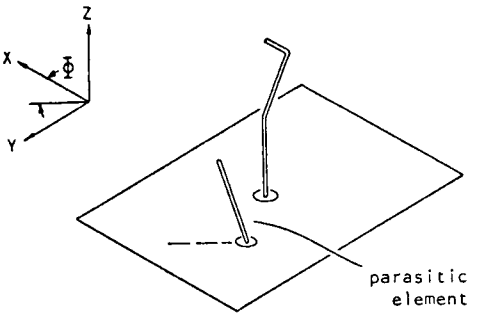

Figure 3: Bent monopole with angled parasitic element providing a circularly polarised contribution

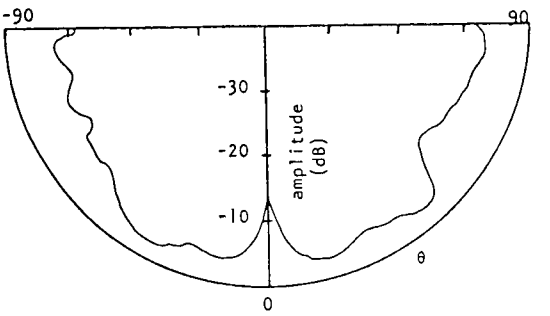

Figure 4a: Co-polar radiation pattern of short range antenna in Φ = 0 plane

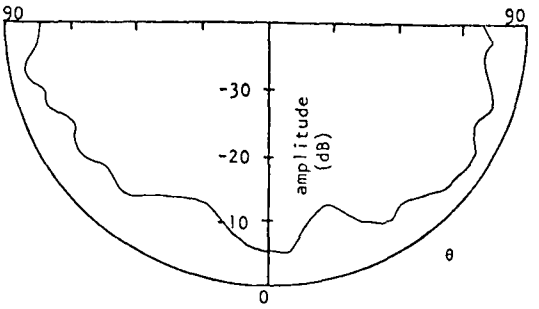

Figure 4b: Co-polar radiation pattern of short range antenna in Φ = 90° plane

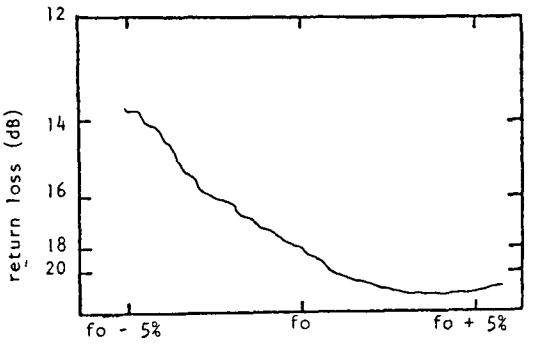

Figure 5: Return loss of short range antenna

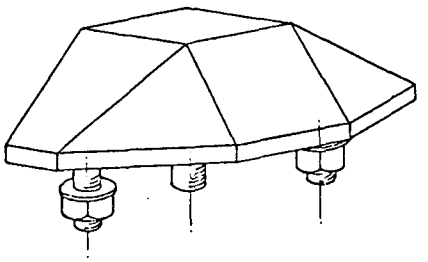

Figure 6: Outline of assembled short range antenna showing wedge faired radome

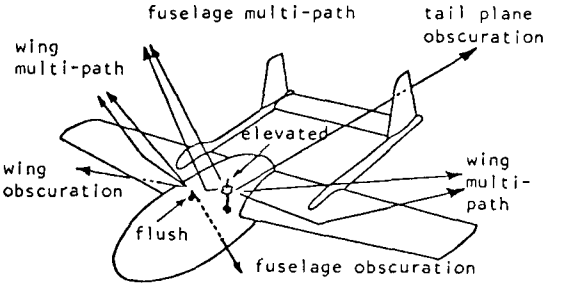

Figure 7: Principal airframe effects at high frequencies

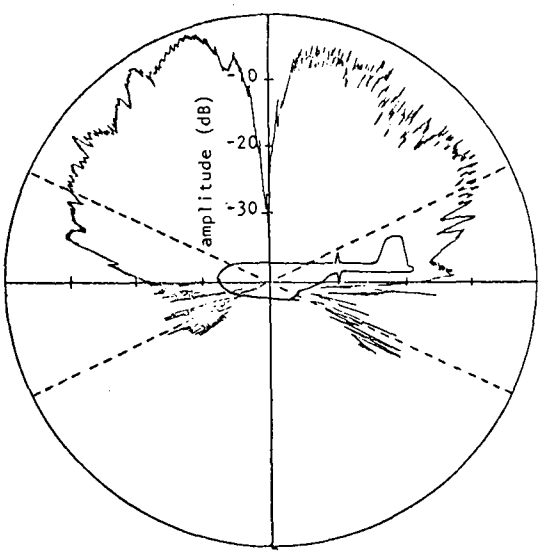

Figure 8: Radiation pattern of stub antenna mounted on top surface of fuselage in pitch plane

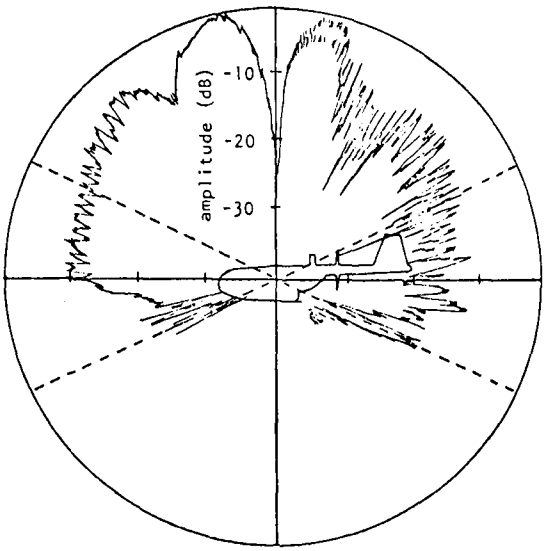

Figure 9: Radiation pattern of biconical antenna mounted 10 wavelengths above the top surface of the fuselage

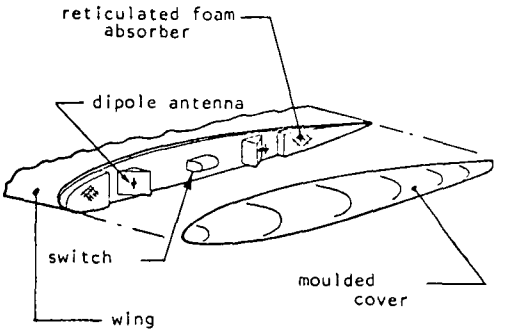

Figure 11: Prototype wing tip antenna system

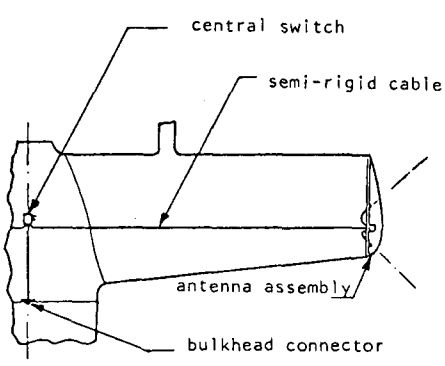

igure 10: Wing tip antenna system

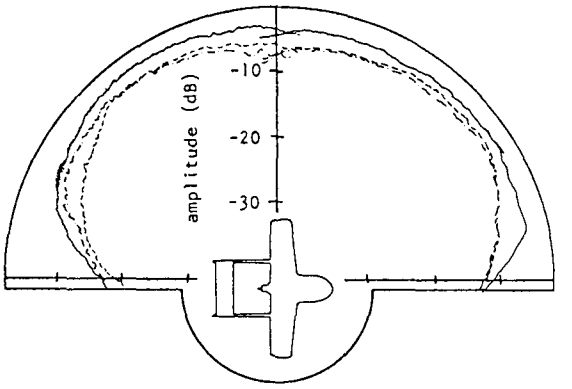

Figure 12: Radiation patterns of prototype wing tip antenna system in horizontal plane

——— roll angle 0°
----- roll angle 30°
— . — roll angle -30°

Publication P22. A.B. HARRIS, B. CLAYDON and K.M. KEEN, *Reducing the sidelobes of Earth station antennas*. International Conference on Communications, Boston, USA, June 1979, Conference Proceedings. pp 6.6.1-6.6.5.

REDUCING THE SIDELOBES OF EARTH-STATION ANTENNAS

A B HARRIS, Telecommunications Development Department, British Post Office
B CLAYDON and K M KEEN, RF Technology Centre, ERA, England

ABSTRACT

With the increasing usage of the geostationary orbit for satellite communications systems the sidelobe radiation performance of earth-station antennas is rapidly becoming a parameter of critical importance.

This paper considers the factors contributing to the wide-angle radiation of typical earth-station antennas, and derives their relative importance. Tighter sidelobe performance specifications are proposed and the necessary design parameters required to meet these specifications are stated. These measures would significantly reduce the minimum spacing between satellites in the geostationary orbit.

INTRODUCTION

In the early days of satellite communications, satellite capacity was limited principally by thermal noise in the receiving antenna relative to the low signal power available from the satellite. As a result earth station specifications placed a strong emphasis on G/T, the ratio of antenna gain to noise temperature. However, with the rapidly increasing number of communication satellites now using the geostationary orbit, interference between satellite systems is becoming the major limitation on communications capacity. This factor imposes a fundamental limit on the number of co-frequency satellites which can be deployed around the geostationary orbit, so there is an urgent need to establish the minimum sidelobe radiation level which could be economically achieved by taking appropriate measures in the design of the antenna.

This paper reports the principal results of a study carried out to determine the limitations on antenna sidelobe performance (Refs 1, 2). Consideration is primarily directed towards large reflector antennas of 400-600 wavelengths diameter, such as the 32 m antennas used at 4 and 6 GHz in the Intelsat system, but the principles deduced apply to all large reflector antennas of more than 50-100 wavelengths diameter.

At present most earth-stations employ axisymmetric Cassegrain antennas, in which the following principal sources of sidelobe radiation can be identified:

(a) Primary-feed spillover

(b) Subreflector edge diffraction.

(c) Main reflector aperture distribution and edge diffraction.

(d) Scattering from the subreflector support structure.

(e) Main reflector profile errors.

Each of these factors will be discussed in turn before we assess their relative significance and the measures which would need to be taken to reduce sidelobe levels below those of current specifications.

The CCIR Reference Curve

$$G = 32 - 25 \log \theta \text{ dBi}$$

has been widely adopted as a specification. In this paper it is used as a baseline against which to compare the performance of particular antennas and the relative significance of the separate contributions to that performance.

PRIMARY-FEED SPILLOVER

In a Cassegrain antenna, sidelobes of the feed horn itself will contribute directly to the far-field radiation pattern of the antenna. Fig 1 shows an example of an early antenna design in which, from an angle of 10° outwards, the feed radiation pattern can clearly be seen underlying the antenna pattern. In beam-waveguide antennas the sidelobes of the horn will still contribute to the sidelobe radiation but lose their regular lobe structure on transmission through the beam-waveguide.

An essential condition, therefore, for an antenna to meet a given specification is that the feed horn should well satisfy that specification. Fortunately the corrugated horn, which is coming into widespread use because of its wide-band pattern symmetry and low cross-polarization, is also capable of excellent sidelobe performance over a wide frequency range.

SUBREFLECTOR EDGE DIFFRACTION

A further high contribution to the wide-angle radiation is spillover of the feed horn main lobe

CH1435-7/79/0000-0037$00.75

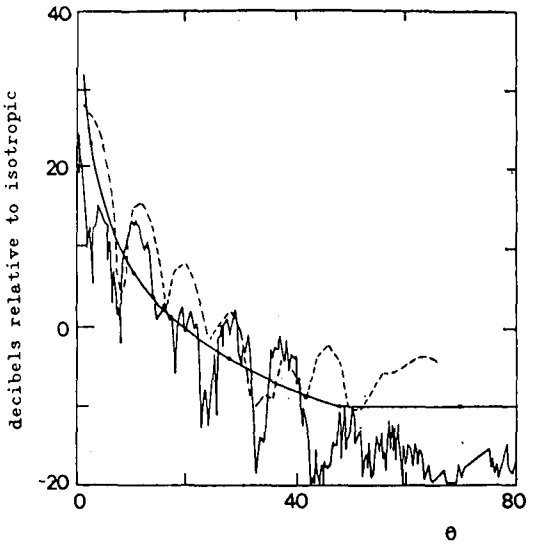

——— Antenna radiation pattern (6.39GHz)
- - - - Primary-feed radiation pattern(6.175GHz)
—•— Reference curve, 32-25logθ

Fig 1 Effects of primary-feed spillover

past the subreflector and diffraction of this radiation by the subreflector edge. The Geometrical Theory of Diffraction may be used to determine in detail the edge diffraction from the subreflector due to the incident radiation from the feed horn. These diffraction effects depend on the geometry of the antenna and on the level of edge illumination. Fig 2 depicts the diffraction effects when the feed edge illumination is varied. The absolute level of the diffraction pattern changes with the edge illumination, with the maximum coinciding approximately with the semi-angle subtended by the subreflector at the feed.

The maximum level of the spillover diffraction lobe can be approximated by the simple formula,

$$S_p \approx G_F + T - 6 \text{ dBi}$$

where G_F is the feed gain and T is the edge illumination taper. Fig 3 shows that the edge illumination taper is the critical parameter. As the subreflector semi-angle is varied, so is the required forward gain of the feed horn so that this parameter has little effect on whether the antenna conforms to a sidelobe specification.

In designing a high-efficiency shaped Cassegrain reflector, a low level of feed edge illumination can be compensated by shaping the

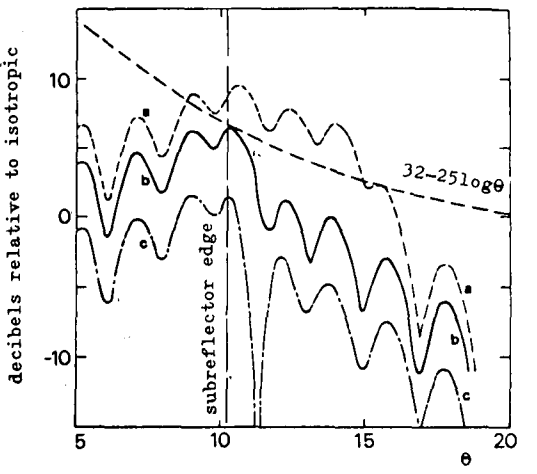

a. -10dB edge taper
b. -13dB edge taper
c. -20dB edge taper

Fig 2 Variation of subreflector diffraction with edge illumination taper

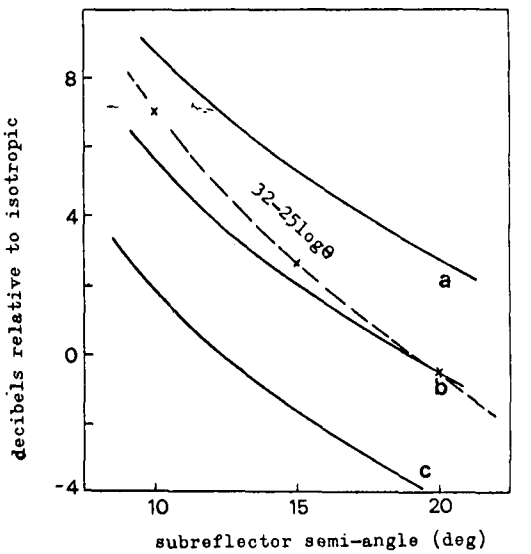

a. -10dB edge taper
b. -15dB edge taper
c. -20dB edge taper

Fig 3 Variation in level of spillover-diffraction lobe with subreflector semi-angle and edge illumination taper

subreflector profile so that the main reflector aperture distribution is essentially uniform. It is therefore feasible to ensure both high efficiency and spillover diffraction lobes below the reference curve using edge tapers of about -15 to -20 dB.

When the diameter of the subreflector is varied, the absolute level of the diffraction pattern at its peak remains unaltered but the periodicity of the ripple and the rate of fall-off change. This rate of fall-off, in any case, decreases faster than 25 log θ so that any violation of the reference curve will be restricted to angles in the vicinity of the subreflector half-angle.

The plane wave radiated by the main reflector is also incident on the subreflector, but the resultant diffraction is generally less significant than that due to the incidence of the feed horn radiation.

MAIN REFLECTOR APERTURE DISTRIBUTION AND EDGE DIFFRACTION

The radiation patterns of different reflector aperture distributions can be assessed using a simplified scalar analysis. The radiation pattern of an unblocked aperture lies well below the reference curve, even in the "worst" case of uniform aperture illumination. The sidelobe pattern is increased by blockage due to the subreflector, but not to the level of the present reference curve. The sidelobe levels may be reduced by lowering the illumination levels at the edge of the blocked region and at the edge of the main reflector.

In some antennas there is a region of high sidelobes around 100°-120° from axis where the radiation from the subreflector spills past the edge of the main reflector. This can also be controlled by shaping the subreflector to taper the illumination sharply at the edge of the main reflector.

SCATTERING FROM THE SUBREFLECTOR SUPPORT STRUCTURE

The contribution of subreflector support blockage to the wide-angle radiation of an axisymmetric Cassegrain antenna arises from two factors:

(a) the spherical wave reflected from the subreflector being blocked before reaching the extremities of the main reflector,

(b) the plane wave emanating from the main reflector aperture being blocked by the support struts.

Spherical wave blocking leads to trapezium-shaped shadowed areas at the periphery of the main reflector. The scattered radiation associated with this may be determined by application of aperture-field techniques since the major contribution is contained close to boresight. For a typical earth-station Cassegrain geometry, the level of radiation reduces quickly away from boresight, reaching the isotropic level of the antenna at 5-10° from axis.

The more important contribution to the wide-angle radiation is the scattering by the support struts of the plane wave reflected from the main reflector aperture. By approximating each strut as a plane strip whose surface current distribution is determined by application of the field boundary conditions, an approximate theoretical model can be constructed for determining the wide-angle radiation envelope (3). For a single strut the predicted scattered field resembles that of a phased line source, and maximises on a conical surface whose angular position depends solely on the inclination of the strut to the aperture plane.

An experimental programme has been carried out to investigate the validity of this theoretical model. Isolation of the scattered field associated with a strut from the far-field response of an antenna is generally difficult as the contribution is of a similar order of magnitude to the sidelobe levels of the reflector. However, by placing a strut in the near-field of an offset reflector antenna with very low sidelobes of its own, the effect of the strut could be isolated (Fig 4).

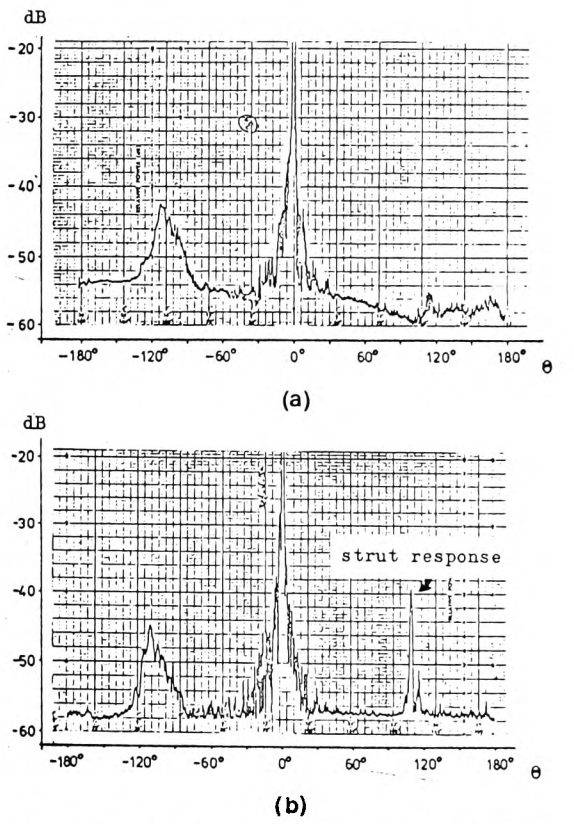

Fig 4 Wide angle radiation patterns from offset reflector relative to peak gain

(a) without strut

(b) with strut

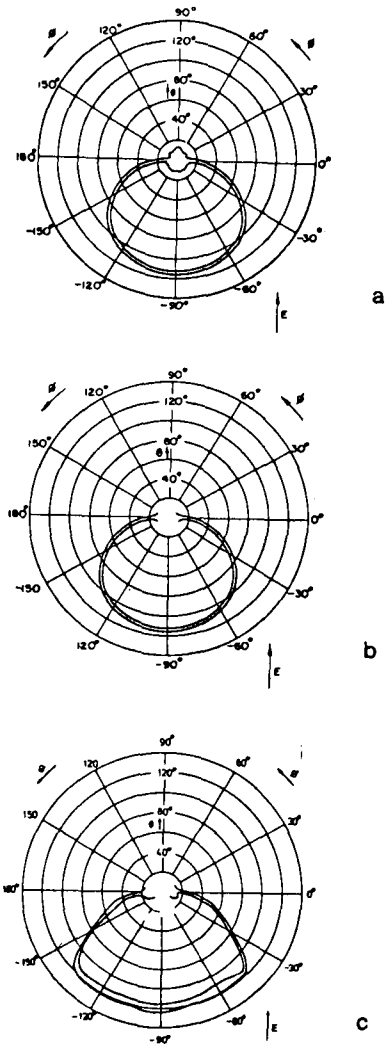

Fig 5 -10 dBi countour plot of radiation from strut:

(a) predicted

(b) measured using circular strut

(c) measured using flat strut

Fig 5 compares the predicted and measured overall -10 dBi countour levels for 3.8λ diameter struts. Good agreement is evident for the circular strut, but the results for the flat strip show additional effects arising from reflection from the flat surfaces or diffraction at the corners. The peak values of the co- and cross-polar responses vary with position along the conical maximum; the predicted and measured values agreed within 5 dB.

The overall radiation envelope due to plane wave blocking from a tripod or quadrupod, as used in earth-station antennas, can be derived from the sum of the patterns of constituent single struts.

MAIN REFLECTOR PROFILE ERRORS

Random profile errors in earth-station antennas arise from several causes. Changes in the gravitational loading with elevation angle, wind and thermal expansion will all tend to cause profile errors with large correlation intervals of the order of the reflector radius. One the other hand, errors in the setting of individual reflector panels or in the original manufacture of the panels will give rise to errors with correlation intervals of the order of a panel size or less. Panel dimensions will vary to some extent with aperture size, but in most antenna designs lie between 1 m and 3 m. The effects of typical profile errors for earth-station antennas of diameter 30 m operating a 6 GHz (4) are shown in Fig 6. Only the errors associated with small correlation intervals are seen to affect the wide-angle radiation and these effects rapidly become negligible with increasing angle. The incidence of sidelobes arising from profile errors is statistical in nature, but in order to include effectively all the sidelobes the curves are drawn to include 99.9% of the sidelobe peaks.

SUMMARY

We are now in a position to consider the limitations on improvements to earth-station sidelobe performance.

Fig 7a indicates the principal factors limiting the performance of a typical earth-station designed to meet current specifications.

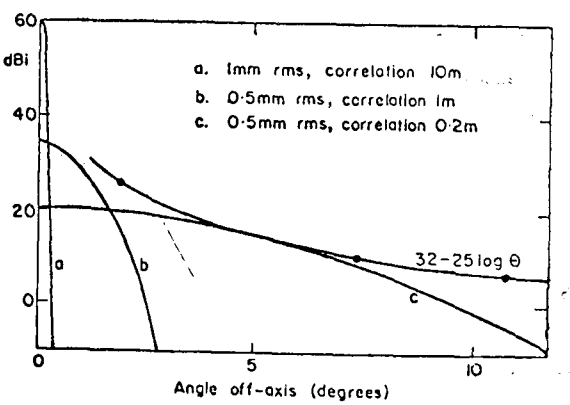

Fig 6 Effect of Random Profile Errors for a 30 m Earth-Station Operating at 6 GHz

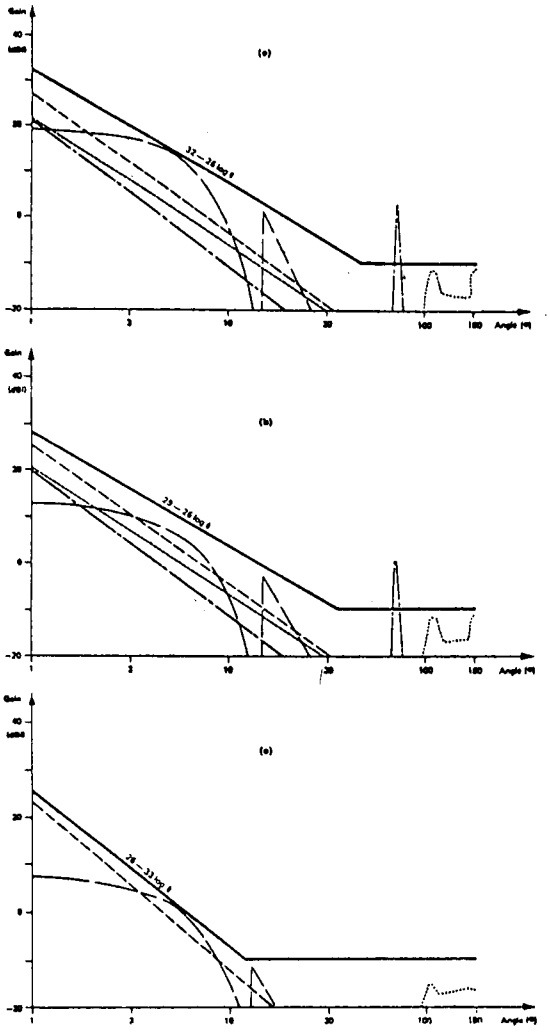

Fig 7 Contribution to the overall sidelobe performance of earth-station antennas:

——— ——— — Main reflector profile errors

——— — ——— — Plane wave blocking

— — — — — Main reflector aperture distribution inc blockage

——— ——— ——— — Subreflector edge diffraction

- - - - - - - - - - - - - Spherical wave blocking

. . . . . Main reflector edge diffraction

——————— 32-25 log θ

It is of axisymmetric Cassegrain type, has a corrugated feed horn with low sidelobes, a subreflector extending to -15 dB of the feed horn main lobe, and within-panel profile errors of 0,5 mm rms.

If the subreflector is extended to increase its edge illumination taper to 20 dB, and the small-correlation-interval profile errors are reduced to 0.25 mm rms, it should be possible to achieve a sidelobe envelope of

$$G = 29 - 25 \log \theta \text{ dBi}$$

(Fig 7b). This envelope is proposed as a suitable design target for the next generation of axisymmetric Cassegrain antennas.

In axisymmetric Cassegrain antennas, however, there is no known means of removing the effects of the subreflector supports from the sidelobe patterns, so there will be restricted angular regions where the sidelobe level will rise to values of the order of -10 dBi. These effects can only be removed by adopting an offset configuration. With all the effects of aperture blockage removed, this type of configuration can lead to much lower sidelobes over the whole radiation pattern. An envelope of

$$G = 26 - 33 \log \theta$$

could then be achieved (Fig 7c). With this sidelobe envelope the minimum spacing between co-frequency geostationary satellites could be significantly reduced; for example the 3° minimum spacing required between Intelsat satellites could be reduced to about 1.6°.

ACKNOWLEDGEMENTS

The authors acknowledge the permission of the Senior Director of Development of the British Post Office to publish this paper.

REFERENCES

(1) Claydon, B, and Keen, K M, 1978. *"Sidelobe Performance of Earth-Station Antennas"*, ERA RF Technology Centre, Report No. RFTC 301076.

(2) Claydon, B, Keen, K M, and Harris, A B, 1978. *"Wide Angle Radiation from Earth Station Antennas"*, IEE International Conference on Antennas and Propagation, London, November 1978.

(3) Kreutel, R W, 1976. *"Wide Angle Sidelobe Envelopes of a Cassegrain Antenna"*, COMSAT Technical Review, 6, 71-88.

(4) Harris, A B, 1978. *"The Contribution of Reflector Profile Errors to Antenna Sidelobe Radiation"*, Electronics Letters, 114, 343-345.

Publication P23. N.A. ADATIA and K.M. KEEN, *Radiation characteristics of a double offset antenna; theory and experiment.* IEEE/URSI APS Symposium Publication, Quebec, June 1980, pp 545-548.

RADIATION CHARACTERISTICS OF A DOUBLE OFFSET ANTENNA: THEORY AND EXPERIMENT *

N A Adatia
RF Technology Centre
ERA Technology Ltd
Leatherhead Surrey
England

K M Keen
Dept of Elect. & Electronic Eng.
University of Surrey
Guildford Surrey
England

The requirement for high gain antennas with low sidelobes and low cross-polar radiation characteristics is becoming an increasingly important feature in planning of many satellite communication missions. This has forced antenna designers to consider not only single offset reflector geometries but also double-offset antenna (DOA) configurations of the type illustrated in Fig (1). In addition to avoiding aperture blocking effects, this antenna allows the primary feed hardware to be located close to the antenna platform thus avoiding long RF transmission paths.

Analysis performed by several workers [1],[2] has shown that the double offset antenna can be designed such that, when fed by conventional linearly polarised primary feed, the depolarisation arising from the two reflectors can be made to cancel. This performance is achieved by matching the scattered radiation fields from the subreflector to the main reflector and, in principle, the technique offers a potential for a broad-band low cross polar performance.

Although such features are highly attractive, there is at present time little information available concerning the overall performance and limitations of (DOA) for spacecraft applications where the choice of reflector parameters is restricted by the volumetric constraints imposed by the launcher shroud. In this situation the design demands a careful consideration of the associated reflector diffraction effects which impair the polarisation purity of the radiated fields. Although theoretical techniques such as the Geomtrical Theory of Diffraction and the physical-optics surface current integration have been employed in the past to assess the level of depolarisation caused by these effects, significant discrepancies have been noted between the predictions obtained from these methods [3]. Attempts to resolve this problem have been further hampered by the lack of reliable experimental data with which the theoretical predictions can be compared.

This paper describes the results of detailed measurements performed on a representative double offset Cassegrain configuration (Fig 1) designed to satisfy some of the principal requirements of a planned European satellite communication mission. The primary objective of this study has been to provide accurate experimental data to validate computer programmes for analysis of DOA systems. In the present work, experimental results are compared with predictions obtained using the physical-optics surface current integration technique.

* This work was supported by the European Space Agency

Examples of the measured and predicted results are provided in Fig (2) - (4). Fig (2) shows the scattered radiation characteristics of the subreflector (in the plane of asymmetry) when illuminated by a linearly polarised pyramidal horn operating at 30GHz. The horn dimensions are selected here to provide an edge illumination taper of -10dB in the principal planes.

Fig (3) shows the overall copolar radiation characteristics in the antenna plane of asymmetry. The peak cross-polar radiation in this plane has been measured at a level of -42dB; predictions indicate peak value of -48dB.

Fig (4) shows the predicted and measured characteristics of the subreflector when illuminated by a circularly polarised corrugated conical horn feed with aperture diameter of 2.8 cms. Although excellent correlation is noted for the radiation in the plane of symmetry, there is considerable discrepancy between theory and experiment for the cross-polar field distribution in the plane of asymmetry. This discrepancy is attributable largely to the edge diffraction effects which are not accurately accounted for in the physical-optics formulation.

Additional measurement data together with the conclusions drawn from the study will be discussed during the presentation.

References

1) H Tanaka, M Miznsawa, "Elimination of cross-polarisation in offset dual reflector antennas", Elec. commun.(Japan) Vol.58, pp 71-78, 1975.

2) Y Mizugutch et al "Offset dual reflector antenna" IEEE Int. Symp. AP-S, Oct.1976, pp 2-5.

3) N A Adatia, "Diffraction effects in dual offset Cassegrain antennas", in IEEE Int.Symp.Digest, AP-S, Washington DC, May 1978.

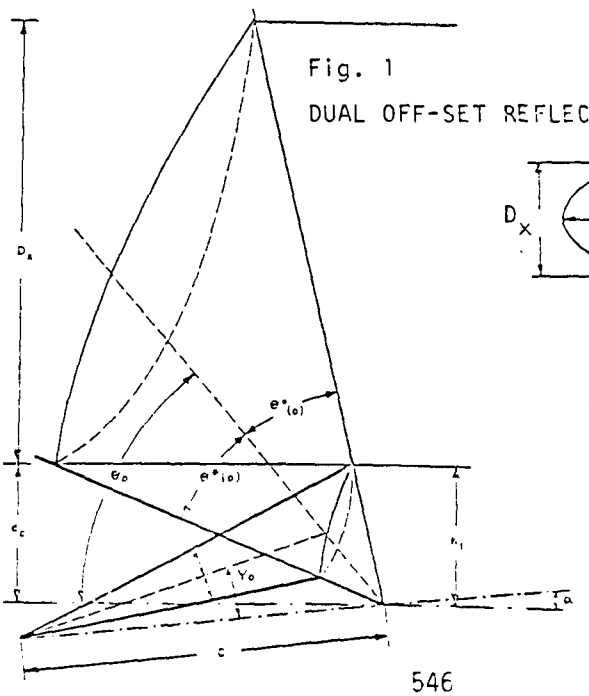

Fig. 1

DUAL OFF-SET REFLECTOR GEOMETRY

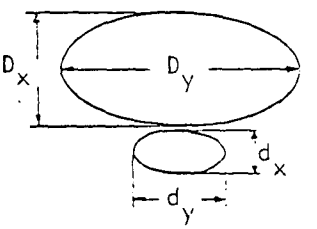

parameter	value
D_x	44.73 cm
D_y	73.1 cm
F	40.4 cm
d_x	13.75 cm
d_y	19.7 cm
C	45.5 cm.
ϵ	1.66
θ_c	52.3°
θ^*	24.6°

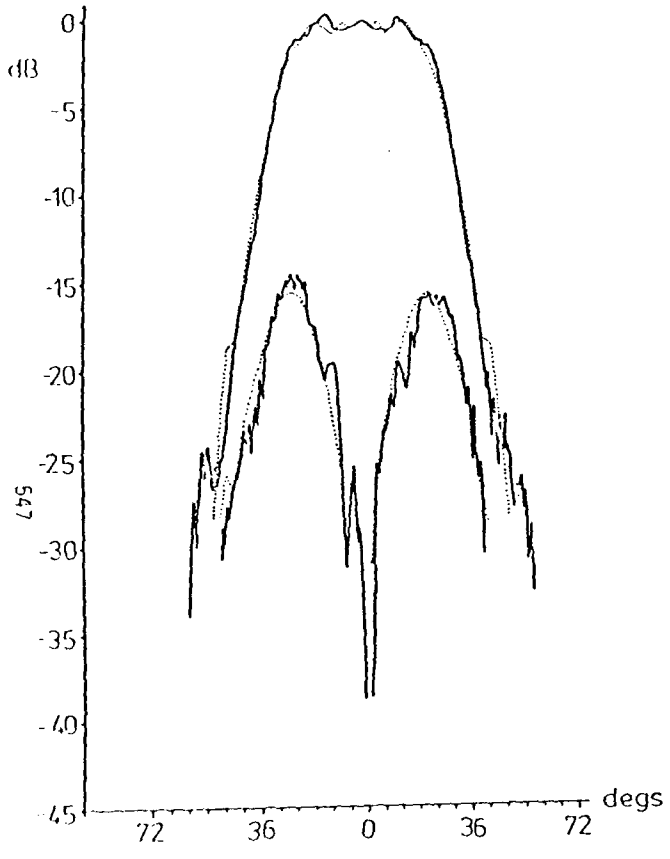

Fig. 2

SUB-REFLECTOR CO AND CROSS POLAR RADIATION PATTERNS IN THE SUB-REFLECTOR H PLANE

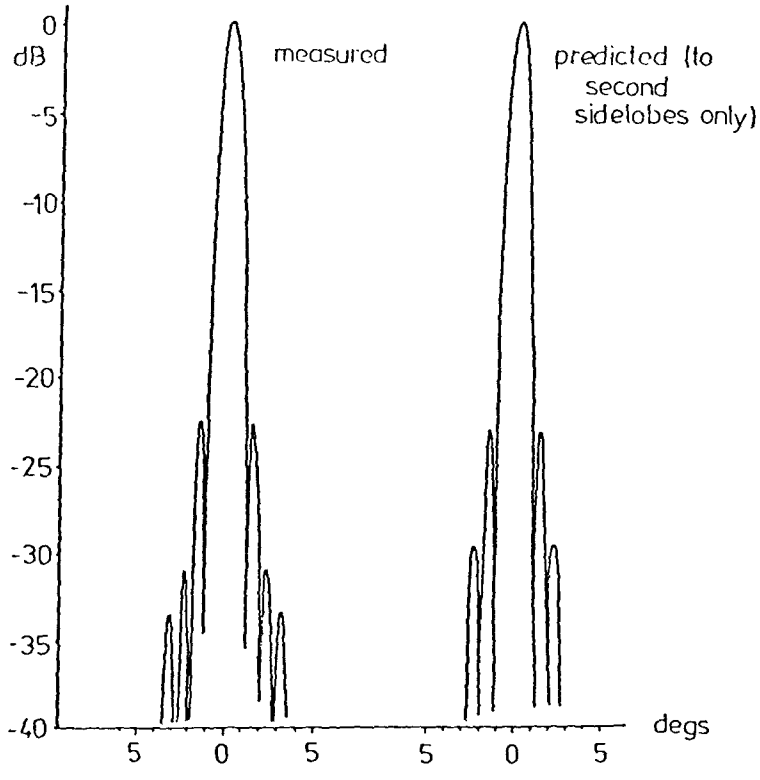

Fig. 3

MEASURED AND PREDICTED RADIATION PATTERNS IN THE ϕ = 90 DEGREE PLANE

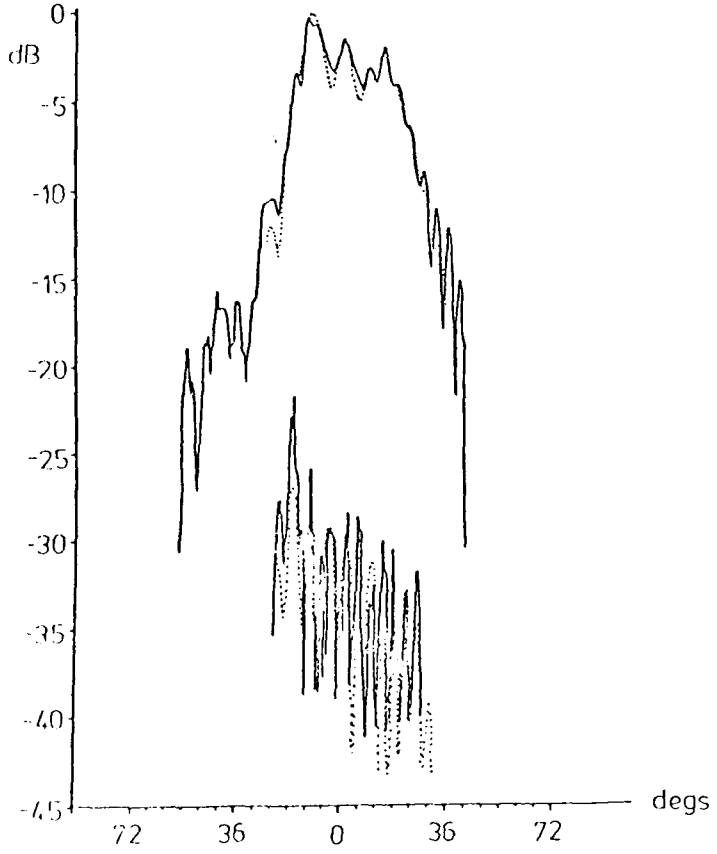

Fig. 4a

SUB-REFLECTOR ASSEMBLY CIRCULAR POLARIZATION CO AND CROSS POLAR PATTERNS IN THE ϕ = 90 PLANE

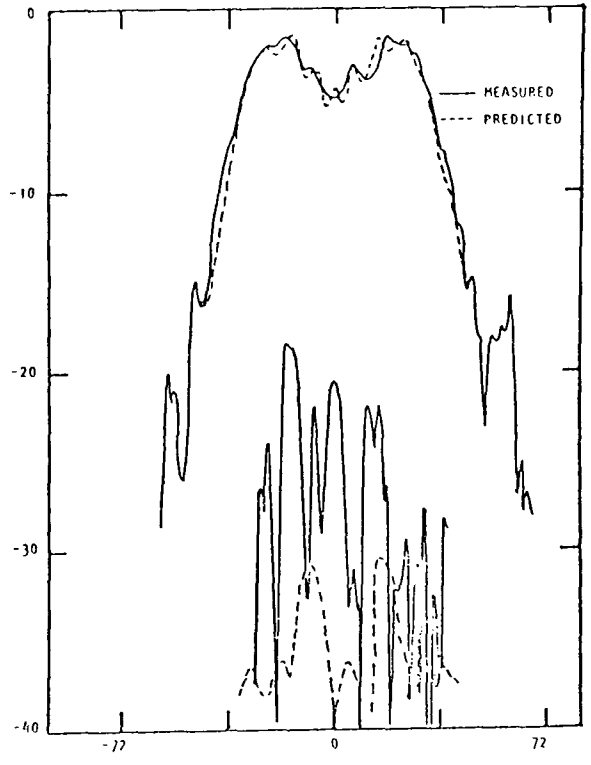

Fig. 4b

PREDICTED AND MEASURED CHARACTERISTICS OF THE SUB-REFLECTOR IN $\phi = 90^{o}$ PLANE WITH CIRCULARLY POLARIZED CONICAL HORN FEED

Publication P24. K.M. KEEN, *A measurement technique for modelling the effects of feed support struts on large reflector antennas.* IEEE Trans-AP, Vol. 28, July 1980, pp 562-564.

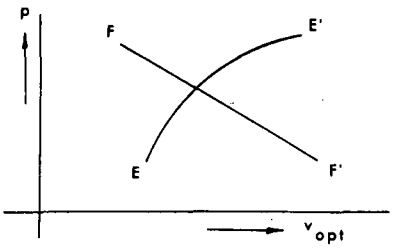

Fig. 2. p versus v_{opt} for minimum gain loss condition.

the distance between the horn aperture and the subreflector had a deviation of less than three percent from the calculated value. This agreement is quite good considering the fact that, in theory, the effects of random surface errors of the parabolic reflector on the phase error are neglected. The overall measured gain differed from the calculated value by less than 0.2 dB. The radiation pattern measurements showed a symmetrical 14 dB down first sidelobe level on either side of the main beam with nulls that were on the average 20 dB down below the sidelobe peaks.

ACKNOWLEDGMENT

The author would like to acknowledge the support and valuable assistance of J.S. Hollis in this development effort.

REFERENCES

[1] J.H. Brunning, "A best fit paraboloid solution to the shaped dual reflector antenna," presented at Symp. U.S. Air Force Antenna Research and Development Program, Nov. 15, 1967.

[2] G.W. Collins, "Shaping of subreflectors in Cassegrainian antennas for maximum aperture efficiency," *IEEE Trans. Antennas Propagat.*, vol. AP-21, pp. 309–313, May 1973.

[3] V. Galindo, "Design of dual-reflector antennas with arbitrary phase and amplitude distributions," *IEEE Trans. Antennas Propagat.*, vol. AP-12, pp. 403–408, July 1964.

A Measurement Technique for Modeling the Effects of Feed Support Struts on Large Reflector Antennas

K. M. KEEN

Abstract—**A measurement technique is described in which frequency scaled models of struts are placed in the near-field region of an offset reflector. In this compact range environment the excitation of the strut model is by plane waves, as would be encountered in the axisymmetrical reflector situation. Far-field radiation patterns are recorded, with and without the strut model in place, and, because of the low sidelobe levels associated with offset reflector antenna systems, it is possible to isolate the far-field response of the strut model. This technique is particularly useful for determining the real effects of structures that are difficult to analyze mathematically, such as latticed struts or metallic geodetic radomes.**

In connection with an investigation into the sidelobe performance of earth station antennas [1], [2], an experimental technique for investigating the far-field response of large axisymmetrical reflector antenna feed support struts has been devised and is described here. Such struts are actually subject to two modes of excitation, i.e., plane wave excitation from the main reflector, plus spherical wave excitation from the feed or subreflector. This latter mode of excitation is in some cases small (depending on the geometry) compared with the plane wave excitation, and the experimental technique as described here only models plane wave excitation which, from each antenna strut, gives rise to scattering which maximizes on a conical surface as illustrated in Fig. 1.

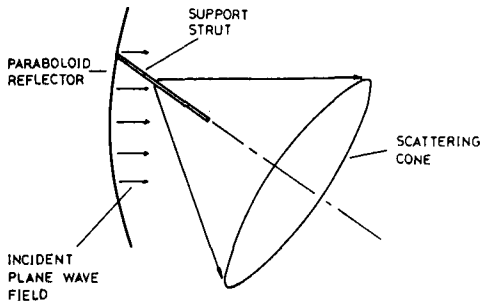

Fig. 1. Scattering cone from one support arm.

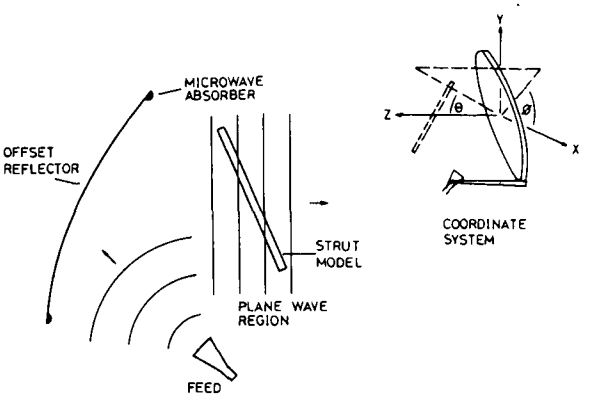

Fig. 2. Measurement arrangement and coordinate system.

With an axisymmetrical reflector antenna system, measurement of the scattering from support struts is difficult, as the contribution from these in the far field is in the presence of large contributions from the main blockage component (i.e., either a subreflector or a feed assembly, depending on whether the antenna system is Cassegrainian or front fed). Sheftman [3] has carried out an excellent experimental study with a 110-in diameter Cassegrain reflector system. However, for the investigation of the effects of particular cross sections of struts, measurements with zero blockage offset reflector systems would appear to offer greater accuracy. For this reason a "pattern difference" offset reflector antenna technique has been devised which allows strut model scattering to be reasonably well isolated from other contributions. Basically, the technique involves placing a strut model in the near field of an offset reflector antenna, as shown in Fig. 2. It is well known from the use of compact antenna ranges [4] that the wavefront is planar in this region, even up to millimeter wave frequencies [5]. Thus representative plane wave excitation can be achieved in this way. With the strut model in the near field of the offset reflector antenna, far-field radiation pattern measurements are made, and these are compared with similar measurements made with the strut model absent, to show the contribution of the strut alone.

Manuscript received October 5, 1979; revised December 24, 1979. This work was supported under a contract from the Telecommunications Development Department, British Post Office.

The author was with the ERA RF Technology Centre, Leatherhead, Surrey, England. He is now with the Department of Electronic and Electrical Engineering, University of Surrey, Guildford, GU2 5XH, Surrey, England.

0018-926X/80/0700-0562$00.75

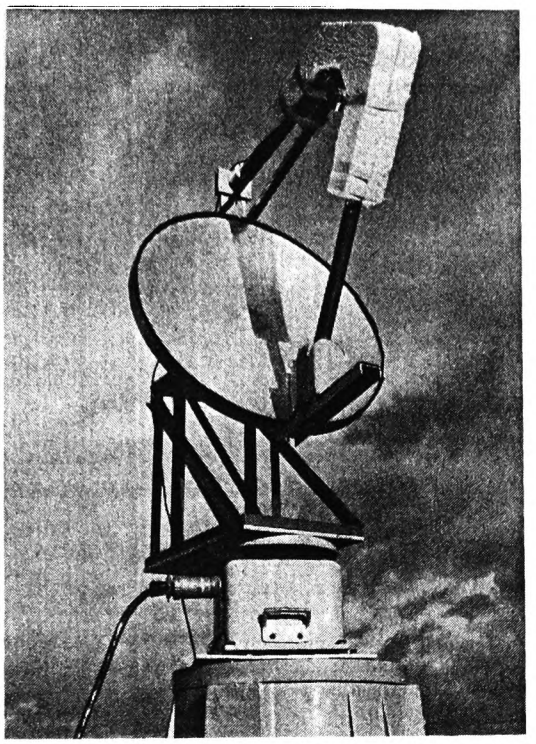

Fig. 3. Offset reflector measurement system with 3.8-wavelength diameter strut model.

This pattern difference technique is possible because of the low wide-angle sidelobe levels that are associated with offset reflector antennas. Typically, strut response levels of −40 dB compared with the main beam peak have been seen with the antenna system used for the earth station antennas measurement program. This antenna system had a gain of approximately 45 dBi. Wide-angle sidelobe levels for the same antenna (minus strut model) were seen to be −55 dB, or thereabouts, below the main beam peak. The accuracy of the pattern difference technique depends on the level of the strut response in comparison with the antenna sidelobe level below it. Suppose E_s is the peak level of a lobe from the strut alone, and E_a is the antenna sidelobe level at the same angular position. Then the recorded value can be anything from $E_s - E_a$, if the fields are in antiphase, to $E_s + E_a$, if the fields are in phase. Thus a level of uncertainty is associated with this technique which depends on the ratio of E_s to E_a. As an example, if the E_s to E_a level difference is 15 dB, a typical value for the measurement technique, the recorded value of E_s has an error spread of 1.4 dB to −1.7 dB about the true value.

Fig. 3 shows an experimental arrangement used for investigating some strut models. It consisted of a 70-cm projected aperture diameter offset reflector fed by a conical corrugated horn. Strut models were placed in the aperture with chosen inclinations using polystyrene foam supports which gave good rigidity but which were found by experiment to be virtually invisible at the 30-GHz measurement frequency. The coordinate system used is shown in the inset in Fig. 2. Before far-field measurements were carried out, near-field probings were made with the reflector and feed system, and these showed that it was necessary to reduce the reflector edge diffraction by putting absorbent material along the reflector periphery. With the absorbent material, near-field probing experiments showed that a useable area of approximately 45 wavelengths in diameter existed in the central portion of the reflector aperture, and that over this zone the amplitude distribution was smooth and with an approximately "cosine on pedestal" taper, the taper level reducing to about −6 dB at the zone edges. This taper was, of course, dependent on the feed used, and different tapers can be arranged with this measurement technique by a suitable choice of feed.

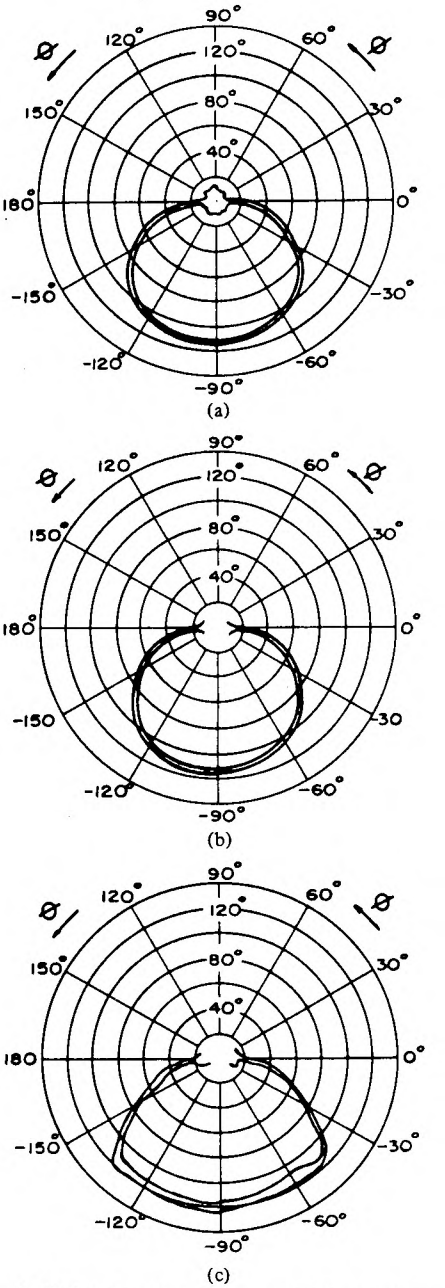

Fig. 4. −10-dB level contour diagrams. (a) Predicted response of a 3.8-wavelength diameter strut inclined at 32.5° to vertical. (b) Measured response corresponding to (a), strut model length 45 wavelengths. (c) Response of a flat strip strut 3.8 wavelengths wide.

The far-field measurements were carried out on a 105-m length elevated mode range with multipath reflection levels lower than −55 dB. "Great circle" cut radiation pattern measurements were made in increments of 15° about the antenna axis so that contour diagrams could be plotted. The available dynamic recording range was of the order of 60 dB.

Fig. 4 illustrates some results obtained with this technique. Fig.

4(b) shows the response of a 3.8-wavelength diameter strut model, actually a 3.8-cm brass tube 45 wavelengths long, inclined at 32.5° to the vertical. Polarization was vertical linear. The scattering cone can be clearly seen, and it compares well with a theoretically predicted response shown in Fig. 4(a). The corresponding horizontal polarization gave a virtually identical contour diagram. Fig. 4(c) is interesting as it is the measured response of a flat strip rectangular strut model 3.8 wavelengths wide and 0.3 wavelengths thick. Instead of a scattering cone, the response is seen to be elongated in the regions around $\theta = -45°$ and $\theta = -135°$.

The above illustrates the usefulness of the technique with regard to real struts or structures that are difficult to model mathematically. For example, lattice struts could be experimentally investigated using this technique. Another area in which the technique is potentially useful is the investigation of depolarization and scattering from metallic frame radome structures.

As described, the technique does not extend to spherical wave excitation. However, by the correct positioning of the feed and strut, this form of excitation could also be included. One final point is that the small amount of level uncertainty connected with the pattern difference technique could be eliminated by making measurements in both amplitude and phase.

ACKNOWLEDGMENT

The author would like to thank Dr. A. W. Rudge for proposing the measurement technique.

REFERENCES

[1] B. Claydon and K.M. Keen, "Sidelobe performance of earth station antennas," ERA RF Technology Ctr., Final Rep., Post Office Contract RD111/863, June 1978.
[2] B. Claydon, K.M. Keen, and A.B. Harris, "Wide angle radiation from earth station antennas," in *Proc. Inst. Elec. Eng. Int. Conf. Antennas and Propagation*, 1978, pp. 218-222.
[3] F.I. Sheftman, "Experimental study of subreflector support structures in a Cassegrainian antenna," MIT Lincoln Lab., Tech. Rep. 416, Sept. 1966.
[4] S. Hollis *et al.*, *Microwave Antenna Measurements*. Scientific Atlanta Inc. June 1980.
[5] A.D. Olver and G. Tong, "Compact antenna range at 35 GHz," *Electron. Lett.*, vol. 13, Apr. 14, 1977.

Pattern Shaping with a Metal Plate Lens

ALEXANDER C. BROWN, JR., MEMBER, IEEE

Abstract—**The metallic parallel plate lens is a viable alternative to both the shaped reflector and the array antenna for beam shaping. A *C*-band antenna using this lens is designed to provide a $\csc^2\theta(\cos\theta)^{1/2}$ power pattern over the angular limits of 60°–80° below horizontal. The Woodward–Levison synthesis technique is applied to determine the required amplitude and phase distribution across the aperture. Initial plate positions and lengths of the lens are determined from geometrical optics and infinite waveguide theory. The positions and lengths of the lens plates are adjusted experimentally until a satisfactory pattern is obtained.**

Manuscript received August 3, 1979; revised January 24, 1980.
The author is with the Goodyear Aerospace Corporation, Arizona Division, Litchfield Park, AZ 85340.

I. INTRODUCTION

In this communication, we describe the design of a shaped beam microwave antenna using a metalic parallel plate lens to provide the shaping. Although the technique is not new [1], it has not been discussed in widely available literature. The lens is easy to construct as it consists simply of flat metal plates. This approach is a viable alternative to the shaped reflector and to the array antenna. In all other respects, this antenna is quite ordinary; a single layer pillbox and flare are used to space feed the lens. The development of this antenna is especially simple as the lens is designed by easy-to-apply synthesis techniques and a simulator, which we describe in Section II.

The antenna is part of a side-looking radar system [2]. The antenna illuminates a swath of ground from 60° to 80° around the roll axis (*H* plane of the antenna) of the aircraft. This depression angle θ is measured positive downward from horizontal. Within these angular limits the beam is shaped to provide a $\csc^2\theta(\cos\theta)^{1/2}$ power pattern. With respect to the direction of flight (*E* plane of the antenna), the beam is conventional and has a beamwidth of 3.5° at the 3-dB points.

This antenna had to satisfy a number of requirements of varying degrees of importance. Most important was the beam shaping requirement. This pattern was allowed to deviate from the $\csc^2\theta\cos^{1/2}\theta$ curve by no more than ±0.5 dB. This requirement simplifies the design of the radar system because no signal compensatory circuitry was required to make up for pattern difficiencies of the antenna. The antenna had to operate at 5.5 GHz (in the *C* band) with an input voltage standing-wave ratio (VSWR) of less than 1.4 over the fairly narrow band of ±7.5 GHz, and should be able to handle 50 kW at 5 psia. Other requirements included −11-dB sidelobes and −20-dB cross polarization, which were not stringent.

An antenna satisfying the above design requirements consists of a single layer pillbox, a 90° flare, and a metal plate lens. The pillbox [3], [4] is a parabolic cylinder reflector between two parallel plates fed from the center by an open waveguide polarized so that the electric field is parallel to the plates. A focal length to dimension (*F*/*D*) ratio of 0.25 is chosen to provide approximately 10 dB of edge taper in the *E* plane. The aperture of the pillbox is increased by a 90° angle flare. Then the pillbox and flare space feed a lens constructed of flat parallel (to the *E* field) metal plates. Fig. 1 shows the *C*-band antenna. The antenna is matched to within 1.4 VSWR over the band by placing an inductive post in the waveguide feed, and the size of WR-187 is sufficiently large to handle the power [5].

II. DEVELOPMENT OF THE ANTENNA

The antenna development consisted of the building and testing of a simulator, a prototype, and a final *C*-band antenna. In Table I the aperture dimensions are given. The simulator was built as a tool to design the lens; consequently, it was simply an *H*-plane sectoral horn with a lens. In effect, it was a slice of a complete antenna as can be seen by comparing Figs. 1 and 2. Both the simulator and the prototype were designed to operate at 11.44 GHz, because at this frequency the ratio of the wavelength and the width of standard *X*-band the WR-90 waveguide is identical to the ratio of the wavelength (at 5.5 GHz) and the width of the WR-187 waveguide. The simulator and the prototype were built to operate in *X* band solely because of facility and test equipment availability. The final *C*-band antenna was tested at the Physical Science Laboratory, New Mexico State University.

0018-926X/80/Q700-0564$00.75

Publication P25. K.M. KEEN, A low blockage, dipole array reflector antenna feed for the lower microwave frequencies. IEEE Trans-AP, Vol. 28, Nov. 1980, pp 914-916.

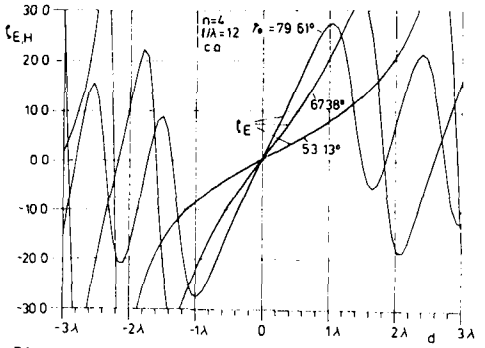

Fig. 3. Phase center location ζ as a function of defocusing d for various angular semiapertures ψ_0.

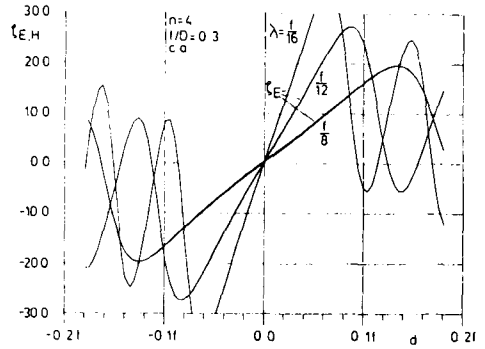

Fig. 4. Phase center location ζ as a function of defocusing d (in focal length f) with operating wavelength λ (in fractions of focal length 4) as a parameter.

From Figs. 3 and 4 we can see that

i) the rate of change of ζ with d generally increases with ψ_0 (or f/λ);

ii) the location of the first maximum of the ζ versus d curve moves toward the coordinate with ψ_0 (or f/λ), while the first maximum itself decreases with ψ_0 (Fig. 3) and increases with f/λ (Fig. 4).

The overall features of these figures (except Fig. 2(c)) can be summarized as follows.

i) The shape of the curve of ζ versus d is somewhat similar to a damped oscillating curve for $d > 0$ or $d < 0$. This means that ζ moves to and fro around the location of $\zeta_{d=0}$ which is near the vertex of the reflector. In general, ζ changes rapidly with d.

ii) The main features of the curves in Figs. 2(a), 3, and 4 are similar to each other. This indicates that d, the amount of defocusing, is a dominant factor in determining the phase center location.

iii) The relative difference between ζ_E and ζ_H, $(\zeta_E - \zeta_H)/\zeta_E$, generally decreases as d increases. At some values of d (e.g., $d = -1.1\ \lambda$ or $1.2\ \lambda$ in Fig. 2(a)) $\zeta_E \cong \zeta_H$. Therefore phase centers in the E and H planes can be brought together by defocusing.

iv) Moving the feed toward the reflector ($d < 0$) has a somewhat stronger effect on the phase center than moving the feed away from the reflector ($d > 0$). This can be easily seen from the unsymmetrical characteristics of curves of ζ versus d about the focus in Figs. 2(a), 3, and 4.

III. DISCUSSION

With an axially defocused feed ($d \neq 0$) the phase center of a paraboloid defined around the main beam direction ($\theta = 0$) is not only a function of n (the primary feed gain function) and $\psi_0 \sim f/D$ (the angular semiaperture), but also a function of d/λ and f/λ. In many practical cases, when discrete data of phase pattern are provided only, the analytical expression (3) may be of little use, and numerical techniques [6], [9] to determine the location of the phase center in a least-square sense must be used.

IV. CONCLUSION

The phase center of a paraboloid with an axially defocused feed is a function of various antenna parameters and the amount of defocusing d. The curves of ζ versus d are unsymmetrical about the focus. By proper defocusing, ζ_E and ζ_H can be brought together.

ACKNOWLEDGMENT

The author is indebted to S. Sastradipradja for discussions. The permission of the Director, Research Laboratories, Telecom Australia, to publish this communication is acknowledged.

REFERENCES

[1] P. G. Ingerson and W. V. T. Rusch, "Radiation from a paraboloid with an axially defocused feed," *IEEE Trans. Antennas Propagat.*, vol. AP-21, pp. 104–106, Jan. 1973.

[2] D. K. Cheng, "On the simulation of Fraunhofer radiation patterns in the Fresnel region," *IRE Trans. Antennas Propagat.*, vol. AP-5, pp. 399–402, Oct. 1957.

[3] M. Landry and Y. Chassé, "Measurement of electromagnetic field intensity in focal region of wide-angle paraboloid reflector," *IEEE Trans. Antennas Propagat.*, vol. AP-19, pp. 539–543, July 1971.

[4] D. Carter, "Phase center of microwave antennas," *IRE Trans. Antennas Propagat.*, vol. AP-4, pp. 597–600, Oct. 1956.

[5] S. Silver, *Microwave Antenna Theory and Design*, MIT Rad. Lab. Series, Vol. 12. New York: McGraw-Hill, 1949, ch. 5, pp. 144–149.

[6] W. V. T. Rusch and P. D. Potter, *Analysis of Reflector Antennas*. New York: Academic, 1970, ch. 4, pp. 145–153.

[7] Y. H. Ja, "Phase center of paraboloidal antennas," *Electron. Lett.*, vol. 15, pp. 784–785, Nov. 1979.

[8] D. Carter, "Wide-angle radiation in pencil beam antennas," *J. Appl. Phys.*, vol. 26, pp. 645–652, June 1955.

[9] Y. H. Ja, "Numerical evaluation of phase centers of corner reflector antennas," *Electron. Lett.*, vol. 15, pp. 1–2, Jan. 1979.

A Low-Blockage Dipole Array Reflector Antenna Feed for the Lower Microwave Frequencies

K. M. KEEN

Abstract—**An antenna is described which was devised as a feed for a small axisymmetrical paraboloid reflector at an operational frequency of just over 1 GHz. The antenna consists of a broadside array of two dipoles on a printed circuit board (PCB), joined by a common**

Manuscript received January 2, 1980; revised July 7, 1980.

The author was with the ERA RF Technology Center, Leatherhead, Surrey, England. He is now with the Department of Electronic and Electrical Engineering, University of Surry, Guildford GU2 5XH, England.

transmission line. Each dipole is backed by a small strip reflector. With this simple array, which has one central feed point, the *H*-plane radiation pattern can be varied independently of the *E*-plane pattern. In addition, the aperture blockage of the feed is small.

At the lower microwave frequencies, aperture-blockage considerations generally dictate the use of dipole-based elements as feeds for full paraboloid reflector antennas, unless the reflectors are comparatively large (e.g., with diameters larger than about 5 λ or so). Unfortunately, the commonly used feeds, for example the dipole-disk and dipole-plate elements [1], have the disadvantage that the *H*-plane radiation patterns are broader than the *E*-plane patterns, because of the fundamental properties of a half-wavelength dipole. This is a particular nuisance in situations where equal *E*- and *H*-plane secondary patterns are required from an axisymmetrical paraboloid. Obviously, to achieve this the reflector aperture illuminations in these planes must be equal, and therefore equal *E*- and *H*-plane primary patterns are needed. This communication describes a simple feed configuration that allows independent control of the *H*-plane pattern and which can exhibit pattern symmetry if required, while maintaining a low-blockage profile.

Fig. 1 shows the feed, which can be conveniently constructed from two copper covered fiberglass printed circuit boards (PCB's). Two half-wavelength dipoles and a common transmission line are formed on one board, and two strip reflectors are formed on the other which is spaced at a quarter of a wavelength behind the first board. The interdipole spacing is chosen to give the required *H*-plane pattern beamwidth. The common transmission line is of the type described by Bawer and Wolfe and used in the output section of their well-known printed circuit balun [2]. Essentially, this transverse electromagnetic (TEM) mode transmission line consists of two coplanar conducting strips with a small gap between them. The characteristic impedance as a function of geometry can be found either from the experimental results in [2] or in the paper by Crampagne, Khoo, and Guiraud [3]. The common line is fed at its center from a coaxial cable with a suitable balun arrangement.

Figs. 2, 3, and 4 show measured results obtained with a development model of the antenna aimed at operation in the region of 1000–1100 MHz. This antenna had an interdipole spacing of 13 cm (0.433 free-space wavelengths at 100 MHz) and a dipole-to-reflector spacing of 7.5 cm. The dimensions of each of the reflector strips were 19 cm by 3 cm. The size of these strips (each only 0.63 by 0.1 λ) was determined as a compromise of the smallest physical feed area transverse to the reflector axis which was sufficient to give an acceptable back-to-front radiation pattern ratio. Fig. 2 shows *E*- and *H*-plane radiation patterns at 1000 MHz, and it can be seen that essentially, pattern symmetry is present over the portion of the main beam which would be used to illuminate a paraboloid reflector. Over a frequency band of ±5 percent or so, the *E*-plane patterns of the feed were found to be virtually independent of frequency, but the *H*-plane pattern beamwidth decreased with increasing frequency, as would be expected with a broadside array, although this effect was seen to be minor. The effect on patterns of reducing the dipole-to-reflector spacing was also investigated, but this was found to be small although the effect on impedance match was detrimental. For this reason the spacing was kept at one-quarter of a free-space wavelength. Pattern measurements also revealed the

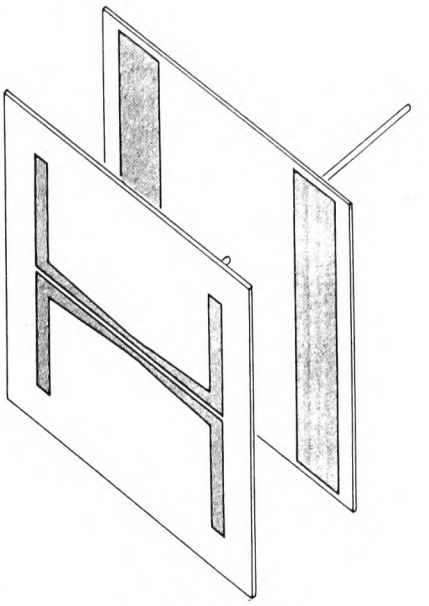

Fig. 1. The antenna.

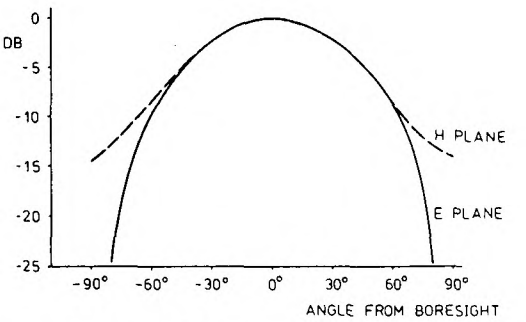

Fig. 2. Measured *E*- and *H*-plane patterns of the 0.43-λ spacing dipole array feed at 1000 MHz.

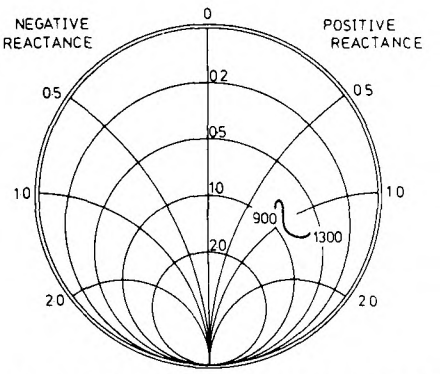

Fig. 3. Smith chart plot of antenna input impedance from 900 to 1300 MHz.

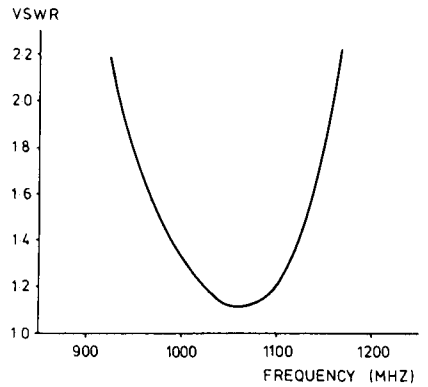

Fig. 4. Measured VSWR of antenna with reactive shunt at input port.

back-to-front ratio of the antenna. Clearly this is dependent on the size of the reflector strips, but even with the low-blockage 19-cm by 3-cm strips of the development antenna, back-to-front ratios of the order of −14 dB were seen.

Fig. 3 shows a Smith chart plot of input impedance from 900 to 1300 MHz referenced to the central feeding point of the common transmission line on the front PCB. The plot is normalized to the 50-Ω characteristic impedance of the coaxial feeding cable. This indicated that, with suitable impedance transformation, the antenna has a respectable impedance match bandwidth of the order of ±15 percent. The plot also showed that with this spacing the resistive part of the input impedance is close to 50 Ω and that a reasonably good match could be obtained directly, by merely nullifying the positive reactance component. Fig. 4 shows the measured voltage standing-wave ratio (VSWR) obtained in this way, by the addition of a reactive shunt at the center of the common interdipole transmission line. It can be seen that the VSWR is good, but it is worth noting that it could be further improved by also matching the resistive component of the input impedance, for example with the transforming balun described by Gans, Kajfed, and Rumsey [4].

As a final comment it should be mentioned that with this form of construction the antenna is an essentially low-cost item, especially in production where conventional PCB etching techniques could be employed. At these frequencies and because, first, the common transmission line sections are short, and second, very few of the fields associated with the dipoles and the common transmission line are contained in the dielectric substrate, ordinary inexpensive printed circuit board materials may often be acceptably efficient, and the expensive microwave PCB materials can be avoided, thus keeping costs down further. The use of some grades of ordinary fiberglass PCB materials for planar antenna structures at the lower microwave frequencies is well-known, and even with Archemedian spiral antennas, where considerable transmission region path lengths exist on the dielectric substrate, the efficiency is only reduced by 0.5 dB when using common PCB materials [5].

REFERENCES

[1] S. Silver, *Microwave Antenna Theory and Design*. New York: McGraw-Hill, 1949.
[2] R. Bawer and J. J. Wolfe, "A printed circuit balun for use with spiral antennas," *IRE Trans. Microwave Theory Tech.*, pp. 319–325, May 1960.
[3] R. Crampagne, G. Khoo, and J. Guiraud, "Analysis and synthesis of MIC transmission lines," *Microwave J.*, pp. 105–126, June 1977.
[4] M. J. Gans, D. Kajfed, and V. H. Rumsey, "Frequency independent baluns," *Proc. IEEE*, vol. 53, p. 647, 1965.
[5] R. Bawer and J. J. Wolfe, "The spiral antenna," in *IRE Int. Conv. Rec.*, Part 1, vol. 8, pp. 84–95, 1960.

On the Edge Mode in the Theory of Thick Cylindrical Monopole Antennas

JACK H. RICHMOND, FELLOW, IEEE

Abstract—**The Fourier transform is employed to develop the theory of thick cylindrical monopole antennas. The tubular monopole with an open end is considered as well as the solid monopole with a flat end. The unknown current or field distribution is expanded in a Fourier series, and Galerkin's method is employed to develop simultaneous equations for the Fourier coefficients. When the edge mode is included among the basis functions, it is found this greatly improves the convergence of the moment-method calculations. Numerical data are included, showing excellent agreement with experimental measurements of the monopole admittance.**

I. INTRODUCTION

Einarsson [1] presents solutions for tubular and solid cylindrical-wire antennas. These solutions are based on a delta-gap model of the generator and thus are not suitable for calculating the susceptance. This objection applies also to the formulations of Chang [2] and King and Wu [3]. Otto [4] employs a realistic magnetic-frill model for the generator and reduces Einarsson's formulation to one equation with one unknown (rather than eight simultaneous equations). It has not been demonstrated that Otto's approximations are applicable to electrically thick antennas, however.

Chang [5] presents a moment-method solution for the thick tubular monopole based on Hallen's integral equation with an extra term corresponding to a radially extended source in the aperture of the coaxial feed cable. Thus an excellent solution is available for the thick tubular antenna, but evidently not for the thick solid cylindrical antenna.

King [11] presents measured admittances of thick monopoles, theoretical results for thick tubular monopoles, and a correction term for higher order modes in the coaxial feed line.

In this communication we present moment-method solutions for tubular and solid cylindrical antennas. In comparison with previous formulations, ours are straightforward. It is demonstrated that the convergence of the solution is greatly improved when the edge mode is included among the basis

Manuscript received January 3, 1980; revised April 29, 1980. This work was supported in part by Contract DAAG29-79-C-0082 between the Army Research Office and the Ohio State University Research Foundation.

The author is with the ElectroScience Laboratory, Department of Electrical Engineering, the Ohio State University, Columbus, OH 43212.

0018-926X/80/1100-0916$00.75

Publication P26. **K.M. KEEN,** ***Satellite antenna measurement techniques*** **Commissioned IEE Review. IEE Proc. Vol. 127, Part A, No. 7, Sept. 1980, pp 417-434.**

Satellite-antenna measurement techniques

K.M. Keen, M.Sc., C.Eng., M.I.E.E.

Indexing terms: *Satellite links, Antennas, Measuring science*

Abstract: Initially, the review takes a brief look at the various types of antenna systems that are used on satellites and shows that in terms of the measurement of their radiation characteristics, they can be categorised into two groups, i.e. low-gain (omnidirectional and quasi-omnidirectional) antennas, and medium- and high-gain antennas. With the first group, the main measurement difficulty lies with the suppression of multipath reflections, and the various range configurations that can be used to avoid or overcome this problem are described. Two of these are, for example, the ground reflection mode range and the use of baffles within an anechoic chamber. Following this, direct measurement ranges applicable to medium- and high-gain antennas are reviewed. These far-field approximation test range configurations include the elevated mode range, either in an outdoor environment or within an anechoic chamber, and the semi-open anechoic chamber. Subsequently, the review considers the various near-field and intermediate distance methods. Finally, some special techniques that have been devised to examine some particular satellite-antenna problems, such as the determination of the r.f. transparency of launch vehicle fairings and the effect of conductive thermal-control paint on satellite-reflector antennas, are presented. The review is principally from a European viewpoint.

1 Introduction

During the last decade there has been a considerable increase in the use of artificial Earth satellites for telecommunication, scientific and military applications. Moreover, the satellites themselves have become more complex, are often larger, and have generally greater capability than previous generations of spacecraft. One of the aspects of satellite engineering in which this increase in capability is evident is in the technology of the antenna systems. This technology has undergone substantial evolution owing to the research and development activities which have been necessary in this field in order that antenna systems are able to meet the stringent performance requirements that exist for current and future satellite programmes. This evolution can be seen, for example, in the polarisation diversity and multibeam reflector antennas and their associated high-performance feeds. Of course, as satellite-antenna systems have become capable of higher performance, then so the measurement of this performance, i.e. the determination of radiation patterns, gain, cross-polarisation levels, beamsquint and so on, has become more exacting, and there has been a corresponding evolution in antenna-measurement methods. It is the purpose of this paper to collate and review the many techniques that have evolved, or are evolving, for satellite-antenna performance measurement. Some of these techniques were developed exclusively for the specific problems of certain satellite systems, but many are applicable to antenna technology in general. Therefore, hopefully, the contents of this review will be of relevance to all readers who have an interest in antenna measurements in the part of the electromagnetic spectrum that extends from v.h.f. to millimetre wave frequencies. The introduction to this review continues with a brief look at some of the various types of satellite antennas.

As suggested in Fig. 1, satellite antennas can be broadly categorised into two groups, i.e. low-gain (omnidirectional and quasi-omnidirectional) and medium- and high-gain types. The low-gain antennas have been seen on satellites since the days of Sputnik 1, particularly the well known turnstile antenna system, which consists of four monopoles on one surface of the spacecraft, the monopoles being fed equally in amplitude and in progressive quadrature phases.[1-4] An example of this is shown in Fig. 2, which is an r.f. model of the British UK 6 satellite, used for radiation-pattern measurements; the four cranked whips of its v.h.f. turnstile system are clearly apparent. The purpose of omnidirectional or quasi-omnidirectional antenna systems on a satellite is usually for telemetry and telecommand functions and quite often, these operations must be carried out before the satellite is in its final orbit and attitude with respect to Earth. For example, it may be necessary to stabilise a tumbling satellite in a transfer orbit by commanding the deployment of some booms. Clearly, the satellite must be capable of receiving the commands in any of its possible transfer-orbit attitudes, and hence the necessity for antenna systems with wide radiation-pattern coverage. Other low-gain antenna systems that have been used in the v.h.f. band include the one shown in Fig. 3, which was developed for the French Symphonie satellite[5] and the quadrifilar helix.[6]

Although the v.h.f. band is still favoured in many cases for telemetry and telecommand operations (a current example is the University of Surrey UOSAT satellite), there is a trend towards S-band frequencies[7] where the sky background-noise level is lower. Also, S-band antennas are physically small (typically the largest dimension would be

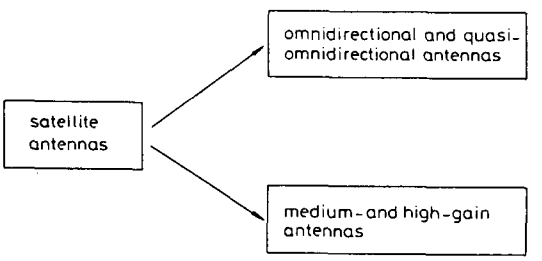

Fig. 1 *Classification of satellite antennas according to measurement considerations*

Paper 865A, first received 10th January and in revised form 20th May 1980. Commissioned IEE Review

Mr. Keen is with the Department of Electronic & Electrical Engineering, University of Surrey, Guildford GU2 5XH, England

0413-702X/80/070417+18 $01.50/0

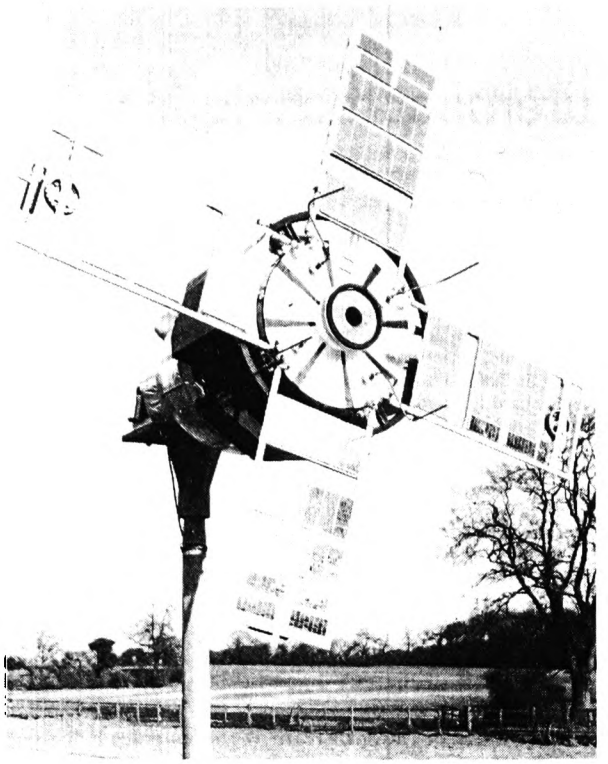

Fig. 2 *R.F. model of the UK 6 satellite*

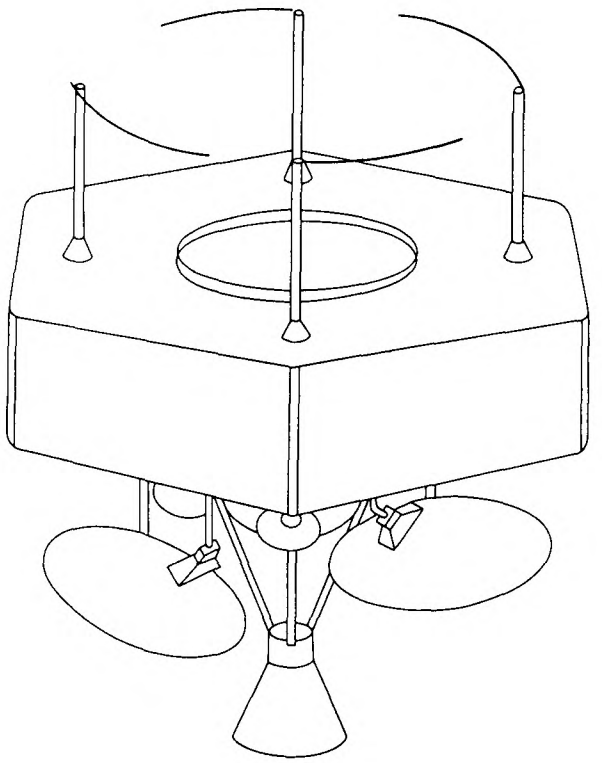

Fig. 3 *Symphonie satellite, showing the v.h.f. antenna system on its upper surface*

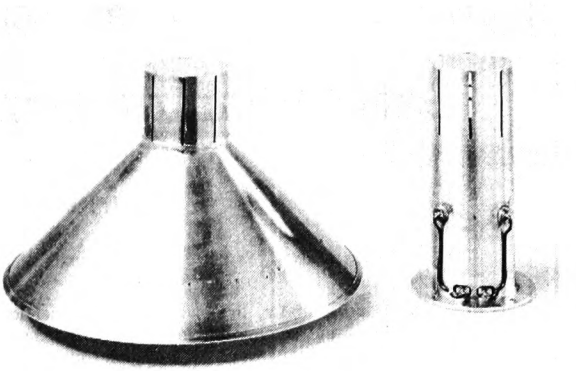

Fig. 4 *Two breadboard versions of an S-band satellite antenna with controllable radiation patterns*

of the order of 30 cm) and, at these frequencies, they have the advantage over v.h.f. systems that the surface-antenna currents responsible for radiation are confined almost entirely to the antenna itself. V.H.F. systems, at the other extreme, function by exciting currents over the surface of the entire spacecraft. Therefore, any booms or appendages on the satellite may have currents induced on them which cause disturbances to the otherwise smooth radiation patterns that would result from the satellite body and antenna whips alone. For this reason, v.h.f. satellite-antenna performance can rarely be predicted at the design stage, but S-band antenna performance can be predicted.

At S-band, the various forms of conical spiral antenna[8, 9] are often used, either as a single antenna giving hemispherical coverage, or in a system which can switch between two antennas mounted on the top and bottom of the spacecraft to give full omnidirectional coverage. Other types of antenna have been developed for use with satellites at S-band; in particular, Reference 10 describes a lightweight slotted cylinder antenna which features a useful degree of radiation pattern control. Breadboard examples of two forms of this antenna are shown in Fig. 4.

All the low-gain antenna systems, whether they are v.h.f. systems operating at about 150 MHz, or S-band antennas operating at just over 2 GHz, present measurement problems as regards their far-field radiation-pattern characteristics, mainly as a result of multipath reflections that would occur on conventional test ranges. Section 2 of this paper describes the measurement techniques that are used to overcome the multipath problem and reviews some other features of low-gain antenna measurements such as the recording of radiation-pattern distribution data.

Fig. 5 is an impression of the ESA large platform satellite L-SAT and shows the antenna farm which illustrates the type of sophisticated antenna systems that are now used to provide spot beams at the higher microwave frequencies. Beamwidths of 1° or less are not uncommon and, with the frequency bandwidth limitations currently encountered, there is an increasing use of polarisation diversity which has spurred the development of low-crosspolarisaton antenna systems.[11] Thus, there has been considerable research and development activity associated with offset reflector antennas which (with suitable feeds) can exhibit improved crosspolarisation characteristics compared with axisymmetrical reflector antennas, as the aperture blockage associated with a feed or subreflector and support struts is eliminated.[12] In fact, the feasibility of multiple beam, dual polarisation, offset reflector antennas using a cluster

of smooth wall feeds with aperture dimensions of just over one wavelength (where this type of feed attains good cross-polarisation characteristics) or by using small aperture octagonal feed horns, has been demonstrated.[13,14] It is interesting to compare Fig. 5, where offset reflector antennas can be seen, with Fig. 6 which shows the ESA OTS satellite, launched in 1978. The reflector antennas on this satellite, front-fed axisymmetrical paraboloids,[15] can be considered to belong to a previous generation of reflector antennas.

Apart from the high-gain spot beam antennas, there is also still interest in medium-gain antennas, such as the Earth coverage type of antenna[16,17] (17° beamwidth from geostationary orbit). Such antennas usually have shaped beams and can have measurement problems of their own, as described later in Section 4 of this review for a particular case. Section 4 deals with near-field and intermediate-distance measurement techniques. Prior to this, Section 3 deals with direct-measurement techniques normally used to evaluate the far-field performances of medium- and high-gain satellite antennas. Section 5 deals with special techniques for particular problems, for example the measurement methods used to determine the r.f. 'transparency' of modified launch vehicle fairings (e.g. the McDonnell Douglas Delta metallic fairing with glass reinforced plastic r.f. windows), and the effects of satellite solar panels on v.h.f. antenna performance.

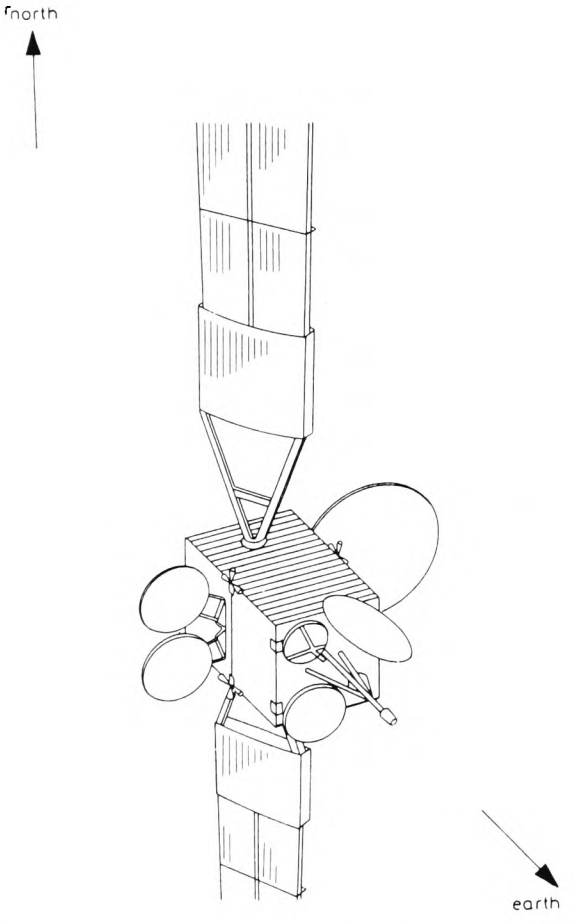

Fig. 5 *Artist's impression of a possible configuration of the ESA L-SAT*

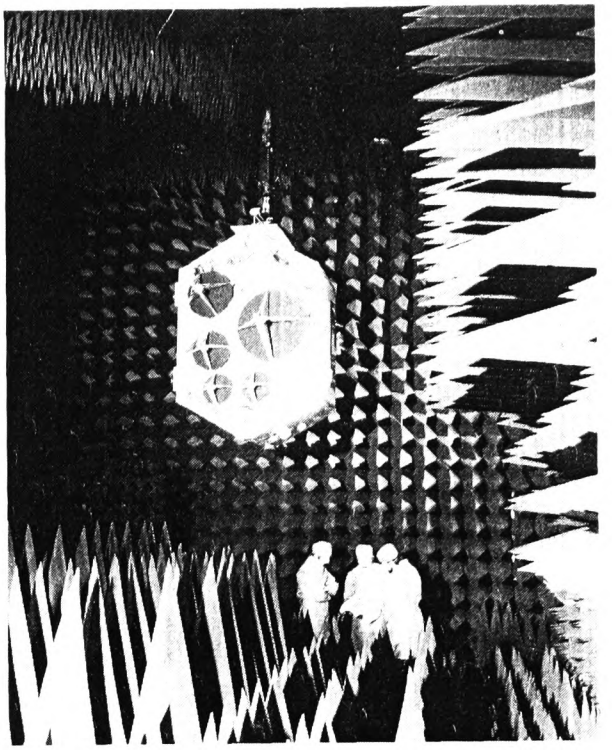

Fig. 6 *OTS satellite undergoing antenna measurements in the British Aerospace Dynamics Group's anechoic chamber*

The spot beam reflector antennas can be clearly seen

To conclude this introduction, it is instructive to look at the antenna systems of a recent satellite to give some idea of the diverse antenna systems that can be seen on any one satellite. Fig. 7 shows the German HELIOS satellite which was used for solar investigation and which travelled close to the Sun (hence the reflective surfaces). The upper central mast carries three antenna systems and there is a fourth antenna, a small horn, inside the lower skirt of the spacecraft.[18] At the base of the mast there is a reflector antenna with a line feed, the reflector itself being formed by a wire grid. Above this is an azimuthally directional medium-gain, 10 element, colinear dipole array antenna. Above this again can be seen a low-gain bicone.

2 Low-gain antenna-measurement techniques

As described in the introduction, the low-gain (omni-directional and quasi-omnidirectional) satellite-antenna systems are usually either v.h.f. systems working at frequencies of about 150 MHz, or S-band systems working at about 2·2 GHz. The principal difference between these, as far as measurements are concerned, is that at v.h.f. the antenna system is actually the entire satellite, but at S-band, the antenna is an isolated entity. In other words, with a v.h.f. antenna, the v.h.f. monopoles excite currents over the spacecraft body and it is the entire system, i.e. spacecraft and monopoles, which radiates. With a smooth-bodied spacecraft, the antenna-pattern coverage is also smooth, but for a spacecraft with appendages such as deployable sensor booms, the currents induced on these structures can cause nulls or dips in the far-field radiation

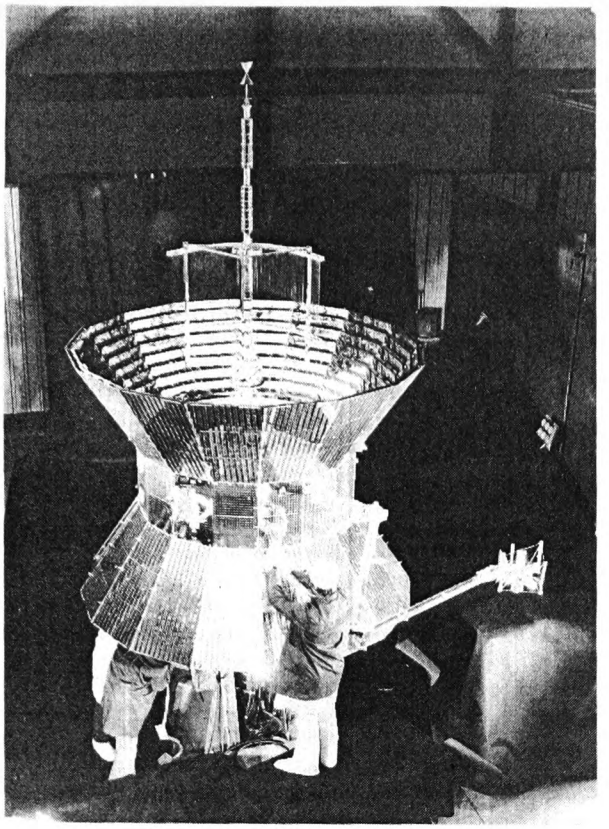

Fig. 7 *HELIOS satellite*

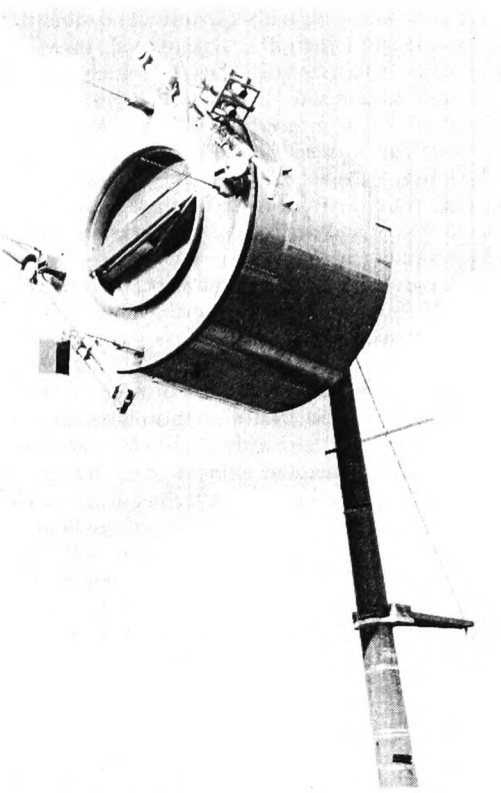

Fig. 8 *R.F. model of GEOS*

pattern. For this reason, v.h.f. antennas can only be measured either with the actual spacecraft, or with an r.f. model of the satellite. Such models are used extensively for v.h.f. antenna development (still largely empirical), and are sometimes referred to as 'tinsats'.[19] One such r.f. model has already been shown in Fig. 2, and Fig. 8 shows another, this being an r.f. model of the ESA GEOS satellite used for the development of the GEOS turnstile antenna system. The four vertical monopoles of the antenna system can be seen, as can the models of the GEOS booms. As a point of interest, the booms on an early version of this particular satellite caused just the sort of problem mentioned earlier, i.e. radiation from these structures upset the symmetry of the radiation distribution which was found to contain nulls in inconvenient directions. For S-band low-gain antenna systems, the surface currents from which the far-field radiation originates are confined mainly to the antenna itself, and so a good deal of antenna investigation can be carried out with the antenna in isolation. However, the antennas do have a certain amount of back radiation which causes scattering from the spacecraft body. Hence, at some stage, the S-band antenna or antennas must be mounted on a representative spacecraft body for measurement.

The radiation patterns of omnidirectional or quasi-omnidirectional antenna systems are always difficult to measure as, using a conventional test range with the antenna under test and a remote antenna on elevated towers or buildings (see Fig. 15), there is little protection from multipath reflections. This is particularly true at v.h.f. where the remote antenna usually has a broad main beam and relatively high sidelobes. Because of this, the general-purpose elevated-mode test range with the typical height and separation distances normally associated with microwave antenna measurements is avoided, and special test-range configurations are used as described below.

Probably the most common type of test range that is used for v.h.f. omnidirectional antennas is the 'ground reflection mode' test range,[20] the principle of which is illustrated in Fig. 9. Basically, a remote antenna, usually a log-periodic dipole array or a Yagi, is placed just above level ground. Interference between the direct ray from the antenna and the ground reflection ray (or, looking at it from a different point of view, the image contribution) gives a vertical radiation pattern which has a broad lobe as shown in the illustration and in which the test antenna* is situated, plus some further narrower lobes which are unimportant. This type of test range is used, for example, at the European Space Research and Technology Centre at Noordwijk, Holland, where an area of ground measuring

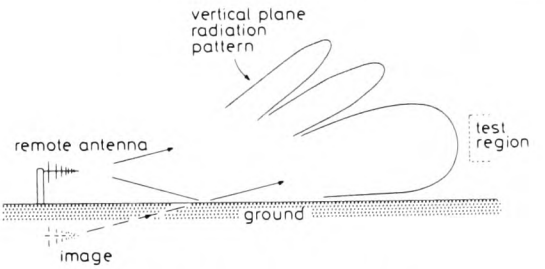

Fig. 9 *Ground-reflection-mode antenna test range*

*'Test antenna' is the normally accepted abbreviation for 'antenna under test'

150 x 100 m has been levelled to an accuracy of ± 2 cm. This allows ground-reflection-mode measurements to be carried out over a frequency range of about 100 MHz to just over 2 GHz.[21] For a particular measurement, the range geometry is calculated from formulas in References 20 or 21, which gives an indication of the required height of the remote antenna above the ground. The resulting amplitude distribution at the test end is, of course, dependent on the ground conditions of the particular test range (e.g. wet or dry soil, snow etc.) and so final adjustments are made empirically by moving a probe antenna across the test aperture to plot the field distribution, which can then be optimised. As the ground reflection characteristics are different for horizontal and vertical linear polarisation, measurements with the two polarisations require different remote antenna heights. Furthermore, measurements in circular polarisation require two linearly polarised remote antennas, each at their respective height above ground, and both fed from a common source via a network comprising a power divider, a phase shifter and an attenuator. The relative amplitudes and phases of the two antennas are then adjusted until an acceptable circular polarisation axial ratio is established at the test aperture. This is usually determined by 'rotating dipole' (or 'polarisation pattern') measurements[20] at selected points in the test aperture.

A different but highly interesting approach is used by the Royal Aircraft Establishment at their Lasham test range,[19] depicted in Fig. 10, which can be used at both v.h.f. and S-band frequencies. At this facility, satellites are mounted on a dielectric pole in front of sloping ground. At the top of the slope is a parabolic dish receiving antenna. Transmission is from the test end, i.e. the satellite, and most of the ground reflections from the slope, are scattered away from the receiving antenna. The small contribution that does arrive at the reflector, and this is from an area just in front of the receiver cabin, arrives at a fairly large angle from the reflector antenna boresight so that (at least when the range is used at u.h.f. frequencies and above) it is discriminated against by the narrow-beam radiation pattern of the receiving antenna. At v.h.f., as the angle between the direct and indirect ray leaving the satellite is minimised (to about 7°) by this geometry, the assumption is made that the signal radiated does not vary appreciably over this angle, between the direct and indirect rays. This is a reasonable assumption for omnidirectional and quasi-omnidirectional radiation patterns. The receiving dish has crossed dipoles as feeds which can be connected via a hybrid, so that the range can be used for measurements in any linear or either hand of circular polarisation.

As stated earlier, elevated mode test ranges with tower heights and range distances normally used for microwave antenna measurements are not employed for v.h.f. measurements because of the multipath reflection problems inherent with such geometries. However, at v.h.f., the required far-field approximation range distance between remote and test antenna (determined by the well known criterion described in the following Section) becomes quite small, and there are some special elevated-mode test ranges used for v.h.f. omnidirectional antenna measurements with high but closely spaced towers as in Fig. 11. With this arrangement, the only multipath contribution is from almost directly below the two antennas, and, even at v.h.f., a reasonably directive remote antenna can be used to discriminate against this. This geometry can also be used with the semi-open anechoic chamber type of facility[22] described in the following Section, which, because of the anechoic chamber around the test antenna, has almost total rejection of the ground reflected ray.

There is considerable advantage in being able to carry out antenna measurements in an indoor environment, away from the weather, especially where flight hardware is involved. Flight hardware usually cannot be taken unprotected outdoors without violating cleanliness stipulations. It has been shown that it is possible to modify a rectangular anechoic chamber in such a way that it can be used for antenna measurements at frequencies as low as 100 MHz.[23] The modified anechoic chamber referred to is at the British Aerospace Dynamics Group's Space Division at Stevenage and has internal dimensions of 18·3 x 7·3 x 7·3 m. Fig. 12 shows how this chamber has been modified for v.h.f.

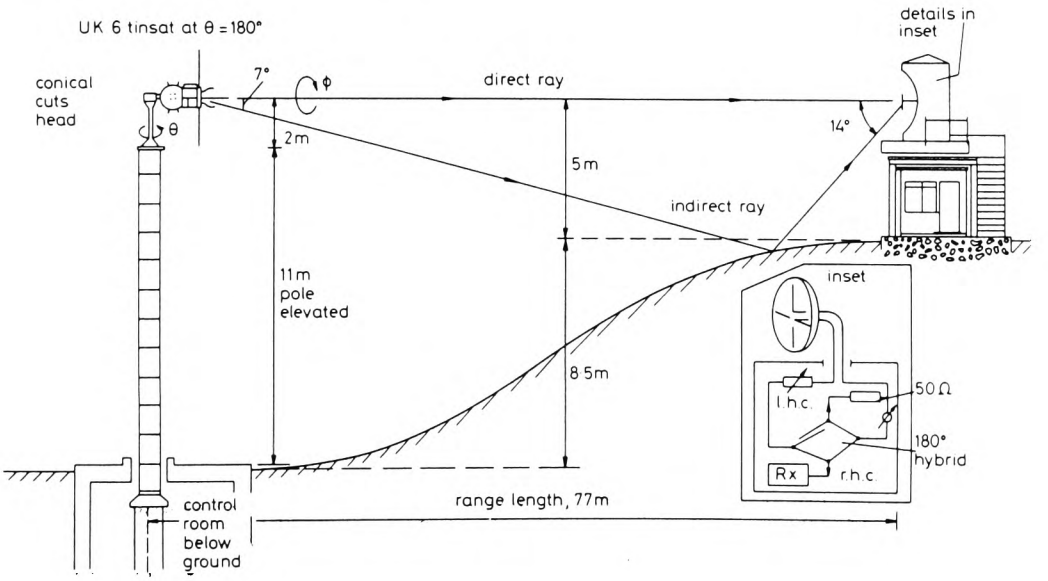

Fig. 10 *Schematic diagram of the Royal Aircraft Establishment model range 1 as Lasham*

measurements by using extra absorbing baffles. The reflectivity level with this internal arrangement has been found to be − 26 dB at 136 MHz in a zone measuring 3 x 2·4 x 2·4 m.

Having described some actual test ranges and techniques for measuring this class of satellite-antenna system, the current Section will now conclude with some remarks on the measurement of gain and directivity. At S-band, gain measurements are relatively straightforward and can be carried out by the substitution method, in which the test antenna is replaced by a standard gain horn of known gain, and the difference in recorded power level then gives the test antenna gain. Commercially available gain standards are usually linearly polarised, and the above procedure applies to linearly polarised test antennas. However, if a test antenna is circularly polarised, the gain can still be determined with a linearly polarised standard gain horn by using Stroka's method[24] in which the axial ratio of the circular polarisation generated by the test antenna must also be found. This can be determined by a 'polarisation pattern' measurement in which a linearly polarised remote antenna is axially rotated about a boresight axis shared between itself and the test antenna.

At v.h.f., gain measurements are very much harder. For these measurements, standard gain dipoles with adjustable dipole lengths and adjustable baluns are available, but, because these are essentially broad-beam devices (unlike standard gain horns), considerable errors can arise from their use. For example, it is not possible to replace a satellite model by a standard gain dipole suspended alone in free space; in practice, the substituted gain standard would be, perhaps, a dipole and attached coaxial cable on a large diameter dielectric tower. And even if the test range has been set up for low multipath errors with a satellite model and its antenna system, it often happens that, because of the different polarisations involved, there is not the same degree of multipath suppression or compensation for the standard gain dipole. Hence, for v.h.f. satellite antennas, the gain is often not evaluated, except as a crude check. Instead, the directivity of the system is found by pattern integration, to give the isotropic level, and allowance is then made for the ohmic losses in the antenna system. The allowance made is usually one half of a decibel, and this is more than adequate for all practical situations.

Directivity measurements with a v.h.f. satellite-antenna system are carried out by sampling the radiation distribution over the entire spherical region about the satellite, in two orthogonal polarisations. The two independent polarisations are essential, because such antenna systems are only able to achieve omnidirectionality by radiating in a variety of polarisations; for example, a cylindrical satellite with a turnstile antenna system might radiate in left-hand circular polarisation in one axial direction, right-hand circular polarisation in the other axial direction, vertical linear polarisation in or near its azimuth plane, and with elliptical polarisations in all other directions, as illustrated in Fig. 13. In practice, the orthogonal polarisations used for the measurements are either left and right circular polarisations or horizontal and vertical linear polarisations. After the data has been processed and the isotropic level found, the original measured data can then be normalised to the isotropic level, to give in effect, normalised radiation pattern maps in the chosen two orthogonal polarisations. This is described in more detail below.

If P_T is the total radiated power, $U_a(\theta, \phi)$ represents the power radiated per unit solid angle in direction θ, ϕ in some polarisation a, and $U_b(\theta, \phi)$ represents the corresponding

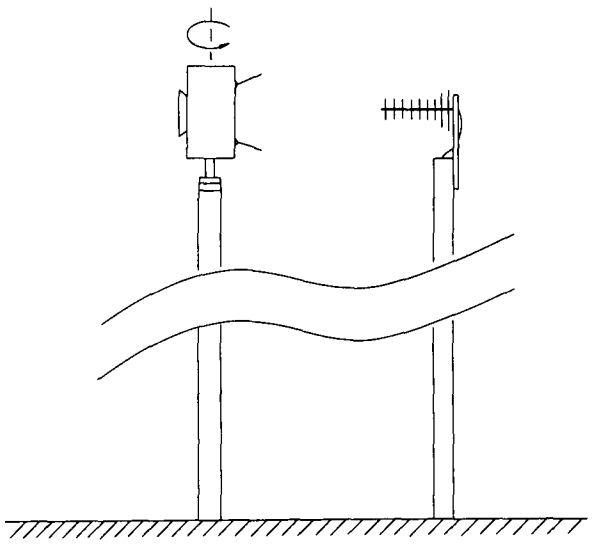

Fig. 11 *Elevated-mode test range with elevation much greater than separation, for v.h.f. antenna measurements*

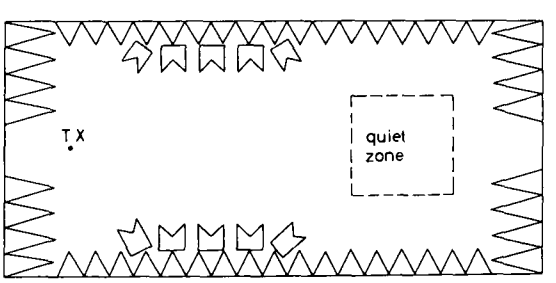

Fig. 12 *British Aerospace Dynamics Group anechoic chamber configuration as used for v.h.f. measurements*

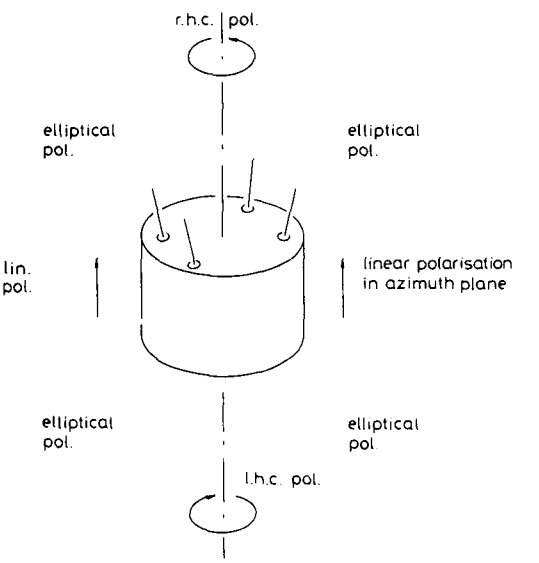

Fig. 13 *Typical distribution of polarisations in a vertical plane from a v.h.f. turnstile-antenna system on a cylindrical satellite*

quantity in the orthogonal polarisation b, then it can be shown that

$$P_T = \iint_{4\pi} U_a(\theta, \phi) \sin\theta d\theta d\phi + \iint_{4\pi} U_b(\theta, \phi) \sin\theta d\theta d\phi$$

If $U_T(\theta, \phi)$ represents the total power radiated per unit solid angle in direction θ, ϕ, then

$$U_T(\theta, \phi) = U_a(\theta, \phi) + U_b(\theta, \phi)$$

hence the partial directivities for each polarisation plus the total power directivity can be expressed as follows:

$$D_a(\theta, \phi) = \frac{4\pi U_a(\theta, \phi)}{P_T}$$

$$D_b(\theta, \phi) = \frac{4\pi U_b(\theta, \phi)}{P_T}$$

$$D_T(\theta, \phi) = \frac{4\pi U_T(\theta, \phi)}{P_T}$$

where, at any angle θ, ϕ, the total power directivity is simply the sum of the partial directivities.

In practice, computer programs exist to do the data processing, for example the one described in Reference 25, which is available from the IEE program library. Such programs print the partial and total directivity values in tabular form as a function of θ and ϕ from which radiation distribution contour maps can be prepared. Fig. 14 shows the upper left-hand extremity of a typical printout; only a small part of this is shown, as such printouts are large (typically 70 cm x 90 cm) and a presentation of a complete sheet here would make the printed characters indiscernible. These maps are highly useful, if not essential, for link budget evaluation, and are almost always used for omnidirectional and quasi-omnidirectional satellite-antenna systems, regardless of frequency band.

The reason for plotting total power directivity values as well as partial directivities is that some ground stations receive satellite telemetry simultaneously in orthogonal polarisations and mix the powers received in the two channels in a ways which, in many cases, is equivalent to total power reception.

As one final comment here, the definition of directivity used above is as follows:

$$D(\theta, \phi) = \frac{U(\theta, \phi)}{(P_T/4\pi)}$$

TIGRA S BAND ...IT< SKIRT

2250 ...HZ

HORIZONTAL LINEAR POLARISATION

BELOW IS A DIGITAL MAP OF THE PARTIAL DIRECTIVITY IN DBI UNITS

PHI	THETA 0.	5.	10.	15.	20.	25.	
0.	-6.1	-5.8	-6.1	-7.3	-8.3	-7.8	.
2.	-6.1	-5.8	-6.1	-7.3	-8.3	-7.8	.
4.	-6.1	-5.8	-6.1	-7.3	-8.3	-7.8	.
6.	-6.1	-5.8	-6.1	-7.3	-8.3	-7.8	.
8.	-6.1	-5.8	-6.1	-7.3	-8.3	-8.1	.
10.	-6.1	-5.8	-6.3	-7.3	-8.3	-8.1	.

Fig. 14 *Photograph of a part of a digital map of directivity values*

where the directivity $D(\theta, \phi)$ and the radiation intensity $U(\theta, \phi)$ are in one specified polarisation ot total power. P_T is the power radiated by the antenna. This definition of directivity is distinct from that for gain, which is defined by:

$$G(\theta, \phi) = \frac{U(\theta, \phi)}{(P_{IN}/4\pi)}$$

where, again, $G(\theta, \phi)$ and $U(\theta, \phi)$ are in one specified polarisation or total power. P_{IN} is the power supplied to the antenna input port. It can be seen that gain takes into account the ohmic losses of the antenna whereas directivity does not.

These definitions are not exactly as specified by the IEEE standards,[26] but it is the author's contention that the above are the ones on common usage. Generally speaking, 'gain' is an antenna parameter which is related to the power supplied to the antenna, and is measured by comparison with a gain standard such as a calibrated horn. In contrast, 'directivity' depends only on the shape of the radiation patterns and is determined by pattern measurements and integration. To introduce a third definition, 'directive gain' is, in the author's opinion, confusing and unnecessary. This also applies to the term 'power gain'. Furthermore, 'directivity' as defined in Reference 26, i.e. as a maximum value only, has no useful meaning for an omnidirectional type of antenna system.

3 Medium- and high-gain antenna-measurement methods

Fig. 15 illustrates the type of antenna-measurement range that is most familiar to microwave antenna engineers. This is the so-called elevated-mode type of range where both the test and the remote antennas are elevated above the ground, often on towers, but sometimes on buildings. By rotating the test antenna in different planes, its radiation patterns can be recorded.

The separation or range distance between the two antennas has to be sufficient to approximate to a 'far-field' distance. Or, looking at it from another point of view, if transmission is from the remote antenna, the test antenna must have a wavefront incident on it that approximates to a plane wave. In practice, a range distance criterion as below is usually adopted:[27]

$$d \geq \frac{2D^2}{\lambda}$$

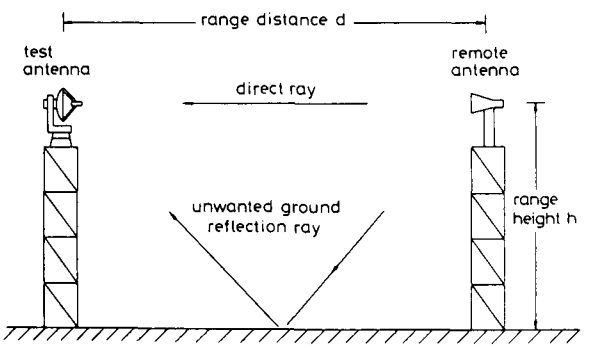

Fig. 15 *Elevated-mode antenna measurement range geometry*

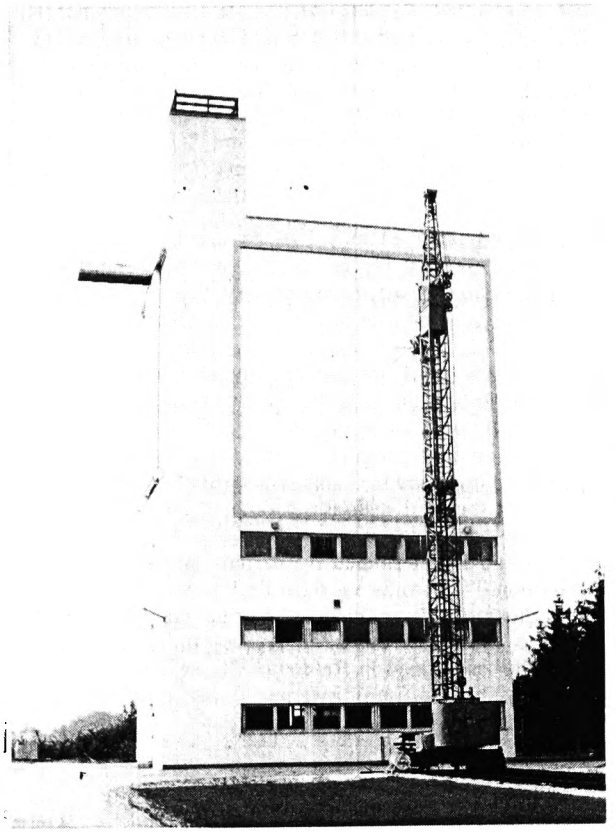

Fig. 16 *Front view of MBB semi-open anechoic chamber facility near Munich*

where D is the antenna aperture diameter, d is the range distance, and λ is the free space wavelength. This criterion is equivalent to a maximum phase error of 22·5° at the test antenna aperture edge, which is a sufficiently good approximation to a plane-wave environment for most measurements. The effect of range distance on the accuracy of recording sidelobe levels has been described by Lyon, Hollis and Hickman in chapter 14 of Reference 20.

Having established the range distance d, the height of the two antennas above the ground is then chosen so that the ground reflected ray is minimised by the antenna radiation patterns. In other words, it is arranged that the antenna-pattern sidelobes pointing at the central ground area are as small as possible. If sidelobe discrimination is insufficient, the ground reflection component can be further reduced by using diffraction fences to screen off the first twenty or so Fresnel zones on the ground.[20] In practice, the 'free space v.s.w.r.' method and aperture probing are two ways of calibrating range performance,[20] and range improvement is usually carried out empirically by making successive calibrations interspersed with changes to the range layout, such as movements or diffraction screens or the deploymant of r.f. absorbent material. The effects of ground reflections on antenna measurements have been investigated by Moeller[28] and his paper contains useful graphs showing, for example, the errors in gain, polarisation purity, and boresight direction measurements, in the presence of ground reflections. In general, at the test aperture, a well sited antenna test range should have a ground reflection contribution level of not greater than −40 dB (compared with the direct path level), and levels of −50 dB are not untypical.[29] Really excellent ranges can

Fig. 17 *Side view of semi-open anechoic chamber facility*

be better than this. Janssen *et al.*[30] have described a range that was accurate over a 90 dB dynamic range, although this was a special elevated mode range with a height to separation ratio of 3:2, limited to the evaluation of corrugated horns.

As stated in Section 2 in connection with low-gain antennas, there is always an advantage in being able to carry out antenna measurements in an 'indoor' environment, especially where flight hardware is involved. For moderate-gain antennas where the range distance is not too great, it is often possible to carry out elevated mode measurements in an anechoic chamber. However, due to the high cost of broadband microwave absorbent material, anechoic chambers are expensive, and although there are quite a number of small chambers in existence (many of which can only be used for feed measurements), plus a few medium-sized chambers, there are relatively few large anechoic chambers. One such large facility of note which has been used for spacecraft work is the radio anechoic chamber of the Technical University of Denmark[31] at Lyngby near Copenhagen. The dimensions of this rectangular chamber are 12 x 14 x 6 m and it is lined with 2 m high broadband pyramidal absorbers. These allow measurements to be carried out at frequencies between 50 MHz and 50 GHz. Because of the large transverse cross-section (12 x 14 m) of this chamber and the effectiveness of the pyramidal absorbers, the chamber has a relatively large quiet zone of 2·5 m diameter and 9·5 m length along its longitudinal centre line. Methods of evaluating radio anechoic chambers have been described by Appel-Hansen.[32]

An ingenious variation on the anechoic chamber arrangement is the Messerschmitt-Bolkow-Blohm GmbH facility at Ottobrunn near Munich.[22] This facility, shown in Figs. 16 and 17, combines the protection, security and convenience of the anechoic chamber environment with the large range distance of the outdoor elevated mode antenna range. Basically, the facility consists of a large anechoic chamber, open on one face but protected from the outdoor environment by an r.f. transparent cover, in the top part of a specially constructed building. Below the chamber is a control room (2nd floor), offices (1st floor) and a dedicated workshop (ground floor). A railway track in front of the building allows the remote antenna tower to be moved to any required distance from the chamber, up to a limit of 80 m. Where longer range distances are required, it is possible to locate a tower beyond the limit of the railway track. Large antennas or other bulky rigs, such as satellite models or aircraft models, can be installed in the chamber

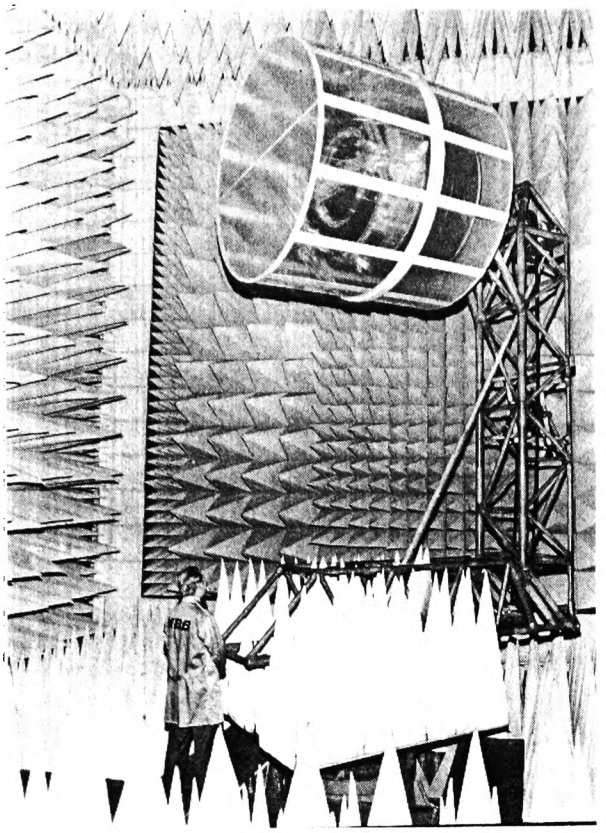

Fig. 18 *GEOS spacecraft encapsulated in r.f. transparent radome to comply with cleanliness requirements*

through metal doors on one side. Positioning is carried out with a 2·5 ton maximum load crane which has a horizontal trackway across the top of the chamber. The advantages of this type of antenna measurement range are clearly obvious, and it is fair to say that, as a general-purpose range, this particular facility is one of the best in Europe.

One last comment concerning anechoic chambers is that, although having an enormous advantage as regards environmental protection, they may still not satisfy the stringent cleanliness requirements imposed on flight hardware. In such cases it is necessary to cover the spacecraft or antenna system with some sort of radome. Fig. 18 shows one such radome fitted to the ESA GEOS spacecraft. This radome was a simple cylindrical construction with a glass-reinforced plastics framework covered by an r.f. transparent plastic film.

4 Near-field and intermediate-distance techniques

In the preceding Section it was shown that medium- and high-gain antennas are normally measured using elevated-mode ranges of one form of another. Unfortunately, there are some situations where this type of test range becomes impractical, unless gross measurement errors can be tolerated. This happens when the antenna to be investigated has such a large aperture in terms of its operating wavelength that the far-field approximation range distance required for its measurement (determined by the $2D^2/\lambda$ criterion) becomes excessively large. There is a rule of thumb for the geometry of elevated-mode ranges which states that the elevation of the antennas above the ground must be at least one tenth the range distance. With elevations lower than this, errors due to ground reflections become untenable. As an illustration, consider a 2 m diameter satellite reflector antenna with an operating frequency of 14 GHz. The minimum range length required for measuring this antenna is, according to the $2D^2/\lambda$ criterion, 373 m. This then implies an elevation of at least 37 m and preferably more: 60 or 70 m would be better. Few antenna measurement facilities can accomodate these dimensional requirements. And when it is considered that satellite antennas need not be constrained by launch vehicle fairing dimensions (for example, the deployable reflector on the NASA ATS-6 satellite has a diameter of nearly 10 m)[33] and that the use of frequencies as high as 30 GHz is under study,[34] the range distance problem can be appreciated.

It should be mentioned that there are a few direct-measurement long-distance antenna ranges in which the ground-reflection problem is at least partially overcome by a suitable choice of location: for example, by transmitting across a valley, or even between two adjacent mountains. However, these ranges are rarely completely satisfactory, either because the multipath error improvement is insufficient or for other reasons such as a lack of dynamic range with the recording apparatus, or even because of the difficulty in erecting antennas in remote sites of limited access.

Curiously, it is not only the electrically large aperture antennas that give rise to range distance problems. It must be remembered that the $2D^2/\lambda$ distance is only an approximation to a far-field distance, and that actually, wavefronts at the test antenna are spherical with path length deviations of $\lambda/16$ at the antenna extremities. Because of this, certain antennas, constrained to have nontapered aperture phase distributions, may require far-field approximation distances much greater than the usually accepted value. For example, in connection with one of the ESA programmes, an *L*-band shaped-beam Earth-coverage reflector antenna with an aperture diameter of 2 m[17,35] was found by computer simulation to require a range distance of greater than 1 km, and a special 'intermediate distance' test range had to be constructed to overcome this problem.[36] The shaped beam antenna referred to, the MARECS satellite antenna, is shown in Fig. 21.

For situations where elevated mode measurement range distances become too long to be practical, measurements can be either carried out using 'near-field' techniques or 'intermediate-distance' techniques. These techniques are their relative merits are described below, following a brief description of the compact range technique[37] which is a special near-field technique in a class of its own. As will be seen, most near-field and intermediate-distance techniques are indirect-measurement methods where field sampling is carried out and then data processing is used to determined the required far-field characteristics. The compact-range technique, however, is a direct-measurement technique, although its use is limited to the measurement of relatively small antennas such as horn feeds. Fig. 19 illustrates a typical compact-range configuration. This type of measurement range makes use of the well known phenomenon that planar wavefronts are generated in the near-field region of reflector antennas and lenses. Although metallic lens compact ranges have been described,[38] the usual form of a compact range is as in Fig. 19. Most often, an offset parabolic reflector is used in preference to an axisymmetrical parabolic reflector to avoid unnecessary aperture

blockage. Edge diffraction from the periphery of the reflector is eliminated either with microwave-absorbent material, or by cutting castellations or triangular 'teeth' in the rim. Direct path screening between the reflector feed and the test antenna is necessary and this is usually accomplished with absorber. In addition, to avoid reflections from the test antenna support arm, this is usually covered in absorber also. It has been shown that the compact range technique can be used at up to millimetre wave frequencies.[39] An unusual application of the compact range principle has been described recently for the measurement of the scattering patterns of the support struts of large reflector antennas.[40]

In general, near-field techniques may be described as methods where a probe is moved across the aperture of a test antenna, and the near-field phase and amplitude sampled. The far-field characteristics of the test antenna are then determined by carrying out a near-field to far-field (n.f.f.f.) transformation of the near-field samplings using data processing techniques.[41,42] The sampling process may be carried out over spherical, planar or cylindrical surfaces. Fig. 20 illustrates one of these; it shows the type of moveable probe carriage arrangement used for planar scanning, where the probe can be moved vertically and horizontally. The relative advantages and disadvantages of using the three types of scanning geometries have been described by Wacker and Newell.[43]

There has been considerable interest in the use of near-field techniques with satellite antennas, particularly the use of spherical scanning. With this geometry, if probing is carried out in phase and amplitude in two orthogonal polarisations, the test antenna performance can be fully characterised and the entire far-field distribution of the antenna

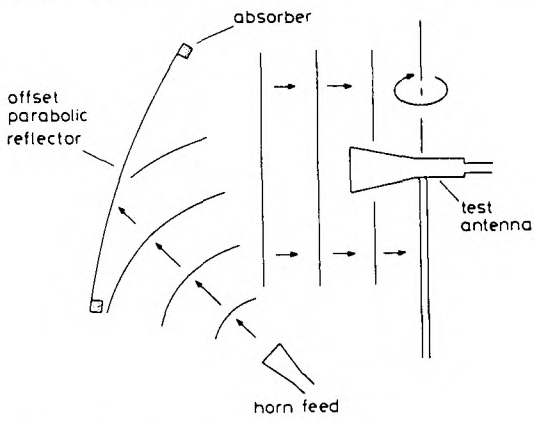

Fig. 19 *One form of compact range*

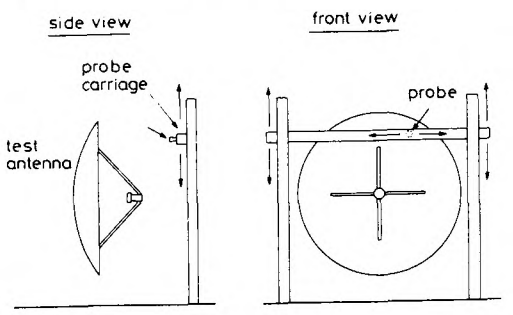

Fig. 20 *Near-field measurement arrangement using the planar probing geometry*

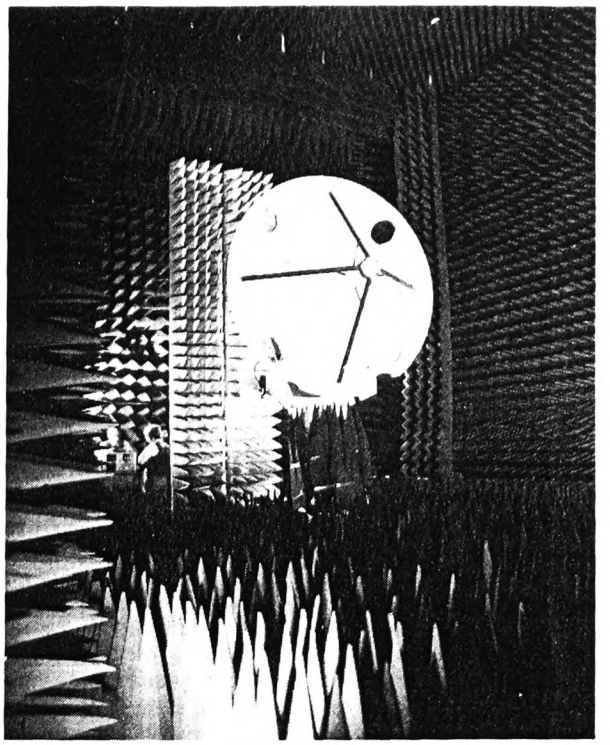

Fig. 21 *Cylindrical scanning near-field facility under development by the British Aerospace Dynamics Group*

The antenna under test is the MARECS satellite shaped beam antenna

can be found by data processing using fast Fourier transform (f.f.t.) techniques. One other advantage of spherical scanning is that it is not necessary to have an accurate probe positioner to move the probe around the antenna. Instead, the probe can be fixed and the test antenna made to scan using a conventional two-axis antenna mount. The feasibility of using spherical scanning for the measurement of satellite antennas has been described by Jensen.[44]

The cylindrical scanning near-field measurement is also being actively developed. This geometry is significantly simpler to deal with theoretically than the spherical scanning case. Also, the scanning mechanism is relatively simple, consisting of a probe with vertical linear motion only and azimuthal rotation of the antenna. This type of scanning ensures that no mechanical changes due to gravitational deflections occur with the test antenna during a measurement cycle. Fig. 21 illustrates the cylindrical scanning facility under development by the British Aerospace Dynamics Group in Stevenage, England.[45] The vertical probe carriage and probe antenna can be clearly seen behind the test antenna, which in this case is the MARECS shaped beam antenna referred to previously.

It can be seen then, that indirect near-field measurement techniques are under active development in Europe. So far, the results are encouraging and the only question concerns the ultimate accuracy obtainable with these techniques. There are measurement errors, for example, associated with the probe. These are of two types. First, the physical presence of the probe alters the field being measured, i.e. some energy is rescattered onto the antenna under test. This effect cannot be corrected for in practice. Secondly,

because the probe has a finite aperture, it measures an average of the field over this aperture rather than the field at a point. This can be corrected for at the cost of some complexity. Larsen[46] has investigated probe correction for spherical scanning and has shown that its use improves measurement accuracy. Investigations in the near future should indicate whether probe scattering causes significant errors, and if so, how the probe can be chosen to minimise these.

Intermediate-distance techniques, which have been reviewed by Keen, Bennett and Wood,[47] offer an alternative to near-field techniques. The basis of these methods is that sampling is carried out at some convenient distance from the antenna between its near-field distance (i.e. right in front of the antenna) and its far-field distance. Typically, a distance of $0{\cdot}5D^2/\lambda$ might be chosen. Apart from this, the techniques are similar to near-field techniques in that the antenna field sampling must be carried out in both amplitude and phase, or in some form that contains combined amplitude and phase data, and then an intermediate distance to far-field distance transformation is carried out by data processing to give the far-field characteristics of the test antenna.

If intermediate-distance techniques are compared with near-field techniques, there are both advantages and disadvantages depending on the type of measurements that are to be carried out. However, there are two general points in favour of intermediate-distance techniques that are worth noting. The first is the elimination of probe errors and the second is that, as the range distance is not critical, intermediate-distance working can be carried out on existing test ranges. This includes large anechoic chambers. In fact, virtually any elevated-mode test range with the necessary turntables, positioners etc. can be extended in capability by being able to adopt intermediate distance working. It must be emphasised, however, that the data processing involved is, as with near-field techniques, somewhat daunting, and a great deal of computer power and time is needed.

Three particular intermediate-distance techniques have been demonstrated so far. These are the University of Sheffield Holographic Technique,[48] the Marconi Research Laboratories Technique[36,49] and the ESTEC technique,[50] being named here after the establishments at which they were developed. The first of these, the holographic technique developed by researchers at the University of Sheffield, uses a 3-antenna arrangement as shown in Fig. 22. Transmission is from a remote antenna and reception is by

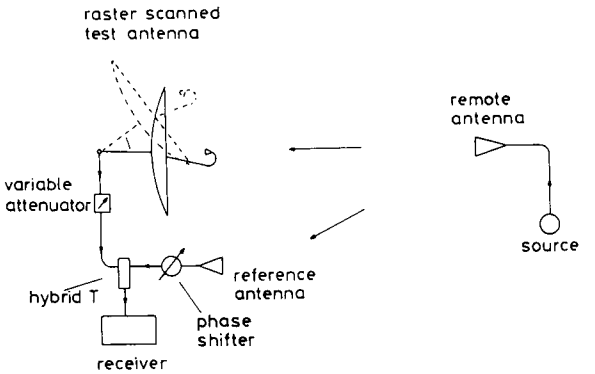

Fig. 22 *University of Sheffield holographic technique*

both the test antenna (moveable) and a static reference antenna which are connected via a hybrid T. An attentuator and a phase shifter are also included in the r.f. circuit. The test antenna is mounted on a two-axis positioning system which carries out raster scanning of the test antenna during which the corresponding hologram is recorded. Originally, optical holograms were produced with this technique which were processed optically, but now electronic data processing techniques are used. The data array formed by regular sampling of the hologram signal is computer-processed using f.f.t. techniques to provide a variety of antenna characteristics, including far-field radiation patterns. One of the powerful features of this measurement method is that antenna surface profile information can also be obtained, and surface deformation and other deviations of paraboloid reflectors can be identified.[51]

The Marconi intermediate-field range was originally developed for bread-board and flight model testing of the MAROTS (now MARECS) satellite antenna. This is basically an outdoor facility using two 13 m towers at 107 m spacing. For tests at L-band the range length is $\triangleq 4D^2/\lambda$. In ordinary circumstances, this length would have been sufficient to permit conventional far-field measurements. However, the special characteristics of the shaped beam antenna precluded this, as described earlier. True near-field probing would also be unsuitable for this type of antenna, because this would place unwanted emphasis on phase measurement accuracy; e.g. 1° phase measurement error would result in 0·2 dB error in the predicted antenna gain.[47]

The range uses conventional azimuth and polar antenna positioners, effectively giving spherical surface probing. The spherical probing data is processed by spherical wave expansion technique which is essentially a rigorous electromagnetic transformation. It is valid regardless of measurement range, and ideally permits all six electromagnetic-field quantities (3 components E, 3 components H) to be individually specified at near- or far-field range. The spherical wave spectrum for the antenna is a standard interface which can be used to transfer data to other computer programs. The 'cutoff' property of the spectrum gives a filtering action to eliminate spurious components of the measured pattern not compatible with the size of the aperture under test.

An overall absolute-measurement accuracy of ± 0·07 dB at J-band has been established experimentally with this technique.[52]

The technique developed at ESTEC is in some ways a hybrid of the two previously described methods, and was developed to extend the capabilities of the conventional far-field approximation antenna test range on the ESTEC site. Basically, the antenna under test is fed in parallel with a second antenna, in order to make interference patterns which are monitored at an intermediate distance. As with the holographic technique, the interference patterns which are monitored at an intermediate distance. As with the holographic technique, the interference patterns contain the essential phase information, although with the ESTEC method the formation of the interference patterns, the phase data extraction and the intermediate to far-field distance transformation are carried out in different ways.

Fig. 23 shows the antenna measurement configuration and Fig. 24 illustrates the circuit which feeds the test and reference antennas. There is an alternative form of circuit arrangement in which the antenna B to antenna C path is

replaced by a cable which combines the interference wave with the direct wave in a directional coupler, this being situated in the line between antenna C and the amplitude receiver. Both forms are, however, equivalent. Essentially the measurement method is as follows. For each conical directional 'cut' in the spherical measurement surface, four separate radiation patterns are recorded. The first is in amplitude only and is made with antenna B switched out. The following three are interference patterns formed by having antenna B switched in so that interference between radiation from antennas A and B can be monitored at antenna C. These three patterns are recorded with the phase shifter set to relative phases of 0°, 90°, and 180°, respectively. This procedure is carried out for the entire spherical envelope surrounding the test antenna, and in two orthogonal polarisations. When all the recording is finished, data processing is carried out in two stages. In the first stage, for each 'cut' and polarisation, the four patterns or sets of recorded data are processed to give an amplitude pattern and a phase pattern. Thus, the first stage is essentially concerned with extracting phase information from interference patterns. In the second stage, the amplitude and phase data is processed by a near field (or intermediate distance) to far-field transformation computer program, which finally gives the required far-field pattern information. At ESTEC, the program SNIFT[53] has been used for the transformation process.

To conclude this Section, it may be said that the range-distance problem encountered with electrically large satellite antennas can be overcome using either near-field or intermediate-distance techniques, all of which rely heavily on data processing.

5 Special techniques for particular cases

This Section contains a miscellaneous collection of antenna or related measurement techniques that have been used for some particular problems connected with satellites, mostly of an unusual kind. Section 5.1 deals with in-orbit satellite antenna measurements; these can be important as a check on the performance of an antenna in its 'real' operating environment. This may be particularly desirable if the satellite or the antenna system is the first of a future series of similar satellites or antennas.

Section 5.2 deals with the transparency of launch vehicle fairings. It is now normal, at least for European launches, to monitor telemetry data from a satellite from the very beginning of its launch phase. In order that telemetry data can be transmitted through the metallic launch-vehicle fairing which covers the satellite for the first part of the launch, the fairing half-shells are fitted with r.f. windows. The location, number and size of the windows must be sufficient to give the required coverage.

In Sections 5.3 and 5.4, the measurement of small gain reductions or changes is described, in connection with the reflectivity of lightweight spacecraft carbon-fibre reinforced plastics reflectors, and in another context, in connection with electrically conductive paint that is sometimes applied to spacecraft bodies (and antenna systems) for dissipating electric currents induced by plasmas.

In Section 5.5, the effects of body-mounted solar panels on v.h.f. omnidirectional antenna systems is considered and a measurement technique used to evaluate the effects is described. Rocket-exhaust plume transparency measurements and results are briefly described in Section 5.6. This can be important as regards, for example, apogee boost motor firing on satellites.

Finally, Section 5.7 deals with crosspolarisation measurements which, with the advent of polarisation diversity antennas, have become of great importance. Some comments and descriptions are given for both linear polarisation and circular polarisation measurements.

5.1 *In-orbit antenna pattern measurements*

Although it has only been done on a few occasions, it is sometimes possible to measure the radiation characteristics of spot beam satellite antennas directly from an orbiting spacecraft, at least over a limited angular region around the boresight direction. This is done either to see if a deployable antenna has fully deployed and has assumed its correct shape, or to monitor the performance of an antenna or group of antennas under varying thermal conditions. Brain[54] has described an in-orbit measurement programme for the ESA OTS-2 satellite, in which the satellite is manoeuvred using its gas jets (north-south movement) and its momentum wheel (east-west movement). These roll and pitch rotations are limited to ± 2°, hence several Earth stations have to be used simultaneously during the antenna tests, and the results integrated.

Other in-orbit measurements have been carried out in the past by flying aircraft through the main beams of high-gain satellite antennas.

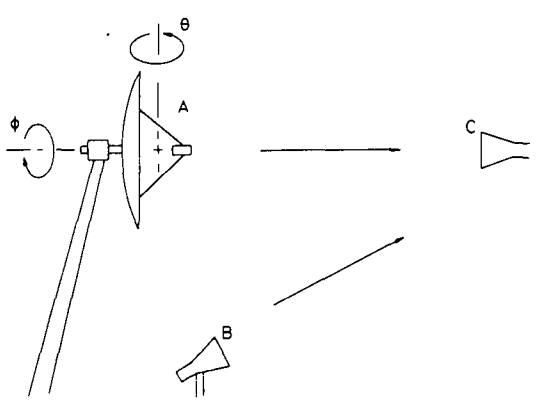

Fig. 23 *Interference pattern intermediate-distance measurement method*

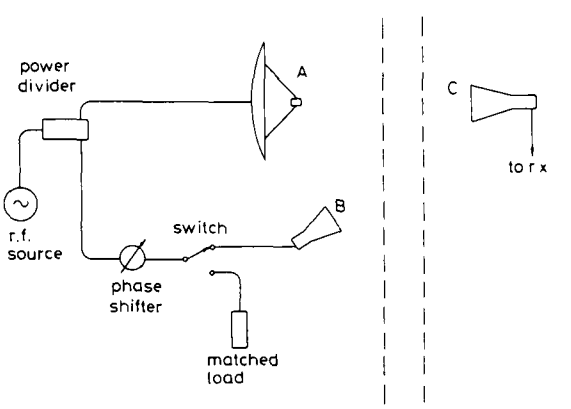

Fig. 24 *Feeding circuit for the interference-pattern method*

5.2 *Launch-vehicle fairing transparency measurements*

Fig. 25, which is based on a version of the much used DELTA launch vehicle, illustrates the positioning of a satellite above the third stage and within the fairing of such a vehicle. The fairing consists of two half-shells which eject at a height of about 120 km. For early satellite launches, the fairing shells were made of fibreglass and were very nearly transparent at r.f. Hence telemetry data could be received from the satellite at all times during the launch phase. This reception of telemetry is considered important by some users, who, if something goes wrong, require to know precisely when the mishap occurs. As satellites became larger, more spacious fairings were needed and the fibreglass shells were replaced by bigger and more rigid metal ones, thus causing a problem with the initial launch-phase telemetry link. Fortunately, and here the DELTA vehicle is specifically referred to, it was possible to specify that fairing access doors were made of fibreglass rather than aluminium alloy. The access doors would then act as r.f. windows. It was also possible to have fibreglass panels fitted in the conical/hemispherical top section of the fairing.

During the development of the ESA GEOS and METEOSAT satellites, a measurements study was carried out with models of the launch vehicle configuration for each case, to ensure telemetry data reception during the initial phase of the launches of these two spacecraft.[55] The study was carried out with 1/5th scale r.f. models of the upper parts of the launch vehicle and a similarly scaled satellite model which was correctly positioned in the fairing.

The factors which affect the 'coverage' of radiation from a launch-vehicle fairing and determine whether a vehicle to ground station link can be maintained during the launch phase are, first, how much energy leaks out of the r.f. windows from the inside of the fairing, and secondly, the combined radiation pattern of the windows on the fairing. For this reason, measurements were carried out in the following way in each case. The satellite was first evaluated alone over the entire spherical region around it, in the way described in Section 2 for determining directivity. Its isotropic level was then found by pattern integration. The same was then done for the launch-vehicle model with the satellite inside so that a digital printout of directivity values was produced, except that the isotropic level was adjusted to the original (satellite only) level. Hence the digital map showed not only the radiation pattern but also the insertion loss of the fairing configuration.

In anticipation that users may want to carry out similar measurements on the fairing configurations of Ariane, the new European launch vehicle, a 1/5th scale model of the upper parts of this launch vehicle is available, as shown in Figs. 26 and 27. These are various r.f. transparent sections on, or available with, the Ariane fairing. Most notable is the reverse cone at the base of the fairing, which is in glass-reinforced plastic. In addition to this, other windows can be provided, as illustrated in Fig. 26.

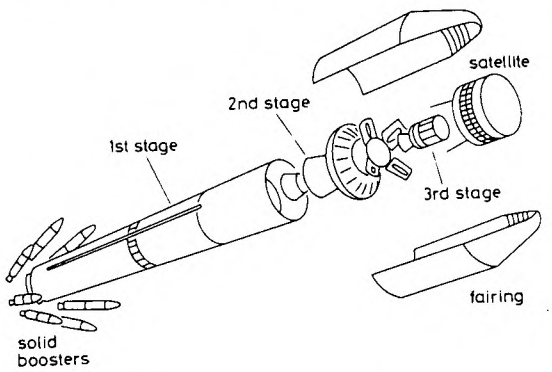

Fig. 25 *Typical positioning of a satellite within a launch vehicle*

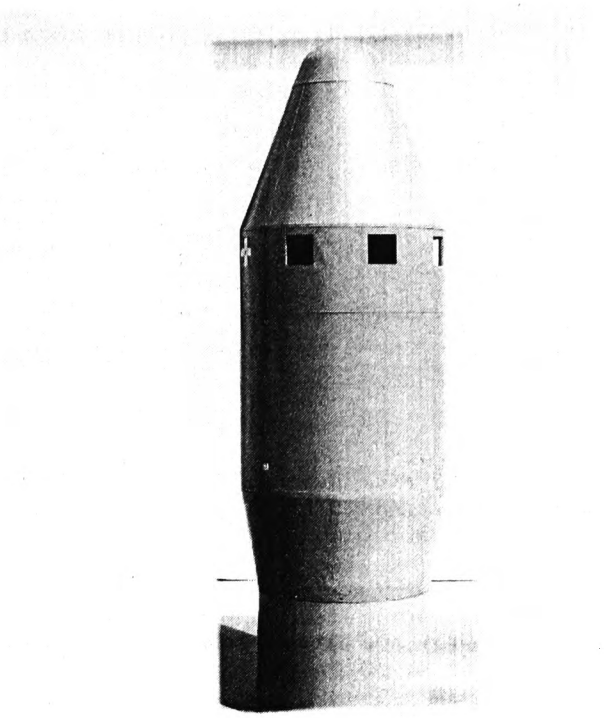

Fig. 26 *Photograph of a $\frac{1}{5}$th scale model of ARIANE fairing*
View of outside

5.3 *Measurements to determine the reflectivity of carbon-fibre plastic reflectors*

Component mass is always a problem on satellites and must be minimised. The development of the carbon-fibre reinforced plastics (c.f.r.p.) which are strong, rigid, lightweight and have a small coefficient of expansion, has provided a uniquely useful material for satellite component parts. This includes antenna reflectors. The low coefficient of expansion is particularly relevant in this context as satellite reflectors are subject to considerable temperature variations from diurnal eclipses. Originally, spacecraft c.f.r.p. reflectors were coated with metal foil. Eventually, though, it was realised that c.f.r.p. is itself a good reflector with the same order of reflectivity as plane metal, subject to certain factors such as frequency, polarisation, surface filling fraction and surface roughness of the material, and the 'lay-up' of the tows of fibres in the c.f.r.p..

Many ways have been devised to evaluate c.f.r.p. as a reflector material. Arguably, the only really satisfactory way is to take an actual c.f.r.p. reflector made in the appropriate way and with the correct surface finish (this is very important) and make gain difference measurements referred to a metallic surface.[56-58] In other words, the reflector is first fitted with an appropriate feed to make

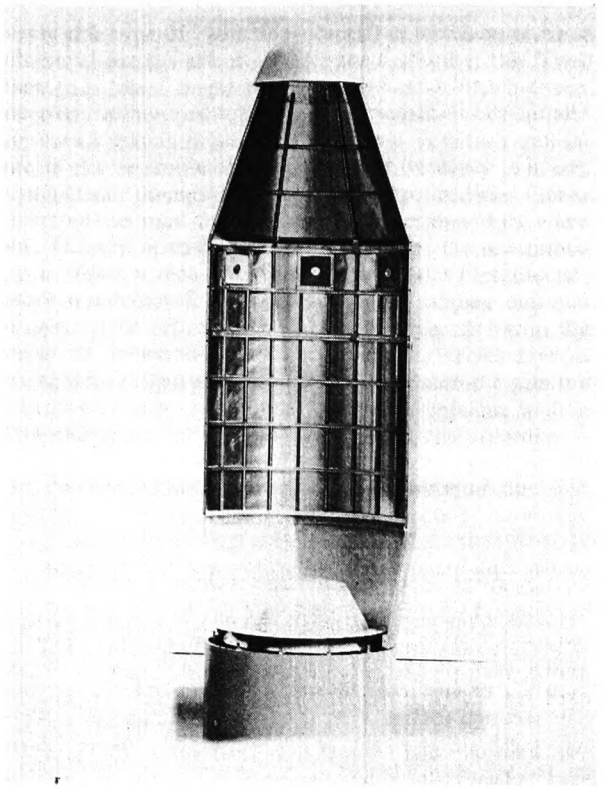

Fig. 27 *Photograph of a $\frac{1}{5}$th scale model of ARIANE fairing*
View of inside

a representative antenna system. The reflector is then metallised in some reversible way, and with the antenna positioned on a suitable measurement range, the gain of the antenna is monitored. The metallisation is then removed and the difference in monitored received power level shows the gain loss, if any, associated with the c.f.r.p. reflector.

Measurements have been carried out in this way by using the substitution method as for gain measurements. That is, the metallised c.f.r.p. antenna gain is established first with reference to a gain standard (or in fact any convenient antenna, since the absolute gain value is not important). The metallisation is then removed and the new gain value established with respect to the same reference antenna as before. However, as gain differences are usually only small fractions of a dB, it is difficult to get the required accuracy with this method and the system shown in Fig. 28 has been found to be more accurate. This is a swept-frequency technique and therefore the reflectivity can be established as a function of frequency over an operating band of interest. This is clearly better than making spot-frequency measurements. Another advantage of this system is that the levels are monitored via a network analyser which measures the test channel to reference channel signal level and which therefore rejects variations in the source level. Only differences occurring in the test channel line are recorded.

A variety of methods of reversible metallisation have been tried, but the simplest and most effective seems to be to coat the reflector with a thin film of automobile grease and then to apply a thin aluminium foil which can be smoothed down to the correct shape. Very accurate metallic surface coverings can be made in this way without much trouble. Such surfaces can be easily removed as can the grease, which may be wiped off using alcohol.

The results of test with various reflectors have shown that gain losses are usually smaller than 0·1 dB especially at the lower frequencies. High modulus (type I) carbon fibre appears to be better than high tensile (type II) fibre, but the most important factors are the filling fraction at the surface (i.e. the ratio of carbon fibre to plastic) which must be high, and the surface smoothness. The reflectivity of c.f.r.p. deteriorates at the higher microwave frequencies (it used to be considered that 15 GHz or thereabouts was the limit of use); however, uncoated c.f.r.p. reflectors operating at much higher frequencies than this have been heard of, although with no published details at the time of writing. One final point concerns polarisation sensitivity; this depends on the lay-up of the fibres and is generally not a problem, but a lay-up with all the surface tows in one direction can give a degree of polarisation sensitivity.

5.4 Effect of conductive thermal-control paint on spacecraft antenna performance

A few years ago it became apparent that spacecraft in Earth orbits are subject to a previously unsuspected form of environmental hazard. System malfunctions and even, occasionally, the complete failure of satellites led to the conclusion that differential electrical charging from hot plasmas can cause highly destructive vacuum arcs. The plasmas are a manifestation of a phenomenon known as substorms, which occur in the Earth's magnetosphere owing to interactions between the solar wind, the Earth's magnetic field and the interplanetary magnetic fields. If a satellite encounters a substorm region, the high-energy electrons in the plasma can cause charging of its components parts to the order of 20 kV. Subsequent electrical breakdown in dielectric materials can cause electromagnetic interference, transient pulses in electronic circuitry burnout of electrical components.

A way to prevent charge build-up is to ensure that satellites are electrically conductive on all external surfaces. This conflicts with the use of thermal-control paints, normally dielectric materials, which are often applied to the spacecraft bodies or appendages for temperature control. If, however, the paint has some additive to make it slightly conductive, it fills the dual role of thermal control and charge build-up inhibition. The possibility of having to

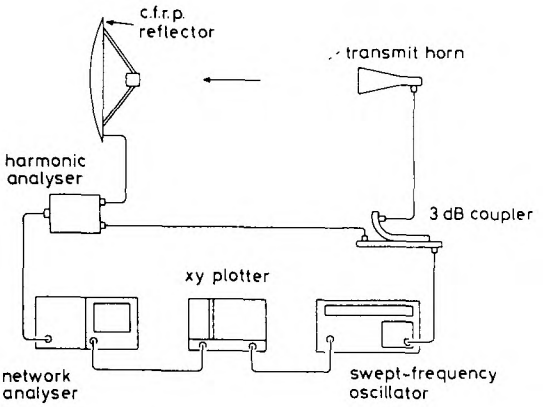

Fig. 28 *Swept-frequency measurement arrangement for recording small gain differences*

apply this type of paint to spacecraft antennas gave rise to doubts about the effect on reflector systems; it was feared that gain losses might occur as a result of the low conductivity of the paint. This led to a measurement study[59] similar to that carried out for the c.f.r.p. reflectors, and the use of the measurement system of Fig. 28 with a particular conductive thermal-control paint. An ordinary metal reflector was used this time at the test channel end, and it was initially coated with the conductive thermal-control paint. After a recording was made on the XY plotter, the paint was removed with chemical paint stripper and then another trace recorded on the plotter. Fig. 29 shows the result of measurements with a particular paint over an 8–12 GHz frequency range. It was seen that the gain loss was smaller than 0·1 dB and therefore acceptable at these frequencies.

5.5 *Effects of body-mounted solar panels at v.h.f.*

As already stated earlier, v.h.f. satellite-antenna systems are effectively not just the monopoles. The mechanism by which radiation occurs is that the monopoles excite currents on the spacecraft body and the whole thing, i.e. spacecraft plus monopoles, is the source of the far-field radiation. Quite often, satellite bodies are covered in solar panels, and therefore it might be thought that, due to the semiconducting nature of the solar cells, surface current losses would lower the efficiency of the 'satellite body and monopoles' radiating system. In fact this does not happen if the solar cells are situated above a metal surface (see Nichols,[2] page 8).

Measurements to verify this were carried out by the author on the ESTEC antenna test range using a full-size cylindrical metal satellite model with a monopole antenna, and in which one body panel could be removed and replaced with a solar panel (see Fig. 30). Measurements were made by monitoring the radiation patterns of the satellite at various θ angles; that is, 'conical cut' radiation patterns were recorded. These were made with and without the solar panel present. If the panel had been lossy, it would have caused a level reduction in the corresponding part of the radiation patterns, but in fact, no effects were seen, and it was concluded that at v.h.f., the solar panel acted identically to a metal one. The particular solar panel used for this investigation was a spare from the ESA GEOS satellite programme.

5.6 *Rocket-engine exhaust plume measurements*

How does a rocket-engine exhaust plume affect electromagnetic waves? Is it transparent, partially transparent or completely opaque? This question is important for situations such as apogee boost motor firing where a large plume could cause the loss of communication links, and has been investigated by Golden, Taylor and Vicente.[60]

On the basis of data obtained during TITAN IIIC flights and 40:1 scale model measurements in an anechoic chamber, these researchers have established that an exhaust gas plume can be represented or modelled, at least to a fair degree of accuracy, by a single metallic disc located transversely across the volume that would be occupied by a plume and with the same external dimension. The application of diffraction theory can then be used to predict the effects on incident waves and the subsequent impact on the communication link.

5.7 *Crosspolarisation measurements*

The use of polarisation diversity antennas with communications satellites has produced a greater interest in antenna crosspolarisation performance and in crosspolarisation measurement. With the type of antennas used for this application, Ludwig's third definition of crosspolarisation is appropriate.[61] Measurements are often required down to levels of −60 dB below the copolar level. Such measurements can be very difficult, especially with regard to mechanical alignment, although the measurement problems for linear crosspolarisation are different from those encountered with circular crosspolarisation. Some comments on the practical aspects of crosspolarisation measurement are given below.

Alignment is the main problem with linear crosspolarisation measurements. Fig. 31 illustrates a linear crosspolarisation measurement system where the remote antenna is rotated about its longitudinal axis to be orthogonally polarised to the test antenna. $\hat{E}_1$ and $\hat{E}_2$ represent the aperture electric-field unit vectors of the two antennas. The accuracy to which this rotational positioning must be accomplished is illustrated in Fig. 32 and it can be seen that

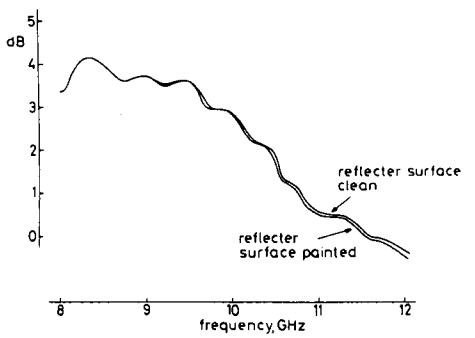

Fig. 29 *Gain difference recording made during a conductive thermal-control paint investigation*

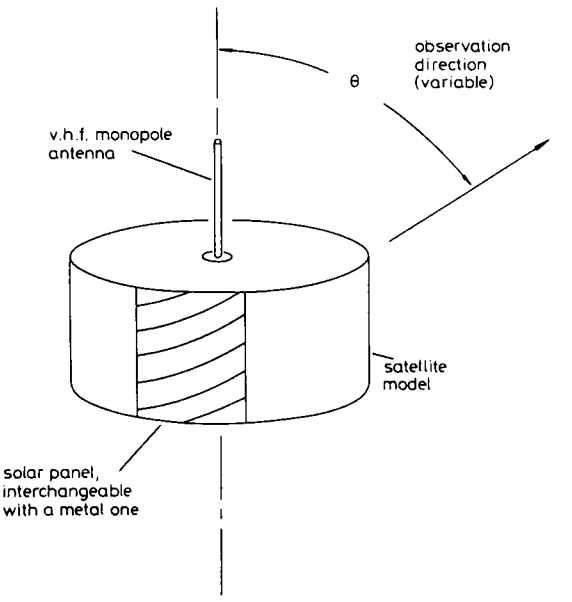

Fig. 30 *Experimental arrangement used to determine radiation losses at v.h.f. associated with body-mounted solar panels*

an alignment accuracy of the order of ± 0·05° is necessary for crosspolar measurements down to − 60 dB. In practice, this accuracy may be obtained by rotating the remote antenna through a step-down gearbox so that very small movements can be made. Also, alignment is generally carried out on a crosspolar null, such as often exists on the boresight of an antenna system.

Linear crosspolarisation can only be measured as shown in Fig. 31 if the remote antenna itself has good crosspolarisation properties, i.e. if the boresight crosspolarisation level is negligibly low. Precisely made (e.g. electroformed) low-flare-angle fundamental mode pyramidal horns are often used for this purpose. If, however, the horn is poorly made, unwanted copolar to crosspolar mode generation may occur within the horn. In such a case, a wire grid across the aperture of the horn can be used to filter out some of the unwanted crosspolar component, although in practice an improvement of only about 6 dB would seem to be achievable without also reducing the copolar level.

Accurate direct circular crosspolarisation measurement is difficult because of the need for accurate polarisers. These should, of course, be capable of producing circular polarisation purity considerably better than the crosspolar level to which measurements are to be made. Typically, then, polarisers with crosspolarisation levels of perhaps − 70 dB are required. Unfortunately, it is very difficult, if not impossible, to achieve this sort of performance over a reasonable bandwidth, and in practice, polariser compensation of some sort may be used such as with the arrangement shown in Fig. 33. Here, unwanted crosspolarisation from the polariser is compensated for in the following way. The slightly elliptically polarised transmitted wave is reduced to two linearly polarised components with their nearly quadrature phase difference, using an orthogonal model transducer (o.m.t.). These components are then modified slightly in amplitude and phase so that when they are recombined, the unwanted circular crosspolarisation component is compensated for. This again is a system that requires the knowledge of a polarisation null for setting up, and when the antennas are mechanically aligned to that null (in practice, usually on boresight) the attenuators and the phase shifter are adjusted to give a zero output on one port of the magic T (the crosspolar port); the other port is then the copolar port. Of course, when the crosspolar port is being monitored, the other must be terminated in a matched load rather than being left open.

Finally, Fig. 34 gives an impression of the difficulty in

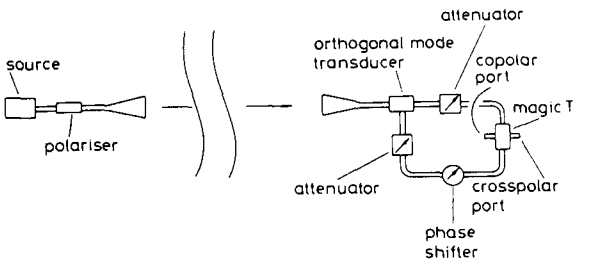

Fig. 33 *One arrangement for accurate circular crosspolarisation measurements using a nonperfect polariser*

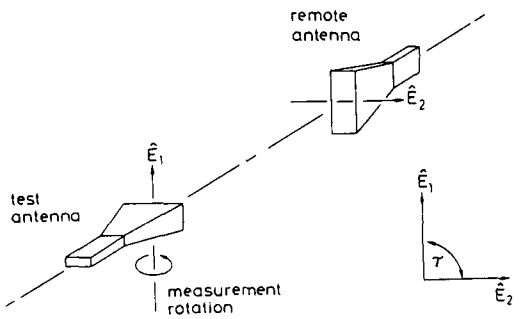

Fig. 31 *Crosspolarisation measurements with linear polarisation*

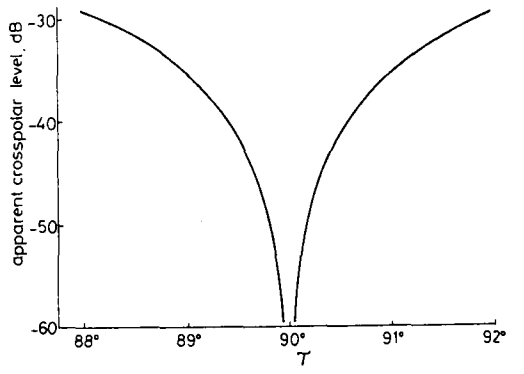

Fig. 32 *Linear crosspolarisation measurements orthogonality graph for two coaxially aligned antennas, each with zero crosspolarisation components on boresight*

τ is the angle between $\hat{E}_1$ and $\hat{E}_2$, as shown in Fig. 31

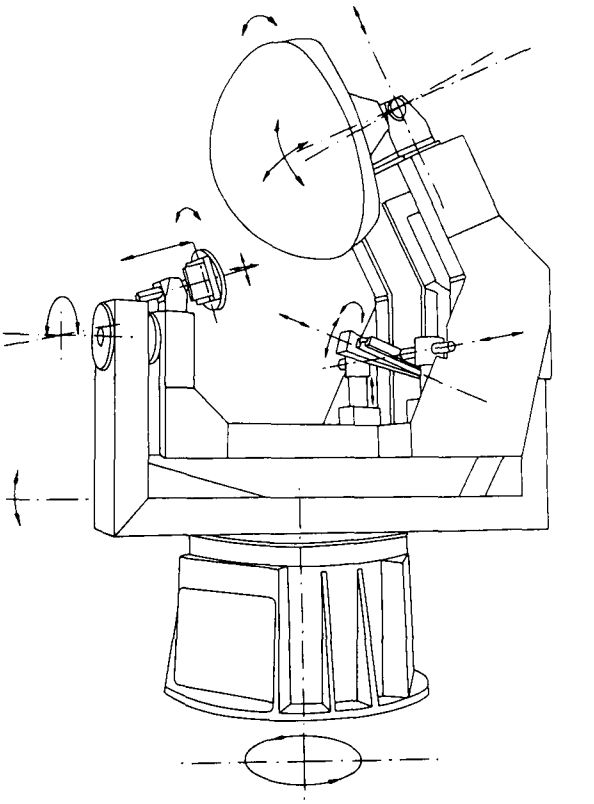

Fig. 34 *Illustration of the available (and necessary) movements required for component alignment on an experimental model of a t.v. broadcast satellite double-offset antenna system*

setting up and in making crosspolarisation (and even copolarisation) measurements on an antenna system with several components, all of which must be correctly and accurately aligned with respect to each other. This diagram shows the available movements on an experimental double offset t.v. satellite antenna that was recently investigated.[62] With the arrangement shown, the inner framework rotated within the out framework, so that different radiation pattern 'cuts' could be made. There were no less than 19 separate movements associated with this rig.

6 Concluding remarks

It is hoped that this review paper has covered all of the measurement techniques and types of test range that have been developed for, or are applicable to, satellite antennas. Some of these techniques, in particular the spherical scanning and cylindrical scanning near-field methods, are still under development and the ultimate accuracy obtainable with n.f.f.f. methods has still to be determined. It is clear, however, that near-field and intermediate-distance techniques will become more widely applied in the future; this must occur if, as seems likely, operating frequencies are raised and antenna diameters become larger. At the same time, it should be remembered that the majority of satellite-antenna measurements are direct measurements made in the conventional way using either elevated mode or ground reflection mode test ranges. In the forseeable future, it is doubtful that indirect methods will take over the role of direct measurements in situations where direct measurements can be conveniently used. Conventional far-field measurements are usually simpler, quicker and give immediate results. It is probably fair to say that they are also more versatile for development work and for final adjustments, for example the fine positioning of a feed for a reflector-antenna system. For this reason, the modern developments of conventional ranges are of considerable interest. Without much doubt, as a general purpose test range *par excellence* for nearly all antenna types, the elevated semi-open anechoic chamber is a particularly fine example as it combines the simplicity and versatility of elevated mode working with the environmental protection of the anechoic chamber.

As this review has been from a European viewpoint, a final appropriate comment concerns the calibration of gain horns. Accurate gain standards are essential for satellite-antenna measurements, but unfortunately, at the time of writing, there is no gain horn calibration service in Europe. At present, horns have to be sent to the National Bureau of Standards in the USA where calibrations are carried out using the 'three antennas' method.[63] The availability of this type of service in Europe is well overdue.

7 Acknowledgments

Although any opinions expressed in this paper are the author's alone, a number of people have helped in the preparation of this review, mainly by supplying diagrams and photographs, but also by giving information and reading and commenting on the draft manuscript. In particular, the author would like to thank M. Sweeting and Q.V. Davis of the University of Surrey, J. Aasted and N.W.T. Neale of the European Space Agency, Noordwijk, Holland, F. Voyner of the British Aerospace Dynamics Group, Stevenage, England, R.W. Hogg of the Royal Aircraft Establishment, Farnborough, England, C. Ancona of STAREC, Massy, France, K. Koob and B. Liesenkotter of Messerschmitt-Bolkow-Blohm GmbH, Ottobrunn, W. Germany, and the author's ex-colleagues at ERA Technology Ltd., Leatherhead, England.

The author would also like to acknowledge assistance from the University of Surrey AVA Unit.

8 References

1 JACKSON, R.B.: 'The canted turnstile as an omnidirectional spacecraft antenna system'. NASA Report X-712-67-441, 1967
2 NICHOLS, S.: 'Satellite turnstile antennas', Naval Research Laboratories (Washington) Report 6907, 1969
3 GREGORWICH, W.S.: 'A tangential turnstile antenna for spacecraft'. Proceedings of the IEEE APS Symposium, 1974, pp. 207–209
4 KEEN, K.M.: 'V.H.F. turnstile antenna performance as a function of antenna geometry on large cylindrical satellites', *Electron. Lett.*, 1977, 13, pp. 654–656
5 ANCONA, C., and DO-BOI, H.: 'The Symphonie satellite VHF circularly polarised antenna with toroidal pattern' *in* 'Antennas for aircraft and spacecraft'. IEE Conf. Publ. 128, 1975, pp. 148–153
6 KILGUS, C.C.: 'Shaped conical radiation pattern performance of the backfire quadrifilar helix' *in* 'Antennas for aircraft and spacecraft'. *ibid.*, 1975, pp. 154–159
7 BRAIN, D.: 'S-band telemetry antenna systems for scientific satellites' *in* 'Antennas for aircraft and spacecraft'. *ibid.*, 1975, pp. 64–67
8 ANCONA, C.: 'A hemispherical coverage conical spiral antenna and its aerospace applications' *in* 'Aerospace antennas', IEE Conf. Publ. 77, 1971, pp. 43–48
9 RUMSEY, V.H.: 'Frequency independent antennas' (Academic Press, 1966), chap. 4
10 ALBERTSEN, N.C., BALLING, P., and LAURSEN, F.: 'New low gain S-band satellite antenna with suppressed back radiation'. Presented at the European Microwave Conference, 1976, pp. 359–363
11 KREUTEL, R.W., DIFONZO, D.F., ENGLISH, W.J., and GRUNER, R.W.: 'Antenna technology for frequency re-use satellite communications' *Proc. IEE*, 1977, 65, (3), pp. 370–378
12 RUDGE, A.W.: 'Offset parabolic reflector antennas'. Course notes for 'Reflector antenna theory and computation', University of Southern California, 1976
13 RUDGE, A.W.: 'Study, design, construction and evaluation of a multiple beam antenna'. ERA RF Technology Centre Report, 1975, under ESTEC contract 2277/74HP
14 RUDGE, A.W., PHILIPPOU, G.Y., and WILLIAMS, N.: 'Low cross polar waveguide horns for multiple-feed reflector antennas' *in* 'Antennas and Propagation', IEE Conf. Publ. 169, 1978, pp. 360–363
15 DORO, G., and SAITTO, A.: 'Dual polarisation antennas for OTS' *in* 'Antennas and spacecraft'. IEE Conf. Publ. 128, 1975, pp. 76–82b
16 AJIOKA, J.S., and HARRY, H.E.: 'Shaped beam antenna for Earth coverage from a stabilised satellite', *IEEE Trans.*, 1970, AP-3, pp. 323–327
17 WOOD, P.J.: 'Shaped beam reflector design for Earth coverage applications' *in* 'Antennas for aircraft and spacecraft'. IEE Conf. Publ. 128, 1975, pp. 47–52
18 HORWATH, L., LIESENKOTTER, B., and TYMANN, G.: 'The antenna system of the HELIOS solar probe'. Proceedings of the international telemetering conference, Los Angeles, Vol. 10, 1974, pp. 40–50
19 HOGG, R.W.: 'Measurement techniques for satellite VHF telemetry antennas'. ESTEC workshop on antenna testing techniques, ESA SP127, 1977, pp. 77–83
20 HOLLIS, J.S., LYON, T.J., and CLAYTON, L., (ed.): 'Microwave antenna measurements' (Scientific Atlanta Inc., 1970)
21 FORD, E.T.: 'The ground reflection mode used on an antenna test site for VHF and UHF measurements' *in* 'Aerospace antennas'. IEE Conf. Publ. 77, 1971, pp. 89–97
22 KOOB., K., and LIESENKOTTER, B.H.C.: 'The semi-open anechoic chamber of the MBB antenna test facility'. ESA workshop on antenna testing techniques, ESA SP127, 1977, pp. 9–13
23 VOYNER, Z.F., and DRAPER, D.: 'Design and evaluation of the rf anechoic chamber at H.S.D.'. *ibid.*, pp. 15–20

24 SROKA, P.J.: 'Monograph saves time on converting antenna gain', *Microwaves*, 1974, 13, pp. 54–55
25 KEEN., K.M.: 'Computer program system for evaluating partial and total antenna directivities from measured data', *Proc. IEE*, 1977, 124, (12), pp. 1117–1120
26 IEEE Standard Definitions of Terms for Antennas', *IEEE Trans.*, 1969, AP-7, pp. 262–269
27 SILVER, S.: 'Microwave antenna theory and design' (McGraw-Hill, 1949), chap. 15
28 MOELLER, A.W.: 'The effect of ground reflections on antenna test range measurements', *Microwave J.*, 1966, 9, pp. 47–54
29 RUDGE, A.W.: 'Antenna radiation measurements at ERA's RF Technology Centre'. ESTEC Workshop on antenna testing techniques, ESA SP127, 1977, pp. 53–56
30 JANSSEN, M.A., BEDNARCZYK, S.M., GULKIS, S., MARLIN, H.A., and SMOOT, G.F.: 'Pattern measurements of a low side-lobe horn antenna', *IEEE Trans.*, 1979, AP-27, pp. 551–555
31 APPEL-HANSEN, J.: 'The radio anechoic chamber of the Technical University of Denmark and its evaluation'. ESTEC Workshop on antenna testing techniques, ESA SP127, 1977, pp. 37–43
32 APPEL-HANSEN, J.: 'Reflectivity level of radio anechoic chambers', *IEEE Trans.*, 1973, AP-21, pp. 490–498
33 RICARDI, L.J.: 'Communication satellite antennas', *Proc. IEE*, 1977, 65, (3), pp. 356–369
34 AASTED, J.: 'Antenna and propagation work in ESA' *in* 'Antennas and propagation'. IEE Conf. Publ. 169, 1978, pp. 230–231
35 COWAN, J.H.: 'A shaped beam antenna for a maritime communications satellite' *in* 'Antennas for aircraft and spacecraft'. IEE Conf. Publ. 128, 1975, pp. 101–106
36 WOOD, P.J., and LOCKETT, N.J.: 'A new type of test range for satellite antenna polar diagram measurements' *in* 'Antennas for aircraft and spacecraft'. IEE Conf. Publ. 128, 1975, pp. 186–191
37 JOHNSON, R.C., ECKER, H.A., and MOORE, R.A.: 'Compact range techniques and measurements', *IEEE Trans.*, 1969, AP-17, pp. 568–576
38 WOONTON, G.A., BORTS, R.B., and CARRUTHERS, J.A.: 'Indoor measurements of microwave antenna radiation patterns by means of a metal lens', *J. Appl. Phys.* 1950, 21, pp. 428–430
39 OLVER, A.D., and TONG, G.: 'Compact antenna range at 35 GHz', *Electron. Lett.*, 1977, 13, pp. 223–224
40 KEEN, K.M.: 'A measurement technique for modelling the effects of feed support struts on large reflector antennas', *IEEE Trans.*, 1980, AP-28, (to be published in July)
41 JOHNSON, R.C., ECKER, H.A., and HOLLIS, J.S.: 'Determination of far-field antenna patterns from near field measurements', *Proc. IEEE*, 1973, 61, pp. 1668–1694
42 HANSEN, J.E.: 'Near field/far field antenna test techniques – general presentation of concepts'. ESTEC workshop on antenna testing techniques, ESA SP127, 1977, pp. 109–114
43 WACKER, P.F., and NEWELL, A.C.: 'Advantages and disadvantages of planar, circular cylindrical, and spherical scanning and description of the NBS antenna scanning facilities'. *ibid.*, pp. 115–121
44 JENSEN, F.: 'The spherical near-field far-field technique and its application to satellite antennas'. *ibid.*, pp. 150–158
45 VOYNER, Z.F.: 'Development of cylindrical near field transformation (CNFT) antenna measurement facility – phase I final report'. British Aerospace Dynamics Group TP7774, 1979
46 LARSEN, F.H.: 'Probe correction of spherical near field measurements of a satellite model'. ESTEC workshop on antenna testing techniques, ESA SP127, 1977, pp. 122–128
47 KEEN, K.M., BENNETT, J.C., and WOOD, P.J.: 'Intermediate distance antenna measurement techniques' *in* 'Antennas and propagation'. IEE Conf. Publ. 169, 1978, pp. 106–110
48 BENNETT, J.C., ANDERSON, A.P., McINNES, P.A., and WHITAKER, A.J.T.: 'Microwave holographic metrology of large reflector antennas', *IEEE Trans.*, 1976, AP-24, pp. 295–303
49 WOOD, P.J.: 'The MAROTS antenna measurement facility'. ESTEC workshop on antenna testing techniques, ESA SP127, 1977, pp. 69–76
50 KEEN, K.M.: 'An interference pattern intermediate distance antenna measurement technique', *IEE J. Microwave Opt. & Acoust.* 1978, 2, (4), pp. 113–116
51 ANDERSON, A.P., BENNETT, J.C., WHITAKER, A.J.T., and GODWIN, M.P.: 'Measurement and optimisation of a large reflector antenna by microwave holography' *in* 'Antennas and propagation'. IEE Conf. Publ. 169, 1978, pp. 128–131
52 WOOD, P.J.: 'The prediction of antenna characteristics from spherical near field measurements – part II, experimental validation', *Marconi Rev.* 1977, pp. 117–155
53 JENSEN, F.: 'SNIFT – computer program for spherical near-field far-field technique'. Appendix E to Ticra Final Report S-45-01 under ESTEC contract 2478/75 AK
54 BRAIN, D.J.: 'In-orbit pattern measurements of the European orbital test satellite' *in* 'Antennas and propagation'. IEE Conf. Publ. 169, 1978, pp. 273–277
55 KEEN, K.M., and MAREIS, H.: 'The radiation characteristics of a metallic launch vehicle fairing with rf windows' *in* 'Antennas for aircraft and spacecraft'. IEE Conf. Publ. 128, 1975, pp. 70–75
56 KEEN, K.M.: 'Gain loss measurements on a carbon fibre composite reflector antenna', *Electron. Lett.*, 1975, 11, pp. 234–235
57 KEEN, K.M.: 'Surface efficiency measurements on a high modulus carbon fibre composite reflector antenna at L- and S-band frequencies', *ibid.*, 1976, 12, pp. 160–161
58 KEEN, K.M., MOLETTE, P., PIEPER, B., HERKERT, C.M., and SCHAEFER, W.: 'Development and testing of a new CFRP reflector design'. Raumfahrtforschung, Band 20, Heft 4, July/August 1976, pp. 173–181
59 KEEN, K.M.: 'The effect of thermal control paint on spacecraft antenna performance', *Electron. Lett.*, 1975, 11, pp. 412–413
60 GOLDEN, K.E., TAYLOR, E.C., and VICENTE, F.A.: 'Diffraction by rocket exhausts', *IEEE Trans.*, 1968, AP-16, pp. 614–616
61 LUDWIG, A.C.: 'The definition of cross polarisation', *ibid.*, 1973, AP-21, pp. 116–119
62 ADATIA, N., KEEN, K.M., WATSON, B.K., CRONE, G., and DANG, N.: 'Study of an antenna system for an experimental TV satellite'. ERA RF Technology Centre Report RFTC 420877, 1979, under ESA contract No. 3285/77/NL/AL(SC)
63 NBS STAFF.: 'More accurate antenna calibration developed', *Telecommun. J.*, 1974, 41, pp. 422–423

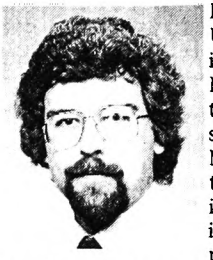

K.M. Keen After gaining a London University B.Sc. with first class honours in 1969, Mr. Keen spent a year at the Nuffield Radio Astronomy Laboratories, Jodrell Bank, from which he subsequently obtained a University of Manchester M.Sc. degree. It was during this time that he first became actively involved with antennas, and this involvement has continued until the present. From 1970, he spent three years in the Antenna Department of the GEC-Marconi Research Laboratories where he was concerned with virtually all aspects of antenna-system research and development. In 1973, he joined the Antennas and Propagation Section of the European Space Research and Technology Centre (ESTEC) in Noordwijk, Holland. At this establishment he had responsibility for the antenna-measurements facility and was involved with spacecraft-antenna development within European industry. He returned to England in 1977 and was a consultant antenna engineer to ERA Technology Ltd. in Leatherhead. In 1979, he joined the University of Surrey in Guildford, as a lecturer in the Department of Electronic & Electrical Engineering. He continues to maintain an interest in antennas via the UOSAT satellite project and various research studies.

Publication P27. **K.M. KEEN and A.K. BROWN,** ***Techniques for the measurement of the cross-polarization radiation patterns of linearly polarized, polarization diversity, satellite ground station antennas.*** **Proceedings IEE, Vol. 129, Part H, No. 3, June 1982, pp 103-108.**

Techniques for the measurement of the cross-polarisation radiation patterns of linearly polarised, polarisation-diversity satellite ground-station antennas

K.M. Keen, B.Sc. (Hons.), M.Sc., C.Eng., M.I.E.E., and A.K. Brown, B.Sc. (Hons.)

Indexing terms: *Antennas, Measurement and measuring*

Abstract: Techniques are presented for the measurement of the cross-polarisation patterns of linearly polarised, frequency re-use ground-station antennas, using a communications satellite as the remote end of the measurement link. Both receive- and transmit-mode cross-polarisation pattern measurements are considered. In both cases, it is shown that an additional antenna with good boresight cross-polarisation characteristics is required for calibration. Correction factors which allow the true cross-polarisation patterns to be computed are derived.

1 Introduction

With the advent of the large communications satellites which employ frequency re-use (polarisation diversity) to increase the available channel capacity, there has become a need for an accurate means of determining the cross-polarisation performance of polarisation-diversity ground-station antennas. The levels of isolation between orthogonal channels of both the ground antenna and the satellite antenna are critical parameters for frequency re-use systems, and antennas in both the space and ground segments are designed to have low cross-polarisation characteristics. As regards antenna-performance testing, however, although there are a number of techniques for measuring the co- and cross-polar patterns of satellite antennas [1], the accurate recording of similar patterns for ground-station antennas is made difficult by the size involved – typically 15 m for an uplink/downlink terminal antenna working at the 11 and 14 GHz frequencies. Conventional direct pattern measurements are precluded by the very long range lengths needed for far-field approximation; even if very long ranges were available, the multipath reflection levels would cause unacceptable measurement errors. The only applicable wholly terrestrial measurement methods would seem to be the intermediate distance techniques [2]. These have been used for co-polar pattern measurements on ground-station antennas, and cross-polar pattern measurements would appear to be feasible also, although more difficult.

Nonterrestrial methods of pattern evaluation have an advantage over terrestrial methods in that far-field distance conditions are met and the ground-station antenna concerned would be evaluated at, or near to, the normal working elevation and therefore under the normal conditions of antenna structure deformation. Non-terrestrial methods consist of either satellite-linked measurements in which a satellite is used as a beacon or as a receiver for conventional direct pattern measurements, or astronomical methods using cosmic sources [3]. As regards the latter, however, the polarisation content of the flux from cosmic radio sources is insufficiently pure for cross-polarisation measurements.

It would seem, then, that direct measurements using a satellite offer the best method of determining ground-station antenna cross-polarisation patterns. There are, however, problems inherent with such measurements, mainly caused by depolarisation and phase dispersion along the satellite/ground station propagation path. These problems are considered here for the case of dual linear-polarisation frequency re-use systems (as will be used for many European satellites) and techniques for cross-polarisation measurements are proposed. A technique for circular-polarisation frequency re-use systems, as are used on US satellites, has been described by DiFonzo [4]. His method utilises a reference antenna which characterises the received wave at the ground. It will be shown that the same approach must be adopted for the linear-polarisation case also. Another published account of circular-polarisation ground-station cross-polarisation measurements using a satellite is due to Kreutel *et al.* [5]. These measurements were, however, made under fortuitous conditions in which the circularly polarised wave transmitted from the satellite was found to have a low cross-polarisation content when received at the ground. Direct measurements were therefore made without the application of any correction factors.

2 Dual-channnel cross-polarisation

Before considering measurement techniques it is necessary to consider what 'cross-polarisation' means in the context of an antenna with two separate and orthogonally polarised feed ports. This has been described in detail elsewhere [11] and will only be briefly reviewed here.

As far as the vector field directions are concerned (as a function of 'look' angle from boresight) it is clear that the well known 'third definition of Ludwig' [6] is applicable and defines the cross-polar field associated with any co-polar field. This definition has been shown to correspond to the quantities that are measured on a normal antenna test range. Wood [7] has shown that, using the above definition, if two orthogonally polarised sources with coincident boresights each launch a co-polarised field, then the two radiated field vectors will be orthogonal at all points in space. This property is, of course, fundamental to the concept of frequency re-use.

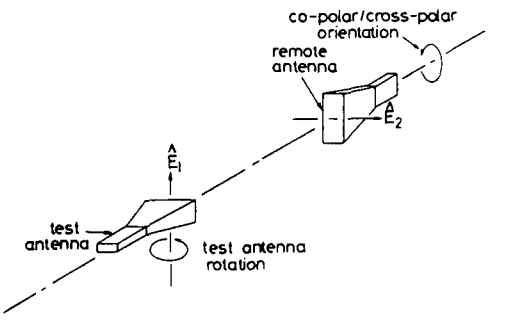

Fig. 1 *Cross-polarisation measurements with linear polarisation and a single-channel test antenna*

Paper 1926H, first received 3rd August 1981 and in revised form 18th February 1982

The authors are with the Department of Electronic & Electrical Engineering, University of Surrey, Guildford, GU2 5XH, England

Fig. 1 illustrates the measurement geometry normally used for cross-polarisation measurements on a one-port linearly polarised antenna such as a pyramidal horn with a rectangular waveguide feed. The co-polar and cross-polar patterns are for the same plane and the same (and only) channel, and are determined by rotating the remotely linearly polarised antenna about its axis. As only one channel exists in the test antenna, we may call measurements of this sort 'single-channel cross-polarisation measurements'.

Although single-channel cross-polarisation measurements may be applied to each channel of an orthogonal two-channel antenna, Ghobrial [8] has shown that, in the ground-station receive mode, this is not appropriate. He maintains that a definition should be adopted for cross-polarisation which predicts the worst possible interference that can occur in a frequency re-use link due to the antenna system. Using Fig. 2, the definition is as follows. With the transmitting satellite antenna polarised along some reference axis, say the x axis, the receiving antenna is adjusted to 'look' at the transmitter, and the feed antenna is oriented to be polarised along the x axis. Co-polar E and H plane radiation patterns can then be taken by rotating the ground antenna in the x-z and y-z planes. The corresponding cross-polar patterns are the same except that the feed antenna on the ground station is re-oriented along the y axis.

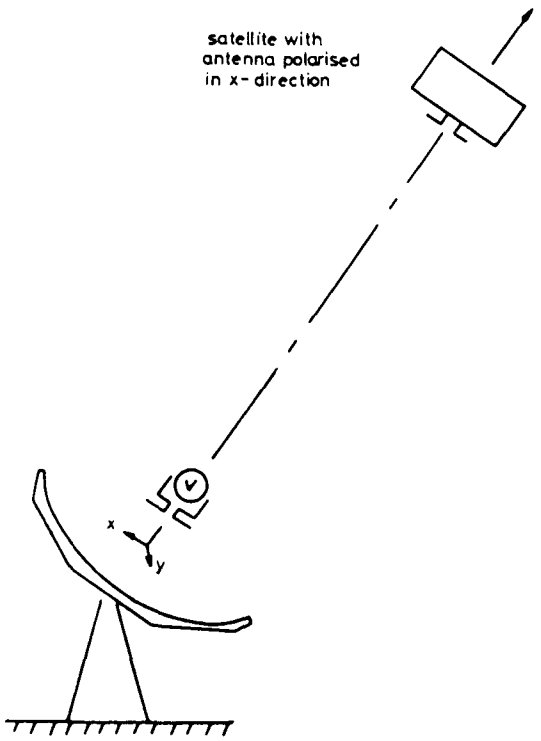

Fig. 2 *On the definition of cross-polarisation with frequency re-use antennas*

Based on the above, 'dual-channel cross-polarisation' can be described in the following way for a ground-station antenna with a coaxially rotatable feed system composed of a dual mode horn and an ortho-mode transducer (OMT). If a purely linearly polarised wave is incident on a dual-polarised ground-station antenna and the antenna feed is aligned with channel 1, co-polar to the wave, then its channel 2 is orthogonal to the wave. If the antenna, OMT etc. are imperfect, as is the case in reality, a cross-polarised component would be received in channnel 2. Thus, in principle, dual-channel cross-polarisation is measured by rotating the antenna for a desired pattern 'cut', with the feed aligned so that one feed port produced a co-polar pattern and the other port gives the corresponding cross-polar pattern.

In the transmit-mode case, the quantity of interest is again the cross-channel interference, and cross-polarisation can be defined as the ratio of the signal levels in the two polarisations when a single ground-station input port is energised. Thus, with a perfect receiving antenna on the satellite and assuming no atmospheric depolarisation etc., a direct measurement of cross-polarisation could be carried out, in theory at least, by recording the signal at one satellite antenna channel, with the other channel being arranged to be in alignment with the co-polar ground-station signal.

3 Receive-mode cross-polarisation measurements

In the ground-station receive mode, it would seem that co- and cross-polarised radiation patterns could be recorded by aligning the antenna feed assembly to a wave from a satellite beacon, and monitoring the two feed ports. In practice, however, the linearly polarised wave from the satellite would not be pure and this would lead to erroneous cross-polar patterns. It is the purpose of this Section to consider the errors and to derive a correction factor which, with some extra ancillary measurements, could be employed to yield the true cross-polar patterns of the ground station.

Suppose that the continuous line plots of Fig. 3 represent a set of real co- and cross-polarised radiation patterns of the ground station. If the satellite beacon wave which is used for the measurements is not perfectly linearly polarised and contains a small cross-polarisation component, then, although this small component would not be significant as regards co-polar pattern measurements and would cause negligible error, the error introduced to the cross-polar pattern measurement would be significant. The effect of the cross-polarised component of the wave would be to give an 'offset' or false relative level to the recorded cross-polar pattern level, of some value as illustrated by the dashed plot of Fig. 3. To derive a correction factor for X in terms of measurable quantities, it is first necessary to consider the nature of the received wave.

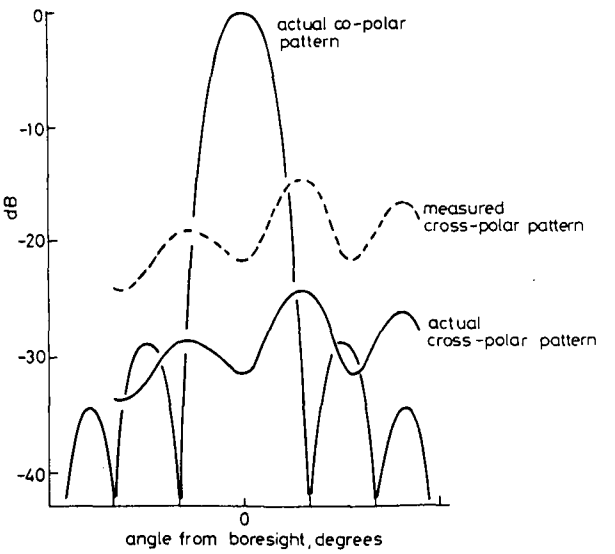

Fig. 3 *Cross-polarisation pattern measurement error caused by imperfectly polarised receive wave*

Assuming that the satellite transmits a single-frequency beacon signal from one channel alone, then the co-polarised component of this beacon signal at the ground would have some orientation about its propagation vector which would

depend on the orientation of the satellite and on the extent of Faraday rotation which occurred along the propagation path. The wave arriving at the ground would consist of co- and cross-polarised components which contained the resolved components generated by the various hardware and propagation-path imperfections. These two components could have any value of relative phase.

As in Fig. 4*a*, we may assign orthogonal x and y axes to the cross-polarised and co-polarised wave components at the ground. However, because there is some phase difference between the field components on these axes, the components would combine to form a polarisation ellipse which would have some value of tilt angle τ relative to the axes. The value of τ would depend on the magnitudes and relative phase of the field components. Thus, at first sight, it would seem that by making a conventional polarisation diagram measurement [9] of the wave with a rotating antenna, it would be possible to establish τ and the ratio $|E_{max}|/|E_{min}|$, giving also then the phase difference δ. These values could then be used for a simple direct correction of measured cross-polarisation patterns.

Unfortunately, in practice it would not be possible to find the tilt angle (and therefore the phase angle δ) as the x and y axes cannot be determined. All that can be done at the ground, as far as orientation is concerned, is to find the major and minor axes of the polarisation ellipse. In fact, this is all that is necessary, as, for measurement purposes, one would not strictly seek the y and x axes, but would use the 'perceived' co- and cross-polar wave components, i.e. the maximum and minimum received components as a function

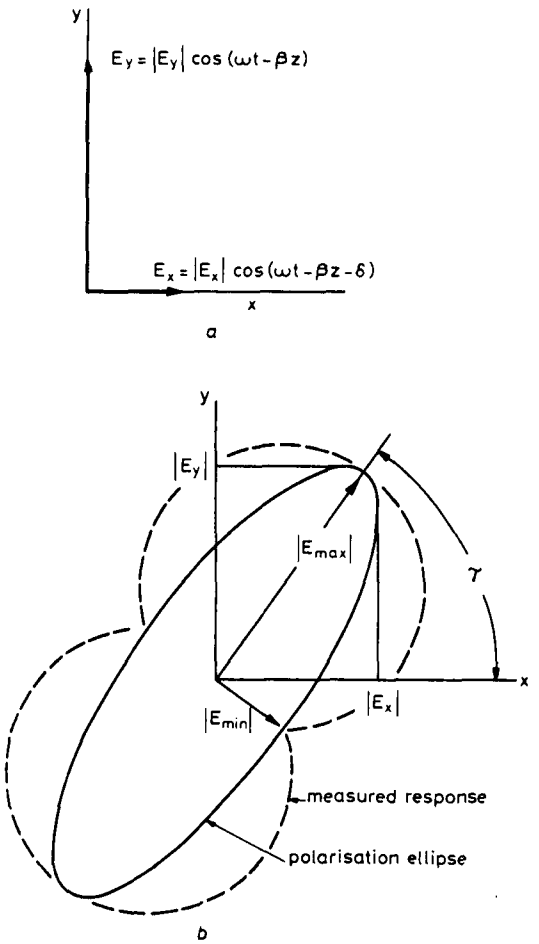

Fig. 4 *Perceived polarisation content of the imperfect beacon wave*

of feed orientation. In other words, if the major and minor axes components of the wave are represented as

$$E_{max} = |E_{max}|e^{j\delta max}$$

and

$$E_{min} = |E_{min}|e^{j\delta min}$$

then these perceived co- and cross-polar components are the ones, with which measurements would be carried out in practice.

An interesting and useful property of these components is that they differ in phase by 90° [10]; in other words

$$|\delta_{max} - \delta_{min}| = \frac{\pi}{2}$$

This implies that it would not be necessary to carry out a separate phase measurement to characterise the wave; a conventional rotating antenna measurement which gave a polarisation plot as in Fig. 4*b* would be sufficient.

Having considered the nature of the imperfect signal with which measurements would be carried out, it is now possible to derive a correction factor for the measured cross-polar pattern.

A ground-station antenna of the type being considered would have two orthogonal receive channels which may be called channels 1 and 2. Co- and cross-polar pattern measurements would be carried out by aligning, say, channel 1 with E_{max} to give the maximum received signal; the E_{min} component would then also be aligned with channel 2. As shown in Fig. 5, antenna-system gain functions may be assigned for each channel and for each polarisation component. Hence g_1^{co} is the system gain function (a complex transfer function) in channel 1 and associated with E_{max} which is aligned with it, and g_1^{cross} is the system gain function in the same channel and associated with E_{min} which is orthogonal to it, and so on. The reason for assigning pairs of gains in this way is, of course, because the antenna response in either channel is not perfectly linearly polarised. It is assumed here that, for radiation-pattern measurements, field strengths or intensity levels would be monitored somewhere in the ground-station RF system, probably at the ends of the waveguide runs from the feed OMT. The gain values shown in Fig. 5, therefore, are attributable to the antenna system down to the monitoring points; the gains are, of course, complex quantities since they must also contain insertion phase terms. This is important as the phase path lengths of channel 1 and channel 2 may be different.

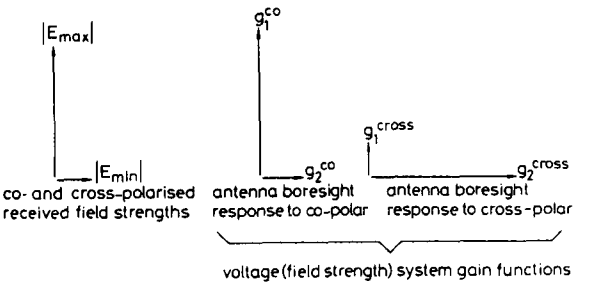

Fig. 5 *Antenna gain functions for the two channels, which can be assigned to the incident co- and cross-polarised components*

In channel 1, the co-polar aligned channel, the total boresight monitored field strength can be written as

$$E_1 = E_{max}g_1^{co} + E_{min}g_1^{cross}$$

but as $|E_{min}|$ would be at least 25 dB below $|E_{max}|$ and

because g_1^{cross} would also be about 25 dB below g_1^{co},

$$E_1 \simeq E_{max} g_1^{co}$$

In channel 2, the cross-polar channel, no such approximation, can be made for the boresight response as it has two components in it of about the same magnitude. If E_2 is the total monitored field strength, then this can be written:

$$E_2 = E_{min} g_2^{cross} + E_{max} g_2^{co}$$

Using the complex exponential notation for convenience, the amplitude and phase values of all terms in the analysis will now be considered.

Let θ represent the relative phase between the received fields E_2 and E_1; then, using E_1 as the phase reference, we can write

$$E_1 = |E_1| e^{j0} = |E_1|$$

$$E_2 = |E_2| e^{j\theta}$$

assuming a phase path-length difference of Δ between channel 2 and channel 1, then, using channel 1 as a reference, we can write

$$g_1^{co} = |g_1^{co}| e^{j0} = |g_1^{co}|$$

$$g_1^{cross} = |g_1^{cross}| e^{j0} = |g_1^{cross}|$$

$$g_2^{co} = |g_2^{co}| e^{j\Delta}$$

$$g_2^{cross} = |g_2^{cross}| e^{j\Delta}$$

Also, if we assume that the OMT channels have similar losses and that the lengths of the waveguide runs from the OMT are not too dissimilar, then

$$|g_2^{cross}| \simeq |g_1^{co}|$$

to a good approximation.

Finally, we know that the incident fields are in phase quadrature, so we may write

$$E_{max} = |E_{max}| e^{j0} = |E_{max}|$$

$$E_{min} = |E_{min}| e^{j(\pm \pi/2)}$$

Leaving out most of the mathematical derivation which has been given elsewhere [11], it can be shown that, using the above, an expression involving $|E_2|$ can be derived as follows:

$$|E_2|^2 = |E_{min}|^2 |g_2^{cross}|^2 + |E_{max}|^2 |g_2^{co}|^2$$

This can be divided by an expression for $|E_1|^2$ derived from an earlier equation to give

$$\frac{|E_2|^2}{|E_1|^2} = \frac{|E_{min}|^2}{|E_{max}|^2} \cdot \frac{|g_2^{cross}|^2}{|g_1^{co}|^2} + \frac{|g_2^{co}|^2}{|g_1^{co}|^2}$$

There are two things to notice in this equation. First, the term on the left-hand side represents the actual (erroneous) recorded cross-polar level. Secondly, the second term on the right-hand side represents the wanted (true) cross-polarisation level, as can be seen from Fig. 5. If, as in Fig. 3, we call this X, we get the simple result that

$$X = \frac{|E_2|^2}{|E_1|^2} - \frac{|E_{min}|^2}{|E_{max}|^2}$$

or, in the decibel notation,

$$X_{dB} = 10 \log_{10} \left[\frac{|E_2|^2}{|E_1|^2} - \frac{|E_{min}|^2}{|E_{max}|^2} \right]$$

By reference to Fig. 6 and the above correction-factor equation, the receive-mode measurement method may now be described. Co- and cross-polar radiation patterns would first be recorded with the ground-station antenna (Fig. 6*a*) by aligning the horn and monitoring the intensity levels at the co- and cross-polar OMT ports as a function of antenna rotation. The recorded cross-polar patterns would be, of course, at an erroneous level at this stage. Wave sampling would then be carried out as in Fig. 6*b* using the high-polarisation-purity linearly polarised ancillary antenna, by axially rotating this antenna and noting the value of $|E_{min}|^2/|E_{max}|^2$ of the polarisation ellipse.

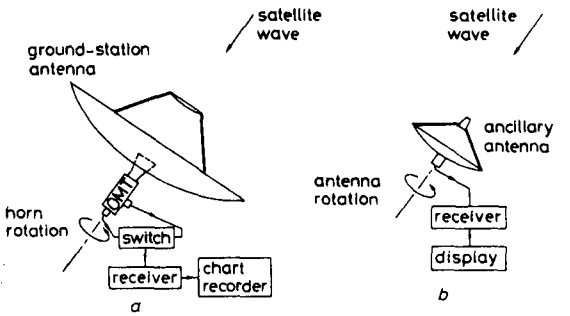

Fig. 6 *Cross-polarisation pattern measurement method in the receive mode*

a ground station antenna measurements
b wave-sampling measurements with an ancillary antenna

4 Transmit-mode cross-polarisation measurements

In this Section, one possible method by which transmit-mode measurements may be made is proposed. Such measurements would be more complicated and difficult to carry out than receive-mode measurements, as an uplink and a downlink plus a second ground station would be involved, as shown in Fig. 7. One point, that is immediately obvious from this diagram, is that only one channel should be used on the downlink during measurements. If, say, channel 1 of the downlink carried the monitored co-polar pattern information, channel 2 the cross-polar information, and both were received in the normal way in orthogonal ground-station channels, there would be many additional errors on the cross-polar information due to the satellite, ground station and downlink path (e.g. channel-insertion gain differences in the satellite, propagation-path depolarisation and the non-ideal ground-station 2 cross-polarisation performance). These errors would be very difficult to correct for. Because of this, a mainly single-channel downlink measurement scheme is proposed here in which only the cross-polar patterns of the ground station under test are determined; the co-polar patterns are not measured, although the boresight co-polar level is found in order to give a reference to the cross-polar levels. It is

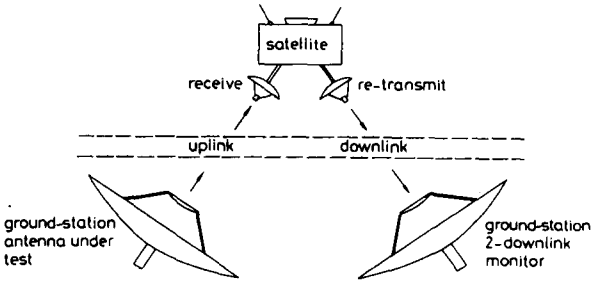

Fig. 7 *Scheme for transit-mode measurements using a second ground station as a downlink receiver*

Co-polar on channel 1, cross-polar on channel 2, both links

also necessary to use an ancillary high-polarisation-purity antenna to transmit to the satellite, to determine the extent of propagation-path depolarisation and satellite-antenna cross-polar degradation, as will be explained below.

Setting aside any polarisation ellipse considerations for the moment, suppose that the ground station under test is transmitting on its channel 1 alone, with the channel 2 input correctly terminated, and with the transmit horn aligned to give a maximum signal on the receive-antenna channel 1 at the satellite. We can then say that, at the satellite, channel 1 monitors the ground-station co-polar pattern, and the orthogonal channel 2 monitors the cross-polar pattern. Consider now the content of the signal received by the satellite from channel 2 of its antenna. This consists not only of ground-station antenna cross-polarisation but also a propagation-path depolarised content (depolarised from the co-polar wave) and a cross-polarisation contribution from the imperfect satellite receive antenna. We may designate the corresponding field quantities as follows:

$$E_{cross} = |E_{cross}| \cos \omega t$$

= ground-station cross-polar component

$$E_{atm} = |E_{atm}| \cos (\omega t + \delta)$$

= atmospheric depolarisation (from channel 1 component)

$$E_{ant} = |E_{ant}| \cos (\omega t + \theta)$$

= component from satellite antenna/OMT

where δ and θ are phase angles referred to the E_{cross} wave. Hence the total received field is

$$E_2 = |E_{cross}| \cos \omega t + \{|E_{atm}| \cos (\omega t + \delta) + |E_{ant}| \cos (\omega t + \theta)\}$$

The term in curly brackets represents unwanted error terms, and in fact we can combine them as one contribution as follows:

$$E_2 = |E_{cross}| \cos \omega t + |E_{err}| \cos (\omega t + \phi)$$

where ϕ is the appropriate phase term.

From the above equation it can be seen that some way of finding the second term on the right-hand side of the equation is needed, so that this factor can be extracted. This can be accomplished as follows.

The ancillary antenna is used to transmit (to a good approximation) a purely linearly polarised wave to the satellite at the appropriate frequency. The ancillary antenna is rotated about its axis, as indicated in Fig. 8, and its received wave at the satellite is monitored via the downlink in channel 2 alone. Now if the propagation path and the satellite receive antenna were both perfect, the polarisation pattern received from the rotated antenna would be a straight line; i.e. the minimum of the pattern would be a zero. In practice, of course, the effects of the atmosphere plus the imperfect antenna give rise to a real minimum, which is in fact a measure of the $|E_{err}|$ term of the last equation.

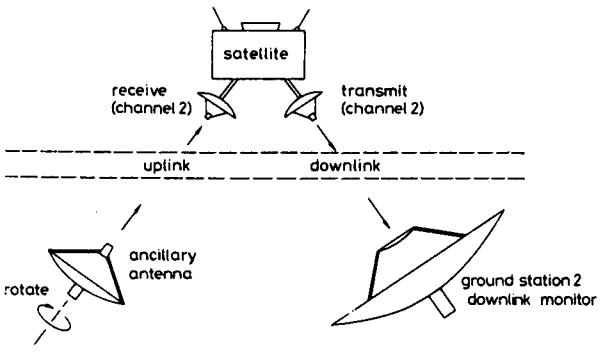

Fig. 8 *Error-term determination using the ancillary linearly polarised antenna*

Looking again at the last equation, this is more usefully expressed in normalised form, referenced to the magnitude of the ground-station boresight co-polar level. If we assume that depolarisation losses are negligible to this component and if we use here dashes to represent normalised field values, then, if $|E^0_{co}|$ is the magnitude of the transmitted boresight co-polar field level, the equation can be rewritten:

$$E'_2 = |E'_{cross}| \cos \omega t + |E'_{err}| \cos (\omega t + \phi)$$

where

$$|E'_{cross}| = \frac{|E_{cross}|}{|E^0_{co}|}$$

and

$$|E'_{err}| = \frac{|E_{err}|}{|E^0_{co}|}$$

It is the normalised value, $|E'_{err}|$, which would actually be found by the measurement illustrated in Fig. 8.

In addition, the phase term ϕ could be measured either by making a direct comparison via a reference channel between the ancillary antenna and ground station 2, if these were in close proximity, or by one of the other methods described in Reference 11. The procedure for measuring ϕ would be to determine the difference in phase that corresponded to changing from the maximum received wave in the satellite channel 2, to the minimum signal in the same channel, as the transmitting ancillary antenna was rotated. It can be seen that this measured value would be the wanted value of ϕ, as the maximum received signal (where the transmit antenna is aligned to give maximum response in channel 2 of the satellite) corresponds to the wave reference phase, and the minimum received signal (which arises from atmospheric depolarisation and the cross-polar response of the satellite antenna + OMT) then gives the error-wave phase as a relative value.

Having established that the amplitude and phase of the error wave are both measurable quantities, the procedure for determining the $|E'_{cross}|$ component, i.e. the wanted ground-station transmitted cross-polar response, can now be described. This procedure would be carried out in four steps as follows:

Step 1

With the ground station under test transmitting on its channel 1 (see Fig. 7), the transmitting ground-station feed is rotated to give the maximum received channel 1 response at ground station 2. When this occurs it can be assumed that the co-polar response of the ground station is correctly aligned to channel 1 at the satellite, and that its orthogonal cross-polar response is therefore aligned with channel 2 at the satellite. After this step is carried out, all further measurements at ground station 2 are carried out on channel 2 alone.

Step 2

Cross-polar radiation patterns of the ground station under test are now measured by rotating this ground-station antenna and monitoring patterns on channel 2 at ground station 2. These mentioned patterns contain, of course, the error-wave content.

Step 3

With the ground-station antenna under test boresighted on

the satellite, the feed is rotated until a maximum value is obtained in channel 2 of the uplink/downlink system. To a good approximation, it can be said that the co-polar boresight ground-station antenna gain with this feed alignment is the same as with the previous alignment, and that the level recorded at ground station 2 in channel 2 can therefore be used as a co-polar level reference.

The feed-rotation co-polar level measurement described above is necessary, as all measurement values must be obtained in the same channel, channel 2, to avoid downlink channel path and system differences.

Step 4

The ancillary antenna measurements are then carried out as described earlier and illustrated in Fig. 8, to determine the amplitude and phase of the error term in the expression for E_2'. The recorded cross-polar patterns (with errors), which would be obtained during step 2 of the above procedure, would actually be recorded in amplitude only, as either field magnitude or intensity levels. The recorded radiation patterns would therefore be in accordance with the following expression, which is a field-intensity expression derived from a previous equation involving E_2':

$$|E_2'|^2 = |E'_{cross}|^2 + |E'_{err}|^2 + 2|E'_{cross}||E'_{err}| \cos \phi$$

This is in normalised form. As $|E_{co}^0|$ is the magnitude of the transmitted boresight co-polar field as measured in step 3 of the procedure described above, the above equation can be rewritten as

$$\frac{|E_2|^2}{|E_{co}^0|^2} = \frac{|E_{cross}|^2}{|E_{co}^0|^2} + \frac{|E_{err}|^2}{|E_{co}^0|^2} + \frac{2|E_{cross}||E_{err}| \cos \phi}{|E_{co}^0|^2}$$

and this equation defines the relationship between the recorded (erroneous) levels – the term on the left-hand side – and the 'true' cross-polarisation pattern levels given by the first term on the right-hand side. The reason for the word 'true' being in quotes will be explained later.

As the equation is a quadratic, the 'true' cross-polarisation pattern terms would have to be determined by numerical root evaluation, probably by using the well known Newton-Raphson method [12]. After finding the 'true' cross-polarisation level numerically, it would then, of course, be expressed in decibel units in the usual way. So the required cross-polar pattern expression would be

$$X_{dB} = 10 \log_{10} \frac{|E_{cross}|^2}{|E_{co}^0|^2}$$

The reason for the word 'true' being in quotes is because the cross-polarisation found as above would not be precisely correct, as one further source of error has been neglected. This arises from the fact that the channel alignments are made by rotating the feed of the ground station under test until maximum signals are received in ground station 2 via the uplink/satellite/downlink path. In other words, channel 2 at the satellite does not receive exactly the E_{err} terms, but actually receives the minimum of the polarisation ellipse at the satellite antenna. This is nearly, but not exactly, equal to the ground-station cross-polar and atmospheric depolarisation terms. Thus there is an error associated with this technique which cannot be compensated for, but which is likely to be small enough to be neglected.

5 Conclusions

For receive-mode cross-polarisation measurements the technique is reasonably straightforward and involves the characterisation of the imperfect satellite beacon wave at the ground, using an ancillary linearly polarised antenna having good polarisation purity. In practice, this would mean a boresight cross-polar level of −50 dB or better. Having characterised the wave, the true receive-mode cross-polarisation patterns can then be determined by applying a correction-factor expression to the erroneous directly measured cross-polarisation pattern.

The high polarisation-purity ancillary antenna would also be necessary for transmit-mode measurements. As has been shown, transmit-mode measurements are quite feasible (subject to limits on dynamic range due to available transmitter powers, receiver sensitivities, noise levels etc) but they are somewhat involved and require the use of satellite up and down links and a second ground station. Also, whereas most of the errors incurred during the measurement can be compensated for, there is one source of error which cannot be corrected, although this is likely to have a small effect on overall accuracy.

Finally, an important point which emerges from considering both receive-mode and transmit-mode cross-polarisation patterns in linear polarisation is that, unlike the circular-polarisation case, the plane in which pattern measurements are made (i.e. the 'cuts') are dependent on the satellite orientation with respect to the line-of-sight between the ground station and the satellite. This means that measurements can only be made for chosen planes of the ground-station antenna if the satellite can be rotated around the line-of-sight by telecommand.

6 Acknowledgments

The authors would like to thank Mr N.W.T. Neale of the European Space Agency for his interest and support.

7 References

1 KEEN, K.M.: 'Satellite antenna measurement techniques', *IEE Proc. A*, 1980, **127**, (7) pp. 417–434
2 KEEN, K.M., BENNETT, J.C., and WOOD, P.J.: 'Intermediate distance antenna measurement techniques' *in* 'Antennas and propagation'. IEE Conf. Publ. 169, Nov. 1978, pp. 106–110
3 BAARS, J.W.M.: 'The measurement of large antennas with cosmic radio sources', *IEEE Trans.*, 1973, **AP-21**, pp. 461–474
4 DiFONZO, D.F.: 'The measurement of Earth station depolarisation using satellite signal sources'. COSMAT Laboratories Tech. Memo. CL-42-75, 1975
5 KREUTEL, R.W., DiFONZO, D.F., ENGLISH, W.J., and GRUNER, R.W.: 'Antenna technology for frequency re-use satellite communications', *Proc. IEEE*, 1977, **65**, pp. 370–378
6 LUDWIG, A.G.: 'The definition of cross-polarisation'. *IEEE Trans.*, 1973, **AP-21**, pp. 116–119
7 WOOD, P.J.: 'Reflector antenna analysis and design' (Peter Perigrinus Ltd., 1980)
8 GHOBRIAL, S.I.: 'Cross-polarisation in satellite and Earth station antennas', *Proc. IEEE*, 1977, **65**, pp. 378–387
9 JASIK, H.: 'Antenna engineering handbook' (McGraw-Hill, 1961) Section 34–6
10 HOLLIS, J.S. *et al.*: 'Microwave antenna measurements' (Scientific Atlanta Inc. 1970) Chap. 3
11 KEEN, K.M., and BROWN, A.K.: 'Techniques for the measurement of the cross-polarised radiation patterns of a dual channel (frequency re-use) ground station antenna'. Document KMK/R5-81, European Space Agency, June 1981
12 WILKES, M.V.: 'Numerical analysis' (Cambridge University Press, 1966)

Publication P28. K.M. KEEN, R.R. GRIME, and B.E. STEMP, *Improvements to a surface wave antenna measurement range with troublesome site effects.* Electronics Letters, Vol. 18, No. 11, May 27 1982, pp 439-440.

TM gain spectra with increasing current. The maximum gain difference at λ_{TM} is 2·2 ± 0·3 dB.

The gain difference between resonant and antiresonant conditions has been evaluated to 1·7 dB and 3 dB for TE and TM polarisations, respectively.

Gain against input power: Fig. 3 shows the gain variation as a function of incident power at amplified input for different values of the injection current. The saturation power is estimated to be 5 to 7 dBm at the operating wavelength. At a 20 dB gain for TE polarisation, the gain will not change by more than 1·5 dB for a current variation of 20 mA (Fig. 2).

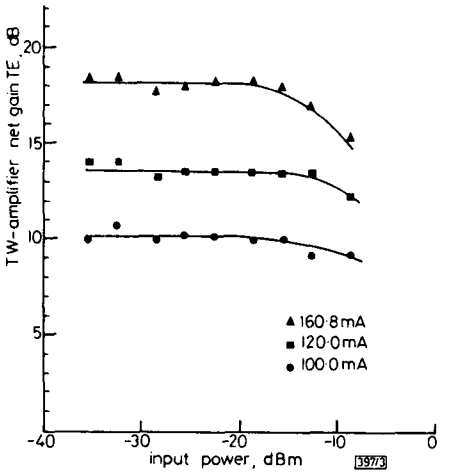

Fig. 3 *TW semiconductor laser amplifiers gain against input power characteristics*

Saturation output level is about 5 dBm

Conclusion: The polarisation sensitivity of a TW-type semiconductor laser amplifier has been reported. The ratio of TM to TE gain coefficients was estimated to be 0·85. A gain difference of about 2 dB has been measured for a TE of 19 dB. For gain values higher than 15 dB, the amplifier was slightly resonant. By using waveguide structures with a better confinement factor and a combination of misaligned stripes and very low reflectivity coatings, a lower gain difference between TE and TM polarisations could be achieved.

Acknowledgments: The author is grateful to F. Favre and M. Monerie for fruitful discussions and to I. Ceres and D. Leclercq of the Laboratoire de l'Horloge Atomique, Orsay, France, for providing the laser amplifier.

J. C. SIMON

CNET LAB/MER/FOG
BP 40, 22301 Lannion, France

13th April 1982

References

1 SIMON, J. C., JOINDOT, I., HUI BON HOA, D., and CHARIL, J.: 'On line GaAs (GaAl)As laser diode amplifier for single mode fiber communication systems'. IOOC '81, San Francisco, April 27–29, 1981, Paper MH2

2 FAVRE, F., JEUNHOMME, L., JOINDOT, I., MONERIE, M., and SIMON, J. C.: 'Progress towards heterodyne-type single-mode fiber communication systems', *IEEE J. Quantum Electron.*, 1981, **QE-17**, pp. 897–906

3 YAMAMOTO, Y., and KIMURA, T.: 'Coherent optical fiber transmission systems', *ibid.*, 1981, **QE-17**, pp. 919–934

4 YAMAMOTO, Y.: 'Noise and error rate performance of semiconductor laser amplifiers in PCM-IM optical transmission systems', *ibid.*, 1980, **QE-16**, pp. 1073–1081

5 KOBAYASHI, S., and KIMURA, R.: 'Injection locking in AlGaAs semiconductor laser', *ibid.*, 1981, **QE-17**, pp. 681–689

6 SMITH, D. W., and MALYON, D. J.: 'Experimental 1·51 μm monomode fibre link containing an injection locked repeater', *Electron. Lett.*, 1982, **18**, pp. 43–44

7 KRESSEL, H., *et al.*: 'Large optical cavity (AlGa)As-Ta As heterojunction laser diode: threshold and efficiency', *J. Appl. Phys.*, 1972, **43**, pp. 561–567

0013-5194/82/110438-02$1.50/0

IMPROVEMENTS TO A SURFACE-WAVE ANTENNA MEASUREMENT RANGE WITH TROUBLESOME SITE EFFECTS

Indexing terms: Antennas, Modelling

A surface-wave antenna measurement range used for ship antenna modelling work has been improved by the development of a novel source antenna. The antenna, a large 'half-truncated' corner reflector, has reduced unwanted range reflections to allow phase measurements to be made to an accuracy of approximately ± 2°. Also, the screening effect of the reflector allows an adjacent range on the same reflecting ground plane to be operated simultaneously without noticeable effect on the surface-wave range performance.

A recent communication[1] has described a proposed technique for the improvement of outdoor antenna measurement ranges which are limited in accuracy by spurious multipath reflections. Although generally applicable, the technique had been devised for one particular ground reflection range used for sensitive phase and amplitude measurements on RF ship models rigged with scaled HF antennas. This range, which is one of the reflection ranges at the Admiralty Surface Weapons Establishment at Funtington, Sussex, is not a ground reflection range in the usual form,[2] i.e. where the test and remote antenna are raised some distance above a reflecting ground plane such that the direct and reflected rays from the remote antenna form a pattern lobe boresighted on the test antenna; these range configurations are quite common and are used, for example, for VHF satellite antenna evaluation.[3] The ground reflection ranges used for ship antenna modelling work are quite different in that the large reflecting plane (usually made from aluminium sheet) represents the sea and has the appropriate conductivity at the scaled frequencies used. Ship model antenna measurement ranges[4,5] can be divided into two types.

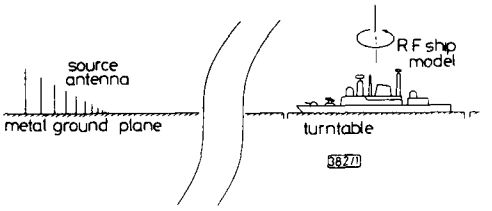

Fig. 1 *Surface-wave range for ship model antenna measurements*

With both of these, the ship model is positioned on an azimuthally rotatable turntable which has its upper surface flush with the reflecting plane. With one type of range, the remote antenna is moveable above and across the model, usually on a GRP boom, so that 'conical cut' radiation patterns can be measured at required elevation angles. With the second type of range, the remote antenna is placed on the reflecting plane as in Fig. 1, and zero elevation angle antenna responses (i.e. surface-wave responses) are measured. It is this type of range for which the improvement technique of Reference 1 was proposed. Fig. 2 illustrates the multipath reflection problem for the particular ASWE range which was designed to operate over a 15 octave frequency bandwidth from VHF to L-band frequencies. This range is particularly sensitive as regards phase measurement where a phase stability of approximately ± 2° is required; at the higher operating frequencies, before the improvements described below were implemented, it was found that even the movement of vegetation by wind caused

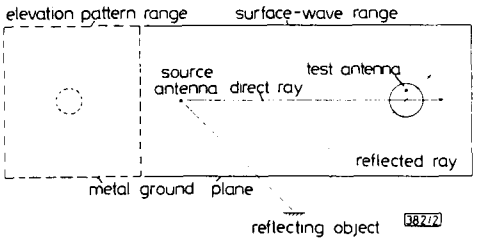

Fig. 2 *Plan of reflection range configuration (not to scale)*

phase measurement errors of greater than ± 2°. The proposed improvement technique involves surrounding the range with a compound elliptical reflecting screen which would direct unwanted multipath rays into absorbers situated at the foci of the compound ellipse.[1] In practice, however, this technique had some potential disadvantages associated with it such as the time and effort needed to construct a complete screen. Also, it was likely that some diffracted rays from the upper edge of the screen would have impinged on the test antenna, and therefore any movements of the screen by wind would have caused a phase jitter to be recorded. For these reasons a different approach was adopted to improve the performance of the range. The technique used and the performance obtained are described below.

The main problem with the type of range shown in Figs. 1 and 2 and the reason for the high levels of multipath reflection lie with the source antenna. To operate in the required way in a surface-wave range environment, the source antenna must be some form of monopole fed against the reflective surface. At the ASWE range, a log-periodic monopole array[6] was used, as this is a wideband device and has some directionality. This is limited, however, and in the azimuth plane the radiation pattern of the antenna is approximately cardioid shaped, thereby causing strong illumination to reflecting objects to the side and even the rear of the measurement range. To overcome this, a novel surface-wave directional source antenna was developed. This is a half-truncated corner reflector, based on a conventional dipole fed corner reflector antenna,[7] but cut in half and fed with a monopole above the reflecting ground plane as shown in Fig. 3. The corner reflector consists of two screens each measuring 3·7 m by 1·9 m. Most of the area of each screen is covered with wire mesh of 4 mm spacing, but the central region of the corner reflector, the most sensitive for the higher frequencies used, consists of two plane aluminium sheets each measuring 1 m by 1 m. A monopole base unit is moveable along the axis of the corner reflector to be 0·5 wavelengths from the reflector apex at the frequency of operation,

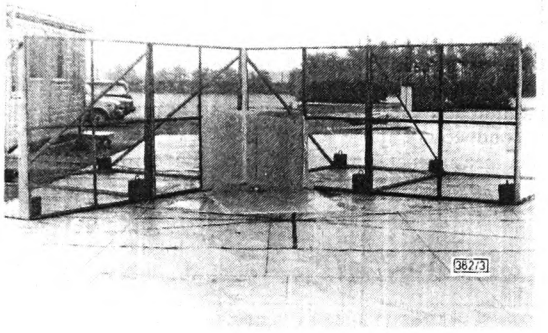

Fig. 3 *Wideband 'half-truncated' corner reflector antenna with moveable monopole feed*

Screen halves are covered with wire mesh

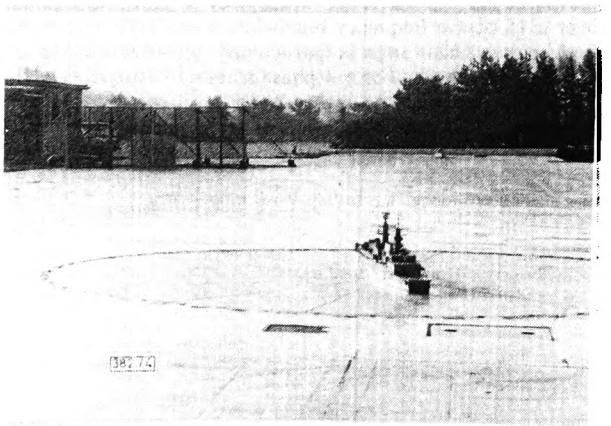

Fig. 4 *Surface-wave range with turntable and ship model in foreground*

and a range of monopole rods of different lengths is available to cover the frequency band. The corner reflector antenna can also be seen in Fig. 4, a photograph of the complete range, taken during a measurement with a ship model which can be seen in the foreground on the 6 m-diameter turntable.

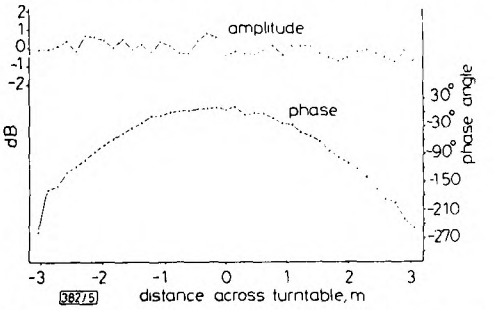

Fig. 5 *Worst-case (highest-frequency) amplitude and phase distribution recorded with a monopole probe moved across turntable*

Fig. 5 shows the measured amplitude and phase distribution across the turntable at the highest operating frequency; this is the worst case and shows the largest wavefront deviations over the 15 octave bandwidth. The distribution was obtained by a relatively crude probing technique whereby a monopole antenna was manually moved across the test aperture between samplings. The data was recorded digitally for computer storage. The phase curvature across the test aperture due to the finite length of the range (37 m) is not of consequence as it can be removed from measured data by computer processing. Operationally, the most important aspect of the range performance is the phase stability. This can be classed into two types, i.e. long-term phase stability or phase drift, and short-term phase stability. The observed long-term component was caused by thermal effects, e.g. solar heating of cables. This was improved from, typically, 360° of phase change in 1 h, to an acceptable value of approximately 5° in 2 h, by shortening all deployed cables as much as possible, and taking care over their physical layout. The short-term phase component, or phase jitter, was caused by multipath reflections from moving objects, e.g. people, and was reduced to better than ± 2° by the measures described above.

As a bonus, the large screens of the corner reflector have been found to give virtually total isolation between the two ranges on the shared ground plane (Fig. 2), and no phase variations are experienced with surface-wave range measurements when the elevation range is operated simultaneously.

Acknowledgment: The authors would like to thank the Director of the Admiralty Surface Weapons Establishment for permission to publish this letter.

K. M. KEEN *7th April 1982*

Keith M. Keen & Associates
'Blackwater', Ifold, Loxwood
Billingshurst, W. Sussex, RH14 0TA, England

R. R. GRIME
B. E. STEMP

Admiralty Surface Weapons Establishment Extension
Hambrook, Chichester, W. Sussex, PO18 8UE, England

References

1 HILL, D. R.: 'New technique to improve antenna measurements in the presence of site reflections', *Electron. Lett.*, 1981, **17**, pp. 257–258
2 HOLLIS, J. S., LYON, T. J., and CLAYTON, L.: 'Microwave antenna measurements' (Scientific Atlanta Inc., 1970)
3 KEEN, K. M.: 'Satellite antenna measurement techniques', *IEE Proc. A*, 1980, **127**, (7), pp. 417–434
4 WOODMAN, K. F., and STEMP, B. E.: 'Shipborne antenna modelling', *Microwave J.*, 1979, pp. 73–81
5 LAW, P. E.: 'Accommodating antenna systems in the ship design process', *Naval Eng. J.*, 1979, pp. 65–75
6 BERRY, D. G., and ORE, F. R.: 'Log-periodic monopole array', IRE Int. Conv. Rec., 1961, Vol. 9, Pt. 1, pp. 76–86
7 JASIK, H.: 'Antenna engineering handbook', 1961, Chap. 11

0013-5194/82/110439-02$1.50/0

Publication P29. **K.M. KEEN,** ***Simple expressions model antenna radiation patterns.***
MICROWAVES & RF, Dec. 1982, pp 65-87.

Simple Expressions Model Antenna Radiation Patterns

Antenna engineers can benefit from these convenient mathematical expressions that describe the main beam regions of radiation patterns.

Keith M. Keen, Consultant Microwave Antenna Engineer, "Blackwater," The Drive, Ifold, Nr. Billingshurst, West Sussex, England RH14 0TA.

DESIGNERS often use tedious and time-consuming methods to determine the radiation pattern of an antenna. Very wide beam-width antennas, such as dipoles positioned in front of reflecting plates or some log-periodic and spiral antennas, can often be calculated by a $(1 + \cos \theta)$ approximation. Slightly more directive patterns, like those associated with log-periodic dipole arrays, can be handled by "fudging" an expression based on the same $(1 + \cos \theta)$ factor plus some higher-order cosine terms.

But even these approximate results become impossible to obtain for more directive antennas. Irregularly shaped patterns, such as those produced by the excitation of higher-order modes, also confound these methods.

Computations minimized

Fourier series offer a better way of describing an antenna's main beam regions. The coefficients of the series can be found from field-strength samples taken from the antenna. Although this method requires the solution of several simultaneous equations, a computer program can handle this chore. The program accompanying this article, for example, can be used for series with as many as 20 terms.

If the pattern is symmetrical about its boresight axis, it can be expressed by the truncated Fourier cosine series shown in Eq. 1 (see "Equations for antenna modeling," p. 87 , which also contains a brief explanation of the mathematical basis of the Fourier method). In Eq. 1, E = the field strength and θ = the measurement angle at which this value occurs. The number of required terms depends on the beam width and complexity of the radiation pattern, and the acceptable degree of approximation.

The Fourier series technique can be used effectively to represent the main beam region of almost any type of radiation pattern shape. Figure 1 shows the E-plane pattern of a microstrip patch antenna. This 100-degree beam-width pattern has been modeled

(continued on next page)

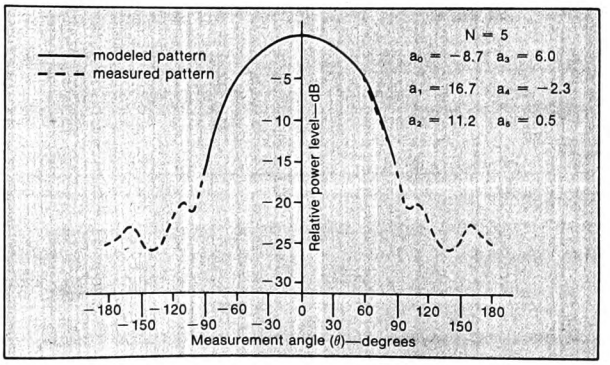

***1. A microstrip patch antenna E-plane pattern** is modeled by a six-term series. The dashed line represents measured data, while the solid line indicates the results of the computer calculation presented in this article. The six Fourier coefficients are also shown.*

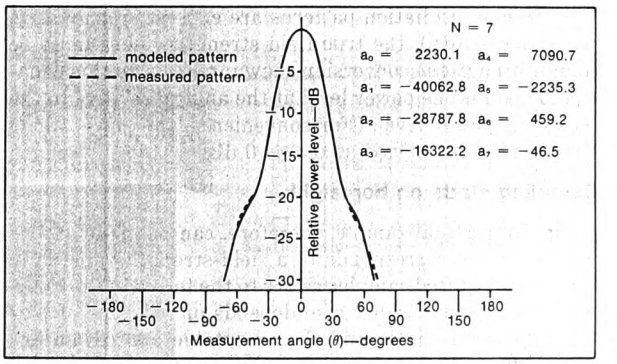

***2. The H-plane pattern for an X-band gain horn** is modeled in the same manner as the microstrip antenna shown in Fig. 1. The narrow beam width necessitates an eight-term Fourier series.*

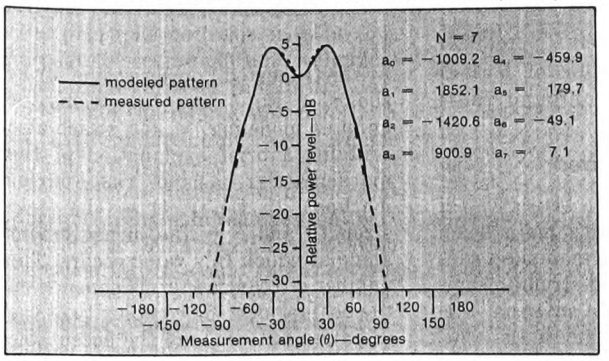

3. Eight terms are also required to model this two-hybrid-mode feed horn *in the E-plane. In each of the three cases shown (Figs. 1, 2, and 3) more of the pattern could have been modeled by using more coefficients.*

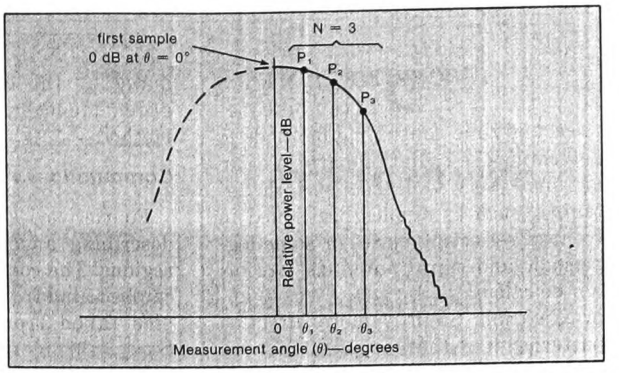

4. A four-term series can be solved by sampling the pattern at three angles *in addition to the boresight axis. Only one side of the symmetrical pattern need be measured.*

by a six-term series. Figure 2 shows a more narrow H-plane pattern produced by an X-band gain horn with a beam width of about 30 degrees. This pattern has been modeled by an eight-term series. Finally, Fig. 3 shows an interesting double-hybrid mode (HE_{11} + HE_{12}) feed-horn pattern, with a dip on the boresight axis. Its E-plane pattern has also been modeled by an eight-term series.

The dashed line in each diagram represents the measured pattern, and the solid line indicates the calculated Fourier series approximation over the main beam region. The Fourier coefficients are also shown in each case.

Although the three examples only model the major portions of the main beams, the entire pattern for each could have been represented by using more coefficients. The portions shown, however, are typically all that are needed.

Although no pencil-beam patterns are illustrated in the figures, if the series includes enough terms, narrow beam patterns of only a few degrees beam width can also be represented through this technique. Unfortunately, the series field representation does not account for phase. Most antennas exhibit flat phase response over the major portion of their main beams. A few do not. Patterns in this latter, generally undesirable group cannot be satisfactorily represented by the series of Eq. 1.

The determination of the Fourier coefficients begins with the sampling of the pattern (Fig. 4). Field strength values are found for a number of angular positions on only one side of the symmetrical pattern.

Since most radiation patterns are expressed in relative power levels (dB), the true field strength values must be found through the conversion shown in Eq. 2. In this equation, $P_{dB}(\theta)$ is the power level at the angle θ relative to the boresight power level. (For convenience, the power along the boresight is always taken as 0 dB.)

Sampling starts on boresight

The first actual sample, therefore, can be made at θ = 0 degrees and corresponds to a field-strength value of 1. Since the required samples relate to the terms in the Fourier series, their number also depends on the type of pattern, its beam width, and the acceptable approximation. The actual number of samples needed to precisely represent the pattern can be calculated by Shannon's sampling theorem,[2] but such an exact representation is seldom required. It is much simpler to use a rule of thumb. For example, four or five samples (in addition to the 0-degree

(concluded on p. 87)

Program listing

```
0: dsp "Fourier
 coeffs prog"
1: dim E[20];
 dim T[20]
2: dim B[21,21]
3: dim A[30];
 dim D[30]
4: 1→M
5: ent N
6: "one":ent
 E[M];ent T[M]
7: 1+M→M
8: if M<N+1;gto
 "one"
9: gsb "sub1"
10: jmp 16
11: "sub1":1→P;
 2→Q
12: "five":1→B[P
 ,1]
13: 1+P→P
14: if P<N+2;
 gto "five"
15: "six":1→B[1,
 Q]
16: 1+Q→Q
17: if Q<N+2;
 gto "six"
18: 2→P
19: "eight":2→Q
20: "seven":cos(
 (Q-1)*T[P-1])→B
 [P,Q]
21: Q+1→Q
22: if Q<N+2;
 gto "seven"
23: P+1→P
24: if P<N+2;
 gto "eight"
25: ret
26: gsb "sub2"
27: jmp 13
28: "sub2":for
 M=2 to N+1
29: for J=M to
 N+1
30: for I=M to
 N+1
31: B[I,J]-B[M-
 1,J]/B[M-1,M-
 1]*B[I,M-1]→B[I
 ,J]
32: next I
33: next J
34: next M
35: 1→S
36: for I=1 to
 N+1
37: S*B[I,I]→S
38: next I
39: ret
40: S→D[1]
41: for G=1 to
 N+1
42: gsb "sub1"
43: for H=1 to
 N+1
44: E[H]→B[H+1,
 G]
45: next H
46: gsb "sub2"
47: S→D[9+G]
48: next G
49: 1→M
50: "four":D[M+
 9]/D[1]→A[M+9]
51: M+1→M
52: if M<N+2;
 gto "four"
53: 10→Z
54: "nine":prt
 A[Z]
55: Z+1→Z
56: if Z<N+11;
 gto "nine"
57: end
```

(continued from p. 66)

value) can be taken for beam widths between 60 and 90 degrees, five or six for those between 30 and 60 degrees, seven or eight for those not exceeding 30 degrees, and so on.

After the coefficients have been calculated, the field-strength series of Eq. 1 can, of course, be converted back to decibel values by using Eq. 3.

As mentioned earlier, a simple computer program can take the mathematical labor out of this procedure. The program (see p. 66) can be run on virtually any machine, from a small capacity desk-top upwards. Although the program has been written in HPL, the well-known Hewlett-Packard language, it can be converted to BASIC or FORTRAN.

When the program is loaded and set to run, it begins by asking for N, the number of samples made, excluding the $\theta = 0$ degrees sample (the value of which is inherent in the program). These N samples correspond to a Fourier series of (N + 1) terms and, consequently, (N + 1) coefficients.

The program then requests that sets of field strength and position data pairs be entered. It calculates the corresponding coefficient for each of the N data pairs by solving the appropriate determinants by a Gaussian elimination technique.[3,4] ••

References

1. E. Kreyszig, *Advanced Engineering Mathematics*, 2nd ed., John Wiley & Sons, New York (1967).
2. C.E. Shannon, "Communication in the presence of noise," *Proceedings of the IRE*, Vol. 37 (1949).
3. C. Froberg, Introduction to Numerical Analysis, 2nd ed., Addison-Wesley Publishing Co., Reading, MA (1969).
4. B.A.M. Moon, *Computer Programming for Science and Engineering*, Butterworth & Co., London (1968).

Equations for antenna modeling

The field pattern of the antenna can be expressed as a Fourier series:

$$E(\theta) = a_o + a_1 \cos\theta + a_2 \cos 2\theta_{..} \text{ etc.} \quad (1)$$

In Eq. 1, E = the field strength and θ = the angle at which this field strength occurs.

To illustrate the mathematical basis of this method, assume that just four coefficients will give an acceptable approximation of a pattern of interest. In this case, the field pattern can be represented as:

$$E(\theta) = a_o + a_1 \cos\theta + a_2 \cos 2\theta + a_3 \cos 3\theta$$

To determine the four unknown coefficients, four field-strength values (E_1 through E_4) must be obtained at their four corresponding angular positions (θ_1 through θ_4). These values give a system of four simultaneous equations:

$$E_1 = a_o + a_1 \cos\theta_1 + a_2 \cos 2\theta_1 + a_3 \cos 3\theta_1$$
$$E_2 = a_o + a_1 \cos\theta_2 + a_2 \cos 2\theta_2 + a_3 \cos 3\theta_2$$
$$E_3 = a_o + a_1 \cos\theta_3 + a_2 \cos 2\theta_3 + a_3 \cos 3\theta_3$$
$$E_4 = a_o + a_1 \cos\theta_4 + a_2 \cos 2\theta_4 + a_3 \cos 3\theta_4$$

From these equations, the values of the coefficients can be found using determinants and Cramer's rule:[3]

$$a_o = \frac{\Delta_o}{\Delta},\ a_1 = \frac{\Delta_1}{\Delta},\ a_2 = \frac{\Delta_2}{\Delta},\ a_3 = \frac{\Delta_3}{\Delta}$$

The Δ terms in the above expressions are the determinants of the four simultaneous equations:

$$\Delta = \begin{vmatrix} 1 & \cos\theta_1 & \cos 2\theta_1 & \cos 3\theta_1 \\ 1 & \cos\theta_2 & \cos 2\theta_2 & \cos 3\theta_2 \\ 1 & \cos\theta_3 & \cos 2\theta_3 & \cos 3\theta_3 \\ 1 & \cos\theta_4 & \cos 2\theta_4 & \cos 3\theta_4 \end{vmatrix}$$

$$\Delta_o = \begin{vmatrix} E_1 & \cos\theta_1 & \cos 2\theta_1 & \cos 3\theta_1 \\ E_2 & \cos\theta_2 & \cos 2\theta_2 & \cos 3\theta_2 \\ E_3 & \cos\theta_3 & \cos 2\theta_3 & \cos 3\theta_3 \\ E_4 & \cos\theta_4 & \cos 2\theta_4 & \cos 3\theta_4 \end{vmatrix}$$

and so on.

The details of the evaluation of the determinants, since they are executed by the accompanying computer program, will not be given here.

Relating field strength and dB's

The field-strength values for an antenna pattern can be found from the relationship:

$$E(\theta) = 10^{\frac{P_{dB}(\theta)}{20}} \quad (2)$$

in which $P_{dB}(\theta)$ is the relative power level, in dB, at the angle θ. Conversely, field strength can be converted back to decibel values by:

$$P_{dB}(\theta) = 20 \log_{10} E(\theta) \quad (3)$$

••

Publication P30. **K.M. KEEN,** ***Antenna system for a new geostationary applications satellite concept.*** **Microwave Systems News, Vol. 13, No. 2, February 1983, pp 64A-64F. (Re-titled *"Plug-ins" Make Geostationary Satellite Antenna Versatile*).**

"Plug-Ins" Make Geostationary Satellite Antenna Versatile

An antenna system using plug-in modules sharing a common main reflector would make multi-payload geostationary applications satellite capabilities easy to upgrade or scale down.

By **Keith M Keen,** Keith M. Keen & Associates

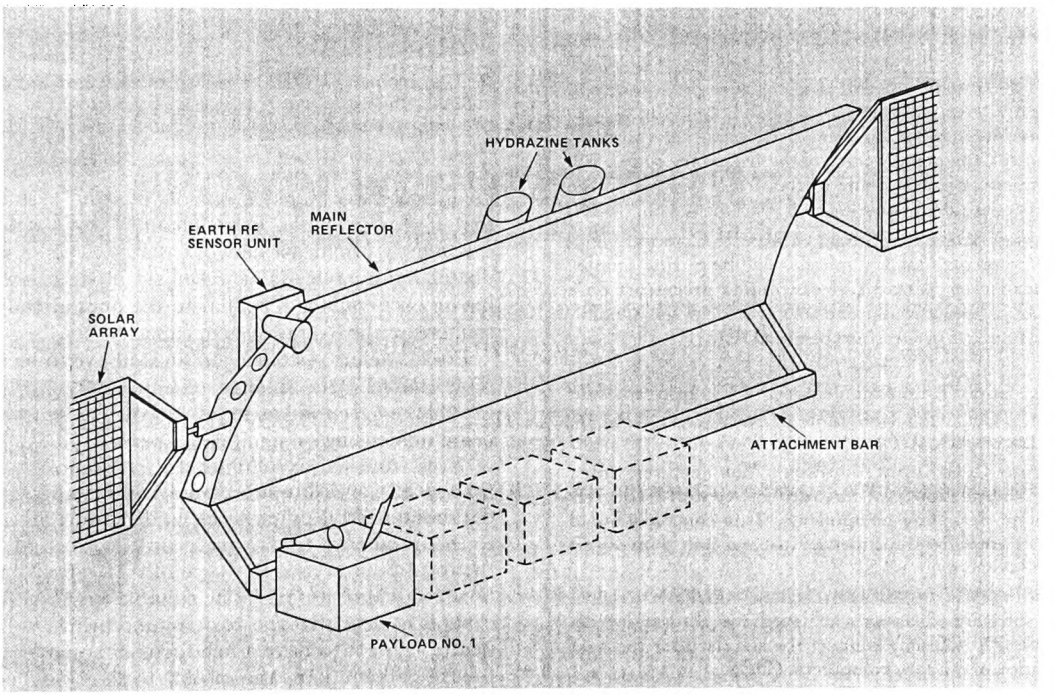

***1. The makeup of the proposed geostationary** applications satellite would consist of a large, shared main reflector and its support structure, plus a pointing mechanism using an RF sensor and hydrazine gas thrusters, and large deployed solar arrays. Applications packages could be attached or removed from the main structure by space shuttle missions.*

Applications satellites such as communications satellites, TV broadcast satellites, and maritime satellites, are made as complete units and launched individually into geostationary orbit by non-recoverable launch vehicles. This is, of course, an expensive process. With the advent of space-shuttle technology, however, it is possible to conceive of a future lower cost alternative in which one large basic structure is placed in geostationary orbit by a space shuttle, and to which applications payload packages can be "plugged-in" or removed as required.[1] Figure 1 shows a system which is proposed here. It consists of a large, shared main reflector and its support structure, plus a pointing mechanism using, for example an RF sensor—or sensors—and hydrazine gas thrusters, and large deployed solar arrays. Applications payload packages, each having its own transponders plus antenna subreflector(s) and feed(s) would be attached to, or removed from, the main structure by space shuttle missions. Typical payload packages would be for TV broadcast to several countries at 12 to 18 GHz, for land mobile communications at L-Band frequencies, for frequency re-use communications at 11 and 14 GHz, and for high capacity videoconference links at 20 and 30 GHz. Clearly, one of the

Keith M. Keen is with Keith M. Keen & Associates, Ifold, Billinghurst, West Sussex RH14 OTA, England; (0403) 72001, Tlx: 858623.

Euroform

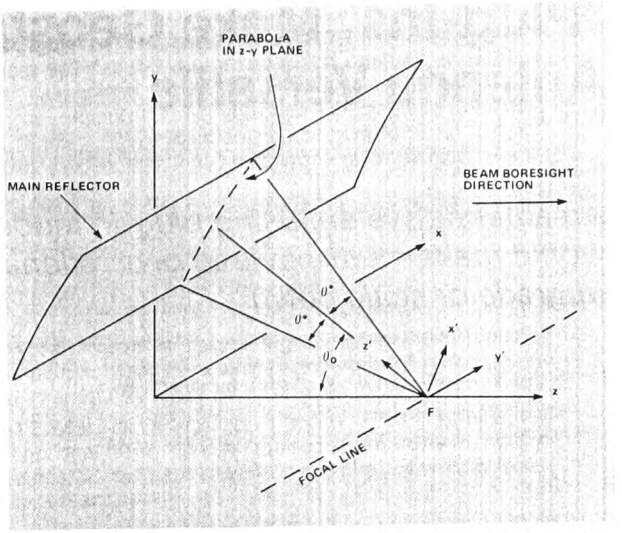

***2. The geometry of the proposed** offset parabolic cylinder main reflector differs in that it does not require that the focal length of the main and subreflectors be the same in each case.*

great advantages for this sort of "plug-in" system would be that if, for example, extra channels were needed for an existing TV broadcast network that was being provided by one or more payloads, it would simply be a matter of adding an extra payload, similar to the ones already deployed, to increase the overall system capacity.

For a satellite system as outlined above to be feasible, the large shared main antenna reflector must in some way be capable of accepting as many "feeds" as necessary, without beam defocusing or significant aperture blockage. The type of large front-fed axisymmetrical paraboloid reflector used for ATS-6[2] for example, would not be applicable since a paraboloid has a point focus, and there is a practical limit to the number of feeds which can be placed at, or near to, the focal point. Also, this type of system has only one feed box and would not really be suitable for the "plug-in" concept. It is clear that the basic requirement for the main reflector is for it to have a line focus or some other extended focus, rather than the point focus of a contentional paraboloid.

The antenna system proposed is an offset parabolic cylinder main reflector with orthogonal offset parabolic cylinder sub-reflectors and suitable feeds for each payload. With this geometry, the main reflector has a line focus of the same length as itself. Also, it is known that two orthogonal parabolic cylinders and a point source feed can be equivalent to a single paraboloid and point source feed, to produce plane wavefronts.[3] This was first demonstrated by Spencer et al.[4] in 1955, who built an antenna consisting of a symmetrical parabolic cylinder, an orthogonal offset parabolic cylinder and a horn feed. More recently, Dragone[5] has demonstrated a derivative of this as a compact satellite antenna. A recent study for the European Space Agency has shown that the double offset parabolic cylinder/corrugated feed Dragone antenna has an improved performance as a frequency re-use Euro-beam and spot-beam antenna for applications such as with the ECS

Continued on page 64F

Continued from page 64B

satellite, compared with existing conventional paraboloid antennas for the same purpose.[6,7]

Figures 2 and 3 show the geometry of the proposed reflector antenna system. This differs from the Spencer et al, and Dragone antennas described in that, with both of these

Applications payload packages, each having its own transponders plus antenna subreflectors and feeds would be attached to the main structure by space shuttle missions.

systems, the focal lengths of the main and sub-reflectors were the same in each case. This is not a fundamental requirement, as can be seen from a geometrical optics appraisal of the behavior of wavefronts in a focused system of two parabolic cylinder reflectors. A point source in the focal line of one parabolic cylinder (whether offset or not) will, after reflection, produce cylindrical wavefronts that appear to emanate from the directrix of the parabola in the plane containing the point source. If the cylindrical (again, whether offset or not) such that the focal line of this reflector coincides with the relevant directrix of the first, the cylindrical wavefronts will then be converted to plane wavefronts.

Figure 2 shows the geometry of the main reflector relative to a cartesian co-ordinate system xyz, where the z direction coincides with the nominal main beam boresight direction. The reflector is defined by its length, the focal

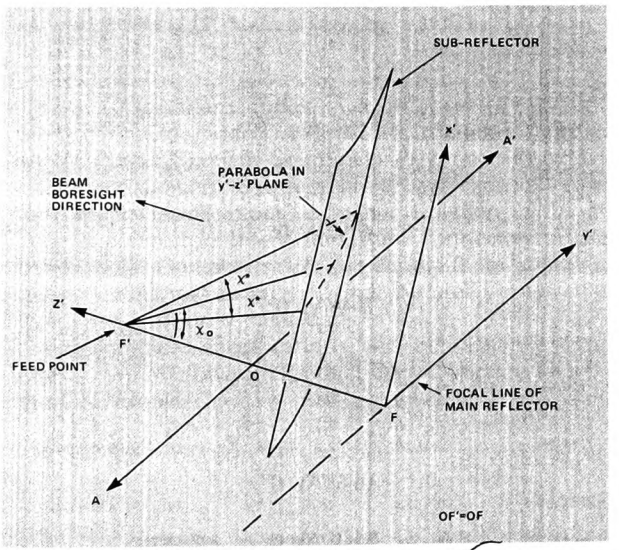

3. The geometry of the proposed offset ~~parabolic~~ cylinder subreflector relative to a second cartesian axes system. The subreflector is defined by the focal length of the parabola in the z'–y' plane and by the offset angles x_o and x* which are also contained in this plane.

length of the parabola in the z–y plane, and by angles θ_o and θ^* in the same way as these angles normally define the boundaries of offset paraboloids, except that they are confined to the z–y plane here. At the point F, the intersection of the focal line of the main reflector and the z axis, a second cartesian axes system x'y'z' is defined so that z' is in the θ' is in the θ_o direction and y' is along the focal line as shown. Figure 3 shows the sub-reflector geometry relative to this co-ordinate system. The sub-reflector geometry relative to this co-ordinate system. The sub-reflector is defined by the focal length of the parabola in the z'–y' plane and by the offset angles x_o and x* which are also contained in this plane. In this diagram, point O and the distance OF' are the origin and the focal length of the parabola. With OF'=OF as shown, the directrix of the parabola coincides with the focal line of the main reflector, as required for collimation. In terms of the profiles for the main reflector and sub-reflectors, if f_m and f_s are the respective focal lengths, then the parabolic arcs are given by

$$y' = 4 f_m z \qquad (1)$$

within

$$\theta_o - \theta^* \text{ to } \theta_o + \theta^*$$

and

$$y'' = 4 f_s (z' - f_s) \qquad (2)$$

within

$$x_o - x^* \text{ to } x_o + x^*$$

To conclude, it should be emphasized that the proposed antenna system is only tentative at this stage. A fully viable system would have to be capable of spot beam, elliptic beam, and multiple spot beam operation, sometimes with polarization diversity. And, although previously published information on the performance of parabolic cylinder antennas suggests that the requirements can be met, these points clearly require further investigation. ■

References

1. *European Space Agency Memorandum* DP PA GB CT 9062, July 29, 1980.
2. L.J. Ricardi, "Communication Satellite Antennas," *Proc. IEEE, Vol. 65, No. 3*, March 1977, pp. 356–369.
3. H. Jasik, *Antenna Engineering Handbook*, McGraw-Hill Book Co., 1961, Section 12.3.
4. R.C. Spencer, F.S. Holt, H.M. Johanson, and J. Sampson, "Double Parabolic Cylinder Pencil-Beam Antenna," *IRE Trans-AP*, January 1955, pp. 4–8.
5. C. Dragone, "An Improved Antenna for Microwave Radio Systems Consisting of Two Cylindrical Reflectors and a Corrugated Horn," *Bell Systems Technical Journal*, Vol. 53, No. 7, September 1974, pp. 1351–1376.
6. Selenia Space Activities Division, "ASTP, Improved Antennas for ECS," *European Space Agency Study Contract 3882/79*, July 1980.
7. G. Doro, and A. Saitto, "Evaluation of the Requirements and Performance of Antenna Systems for the European Telecommunication Satellites," *International Scientific Meeting on Space Satellites and Telecommunications*, March 1979, pp. 522–531.

Publication P31. K.M. KEEN, *New technique for the evaluation of the scattering cross-sections of radar corner reflectors.* IEE Proceedings, Vol. 130, Part H, No. 5, August 1983, pp 322-326.

New technique for the evaluation of the scattering cross-sections of radar corner reflectors

K.M. Keen, M.Sc., C.Eng., M.I.E.E.

Indexing terms: *Radar and Radionavigation, Scattering cross-sections*

Abstract: A numerical technique has been developed for the evaluation of the monostatic radar cross-sections of any regular shape of corner reflector consisting of three orthogonal plates. During a data processing sequence, for any given angle of incidence, the reflector effective area is mapped out by a series of boundary lines which enclose the projections of the real and image apertures of the reflector on an oblique plane, this plane being orthogonal to the incident ray direction and passing through the reflector apex. The area, which can be related to the scattering cross-section, is then computed by an integration process which involves logical decisions regarding the choice of boundary lines. The technique has been applied to a particular reflector geometry consisting of two triangular plates and one square plate, developed for use with the European SAR-580 project.

1 Introduction

Trihedral corner reflectors consisting of three mutually orthogonal metal plates are well known as passive radar beacons and as standards for the experimental determination of radar cross-section values [1]. Fig. 1 shows the

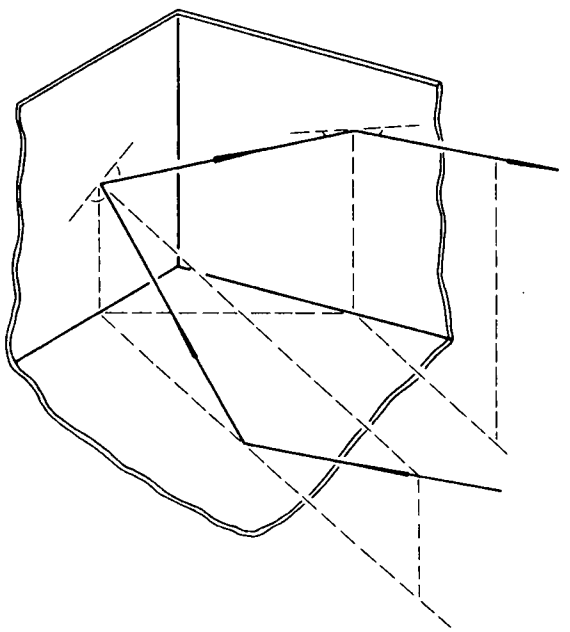

Fig. 1 *Ray optics reflection mechanism in trihedral corner reflector*

mode of operation of such reflectors which, as long as the aperture dimensions are greater than 2 or 3 wavelengths, is almost entirely of a geometrical optics nature. Over a wide angular region about the axis of symmetry through the reflector apex, many of the rays in a plane wavefront incident on the reflector will undergo three reflections and emerge in an exactly reversed direction. Moreover, the path lengths for all triple reflection ray paths are the same. Thus corner reflectors exhibit large radar cross-sections over wide angular regions, the actual value of the cross-section and the extent of the angular coverage being dependent on the shape of the three metal plates.

Analytic expressions for the two best known corner reflector shapes, i.e. symmetrical triangular-sided and square-sided reflectors, have been derived by Spencer [2]. The analysis is somewhat involved, however, and leads in each case to a set of different expressions for the effective area, corresponding to various angular regions of incident wave direction. A more general method of establishing effective area has been described by Robertson [3] who showed that for regular plate shapes, equivalent corner-reflector flat-plate area can be established for any angle of incidence, by the projection of the real and image apertures onto an imaginary plane through the apex of the reflector, this plane being orthogonal to the incident ray direction; the image aperture is the inversion of the real aperture with respect to the apex. The effective area is then the area of overlap between these two projected areas, and corresponds to the region over which triple reflections occur. Outside this common area, the regions relating to just one projected area correspond to zones where only double reflections occur; these rays do not return in the reverse incident ray direction. Using this approach, an effective area for any given incident-wave direction can be determined graphically, i.e. by drawing the projected real and image apertures and measuring the common area. Alternatively, trigonometrical expressions can be found for the area, although this is tedious and must be done for a number of cases, as the shape of the common area undergoes fundamental changes as the incident ray direction is varied.

Although still based on Robertson's projected aperture concept, a new general purpose technique for determining effective areas has been developed and is the subject of this paper. The basis of the technique is that the area mapping is carried out for any specified aperture shape by computer processing which, for every aspect angle under consideration, continues by evaluating the projected effective area by an integration process. The theory for this is given in the following two Sections in the context of the reflector shape shown in Fig. 2. This shows one of the ground marker targets used in the European SAR-580 programme in which an airborne synthetic aperture radar is used for Earth sensing; the reflectors give precise information on position and reflection level. Several sizes of reflector are available, but in each case, the reflector consists of two triangular sides and a square base plate.

Paper 2620H, first received 22nd July 1982 and in revised form 18th January 1983

Mr. Keen is with Keith M. Keen & Associates, Ifold, West Sussex, RH14 0TA, England

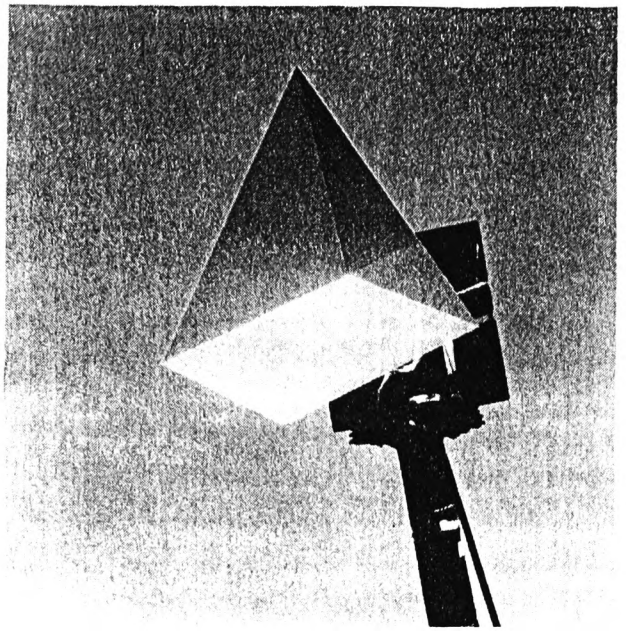

Fig. 2 *SAR-580 corner reflector*

2 Boundary line mapping of the projected area

Fig. 3 shows the reflector geometry contained within a cartesian co-ordinate system which has its origin at the reflector apex and its three axes along the orthogonal intersections of adjacent planes. The 'end-points' or aperture limits of the reflector are therefore the points A, B, C and D, which have co-ordinates $(\tau, 0, 0)$, $(0, \tau, 0)$, $(0, 0, \tau)$ and $(\tau, \tau, 0)$ respectively, where τ is the side dimension (along an intersection line) of the reflector. With this co-ordinate system, the direction of an incident ray is specified by the direction cosines l, m and n. Fig. 4 illustrates the projection of the real aperture limits onto the oblique plane through the reflector apex, this plane being orthogonal to the l, m, n direction. The projections from A, B, C and D, each have the same l, m, n direction cosines, and these meet the plane at A', B', C' and D'. Lines between these points then define the boundaries of the projected real aperture. The projected image aperture is formed in the same way, except that image aperture limits, the images of A, B, C and D with respect to the reflector apex, are projected orthogonally onto the plane from the reverse side, to form points A", B", C" and D". Lines between these points define the boundaries of the projected image aperture.

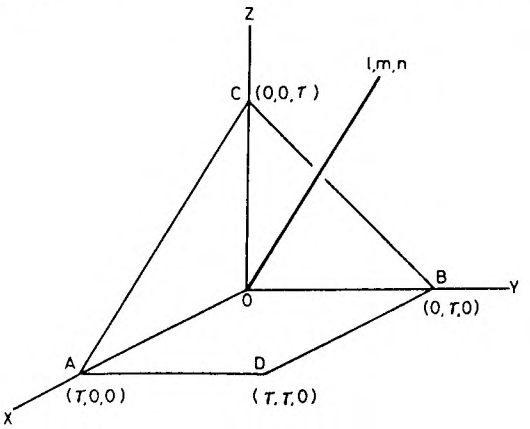

Fig. 3 *Corner reflector geometry and coordinate system*

At this stage it is instructive to look at some of the shapes of the effective areas which occur for different l, m, and n values. Fig. 5 shows four cases, the first being for $l = m = n$ i.e. along an axis of symmetry through the apex. The second and third are both in the vertical plane of symmetry through the reflector, for cases $l = m < n$ and $l = m > n$, i.e. above and below the axis of symmetry, respectively. The fourth is for $l \simeq n < m$. These diagrams illustrate the way in which the shape of the effective area changes.

As a point of interest, the three dimensional 'optical model' described by Crispin and Siegel [1], and which can be easily constructed from cardboard, is an invaluable aid in establishing effective area shapes.

The first stage of the evaluation technique is the calculation of the two dimensional co-ordinates of the projected points on the oblique plane. This is accomplished by a co-ordinate system transformation between the cartesian co-ordinate system of Fig. 3 and a new cartesian co-ordinate system $OX'Y'Z'$ containing the oblique plane and the incident ray direction as in Fig. 4. The second co-ordinate system has the same origin as the first, has its OZ' axis along the l, m, n direction and its OX' and OY' axes in the oblique plane. The OX' axis is defined as the orthogonal projection of the OX axis; this then fully defines the second co-ordinate system in terms of the first. If (x, y, z) represents any points with respect to the $OXYZ$ co-ordinate system, and (x', y', z') represents the same point but expressed in the $OX'Y'Z'$ system, the co-ordinates x' and y' are the wanted co-ordinates on the two dimensional $OX'Y'$ system in the oblique plane. Thus the required co-ordinates of the projected points can be established by a co-ordinate transformation process.

Fig. 6 shows the two co-ordinate systems which are related by pure compound rotation. The transformation from one co-ordinate to the other is given by the matrix equation:

$$\begin{bmatrix} x' \\ y' \\ z' \end{bmatrix} = \begin{bmatrix} \sin\alpha & -\cot\alpha\cos\beta & -\cot\alpha\cos\gamma \\ 0 & \operatorname{cosec}\alpha\cos\gamma & -\operatorname{cosec}\alpha\cos\beta \\ \cos\alpha & \cos\beta & \cos\gamma \end{bmatrix} \begin{bmatrix} x \\ y \\ z \end{bmatrix} \quad (1)$$

where α, β, and γ are the angles between the incident ray and the OX, OY and OZ axes, respectively. In practice only the x' and y' co-ordinate values are needed.

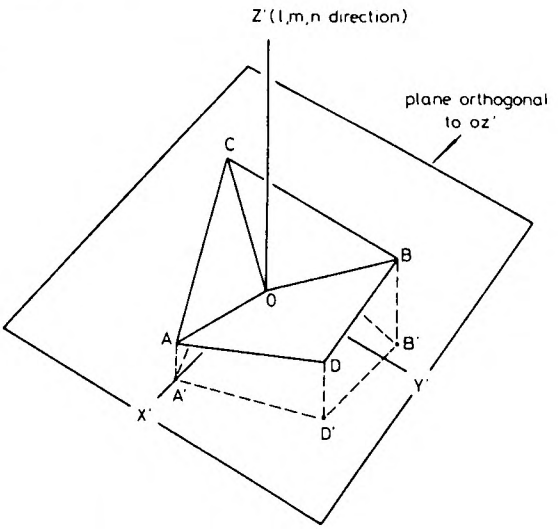

Fig. 4 *Projection of real aperture limits onto the oblique plane*

Using the above equations, the oblique plane coordinates are calculated for the projection of the points A, B, C and D, and for their images. The slope and intercept of each of the area boundary lines passing through pairs of points is then calculated so that the equations of the 8 lines are known. These may be represented by the matrix equation below:

$$y' = \begin{pmatrix} m_1 \\ m_2 \\ m_3 \\ \vdots \\ m_8 \end{pmatrix} x' + \begin{pmatrix} c_1 \\ c_2 \\ c_3 \\ \vdots \\ c_8 \end{pmatrix} \quad (2)$$

In each case, the appropriate slope and intercept values are calculated from equations of the form

$$m_n = \frac{y'_r - y'_k}{x'_r - x'_k} \quad (3)$$

$$c_n = y'_k - \left(\frac{y'_r - y'_k}{x'_r - x'_k}\right) x'_k \quad (4)$$

When this is carried out using a computer program, some care must be taken, of course, for cases where slopes become infinite i.e. when the lines are vertical.

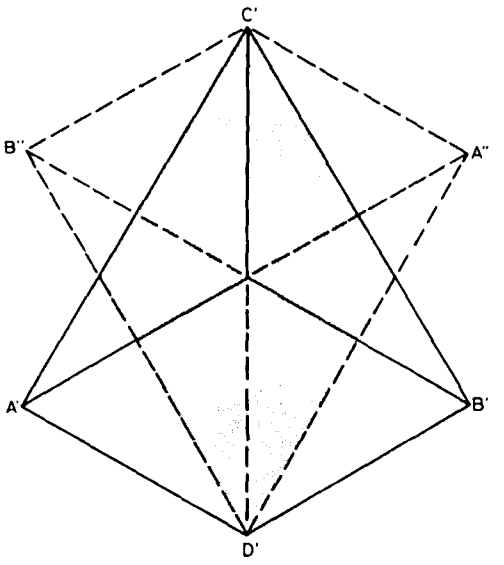

a

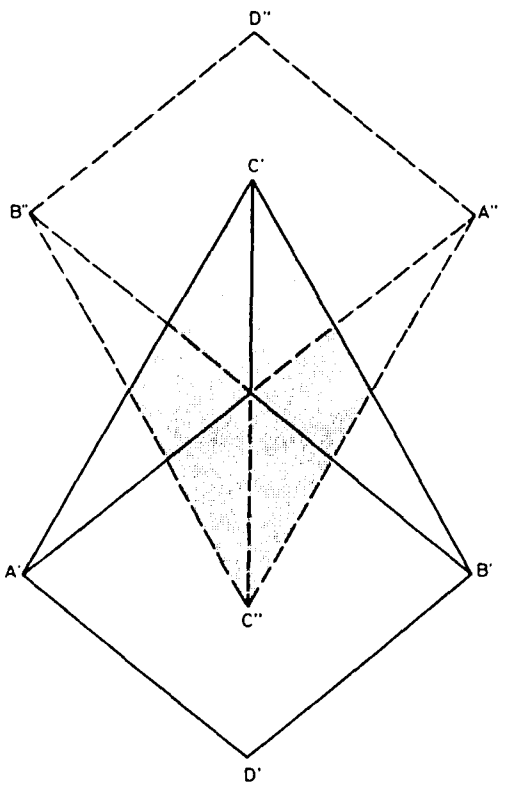

b

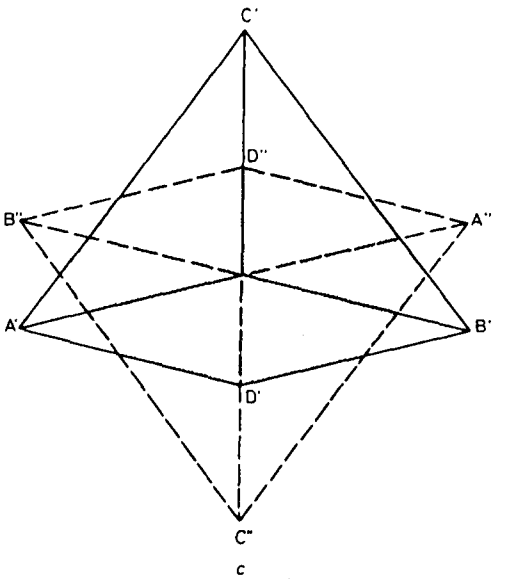

c

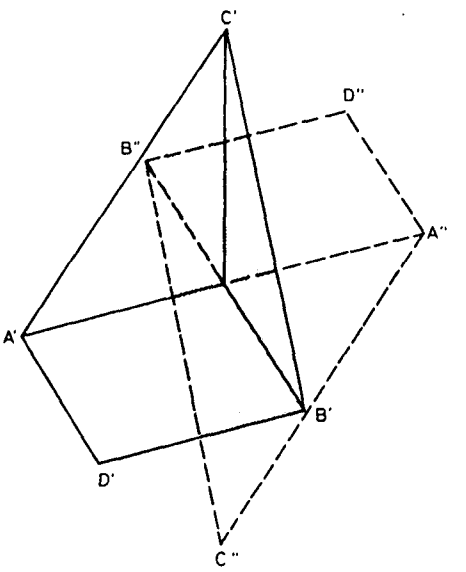

d

Fig. 5 *Effective area of corner reflector*
a $l = m = n$
b $l = m < n$
c $l = m > n$
d $l \neq n < m$

3 Integration over effective area

Fig. 7 illustrates the integration process. As the projected effective area is always symmetrical about the Y' axis, it is only necessary to determine the bounded area in the first and fourth quadrants, which is then doubled. The integration process which gives the effective area for any incident ray direction l, m, n can be described as below:

$$A_{eff}(l, m, n) = 2\left\{\int_0^{\bar{x}'} (y'_U - y'_L)\, dx' + \Delta A\right\} \quad (5)$$

where y'_U and y'_L are upper and lower boundary values, $\bar{x}'$ is the x' value where a boundary line cuts the X' axis, and ΔA is the area beyond $\bar{x}'$ which is nearly always triangular and can be easily determined.

In computational practice, the integration is actually carried out by summing elemental areas i.e.

$$A_{eff}(l, m, n) = 2\left\{\sum_{0 \to \bar{x}'} \delta A + \Delta A\right\} \quad (6)$$

Fig. 8 illustrates the elemental strips of area that are summed, and the area of a strip between two boundary lines is

$$\delta A = \left[\frac{(y'_A - y'_C) + (y'_B - y'_D)}{2}\right] \delta x' \quad (7)$$

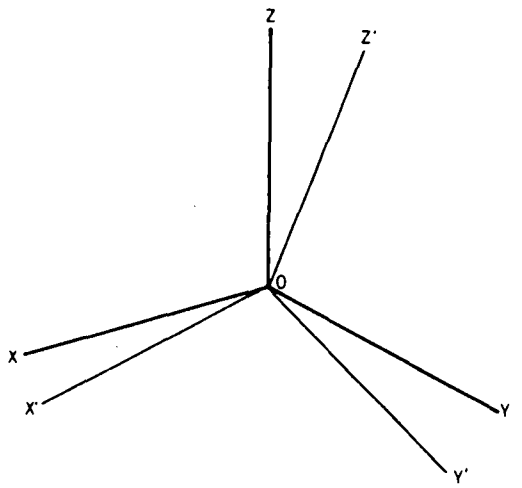

Fig. 6 *Transformation of cartesian coordinate systems by compound rotation about the shared origin*

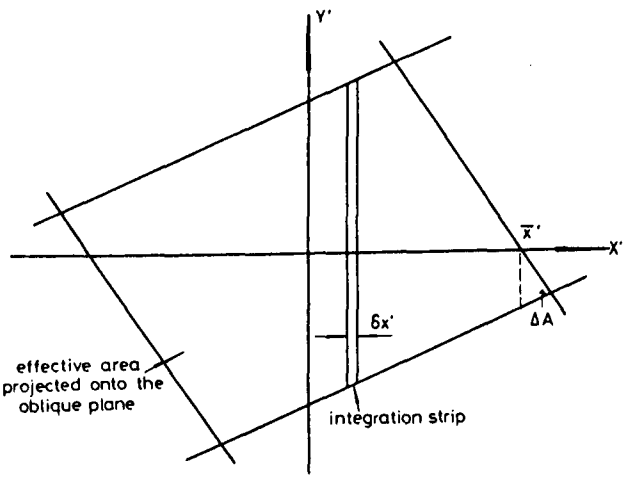

Fig. 7 *Integration process*

This is an exact value. Sometimes, however, the strip covers the intersection of two boundary lines as in Fig. 8*b*, and an error equal to the shaded triangular region occurs. This can only happen two or three times and by making $\delta x'$ small the error can be made negligible. A Romberg type of routine [5] is useful here.

Calculation of ΔA 'excess area' value is reasonably straightforward using a computer program, as each of the boundary lines can be identified by its matrix number. Care must be taken, however, to ensure that all possible excess area shapes can be evaluated.

Once evaluated, the effective area for any incident-ray direction can be related to the equivalent scattering cross-section, σ, using

$$\sigma(l, m, n) = \frac{4\pi}{\lambda^2} [A_{eff}(l, m, n)]^2 \quad (8)$$

where λ is the wavelength.

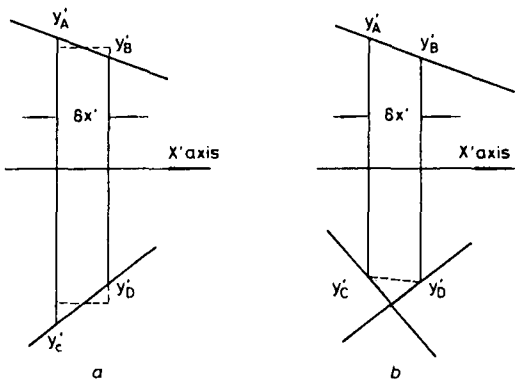

Fig. 8 *Elemental areas summed during the integration process*
a between two boundary lines
b between three boundary lines

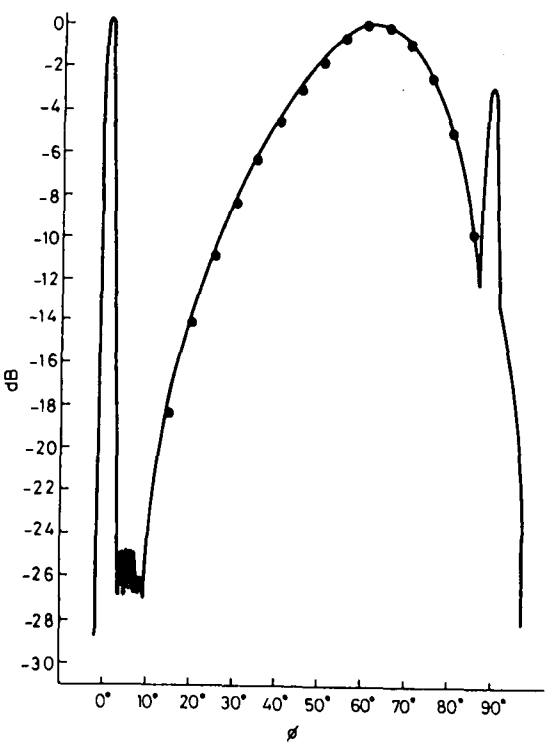

Fig. 9 *Comparison of measured and predicted results*
The continuous line is a $\phi = 45°$ plane pattern of a 90 cm side dimension reflector. Dots are predicted values at 5° intervals

Figs. 9 and 10 show some results obtained with this technique, applied to a reflector with $\tau = 90$ cm and for a frequency of 5.3 GHz. Fig. 9 shows a comparison between predicted and measured results for the $\phi = 45°$ plane. The measurements were made on a 52 m slant geometry range using a CW system with a 100 dB nulling capability. Good agreement can be seen. The maximum value of the scattering cross-section for the SAR-580 reflectors occurs at $\theta = 61.4°$ and $\phi = 45°$. For the 90 cm side size, the maximum values of scattering cross-section and effective area were computed to be 1778.95 m^2 and 0.673 m^2 respectively. Fig. 10 shows a predicted contour plate of the inner region of the reflection level distribution; the pattern ripples shown in this diagram have been observed during measurements.

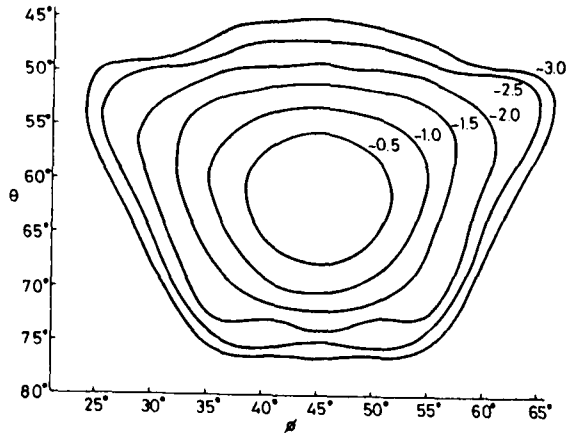

Fig. 10 *Predicted contour plot of reflection levels*
Contours are at 0.5, 1.0, 1.5, 2.0, 2.5 and 3.0 dB below the peak level

4 Acknowledgments

This work was carried out for the European Space Agency under ESTEC Contract No. 4947/81/NL/MS, and the author is grateful to A. Woode of ESTEC, Noordwijk, Holland for encouragement and helpful discussions. The author would also like to thank M.B. Barnes, R.D. Kenwood and D.W. Goode of the Royal Aircraft Establishment, Farnborough, England.

5 References

1 CRISPIN, J.W., and SEIGEL, K.M.: 'Methods of radar cross-section analysis' (Academic Press, 1968).
2 SPENCER, R.C.: 'Optical theory of the corner reflector'. MIT Radiation Laboratory Report No. 433, March 1944
3 ROBERTSON, S.D.: 'Targets for microwave radar navigation', *Bell Syst. Tech. J.*, 1947, **26**, pp. 852–869
4 REKTORYS, K. (Ed.): 'Survey of applicable mathematics', (Iliffe, 1969) Chap. 6
5 FROBERG, C.: 'Introduction to numerical analysis' (Addison-Wesley Publishing Co., 1974)

Publication P32. K.M. KEEN, *Ground station antenna cross-polarization measurements with an imperfectly polarized ancillary antenna.* Electronics Letters, Vol. 18, No. 21, Oct. 14 1982, pp 924-926.

where C is a power conversion constant.

$E_n \angle \psi_n$ at the nth antenna element is a consequence of m incident rays having relative phase shifts with respect to the first antenna element ($n = 0$, $\psi_0 = 0$) such that

$$E_n^c \triangleq E_n \angle \psi_n = \sum_{k=0}^{m-1} A_k Z_k^n \qquad n = 0, 1, 2, \ldots, 2m-1$$

and

$$Z_k = e^{j\alpha_k}$$

where A_k is the amplitude and α_k is the relative phase of the kth incident ray.

The solution for Z_k for $k = 0, 1, 2, \ldots, m-1$ can be obtained by assuming that there exists a polynomial $S(z)$ with z in the form $e^{j\alpha}$;

$$S(z) = z^m + C_{m-1} z^{m-1} \ldots + C_0$$

whose zeros are $Z_0, Z_1, \ldots, Z_{m-1}$, such that

$$S(Z_k) = 0 \qquad k = 0, 1, 2, \ldots, m-1$$

Following the solution of Moody,[1] the coefficients of $S(z)$, i.e. $C_{m-1}, \ldots, C_0$, can be found from the following matrix equation:

$$\begin{bmatrix} E_0^c & E_1^c & \ldots & E_{m-1}^c \\ E_1^c & E_2^c & \ldots & \\ \vdots & & & \\ E_{m-1}^c & & & E_{2m-2}^c \end{bmatrix} \begin{bmatrix} C_0 \\ \vdots \\ C_{m-1} \end{bmatrix} = - \begin{bmatrix} E_m^c \\ \vdots \\ E_{2m-1}^c \end{bmatrix}$$

Hence the roots of $S(z)$ can now be determined. Each unique root of $S(z)$ represents one direction of the incident rays. With this solution, the amplitudes of the incident rays can also be determined by

$$\begin{bmatrix} 1 & 1 & \ldots & 1 \\ Z_0 & Z_1 & \ldots & Z_{m-1} \\ \vdots & & & \\ Z_0^{m-1} & Z_1^{m-1} & \ldots & Z_{m-1}^{m-1} \end{bmatrix} \begin{bmatrix} A_0 \\ \vdots \\ A_{m-1} \end{bmatrix} = \begin{bmatrix} E_0^c \\ \vdots \\ E_{m-1}^c \end{bmatrix}$$

Application of this technique to resolve m incident rays on an antenna array would require less hardware than comparable systems. It could also be incorporated into a digitally controlled, interference cancelling antenna where null forming algorithms could be used to synthesise and optimise a suitable radiation pattern to achieve maximum signal/noise ratio. An added advantage of the deterministic interference cancelling antenna approach of this kind over well known analogue adaptive arrays is that the transient response time is no longer a function of the strength of the incident ray but depends on the speed of the digital control processor used and the efficiency of its control algorithm. Furthermore, the need to generate or provide a reference signal, as in some other adaptive arrays, is avoided. Knowing the direction of the desirable signal in advance, algorithms to counter slow pulsating interference can also be devised without difficulty.

Y. C. CHEAH*
F. J. PAOLONI

Department of Electrical & Computer Engineering
The University of Wollongong
PO Box 1144, Wollongong, NSW 2500, Australia

* On leave from N.Z. Post Office

18th August 1982

References

1 MOODY, M. P.: 'Resolution of coherent sources incident on a circular antenna array', *Proc. IEEE*, 1980, **68**, pp. 276–277
2 HACKETT, C. M.: 'Adaptive arrays can be used to separate communication signals', *IEEE Trans.*, 1981, **AES-17**, pp. 234–247
3 LEAVITT, M. K.: 'A phase adaptation algorithm', *ibid.*, 1976, **AP-24**, pp. 754–756

0013-5194/82/210923-02$1.50/0

GROUND STATION ANTENNA CROSSPOLARISATION MEASUREMENTS WITH AN IMPERFECTLY POLARISED ANCILLARY ANTENNA

Indexing terms: Antennas, Polarisation

A technique has been described for measuring the crosspolarisation radiation patterns of linearly polarised, frequency reuse satellite ground station antennas, using a satellite as the remote source. This involves sampling of the imperfect satellite wave with a high polarisation purity ancillary antenna, and the application of a correction factor to the measured crosspolarisation levels. In practice, the ancillary antenna may have a small but finite crosspolarisation level, and error levels due to this are of interest. Error level expressions are given here, and some typical results are considered.

In a recent publication,[1] ways have been considered by which the crosspolarisation radiation patterns of linearly polarised, polarisation diversity (i.e. dual-channel) ground station antennas can be measured using a communications satellite as a far-field source. In the ground station antenna receive mode, the problem with using a satellite as a remote linearly polarised beacon is that the wave arriving at the ground is not purely linearly polarised. Because of the imperfections of the satellite antenna and depolarisation by the propagation path, the incident wave is elliptically polarised with an axial ratio of the order of 30 dB. The effect is that if ground station antenna pattern measurements are made with one antenna channel aligned to the received wave ellipse major axis to give 'copolar' patterns, and the other orthogonal channel there aligned to the minor axis of the ellipse, then the 'crosspolar' patterns measured with this channel would be at an erroneous level, as shown in Fig. 1, due to the reception of the minor axis compo-

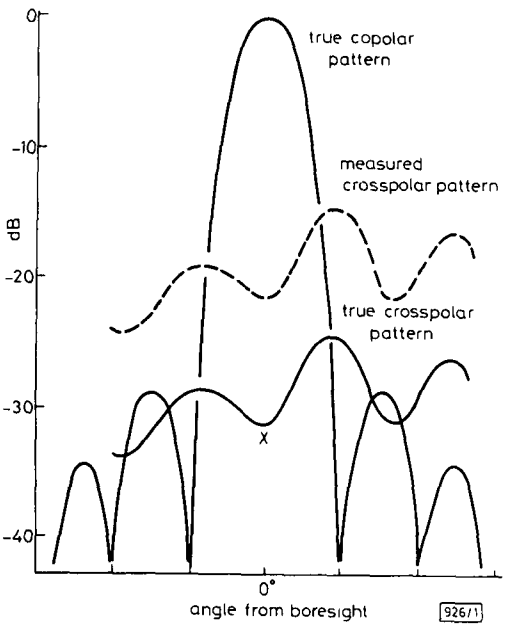

Fig. 1 *Crosspolarisation pattern measurement error caused by imperfectly polarised, received satellite wave*

nent of the polarisation ellipse. However, by using an ancillary linearly polarised antenna to sample the incident wave, as shown in Fig. 2, a correction factor can be used which gives the true crosspolarisation level X for any antenna orientation, in terms of the perceived (erroneous) crosspolarisation level and the axial ratio of the satellite wave polarisation ellipse. In decibel units the correction factor expression is

$$X = 10 \log_{10} \left\{ \frac{|E_2|^2}{|E_1|^2} - \frac{|E_{min}|^2}{|E_{max}|^2} \right\} \qquad (1)$$

where $|E_1|$ is the magnitude of the received field level in the antenna copolar channel, and $|E_2|$ is the equivalent quantity

in the crosspolar channel, and therefore the quantity $|E_2|^2/|E_1|^2$ is the directly measured and erroneous crosspolarisation level. The quantities $|E_{min}|$ and $|E_{max}|$ are the minimum and maximum field strength magnitudes of the polarisation ellipse.

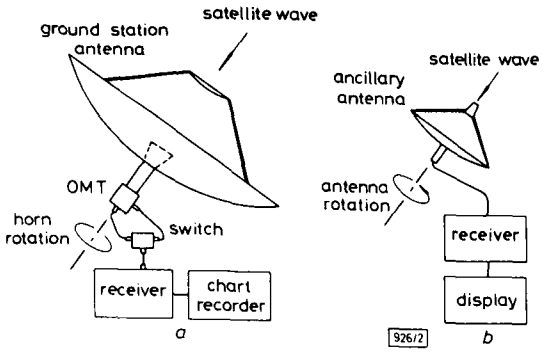

Fig. 2 *Crosspolarisation pattern measurement method*

a Ground station antenna measurements

b Received wave sampling measurements using an ancillary antenna

Eqn. 1 was mathematically derived elsewhere,[1] but an understanding and justification of it follows from a consideration of the contributions that enter the antenna channel being monitored for crosspolarisation (call it channel 2). These are all the ground station antenna crosspolarisation contributions which, in some way, initially derive from the polarisation ellipse field strength maximum (to which the copolar channel—channel 1—is aligned) and the ellipse minimum contribution which is in phase quadrature with the ellipse maximum field. The main crosspolarisation components retain the phase of the copolar components—for example: crosspolarisation components due to imperfect orthogonality of orthogonal-mode transducer and horn components; horn/reflector crosspolarisation due to the horn not being a perfect Huygens source for an axisymmetric reflector;[2] or the horn being not perfectly polarisation matched for an offset paraboloid reflector.[3] This phase similarity is not necessarily true of all contributions, but the net effect is a crosspolarisation phase equal, or at least near to, the copolar phase. Thus, in channel 2, the total crosspolarisation field and the ellipse minimum field will be in or near to phase quadrature, and this is the basis of eqn. 1.

Eqn. 1 is appropriate if the ancillary antenna of Fig. 2 has negligible crosspolarisation on boresight, compared with the wave crosspolarisation levels it has to accurately sampled. For a satellite wave axial ratio of the order of 30 to 40 dB, the ancillary antenna crosspolarisation level should be no greater than perhaps −60 dB. Unfortunately it is difficult to make a large, high-gain ancillary antenna with this level of performance, and, in practice, crosspolarisation levels of only −40 dB to −50 dB could be expected. This finite crosspolarisation would produce errors in the wave sampling as indicated in Fig. 3. This would then give errors in the predicted crosspolarisation level of eqn. 1, although if the ancillary antenna crosspolarisation level was not excessive, the error level could be acceptable. Clearly, it is necessary to establish the level of error that would result from an imperfectly polarised ancillary antenna, and this is described below.

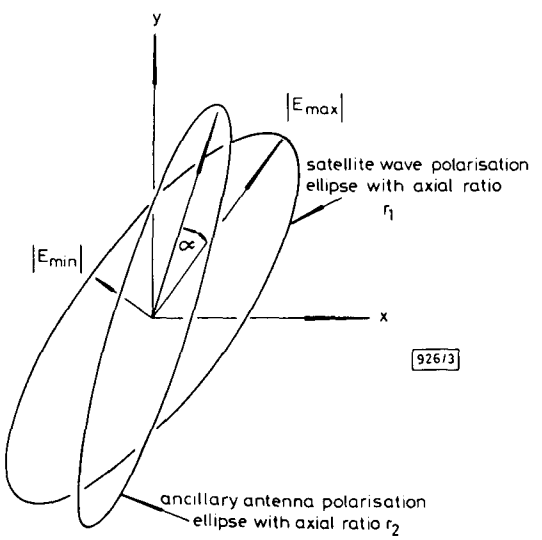

Fig. 3 *Satellite wave polarisation ellipse sampling with a nonperfect ancillary antenna*

r_1 is axial ratio of satellite wave ellipse; r_2 is axial ratio of ancillary antenna ellipse

Fig. 3 shows the situation; the satellite wave, which has an axial ratio r_1, is sampled by an antenna with polarisation ellipse axial ratio r_2. Hatkin[4] has shown that, for an interellipse orientation of α, the field strength E induced in the receiving antenna is given by

$$E^2 = k\left[\frac{1}{2} \pm \frac{2r_1 r_2}{(1+r_1^2)(1+r_2^2)} + \frac{(1-r_1^2)(1-r_2^2)}{2(1+r_1^2)(1+r_2^2)}\cos 2\alpha\right] \quad (2)$$

where k is a constant; the positive sign applies if the ellipses have the same sense (or 'hand') of rotation, and the negative sign applies for opposite senses.

From eqn. 2, the sampled satellite wave field strength term of eqn. 1 becomes:

$$\frac{|E'_{min}|^2}{|E'_{max}|^2} = \frac{\frac{1}{2} \pm \frac{2r_1 r_2}{(1+r_1^2)(1+r_2^2)} - \frac{(1-r_1^2)(1-r_2^2)}{2(1+r_1^2)(1+r_2^2)}}{\frac{1}{2} \pm \frac{2r_1 r_2}{(1+r_1^2)(1+r_2^2)} + \frac{(1-r_1^2)(1-r_2^2)}{2(1+r_1^2)(1+r_2^2)}} \quad (3)$$

where primes are used to indicate that inaccuracies are present.

Hence, from eqns. 1 and 3 we see that, if the ancillary antenna is perfect, the predicted crosspolarisation level is

$$X = 10\log_{10}\left[\frac{|E_2|^2}{|E_1|^2} - \frac{1}{r_1^2}\right] \quad (4)$$

whereas, if the ancillary antenna has a finite axial ratio r_2, the less accurate predicted level is

$$X' = 10\log_{10}\left[\frac{|E_2|^2}{|E_1|^2} - \frac{\frac{1}{2} \pm \frac{2r_1 r_2}{(1+r_1^2)(1+r_2^2)} - \frac{(1-r_1^2)(1-r_2^2)}{2(1+r_1^2)(1+r_2^2)}}{\frac{1}{2} \pm \frac{2r_1 r_2}{(1+r_1^2)(1+r_2^2)} + \frac{(1-r_1^2)(1-r_2^2)}{2(1+r_1^2)(1+r_2^2)}}\right] \quad (5)$$

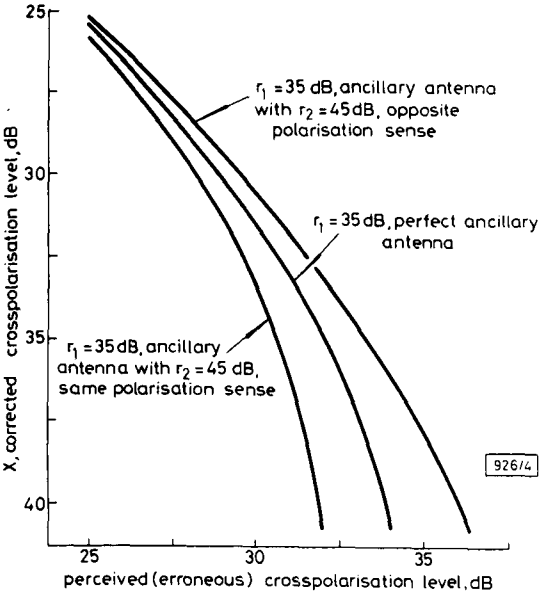

Fig. 4 *True crosspolarisation level as a function of measured level for a satellite wave axial ratio of 35 dB and a perfectly polarised ancillary antenna (centre curve)*

Outer curves show the errors in predicted levels due to a nonperfectly polarised ancillary antenna with a 45 dB axial ratio, for both polarisation senses

where the positive signs apply to same-sense ellipses and negative signs to opposite-sense ellipses.

Fig. 4 shows some results from eqns. 4 and 5 for typical axial ratio values, i.e. $r_1 = 35$ dB and $r_2 = 45$ dB. The graph shows the predicted (corrected) crosspolarisation level as a function of the recorded level. The centre curve is from eqn. 4 and corresponds to a perfect ancillary antenna, whereas the outer curves are from eqn. 5, corresponding to the nonperfect 45 dB axial ratio ancillary antenna cases. The difference between the inner and the outer curves shows the inaccuracies introduced by the imperfect ancillary antenna.

Acknowledgment: The author would like to thank N. W. T. Neale of the European Space Research & Technology Centre (ESTEC) Noordwijk, Holland, for suggesting this addition to earlier work.

K. M. KEEN

Keith M. Keen & Associates
Ilford, W. Sussex RH14 0TA, England

9th September 1982

References

1 KEEN, K. M., and BROWN, A. K.: 'Techniques for the measurement of the cross-polarisation radiation patterns of linearly polarised, polarisation-diversity satellite ground-station antennas', *IEE Proc. H, Microwaves, Opt. & Antennas*, 1982, **129**, (3), pp. 103–108
2 LOVE, A. W.: 'Some highlights in reflector antenna development', *Radio Sci.*, 1976, **11**, pp. 671–684
3 RUDGE, A. W., and ADATIA, N. A.: 'New class of primary feed antennas for use with offset parabolic reflector antennas', *Electron. Lett.*, 1975, **11**, pp. 597–599
4 HATKIN, L.: 'Elliptically polarised waves', *Proc. IRE*, 1950, **38**, p. 1455

0013-5194/82/210924-03$1.50/0

CASCADED BANDPASS *v*TH-LAW DEVICES

Indexing terms: Signal processing, Nonlinear systems

The effect of the *n*-cascaded bandpass *v*th-law devices on the sum of a strong signal and a weak signal is analysed. It is shown that if any of the nonlinear devices is a hard-limiter, the *n*-cascaded nonlinearities have the same effect as that of a single hard-limiter. If two such cascaded *n* *v*th-law devices (differing in at least one *v*th-value) or two complex bandpass nonlinearities are connected in parallel, we obtain the generalised form of a 'power-division' multiplex system which utilises a feed-forward across a limiter technique.

This letter analyses the effect of the *n*-cascaded bandpass *v*th-law devices on the sum of a strong signal and a weak signal (Fig. 1). It is also shown that if any of the nonlinear devices is a hard-limiter, the *n*-cascaded nonlinearities have the same effect as that of a single hard-limiter as shown in Fig. 2. If two such cascaded *n* *v*th-law devices (differing in at least one *v*th value) are added in parallel, we obtain the generalised form of a 'power-division' multiplex system which utilises the feed-forward across a limiter technique.[1] This system has applications in improving the efficiency of frequency-space utilisation through the feasibility of separating two or more cochannel carriers and in improving the stronger-signal capture characteristics of an FM receiver.

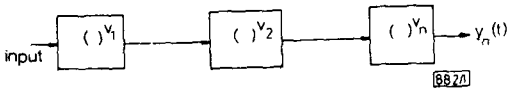

Fig. 1 *Cascaded n vth-law devices*

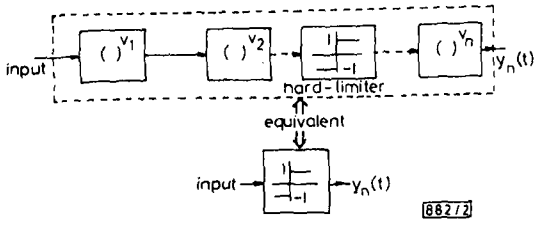

Fig. 2 *Cascaded (n − 1) vth-law devices and one hard-limiter*

Let the input to a nonlinear device be

$$S(t)\cos(\omega_0 t + \theta(t)) + N(t)\cos(\omega_0 t + \varphi(t)) \tag{1}$$

where $S(t)$ and $N(t)$ are the envelope, and $\theta(t)$ and $\varphi(t)$ are the phase of the signal and noise, respectively.

Under the condition that $(N(t)/S(t)) = a \ll 1$, the input in eqn. 1 can be written as

$$\mathrm{Re}\{A(t)\exp(j(\omega_0 t + \alpha(t)))\} \tag{2}$$

where

$$A(t) = N[1 + 2a\cos(\varphi - \theta)]^{1/2}$$

and

$$\alpha(t) \cong \theta + a\sin(\varphi + \theta) \tag{3}$$

In eqn. 3, φ and θ denote $\varphi(t)$ and $\theta(t)$, respectively.

Assuming the nonlinear device has a power-law transfer equation

$$\begin{aligned} y &= x^{v_1} \quad x \geq 0 \\ &= 0 \quad x < 0 \end{aligned} \tag{4}$$

one obtains the output of the nonlinear device as

$$\begin{aligned} y_1(t) &= K_{v_1} N^{v_1}[1 + 2a\cos(\theta - \varphi)](v_{1/2}) \\ &\quad \times \exp j(\varphi + a\sin(\theta - \varphi) + \omega_0 t) \\ &= K_{v_1} N^{v_1}[\cos(\omega_0 t + \varphi) + (a/2)(v_1 + 1) \\ &\quad \times \cos(\omega_0 t + \theta) + (a/2)(v_1 - 1) \\ &\quad \times \cos(\omega_0 t + 2\varphi - \theta)] \end{aligned} \tag{5}$$

where

$$K_{v_1} = \frac{\Gamma(v+1)}{2^v \Gamma((v+3)/2)\Gamma((v+1)/2)}$$

(see Reference 2).

If $y_1(t)$ is fed to a second nonlinear device,

$$\begin{aligned} y &= x^{v_2} \quad x \geq 0 \\ &= 0 \quad x < 0 \end{aligned} \tag{6}$$

then, after rewriting $y_1(t)$ in phasor form, one can obtain the output of the second nonlinear device (similar to eqn. 5) as

$$\begin{aligned} y_2(t) &= (K_{v_1} N^{v_1})^{v_2} K_{v_2}[\cos(\omega_0 t + \varphi) \\ &\quad + (a/2)(v_1 v_2 + 1)\cos(\omega_0 t + \theta) \\ &\quad + (a/2)(v_1 v_2 - 1)\cos(\omega_0 t + 2\varphi - \theta)] \end{aligned} \tag{7}$$

Generalising the above result to *n* *v*th-law devices in cascade, one can obtain

$$\begin{aligned} y_n(t) &= K_0[\cos(\omega_0 t + \varphi) + (a/2)(v_1 v_2 \ldots v_n + 1) \\ &\quad \times \cos(\omega_0 t + \theta) + (a/2)(v_1 v_2 \ldots v_n - 1) \\ &\quad \times \cos(\omega_0 t + 2\varphi - \theta)] \end{aligned} \tag{8}$$

where K_0 depends on v_i, $i = 1, 2, \ldots, n$ and $N(t)$.

From eqn. 8 it is obvious that, if any of the nonlinear devices is a hard-limiter (say $v_2 = 0$), $y_n(t)$ is the same as when only one hard-limiter is used between the input and the output.

guide. These lasers emit either in a coupled, first-order mode, or as two independent lowest-order uncoupled lasers. At 25°C we find $I_{th} = 25$–30 mA and η at threshold is 0·5–0·6. The output power for the laser in Fig. 2 at 100 mA was 15 mW/facet in the lowest-order mode. The optical spectrum typically consists of 2–3 longitudinal modes spaced by 11·25 Å (Fig. 3).

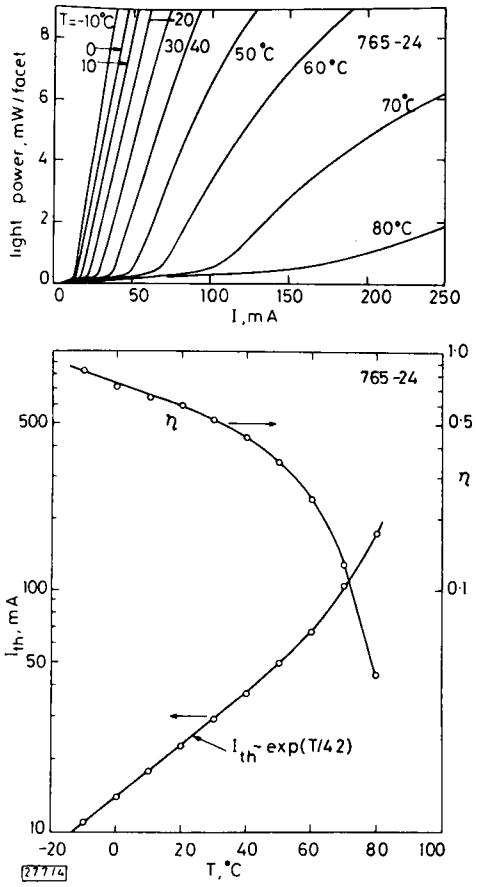

Fig. 4

a Temperature dependence of light output on pulsed current showing laser emission up to 80°C
b Temperature dependence of I_{th} and η

Plots of the light output against pulsed current at several temperatures are shown in Fig. 4*a*. The temperature dependence of I_{th} and the initial value of η are shown in Fig. 4*b*. Up to 40°C the light output is reasonably linear, and I_{th} has the characteristic temperature dependence with $T_0 = 42$°C. At higher temperatures the nonlinearity of the light output increases, I_{th} increases nonexponentially with temperature, and the quantum efficiency decreases. The results indicate the presence of an effective additional leakage current at high temperatures in addition to the various intrinsic mechanisms presumed responsible for the lower temperature T_0.[8] Such behaviour has been observed in a variety of other InGaAaP laser structures. It has been observed that the break in the exponential $I_{th}(T)$ dependence is not present in optically pumped lasers suggesting that this additional leakage is associated with the forward-biased *p-n* junction.

We are indebted to H. G. White, R. M. Mikulyak, C. G. Fleming and A. Savage for technical assistance. The InP substrates were grown by Western Electric Engineering Research Center, Princeton, New Jersey.

J. P. VAN DER ZIEL
H. TEMKIN
R. A. LOGAN

Bell Laboratories
600 Mountain Avenue
Murray Hill, NJ 07974, USA

4th January 1983

References

1 DEVLIN, W. J., WALLING, R. H., FIDDYMENT, P. J., HOBBS, R. E., MURRELL, D., SPILLETT, R. E., and STEVENTON, A. G.: 'Low-threshold channelled-substrate buried crescent InGaAsP lasers emitting at 1·54 μm', *Electron. Lett.*, 1981, **17**, pp. 651–653
2 DEVLIN, W. J., WALLING, R. H., FIDDYMENT, P. J., HOBBS, R. E., MURRELL, D., SPILLETT, R. E., STEVENTON, A. G., and NEWMAN, D. H.: 'Low threshold channelled substrate buried crescent InGaAsP lasers as sources for 1·55 μm optical communication systems'. Presented at Int. Symp. GaAs and related compounds, Japan, 1981, Inst. Phys. Conf. Ser. No. 63: Chap. 12, pp. 567–568
3 LOGAN, R. A., VAN DER ZIEL, J. P., TEMKIN, H., and HENRY, C. H.: 'InGaAsP/InP (1·3 μm) buried crescent lasers with separate optical confinement', *Electron. Lett.*, 1982, **18**, pp. 895–896
4 WESTBROOK, L. D., NELSON, A. W., and HATCH, C. B.: 'Low threshold 1·55 μm InGaAsP lasers double clad with InGaAsP confining layers', *ibid.*, 1981, **17**, pp. 952–953
5 PEARSALL, T. P., QUILLEC, M., and POLLACK, M. A.: 'The effect of substrate orientation on the liquid-solid distribution coefficients for $Ga_xIn_{1-x}As$ in the temperature range 600–700°C', *Appl.bPhys. Lett.*, 1979, **35**, pp. 342–344
6 OOMURA, E., HIBUCHI, H., HIRANO, R., NAMIZAKI, H., MUROTANI, T., and SUSAKI, W.: 'Transverse mode control in InGaAsP/InP buried crescent diode lasers', *Electron. Lett.*, 1981, **17**, pp. 83–84
7 NAHORY, R. E., POLLACK, M. A., and DEWINTER, J. C.: 'Temperature dependence of InGaAsP double-heterostructure laser characteristics', *ibid.*, 1979, **15**, pp. 695–696
8 YAMAKOSHI, S., SANADA, T., WADA, O., UMEBU, I., and SAKURAI, T.: 'Direct observation of electron leakage in InGaAsP/InP double heterostructure', *Appl. Phys. Lett.*, 1982, **40**, pp. 144–146

0013-5194/83/030113-03$1.50/0

PREDICTION OF SCATTERING CROSS-SECTION REDUCTIONS DUE TO PLATE ORTHOGONALITY ERRORS IN TRIHEDRAL RADAR REFLECTORS

Indexing terms: Antennas, Scattering, Reflector antennas

A method is presented for the determination of the reduction in scattering cross-section levels due to angular errors between plates in trihedral radar corner reflectors. The method applies to any regular reflector shape and for any incident ray direction in the reflector main beam zone; it owes its viability to a recently developed technique for determining trihedral reflector effective areas. The analysis is not exact, but gives good agreement with experimental results for a wide range of reflector sizes.

Trihedral reflectors consisting of three orthogonal flat plates are perhaps the most widely used of the passive radar targets. Developed in the 1940s as calibration and navigation targets,[1,2] trihedral reflectors have the property that, over an appreciable angular zone, the majority of rays incident within a reflector will undergo three reflections and emerge in an exactly reversed direction, as illustrated in Fig. 1. Reflectors of more than about 10 wavelengths side dimension operate mainly as ray-optical devices and may be quite accurately analysed using geometrical optics, although the addition of GTD contributions from edges and corners is necessary for

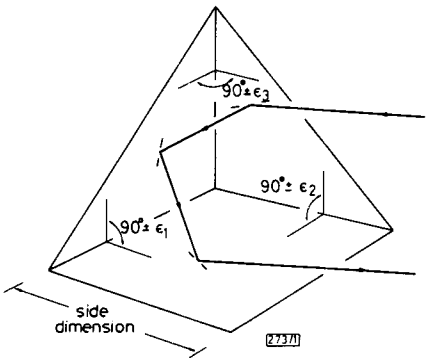

Fig. 1 *SAR-580 corner reflector geometry and definition of error angles*

Publication P33. K.M. KEEN, *Prediction of scattering cross-section reductions due to plate orthogonality errors in trihedral radar reflectors.* Electronics Letters, Vol. 19, No. 3, February 3 1983, pp 115-117.

guide. These lasers emit either in a coupled, first-order mode, or as two independent lowest-order uncoupled lasers. At 25°C we find $I_{th} = 25$–30 mA and η at threshold is 0·5–0·6. The output power for the laser in Fig. 2 at 100 mA was 15 mW/facet in the lowest-order mode. The optical spectrum typically consists of 2–3 longitudinal modes spaced by 11·25 Å (Fig. 3).

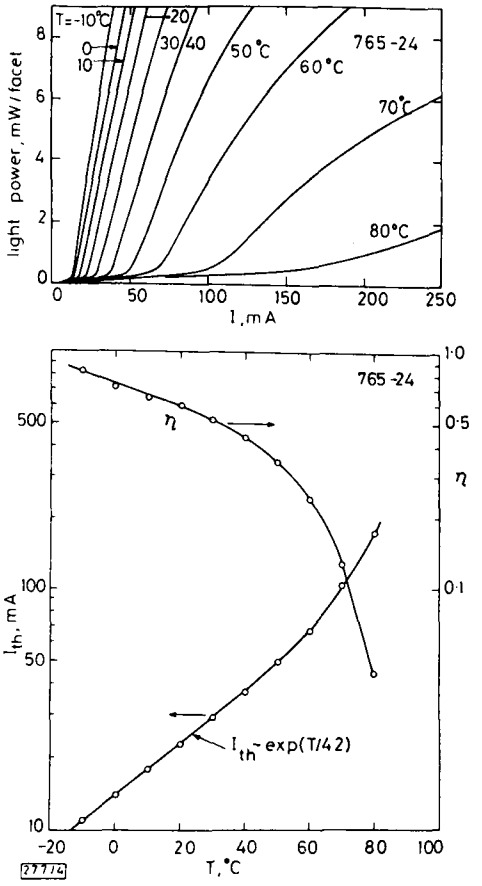

Fig. 4

a Temperature dependence of light output on pulsed current showing laser emission up to 80°C
b Temperature dependence of I_{th} and η

Plots of the light output against pulsed current at several temperatures are shown in Fig. 4*a*. The temperature dependence of I_{th} and the initial value of η are shown in Fig. 4*b*. Up to 40°C the light output is reasonably linear, and I_{th} has the characteristic temperature dependence with $T_0 = 42$°C. At higher temperatures the nonlinearity of the light output increases, I_{th} increases nonexponentially with temperature, and the quantum efficiency decreases. The results indicate the presence of an effective additional leakage current at high temperatures in addition to the various intrinsic mechanisms presumed responsible for the lower temperature T_0.[8] Such behaviour has been observed in a variety of other InGaAaP laser structures. It has been observed that the break in the exponential $I_{th}(T)$ dependence is not present in optically pumped lasers suggesting that this additional leakage is associated with the forward-biased *p-n* junction.

We are indebted to H. G. White, R. M. Mikulyak, C. G. Fleming and A. Savage for technical assistance. The InP substrates were grown by Western Electric Engineering Research Center, Princeton, New Jersey.

J. P. VAN DER ZIEL
H. TEMKIN
R. A. LOGAN

Bell Laboratories
600 Mountain Avenue
Murray Hill, NJ 07974, USA

4th January 1983

References

1 DEVLIN, W. J., WALLING, R. H., FIDDYMENT, P. J., HOBBS, R. E., MURRELL, D., SPILLETT, R. E., and STEVENTON, A. G.: 'Low-threshold channelled-substrate buried crescent InGaAsP lasers emitting at 1·54 μm', *Electron. Lett.*, 1981, **17**, pp. 651–653
2 DEVLIN, W. J., WALLING, R. H., FIDDYMENT, P. J., HOBBS, R. E., MURRELL, D., SPILLETT, R. E., STEVENTON, A. G., and NEWMAN, D. H.: 'Low threshold channelled substrate buried crescent InGaAsP lasers as sources for 1·55 μm optical communication systems'. Presented at Int. Symp. GaAs and related compounds, Japan, 1981, Inst. Phys. Conf. Ser. No. 63: Chap. 12, pp. 567–568
3 LOGAN, R. A., VAN DER ZIEL, J. P., TEMKIN, H., and HENRY, C. H.: 'InGaAsP/InP (1·3 μm) buried crescent lasers with separate optical confinement', *Electron. Lett.*, 1982, **18**, pp. 895–896
4 WESTBROOK, L. D., NELSON, A. W., and HATCH, C. B.: 'Low threshold 1·55 μm InGaAsP lasers double clad with InGaAsP confining layers', *ibid.*, 1981, **17**, pp. 952–953
5 PEARSALL, T. P., QUILLEC, M., and POLLACK, M. A.: 'The effect of substrate orientation on the liquid-solid distribution coefficients for $Ga_xIn_{1-x}As$ in the temperature range 600–700°C', *Appl.bPhys. Lett.*, 1979, **35**, pp. 342–344
6 OOMURA, E., HIBUCHI, H., HIRANO, R., NAMIZAKI, H., MUROTANI, T., and SUSAKI, W.: 'Transverse mode control in InGaAsP/InP buried crescent diode lasers', *Electron. Lett.*, 1981, **17**, pp. 83–84
7 NAHORY, R. E., POLLACK, M. A., and DEWINTER, J. C.: 'Temperature dependence of InGaAsP double-heterostructure laser characteristics', *ibid.*, 1979, **15**, pp. 695–696
8 YAMAKOSHI, S., SANADA, T., WADA, O., UMEBU, I., and SAKURAI, T.: 'Direct observation of electron leakage in InGaAsP/InP double heterostructure', *Appl. Phys. Lett.*, 1982, **40**, pp. 144–146

0013-5194/83/030113-03$1.50/0

PREDICTION OF SCATTERING CROSS-SECTION REDUCTIONS DUE TO PLATE ORTHOGONALITY ERRORS IN TRIHEDRAL RADAR REFLECTORS

Indexing terms: Antennas, Scattering, Reflector antennas

A method is presented for the determination of the reduction in scattering cross-section levels due to angular errors between plates in trihedral radar corner reflectors. The method applies to any regular reflector shape and for any incident ray direction in the reflector main beam zone; it owes its viability to a recently developed technique for determining trihedral reflector effective areas. The analysis is not exact, but gives good agreement with experimental results for a wide range of reflector sizes.

Trihedral reflectors consisting of three orthogonal flat plates are perhaps the most widely used of the passive radar targets. Developed in the 1940s as calibration and navigation targets,[1,2] trihedral reflectors have the property that, over an appreciable angular zone, the majority of rays incident within a reflector will undergo three reflections and emerge in an exactly reversed direction, as illustrated in Fig. 1. Reflectors of more than about 10 wavelengths side dimension operate mainly as ray-optical devices and may be quite accurately analysed using geometrical optics, although the addition of GTD contributions from edges and corners is necessary for

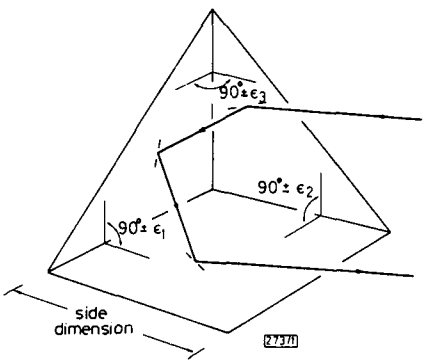

Fig. 1 *SAR-580 corner reflector geometry and definition of error angles*

very accurate pattern determination.[3] Robertson[2] has shown how the effective area of a trihedral reflector can be determined by mapping the real and image apertures of a reflector onto an oblique plane through the reflector apex, the plane being orthogonal to the direction of the incident rays. This procedure has recently been adapted to a computer processing technique which uses numerical integration to determine effective areas at any angle of incidence, for any regular trihedral reflector shape.[4] There is currently considerable interest in trihedral reflectors as ground targets for the calibration of airborne and spaceborne remote-sensing, synthetic-aperture radars. Fig. 1 shows the geometry of the type of ground targets developed for the European SAR-580 programme.[5] As accurate predictions of reflection level are required for this type of calibration, it is necessary that the effect on scattering cross-section due to nonorthogonal alignment of reflector plates caused by construction accuracy limitations can be computed. A procedure for accomplishing this, which depends on the method for finding the effective area at any direction of incidence,[4] and which is based on the description of the physical mechanism involved given by Spencer,[1] is outlined below.

Following Spencer, the theory development is best carried out by first considering the simplest dihedral reflector case. A dihedral radar reflector consists of only two orthogonal plates and will give a return in the reversed incident wave direction by two reflections, but only in the plane orthogonal to both plates.

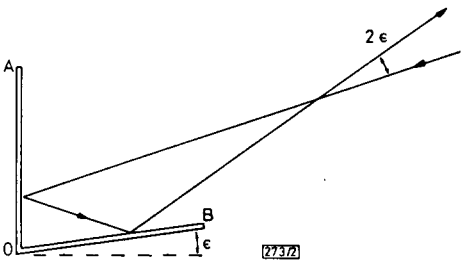

Fig. 2 *Dihedral reflector orthogonality error*

Angular error ε causes a beam squint of 2ε on ray incident on plane reflector OA

Fig. 2 shows a dihedral reflector with an angular orthogonality error ε. A ray incident on plate OA will emerge from plate OB with an angular displacement of 2ε from the reversed incident ray direction. Similarly, a ray incident on plate OB also emerges with an angular displacement of 2ε, but this time on the other side of the incident beam direction. Thus, as shown in Fig. 3, the angular error causes the returned component to be split into two diffraction patterns with a separation of 4ε between beam peaks, the sum of which gives the actual reflection level.

Each of the diffraction patterns has a field distribution of the form

$$E(\theta) = \tfrac{1}{2}KF(\theta, a_\lambda) \tag{1}$$

where $F(\theta, a_\lambda)$ is the Fourier transform of the appropriate aperture distribution a_λ, K is a constant containing distance and other factors which are not relevant here, and the factor of $\frac{1}{2}$ has been introduced as there are two equal diffraction patterns which would normally be one, for $\varepsilon = 0°$. The angle θ is the angle from beam peak for each diffraction pattern. As

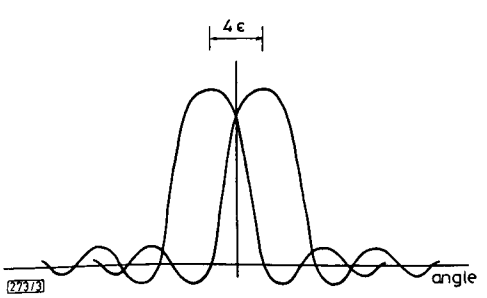

Fig. 3 *Diffraction pattern doubling due to error angle ε*

we are only interested in the sum of the patterns in the reversed incident ray direction, $\theta = 2\varepsilon$ in both cases.

Adding the two equal phase and amplitude contributions at $\theta = 2\varepsilon$ (pattern symmetry is assumed) and normalising with $\varepsilon = 0°$, i.e. no-error case, gives the level reduction in decibels due to a plate orthogonality error ε as

$$L_{dB} = 20 \log_{10} F(2\varepsilon, a_\lambda) \tag{2}$$

To use this function it is necessary to determine a_λ and the distribution, and then find the Fourier transform. This has been done for the dihedral case[3] but will not be repeated here. Of greater interest is the extension of the above to the trihedral reflector case. The same mechanism occurs except that an error in one reflector plate causes two beams to be formed, errors in two plates cause four beams, and errors in all three plates cause six beams; these combine 'in-phase' in pairs in the way described above. The errors may be treated separately and added as below:

$$L_{dB} = L^1_{dB} + L^2_{dB} + L^3_{dB} \tag{3}$$

where each of the terms on the right-hand side is a Fourier transform expression of the form of eqn. 2, but with its associated error angle, e.g. angles ε_1, ε_2 and ε_3 of Fig. 1.

The appropriate values of a_λ are not easy to determine exactly, but from an examination of effective area shapes, a good approximation is the semi-minor diameter of a hexagon with an area equal to the effective area. Thus,

$$a_\lambda = \frac{1}{2\lambda}\sqrt{\frac{A_{eff}(l, m, n)}{0{\cdot}87}} \tag{4}$$

where λ represents wavelength and $A_{eff}(l, m, n)$ is the effective area which is a function of the direction cosines of the incident beam. For the Fourier transform functions, again it is not easy to get an exact formulation, but a close approximation can be obtained from a knowledge of the distributions involved, to give the same sort of pattern shape and beamwidth. A linear cosine distribution is a fair representation, and therefore the following function has been used:

$$F(2\varepsilon, a_\lambda) = \frac{\left[\frac{\pi}{2}\right]^2 \cos[\pi a_\lambda \sin(2\varepsilon)]}{\left[\frac{\pi}{2}\right]^2 - [\pi a_\lambda \sin(2\varepsilon)]^2} \tag{5}$$

The above procedure is a good approximation for most trihedral reflector shapes; the value of the effective area must, of course, be determined for the appropriate shape. Applying the above to triangular-sided reflectors, comparison with published measured results on boresight level reductions[6] shows agreement of better than 0·1 dB per error up to values of half a degree for reflector sizes ranging from 15 to 35 wavelengths side dimension. Fig. 4 shows boresight level reductions for a 90 cm size SAR-580 reflector at 5·3 GHz. Computed patterns given elsewhere[3] are interesting as they show that the beam peak error reduces with angle from peak as a consequence of the diminishing effective area.

Acknowledgment: This work was carried out for the European Space Agency under ESTEC Contract 4947/81/NL/MS, and

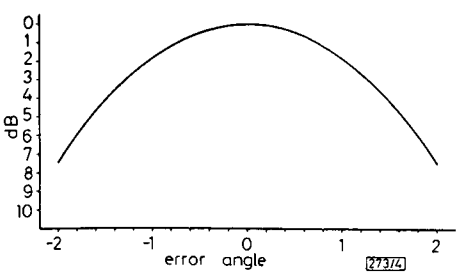

Fig. 4 *Boresight reflection level reduction due to orthogonality errors at all three plate intersections for a 90 cm side dimension SAR-580 reflector at 5·3 GHz*

the author is grateful to A. Woode of ESTEC, Noordwijk, Holland, for support and helpful discussions.

K. M. KEEN *24th December 1982*

Keith M. Keen & Associates
Ifold, Loxwood, West Sussex RH14 0TA, England

References

1 SPENCER, R. C.: 'Optical theory of the corner reflector'. MIT Rad. Lab. Report ATI-5783, 1944
2 ROBERTSON, S. D.: 'Targets for microwave radar navigation', *Bell Syst. Tech. J.*, 1947, pp. 852–869
3 KEEN, K. M.: 'Theory and software development for the accurate prediction of the scattering cross-section patterns of modified corner reflectors'. Keith M. Keen & Associates Final Report KMK/FR.RCS-82 under ESTEC Contract 4947/81/NL/MS, Dec. 1982
4 KEEN, K. M.: 'A new technique for the evaluation of the scattering cross-sections of radar corner reflectors', *IEE Proc. H, Microwaves, Opt. & Antennas*, to be published
5 CORR, D. G., WOODE, A. D., and BRUZZI, S.: 'The SAR-580 calibration site at RAE, Bedford', *Int. J. Remote Sensing*, 1980, **3**, pp. 223–227
6 JASIK, H.: 'Passive reflectors' *in* 'Antenna engineering handbook' (McGraw-Hill Book Co., 1961), Chap. 13

0013-5194/83/030115-03$1.50/0

IN SITU MASS SPECTROMETRIC INVESTIGATION OF METALLISED InP SAMPLES DURING ANNEALING

Indexing terms: Semiconductor devices and materials, Semiconductors (III–V), Ohmic contacts, Schottky contacts

In situ mass spectrometry was used to study the interaction of the metal-InP system. In the presence of a thin gold layer on the crystal surface the phosphorus yield showed characteristical peak against temperature with a relatively high rate of evaporation. Contact systems containing gallium and indium were also investigated. A thin Ga layer deposited into the gold film eliminated the characteristical phosphorus losses.

Introduction: InP is a direct bandgap semiconductor which is particularly well suited for microwave and optoelectronic devices.

Low-resistance ohmic contacts to InP have been obtained using gold- and silver-based metallisation systems. The as-deposited metallisation shows Schottky-character, and a suitable postdeposition annealing converts it into ohmic contact. It is well known that a high alloying temperature or too long an alloying time can destroy the compound semiconductor.[1] This decomposition is greatly enhanced by the layers on the surface of the crystals.[2] For the *in situ* investigation of the metal-semiconductor interaction a mass spectrometric method was proposed.[3] The main advantage of this *in situ* method is that the temperature dependence on decomposition can be obtained. This method was applied to the investigation of GaAs, GaP[4] and GaAlAs.[5]

Gallium-containing contact systems have been applied to making contacts to GaAs.[6] This thin gallium layer, codeposited with the metallisation, causes a drastic change in the interaction.[7]

In this letter we briefly report on our mass spectrometric study of the decomposition of *n*-InP covered with a single metallic layer. Gallium- and indium-containing contact systems were also investigated and compared.

Experimental: This study was carried out using LEC-pulled InP of ⟨100⟩ and of ⟨111⟩ orientations. *N*-type InP was doped with either Sn or Te, and the carrier concentration was about 10^{17} cm^{-3}. No epitaxial layers were used. Various types of metallisations were studied, but in this letter data concerning only the most interesting layer systems will be published. They are 400 nm-thick gold layer, 400 nm-thick gold layer + 100 nm-thick In layer + 400 nm Au layer and 400 nm-thick gold layer + 100 nm-thick Ga layer + 400 nm Au layer.

For comparison, InP slices without metallisation were also investigated. The experimental set-up has been described in our previous work.[4] The QML-51 Riber quadrupole mass spectrometer was supplied with a six-channel peak selector made in Atomki Debrecen, Hungary. The chamber of the mass spectrometer was cooled by liquid nitrogen during the measurements. The pressure in the chamber of the mass spectrometer was lower than 10^{-3} Pa.

Results: In Figs. 1 and 2 the P_1 and P_4 yields against temperature can be seen from InP samples covered by Au, Au-In-Au and Au-Ga-Au contact layers. We also registered the P_2 species. The rates of the several phosphorus species are supposed to be essentially temperature-dependent. Au-InP contact systems at 440°C show large peak similarly to Au-GaAs contact system.[4]

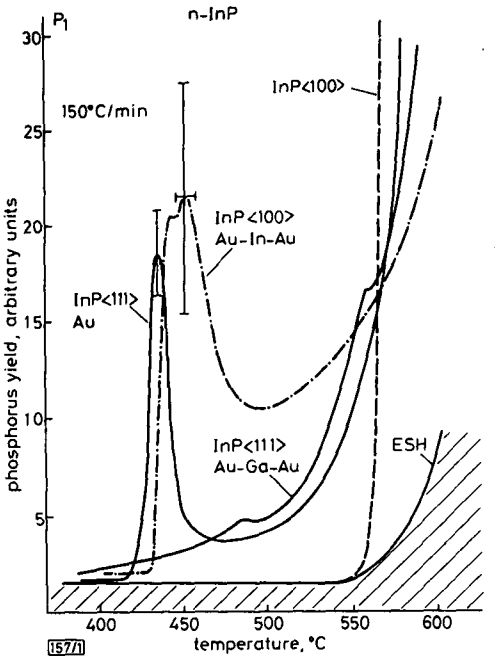

Fig. 1 *Phosphorus (P_1) yield from n-InP covered by contact layers*
– – – – uncovered InP samples
//////// background (empty sample holder, ESH)

Using Au-In-Au contacts we also experienced large peaks at slightly higher temperatures. The curves seem to have two maxima, one of them sometimes appearing as a shoulder.

The points in Figs. 1 and 2 are averages of several measurements, and the scattering of the temperature and phosphorus yield belonging to the extremes is also shown. In spite of the large scattering the shape of the curves obtained for the same type of samples was very similar.

In contrast with the results obtained using Au-In-Au contacts, a 100 nm-thick Ga layer between two Au layers can practically eliminate the large phosphorus peaks. It is in good accordance with the results reported in Reference 7.

In the case of free InP surface the evaporation increased very abruptly above 550°C.

Other contacts were also investigated. For example, Ag contacts showed peaks at about 550°C. In the case of Ni contact no peaks of any kind were observed, and even at 600°C the phosphorus yield was relatively low.

We also investigated the effect of repeated annealing. No peaks were observed and the yield was always less than in the case of the first annealing.

Publication P34. **K.M. KEEN, *Use of radio telescopes or satellite Earth station antennas as ultra-high scattering cross-section calibration targets for spaceborne remote sensing radars.* Electronics Letters, Vol. 19, No. 6, March 17 1983, pp 225-226.**

3 KAMINOW, I. P., and CARRUTHERS, J. R.: 'Optical waveguiding layers in lithium niobate and lithium tantalate', *Appl. Phys. Lett.*, 1973, **22**, pp. 326–328
4 TIEN, P. K., and ULRICH, R.: 'Theory of prism-film coupler and thin film light guides', *J. Opt. Soc. Am.*, 1970, **60**, pp. 1325–1337
5 BRICE, J. C.: 'The cracking of Czochralski-grown crystals', *J. Cryst. Growth*, 1977, **42**, pp. 427–430

0013-5194/83/060223-03$1.50/0

USE OF RADIO TELESCOPES OR SATELLITE EARTH STATION ANTENNAS AS ULTRA-HIGH SCATTERING CROSS-SECTION CALIBRATION TARGETS FOR SPACEBORNE REMOTE SENSING RADARS

Indexing terms: Antennas, Radio telescopes, Radar

Spaceborne synthetic aperture and scatterometer radars currently under development for earth remote sensing may require the provision of ground calibration targets with very large scattering cross-sections. One way of providing these would be to adapt existing parabolic radio telescopes or satellite earth station antennas by replacing the feed by a metallic sphere. A dichroic surface would facilitate tracking.

Over the past 15 years there has been a rapidly rising interest in the use of spaceborne scatterometers and synthetic aperture radars for a variety of geophysical applications such as oceanography, agriculture, forestry and ice mapping.[1] The European Space Agency, for example, is currently developing the ERS-1 satellite, which will have a C-band earth sensing radar module. The module will operate in three radar modes: two SAR modes of different resolutions and a scatterometer mode. This type of instrument requires operational calibration, both internal and using known returns from suitable ground targets, to determine essential information such as radiometric response, system resolution and geometric fidelity. Calibration procedures for the ERS-1 module will shortly be studied, and this will involve a detailed investigation of ground calibration targets. At this stage, however, it seems likely that there will be a need for point source targets, either passive or active, with very high return levels. A technique for the adaption of existing parabolic reflector radio telescopes or satellite earth station antennas with the normal tracking facilities, as passive ultra-high reflection level ground targets of known scattering cross-section, is the subject of this letter.

An axisymmetrical parabolic reflector as used for large ground station antennas and for some types of radio telescope is fundamentally a ray-focusing device. In the receive mode it essentially converts plane waves into spherical waves which are centred on the focal point of the reflector, where a small antenna (the 'feed') or a subreflector is located. In the transmit mode it does the same thing in reverse, i.e. it essentially converts spherical waves emanating from the feed (or subreflector) to plane waves. Thus a parabolic reflector antenna could be used as a passive radar reflector by placing a metallic sphere at its focus, as in Fig. 1, which shows the adaption of a front-fed antenna system; the sphere would convert converging spherical incident waves to reflected diverging spherical waves. The principle would also apply to a Cassegrain antenna system, where either the hyperboloid subreflector or the feed could be replaced by a metallic sphere. The beamwidth of a radar reflector of this sort would, of course, be very narrow, and the system would only work in one direction, i.e. along (or, at least, close to) the paraboloid axis.

Values of scattering cross-sections as functions of reflector size and radar wavelength can be determined using the general relationship between scattering cross-section σ and effective area A.[2] Introducing an efficiency factor μ, analogous to the aperture efficiency factor used in antenna calculations, an expression may be derived as below:

$$\sigma = \mu \frac{4\pi A^2}{\lambda^2} \tag{1}$$

where λ represents wavelength. For a reflector with a circular aperture of diameter D, the above can be more conveniently expressed as

$$\sigma = \mu \frac{\pi^3 D^4}{4\lambda^2} \tag{2}$$

The value of μ would be of the order of 0·5. Using this, values of boresight scattering cross-sections have been calculated for a range of typical earth station antenna and radio telescope reflector diameters for the 5·3 GHz radar frequency of the ERS-1 satellite. These are shown in Table 1, and it can be seen that the values are very high, even for relatively small reflectors.

Table 1 VALUES OF RADAR SCATTERING CROSS-SECTIONS FOR A RANGE OF EXISTING REFLECTOR SIZES AT 5·3 GHz

Reflector diameter	σ at 5·3 GHz
m	m^2
5	$7{\cdot}6 \times 10^5$
15	$6{\cdot}1 \times 10^7$
25	$4{\cdot}7 \times 10^8$
65	$2{\cdot}2 \times 10^{10}$

The practical application of this ground target technique would require accurate tracking. This could be carried out in the normal way with a tracking feed, utilising a satellite beacon signal at a frequency well removed from the radar frequency. As shown in Fig. 2, the tracking feed could be incorporated within a reflecting sphere if the sphere was dichroic, allowing transmission at the beacon frequency but acting as a reflector at the radar frequency. A number of frequency-selective structures are known which would facili-

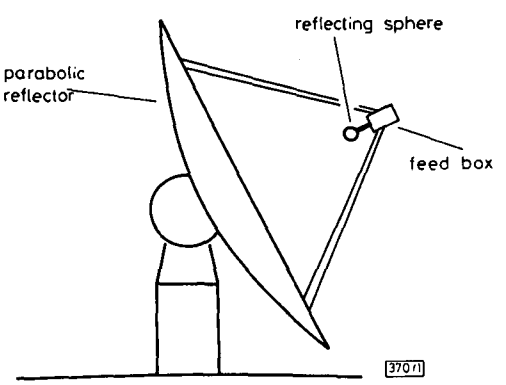

Fig. 1 *Radio telescope or satellite earth station antenna adapted as a high-reflection radar calibration target*

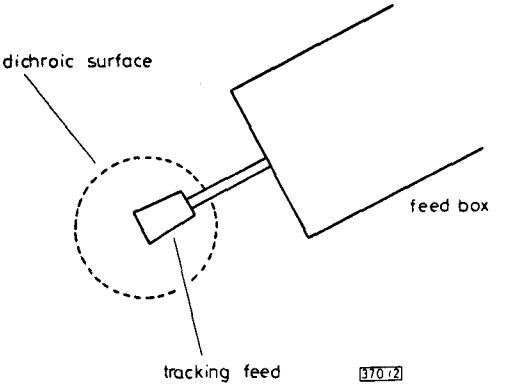

Fig. 2 *Tracking arrangements, using a tracking feed within a dichroic sphere*

tate this: for example, Jerusalem cross and concentric ring arrays.[3,4]

The accurate determination of σ for any given antenna geometry could be determined using the various analytical techniques that have been applied to other radar reflector structures.[5,6]

Acknowledgment: This work was carried out for the European Space Agency under ESTEC contract 4947/81/NL/MS, and the author is grateful to A. Woode of ESTEC, Noordwijk, Holland, for support and helpful discussions.

K. M. KEEN

Keith M. Keen & Associates
Ifold, Loxwood, W. Sussex RH14 0TA, England

2nd February 1983

References

1 LONG, M. W.: 'Radar reflectivity of land and sea' (Lexington Books, 1975)
2 ROBERTSON, S. D.: 'Targets for microwave radar navigation', *Bell Syst. Tech. J.*, Oct. 1947, pp. 852–869
3 PARKER, E. A., HAMDY, S. M. A., and LANGLEY, R. J.: 'Arrays of concentric rings as frequency-selective surfaces', *Electron. Lett.*, 1981, **17**, pp. 880–881
4 LANGLEY, R. J., and DRINKWATER, A. J.: 'An improved empirical model for the Jerusalem cross', *IEE Proc. H, Microwaves, Opt. & Antennas*, 1982, **129**, (1), pp. 1–6
5 KEEN, K. M.: 'Theory and software development for the accurate prediction of the scattering cross-section patterns of modified trihedral corner reflectors'. Keith M. Keen & Associates report KMK/FR.RCS-82. Final report under ESTEC contract 4947/81/NL/MS, Dec. 1982
6 CRISPIN, J. W., and SIEGEL, K. M.: 'Methods of radar cross-section analysis' (Academic Press, 1968)

0013-5194/83/060225-02$1.50/0

YIELD ESTIMATION MODEL FOR VLSI ARTWORK EVALUATION

Indexing terms: Modelling, VLSI design, Mask defects, Yield model

In the letter a model which describes limitations of a manufacturing yield in terms of an IC artwork and a lithography characterisation is proposed. Density and distribution of diameters of defects present in the mask, as well as line-width fluctuations, are taken into account.

Introduction: Recent progress in VLSI technology and development of new design methodologies have created new demand for a model relating an IC artwork description and a statistical characterisation of the lithography progress to an estimate of manufacturing yield. Such a model is needed for: (i) estimation of a contribution of the optical defects present in the mask into a degradation of the manufacturing yield; (ii) prediction of the mask-limited yield from automatic mask inspection data; (iii) optimisation of the simplified design rules[1] with regard to the quality of the available lithography process. Models aiming to solve part of the above goals have been published since the early 1960s. First, for an approximate estimation of the yield models were applied dealing with an average density of optical defects in the mask.[2] Then, more realistic but more complex models were applied for solving the second and third of the above tasks (see, for example, References 3 and 4). Unfortunately, none of the existing approaches is general enough to cover all the phenomena which are essential in solving problems (i) to (iii) with a single model. The other disadvantage of the existing models is that they refer to the defect in the mask rather than to the physical meaning of its image in silicon. In this letter we propose a model which should be suitable for analysis of VLSI artworks and technologies. It is intended as a tool for solving the above-mentioned goals, and seems to be free of previously mentioned disadvantages of the approaches reported elsewhere.

Defect: The optical defects in the mask may cause the following catastrophic deformations of the IC layout: a break of the conducting path, unintended short-circuit between some active areas and unwanted appearance of an active or parasitic device. We assume that these deformations occur if the distance w_d between deformed edges of the conducting path is less than a certain critical value w_{cr} (see Fig. 1*a*) or if a diameter D_d of a circle described on the unwanted device is greater than d_{cr} (see Fig. 1*b*). Of course, the values of w_{cr} and d_{cr} depend on a physical meaning of the considered layer and are determined by the critical values of current densities, breakdown voltages etc. Thus, in general, the estimation of the yield, i.e. the probability that an IC is not catastrophically deformed, consists in searching for the probability that, for each defect present in the mask, $w_d > w_{cr}$ or $D_d < d_{cr}$.

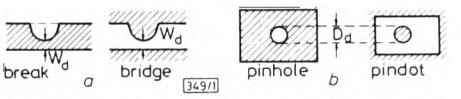

Fig. 1 *Deformations caused by optical defects in mask*

Simplified yield estimation model: To develop a general model we first consider a single mask composed of conducting paths with parallel edges and a uniform width. Moreover, we consider the path breaks only, and we assume that defects in the mask can be described by circles having radius† R and uniform distribution on the entire area of the mask, given by D. Since the defect in the mask causes catastrophic deformation, i.e. it is a killer defect, when $w_d \leq w_{cr}$, then (see Fig. 2) it reduces the yield when its centre is located within a belt having the width $w_f = w - 2[w - (R + w_{cr})]$, where w is the

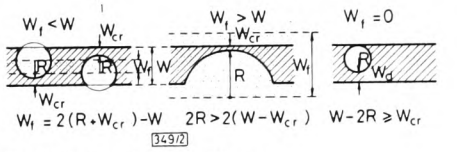

Fig. 2 *Critical belt (dotted area)*

width of the path in the mask. Note, however, that the image from the mask is transformed onto the surface of silicon with a random deformation caused by the inaccuracy of the lithography process. We described a difference in the location of an edge in the mask and its actual location in silicon by a random variable ΔW, which is defined by a Gaussian density function $f(\Delta W)$. Therefore, the actual radius of the defect in silicon is $R_z = R + \Delta W$, where R_z is a random variable having a distribution given by $f(R_z)$, which is a composition of $f(R)$ and $f(\Delta W)$. Thus, the actual distance between two edges of the conducting path is $w - 2\Delta W$, and the actual width of the critical belt w_f on the surface of silicon becomes $2R_z + 2w_{cr} - w$. Knowing the area of the critical belt and the distribution of R_z one can evaluate the probability of the event that the centres of the defects are out of the critical area, i.e. the yield. In order to accomplish this we divide the range of changes of R_z into n segments $[R_z^i, R_z^{i+1}]$ and we compute for each $i = 1, 2, \ldots, n$, $A_f^i = Lw_f^i$, where w_f^i is the width of the critical belt computed for $R_z^{i*} = (R_z^i + R_z^{i+1})/2$ and L is a total length of the conducting path in the mask. Thus, one can show that the yield is as follows:

$$Y = \sum_{i=1}^{n+1} \int_{R_1}^{R_z^{i+1}} f(R_z)\, dR_z \exp\left[-DA_f^i \int_{R_z^i}^{R_z^{i+1}} f(R_z)\, dR_z \right] \quad (1)$$

This can be done by applying a formula for a total probability and the Poisson theorem.[5]

Yield estimation procedure: Eqn. 1 was developed for a single mask under rather unrealistic assumptions. Here, we give an

† R is a random variable described by a probability function $f(R)$

this process the Auger recombination is 5 times stronger than the radiative recombination for $n = 3 \times 10^{18}$ cm^{-3}.

In conclusion, we find that for the 1·3 μm InGaAsP laser studied the radiative recombination coefficient decreases with charge density. Indications are also strong that the active region is lightly doped and the Auger coefficient is relatively small in agreement with the results of Su *et al.*[1]

Acknowledgment: One of the authors (W. Streifer) wishes to acknowledge informative discussions with Dr. R. Olshansky and G. H. B. Thompson throughout the course of this work and with Dr. T. L. Paoli concerning the differential carrier lifetime. We also appreciate receiving detailed data relating to sample 194-2.

D. YEVICK
W. STREIFER

Xerox PARC
3333 Coyote Hill Road, Palo Alto, CA 94304, USA

11th October 1983

References

1 SU, C. B., SCHLAFER, J., MANNING, J., and OLSHANSKY, R.: 'Measurement of radiative recombination coefficient and carrier leakage in 1·3 μm InGaAsP lasers with lightly doped active layers', *Electron. Lett.*, 1982, **18**, pp. 1108–1110

2 STERN, F.: 'Calculated spectra dependence of gain in excited GaAs', *J. Appl. Phys.*, 1976, **47**, pp. 5382–5386

3 THOMPSON, G. H. B.: 'Analysis of radiative and nonradiative recombination law in lightly doped InGaAsP lasers', *Electron. Lett.*, 1983, **19**, pp. 154–155

FAST ALGORITHM FOR THE EXACT DETERMINATION OF THE MAPPED EFFECTIVE AREAS OF TRIHEDRAL RADAR REFLECTORS

Indexing terms: Radar, Reflectors

A computer processing technique has recently been described for the evaluation of monostatic scattering cross-sections of regularly shaped trihedral radar reflectors, the final stage of which involves the determination of an effective area mapped out by orthogonal projections of real and image aperture boundary lines on an oblique plane. Previously the area determination was carried out by an integration process plus a geometrical procedure. An alternative method described here reduces the area to a set of triangles which are evaluated and summed: this gives an exact value and is approximately 50 times faster in computer CPU time.

The current interest in the use of trihedral radar corner reflectors as ground targets for the calibration of synthetic aperture radars and scatterometers carried by remote sensing satellites has resulted in some extensions to the original analytical work on corner reflectors, carried out in the 1940s.[1,2] Recently, a new method has been described for evaluating the geometrical optics monostatic effective area (and therefore, scattering cross-section) of any regularly shaped trihedral reflector, for any incident ray direction.[3]

This method, which uses computer evaluation, is basically as follows. For any direction of incident ray, the effective area is mapped out by the orthogonal projections of the reflector aperture boundary lines (transposed about the reflector apex) onto an oblique plane; this plane is perpendicular to the incident ray direction and passes through the corner reflector apex. The orthogonal projection process is carried out by a co-ordinate transformation involving a compound rotation to a two-dimensional Cartesian co-ordinate system on the oblique plane with co-ordinate axes $0X'$ and $0Y'$. The result of this stage of the overall procedure is a set of projected lines of known slopes and intercepts in the $X'Y'$ co-ordinate system; these define the boundaries of the effective area. The final stage of the procedure then is to evaluate the area. Originally, this was carried out by the perfectly valid but rather lengthy process as in Fig. 1 which shows a typical effective area half mapping (the effective area is symmetrical about the $0Y'$ axis). This process is in two parts: first, integration of the area is carried out by trapezoidal strip summation, up to the position $\bar{X}'$ of the first crossing of the X'-axis; secondly, geometrical evaluation is used to find the portion of area remaining beyond $\bar{X}'$. The integration process is not exact, and has to be carried out with small δx values in order to make errors negligible. Also, the geometrical procedure to determine the remaining area is prolix in terms of computer program length and running time.

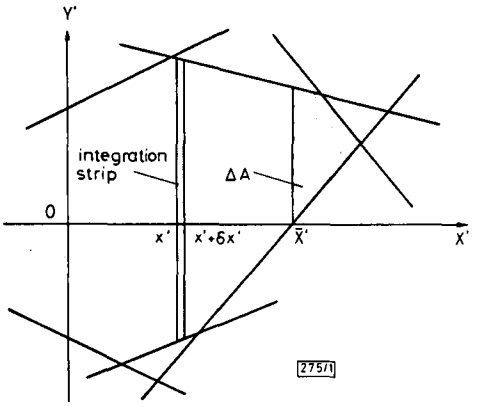

Fig. 1 *Effective area determination by strip integration and geometrical area calculation*

With experience of the scattering cross-section prediction method it became clear that evaluation of mapped effective areas could be carried out in a more efficient and exact way. This alternative technique is the subject of this letter.

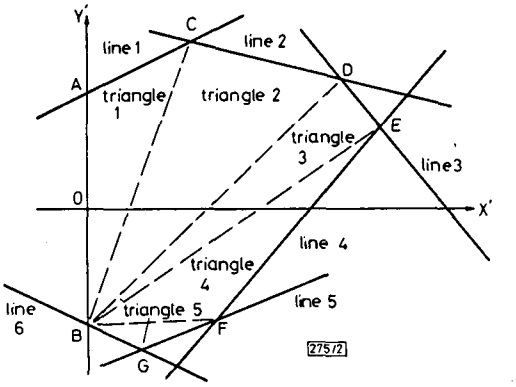

Fig. 2 *Alternative effective area determination method*

Polygon of n sides is divided into $n - 2$ triangles which are separately evaluated and then summed

Fig. 2 shows the alternative area evaluation technique applied to the same set of boundary lines as in Fig. 1. The technique is based on the simple fact that a polygon of n sides can be divided into $n - 2$ triangles, and that the area of each triangle can always be determined from the length of its sides (and therefore from a knowledge of the co-ordinates of its corners) using Heron's formula,[4] i.e.

$$\text{area} = \sqrt{[s(s-a)(s-b)(s-c)]}$$

where a, b and c are the side lengths and s is the semiperimeter

$$s = \tfrac{1}{2}(a + b + c)$$

For the half effective area shape shown, the seven-sided polygon consisting of the $0Y'$-axis and lines 1 to 6 (as assigned in clockwise order) can be reduced to five triangles with a common corner; this may be either the lowest positive Y'-axis intercept A, or the highest negative Y'-axis intercept B. Fig. 3 is an outline flowchart for a software subroutine which carries out area evaluation in this way. Initially all slope and intercept data for the projected real and image aperture boundary

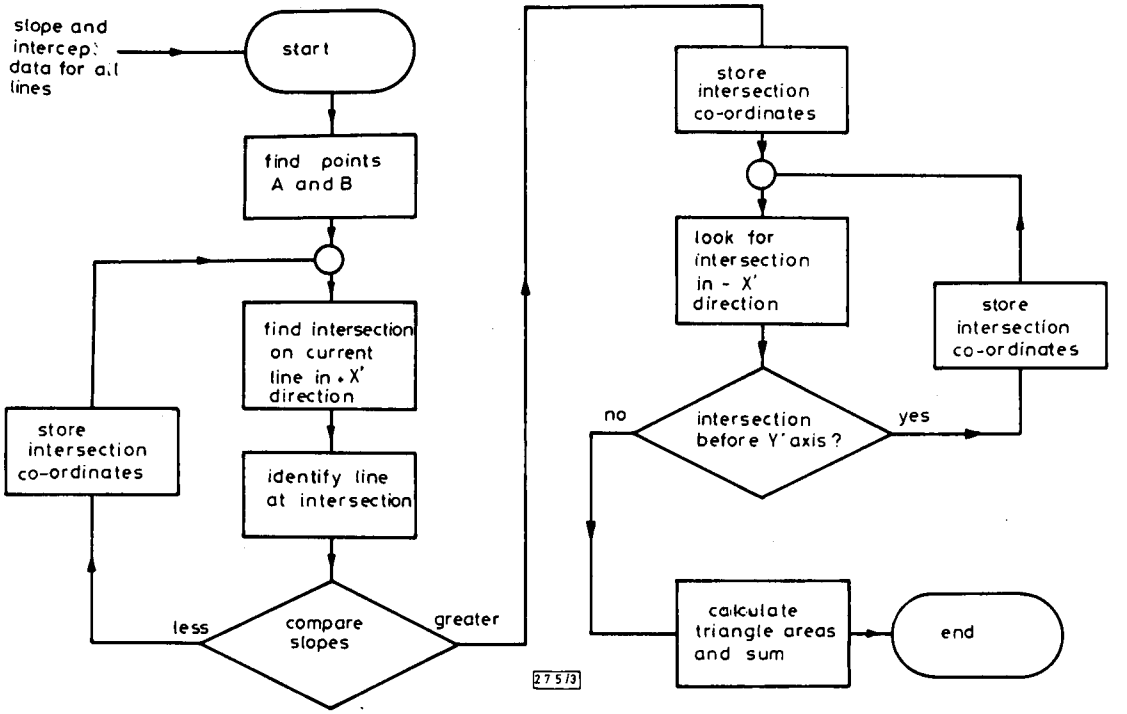

Fig. 3 *Outline flowchart for the effective area determinations using a reduction to n − 2 triangles*

lines are supplied. The lowest positive and highest negative Y'-axis intercepts are then found; these are the points A and B. Point A also defines line 1 as it is the line with this Y' intercept value. However, care must be taken with this and similar line and point matching: more than one line might cross the Y'-axis at A but only the one with the lowest slope is of interest as this forms part of the area boundary; other lines do not.

Following the identification of line 1, the procedure shown in the flowchart of Fig. 3 consists basically of two loops and a summation process. In both loops, the effective area boundary is traversed in a clockwise direction from point A on the $+Y'$-axis to point B on the $-Y'$-axis: the first loop operates when the boundary traversal corresponds to a movement in the positive direction along the $0X'$-axis, or a zero horizontal movement (i.e. with a vertical line); the second loop corresponds to a movement in the negative direction along the $0X'$-axis. In these loops, the intersection points of interest are found and stored. The final stage is the calculation of the $n-2$ triangle areas using Heron's formula, and summation to give the required effective area.

The above procedure is clearly superior to the previous technique using strip integration, as it is exact and involves only a small fraction of the number of calculations required previously. A subroutine in Fortran has been used successfully with the three trihedral reflector shapes, i.e. triangular-sided corner reflectors, square-sided corner reflectors and SAR-580 corner reflectors.[3] Reflection patterns agree with those calculated using strip integration, but the computational speed was seen to be improved by a factor of about 50.

Acknowledgment: This work was carried out for the European Space Agency under Rider 1 to ESTEC contract 4947/81/NL/MS, and the author is grateful to A. D. Woode of ESTEC, Noordwijk, Holland, for support and helpful discussions.

K. M. KEEN

Keith M. Keen & Associates
Ifold, Loxwood, W. Sussex RH14 0TA, England

6th October 1983

References

1 SPENCER, R. C.: 'Optical theory of the corner reflector'. MIT Rad. Lab. Report ATI-5783, 1944
2 ROBERTSON, S. D.: 'Targets for microwave radar navigation', *Bell Syst. Tech. J.*, 1947, pp. 852–869
3 KEEN, K. M.: 'A new technique for the evaluation of the scattering cross-sections of radar corner reflectors', *IEE Proc. H, Microwaves, Opt. & Antennas*, 1983, **130**, (5), pp. 322–326
4 REKTORYS, K.: 'Survey of applicable mathematics' (Iliffe Books, 1969)

SIMPLE MEASUREMENT METHOD FOR POLARISATION MODAL DISPERSION IN POLARISATION-MAINTAINING FIBRES

Indexing terms: Optical fibres, Polarisation

A new method for polarisation modal dispersion measurement of polarisation-maintaining fibres is presented. By using a laser diode and a Michelson interferometer, polarisation modal dispersion is determined from the path difference between the two interference peaks which arise from the interference between HE_{11}^x and HE_{11}^y modes.

Introduction: Polarisation-maintaining fibres are essential for coherent optical communication systems and fibre sensor systems. One of the important characterisations for polarisation-maintaining fibres is to measure the polarisation modal dispersion accurately. Many methods for the polarisation modal dispersion measurement have been proposed so far.[1-3] Among these techniques, the spatial technique[3] is the most accurate. However, the reported measurement procedure is rather complicated. First one must set up a modified Twyman–Green interferometer without a test fibre so that the optical path difference between the two arms of the interferometer equals zero. Next, the test fibre is set and one of the mirrors is moved so that the maximum visibility is again obtained. When light source power is low, the interference visibility is difficult to observe. This letter proposes a simple and highly accurate method using a Michelson interferometer.

Principle: When the electric field envelopes of the HE_{11}^x and HE_{11}^y modes are $F_x(t)$ and $F_y(t)$, respectively, the electric field after passing through an analyser whose polarisation plane matches the direction of 45° with respect to the principal axis

Publication P36. **K.M. KEEN, *Antenna circular polarization deterioration due to feeder errors.* Microwave Systems News, May 1984, pp 102-108.**

(Re-titled *Feeder Errors Cause Antenna Circular Polarization Deterioration)*

ANTENNAS

Many types of circularly polarized antennas achieve polarization performance by feeding orthogonal radiating elements with a quadrature hybrid. In practice, hybrids are not perfect, and elliptical polarization can result.

Feeder Errors Cause Antenna Circular Polarization Deterioration

By
Keith M. Keen
Keen Associates

Many types of antennas that are designed to work in circular polarization consist of orthogonal pairs of linearly polarized elements fed with equal amplitudes but 90° phase difference, provided by a quadrature hybrid and two equal-length cables between the hybrid and the antenna. A well-known example is the crossed half-wavelength dipole antenna;[1] this is sometimes used as a circular polarization feed for parabolic reflector antennas and also, as shown in Figure 1, for short-backfire antennas. Other examples of orthogonal element-pair antennas fed via a quadrature hybrid for circular polarization are the quadrifilar helix antenna,[2] the four-turn conical spiral,[3] some VHF turnstile antennas,[4] and crossed log-periodic dipole arrays.[5]

With such antennas, if the hybrid is perfect and the feeder cables are exactly the same length, the polarization response in the antenna boresight direction is perfectly circular. If, however, the hybrid does not provide exactly equal amplitudes with an exactly 90° phase difference at its two output ports (as happens in practice), and also if there is an additional phase error in the feeder cables between the hybrid and the antenna, elliptical, rather than circular, polarization results. Figure 2 is a useful set of curves which shows antenna boresight axial ratio as a function of amplitude and phase errors in hybrid and feeder. On the graph, the amplitude error is simply the ratio of the two amplitudes in dB, and the phase error is the departure from 90°.

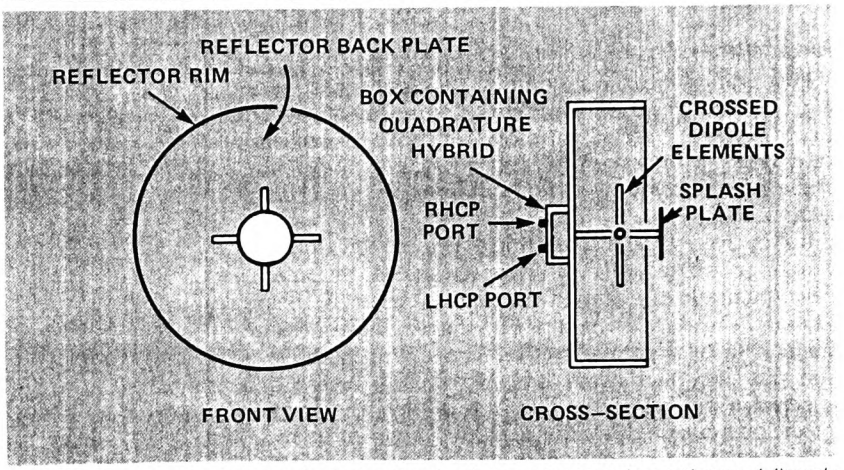

***1. The short-backfire antenna** is one example of an antenna using orthogonal linearly polarized radiating elements (crossed dipoles) fed with a quadrature hybrid, for circular polarization.*

Derivation of Graph

In the far field, the boresight polarization ellipse can be described by two orthogonal linearly polarized field components in a Cartesian coordinate system where the x and y axes are parallel to the antenna elements:[6]

$$E_x = E_1 \sin \omega t$$

$$E_y = E_2 \sin (\omega t + \delta)$$

Keith M. Keen is with Keen Associates, Ifold, West Sussex RH14 OTA, England; Tel.: (0403) 752001.

Continued on page 107

Continued from page 102

E_1 and E_2 are proportional to the two amplitudes at the antenna element pairs, and δ is the phase difference between them. Using the usual polarization ellipse diagram,[6] the following may be defined

$$\gamma = \tan^{-1} \frac{E_2}{E_1} \quad 0° \leq \gamma \leq 90°$$

and

$$\epsilon = \cot^{-1} (\mp AR)$$
$$-45° \leq \epsilon \leq +45°$$

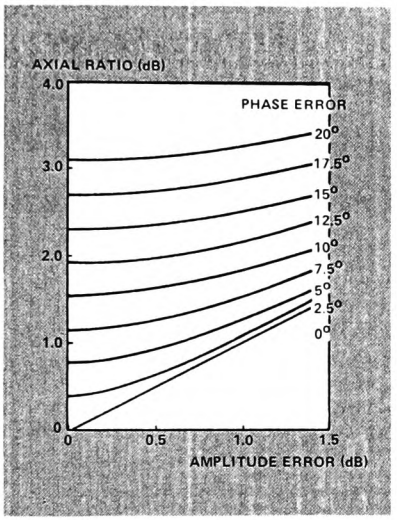

***2. Antenna boresight axial ratio** is shown as a function of hybrid and feeder line phase and amplitude errors. Phase errors are departures from 90°, and may be positive or negative. The amplitude error may also be positive or negative.*

where AR is the axial ratio, i.e., the length of the major ellipse axis over the length of the minor axis. In decibels, this is expressed as

$$AR_{dB} = 20 \log_{10} AR$$

These quantities may be related by the relationship[6]

$$\sin 2\epsilon = \sin 2\gamma \sin\delta$$

and this is the basis of Figure 2.

The above equations are symmetrical in that it does not matter which way the amplitude imbalance occurs, i.e., whether E_2 is greater than E_1 or vice versa, or whether the phase error (a departure from $\delta = 90°$) is positive or negative. This means that the axial ratio is the same for all cases, although the orientation of the polarization ellipse may not be.

Example of Use

A short-backfire antenna, constructed with crossed dipole elements for circular polarization operation as a satellite-terminal antenna over a frequency band of 1550 to 1661 MHz, contains a commercially available quadrature hybrid with an amplitude equality specification of 0.2 dB and a phase departure from 90° specification of ±4°. The cables

between dipoles and hybrid ports are equal to a tolerance equivalent to ±1° in this frequency band. For this antenna then, the worst-case total feeding error would be 0.2 dB in amplitude and 5° in phase, which, from Figure 2, would produce elliptical polarization with an axial ratio of just under 0.8 dB.

Other Uses of the Graph

The graph in Figure 2 is applicable to any situation where a perfectly circularly polarized wave is degraded by amplitude and/or phase difference modifications, relative to two orthogonal planes in the direction of propagation. A good example of this is a perfectly circularly polarized wave obliquely incident on a planar dielectric radome wall as in Figure 3. For oblique incidence at some angle θ, transmission loss in a radome wall is different for parallel-linear and perpendicular-linear polarizations, where "parallel" and "perpendicular" refer to the plane of incidence on the wall. The parallel and perpendicular insert phases (differences between radome wall path length phases and that due to free space) are also different.[1] Thus, the radome wall degrades the circularly polarized wave to an elliptical one, the axial ratio of which may be determined using Figure 2, after calculating the parallel and perpendicular transmission losses and insert phases with the appropriate radome-wall formulas.[1] ■

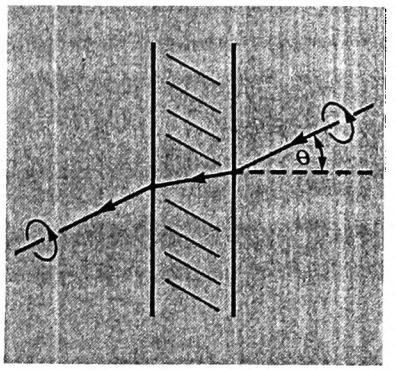

***3. In this circularly polarized wave** incident at angle θ on a planar radome wall, differences in parallel and perpendicular transmission losses and insert phases (relative to plane of incidence) cause degradation to elliptical polarization.*

References

1. H. Jasik, *Antenna Engineering Handbook*, McGraw-Hill Book Co., 1961.
2. C.C. Kilgus, "Resonant Quadrifilar Helix Design," *Microwave Journal*, Dec. 1970, pp. 49-54.
3. C. Ancona, "A Hemispherical Coverage Conical Spiral Antenna and Its Aerospace Applications," *IEEE Conference on Spacecraft Antennas* 1971, pp. 43-48.
4. A. W. Rudge, K. Milne, A.D. Olver, and P. Knight, *The Handbook of Antenna Design*, Vol. 2, Peter Perigrinus Ltd., 1983.
5. Scientific Atlanta Inc., *Instrumentation Products Catalog 1982.*
6. J.D. Kraus, *Radio Astronomy*, McGraw-Hill Book Co., 1966.

Publication P37. K.M. KEEN, *Design criterion for inclined planar radomes on radar corner reflectors used for spaceborne SAR calibration.* Electronics Letters, Vol. 21, No. 12, June 6 1985, pp 548-549.

The corresponding counter value yields

$$T_{RT} = t_4 - t_1 = 2T_D + T_E + T_F \quad (1)$$

and with T_E known by measurement and T_F known by design, the transmission delay T_D between the accessing ground station and the satellite is

$$T_D = \tfrac{1}{2}(T_{RT} - T_E - T_F) \quad (2)$$

and this is readily evaluated by the accessing ground station.

Because the synch-request burst can have a very short duration, then interference with signals transmitted by other operational ground stations is significantly reduced by this initial acquisition method. The time required to achieve initial acquisition is given by eqn. 1. Also, if it is desired to minimise the probability of error in the T_E value, the corresponding estimate may be achieved several times by repeatedly transmitting the synch-request burst for a predetermined number of required measurements.

Tracking: This is the process which enables a ground station to adjust its timing of data transmissions according to the time delay variation between the ground station and the satellite. This delay variation is caused mainly by satellite-orbit perturbation and satellite-clock instability.

Tracking in this new method is achieved by passing synch bursts transmitted down from the satellite through an aperture gate in the ground station. When the ground station is synchronised the synch burst coincides with the centre of the aperture gate, as shown in Fig. 2*a*. Any deviation of the synch-burst falling edge from the aperture reference time T_R is easily measured using a counter-to-count reference clock pulse. For example, if T_D is increased by a time t_d (see Fig. 2*b*), then the counter starts counting up from zero at the end of the T_R period and stops when the synch-burst falling edge is detected.

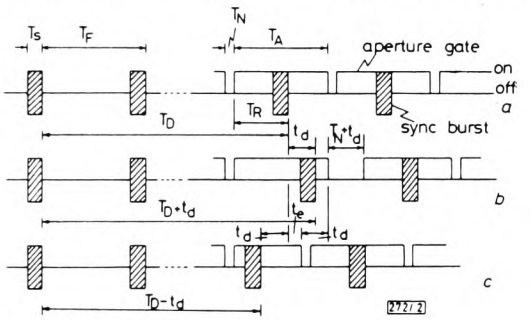

Fig. 2 *Tracking timing diagram*

a Synchronised case
b T_D increased by t_d
c T_D decreased by t_d

The corresponding counter value yields a measure of t_d, and this is added to the next aperture gate off-duration T_N, and thereby adjusts the timing to achieve synchronisation.

Alternatively, if T_D is decreased by a time t_d (see Fig. 2*c*), then the counter starts counting up from zero when the synch-burst falling edge is detected and stops at the end of the T_R period. The corresponding counter value yields a measure of t_d and the aperture gate on-duration is extended beyond the T_R time by a time equal to

$$t_e = T_A - T_R - t_d \quad (3)$$

and with t_d known by measurement and T_A and T_R known by design, the timing is adjusted by turning the aperture gate off at a time equal to $T_R + t_e$, thereby achieving synchronisation. If no synch bursts or more than one synch burst have been detected within the aperture gate, this indicates that the ground station has lost synchronism, and reacquisition (initial acquisition) is then required.

Several advantages of this new approach to tracking are readily apparent, namely (*a*) there is no up-link influence, (*b*) the time required to measure the delay variation between the ground station and the satellite is half of the time required by the synch window method, (*c*) the problem of burst signal intermodulation, which is inherent in the synch window method, is eliminated, and (*d*) a ground station does not lose synchronisation until the delay variation t_d exceeds $|\pm\frac{1}{2}(T_F - T_N - T_S)|$, and consequently the possibility of losing synchronisation is very low, and normally it is only necessary for the satellite to respond to one initial acquisition request, based on a first-come first-served basis. This reduces the satellite hardware and the required reserved space in the synch burst.

L.-K. SHARK
T. J. TERRELL
R. J. SIMPSON

School of Electrical & Electronic Engineering
Lancashire Polytechnic
Preston PR1 2TQ, United Kingdom

26th April 1985

References

1 SCHMIDT, W. G.: 'An on-board switched multiple-access system for millimeter-wave satellites'. Proc. INTELSAT/IEE int. conf. digital satellite commun., Nov. 1969, pp. 399–407
2 RAPUANO, R. A., and SHIMASAKI, N.: 'Synchronisation of earth stations to satellite-switched sequences'. Proc. AIAA 4th commun. satellite syst. conf., Apr. 1972, AIAA paper 72-545
3 JEFFERIS, A. K., and HODSON, K.: 'New synchronisation scheme for communication-satellite time-division multiple-access systems', *Electron. Lett.*, 1973, **9**, pp. 566–568
4 CARTER, C. R., DE BUDA, R., and HAYKIN, S. S.: 'A new system synchronization technique for the switching satellite', *IEEE Trans.*, 1977, **COM-25**, pp. 455–458
5 CARTER, C. R.: 'Survey of synchronization techniques for a TDMA satellite switched system', *ibid.*, 1980, **COM-28**, pp. 1291–1301

DESIGN CRITERION FOR INCLINED PLANAR RADOMES ON RADAR CORNER REFLECTORS USED FOR SPACEBORNE SAR CALIBRATION

Indexing terms: Radar, Radar cross-sections

Larger corner reflector ground targets currently planned for spaceborne SAR calibration will require planar A-sandwich radome covers for weather protection and mechanical stability. The radomes must be inclined with respect to reflector apertures, however, to avoid scattering cross-section uncertainties in the target beam peak direction. A criterion for inclination angle is derived here.

It is currently planned that a number of trihedral corner reflectors as in Fig. 1*a* will be deployed as ground calibration targets for the remote-sensing synthetic-aperture radar system of the ERS-1 satellite, due for launch in 1988. The ground targets will be big, with side dimensions (OA) of 2 m, giving a peak scattering cross-section level (σ_{max}) of just over 43 dB. For calibration of the SAR, accurate knowledge of σ_{max} values will be necessary, and this will be determined by physical measurement of individual targets and computer prediction using methods described recently, which take construction tolerances into account.[1–3] The effect on σ_{max} due to radome covers, which will be necessary for environmental protection and the preservation of known σ_{max} values under most weather conditions, as well as for mechanical stability, will also be determined by computation using well known radome formulas.[4] For electromagnetic, mechanical and cost reasons, a planar A-sandwich construction consisting of two GRP 'skins' and a plastic foam core with optimised dimensions for minimum transmission loss, has been found to be the optimum form of radome. However, if this type of radome is placed directly across the aperture of a corner reflector, large uncertainties in σ_{max} arise, owing to the small but finite reflection coefficient of the planar cover.

A planar radome cover situated across the aperture of a corner reflector as in Fig. 1*a* would be orthogonal to the reflector beam peak boresight direction. Thus, rays incident on the target along the boresight direction would produce a reflected component from the front surface of the radome; i.e.

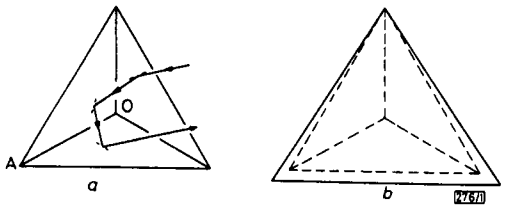

Fig. 1 *Ground target corner reflector configuration (a) and corner reflector with inclined planar radome (b)*

the surface would act as a large plane reflector of low reflectivity. This reflected component would interfere with the main outgoing rays (from the triple reflection process within the corner reflector) and therefore, depending on the phase relationship, could produce a change in σ_{max}. Furthermore, after triple reflection within the corner reflector, before leaving the target there would be another normal incidence traverse of the planar radome, and therefore another reflected component would be generated. This component would, in turn, pass back into the reflector, undergo triple reflection and (ignoring further radome reflections) then be returned along the beam peak direction. There would, therefore, be two normal incidence radome reflection contributions which could interfere with the main returned component from the reflector. As it would not be practical to determine the relative phases associated with these components, it is not possible to predict the change in σ_{max} due to interference; the only prediction that may be made is for the limits in variation in σ_{max} corresponding to fully 'in-phase' and 'out-of-phase' constructive and destructive interference between the three components. Fig. 2 (solid lines) shows these limits of uncertainty in σ_{max} as a function of radome reflection coefficient. Taking into account constructional tolerances, e.g. variations in core thickness, reflection coefficients of the order of -30 dB to -40 dB are appropriate for the proposed ERS-1 target radomes, corresponding to an unacceptable uncertainty in σ_{max} of the order of $\pm 0{\cdot}6$ dB.

To avoid uncertainties in scattering cross-section levels in the beam peak direction, which is where calibration will be made (targets will be carefully positioned in elevation and azimuth) it is proposed that radomes will be inclined in the vertical plane, as shown in Fig. 1*b*. The effect of this would be to divert radome reflection components by an angular separation equal to twice the radome inclination θ from the orthogonal (across aperture) position. It is necessary, however, to find a criterion for choosing θ which, for mechanical reasons, should be as small as possible. A criterion for θ is derived below.

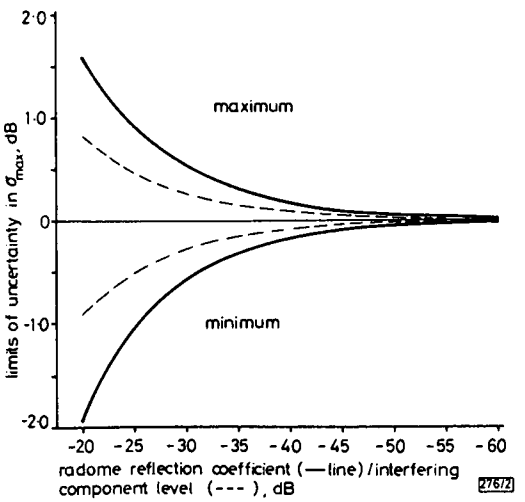

Fig. 2 *Scattering cross-section level uncertainty limits in beam peak direction*

Fig. 3 shows diffraction patterns in the vertical plane through the beam peak boresight in which the reflector diffraction pattern is centred. It is assumed that the two radome reflection components combine 'in-phase' (worst-case situation) to form the lower level diffraction pattern, which

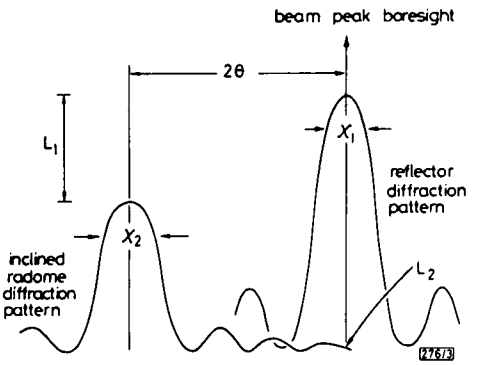

Fig. 3 *Reflector and inclined radome diffraction patterns in elevation plane through main beam boresight*

would be separated from the reflector diffraction pattern by twice the radome inclination angle θ. The criterion for θ must be such as to ensure that L_2, the level of the radome diffraction pattern, is negligibly small in the boresight direction. The broken curves in Fig. 2 show the uncertainty in σ_{max} due to a single interfering component and it may be seen that a level L_2 of -50 dB would give a negligible uncertainty of $\pm 0{\cdot}03$ dB. As it is known that L_1 would be at least -30 dB, a criterion may therefore be formed on the basis of 2θ being sufficiently wide to ensure a radome diffraction pattern sidelobe level of -20 dB. From a knowledge of typical diffraction patterns,[4] this level is normally attained at an angular distance of about four beamwidths from beam peak. Hence θ may be chosen according to

$$2\theta \geq 4\chi_2 \tag{1}$$

where χ_2 is the halfpower beamwidth of the radome diffraction pattern, approximately given by[4]

$$\chi_2 \simeq \frac{60^\circ}{a_\lambda} \tag{2}$$

where a_λ is the appropriate linear dimension in wavelengths (the vertical radome dimension). Hence the required criterion is

$$\theta \geq \frac{120^\circ}{a_\lambda} \tag{3}$$

Acknowledgments: Thanks are due to A. D. Woode and R. V. Gelsthorpe of ESTEC, Netherlands, for useful discussions. This work was carried out under ESA contract 5963/84/NL/GM(SC).

K. M. KEEN

Keen Associates
Ifold, West Sussex RH14 0TA, United Kingdom

29th April 1985

References

1 KEEN, K. M.: 'New technique for the evaluation of the scattering cross-sections of radar corner reflectors', *IEE Proc. H, Microwaves, Opt. & Antennas*, 1983, **130**, pp. 322–326

2 KEEN, K. M.: 'Fast algorithm for the exact determination of the mapped effective areas of trihedral corner reflectors', *Electron. Lett.*, 1983, **19**, pp. 1014–1015

3 KEEN, K. M.: 'Prediction of scattering cross-section reductions due to plate orthogonality errors in trihedral radar reflectors', *ibid.*, 1983, **19**, pp. 115–117

4 JASIK, H. (Ed.): 'Antenna engineering handbook' (McGraw-Hill Book Co., 1961)

Publication P38. K.M. KEEN, *Simple pattern prediction procedure for satellite antenna contoured beams.* Microwave Journal, October 1985, pp 149-153.

Simple Pattern Prediction Procedure for Satellite Antenna Contoured Beams

K.M. Keen
Keen Associates
Ifold, West Sussex, England

A relatively simple satellite antenna contoured beam prediction procedure, sufficiently accurate for many applications, is presented. The method is intended for early system studies or planning, prior to detailed investigation where more sophisticated procedures based on detailed antenna designs would be used. The expressions given here are easily transformed to a small computer program that may be run on a personal computer and requires minimum inputs.

Introduction

Many communications and direct broadcast satellites have contoured beam downlink antenna systems in order to maximize flux density over a given geographic area. The usual type of antenna is an offset parabolic reflector system with an array of small aperture feeds; the contoured beam is synthesized by the addition of spatially separated constituent beams of the same polarization, usually with equal phases.[1]

There are very accurate and sophisticated ways of predicting patterns for fully specified antenna systems,[1,2] but a simple "first order" technique of pattern shape prediction is more useful for initial studies by system planners who would not wish to undertake a detailed antenna design at that stage. This paper describes such a simplified technique.

Figure 1 shows the coordinate system relevant to the procedure; the OXYZ axes are conventional cartesian, with the OZ axis originating at the "center" of the contoured beam. It is assumed that the antenna system consists of a circular projected aperture reflector and that there are N feeds, each of which produces a circularly symmetric beam of the same half power beamwidth x. Relative to the axes shown, the n^{th} beam would be boresighted on direction (θ_n, ϕ_n) in conventional spherical coordinates (direction OP).

The direction OQ represents some general observation position (θ, ϕ). The pattern prediction procedure is essentially a synthesis technique where the number of beams and their relative angular positions are specified and the resulting contoured beam pattern is generated. With a computer program based on the method, it is necessary for the user to specify only the following inputs:

- Antenna reflector diameter d and wavelength λ or constituent beam half power beamwidth χ
- The number of constituent beams, N
- The angular positions of each beam (θ_n, ϕ_n)
- The relative amplitude a_n, associated with each beam.

Contoured Beam Synthesis

The first step is to establish an expression for representing any of the N circularly symmetric constituent beams. In practice, contoured beam satellite antenna require feed clusters with closely spaced feeds for correct beam positioning. Because the feeds are close, they have to have small apertures; this results in relatively wide primary antenna beamwidths and therefore relatively high reflector edge illumination values, a figure of -5 dB being typical. For a circular aperture of diameter d, a -5 dB edge taper and a wavelength λ, the far zone electric field expression is[3]

$$E(\theta_n') = \frac{0.562\, F_1(\theta_n') + 0.219\, F_2(\theta_n')}{0.781} \quad (1)$$

where

$$F_1(\theta_n') = \frac{2\, J_1(\pi d_\lambda \sin\theta_n')}{\pi d_\lambda \sin\theta_n'} \quad (2)$$

and

$$F_2(\theta_n') = \frac{8\, J_2(\pi d_\lambda \sin\theta_n')}{(\pi d_\lambda \sin\theta_n')^2} \quad . \quad (3)$$

[Continued on page 150]

[From page 149] KEEN

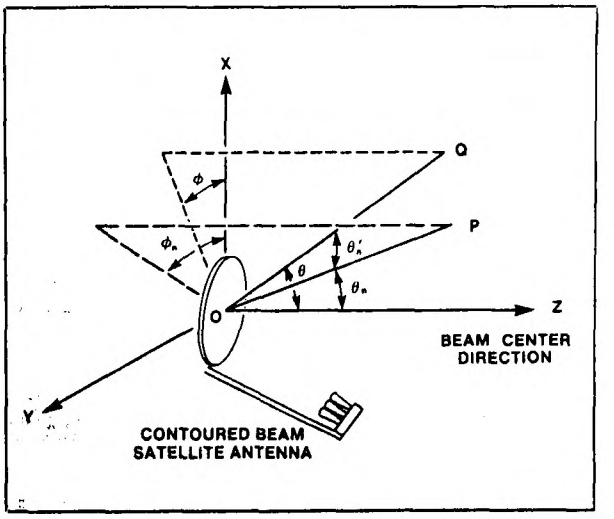

Fig. 1 Cartesian/spherical coordinate system for contoured beam prediction procedure.

These equations are in terms of the n^{th} beam and the angle from the n^{th} beam boresight direction. J_1 and J_2 are Bessel functions, and for computational purposes, it should be noted that both functions given in Equations 2 and 3 go to 1 when θ'_n goes to 0. The parameter d_λ is the ratio of d and λ. If constituent beam half power beamwidth is to be used as an input rather than reflector diameter and wavelength, a value of d_λ for Equations 2 and 3 may be determined from the antenna beamwidth approximation expression appropriate for the -5 dB illumination taper:

$$\chi = \frac{65^\circ}{d_\lambda} \tag{4}$$

where χ is in degrees.

The next step is to interpret the angles θ'_n for each beam in terms of the general direction (θ, ϕ) and the constituent beam boresight direction represented by (θ_n, ϕ_n) for the n^{th} beam. From a well known theorem in solid geometry which relates the angle between two vectors to their direction cosines, it may easily be shown that

$$\theta'_n = \cos^{-1}[\sin\theta \sin\theta_n (\cos\phi \cos\phi_n + \sin\phi \sin\phi_n) + \cos\theta \cos\theta_n]. \tag{5}$$

Finally, the synthesized contoured beam field pattern is found by the summation of the N constituent beams with their relative amplitude values, i.e.

$$E_s(\theta,\phi) = \sum_{n=1}^{N} a_n E_n(\theta'_n). \tag{6}$$

The corresponding normalized power pattern (in dB) is then given by

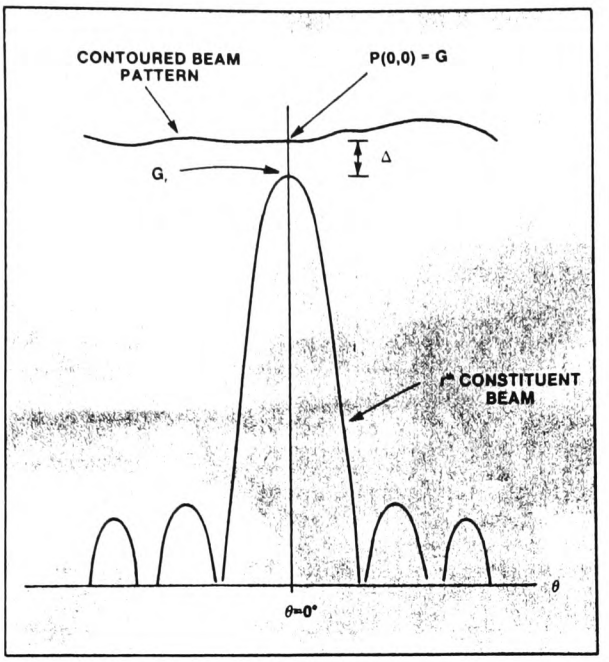

Fig. 2 Gain and pattern level relationships between contoured beam and r[th] constituent beam, boresighted at $\theta = 0°$.

$$P(\theta,\phi) = 10 \log_{10} \left[\frac{E_s^2(\theta,\phi)}{E_s^2(0,0)} \right] \quad (7)$$

where normalization is referenced to the power level at $\theta = 0°$, $\phi = 0°$.

Gain and EIRP Referencing

Contoured beam patterns given by Equation 7 are in dB relative to the power level at $\theta = 0°$, $\phi = 0°$ (P(0,0) in Figure 2). It is of greater interest, however, to know contoured beam pattern levels in terms of antenna gain and satellite EIRP. Expressions that may be used to relate $P(\theta,\phi)$ to these parameters are given. A well known expression for the gain of an antenna with a single circularly symmetric beam with half power beamwidth ϵ (in degrees) is [3]

$$\text{gain} = \frac{26{,}000}{\epsilon^2}$$

From this it may be shown that if the r[th] constituent beam has its boresight at $\theta = 0°$, $\phi = 0°$ as in Figure 2, then the gain G, relating to this beam is (in dB)

$$G_r = 10 \log_{10} \left[\frac{26{,}000\, a_r^2}{x^2 \sum_{n=1}^{N} a_n^2} \right] \quad (8)$$

Only if the power level (0,0) corresponds to gain G in decibels is it necessary to establish the level difference Δ (in decibels) in Figure 2, to give G in terms of G_r and

[Continued on page 152]

[From page 151] **KEEN**

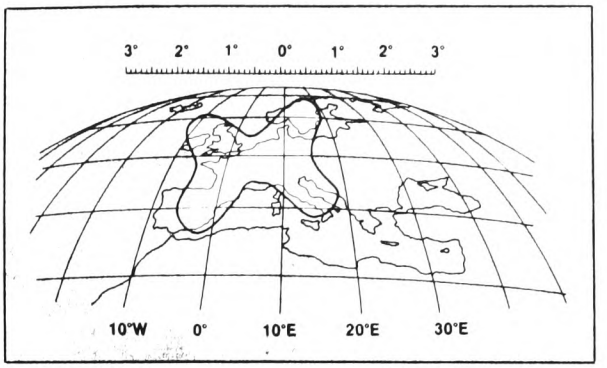

Fig. 3 33 dB gain plot of 2 m diameter satellite antenna contoured beam at 12 GHz.

Δ. It is easy to show that

$$\Delta = 10 \log_{10} \frac{\left[\sum_{n=1}^{N} a_n E_n(0)\right]^2}{a_i^2 E_i^2(0)} \quad (9)$$

and therefore

$$G = G_i + \Delta \quad (10)$$

giving an antenna gain reference level for P(0,0). If the satellite transmitted power level W (in dBW) also is known, then the EIRP at $\theta = 0$, $\phi = 0$ is[4]

$$EIRP = G + W \quad (11)$$

Example

Figure 3 shows a computed contoured beam shape plotted on the usual type of orthographic projection map that corresponds to a particular satellite position in the geostationary orbit. The computation was for a 2 m diameter satellite antenna at 12 GHz with five constituent beams as described in Table 1; the contour line is at a gain level of 33 dB.

Figure 4 shows the five constituent beams (-3 dB levels are plotted) and their positions relative to the cartesian axes system and the chosen beam center.

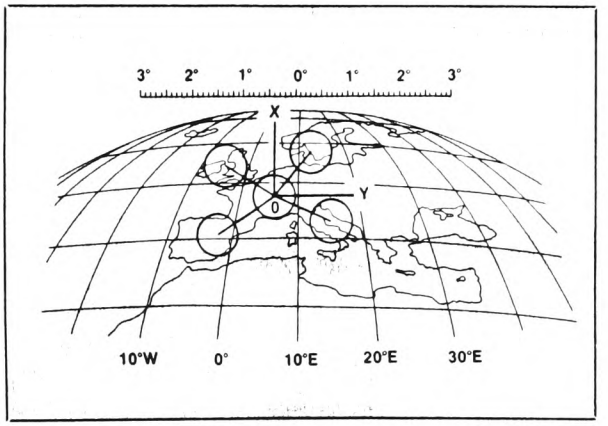

Fig. 4 Angular positions and half power levels of the five constituent beams in the contoured beam shown in Figure 3.

BEAM PARAMETER VALUES RELATING TO CONTOURED BEAM SHOWN IN FIGURE 3

n	Constituent Beam	θ_n	ϕ_n	a_n
1	Beam 1, Central Europe	0	0	10
2	Beam 2, Sweden	1.1°	40°	1.0
3	Beam 3, Italy	1.2°	113°	1.0
4	Beam 4, Spain	1.3°	236°	1.0
5	Beam 5, UK	1.1°	302°	1.0

Conclusion

The procedure described here is relatively simple, yet accurate enough for many applications. It does not take into account antenna performance degradations due to beam squinting such as constituent beam gain reductions, and sidelobe level changes, or pattern distortions due to mutual coupling between feeds. Still, these effects are generally small and may be neglected if only a first order prediction is required. Also, the procedure as given here is only for "in-phase" beams as, in practice, most systems of this sort are. The expressions may be easily modified, however, to give constituent beam phase as a variable, along with beam amplitude.

Acknowledgment

The procedure described here is based on part of a subcontract study carried out for Communication Systems Research Ltd. of Ilkley, Yorkshire, England in 1984. ■

References

1. Rusch, W.T., "Reflectors With Contoured Beams," in *The Handbook of Antenna Design*, Vol. 1, ed. by A.W. Rudge et al, Peter Perigrinus Ltd., 1982.
2. "Study of Software for Optimization of Contoured Beam Reflector Antennas," TICRA A/S Final Report No. S-128-02, under ESTEC Contract No. 4188/77/NL/DG(SC), January 1981.
3. Stutzman, W.L., Thiele, G.A. "Antenna Theory and Design," John Wiley and Sons Inc., 1981.
4. Sinnema, W., "Electronic Transmission Technology," Prentice-Hall Inc., 1979.

Since 1982, **Keith M. Keen** *has run a small microwave antenna business. Keen Associates, in the south of England. The entire spectrum of antenna engineering work is undertaken, varying from design, production and testing to software development and consultancy.*

Keen holds a BSc degree from the University of London and an MSc degree from the University of Manchester. He has authored more than 40 publications on antenna and microwave engineering.

Publication P39. **K.M. KEEN,** ***Method permits gain estimation for very wide beam satellite terminal antennas.*** **Microwave Systems News, October 1985, pp 83-87.**

Method Permits Gain Estimation for Very-Wide-Beam, Satellite-Terminal Antennas

By
K.M. Keen
Keen Associates

Ideal pattern analysis reveals the gain vs. coverage relationship for very-wide-beam, satellite-terminal antennas.

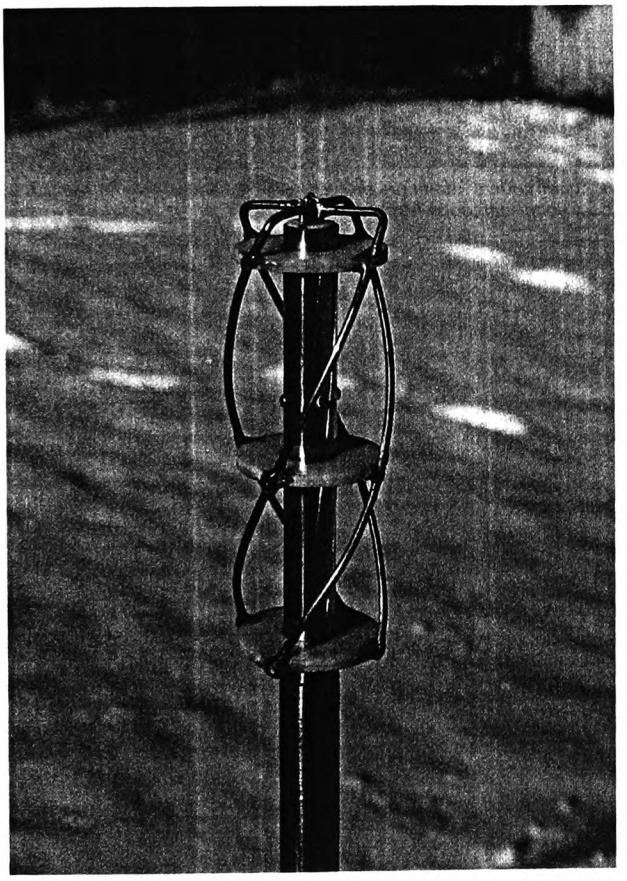

1. This experimental very-wide-beamwidth quadrifilar-helix antenna was developed for low-gain, maritime satellite-terminal applications.

There is considerable interest in very-wide-beamwidth, circularly polarized antennas for satellite-terminal applications at L-band frequencies. One reason for this is the anticipation of the NAVSTAR global positioning system, which will consist of 18 satellites in six orbital planes. Ground receivers will have to deal with multiple satellite signals from anywhere in the sky; and therefore hemispherical-coverage-type antennas will be required. A wide-beamwidth antenna for this application was described in the November 1984 issue of *Microwave Systems News*.[1]

There is also growing interest in simple, low-cost, low-data-rate, satellite-communication terminals for small ships and for "land-mobiles" such as long-distance trucks. For example, the European Space Agency has a program called PROSAT for the promotion of small-terminal techniques for maritime, land-mobile, and aeronautical applications.[2] Some of these applications require very-wide-beam antennas. In particular, small ships liable to pitching and rolling in rough seas would require antennas with coverages well in excess of hemispherical, to ensure viable communication links over a range of geographical positions. Figure 1 shows an experimental model of a small ship-terminal antenna that was investigated recently. In one form, with an inverted metallic cone above it, a beamwidth of 240° was achieved.

One problem associated with these wide-coverage antennas, particularly for systems-planning engineers, is to predict what sort of antenna gain is achievable for a given coverage. The well-known numerical-approximation expression of gain as a function of beamwidth, which for a symmetrical beam of half-power width χ is[3]

$$\text{gain} = \frac{26{,}000}{\chi^2} \qquad \text{(A)}$$

This expression only applies to "pencil" beams, and is not appropriate for beamwidths of the order of 180°. For this reason, a useful gain vs. coverage graph has been produced for very-wide-beam terminal antennas (Fig. 2).

The gain vs. coverage graph is based on directivity computations of ideal radiation patterns (Fig. 3), using the coordinate system shown in Figure 4. Patterns are assumed to be symmetrical about the antenna main axis, and have a constant pattern level down to $\theta = \theta_o$. The beamwidth is therefore 2_o. The gain vs. coverage graph has been prepared for four values of back-lobe/side-lobe level: −10 dB, −15 dB, −20 dB, and no back lobe. Also, an overall antenna loss of a quarter of a decibel has been assumed. Details of the analysis from which the coverage graph was prepared are given in the following section. This also contains Equation 5, a useful expression for easy directivity computations of wide-beam, symmetrical radiation patterns with non-ideal shapes.

K.M. Keen is with Keen Associates, Ifold, Loxwood, West Sussex RH14 OTA, England; Tel: 44 403 752001.

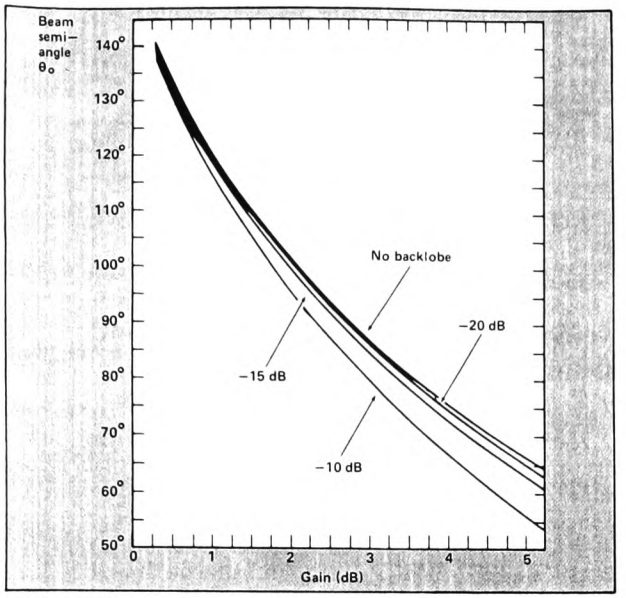

2. The ideal beam semi-angle θ_0 is shown as a function of gain for various back-lobe/side-lobe levels (assumes 0.25-dB loss).

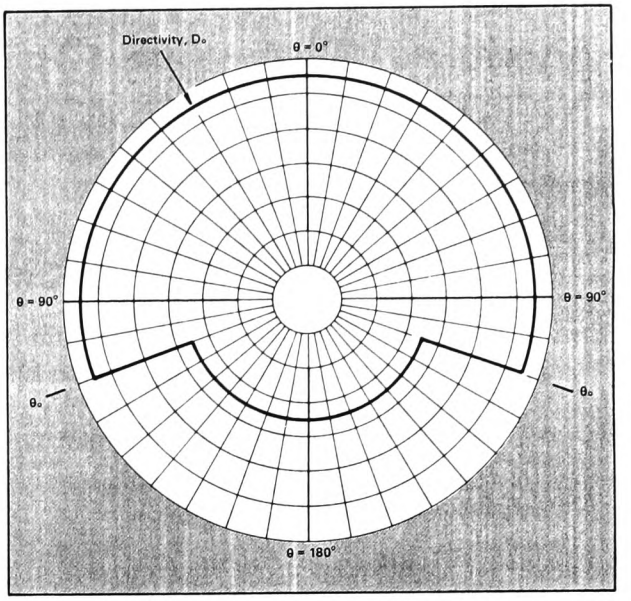

3. In this ideal radiation pattern with coverage to angle θ_0, the back-lobe/main-lobe level ratio is k.

The gain vs. coverage graph in Figure 2 is easy to use and is applicable in a number of ways. One use is to show what sort of coverage is possible for a given gain level. For example, a gain level of 3 dB corresponds to a beam semi-angle range of 80° to 87°, depending on back-lobe level. This gives a good indication of what is achievable with real antennas such as conical spirals and quadrifilar helices when developed for this gain value. Another use is to show what sort of gain is achievable for specified coverages. For example, for a 240° beamwidth coverage for a particular ship-terminal antenna, a constant main-beam-level antenna could be expected to have a gain of a little less than one dB.

Gain Calculation Expressions

Referring to the spherical coordinate system shown in Figure 4, the definition of antenna gain in direction, θ, ϕ is[4]

$$G(\theta,\phi) = \frac{4\pi U(\theta,\phi)}{P_{IN}} \qquad (1)$$

where $U(\theta, \phi)$ is radiation intensity in direction θ, ϕ and P_{IN} is the total power supplied to the antenna. Gain is therefore a function of both radiation-pattern shape and antenna losses. Another related parameter is *directivity* in direction θ, ϕ, which is in terms of total radiated power P_T (rather than input power) and is therefore dependent on pattern shape only.

$$D(\theta,\phi) = \frac{4\pi U(\theta,\phi)}{P_T} \qquad (2)$$

Directivity and gain* are related by antenna efficiency η,

$$G(\theta,\phi) = \eta D(\theta,\phi)$$

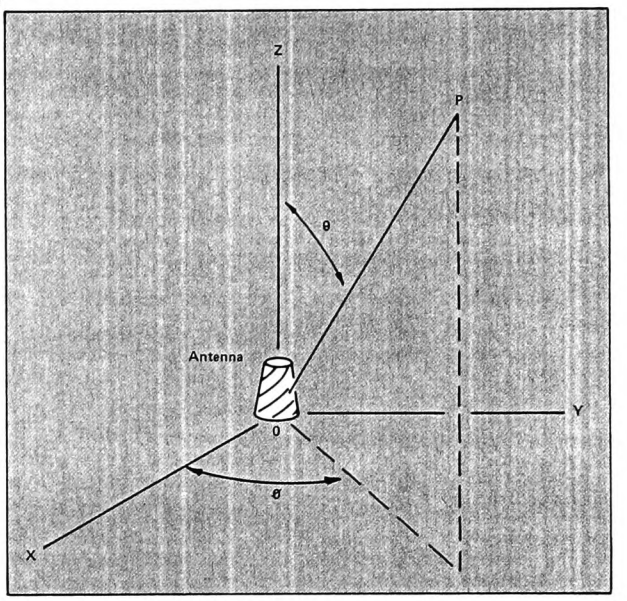

4. The gain vs. coverage graph in Figure 2 uses this coordinate system.

Equation 2 may be rewritten

$$D(\theta,\phi) = \frac{4\pi U(\theta,\phi)}{\int_0^{2\pi}\int_0^{\pi} U(\theta,\phi)\sin\theta\,d\theta\,d\phi} \qquad (4)$$

Sometimes the terms "directive gain" and "power gain" are used instead of "directivity" and "gain," but this can be confusing. The terms used above are, however, the ones in most common use.[4,5]

This expression simplifies, as only radiation patterns with symmetry about the OZ axis in Figure 4 are being considered. Also, radiation intensity is proportional to radiation-pattern relative power level $P(\theta)$ (as would be seen on a measured radiation-pattern diagram), and therefore Equation 4 reduces to

$$D(\theta) = \frac{2P(\theta)}{\int_0^{\pi} P(\theta) \sin\theta d\theta} \qquad (5)$$

This is a useful expression for computing the directivity of symmetric beam antennas from a measured radiation pattern.[5] Pattern levels are sampled at convenient intervals of θ, and a numerical integration is made using Simpson's rule.

Figure 3 shows the ideal pattern that is considered here. The pattern has symmetry about the OZ axis and therefore is independent of ϕ. It is defined by

$$P(\theta) = 1 \qquad 0 \leqq \theta \leqq \theta_0$$

$$P(\theta) = k \qquad \theta_0 < \theta \leqq \pi$$

where k is some back-lobe level relative to the main beam level of 1. The directivity, corresponding to $P(\theta) = 1$, is D_o.

Putting these values into Equation 5 and integrating gives

$$\theta_0 = \cos^{-1}\left[\frac{1 + k - \left(\frac{2}{D_0}\right)}{1 - k}\right] \qquad (6)$$

from which the graph shown in Figure 2 was prepared. Equation 6 was used to compute pattern-coverage limits for given directivity values and for back-lobe levels of −10 dB, −15 dB, −20 dB, and for k = 0. To convert from directivity to gain, antenna losses of 0.25 dB were assumed—an appropriate figure for a small antenna such as a conical spiral or quadrifilar helix. ■

References

1. R. Eschenbach and R. Helkey, "Performance/Cost Ratio Optimized for GPS Receiver Design," *Microwave Systems News*, November 1984, pp. 43-52.
2. R. Rogard, "The PROSAT Programme," *European Space Agency Bulletin*, November 1982, pp. 75-80.
3. W.L. Stutzman and G.A. Thiele, *Antenna Theory and Design* (John Wiley and Sons, Inc., 1981).
4. J.S. Hollis, T.J. Lyon, and L. Clayton, *Microwave Antenna Measurements* (Scientific Atlanta, Inc., 1970).
5. K.M. Keen, "Computer Program System for Evaluating Partial and Total Antenna Directivities from Measured Data," *Proc. IEE*, Vol. 124, No. 12 (December 1977), pp. 1117-1120.

Publication P40. **K.M. KEEN,** ***Simple impedance transforming feed system for low-gain quadrifilar and bifilar satellite terminal antennas.*** **Electronics Letters, Vol. 24, No. 5, March 1988, pp 278-279.**

period was 0·2 ms. The threshold current was 250 mA. The maximum output power was as high as 210 mW, although it was limited by the capacity of the current source used. The output power was increased by a factor of 1·4 by the AR coating.

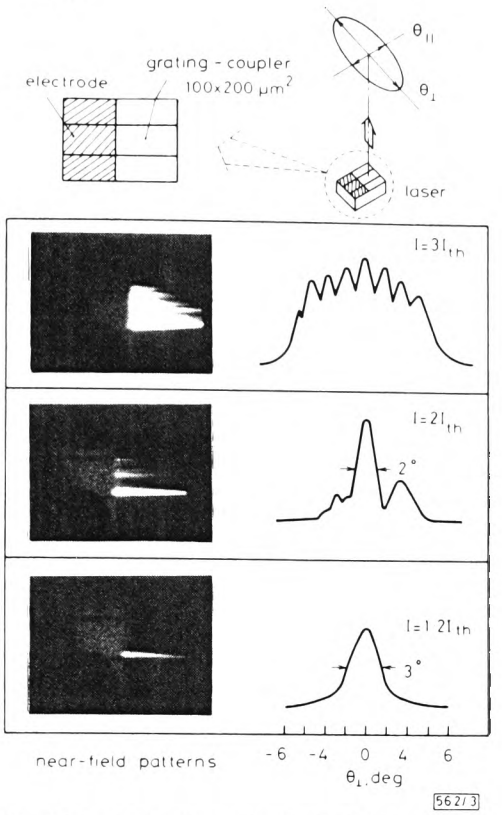

Fig. 3 *Near-field and corresponding far-field patterns perpendicular to cavity at various injection levels*

Near-field patterns were observed by an infra-red camera

Fig. 3 shows the near field and the corresponding far field patterns perpendicular to the cavity at various injection levels. A nonuniform spatial power distribution was observed across the cavity. Its full width at half maximum (FWHM) value (w_p) was 15 μm at $I = 1{\cdot}2I_{th}$, and the corresponding FWHM beam divergence angle ($\theta_\perp$) was 3°, which agrees well with that calculated as emitted from the uniform 15 μm aperture. At $I = 2I_{th}$, w_p was increased to 22 μm, and $\theta_\perp$ was decreased to 2°. However, weak lateral submodes were observed, which caused the other peak in the far field pattern. For $I \gtrsim 3I_{th}$, the lateral modes were completely multimoded, and therefore multilobed far field patterns were observed, and the FWHM angle was increased. We should optimise the stripe width to obtain a stable, narrow beam divergence angle.

The laser oscillated in a single longitudinal mode ($\lambda \simeq 866$ nm) at low excitation levels ($I \lesssim 1{\cdot}2I_{th}$). For $I > 1{\cdot}2I_{th}$, however, multilongitudinal mode oscillation was observed mainly owing to the instability of the lateral mode. The FWHM beam divergence angle ($\theta_\parallel$) parallel to the cavity was increased by the multimode oscillation. The observed angles at $I = 1{\cdot}2I_{th}$, $2I_{th}$, and $3I_{th}$ were 0·22°, 0·32°, and 0·72°, respectively. These values agree well with those calculated taking account of the multilongitudinal mode oscillation.

Conclusion: We have fabricated an SE MQW DFB laser with an integrated broad area grating-coupler. A narrow beam divergence angle of 2° × 0·32° (at $I = 2I_{th}$) and a maximum output power of 210 mW were obtained. The optimisation of the stripe width will lead to a stable, narrow beam divergence angle.

S. NODA
K. KOJIMA
K. KYUMA

Central Research Laboratory
Mitsubishi Electric Corporation
8-1-1, Tsukaguchi-Honmachi
Amagasaki, Hyogo 661, Japan

8th December 1987

References

1 EVANS, G. A., HAMMER, J. M., CARLSON, N. W., ELIA, F. R., JAMES, E. A., and KIRK, J. B.: 'Surface-emitting second order distributed Bragg reflector laser with dynamic wavelength stabilization and far-field angle of 0·25', *Appl. Phys. Lett.*, 1986, **49**, pp. 1200–1202

2 MITSUNAGA, K., KAMEYA, M., KOJIMA, K., NODA, S., KYUMA, K., HAMANAKA, K., and NAKAYAMA, T.: 'CW surface-emitting grating-coupled GaAs/AlGaAs distributed feedback laser with very narrow beam divergence', *Appl. Phys. Lett.*, 1987, **50**, pp. 1788–1790

3 KOJIMA, K., NODA, S., MITSUNAGA, K., KYUMA, K., and HAMANAKA, K.: 'Continuous wave operation of a surface-emitting AlGaAs/GaAs multiquantum well distributed Bragg reflector laser', *Appl. Phys. Lett.*, 1987, **50**, pp. 1705–1707

4 NODA, S., KOJIMA, K., MITSUNAGA, K., KYUMA, K., HAMANAKA, K., and NAKAYAMA, T.: 'Monolithic integration of an AlGaAs/GaAs multiple quantum well distributed feedback laser and a grating coupler for surface emission', *Appl. Phys. Lett.*, 1987, **51**, pp. 1200–1202

5 NODA, S., KOJIMA, K., MITSUNAGA, K., KYUMA, K., HAMANAKA, K., and NAKAYAMA, T.: 'Ridge waveguide AlGaAs/GaAs distributed feedback lasers', *IEEE J. Quantum Electron.*, 1987, **QE-23**, pp. 188–193

SIMPLE IMPEDANCE TRANSFORMING FEED SYSTEM FOR LOW-GAIN QUADRIFILAR AND BIFILAR SATELLITE TERMINAL ANTENNAS

Indexing terms: Antennas, Antenna feeders, Satellite links

An impedance transforming balun feeder system has been devised for low-gain antennas such as quadrifilar helices and spirals, consisting of four coaxial cables and a microstrip circuit. The arrangement allows physically orthogonal 'balanced pair' outputs with quadrature phasing, in space limited configurations.

There is currently great interest in wide beam circularly polarised L-band antennas, for low data rate, low cost satellite earth station applications, and also for satellite GPS (global positioning system) receivers. Common antennas for these applications are quadrifilar helices,[1] bifilar conical spirals,[2] and quadrifilar conical spirals.[3] These radiators require quite complex feed systems. For example, a quadrifilar helix antenna has four, resonant length, wire radiating elements; these are fed as two orthogonal balanced mode pairs in phase quadrature. Thus the feed system must provide an output of two orthogonal sets of balanced lines with the correct impedances for matching to the antenna radiating elements, with relative phases in quadrature, and with equal amplitudes, from an input of (usually) a single 50 Ω connector and coaxial cable. The customary solution for feeding a quadrifilar helix antenna is to incorporate a phase quadrature device such as a 3 dB hybrid or branch-line coupler (realised in microstrip or stripline) connected to an orthogonal pair of impedance transforming baluns via two coaxial cables, each impedance transforming balun consisting of a coaxial cable quarter wavelength balun, followed by a quarter wavelength 'twin-wire' impedance transformer. Such an arrangement is quite complex mechanically, and involves the assembly of a number of critical tolerance parts into a small volume (e.g. a central balun shielding tube). An alternative, mechanically simpler, feed arrangement has been devised and is described below. It is applicable to a wide range of quadrifilar and bifilar element antennas, with impedances ranging from about 40 to 250 Ω.

Fig. 1 shows the feed system for a quadrifilar antenna. It consists, basically, of four coaxial cables, plus a small microstrip board in which a 50 Ω input line is transformed to a lower impedance line with a simple quarter wavelength section transformer. At the top of the feed system formed by the four cables, i.e. at the antenna element feed point, each

diametrically opposed pair of cables forms a balanced output. That is, cables 1 and 3 have antiphase lengths, as do cables 2 and 4. With the outer conductors of the cables shorted, the inner conductors of each opposed pair provide a balanced 'twin-wire' output line with twice the impedance of that of one cable.[4] Thus cables 1 and 3 provide one balanced output, and cables 2 and 4 provide a second, physically orthogonal balanced output which, because of the cable lengths, is in phase quadrature with the first pair. The lower ends of the four cables are simply joined directly to the microstrip board (as a four way microstrip to coaxial line power divider) at the end of the low impedance section line; the width of this line is chosen to give an impedance of one quarter of the coaxial cable impedance, to preserve impedance match at this interface. The impedance of the coaxial cables is chosen to be as near as possible to half the antenna impedance (measured in terms of pairs of radiating elements).

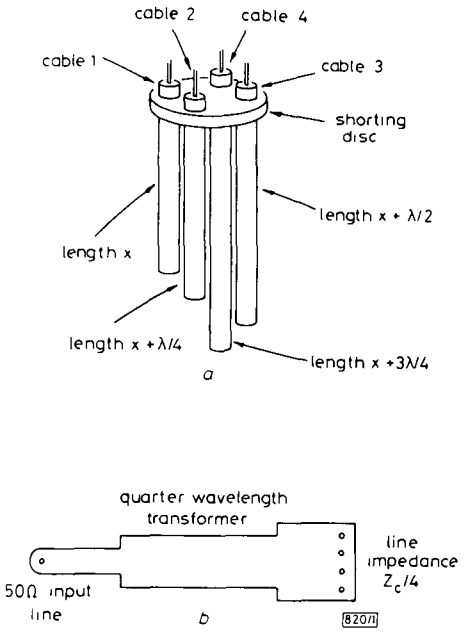

Fig. 1 *Feed system*

a Arrangement of coaxial cables
b Microstrip line configuration
λ represents wavelength in cable medium

Fig. 2 shows the measured impedance match of a wide beamwidth quadrifilar element satellite terminal antenna with a feed system as described above. The antenna is designed to operate over the well known L-band satellite communications frequencies, i.e. 1530 to 1545 MHz downlink and 1631·5 to 1646·5 MHz uplink; also with a GPS receive capability at the 1575·42 MHz L1 frequency. It can be seen that the antenna VSWR is better than 1·2 : 1 over the frequency ranges of interest.

A simpler form of the above described feed system is applicable to bifilar element antennas. Here, only two cables are necessary, corresponding to cables 1 and 3 in Fig. 1*a*. The microstrip line would have an output linewidth corresponding to half the cable impedance, for impedance matching at this interface.

To conclude, the feed system is a relatively simple arrangement, applicable to a number of quadrifilar and bifilar element antenna types. Microwave frequency coaxial cables are available with a range of impedance values, e.g. 25, 35, 50, 75 and 95 Ω, and it is therefore possible to achieve good impedance match performance with antenna impedances varying from less than 50 Ω to over 200 Ω.

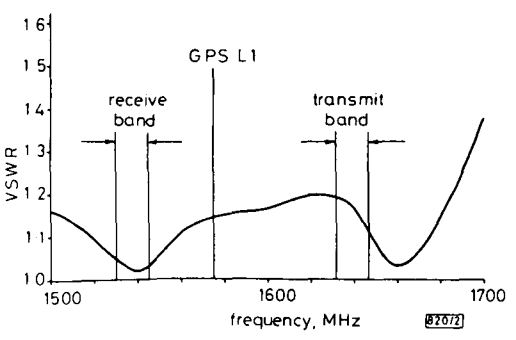

Fig. 2 *Impedance characteristics of a wide beamwidth quadrifilar satellite terminal antenna, measured at its coaxial input connector*

K. M. KEEN
Keen Associates
Ifold, W. Sussex RH14 0TA, United Kingdom

19th January 1988

References

1 KILGUS, C. C.: 'Resonant quadrifilar helix design', *Microwave J.*, December 1970, pp. 49–54
2 DYSON, J. D.: 'The characteristics and design of the conical log-spiral antenna', *IEEE Trans.*, 1965, **AP-13**, pp. 488–499
3 ANCONA, C.: 'A hemispherical coverage conical spiral antenna and its aerospace applications'. IEE Conference 'Spacecraft Antennas' 1971, pp. 43–48
4 DYSON, J. D., and GINOVSZKY, R.: 'Balanced transmission line measurements using coaxial equipment', *IEEE Trans.*, 1971, **MTT-19**, pp. 94–96

STRAINED GaInAs-BASE HOT ELECTRON TRANSISTOR

Indexing terms: Semiconductor devices and materials, Transistors

A hot electron transistor (HET) which has a strained GaInAs base and a graded AlGaAs collector barrier was grown on a GaAs substrate by metalorganic chemical vapour deposition. In this device, the difference in energy levels between the *L*-band minima of the base and the top of the collector barrier is wider than that in GaAs-base HETs, which results in a common emitter current gain β (collector current/base current) as high as 30.

Hot electron transistors (HETs) are attractive as high-speed devices since only high-speed electrons (ideally, only ballistic electrons)[1,2] pass to the collector. The current gain of HETs is, however, not yet large enough for practical application. Recently, we obtained evidence that electron transfer from the Γ to the *L*-band minima causes a large reduction in the transfer ratio α (collector current I_c/emitter current I_e) in AlGaAs/GaAs HETs.[3] Since GaInAs has a wider $\Gamma - L$ valley separation than GaAs, the use of GaInAs as the base material should increase the current gain. It has been reported[4] that $Ga_{0.5}In_{0.5}As$-base HETs lattice matched to InP have higher current gains than AlGaAs/GaAs HETs. It is worth noting here that if severe scattering (other than intervalley scattering) is not present, a high current gain can be expected when the $\Gamma - L$ valley separation is made slightly wider than that of GaAs. In this letter, we report on a remarkable increase in current gain achieved by replacing the GaAs base of an AlGaAs/GaAs HET with a lightly doped strained $Ga_{0.8}In_{0.2}As$ base.

Fig. 1 shows the schematic structure of the device. The device was grown by metalorganic chemical vapour deposition (MOCVD) at 730°C. An *n*-GaAs collector layer was first grown on an n^+-GaAs substrate, followed by an $Al_{0.3}Ga_{0.7}As$ collector barrier 140 nm thick, an $Al_xGa_{1-x}As$ graded layer 10 nm thick, a strained $Ga_{0.8}In_{0.2}As$ base 30 nm thick, an $Al_{0.3}Ga_{0.7}As$ emitter barrier 15 nm thick, and an *n*-GaAs emitter 200 nm thick. The doping density in the emitter, base, and collector is 5×10^{17} cm^{-3}. The Al content x in the graded $Al_xGa_{1-x}As$ layer was varied from $x = 0$ to $x = 0.3$. This grading layer was introduced so that the top of the collector barrier would be effectively lowered as the collector bias V_{cb} was increased. A schematic band diagram of the device is

Publication P41. **K.M. KEEN,** ***Developing a Standard-C antenna.*** **Microwave Systems News, June 1988, pp 52-54.**

DESIGN NOTE

Developing a Standard-C Antenna

A quadrifilar-helix antenna with helical radiators on a flexible printed-circuit laminate, and a printed-microstrip feed system, is designed for standard-C satellite-communications terminals on small ships.

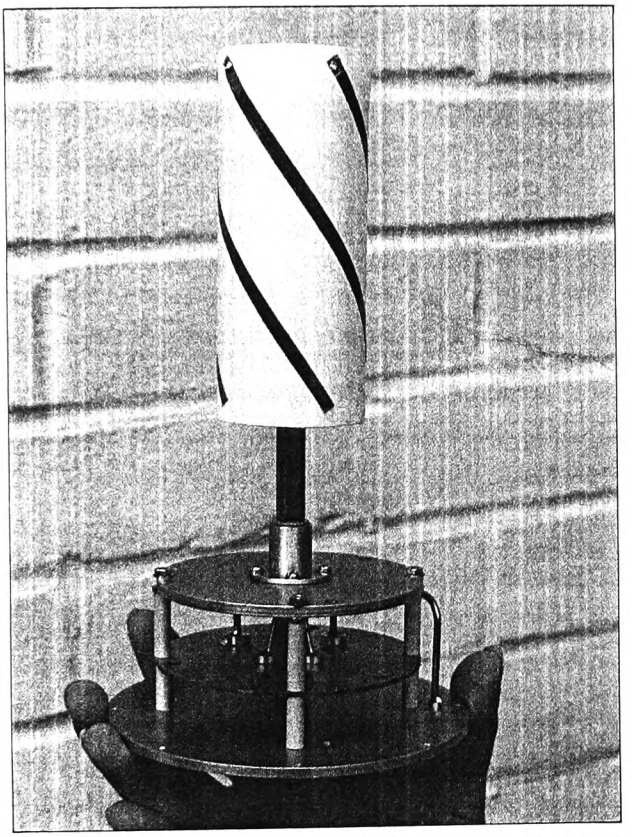

1. The standard-C antenna is shown with radome removed. (Photo courtesy of Keen Associates)

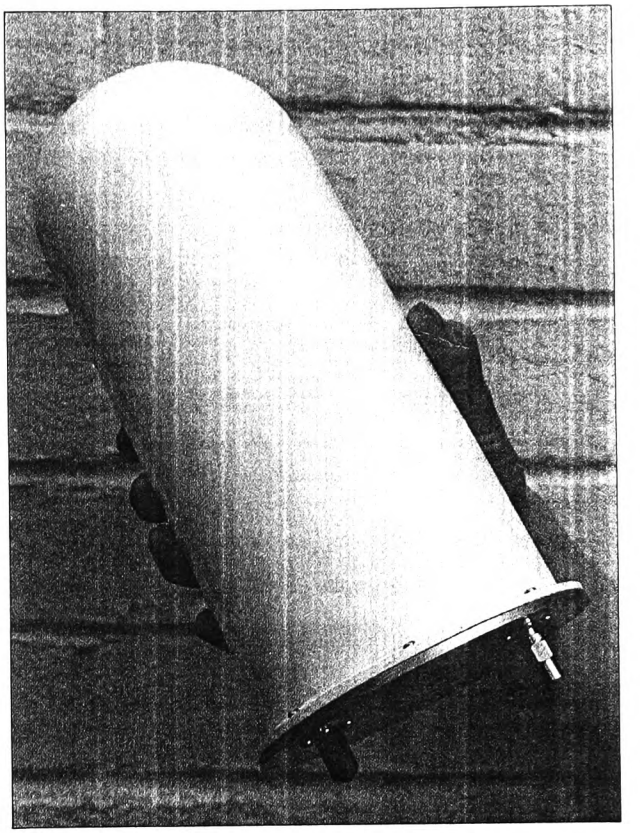

2. The complete standard-C antenna unit can be seen with the glass-reinforced plastic radome. (Photo courtesy of Keen Associates)

By
K.M. Keen
Keen Associates

A standard-C ship Earth station has been specified to be a low-cost, mobile satellite-communications terminal that is simple to install and use. The primary communications function is text and data message transfer. The low-cost aspect of the standard-C terminal makes it particularly applicable for small ships such as trawlers and small cargo vessels. The system operates with a receive frequency band of 1530 to 1545 MHz, and a transmit band of 1631.5 to 1646.5 MHz. The specifications for antennas for standard-C terminals are given fully in the *INMARSAT Standard-C System Definition Manual*.[1] Basically, the requirements are for a low-cost, circularly polarized antenna with a greater-than-hemispherical radiation-pattern coverage. An investigation has been carried out on potentially applicable antenna configurations, culminating in the development of the antenna shown without and with its radome (Figs. 1 and 2).

The antenna is a quadrifilar-helix radiator[2] with three-quarter-wavelength, half-turn, resonant radiating elements. The antenna geometry is chosen to give a radiation-pattern half-power beamwidth of the order of 220 degrees. Figure 3 shows the antenna configuration. Quadrifilar-helix antennas usually have wire-radiating elements. However, for this antenna, a conformally mapped printed-circuit form of construction was devised to achieve dimensional-construction accuracy at low cost and in volume produc-

K.M. Keen is with Keen Associates, Ifold, Loxwood, West Sussex, England RH14 OTA; 44-403-752001.

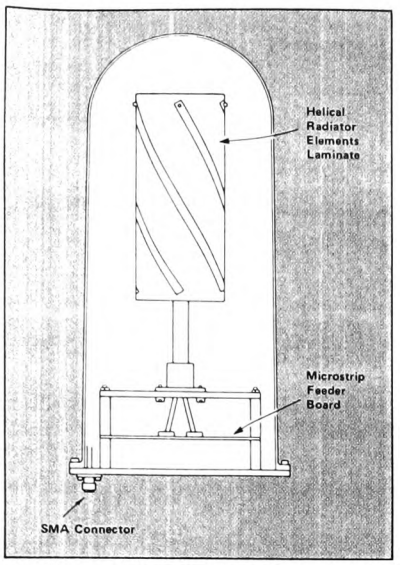

3. The antenna configuration is diagrammed.

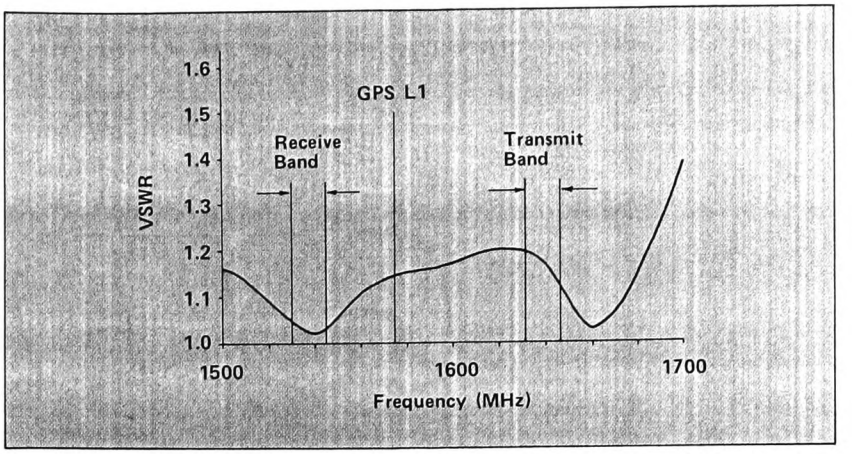

4. The antenna impedance characteristics are measured at the base-plate SMA connector.

tion. The printed cylinder with the helical elements is initially a flat plastic sheet with straight-line copper strips. These are simply wrapped around dielectric-support discs to form a cylinder with the required helical copper-strip geometry.

The radiating elements of the antenna are fed in progressive phase quadrature by a feeder system consisting of a microstrip circuit above the antenna base plate, and an arrangement of cables. This relatively simple feed system achieves a good antenna-impedance match (Fig. 4). The VSWR is better than 1.2:1 in both the receive and the transmit frequency bands.

Figure 5 shows typical vertical-plane radiation patterns. These correspond to the center frequencies of the receive and transmit bands, respectively. The hard lines are the copolarization (RHCP) patterns, and the dotted lines are cross-polarization (LHCP) patterns.

A useful feature of the antenna is that it operates at the GPS L1 frequency also, allowing the possibility of combined standard-C communications and GPS navigation functioning. Various forms of the antenna have been used successfully in standard-C/enhanced-group call-system trials.[3] ■

Acknowledgments

The initial antenna investigation and development was carried out for INMARSAT, and further development has been carried out subsequently. Antennas with an enhanced mechanical configuration have been developed by C and S Antennas, Rochester, England.

References

1. *INMARSAT Standard-C System Definition Manual*, March 1987.
2. C.C. Kilgus, "Resonant Quadrifilar Helix Design," *Microwave Journal*, December 1970, pp. 49–54.
3. "Perfect Results From Initial Group Call Tests," *Ocean Voice*, July 1987, pp. 8–9.

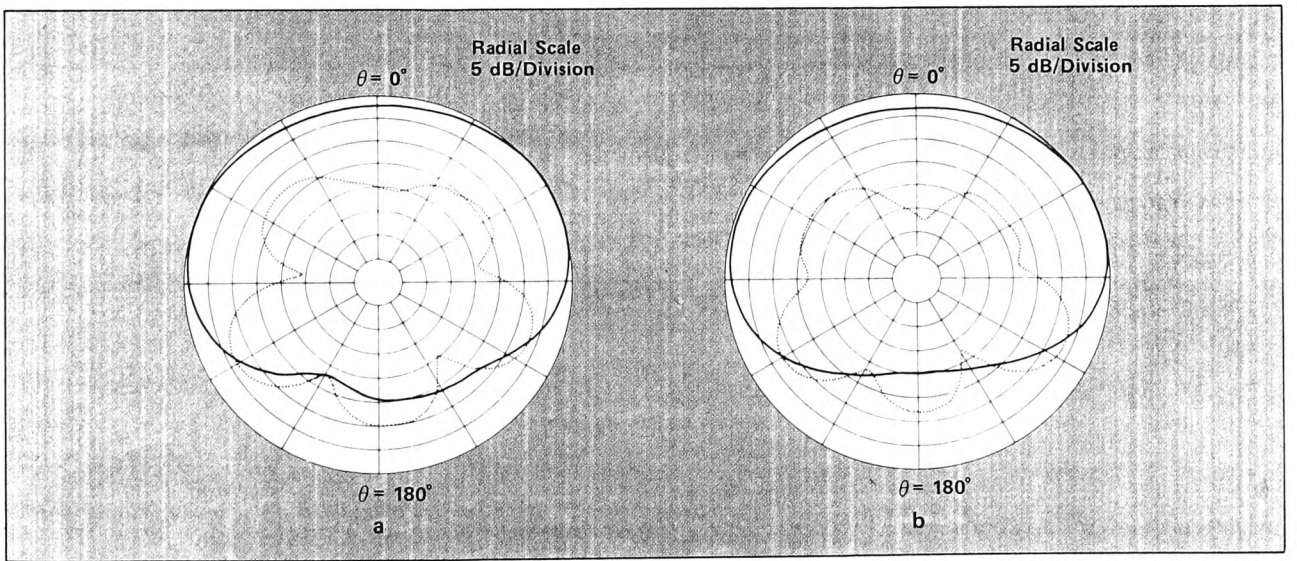

5. The vertical-plane radiation patterns (copolarized and cross-polarized) are plotted at the center frequency of (a) the receive band and (b) the transmit band.

Publication P42. K.M. KEEN, *Low profile cavity antenna with small pitch angle helix feed.* Electronics Letters, Vol. 29, No. 5, 4th March 1993, pp 501-502.

the g_m dispersion of MESFETs with the LTG GaAs passivation is less than that of a MESFET without passivation. In contrast to the case for the MESFET without surface passivation, the R_{out} of MESFETs with LTG GaAs passivation does not decrease when the frequency increases. Because g_m and R_{out} determine the voltage gain, the performance of MESFETs with LTG GaAs passivation layers will not deteriorate with increased operating frequency. Based on the dispersion results reported here and the high breakdown voltages already demonstrated, LTG GaAs is ideal for passivating the surface of GaAs MESFETs.

Acknowledgment: This work was supported by the U.S. Department of the Air Force, in part by a specific program sponsored by the Air Force Office of Scientific Research.

19th January 1993

C. L. Chen, F. W. Smith, L. J. Mahoney, M. J. Manfra, and A. R. Calawa (*Lincoln Laboratory, Massachusetts Institute of Technology, Lexington, Massachusetts 02173-9108, USA*)

References

1 SMITH, F. W., CALAWA, A. R., CHEN, C. L., MANFRA, M. L., and MAHONEY, L. J.: 'New MBE buffer used to eliminate backgating in GaAs MESFET's', *IEEE Electron Device Lett.*, 1988, **9**, pp. 77–80

2 CHEN, C. L., MAHONEY, L. J., MANFRA, M. J., SMITH, F. W., TEMME, D. H., and CALAWA, A. R.: 'High-breakdown-voltage MESFET with a low-temperature-grown GaAs passivation layer and overlapping gate structure', *IEEE Electron Device Lett.*, 1992, **13**, pp. 335–337

3 KACHWALLA, Z.: 'Characterizing traps in MESFETs using internal transconductance (g_m) frequency dispersion', *Solid-State Electron.*, 1988, **31**, pp. 1315–1320

4 LADBROOKE, P. H., and BLIGHT, S. R.: 'Low-field low-frequency dispersion of transconductance in GaAs MESFET's with implications for other rate-dependent anomalies', *IEE Trans.*, 1988, **ED-35**, pp. 257–267

5 GOLIO, J. M., MILLER, M. G., MARACAS, G. N., and JOHNSON, D. A.: 'Frequency-dependent electrical characteristics of GaAs MESFETs', *IEEE Trans.*, 1990, **ED-37**, pp. 1217–12227

LOW PROFILE CAVITY ANTENNA WITH SMALL PITCH ANGLE HELIX FEED

K. M. Keen

Indexing terms: Antennas, Antenna feeders, Dipole antennas, Helical antennas, Resonators

A simple, circularly polarised, cavity-backed antenna is described which has a two turn low pitch angle helix feed. The helix is terminated in a strip monopole for improved axial ratio. The antenna is approximately one third of the size of an equivalent conventional monofilar helix antenna.

Antenna configuration: The antenna is similar to the cavity backed dipole and crossed dipole antennas described by Ehrenspeck [1] and Wong and King [2], except that in this case, a low pitch angle helix of the type described by Nakano *et al.* [3] is used as the radiating source.

Fig. 1 shows the antenna configuration which consists of a cylindrical metal cavity of diameter D and rim depth w, around a two turn monofilar wire helix with a pitch angle of 5·5°. Unlike the radiator described in Reference 3, the helix has a peripheral, rather than a central, feed point. Also, the helix is terminated in a strip monopole of length equal to the helix diameter d, to improve the axial ratio performance. The cavity rim depth w is a little larger than the axial length of the helix; this allows a planar RF window to be incorporated across the cavity aperture, which is a useful practical feature for weather protection.

Measured performance: The performance of an antenna that was designed for a centre frequency of 1590 MHz and operation in RHCP, is shown in Figs. 2–4. The antenna dimensions were $D = 180$ mm ($0{\cdot}95\lambda$), $w = 43$ mm ($0{\cdot}23\lambda$) and $d = 60$ mm (λ/π), where λ represents the free space wavelength at 1590 MHz. The helix wire diameter was 1·6 mm, and the monopole strip width was 6 mm. The RF window was 1·5 mm thick polystyrene.

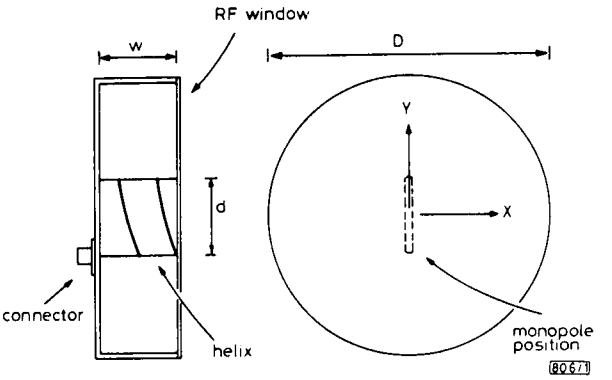

Fig. 1 *Antenna configuration*

Fig. 2 shows the radiation pattern performance of the antenna, at and near to the design frequency. The diagram shows co- and crosspolarisation patterns (i.e. RHCP and LHCP patterns) measured at 1550 MHz. With conventional spherical/Cartesian co-ordinates, the measurement plane was the X–Z plane of the co-ordinate system shown in Fig. 1 (the Z axis is not illustrated, but extends forward of the antenna) and the angle θ is the angle from the Z axis. Copolarisation patterns were found to be essentially independent of the plane of measurement, and with a half power beamwidth of ~65°.

Fig. 3 shows the measured boresight axial ratio as a function of frequency (continuous line). The effect of the monopole

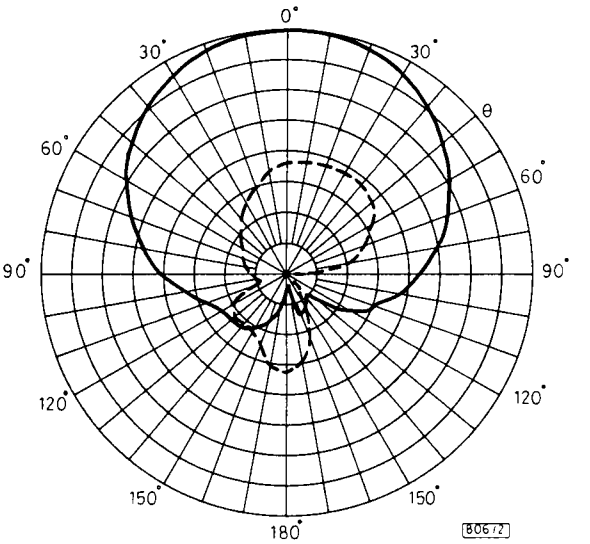

Fig. 2 *Radiation pattern*
Radial scale is 5 dB per division

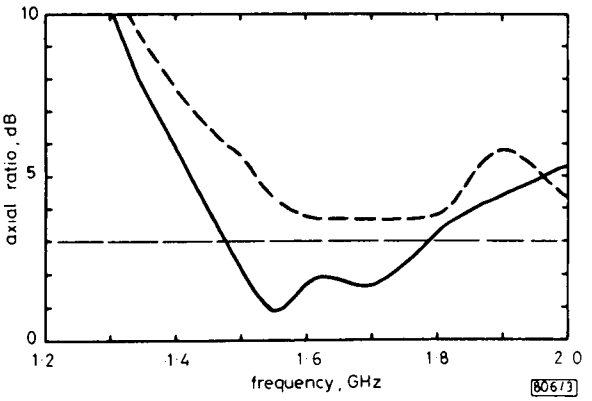

Fig. 3 *Boresight axial ratio*

termination strip at the end of the helix as an axial ratio improvement device can be seen from the dashed line, which shows the measured axial ratio of the antenna with the monopole strip removed.

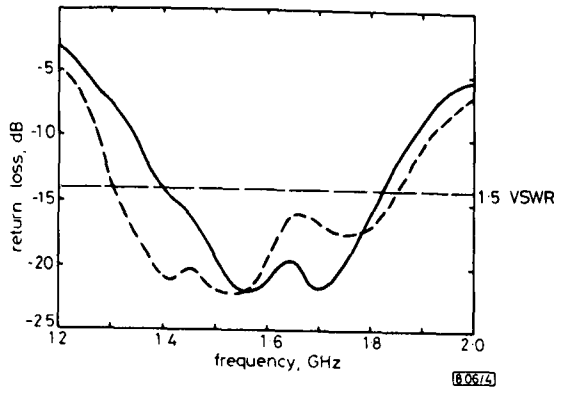

Fig. 4 *Return loss*

Fig. 4 (continuous line) shows the measured return loss of the antenna after impedance matching by incorporating a tapered transition in the first quarter turn of the helix, in the way described by Kraus [4]. An input VSWR of better than 1·5 was easily achieved for a 25% bandwidth. The dashed line in Fig. 4 shows the return loss of the antenna with the monopole termination strip removed.

Conclusions: A simple and compact cavity backed circularly polarised antenna has been demonstrated which has good radiation pattern, axial ratio and impedance match characteristics. An equivalent conventional monofilar helix antenna [5] would have a baseplate diameter of about the same size as the cavity antenna diameter D, but the helix length would be about three times the cavity antenna rim depth w.

27th January 1993

K. M. Keen (*Keen Associates, Ifold, Billingshurst, West Sussex RH14 0TA, United Kingdom*)

References

1 EHRENSPECK, H. W.: 'A new class of medium-size high efficiency reflector antennas', *IEEE Trans.*, 1974, **AP-22**, pp. 329–331

2 WONG, J. L., and KING, H. E.: 'A cavity-backed dipole antenna with wide bandwidth characteristics', *IEEE Trans.*, 1973, **AP-21**, pp. 725–727

3 NAKANO, H., TAKEDA, H., HONMA, T., MIMAKI, H., and YAMAUCHI, J.: 'Extremely low-profile helix radiating a circularly polarized wave', *IEEE Trans.*, 1991, **AP-39**, pp. 754–757

4 KRAUS, J. D.: 'A 50-ohm input impedance for helical beam antennas', *IEEE Trans.*, 1977, **AP-25**, p. 913

5 KRAUS, J. D.: 'Antennas', chap. 7 *in* 'The helical antenna' (McGraw-Hill Book Co., 1988), 2nd edn.

THEORETICAL ANALYSIS OF SEMICONDUCTOR OPTICAL AMPLIFIER WAVELENGTH SHIFTER

I. Valiente, J. C. Simon and M. Le Ligne

Indexing terms: Optical amplifiers, Lasers

A theoretical analysis of a wavelength shifter based on a semiconductor optical amplifier is presented, with special attention paid to practical features such as wavelength dependence of the required pump power, and dynamic response related to system aspects.

Introduction: Wavelength shifters will be key components in future all optical switching devices. Recently, Glance *et al.* [1] and Durhuus *et al.* [2] experimentally demonstrated the possibility of using a semiconductor optical amplifier as a broadband wavelength shifter for ASK modulated signals. In this scheme, the gain at any wavelength in the amplifier bandwidth is modulated through the gain saturation effect [3] by a strong input signal called 'pump', provided the data rate is smaller than the reciprocal of the gain recovery time constant [4]. If an input CW 'probe' wave at a different wavelength is present in the amplifier, the information on the pump wave will be duplicated on the probe but with the complementary ASK pattern, because when the pump is 'high, the signal gain is 'low', and vice versa. We report, for the first time to our knowledge, a theoretical analysis of this type of wavelength shifter. The addressed features are: wavelength dependence of required pump power, pulse spectrum distortion and transient response.

Theoretical model: We consider the propagation of pump and probe waves through a TW amplifier. The model is based on that reported by Agrawal and Olsson [5] using the slowly varying envelope approximation for fields, which is quite realistic for pulse durations greater than 100 ps:

$$\frac{\partial}{\partial z} U_i(z, \tau) = \frac{\Gamma g_i(n) - \alpha_{int}}{2} U_i \tag{1a}$$

$$\frac{\partial}{\partial z} \Phi_i(z, \tau) = -\frac{\Gamma g_i(n) \alpha_H}{2} \Phi_i \tag{1b}$$

where $i = s, p$ stands, respectively, for probe and pump waves, $U_i = (P_i)^{1/2}$ is the wave amplitude, ϕ_i is the phase, P_i is the power, $\Gamma = (\partial/\partial n_c) n_{eff}$ is the amplification factor as defined by Vassallo [6], $g_i(n) = g(\lambda_i, n)$ is the material gain coefficient, α_{int} is the nonresonant loss coefficient, α_H is the linewidth enhancement factor, and $\tau = t - z/v_g$ is the reduced time as measured in a reference frame moving with the pulse. In the active waveguide the carrier density n is given by

$$\frac{\partial}{\partial \tau} n(z, \tau) = \frac{I}{edwL} - Cn^3 - Bn^2 - \frac{\Gamma}{wd}\left[g_s(n) \frac{P_s(z, \tau)}{\hbar\omega_s} + g_p(n) \frac{P_p(z, \tau)}{\hbar\omega_p} \right] \tag{2}$$

where C is the Auger recombination coefficient, B is the recombination coefficient for radiative transition and carrier leakage through heterojunctions, and d, W, L are active layer thickness, width and length, respectively.

To integrate these coupled equations along the z-axis, the amplifier is divided into N_s subsections [7]. It is assumed that the carrier density is uniform in each subsection, and that the input pulse envelope time variation is negligible during a transit time through each section. Thereby, eqn. 2 can be rewritten as

$$\frac{\partial}{\partial \tau} n_k(\tau) = \frac{I}{edwL} - Cn_k^3 - Bn_k^2 - \frac{\Gamma}{wd}\left[g_s(n_k) \frac{\bar{P}_{s,k}(\tau)}{\hbar\omega_s} + g_p(n_k) \frac{\bar{P}_{p,k}(\tau)}{\hbar\omega_p} \right] \tag{3a}$$

$$\bar{P}_{i,k}(\tau) = \frac{\exp\{[\Gamma g_i(n_k) - \alpha_{int}]\,\Delta z\} - 1}{[\Gamma g_i(n_k) - \alpha_{int}]\,\Delta z} P_{i,k-1}(\tau) \tag{3b}$$

where $k = 1$, N_s corresponds to the kth section, and $P_{i,k-1}(\tau)$ is the power at the amplifier input if $k = 1$, and the kth section output power for $k > 1$ otherwise. The Runge–Kutta method is used for time integration. The following numerical parameters are used in this work: $B = 1{\cdot}7 \times 10^{-9}$ exp $(-T/77) + 1{\cdot}2 \times 10^{-9}\,\text{cm}^{-3}\,\text{s}^{-1}$, $C = 4 \times 10^{-29}\,\text{cm}^6\,\text{s}^{-1}$, $d = 0{\cdot}33\,\mu\text{m}$, $w = 0{\cdot}75\,\mu\text{m}$, $L = 400\,\mu\text{m}$, $\Gamma = 0{\cdot}588$, $\alpha_{int} = 10{\cdot}5\,\text{cm}^{-1}$ and $\alpha_H = 5$.

For $g(\lambda_i, n)$ we used the model of Osiński and Adams [8], but with a numerical integration for the gain function. The ionisation energy of localised states $E_l = 62{\cdot}67$ meV and percentage of As composition $y = 0{\cdot}93$ (in the $Ga_xIn_{1-x}As_yP_{1-y}$ active layer material) were used as fitting parameters to obtain a small signal gain of 27 dB at peak gain wavelength of

Publication P43. K.M. KEEN, *Antenna design offers compact size and low cost.* Microwaves and RF, August 1996, pp 77-78.

ANTENNA DESIGN OFFERS COMPACT SIZE AND LOW COST

This circularly-polarized cavity antenna achieves reduced size by incorporating a two-turn, low-pitch-angle helix.

COMMERCIAL applications such as portable communication systems have generated a need for antenna designs that offer a combination of compact size and low cost. A circularly-polarized cavity-antenna scheme meets these requirements by using a two-turn, low-pitch-angle helix. This results in a simple structure that is one-third the size of conventional helix antennas.

The design is similar to cavity-backed dipole and crossed-dipole antennas described by Ehrenspeck[1] as well as Wong and King.[2] However, the new design differs from the older antennas in that a two-turn, low-pitch-angle helix radiator (of the type described by Nakano *et al.*[3]) is used to excite the cavity. This allows for the large reduction in antenna size compared to axial-mode (Kraus-type) helix antennas. In fact, since the helix length is shorter than the quarter-wavelength cavity depth, the cavity can be fully sealed with an RF window across the antenna aperture in order to provide weather protection.

KEITH M. KEEN, Director, Keen Associates, Ifold, Loxwood, Billingshurst, West Sussex RH14 OTA, United Kingdom; (44) 1403-752001.

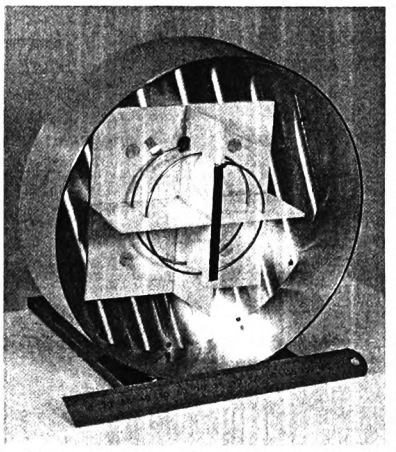

1. The cavity antenna (shown without its cover) uses a monofilar-wire helix, coaxial connector, and strip-monopole termination to achieve low-cost fabrication.

The antenna's simple design (Fig. 1) also contributes to lower fabrication costs. The cavity contains a two-turn helix formed with monofilar wire at a pitch angle of 5.5 deg. The helix is directly joined to a coaxial connector which is mounted on the back of the cavity. A strip monopole is used to terminate the helix, as this approach has been found to improve the antenna's axial ratio.[4]

MATCHING NETWORK

Impedance matching is achieved with a microstrip "tab" on the first quarter turn of the helix. This method is often used to achieve 50-Ω impedance matching with conventional monofilar helical antennas.

2. Typical results indicate that the copolarization-pattern shapes are independent of the measurement plane through the cavity axis.

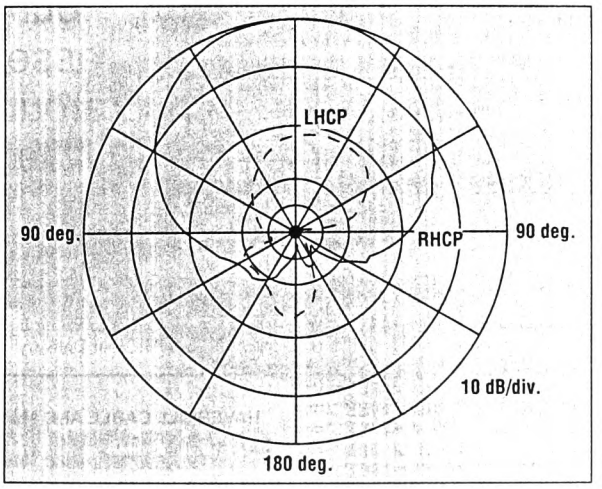

CAVITY ANTENNA

When realized with a circular-profile cavity, this type of antenna structure achieves approximately 7.0-to-9.5-dBic gain depending on the cavity diameter, which can range from 0.8λ to λ (where λ represents the wavelength). The antenna can also be formed with a square-profile cavity.

Figure 2 shows a typical antenna radiation pattern, which was obtained with a cavity diameter of 18 cm and a helix diameter of 6 cm. The helix-wire diameter is 1.6 mm while the monopole strip width is 6 mm. The helix is "right-handed" so that the antenna operates in right-hand circular polarization (RHCP). The plot demonstrates that the copolarization patterns are essentially independent of the measurement plane through the cavity axis.

With the microstrip-tab matching device, an input VSWR of better than 1.50:1 is easily obtained across a 25-percent bandwidth. In addition, a boresight axial ratio of less than 3 dB is achieved across a bandwidth of 19 percent.

An important feature of the cavity antenna is that its length in the cavity-axis direction is approximately one third that of a conventional monofilar helix antenna. This allows for the use of the antenna in applications where small size is essential. For instance, Mini-M vehicle terminals for the Inmarsat system employ a radome-covered antenna unit with a height of 20 cm and a diameter of 24 cm. In this configuration, the cavity antenna is mechanically steered by azimuth rotation only. Elevation pointing is provided by manual adjustment.

A smaller version of the cavity antenna is under development. This version incorporates dielectric loading to achieve smaller cavity dimensions. The dielectric material used is a composite consisting of titanium-dioxide powder (which is produced at low cost in very large quantities as a white paint pigment) in a matrix that is initially a liquid but which hardens after chemical curing. As a result, the composite provides mechanical pliability for the cavity design. ••

References

1. H.W. Ehrenspeck, "A New Class of Medium-Size, High-Efficiency Reflector Antennas," *IEEE Transactions on Antennas and Propagation*, March 1974, pp. 329-331.
2. J.L. Wong and H.E. King, "A Cavity-Backed Dipole Antenna with Wide-Bandwidth Characteristics," *IEEE Transactions on Antennas and Propagation*, September 1973, pp. 725-727.
3. H. Nakano *et al.*, "Extremely-Low-Profile Helix Radiating a Circularly-Polarized Wave," *IEEE Transactions on Antennas and Propagation*, June 1991, pp. 754-757.
4. K.M. Keen, "Low-Profile Cavity Antenna with Small-Pitch-Angle Helix Feed," *Electronic Letters*, March 1993, pp. 501-502.

SPEAK YOUR MIND!

Please let us know what you think of this article by circling one of the following numbers on the Reader Service Card. The article was:

Very Useful	Useful	Not Useful
CIRCLE 507	CIRCLE 508	CIRCLE 509

Publication P44. K.M. KEEN, D. SMITH, and B.S. LEE, *Reduced range antenna measurements for small satellite terminal applications*, Eighth International Seminar on Electrodynamics and Techniques of Microwaves and EHF, Moscow, September 1996, pp 36-40.

Электродинамика и техника СВЧ и КВЧ, 1996, т.4, № 4, с. 36

K.Keen, D. Smith, B.S. Lee[*]

REDUCED RANGE ANTENNA MEASUREMENTS FOR SMALL SATELLITE TERMINAL APPLICATIONS

1. *Introduction.* Ideally an antenna range, of the conventional type will have a range length, distance between test antenna and remote antenna, which is large enough for approximate plane wave conditions to exist. In practice, however, range lengths are sometimes much shorter than would be ideal with the result that the test antenna will be measured with an appreciable phase error across its aperture. A consequence of this phase error is that antenna gains measured on a short, or reduced length, range have lower values than true far field antenna gain values.

By investigating the gain reduction factors associated with operating circular aperture test antennas and pyramidal reference antennas it is hoped to provide correction factors to enable reduced gain antenna measurements to be compared with far field antenna results. It is also hoped to determine the operational limits for conducting antenna measurements within an anechoic chamber of 4m length located at Matra-Marconi Space, Poynton, U.K.

2. *Circular Aperture Gain Reduction Factors.* A method for determining the gain reduction factor, F, for a circular aperture of diameter, D , has been described by Silver [1], Jull [2] and Clarke and Brown [3]. This method involves the evaluation of the Fresnel diffraction integral for the circular aperture at a short range distance, R, along the aperture axis.

The Fresnel integral has the form

$$E = j/\lambda \cdot \left(exp(-jkR)/R\right) \cdot \int_0^{2\pi} \int_0^a A(r,\phi) \cdot exp\left(-jk\left(r/2R\right)\right) \cdot r \cdot dr \cdot d\phi \ ,$$

where A(r,ϕ) is the aperture distribution.

This integral has been evaluated numerically using a personal computer for a variety of aperture distributions:

2.1. *Uniform Distribution.* This considerably simplifies the integral and ultimately gives an expression for the reduced range gain reduction factor

[*] University of Northumbria at Newcastle, England

$$F = -20\ log(sin(x)/x), \quad (dB)$$

where $x = \pi D^2 / 8\lambda R$ (rads).

2.2. *Non-Uniform Distribution.* The gain reduction factors for a number of non - uniform aperture distributions have been evaluated. These have included radial squared tapers, with and without a pedestal level. This allows a suitable field level to be assigned to the aperture edge, e.g. -10 dB. Aperture illuminations following Bessel distributions, of the form found in corrugated feed horns, have also been computed.

2.3. *Aperture Blockage.* For an axi-symmetric Cassegrain fed antenna the effects of aperture blockage caused by the subreflector can also be investigated. These investigations can consider both uniform and non-uniform illuminations as described above.

The gain reduction factors, in dB, for a 60 cm diameter circular aperture under various illumination conditions when operated at X-band on a 4m range are given in Table 1.

Table 1. Gain Reduction Factors, dB, for 0.6m Dia. Circular Aperture

Normalised Frequency	Uniform Illumination	Tapered Illumination on Pedastal	Uniform Illumination with Blockage(0.20D)
0.924	1.084	0.710	1.062
0.936	1.115	0.730	1.093
0.949	1.147	0.750	1.123
0.962	1.179	0.771	1.155
0.975	1.211	0.792	1.186
0.987	1.244	0.813	1.218
1.000	1.277	0.834	1.251
1.013	1.311	0.856	1.284
1.025	1.345	0.877	1.318
1.038	1.380	0.900	1.352
1.051	1.415	0.922	1.386
1.064	1.451	0.945	1.421

3. *Pyramidal Horn Antenna Gain Reduction.* A method for determining the gain reduction factors due to reduced range length for pyramidal horns

has been given by Jull [4]. This method is somewhat protracted and involves solution of the Fresnel equations. Jull has presented some graphical data which can be used to estimate the gain reduction factors.

The gain reduction factor is given by

$$F = (R'_E \mp R'_H) - (R_E \mp R_H), \qquad \text{(dB)}$$

where R'_E and R'_E refer to the reduced range conditions and R_E and R_H refer to the far field conditions.

In this case the method of Jull is followed with the gain reduction factors evaluated numerically.

Overall Gain Reduction Factor. When conducting antenna measurements on a reduced length range the gain reduction factors of both test antenna, F_T, and reference antenna, F_R , must be taken into account. For antenna gain measurements taken using the Friis transmission formula the relationship between reduced range gain, $G_{Red.Range}$, and far field gain, $G_{FarField}$ is

$$G_{Far\ Field} = G_{Red.\ Range} + (F_T + F_R), \qquad \text{(dB)}$$

The overall gain correction factors for a 60 cm diameter antenna with a 20 *dB* standard gain pyramidal horn measured on a 4 *m* range are shown in Table 2.

Table 2. Overall Gain Reduction Factors for 60 *cm* Antenna on 4 *m* Range

Normalised Frequency	Test Antenna Gain Reduction Factor	Reference Antenna Gain Reduction Factor	Total Reduction Factor
0.924	1.08	0.12	1.20
0.987	1.23	0.12	1.35
1.006	1.28	0.13	1.41
1.070	1.46	0.13	1.59

Reduced range gain measurements have been performed on a 60 *cm* diameter Cassegrain antenna with aperture blockage, d = D/5 and are shown in Figure 1 together with far field results taken for the same antenna. The gain reduction due to reduced range measurements is apparent.

Also shown in Figure 1 are corrected values using computed gain reduction factors. The agreement obtained is satisfactory for the present application being within 0.5 *dB*. Whilst the present investigation has concentrated upon an antenna of 60 *cm* diameter the gain reduction variation with antenna aperture has been calculated for the 4 *m* chamber and is shown in Figure 2. The rapid rise in gain reduction factor for antennas of apertures

in excess of 60 *cm* indicates that this is a reasonable limit for operation within the existing chamber.

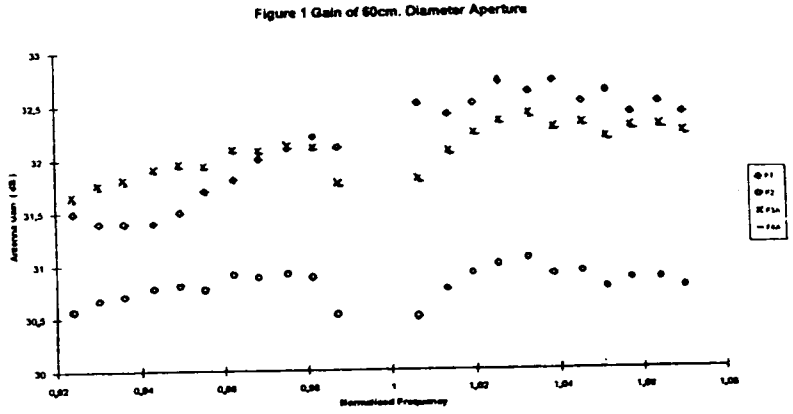

Fig.1. Gain of 60 cm. Diameter aperture.
F1 - Far Field Gain; F2 - Reduced Range Gain No Correction;
F3 - Reduced Range Gain Correction Uniform Illumination No Blockage;
F4 - Reduced Range Gain Correction Uniform Illumination With Blockage.

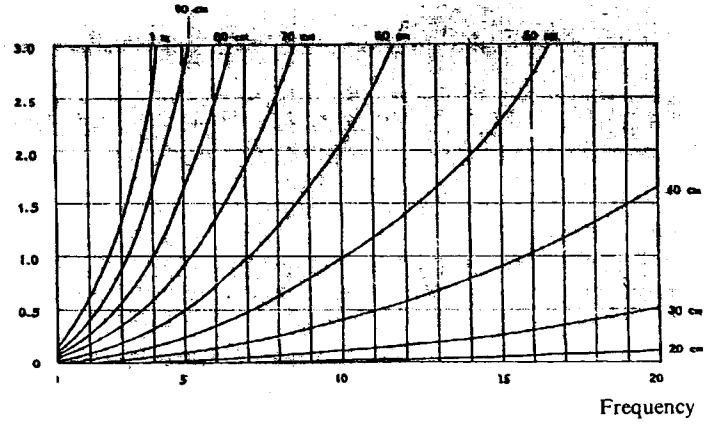

Fig.2. Gain Reduction Factor for Circular Aperture on 4 m Range.

4. *Conclusions.* The effects of measuring antenna gain on reduced length ranges has been investigated. Gain reduction factors for both test and reference antennas have been evaluated. A variety of test antenna illumination conditions have been considered including the effects of aperture blockage. Corrected reduced range antenna gain results show satisfactory agreement with far field measurements for antennas operated at X-band.

References

1. *Silver S.* Microwave Antenna Theory and Design. -McGraw Hill Book Co. , 1949.

2. *Jull E.V.* Aperture Antennas and Diffraction Theory. -Peter Peregrinus Ltd., 1981.

3. *Clarke R.H., Brown J.* Diffraction Theory and Antennas. -Ellis Horwood Ltd., 1980.

4. *Jull E.V.* Finite range gain of sectoral and pyramidal horns // Electronic Letters, 1970. -Vol.6. -Pp.680-681.

Сокращенные размеры диапазонной антенны для бортовых применений.
K.Keen, D. Smith, B.S. Lee

Исследовано воздействие измерения коэффициента усиления антенны на сокращенные диапазоны. Представлены опытные данные. Для двух контрольных случаев оценены коэффициенты усечения КУ. Правильное использование коэффициента усечения КУ дает хорошее согласование теории с экспериментом.

Разработка компактной, хорошо исполненной, дешевой безэховой камеры СВЧ и КВЧ.
D.Geen, D. Smith

В данной работе подробно описана конструкция, характеристики и работа компактной безэховой камеры. В комплекте с простейшими измерительными приборами возможно производство антенных измерительных систем низкой стоимости и высокого качества.

Данилов А.А.[*], *Кузьмин О.А.*[*], *Неганов В.А.*[*]

ПРОЕКТИРОВАНИЕ ПЕРЕХОДОВ НА ОСНОВЕ ФИЛЬТРУЮЩИХ СТРУКТУР

1. *Введение.* При проектировании современной радиотехнической аппаратуры СВЧ и КВЧ диапазонов для эффективного снижения массогабаритных параметров при одновременном увеличении надежности и наращивании функциональных возможностей часто используются широкополосные переходы (ШПП) с одной линии передачи (ЛП) на другую [1,2]. Существенным ограничением имеющихся конструктивных решений ШПП [2-4] на реализацию ширины полосы рабочих частот и требуемые амплитудно-частотные (АЧХ) и фазочастотные (ФЧХ) характеристики является то, что они состоят из нескольких однородных резонансных элементов, у которых на частотах, близко расположенных к верхней границе, имеется максимальный уровень ослабления, препятствующий расширению полосы рабочих частот. Выше по частоте находится вторая (паразитная - в терминах фильтрующих структур) полоса пропускания. Так, например, широко используемый однородный полуволновый замкнутый резонатор на щелевой линии, включенный в центре параллельно в цепь, имеет вторую полосу пропускания с центральной частотой в два раза выше средней рабочей частоты. Между основной и паразитной полосой пропускания существует максимальный уровень ослабления на частоте в полтора раза выше средней рабочей частоты, что ограничивает перекрытие рабочих частот ШПП октавным диапазоном. Другой существенной особенностью имеющихся конструкций ШПП является то, что отрезки ЛП на входе и выходе выполняются в виде широкополосных элементов связи. Для увеличения функциональных возможностей ШПП эти отрезки можно выполнить в виде резонаторов и таким образом повысить помехозащищенность аппаратуры за счет повышения частотной селекции переходов, в том числе установкой максимального уровня ослабления дополнительных резонаторов на входе и выходе на необхо-

[*] Поволжский институт информатики, радиотехники и связи; 443010 Самара-10, ул.Л.Толстого, 23; тел.(8462) 32.58.53.

Publication P45. K.M. KEEN, D. SMITH, and B.S. LEE, *Improved form of backfire bifilar helix conical beam antenna.* Microwave and Optical Technology Letters, Vol 14, No 5, April 5 1997, pp 278-280.

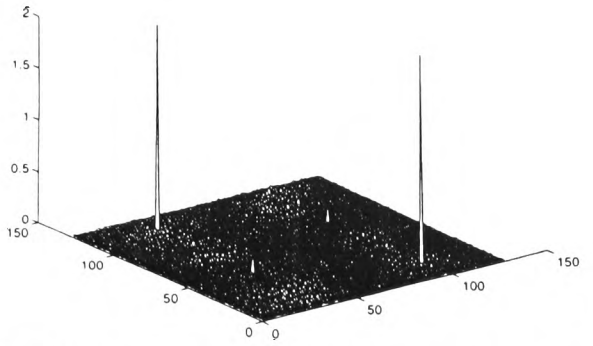

Figure 9 Zero-thresholded correlation output for the AMPOF-based JFT model

JFT based on AMPOF PSF yields better performance in terms of the normalized peak power, peak-to-side-lobe ratio, discrimination ratio, and correlation width. Median computation and thresholding of the binarized JFT are sequential in nature, and therefore time consuming. The proposed JFT model drastically reduces the amount of time because it involves neither any median-based thresholding nor postmultiplication of the fringe pattern. Although the results mentioned here are scene specific, the trend is similar for a wide range of images that we have studied. This scheme can easily be applied to any optimal pattern recognition filter.

REFERENCES

1. P. D. Gianino and J. L. Horner, "Phase-Only Matched Filtering," *Appl. Opt.*, Vol. 23, 1984, pp. 812–816.
2. F. T. S. Yu and J. E. Ludman, "Microcomputer Based Programmable Joint Transform Correlator for Automatic Pattern Recognition and Identification," *Opt. Lett.*, Vol. 11, 1986, pp. 395–397.
3. B. Javidi and C. Kuo, "Joint Transform Image Correlation Using a Binary Spatial Light Modulator at the Fourier Plane," *Appl. Opt.*, Vol. 27, 1988, pp. 663–665.
4. A. VanderLugt, "Signal Detection by Complex Spatial Filtering," *IEEE Trans. Inf. Theory*, Vol. IT-10, 1964, pp. 139–145.
5. A. A. S. Awwal, M. A. Karim, and S. R. Jahan, "Improved Correlation Discrimination Using an Amplitude-Modulated Phase-Only Filter for Optimum Recognition," *Appl. Opt.*, Vol. 29, 1990, pp. 233–236.
6. O. Perez and M. A. Karim, "An Efficient Implementation of Joint Fourier Transform Correlation Using a Modified LCTV," *Microwave Opt. Technol. Lett.*, Vol. 2, 1989, pp. 193–196.
7. B. Javidi, "Nonlinear Joint Power Spectrum Based Optical Correlation," *Appl. Opt.*, Vol. 28, 1989, pp. 2358–2367.
8. S. K. Rogers, J. D. Cline, and M. Kabrisky, "New Binarization Techniques for Joint Transform Correlation," *Opt. Eng.*, Vol. 29, 1990, pp. 1018–1093.
9. M. S. Alam, A. A. S. Awwal, and M. A. Karim, "Improved Correlation Discrimination Using Joint Fourier Transform Optical Correlator," *Microwave Opt. Technol. Lett.*, Vol. 4, 1991, pp. 103–106.
10. M. S. Alam and M. A. Karim, "Fringe-Adjusted Joint Transform Correlator," *Appl. Opt.*, Vol. 32, 1993, pp. 4351–4356.
11. S. Vallmitjana, A. Carnicer, E. Martin-Badosa, and I. Juvells, "Nonlinear Filtering in Object and Fourier Space in a Joint Transform Optical Correlator: Comparison and Experimental Realization," *Appl. Opt.*, Vol. 34, No. 20, 1995, pp. 3942–3949.
12. J. Wang and B. Javidi, "Multiobject Detection Using the Binary Joint Transform Correlator with Different Types of Thresholding Methods," *Opt. Eng.*, Vol. 33, 1994, pp. 1793–1805.
13. B. Javidi, and S. F. Odeh, "Multiple Object Identification by Bipolar Joint Transform Correlation," *Opt. Eng.*, Vol. 27, 1988, pp. 295–300.
14. B. V. K. Vijaya Kumar and L. Hassebrook, "Performance Measures for Correlation Filters," *Appl. Opt.*, Vol. 29, 1990, pp. 2997–3006.

CCC 0895-2477/97

IMPROVED FORM OF BACKFIRE BIFILAR HELIX CONICAL BEAM ANTENNA

K. M. Keen,[1] D. Smith,[2] and B. S. Lee[3]
[1] Keen Associates
Ifold, West Sussex RH14 OTA, United Kingdom
[2] Department of Electrical, Electronic Engineering and Physics
University of Northumbria at Newcastle
Newcastle upon Tyne NE1 8ST, United Kingdom
[3] Matra Marconi Space UK Ltd.
First Avenue
Poynton, Stockport, Cheshire SK12 1NE, United Kingdom

Received 5 November 1996

ABSTRACT: *The nonresonant-length backfire bifilar helix is often used as a vehicle satcom antenna, as it has a circularly polarized conical beam with azimuthal symmetry. Some antenna configurations, however, exhibit poor back-lobe levels. It is shown that radiation patterns can be significantly improved by correct termination of the helix. © 1997 John Wiley & Sons, Inc.* Microwave Opt Technol Lett 14: 278–280, 1997.

Key words: *antennas; helical antennas; bifilar helix antenna*

1. INTRODUCTION

Backfire bifilar helix antennas with nonresonant-length helical wires and small diameters have the ability to form conical-shaped beams that are circularly polarized. This was first demonstrated by Patton [1], and for this reason the antenna is sometimes referred to as the Patton coil [2]. With the use of the coordinate system shown in Figure 1, this type of antenna exhibits a conical beam with a peak at some value of θ between 0° and 90°, and with symmetry about the Z axis, when the two helical conductors are excited in antiphase at the top T and with the helical windings shorted together at the bottom, at O. The elevation angle of the beam peak depends on the helix diameter and pitch angle, and the beamwidth of the conical beam depends on the overall length (and therefore the number of turns) of the helix. In general, more turns give narrower beamwidths. The sense of the helical windings determines whether the antenna operates in RHCP or LHCP.

Because of the conical beam shape, this type of antenna is often used for satcom terminals on vehicles. Terminal antenna dimensions are typically 3–5 wavelengths in length and 0.05–0.1 wavelength in diameter. Antennas with mechanically variable helix dimensions have been demonstrated. With these, the beam elevation angle can be manually adjusted for a wide range of satellite elevation angles [3].

One disadvantage of the backfire bifilar helix antenna is that with some configurations, the radiation pattern back-lobe levels are high. Kilgus [4] has shown that this problem can be overcome with a more complex quadrifilar form of backfire

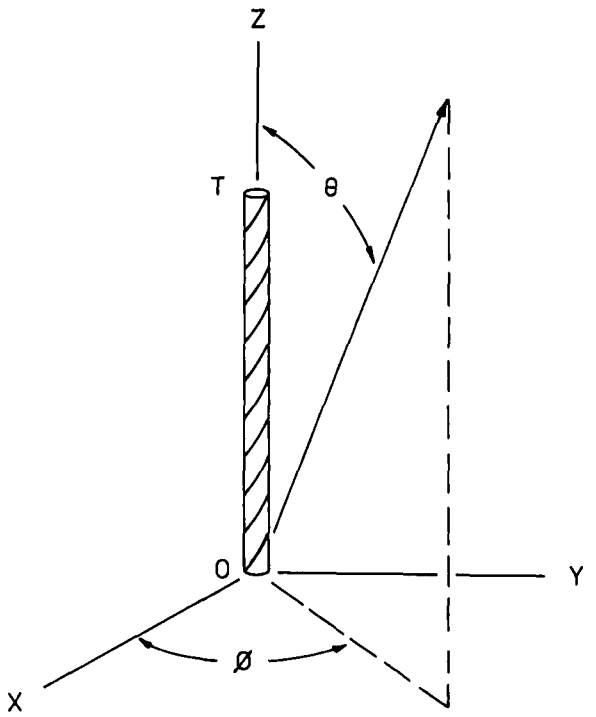

Figure 1 Antenna coordinate system

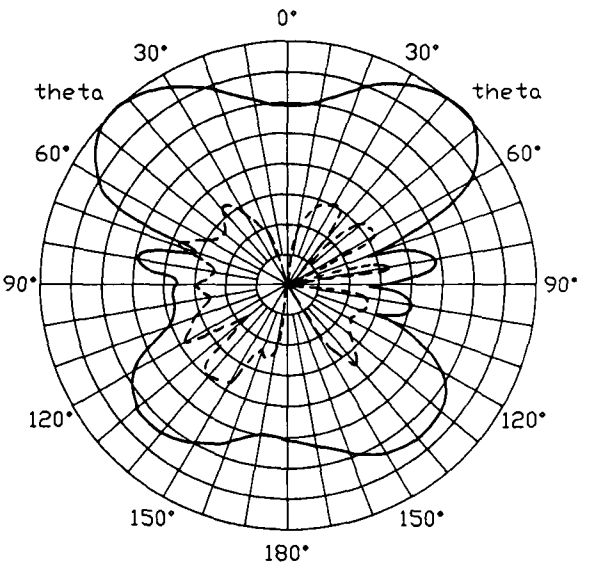

Figure 2 Radiation pattern of the bifilar helix antenna at 1525 MHz. Radial scale is 5 dB per division. Solid line, RHCP; dashed line, LHCP. $\phi = 0°$

helix antenna (not to be confused with the well-known resonant quadrifilar helix antenna), which essentially consists of two interwound backfire bifilar helix elements with a 90° axial rotation offset between them. These two bifilar helices are excited in phase quadrature, so that there is constructive wave interference in the upper hemispherical region of the antenna (i.e., above the OXY plane in Figure 1) and destructive interference in the lower hemispherical region. Although this scheme works well, it can be very difficult to implement in practical antennas, because a feed system of some type is required, which will excite the four helical conductors at the top point T with equal amplitudes and relative phases of 0°, 90°, 180°, and 270°. And because the antenna diameter is small, there is very little space available for a complex feed system within the helix tube or support framework. In contrast, the bifilar backfire helix can have a very simple and compact feed arrangement; for example, a coaxial cable with a split-tube balun at the top. This balun provides a 4:1 impedance transformation [5], so if a 50-Ω cable is used, a good impedance match can be easily obtained with the antenna, which has a radiation resistance on the order of 200 Ω. Because of the difficulty in providing compact feed systems for backfire quadrifilar helix conical beam antennas, a technique for reducing the back-lobe levels of bifilar antennas was investigated experimentally, as is described below.

2. EXPERIMENTAL INVESTIGATION

Figure 2 shows the copolarization (RHCP) and cross-polarization (LHCP) radiation patterns in a vertical plane of a backfire bifilar helix antenna that was designed to give a conical beam with a peak at an elevation angle of 45°, at mid L-band frequencies, in RHCP. The antenna is 55 cm long and 1.5 cm in diameter, and has 5.3 turns and a pitch angle of 66°. It can be seen that, although the radiation characteristics are good in the antenna upper hemisphere region, the copolarization back-lobe levels are high at about −8 dB below the main beam peak. From this radiation-pattern polar diagram and others that were obtained with different antenna configurations, the mechanism by which back lobes are generated became clear. For a transmitting antenna, antiphase (balanced mode) excitation at the top of the bifilar helix causes a traveling wave to progress down the helical transmission line, producing the main beam by backfire radiation. The traveling wave is attenuated by radiation, but with antennas of only a few turns at least, the wave still has a significant amplitude when it arrives at the short at the bottom of the bifilar helix. At this point, the wave is reflected back in the upward direction, and this reflected component then radiates in backfire to produce the unwanted backlobes, which are an attenuated mirror image of the conical mainbeam. This explanation suggests that bifilar helix antennas of this type should be terminated in a matched resistive load, rather than a short, as in normal practice. An experimental investigation was therefore carried out with the antenna described above, with the short replaced by resistive loads of various types and resistance values.

Figure 3 shows the improved copolarization radiation pattern that was obtained with the antenna with the bifilar helix terminated in a 200-Ω metal film resistor. By comparison with Figure 2 it can be seen that the back-lobe level is reduced from −8 to −21 dB below the main beam peak.

3. CONCLUSIONS

A big improvement in the radiation pattern performance of backfire bifilar helix conical beam antennas with nonresonant length elements can be obtained by replacing the helix termi-

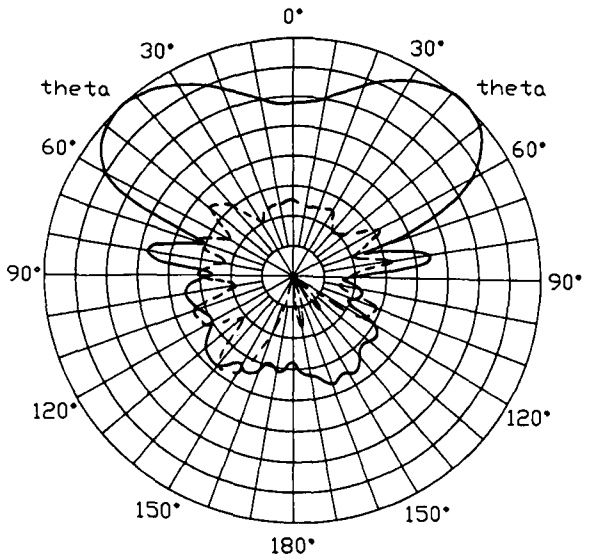

Figure 3 Radiation pattern of the antenna at 1525 MHz, with the end short replaced by a 200-Ω resistor. Radial scale is 5 dB per division. Solid line, RHCP; dashed line, LHCP. $\phi = 0°$

nation shorting wire used in current practice with a matched resistive load. Measurements have also shown that this modification has no adverse effect on either antenna gain in the main beam or the excellent return-loss characteristics that are obtainable with this type of antenna.

REFERENCES

1. W. T. Patton, "The Backfire Helical Antenna," Ph.D. thesis, University of Illinois, 1963.
2. J. D. Kraus, *Antennas* (2nd ed.) McGraw-Hill, New York, 1988.
3. C. D. McCarrick, "A Vertically Mounted, Elevation Steerable, Vehicular Antenna for Mobile Satellite Communications," *Via Satellite*, Oct. 1991, pp. 64–65.
4. C. C. Kilgus, "Shaped-Conical Radiation Pattern Performance of the Backfire Quadrifilar Helix," *IEEE Trans. Antennas Propagat.*, Vol. AP-23, May 1975, pp. 392–397.
5. R. C. Johnson and H. Jasik (Eds.), *Antenna Engineering Handbook*, McGraw-Hill, New York, 1984.

CCC 0895-2477/97

PLANAR CHIROWAVEGUIDE WITH DISCONTINUITIES

Xinzhang Wu[1] and Dwight L. Jaggard[1]
[1] Complex Media Laboratory
Moore School of Electrical Engineering
University of Pennsylvania
Philadelphia, Pennsylvania 19104

Received 10 October 1996

ABSTRACT: *We propose and develop an exact and efficient approach to analyze the effect of discontinuities on guided waves for open planar chirowaveguides. We use a technique that combines a one-dimensional finite-element method for the eigenvalue problem in the transverse direction with a rigorous mode-matching procedure for the discontinuities in the longitudinal direction. Both the scattering of discrete spectra surface-wave modes and the continuous spectra radiation and evanescent modes are discussed in this article. Equivalent transmission-line networks are introduced in the longitudinal direction so that multimode network theory can be used to simplify the analysis. Features such as symmetrical properties of the structure are also discussed. Based on the analysis, we investigate mode conversion and radiation characteristics and propose a mode converter whose converted power is over 90% for moderate values of the chirality parameter.* © *1997 John Wiley & Sons, Inc.* Microwave Opt Technol Lett 14: 280–284, 1997.

Key words: *chiral material; chirowaveguide; finite-element method; mode-matching method; discontinuity*

I. INTRODUCTION

During the past decade, attention has been focused on electromagnetic chirality [1, 2] and its potential applications to microwave and optical-wave guided structures. Although the characteristics of a uniform chirowaveguide have been extensively investigated [3–6], the analysis of discontinuities in open chirowaveguides becomes a significant tool in the design of versatile chirowaveguide circuits. Mariotte and Engheta analyzed the reflection and transmission of guided electromagnetic waves at an air-chiral interface and for a chiral slab in a parallel-plate waveguide and provided a means to measure the chirality admittance for a closed chirowaveguide [7]. Using a hybrid method, we consider here the open-waveguide case with discontinuities. For these open structures, the non-surface-wave modes comprise a continuous spectrum in addition to the surface-wave modes. In our analysis, we follow the customary procedure of discretizing the continuous spectrum [8] by placing perfectly conducting walls far above and below the planar chirowaveguide. This structure supports, in addition to the surface waves, an infinite number of higher non-surface-wave modes, some propagating and the remainder nonpropagating. The backward (or forward) radiation power of the open discontinuity structure can be obtained by the summation of the powers of the reflected (or transmitted) higher propagating non-surface-wave modes. We note that the presence of these bounding planes does not affect the essential physics of the propagation or scattering process.

In this Letter, the scattering characteristics of the discontinuities in open planar chirowaveguides are investigated by a method that combines the one-dimensional finite-element method for the eigenvalue problem in the transverse direction with a rigorous mode-matching procedure for the discontinuities in the longitudinal direction. Equivalent transmission lines are introduced in the longitudinal direction, so that multimode network theory can be used to facilitate the mode-matching analysis for complex structures. The symmetrical properties of the discontinuity structure both in the transverse direction and in the longitudinal direction are investigated so that the analysis can be simplified.

Numerical results of reflection, transmission, and radiation effects of double step discontinuities are investigated as an example of discontinuities in chirowaveguide. Here, we especially emphasize the coupling effect between the R_0 mode (corresponding to the TE_0 mode for nonchirowaveguides) and the L_0 mode (corresponding to the TM_0 mode for nonchirowaveguide).

II. THEORY

The double step discontinuity under consideration is shown in Figure 1. We first analyze the eigenvalue problem of each uniform waveguide and then use the mode-matching method

Publication P46. United States Patent No. 5,539,414, Folded Dipole Microstrip Antenna. July 23 1996. Inventor: K.M. Keen. Assignee: Inmarsat, London.

US005539414A

United States Patent [19]

Keen

[11] Patent Number: 5,539,414

[45] Date of Patent: Jul. 23, 1996

[54] **FOLDED DIPOLE MICROSTRIP ANTENNA**

[75] Inventor: **Keith M. Keen**, Billingshurst, England

[73] Assignee: **Inmarsat**, London, England

[21] Appl. No.: **116,243**

[22] Filed: **Sep. 2, 1993**

[51] **Int. Cl.**[6] **H01Q 1/38**; H01Q 9/26

[52] **U.S. Cl.** ..... **343/700 MS**; 343/702; 343/803

[58] **Field of Search** ..... 343/700 MS, 702, 343/725, 793, 794, 803; H01Q 1/38, 9/26, 9/28

[56] **References Cited**

U.S. PATENT DOCUMENTS

3,813,674	5/1974	Sidford	343/727
4,084,162	4/1978	Dubost et al.	343/700
4,426,649	1/1984	Dubost et al.	343/803
4,498,085	2/1985	Schwarzmann	343/803
4,817,196	3/1989	MacNak et al.	455/193
4,862,516	8/1989	MacNak et al.	455/193
4,873,527	10/1989	Tan	343/718
4,899,162	2/1990	Bayetto et al.	343/803
4,980,694	12/1990	Hines	343/702
4,992,799	2/1991	Garay	343/702
5,289,198	2/1994	Altshuler	343/802
5,410,749	4/1995	Siwiak et al.	455/280

FOREIGN PATENT DOCUMENTS

0331486	9/1989	European Pat. Off. .	
0531164	3/1993	European Pat. Off. .	
2621452	11/1976	Germany	343/803
85/02719	11/1984	WIPO .	

OTHER PUBLICATIONS

Robert E. Munson, "Conformal Microstrip Antennas," *Microwave Journal*, Mar. 1988, pp. 91–92, 94, 98, 100, 104, 106, 108–109.

G. Dubost et al., "Theory and Applications of Broadband Microstrip Antennas"; 6th European Microwave Conference; pp. 275–279 (Sep. 1976).

M. C. D. Maddocks; "Array Elements for a DBS Flat-Plate Antenna"; BBC Research Department Report; pp. 1–10; (Jul. 1988).

Primary Examiner—Donald T. Hajec
Assistant Examiner—Tan Ho
Attorney, Agent, or Firm—Banner & Allegretti

[57] **ABSTRACT**

A folded dipole microstrip antenna is disclosed herein. The microstrip antenna includes a dielectric substrate for defining a first mounting surface and a second mounting surface substantially parallel thereto. A folded dipole radiative element is mounted on the second mounting surface. The microstrip antenna further includes a microstrip feed line, mounted on the first surface, for exciting the radiative element in response to an excitation signal. In a preferred implementation of the microstrip antenna an excitation signal is applied to the microstrip feed line through a coaxial cable. In such a preferred implementation the folded dipole radiative element includes a continuous dipole arm arranged parallel to first and second dipole arm segments separated by an excitation gap. The feed element is mounted in alignment with the excitation gap and is electrically connected to the continuous dipole arm. The antenna may additionally include a ground plane reflector separated from the folded dipole radiative element by a dielectric spacer for projecting, in a predetermined direction, electromagnetic energy radiated by the folded dipole radiative element. The thickness of the dielectric spacer between the ground plane reflector and the folded dipole radiative element is selected such that the impedance presented by the antenna to the coaxial cable is approximately fifty ohms.

2 Claims, 5 Drawing Sheets

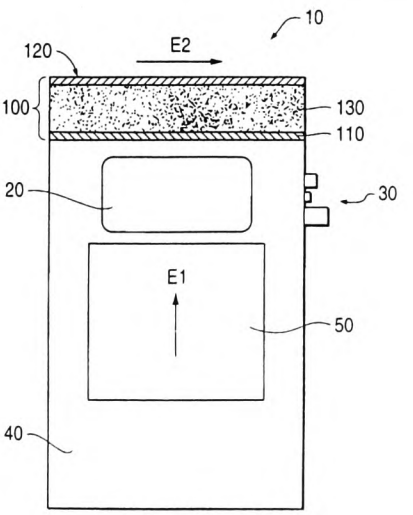

FIG. 1

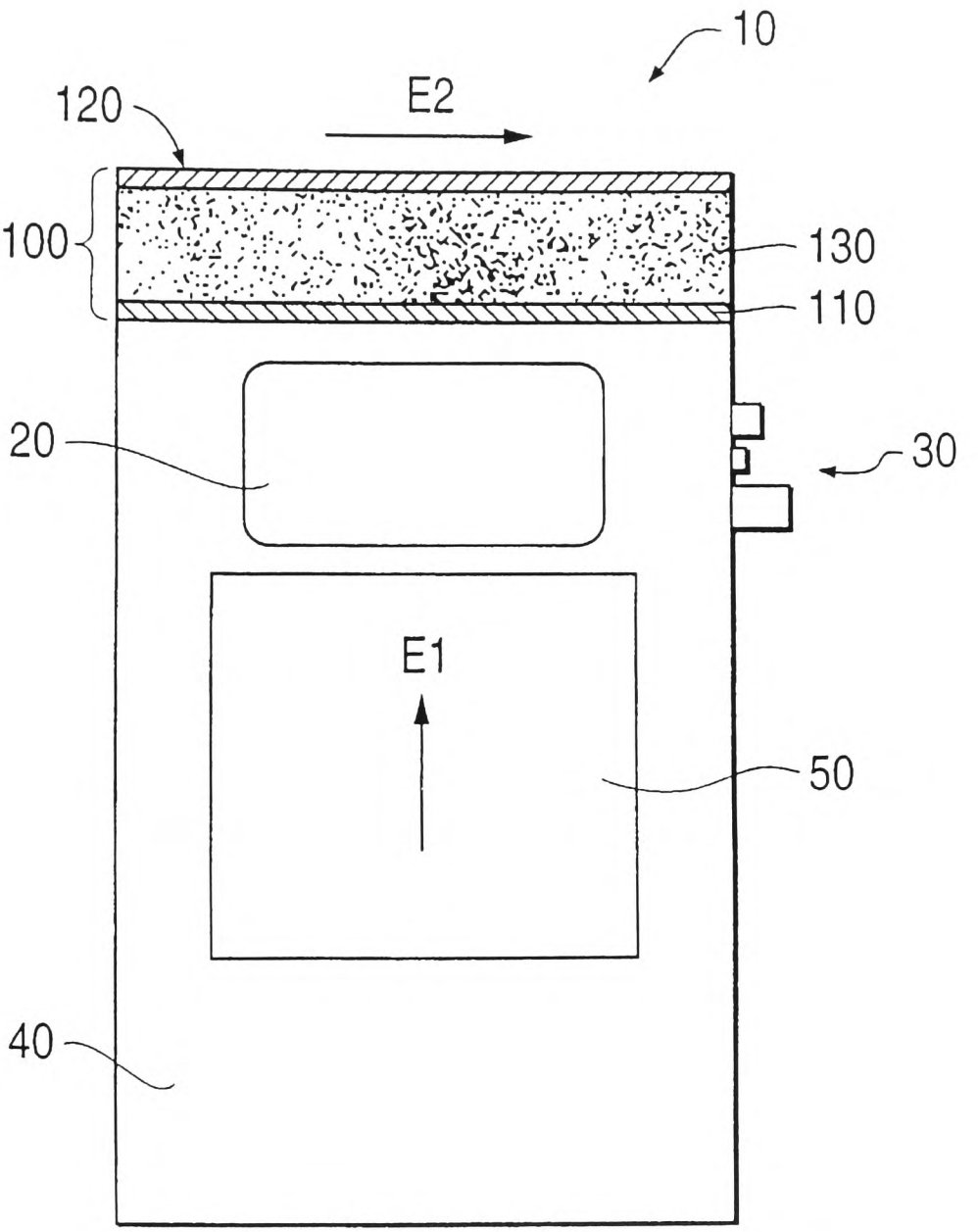

FIG. 2

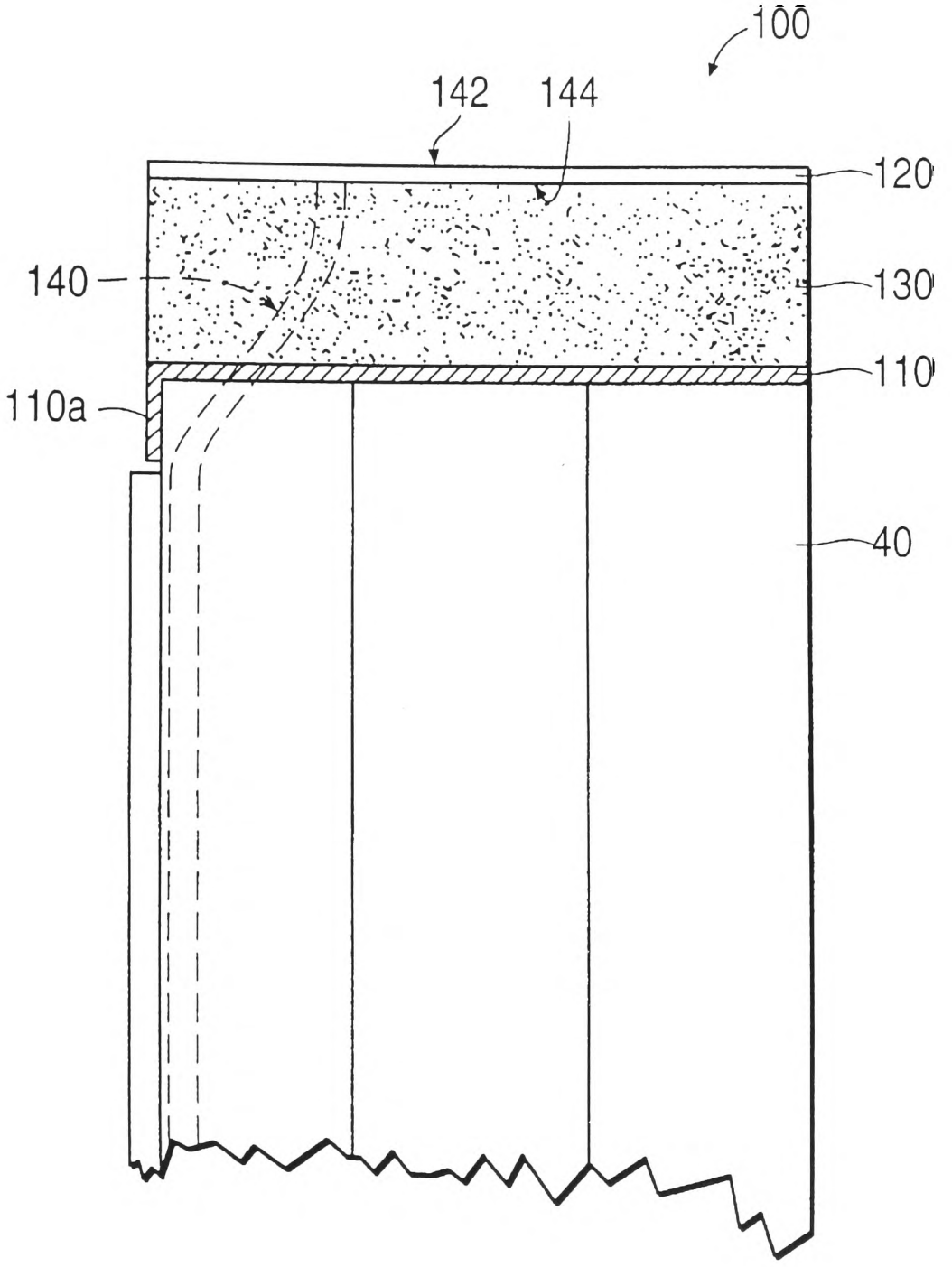

FIG. 3

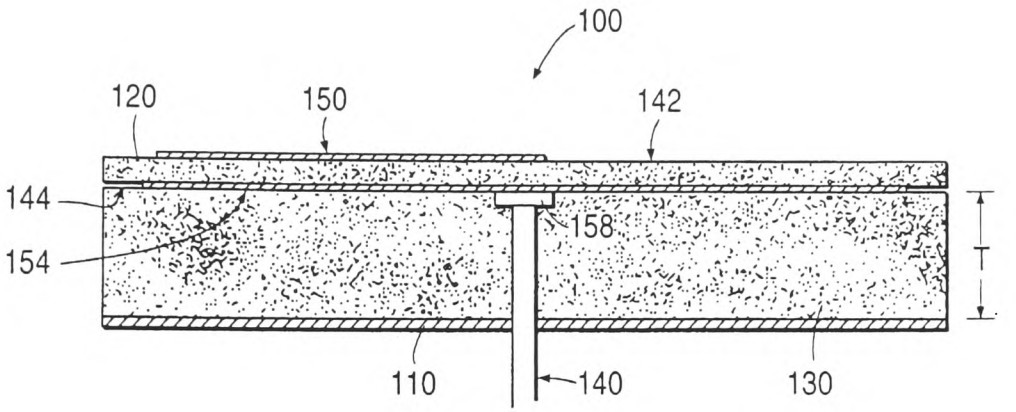
100
120
150
142
144
154
158
110
140
130

FIG. 4

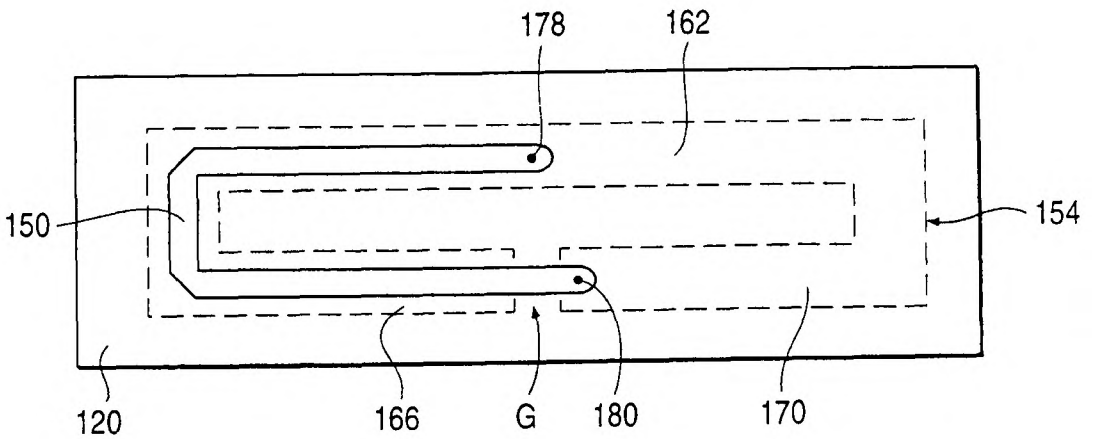
178
162
150
154
120
166
G
180
170

FIG. 5a

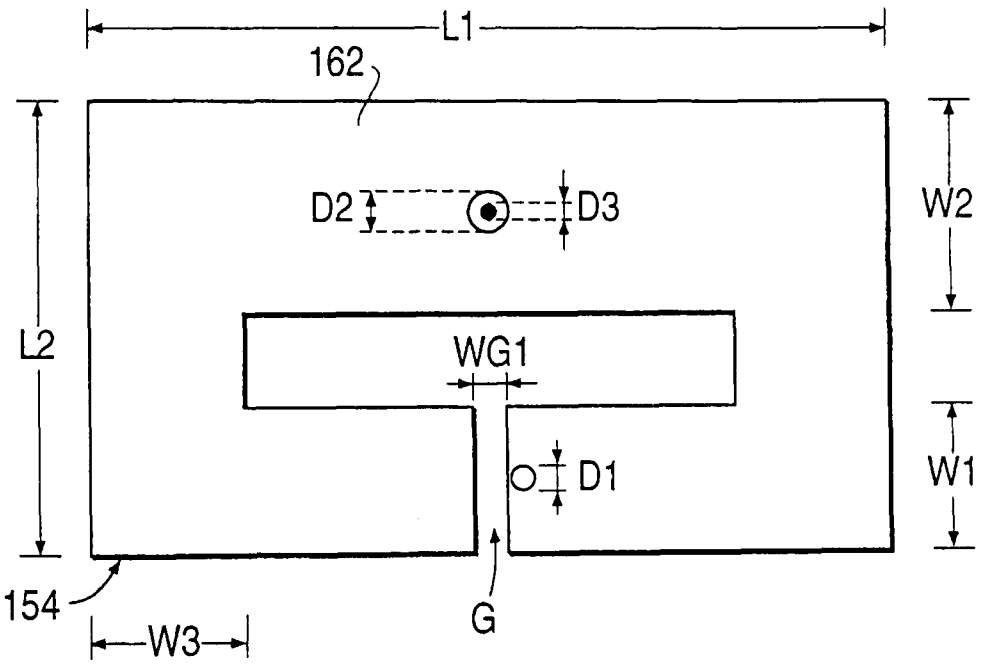

FIG. 5b

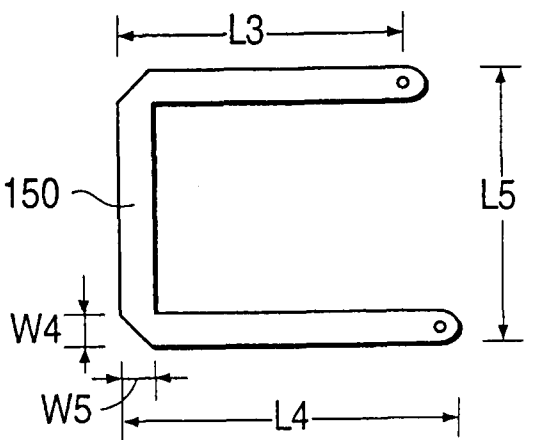

FIG. 6

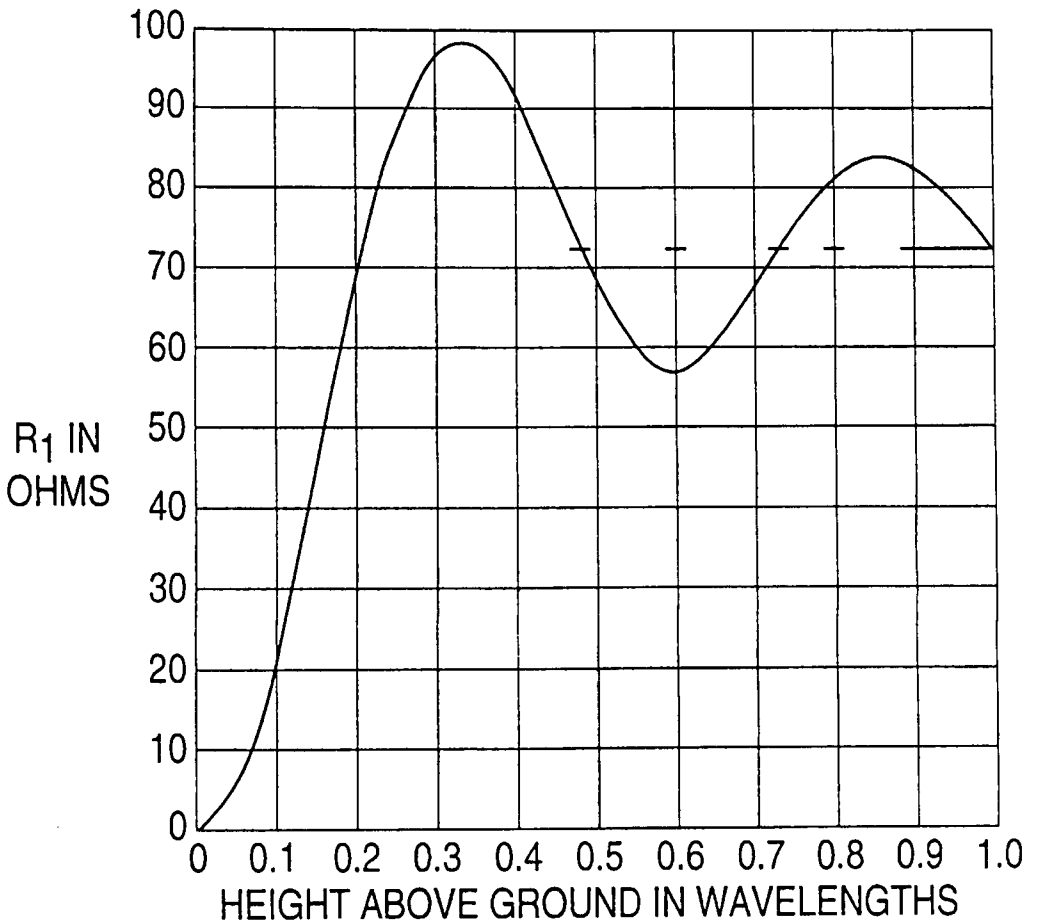
100
90
80
70
60
50
40
30
20
10
0
R_1 IN OHMS
0 0.1 0.2 0.3 0.4 0.5 0.6 0.7 0.8 0.9 1.0
HEIGHT ABOVE GROUND IN WAVELENGTHS

FOLDED DIPOLE MICROSTRIP ANTENNA

The present invention relates to the field of microstrip antennas, and particularity to microstrip antennas used in miniature portable communications devices.

BACKGROUND OF THE INVENTION

In the design of portable radio equipment, and in particular personal paging devices, size is an extremely important factor. Many previous paging devices employed relatively large receive antennas, thereby significantly increasing overall device dimensions. Antennas of this scale were generally required as a consequence of the use of relatively low RF paging frequencies, and also so as to ensure adequate reception of the paging signals. Specifically, high antenna gain is desirable, and under certain conditions may in fact be necessary to ensure achievement of full receiver range capability. However, size constraints preclude incorporation of conventional high gain antenna configurations into paging receivers designed to be relatively compact.

The large size of many conventional paging receivers has required that they be mounted on the side of the body, usually through attachment to the belt or through placement in a pocket. Recently, however, it has been desired to realize paging devices sufficiently compact to be, for example, worn on the wrist. One advantage offered by wrist-carried paging receivers is that they may be held in front of the face, thereby facilitating viewing or adjustment by the user.

Existing wrist-carried paging receivers often include simple loop type antennas responsive to the magnetic field component of the RF signal. In such antennas the loop element is generally disposed within the wrist band of the user. Although this type of antenna system has tended to provide only marginal performance, it enables the loop antenna to be concealed within the wrist band housing. However, this arrangement is of advantage only if it is desired that the attachment mechanism consist of a wrist band or other loop-type device. Accordingly, it would be desirable to provide an antenna system which is capable of being implemented within a paging receiver of compact dimension, and which does not presuppose a particular type of attachment mechanism.

As noted above, receive antennas incorporated within conventional terrestrial paging devices have tended to be somewhat large, partially as a consequence of the use of relatively low paging frequencies (e.g., <1 GHz). However, existing satellite communications systems operative at, for example, 1.5 or 2.5 GHz, afford the opportunity for paging receiver antennas of smaller scale. Antennas operative at these frequencies would need to have gains sufficiently low to project broad radiation patterns, thus enabling reception of paging signals from a broad range of angles. This is required since terrestrial deception of satellite signals is based not only upon line-of-sight transmissions, but also upon transmissions scattered and reflected by objects such as buildings, roads, and the like. Hence, it is an object of the present invention to provide a compact antenna capable of receiving paging signals from communication satellites.

SUMMARY OF THE INVENTION

In summary, the present invention comprises a folded dipole microstrip antenna. The microstrip antenna includes a dielectric substrate for defining a first mounting surface and a second mounting surface substantially parallel thereto. A folded dipole radiative element is mounted on the second mounting surface. The microstrip antenna further includes a microstrip feed line, mounted on the first surface, for exciting the radiative element in response to an excitation signal.

In a preferred embodiment of the microstrip antenna an excitation signal is applied to the microstrip feed line through a coaxial cable. In such a preferred embodiment the folded dipole radiative element includes a continuous dipole arm arranged parallel to first and second dipole arm segments separated by an excitation gap. The feed element is mounted in alignment with the excitation gap and is electrically connected to the continuous dipole arm. The antenna may additionally include a ground plane reflector for projecting, in a predetermined direction, electromagnetic energy radiated by the folded dipole radiative element, as well as for effecting an impedance match between the antenna and a 50 ohm transmission line system.

BRIEF DESCRIPTION OF THE DRAWINGS

Additional objects and features of the invention will be more readily apparent from the following detailed description and appended claims when taken in conjunction with the drawings, in which:

FIG. **1** shows a personal paging receiver in which is incorporated the folded dipole antenna system of the present invention.

FIG. **2** provides an illustration of the microstrip structure of the inventive folded dipole antenna.

FIG. **3** depicts a preferred implementation of the folded dipole antenna in greater detail, providing a cross-sectional view from which the housing has been omitted for clarity.

FIG. **4** shows a partially see-through top view of a preferred embodiment of the folded dipole antenna.

FIG. **5***a* provides a scaled representation of a folded dipole microstrip circuit element.

FIG. **5***b* provides a scaled representation of a feeder line microstrip circuit element.

FIG. **6** is a graph showing the driving point resistance at the center of a horizontal ½ wavelength antenna as a function of the height thereof above a ground plane.

DESCRIPTION OF THE PREFERRED EMBODIMENT

Referring to FIG. **1**, there is illustrated a personal paging receiver in which is incorporated the folded dipole antenna system of the present invention. The paging receiver designated generally as **10** includes a display **20** and input switches **30** for operating the paging receiver in a manner well known to those of ordinary skill in the art. The receiver **10** is disposed within a housing **40**, a lateral side of which provides a surface for mounting an auxiliary microstrip patch antenna **50**. In addition, the housing **40** defines a first end surface on which is mounted the folded dipole antenna **1 00** of the present invention. As is indicated by FIG. **1**, the auxiliary patch antenna **50** is designed to project a radiation pattern having an electric field orientation E1 transverse to the electric field orientation E2 of the inventive dipole antenna **100**. This combination of antennas facilitates improved reception of paging signals of diverse polarization and angle of incidence. In an exemplary implementation the folded dipole antenna **100** is designed to receive paging signals broadcast via satellite at a frequency of 1542 MHz.

As Shown in FIGS. **1** and **2**, the inventive folded dipole antenna **100** is implemented using a microstrip structure comprising an antenna ground plane **110**, a microstrip lami-

nate board **120**, and a foam spacer **130** interposed therebetween. The antenna **100** will generally be attached to the housing **40** by gluing the ground plane **110** thereto using, for example, a hot-melt plastic adhesive. The ground plane **110** may be fabricated from a metallic sheet having a thickness within the range of 0.5 to 2.0 mm, and includes an external segment **110***a* for connection to a lateral side of the housing **40**. The foam spacer **130** may be fabricated from, for example, polystyrene foam having a dielectric constant of approximately 1.2. The thickness of the foam spacer **130** is selected in accordance with the desired impedance, typically 50 ohms, to be presented by the antenna **100** to a coaxial cable **140** (FIG. **2**).

Referring to FIG. **2**, the cable **140** extends from receive electronics (not shown) into the foam spacer **130** through a slot defined by the ground plane **110**. As is described below, the inner and outer conductors of the coaxial cable **140** are connected, using a conventional coaxial-to-microstrip transition, to printed microstrip circuit elements disposed on the upper and lower surfaces **142** and **144**, respectively, of the laminate board **120**. In a preferred embodiment the microstrip laminate board comprises a Duroid sheet, typically of a thickness between 1 and 2 mm, produced by the Rogers Corporation of Chandler, Ariz. Microstrip substrates composed of other laminate materials, e.g., alumina, may be utilized within alternative embodiments of the folded dipole antenna.

FIG. **3** illustrates the folded dipole antenna **100** in greater detail, providing a cross-sectional view from which the housing **40** has been omitted for clarity. As shown in FIG. **3**, a feeder line **150** comprising microstrip circuit elements is printed on the upper surface **142** of the microstrip laminate board **120**. In addition, a folded microstrip dipole element **154** is printed on the lower surface **144** of the board **120**. In an exemplary embodiment the center conductor of the coaxial cable **140** extends through the laminate board **120** into electrical contact with the feeder line **150**. Similarly, the outer conductor of the coaxial cable **140** makes electrical contact with the folded dipole **154** through the outer collar of a coaxial-to-microstrip transition **158**.

Referring to FIG. **4**, there is shown a partially see-through top view of the folded dipole antenna **100**. As shown in FIG. **4**, the folded dipole microstrip, element generally indicated by the dashed outline **154** includes a continuous arm **162**, as well as first and second arm segments **166** and **170**. The first and second arm segments **166** and **170** define an excitation gap G which is spanned from above by the feeder line **150**. In the preferred embodiment the folded dipole **154** excites the feeder line **150** across the excitation gap G, which results in an excitation signal being provided to receive electronics (not shown) of the paging receiver via the inner conductor **178** of the coaxial cable **140**. In this regard the folded dipole **154** provides a ground plane for the feeder line **150**, and is in direct electrical contact therewith through a wire connection **180** extending through the microstrip board **120**.

The ground plane **110** (FIG. **3**) operates as an antenna reflector to project electromagnetic energy radiated by the folded dipole **154**. Specifically, ground plane **110** redirects such electromagnetic energy incident thereon in directions away from the receiver housing **40**. Although in the preferred embodiment of FIG. **1** it is desired to maximize the radiation directed away from the receiver housing **40**, in other applications it may be desired that the folded dipole antenna produce beam patterns in both vertical directions relative to the folded dipole **154**. Accordingly, it is expected that in such other applications that the dipole antenna would be implemented absent a ground plane element.

In an exemplary embodiment the folded dipole **154** and feeder line **150** microstrip circuit elements are realized using a laminate board having a pair of copper-plated surfaces. Each surface is etched in order to produce copper profiles corresponding to the folded dipole and feeder line elements. Alternatively, these elements could be realized by directly plating both sides of a laminate board with, for example, gold or copper, so as to form the appropriate microstrip circuit patterns.

FIGS. **5***a* and **5***b* provide scaled representations of the folded dipole **154** and feeder line **150** microstrip circuit elements, respectively. In the representation of FIGS. **5***a* and **5***b* the dimensions of the feeder line and dipole have been selected assuming an operational frequency of 1542 MHz and a laminate board dielectric constant of approximately 2.3. The dimensions corresponding to length (L), width (W), and diameter (D) parameters of the microstrip elements represented in FIG. **5** are set forth in the following table.

TABLE I

Parameter	Dimension (mm)
L1	60
L2	30
W1	10
W2	14
W3	10
D1	01
D2	04
D3	01
WG1	02
L3	25
L4	27.5
L5	18
W4	4.7
W5	4.7

It is noted that parameter D3 refers to the diameter of the circular aperture defined by the laminate board **20** through which extends the center conductor of coaxial cable **140**. Similarly, the parameter D2 corresponds to the diameter of a circular region of the continuous dipole arm **162** from which copper plating has been removed proximate the aperture specified by D3. This plating removal prevents an electrical short circuit from being developed between the center coaxial conductor and the folded dipole **154**. In the preferred implementation an end portion of the center coaxial conductor is soldered to the microstrip feeder line **150** after being threaded through the laminate board **120** and the dipole arm **162**.

One feature afforded by the present invention is that the overall size of the dipole antenna may be adjusted to conform to the dimensions of the paging receiver housing through appropriate dielectric material selection. For example, the microstrip circuit dimensions given in TABLE I assume an implementation using Duroid laminate board having a dielectric constant of approximately 2.3. A smaller folded dipole antenna could be realized by using a laminate board consisting of, for example, a thin alumina substrate.

Referring again to FIG. **3**, it is observed that the separation between the folded dipole **154** and the ground plane **110** is determined by the thickness T of the foam spacer **130**. The thickness T and dielectric constant of the foam spacer **130** are selected based on the desired impedance to be presented by the folded dipole antenna. For example, in the preferred embodiment it is desired that the impedance of the folded dipole antenna be matched to the 50 ohm impedance of the coaxial cable **140**. As is described below, one technique for determining the appropriate thickness T of the foam spacer

130 contemplates estimating the driving point impedance of the folded dipole antenna. Such an estimate may be made using, for example, a graphical representation of antenna impedance such as that depicted in FIG. 6.

In particular, FIG. 6 is a graph of the impedance of a conventional ½ wavelength dipole antenna situated horizontally above a reflecting plane, as a function of the free-space wavelength separation therebetween. As is indicated by FIG. 6, the impedance for large separation distances is approximately 73 ohms, and is less than 73 ohms if the dipole is situated close to (e.g., less than 0.2 wavelengths) and parallel with a reflecting plane. A folded ½ wavelength dipole exhibits an impedance approximately four times greater than the impedance of a conventional ½ wavelength dipole separated an identical distance from a reflecting plane. Accordingly, the separation required to achieve an impedance of 50 ohms using a folded dipole is equivalent to that necessary to attain an impedance of 12.5 ohms using a conventional ½ wavelength dipole. In order to use FIG. 6 in estimation of the impedance of a folded dipole separated from a reflecting plane by a dielectric spacer the free-space separation distance must be further reduced by the factor $1/\sqrt{\epsilon}$, where ϵ denotes the dielectric constant of the spacer.

Thus, in accordance with FIG. 6, the separation required to achieve an impedance of 50 ohms for a folded ½ wavelength dipole, using a dielectric space with a dielectric constant of approximately 1.2 would be approximately $(1/\sqrt{1.2})\times 0.075$ wavelengths, or approximately 0.07 wavelengths. Thus, the present invention allows the use of a relatively thin dielectric spacer.

While the present invention has been described with reference to a few specific embodiments, the description is illustrative of the invention and is not to be construed as limiting the invention. Various modifications may occur to those skilled in the art without departing from the true spirit and scope of the invention as defined by the appended claims.

What is claimed is:

1. An antenna for a paging receiver, said paging receiver being disposed within a housing, said antenna comprising:

a folded dipole microstrip antenna attached to a first external surface of said housing, said microstrip antenna including a dielectric substrate for defining a first mounting surface and a second mounting surface substantially parallel to said first mounting surface, a folded dipole element mounted on said second mounting surface, said folded dipole element including a continuous arm and first and second dipole arm segments arranged substantially parallel to said continuous arm, a microstrip feed line mounted on said first surface in alignment with an excitation gap defined by ends of said first and second folded dipole arm segments, a reflector for redirecting an electromagnetic energy pattern associated with said folded dipole microstrip antenna away from said housing, wherein said folded dipole element is positioned between said reflector and said microstrip feed line, and means for supplying a received signal from said microstrip feed line to said paging receiver; and

an auxiliary antenna mounted on a second external surface of said housing.

2. The antenna of claim 1, including a dielectric spacer interposed between said reflector and said folded dipole element, wherein thickness of said dielectric spacer is selected such that the impedance presented by said folded dipole microstrip antenna is approximately fifty ohms.

* * * * *